European Commission

EUROPEAN ATLAS OF NATURAL RADIATION

Joint Research Centre

European Commission

EUROPEAN ATLAS OF NATURAL RADIATION

Joint Research Centre

Preamble

Publication details

To refer to this 1st edition of the European Atlas of Natural Radiation please cite as follows:

Cinelli, G., De Cort, M. & Tollefsen, T. (Eds.), *European Atlas of Natural Radiation*, Publication Office of the European Union, Luxembourg, 2019.

The full version of this atlas will be available online at: https://remon.jrc.ec.europa.eu/About/Atlas-of-Natural-Radiation

This URL gives access to the index and leads to an interactive map interface where map layers compiled using the convergence of evidence concept can be interrogated.

Individual pages in this atlas contain QR codes which, when scanned, bring the reader to the exact online location to access the related page content.

Luxembourg: Publications Office of the European Union, 2019.

© European Union, 2019.

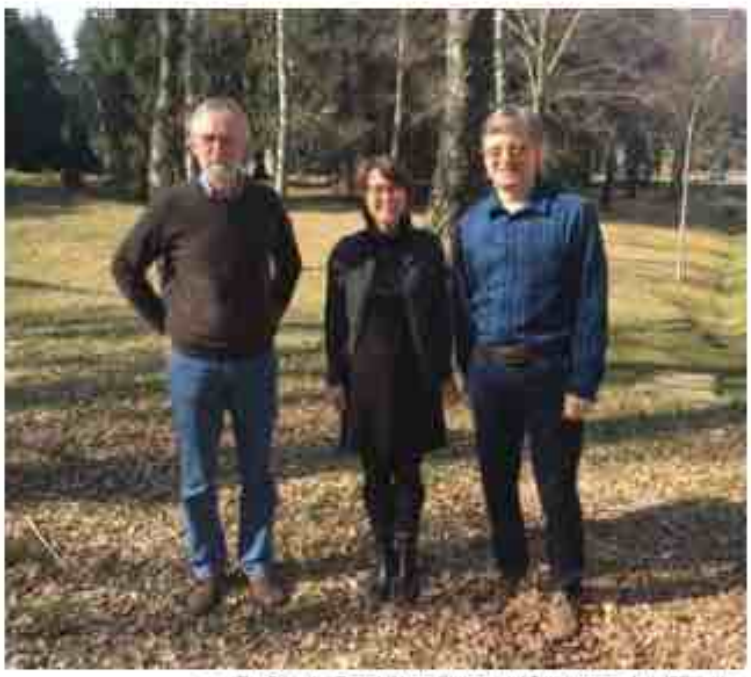

The Editorial Board (Marc, Georgia and Tore) pictured at JRC, Ispra.
Source: EANR, EC-JRC, 2019

Copyright notice and disclaimer

© European Union, 2019

The information and views set out in this book are those of the authors and do not necessarily reflect the official opinion of the European Union. Neither the European Union institutions and bodies nor any person acting on their behalf may be held responsible for the use which may be made of the information contained therein.

The reuse policy of the European Commission is implemented by Commission Decision 2011/833/EU of 12 December 2011 on the reuse of Commission documents (OJ L 330, 14.12.2011, p. 39).

Reuse is authorised, provided the source of the document is acknowledged and its original meaning or message is not distorted. The Commission is not liable for any consequence stemming from the reuse of this publication.

Reuse of photos/figures/diagrams/data with source: EANR, EC-JRC, 2019 is authorised.

For reuse of photos/figures/diagrams/data of a third-party source (i.e. any other than EANR, EC-JRC, 2019), permissions must be sought directly from the source.

Sources are indicated throughout the Atlas by: Source: [identification of the source].

Published by the Publications Office of the European Union, L-2995 Luxembourg, Luxembourg.

European Atlas of Natural Radiation

Printed version

ISBN 978-92-76-08259-0
doi:10.2760/520053
Catalogue number KJ-02-19-425-EN-C

Online version

ISBN 978-92-76-08258-3
doi:10.2760/46388
Catalogue number KJ-02-19-425-EN-N

2019 – 190 pp. – 30.1 × 42.4 cm

Cartographic Representations

Underlying cartographic features depicted on the maps in this atlas are derived from the Digital Chart of the World and Lovell Johns Cartographic Base. These data do not have any explicit legal status; hence, no legal aspects should be derived from the information depicted on any of the maps in this publication.

http://en.wikipedia.org/wiki/Digital_Chart_of_the_World

www.lovelljohns.com

Due to the resolution of the underlying data which is often still too large to represent small islands, the maps represented in this atlas might not or not always represent a number of small Pacific islands. These are included in the interactive online version when provided in the datasets.

All the maps are represented according to the Robinson projection.

Disclaimer of Liability

This is a publication of the Joint Research Centre (JRC), the European Commission's science and knowledge service. It aims to provide evidence-based scientific support to the European policymaking process. The scientific output expressed does not imply a policy position of the European Commission. Neither the European Commission nor any person acting on behalf of the Commission is responsible for the use that might be made of this publication. For information on the methodology and quality underlying the data used in this publication for which the source is neither Eurostat nor other Commission services, users should contact the referenced source. The designations employed and the presentation of material on the maps do not imply the expression of any opinion whatsoever on the part of the European Union concerning the legal status of any country, territory, city or area or of its authorities, or concerning the delimitation of its frontiers or boundaries.

Design and graphic support

Final design and graphic support by Lovell Johns Limited, 10 Hanborough Business Park, Long Hanborough, Witney, Oxfordshire, OX29 8RU, United Kingdom.

http://www.lovelljohns.com

Lovell Johns

GETTING IN TOUCH WITH EU

In person

All over the European Union there are hundreds of Europe Direct information centres. You can find the address of the centre nearest you at: https://europa.eu/european-union/contact_en

On the phone or by email

Europe Direct is a service that answers your questions about the European Union. You can contact this service

- by freephone: 00 800 6 7 8 9 10 11 (certain operators may charge for these calls),
- at the following standard number: +32 22999696, or
- by electronic mail via: https://europa.eu/european-union/contact_en

FINDING INFORMATION ABOUT THE EU

Online

Information about the European Union in all the official languages of the EU is available on the Europa website at: https://europa.eu/european-union/index_en

EU publications

You can download or order free and priced EU publications from EU Bookshop at: https://publications.europa.eu/en/publications. Multiple copies of free publications may be obtained by contacting Europe Direct or your local information centre (see https://europa.eu/european-union/contact_en).

Acknowledgements

The European Atlas of Natural Radiation (EANR) is the result of fruitful collaborations between more than 100 experts from national and international institutions, universities and research centres around Europe. We acknowledge all of the contributing Authors and Reviewers: without their contributions, support and encouragement this publication would not have been possible.

We would like to thank the Advisory Committee, Valeria Gruber and Peter Bossew, for having worked from the begin of the project with constant passion and dedication as well as Gregoire Dubois, who, as one of the founders of the Atlas project, did invaluable work to explore and develop the concept and establishing a European network of institutions and experts.

Two head of units, Franck Wastin and Willem Janssens are acknowledged for their managerial support to the project.

We also would like to express our great thanks to the JRC Radioactivity Environmental Monitoring group (JRC, Ispra), in particular Luca De Felice, Konstantins Bogučarskis, Stefano Vanzo, Pier Valerio Tognoli and Daniel Jianu for their constant assistance in technical issues and in developing the EANR website. Also, for providing support, we acknowledge Elena Moneta, Fanny May and Gabriele Tamborini.

Our special thanks go to Ian Dewsbery from Lovell Johns Ltd. (UK) for his professional guidance in graphic design and cartography, for keeping our scientific, sometimes over-enthusiastic, ideas within publication limits and for turning these into an attractive and modern-looking atlas. William Adnams gave his expertise in GIS/cartographic matters, Clare Varney provided graphical assistance and Symon Porteous for smoothing out the contractual details.

The EU Publications Office and the JRC Central IP Service are acknowledged for their assistance and guidance.

The topic of natural radiation is of great significance to the scientific community, population and national authorities; the latter are thanked for their support and for their agreement on the final version of the maps. We apologise for any unintentional omissions, it is impossible to credit all people who give their direct or indirect contribution.

This QR code points to the full online version of the Atlas, where the most updated content may be freely accessed :

Contributors

Editorial Board

Cinelli, Giorgia	European Commission, Joint Research Centre, Ispra, Italy
De Cort, Marc	European Commission, Joint Research Centre, Ispra, Italy
Tollefsen, Tore	European Commission, Joint Research Centre, Ispra, Italy

Advisory Committee

Bossew, Peter	German Federal Office for Radiation Protection, Berlin, Germany
Gruber, Valeria	Austrian Agency for Health and Food Safety, Department for Radon and Radioecology, Linz, Austria

Contributing Authors

Achatz, Michaela	German Federal Office for Radiation Protection, Berlin, Germany
Ajtić, Jelena	Faculty of Veterinary Medicine, University of Belgrade, Belgrade, Serbia
Ballabio, Cristiano	European Commission, Joint Research Centre, Ispra, Italy
Barnet, Ivan	Czech Geological Survey, Prague, Czech Republic
Borelli, Pasquale	Environmental Geosciences, University of Basel, Basel, Switzerland
Bossew, Peter	German Federal Office for Radiation Protection, Berlin, Germany
Brattich, Erika	Department of Physics and Astronomy, Alma Mater Studiorum University of Bologna, Bologna, Italy
Briganti, Alessandra	Department of Science, Roma Tre University, Rome, Italy
Castelluccio, Mauro	Department of Science, Roma Tre University, Rome, Italy
Chiabetto, Enrico	Regional Agency for the Protection of the Environment, Piemonte, Italy
Cinelli, Giorgia	European Commission, Joint Research Centre, Ispra, Italy
Ciotoli, Giancarlo	National Research Council, Rome, Italy
Coletti, Chiara	Department of Geosciences, University of Padova, Padova, Italy
Cucchi, Anselmo	Regional Agency for the Protection of the Environment, Piemonte, , Italy
Daraktchieva, Zornitza	Centre for Radiation, Chemical and Environmental Hazards, Public Health England, Chilton, UK
De Cort, Marc	European Commission, Joint Research Centre, Ispra, Italy
Domingos, Filipa	Department of Earth Sciences, University of Coimbra, Coimbra, Portugal
Dudar, Tamara	Department of Environmental Studies, National Aviation University, Kiev, Ukraine
Elío, Javier	Trinity College Dublin, Dublin, Ireland
Falletti, Paolo	Regional Agency for the Protection of the Environment, Piemonte, Italy
Ferreira, Antonio	British Geological Survey, Keyworth, UK
Finne, Ingvild Engen	Norwegian Radiation and Nuclear Safety Authority, Østerås, Norway
Fuente Merino, Ismael	University of Cantabria, Santander, Spain
Galli, Gianfranco	Istituto Nazionale di Geofisica e Vulcanologia, Rome, Italy
García-Talavera, Marta	Consejo de Seguridad Nuclear, Madrid, Spain
Gruber, Valeria	Department for Radon and Radioecology, Austrian Agency for Health and Food Safety, Linz, Austria
Gutiérrez Villanueva, José-Luis	Radonova Laboratories, Uppsala, Sweden
Hernandez Ceballos, Miguel Angel	European Commission, Joint Research Centre, Ispra, Italy
Hoffmann, Marcus	Radon Competence Centre, University of Applied Sciences and Arts of Southern Switzerland, Canobbio, Switzerland
Iurlaro, Giorgia	Italian National Agency for New Technologies, Energy and Sustainable Economic Development, Ispra, Italy
Ivanova, Kremena	National Centre of Radiobiology and Radiation Protection, Sofia, Bulgaria
Jones, Arwyn	European Commission, Joint Research Centre, Ispra, Italy
Kovalenko, Grygoriy	Ukrainian Scientific Research Institute of Ecological Problems, Kharkiv, Ukraine
Kozak, Krzysztof	Institute of Nuclear Physics IFJ-PAN, Krakow, Poland
Lawley, Russell	British Geological Survey, Keyworth, UK
Lehné, Rouwen	Hessian Agency for Nature Conservation, Environment and Geology, Darmstadt, Germany
Lister, Bob	British Geological Survey, Keyworth, UK
Long, Stephanie	Environmental Protection Agency, Dublin, Ireland
Lucchetti, Carlo	Department of Science, Roma Tre University, Rome, Italy
Magnoni, Mauro	Regional Agency for the Protection of the Environment, Piemonte, Italy
Matolin, Milan	Faculty of Science, Charles University, Prague, Czech Republic
Mazur, Jadwiga	Institute of Nuclear Physics IFJ-PAN, Krakow, Poland
Mazzoli, Claudio	Department of Geosciences, University of Padova, Padova, Italy
Mollo, Mara	Mara Mollo Total Consulting, Vercelli, Italy
Mostacci, Domiziano	Department of Industrial Engineering, Alma Mater Studiorum University of Bologna, Bologna, Italy
Mundigl, Stefan	Radiation Protection and Nuclear Safety Unit, European Commission, Directorate-General Energy, Luxembourg, Luxembourg
Nesboi, Dieter	Hessian Agency for Nature Conservation, Environment and Geology, Darmstadt, Germany
Neves, Luis	Department of Earth Sciences, University of Coimbra, Coimbra, Portugal
Nikolov, Jovana	Faculty of Sciences, Department of Physics, University of Novi Sad, Novi Sad, Serbia
Nogarotto, Alessio	University of Bologna, Bologna, Italy
Onischenko, Aleksandra	Institute of Industrial Ecology, Russian Academy of Sciences, Ekaterinburg, Russia
Orgiazzi, Alberto	European Commission, Joint Research Centre, Ispra, Italy
Pacherova, Petra	Czech Geological Survey, Prague, Czech Republic
Panagos, Panos	European Commission, Joint Research Centre, Ispra, Italy
Pereira, Alcides	Department of Earth Sciences, University of Coimbra, Coimbra, Portugal
Pokalyuk, Vladimir	Institute of Environmental Geochemistry, National Academy of Sciences of Ukraine, Kiev, Ukraine
Quindós Poncela, Luis Santiago	University of Cantabria, Santander, Spain
Sassi, Raffaele	Department of Geosciences, University of Padova, Padova, Italy
Smedley, Pauline	British Geological Survey, Keyworth, UK
Soligo, Michele	Department of Sciences, Roma Tre University, Rome, Italy
Stoulos, Stylianos	Nuclear Physics Laboratory, Aristotle University Thessaloniki, Thessaloniki, Greece
Szabó, Katalin	Nuclear Security Department, Hungarian Academy of Sciences, Centre for Energy Research, Budapest, Hungary
Taht-Kok, Krista	Geological Survey of Estonia, Tallinn, Estonia
Todorović, Nataša	Faculty of Sciences, Department of Physics, University of Novi Sad, Novi Sad, Serbia
Tollefsen, Tore	European Commission, Joint Research Centre, Ispra, Italy
Tuccimei, Paola	Department of Sciences, Roma Tre University, Rome, Italy
Turtiainen, Tuukka	Radiation and Nuclear Safety Authority, Helsinki, Finland
Tye, Andrew	British Geological Survey, Keyworth, UK
Udovičić, Vladimir	Institute of Physics, Belgrade, Serbia
Vasilyev, Aleksey	Institute of Industrial Ecology, Russian Academy of Sciences, Ekaterinburg, Russia
Verdelocco, Stefania	Conseil et Etude en Radioprotection, Ispra, Italy
Vekhovtsev, Valentyn	Institute of Environmental Geochemistry, National Academy of Sciences of Ukraine, Kiev, Ukraine
Voltaggio, Mario	Istituto di Geologia Ambientale e Geoingegneria, National Research Council, Rome, Italy
Zhukova, Olga	Republican Centre for Hydrometeorology, Control of Radioactive Contamination, and Environmental Monitoring, Minsk, Belarus
Zhukovsky, Michael	Institute of Industrial Ecology, Russian Academy of Sciences, Ekaterinburg, Russia

Reviewers

Bochicchio, Francesco	National Center for Radiation Protection and Computational Physics – Italian National Institute of Health, Rome, Italy
Braga, Roberto	Universita' of Bologna, Dipartimento di Scienze Biologiche, Geologiche e Ambientali, Bologna, Italy
Carpentieri, Carmela	National Center for Radiation Protection and Computational Physics – Italian National Institute of Health, Rome, Italy
Castellani, Carlo Maria	Italian National Agency for New Technologies, Energy and Sustainable Economic Development, Bologna, Italy
Christian, Di Carlo	National Center for Radiation Protection and Computational Physics – Italian National Institute of Health, Rome, Italy
De France, Jennifer	World Health Organization, Department of Public Health, Environmental and Social Determinants of Health, Geneva,Switzerland
Dehandschutter, Boris	Federal Agency for Nuclear Control, Bruxelles, Belgium
Elío, Javier	Geology, School of Natural Sciences, Trinity College, Dublin, Ireland
Fontana, Claudia	Centro di ricerca Agricoltura e Ambiente, Rome, Italy
German, Olga	International Atomic Energy Agency, Radiation Safety and Monitoring Section, Vienna, Austria
Grossi, Claudia	Universitat Politècnica de Catalunya, Barcelona, Spain
Gruber, Valeria	Austrian Agency for Health and Food SafetyDepartment for Radon and Radioecology, Linz, Austria
Hernandez-Ceballos, Miguel Angel	European Commission, Joint Research Centre, Ispra, Italy
Iurlaro, Giorgia	Italian National Agency for New Technologies, Energy and Sustainable Economic Development, Ispra, Italy
Jobbagy, Viktor	European Commission, Joint Research Centre, Geel, Belgium
Matolin, Milan	Charles University, Faculty of Science, Institute of Hydrogeology, Engineering Geology and Applied Geophysics , Prague, Czech Republic
McLaughlin, James	School of Physics, University College Dublin, Dublin, Ireland
Mundigl, Stefan	European Commission, Directorate-General Energy, Radiation Protection and Nuclear Safety Unit, Luxembourg, Luxembourg
Neznal, Matej	RADON v.o.s., Prague, Czech Republic
Perez, Maria Del Rosario	World Health Organization, Department of Public Health, Environmental and Social Determinants of Health, Geneva, Switzerland
Rossi, Francois	European Commission, Joint Research Centre, Petten, Netherlands
Sangorgi, Marco	European Commission, Joint Research Centre, Ispra, Italy
Simic, Zderko	European Commission, Joint Research Centre, Petten, Netherlands
Socciarelli, Silvia	Centro di ricerca Agricoltura e Ambiente, Rome, Italy
Tolton, Richelle	International Atomic Energy Agency, Radiation Safety and Monitoring Section, Vienna, Austria
Venoso, Gennaro	National Center for Radiation Protection and Computational Physics – Italian National Institute of Health, Rome, Italy

The European Radon Association (ERA) (http://radoneurope.org/) contributed by writing the summary for each chapter. The following ERA-members are acknowledged:

Dehandschutter, Boris	Federal Agency for Nuclear Control, Bruxelles, Belgium
Gutierrez, Villanueva Jose Luis	Radonova Laboratories, Uppsala, Sweden
Hansen, Maria	GM Scientific, Bristol, UK
Hurst, Stephanie	Saxon state ministry of the environment and agriculture Radiation Protection, Genetic Engineering, Chemicals, Dresden Germany
Kozak, Krzysztof	Institute of Nuclear Physics IFJ-PAN, Krakow, Poland
Mazur, Jadwiga	Institute of Nuclear Physics IFJ-PAN, Krakow, Poland
McLaughlin, James	University College Dublin School of Physics Dublin, Dublin, Ireland
Nilsson, Per	Driftwood consulting, Visby, Sweden
Pressyanov, Dobromir	University of Sofia, Sofia, Bulgaria
Ringer, Wolfang	Austrian Agency for Health and Food Safety Department for Radon and Radioecology, Linz, Austria
Udovicic, Vladimir	Institute of Physics, Belgrade, Serbia

Contents

Preamble 2

Publication details 2

Contributors 3

Foreword 9

Chapter I – Rationale 10

1.1 Introduction 12

1.2 Legal basis and requirements on protection from exposure to natural radiation sources 14

Chapter 2 – General background information 16

2.1 Radiation physics 18

2.1.1 Different kinds of radiation 18

2.1.2 Biological effects of ionising radiation 20

2.2 Sources of radiation 21

2.2.1 Natural sources of radiation 21

2.2.2 Radon 26

2.2.3 Environmental and exposure pathways 31

2.2.4 Radiation dosage chart 32

2.2.5 Case study: Ukraine 34

2.3 Geology 35

2.3.1 Geological influence on radiation 35

2.3.2 Simplified description of European geology 37

Case study: Simplified description of the Ukrainian geology 40

2.3.3 Simplified description of European soil 41

2.4 Statistics, measurement, mapping 44

2.4.0 From sampling to mapping 44

2.4.1 Observed and observation process 44

2.4.2 Accuracy, precision and representativeness 44

2.4.3 Scale, coverage, resolution and precision 45

2.4.4 Geometry of point samples 47

2.4.5 Network and survey design 49

2.4.6 Mapping 50

2.4.7 Interpretation, documentation, quality assurance 51

Case study: Soil-gas survey design 52

2.5 Measurements methods 54

2.5.1 Introduction 54

2.5.2 Gamma, alpha and beta particles detection 54

2.5.3 Spectrometric analysis 55

2.5.4 Radon measurements 57

Chapter 3 – Terrestrial radionuclides 58

3.1 Uranium 60

3.1.1 Uranium in rock-forming minerals 60

3.1.2 Uranium in the soil – plant system 61

3.1.3 Natural exposure to uranium by biota 61

3.1.4 European map of uranium concentration in topsoil 62

Plate 1: Map of estimated total concentration of uranium in topsoil over Europe 66

3.2 Thorium 69
3.2.1 Thorium in rock minerals 69
3.2.2 Thorium in the soil – plant system 69
3.2.3 Natural exposure to thorium by biota 69
3.2.4 European map of thorium concentration in topsoil 69
Plate 2: Map of estimated total concentration of thorium in topsoil over Europe 74
3.3 Potassium 77
3.3.1 Potassium in rock minerals 77
3.3.2 Potassium in the soil – plant system 77
3.3.3 Natural exposure to potassium by biota 77
3.3.4 European map of potassium concentration in topsoil 78
Plate 3: Map of estimated total concentration of K_2O in topsoil over Europe 80
3.4 European maps of uranium, thorium and potassium concentration in bedrock 84
3.4.1 Discussion and conclusions 86

Chapter 4 – Terrestrial radiation 88
4.1 Source of terrestrial natural radiation 90
4.1.1 Radioactivity properties of K, Th and U 90
4.1.2 Radioactivity as a function of rock type 90
4.1.3 Terrestrial gamma rays in the environment 91
4.2 Dose rate 91
4.2.1 Ambient dose rate 91
4.2.2 Components of the ambient dose rate signal and its decomposition 92
4.2.3 Variability of natural terrestrial dose rate 92
4.2.4 Variability of dose rate from nuclear fallout 93
4.3 Materials and methods 94
4.3.1 Dose rate in geophysical research 94
4.3.2 Dose rate calculation from geochemical data 95
4.3.3 Dose rate in the EURDEP system 95
4.3.4 New technical developments 98
4.4 Terrestrial dose rate mapping 99
4.4.1 General overview 99
4.4.2 European Terrestrial Gamma Dose Rate Map 100
4.4.3 Work in progress: Using EURDEP data to map terrestrial gamma dose rate 101
Plate 4: European Terrestrial Gamma Dose Rate Map 102
Plate 5: European Annual Terrestrial Gamma Dose Map 104
Case study: Piedmont (Italy), soil and rock samples 106

Chapter 5 – Radon 108
Radon, 'From Rock to Risk' – The geogenic compartment 110
5.1 Radon in soil gas 112
5.1.1 Introduction 112
5.1.2 Measurement methods 113
5.1.3 Applications 115
5.1.4 Challenges to developing a European map 118
5.2 Radon exhalation rate 118
5.2.1 Introduction 118

5.2.2 Measurement methods 118
5.2.3 Application: Proposal for a classification scheme for building materials based on radon and thoron exhalation rates 120
5.3.4 Challenges to developing a European map 120
Case study: Radon exhalation measurements in the laboratory 121
5.3 Outdoor radon 122
5.3.1 Introduction 122
5.3.2 Measurement methods 122
5.3.3 Applications 123
5.3.4 Challenges to developing a European map 124
Case study: Continuous monitoring of outdoor radon 125
5.4 Indoor radon 126
5.4.1 Introduction 126
5.4.2 Materials and methods for indoor radon measurements 126
5.4.3 The European Indoor Radon Map 129
Plate 6: European Indoor Radon Map: Number of measurements per grid cell 130
Plate 7: European Indoor Radon Map: Indoor radon concentration. Arithmetic means per grid cell 132
5.4.4 How can the dose due to radon be estimated? 135
Case study: Radon measurements in large buildings 137

Chapter 6 – Radionuclides in water and river sediments 138
6.1 Introduction 140
6.2 Natural radionuclides in ground and surface water 140
6.2.1 Radon 140
6.2.2 Radium 141
6.2.3 Uranium 141
6.2.4 Thorium 142
6.2.5 Lead and polonium 142
6.2.6 Tritium 142
6.3 Measurement methods 142
6.3.1 Introduction 142
6.3.2 Sampling of water and sample pre-treatment 142
6.3.3 Determination of gross alpha/beta activities 143
6.3.4 Measurement methods for uranium and its daughter radioisotopes 144
6.3.5 Radon 144
6.3.6 Measurement methods for tritium 145
6.3.7 Radionuclides in river sediments 145
6.4 Activity concentration of natural radionuclides in water 145
6.5 Applications 147
6.5.1 Introduction 147
6.5.2 Ground water dating 147
6.5.3 Ground water flux 147
6.5.4 Ground water provenance and processes 147
6.5.5 Sedimentation rates 147
6.6 Challenges to improving radioactivity measurements in water and developing a European map 147

Chapter 7 - Radionuclides in food 148
7.1 Materials and methods 150
7.1.1 Natural radiocativity in food 150
7.1.2 Measurement of natural radionuclides in food 151
7.1.3 Activity concentration of natural radionuclides in food 152
7.2 Applications 154
7.2.1 Dose calculation 154
7.2.2. Example of dose assessment of public exposure for food ingestion 156
7.3 Discussion and conclusions 156

Chapter 8 – Cosmic radiation and cosmogenic radionuclides 158
8.1 Cosmic-ray dose map 161
8.1.1. Introduction 161
8.1.2. Materials and methods 161
Plate 8: The European Annual Cosmic-Ray Dose Map 162
8.1.3. Discussion and conclusions 164
8.2 Cosmogenic radionuclides 165
8.2.1. Introduction 165
8.2.2. Environmental applications 165
8.2.3. Databases 166
8.2.4. An overview of research activities on beryllium-7 166
8.2.5. Conclusions 168
Case study: An overview of beryllium-7 concentrations in Europe in 2006 169

Chapter 9 – Annual effective dose from natural environmental radiation 170
9.1 Introduction 172
9.2 Materials and methods 172
9.2.1 Dose calculation 172
9.2.2 Input data 172
9.3 Results 173

Chapter 10 – References and Appendices 176
References 176
Appendix 1 - The International System of Units (SI) 186
Appendix 2 - Country ISO codes 187
Appendix 3 - List of national competent authorities 188
Appendix 4 - Periodic Table of the Elements 189

Gríðafellsfoss, Iceland, lit by the aurora borealis
Source: alexander mila on Unsplash

Foreword

Under the Euratom Treaty, the European Commission (EC) is mandated to collect, verify and report information on radioactivity levels in the environment (European Union, 2016). In this context the Joint Research Centre (JRC) of the European Commission, as a part of its institutional support programme to DG Energy, operates and maintains the Radioactivity Environmental Monitoring database (REMdb), which contains the environmental radioactivity monitoring data provided by the European Union Member States on an annual basis. The REM database also serves as a historical data pool of radioactivity information related to the Chernobyl accident (26 April 1986). In 1998, the JRC published the Atlas on Caesium-137 Deposition on Europe after the Chernobyl Accident (European Union, 1998), which is still available on-line.

All this information aims at monitoring artificial radioactivity, i.e. radioactivity introduced by man into the environment. However, natural ionising radiation is an important contributor to the exposure of members of the public. The human population is continuously exposed to ionising radiation from several natural sources that can be classified into two broad categories: high-energy cosmic rays incident on the Earth's atmosphere and releasing secondary radiation (cosmic contribution); and radioactive nuclides generated during the formation of the Earth and still present in the Earth's crust (terrestrial contribution). The terrestrial contribution is mainly composed of the radionuclides of the uranium and thorium decay chains together with radioactive potassium. In most circumstances, radon, a noble gas produced in the radioactive decay of uranium, is the most important contributor to radiation exposure. To gain a clearer overview of the radioactive nature of the environment, the JRC embarked on the European Atlas of Natural Radiation. This Atlas aims to provide reference values and generate harmonised data for the scientific community and national competent authorities. At the same time, it should help the public to become familiar with the naturally radioactive environment.

In this Atlas, the editors aim to present the current state of knowledge of natural radioactivity, by giving general background information, and describing its various sources. It is a compilation of contributions and reviews received from more than 100 experts in their field: they come from universities, research centres, national and European authorities, and international organisations.

The Atlas also contains a chapter on the legal basis and requirements on protection from exposure to natural radiation sources. It presents the latest Basic Safety Standards Directive (European Union, 2013), which, for the first time, introduces legally binding requirements on the protection from exposure to natural radiation sources and, more specifically, to radon. It stipulates, *inter alia*, that all EU Member States must establish national radon action plans, define reference levels for indoor radon concentrations in dwellings and in workplaces, and identify and delineate radon-priority areas.

The Atlas is complemented by a collection of European maps displaying the levels of natural radioactivity caused by different sources. As a first step, the JRC started to prepare a European map of indoor radon: it shows 'means over 10 km × 10 km grid cells of long-term indoor radon concentration in ground-floor rooms of dwellings.' At present (December 2019), 35 European countries participate to this map.

Maps of uranium, thorium and potassium concentration in soil, covering most European countries, have been created, while maps of uranium, thorium and potassium concentration in bedrock are available for some countries. A methodology has been developed (based on ambient dose equivalent rate measurements), while European maps have been created using uranium, thorium and potassium concentration in soil. Moreover, a European annual cosmic-ray dose map has been completed.

This publication is the result of collaboration between scientists and policy-makers in EU Member States and beyond. To this end, the JRC has organised and hosted several international workshops and meetings to promote and disseminate the results of this Atlas, as well as to discuss topics linked to natural radioactivity.

This Atlas provides reference values and makes harmonised datasets available to the scientific community and national competent authorities.

In parallel, it may serve as a guide to the public:

- to familiarise itself with natural radioactivity; and
- to be informed about levels of natural radioactivity caused by different sources.

The publication of this work would not have been possible without the invaluable help and support of all European authorities who provided us with the most current data and information, as well as the national and international experts and scientists who assisted in writing the text parts, and colleagues who provided graphic and photographic material.

This Atlas is addressed to all who are concerned with radioactivity in the European environment.

M. Betti
Director
Nuclear Safety and Security
Directorate-General Joint Research Centre

M. Garribba
Director
Nuclear Energy, Safety and ITER
Directorate-General Energy

Official Journal
of the European Union
Legislation

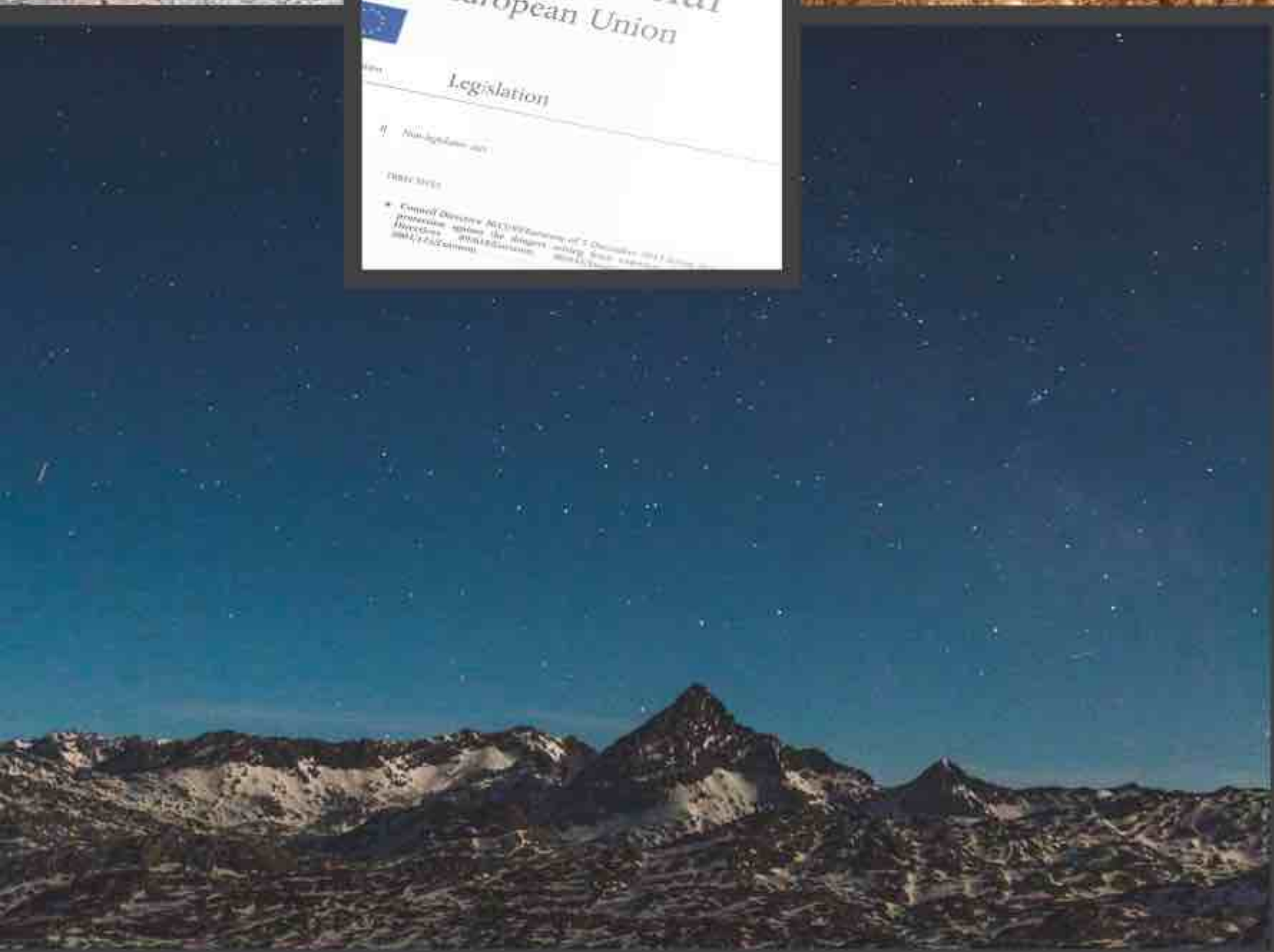

EUROPEAN UNION

THE EURATOM TREATY
CONSOLIDATED VERSION

2016

Chapter 1
Rationale

Natural ionising radiation is considered the largest contributor to the collective effective dose received by the world's population. Man is continuously exposed to ionising radiation from several sources that can be grouped into two categories: first, high-energy cosmic rays incident on the Earth's atmosphere and releasing secondary radiation (cosmic contribution); and, second, radioactive nuclides generated when the Earth was formed and still present in its crust (terrestrial contribution). Terrestrial radioactivity is mostly produced by the uranium (U) and thorium (Th) radioactive families together with potassium (^{40}K), a long-lived radioactive isotope of the elemental potassium. In most cases, radon (^{222}Rn), a noble gas produced by radioactive decay of the ^{238}U progeny, is the major contributor to the total dose.

This European Atlas of Natural Radiation has been conceived and developed as a tool for the public to become familiar with natural radioactivity; be informed about the levels of such radioactivity caused by different sources; and have a more balanced view of the annual dose received by the world's population, to which natural radioactivity is the largest contributor. At the same time, it provides reference material and generates harmonised data, both for the scientific community and national competent authorities.

Intended as an encyclopaedia of natural radioactivity, the Atlas describes the different sources of such radioactivity, cosmic and terrestrial, and represents the state-of-the art of this topic. In parallel, it contains a collection of maps of Europe showing the levels of natural sources of radiation.

This work unfolds as a sequence of chapters: the rationale behind; some necessary background information; terrestrial radionuclides; radon; radionuclides in water and river sediments; radionuclides in food; cosmic radiation and cosmogenic radionuclides. The final chapter delivers the overall goal of the Atlas: a population-weighted average of the annual effective dose due to natural sources of radon, estimated for each European country as well as for all of them together, giving, therefore, an overall European estimate.

As a complement, this introductory chapter offers an overview of the legal basis and requirements on protecting the public from exposure to natural radiation sources. In Europe, radiation has a long tradition. Based on the Euratom Treaty, the European Atomic Energy Community early established a set of legislation for protecting the public against dangers arising from artificial ('man-made') ionising radiation, but this scope has since been extended to include natural radiation. Indeed, the recently modernised and consolidated Basic Safety Standards Directive from 2013 contains detailed provisions on the protection from all natural radiation sources, including radon, cosmic rays, natural radionuclides in building material, and naturally occurring radioactive material.

Clockwise from top-left:

A profile of a typical well drained soil under temperate forest and shows evidence of the main soil processes: humus formation, weathering, leaching and clay translocation.
Source: Eska Michek

Harvesting the wheat crop, Turkey
Source: mert tuna on Unsplash

Cover of the EURATOM Treaty (consolidated version)
Source: https://www.ramdhuma.europa.eu/en/documents-publications/publications/euratom-treaty

Starlit sky over Steinernes Meer, Schönau am Königssee, Germany
Source: Manuel Will on Unsplash

Cover of Council Directive 2013/59/Euratom (Basic Safety Standards Directive)
Source: https://eur-lex.europa.eu/legal-content/EN/TXT/?uri=CELEX:32013L0059

Rationale

1.1 Introduction

In order to describe the history and the motivation behind the European Atlas of Natural Radiation (EANR), this section seeks to answer four simple questions:

a. Who has developed the EANR?

b. Why has the EANR been created?

c. What does the EANR contain?

d. How is the EANR structured?

a. Who has developed the EANR?

The European Commission (EC) develops and operates systems for collecting, checking and reporting information about the levels of radioactivity in Europe's environment on a continuous basis for routine and emergency conditions. This endeavour is in line with its mission, based on the Euratom Treaty Articles 35, 36 and 39 (European Union, 2016), which are quoted below:

Art. 35: *Each Member State shall establish the facilities necessary to carry out continuous monitoring of the level of radioactivity in the air, water and soil and to ensure compliance with the basic standards.*

The Commission shall have the right of access to such facilities, it may verify their operation and efficiency.

Art. 36: *The appropriate authorities shall periodically communicate information on the checks referred to in Article 35 to the Commission so that it is kept informed of the level of radioactivity to which the public is exposed.*

Art. 39: *The Commission shall set up within the framework of the Joint Nuclear Research Centre, as soon as the latter has been established, a health and safety documentation and study section.*

In particular, this section shall have the task of collecting the documentation and information referred to in Articles 33, 36 and 37 and of assisting the Commission in carrying out the tasks assigned to it by this Chapter.

In this framework, since 1987, the **Radioactivity Environmental Monitoring (REM) group** of the EC Joint Research Centre (JRC) supports the European Commission in its responsibilities to provide qualified information on the levels of environmental radioactivity, both for routine and emergency situations, through the following activities:

Radioactivity Environmental Monitoring database (REMdb)

The Radioactivity Environmental Monitoring database (REMdb) was created in the aftermath of the Chernobyl accident (1986) by the European Commission (EC) – Directorate-General Joint Research Centre (DG JRC), located in Ispra, Italy. Since then it has been maintained there with the aim to keep a historical record of the Chernobyl accident and to store the radioactivity monitoring data gathered through the national environmental monitoring programmes of the Member States (MSs). By collecting and checking this information in the REMdb, JRC supports the DG for Energy in its responsibilities to return qualified information to the MSs (competent authorities and general public) on the levels of radioactive contamination of the various compartments of the environment (air concentration, surface and drinking water, milk and mixed diet) on the European Union scale. The REMdb has been accepting data on radionuclide concentrations from European Union (EU) MSs in both environmental samples and foodstuffs from 1984 onwards. To date, the total number of data records stored in REMdb exceeds 5 million, in this way providing the scientific community, authorities and the general public with a valuable archive of environmental radioactivity topics in Europe. For further information about the REMdb, see: https://rem.jrc.ec.europa.eu/RemWeb/.

ECURIE and EURDEP

After the Chernobyl accident, and in order to improve the international emergency preparedness and response procedures the European Commission defined and put in place a Decision (Council Decision 87/600/EURATOM) that essentially obliges a country that intends to implement widespread countermeasures for protecting its population to notify the European Commission without delay. The same Council Decision also specifies that radiological monitoring data have to be exchanged and made available. Over the past 25 years, the European Commission has invested in improving the rapid exchange of information and data in the event of a major accident. The resulting mechanisms for the early phase of emergency support are the early notification system ECURIE (European Community Urgent Radiological Information Exchange) and the automatic data exchange platform EURDEP (European Radiological Data Exchange Platform). 39 countries exchange real-time monitoring information collected from more than 5 500 automatic surveillance systems once per hour in a standard data-format through secure ftp and web-services. This large-scale data harmonisation and exchange system for radioactivity measurements is unique in the world. The clear concept behind EURDEP is to better equip the decision makers with notified and continuous information available in the form of real-time monitoring data to define the most appropriate countermeasures. For further information, see the EURDEP website: https://eurdep.jrc.ec.europa.eu.

Nuclear Emergency Preparedness and Response

Over the past years, the REM group has undertaken several research and training activities on Nuclear Emergency Preparedness and Response (NEP&R), based on the use of trajectory models and atmospheric dispersion models (ADMs) as well as procedures to improve harmonisation of the monitoring data. For further information, see: https://rem.jrc.ec.europa.eu/RemWeb/ and https://remon.jrc.ec.europa.eu/.

European Atlas of Natural Radiation

After the European Commission published the 'Atlas of Caesium Deposition on Europe after the Chernobyl Accident' (European Communities, 1998), the REM group of the JRC embarked on a European Atlas of Natural Radiation (EANR) with the support of the relevant national/international organisations and the scientific community (see Preamble).

b. Why has the EANR been created?

Natural radioactivity or ionising radiation is considered to be the largest contributor to the collective effective dose received by the world's population. Man is continuously exposed to ionising radiation from several natural sources that can be classified in two broad categories: high-energy cosmic rays incident on the Earth's atmosphere and releasing secondary radiation (cosmic contribution); and radioactive nuclides generated during the formation of the Earth and still present in the Earth's crust (terrestrial contribution). Terrestrial radioactivity is mostly produced by the uranium (U) and thorium (Th) radioactive families together with potassium (^{40}K), which is a long-lived radioactive isotope of the elemental potassium. In most circumstances, radon (^{222}Rn), a noble gas produced in the radioactive decay of

The Joint Research Centre of the European Commission

The European Union

The European Union (EU) is an economic and political association of European countries with a combined population of over 500 million inhabitants (7.3% of the world's population) and an economy representing approximately 20% of global Gross Domestic Product (GDP). The EU has evolved from the original six countries of the European Coal and Steel Community (1951) and the European Economic Community (1958), to 28 Member States. The term 'European Union' was established under the 1993 Maastricht Treaty. The EU is represented at the United Nations, the WTO, the G8 and the G20. The EU operates through a system of supranational independent institutions and intergovernmental negotiated decisions adopted by the Member States. Important EU institutions include the European Commission, the Council of the European Union, the Court of Justice of the European Union, and the European Central Bank. The members of the European Parliament are elected every five years by EU citizens.

The European Commission

The European Commission is the executive body of the EU responsible for proposing legislation, verifying the implementation of the decisions, upholding the Union's treaties and the day-to-day running of the EU. The Commission acts as a cabinet government, with 28 Commission members – one representative per Member State. The Commission is composed of thirty-four Directorates-General.

The Joint Research Centre (JRC) is the European Commission's science and knowledge service which employs scientists to carry out research in order to provide independent scientific advice and support to EU policy. As the Commission's in-house science service, the Joint Research Centre's mission is to provide EU policies with independent, evidence-based scientific and technical support throughout the whole policy cycle. Its work has a direct impact on the lives of citizens by contributing with its research outcomes to a healthy and safe environment, secure energy supplies, sustainable mobility and consumer health and safety. The JRC draws on over 50 years of scientific work experience and continually builds its expertise based on its scientific Directorates, which host specialist laboratories and unique research facilities. They are located in Belgium (Brussels and Geel), Germany, Italy, the Netherlands and Spain. While most of the scientific work serves the policy Directorates-General of the European Commission, the JRC addresses key societal challenges while stimulating innovation and developing new methods, tools and standards. The JRC shares know-how with the Member States, the scientific community and international partners. The JRC collaborates with over a thousand organisations worldwide whose scientists have access to many JRC facilities through various collaboration agreements.

https://ec.europa.eu/jrc/en/about

Directorate for Nuclear Safety and Security

The mission of the JRC Directorate G for Nuclear Safety and Security to implement the JRC Euratom Research and Training Programme, to maintain and disseminate nuclear competences in Europe, serving both "nuclear" and "non-nuclear" Member States.

A strong cooperation and complementarity with their national organisations is of key relevance.

Directorate G supports the relevant policy DGs with independent, technical and scientific evidence in the areas of nuclear safety, security and safeguards.

Directorate G is also an active key partner in international networks and collaborates with international organisations and prominent Academia and Research Institutes.

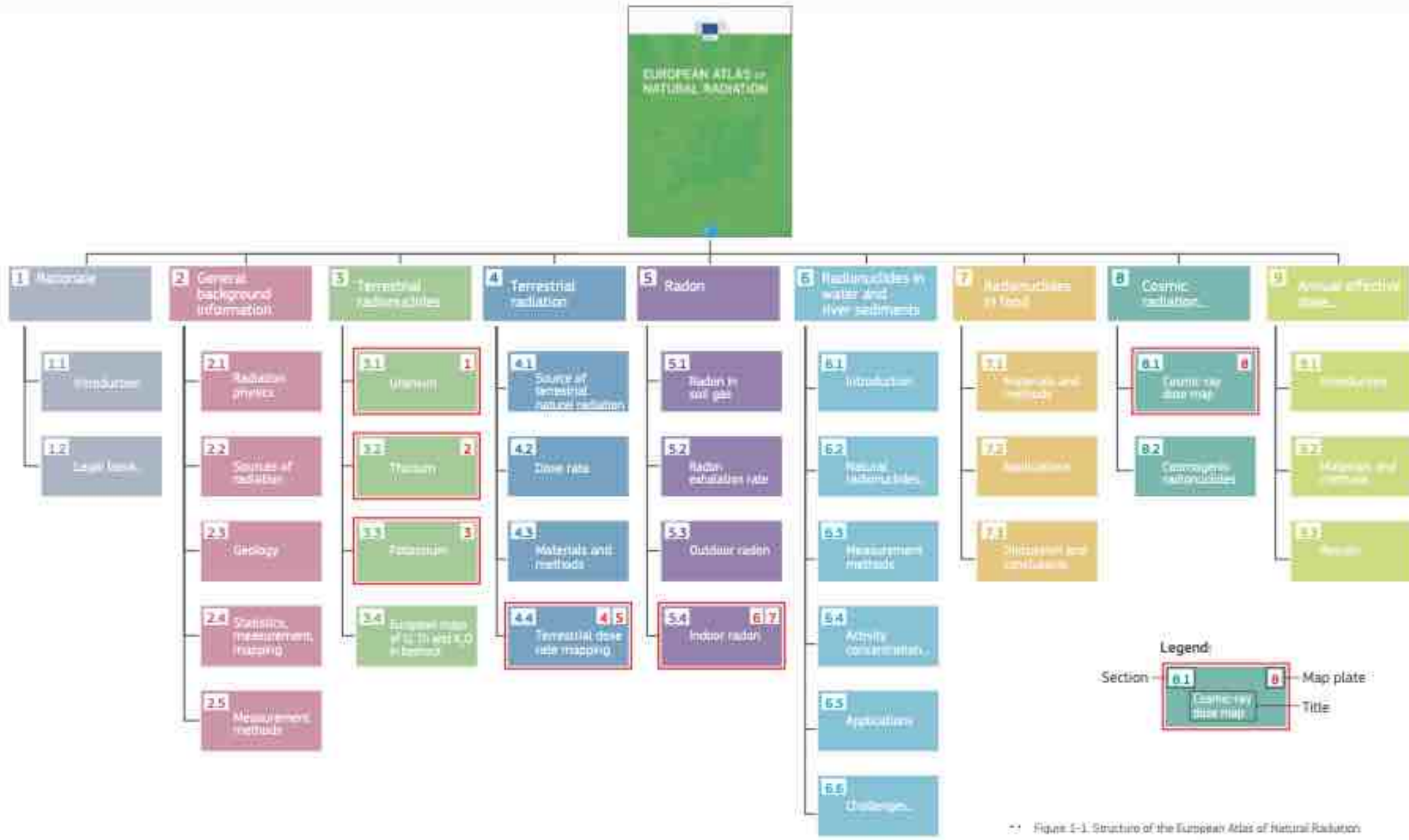

Figure 1-1. Structure of the European Atlas of Natural Radiation

the ^{238}U progeny, is the major contributor to the total dose. Indeed, this Atlas is intended as a tool for the public to:

- familiarise itself with natural radioactivity;
- be informed about the levels of natural radioactivity caused by different sources;
- have a more balanced view of the annual dose received by the world's population, to which natural radioactivity is the largest contributor; and
- make direct comparisons between doses from natural sources of ionising radiation and those from man-made (artificial), and hence to better understand the latter.

JRC mission statement

JRC in brief

- As the European Commission's science and knowledge service, the Joint Research Centre (JRC) supports EU policies with independent scientific evidence throughout the whole policy cycle.
- The JRC creates, manages and makes sense of knowledge and develops innovative tools and makes them available to policy makers.
- The JRC anticipates emerging issues that need to be addressed at EU level and understand policy environments.
- The JRC collaborates with over a thousand organisations worldwide whose scientists have access to many JRC facilities through various collaboration agreements.
- JRC's work has a direct impact on the lives of citizens by contributing with its research outcomes to a healthy and safe environment, secure energy supplies, sustainable mobility and consumer health and safety.
- The JRC draws on over 50 years of scientific experience and continually builds its expertise in knowledge production and knowledge management.
- The JRC hosts specialist laboratories and unique research facilities and is home to thousands of scientists.

Moreover, it provides reference material and generates harmonised data for the scientific community and national competent authorities. The latter could use the information to implement the Basic Safety Standard Directive (European Union, 2013b) regarding aspects linked to natural radiation (e.g. to develop national radon action plans).

Therefore, the EANR is in line with the mission of the European Commission, based on the Euratom Treaty (European Union, 2016), which is to collect, check and report information on radioactivity levels in the environment.

c. What does the EANR contain?

The European Atlas of Natural Radiation could be considered as an encyclopaedia of natural radioactivity. It describes the different natural sources of natural radioactivity, cosmic and terrestrial, in detail and represents the present state-of-the-art of this topic.

Moreover, it contains a collection of maps of Europe showing the levels of natural sources of radiation.

Europe: geographical area

In the EANR, Europe has been considered with the geographical extension of the continent defined as:

'bordered in the North by the Arctic Ocean, on the west by the Atlantic Ocean, and on the south (west to east) by the Mediterranean Sea, the Black Sea, the Kuma-Manych Depression, and the Caspian Sea. The continent's eastern boundary (north to south) runs along the Ural Mountains and then roughly southwest along the Emba (Zhem) River, terminating at the northern Caspian coast.' (Encyclopædia Britannica, 2019).

The spatial coverage of the maps shown in the Atlas varies from map to map, depending on the data that were available to create the maps. For some maps, European-wide databases have been used, while for others the national authorities that agreed to join the Atlas project have provided the data.

d. How is the EANR structured?

The European Atlas of Natural Radiation is structured as depicted in Figure 1-1, namely:

Chapter 1 – Rationale

It presents the rationale behind the EANR, giving an overview of the European institutions involved in this project. Moreover, the legal basis and requirements on protection from exposure to natural radiation sources are described in detail.

Chapter 2 – General background information

It provides the background information necessary to understand:

- how ionising radiation works;
- why it is present in our environment; and
- how it can be represented on a map.

Chapter 3 – Terrestrial radionuclides

It gives a detailed description of the three main terrestrial radionuclides: uranium and thorium, with their decay chains, and potassium-40. Moreover, it explains the materials and methods used to produce European maps of radionuclide concentration in soil and in bedrock and and displays these maps.

Chapter 4 – Terrestrial radiation

It describes the gamma radiation from terrestrial sources (uranium and thorium with their decay chains and potassium) that represents an important component to the natural radiation environment. The methodologies used to map the terrestrial gamma dose rate are described and the European Annual Terrestrial Gamma Dose Map is displayed. It shows the annual effective dose rate that a person would receive from terrestrial radiation, if she/he spends all the reference time in a location in which the soil has fixed uranium, thorium and potassium concentrations.

Chapter 5 – Radon

It focuses on the noble, naturally occurring radioactive gas called radon (^{222}Rn), which is the largest contributor to the dose due to natural radiation received by the global population.

The chapter is divided into the following sections that describe the different steps from radon source to its accumulation in indoor space: radon in soil gas; radon exhalation; outdoor radon;

and indoor radon.

Finally, based on survey data received from 35 European countries participating on a voluntary basis, a European map of indoor radon concentration has been created. It shows the arithmetic means over 10 km × 10 km grid cells of annual indoor radon concentration in ground-floor rooms.

Chapter 6 – Radionuclides in water and river sediments

It describes in detail the natural radionuclides, released from rock surfaces, present in water and river sediments. Besides radionuclides in the uranium and thorium series (including radon), potassium-40 (^{40}K), tritium (^{3}H), carbon-14 (^{14}C) and other natural radionuclides may occur in water. The European legislation on the level or natural radionuclides in water, as well as the international recommendation, is explained.

Moreover, the main measurement techniques used to detect radionuclides in water are described.

Chapter 7 - Radionuclides in food

This chapter describes the pathways of natural radionuclides from soil to food, the radionuclides of interest as well as measurements of radioactivity in foodstuffs. Furthermore, typical activity concentrations in various foodstuffs in European countries are given, and finally the main factors controlling the dose due to ingestion of food are illustrated.

Chapter 8 – Cosmic radiation and cosmogenic radionuclides

This chapter addresses the effects from cosmic radiation. Cosmic rays are atomic nuclei accelerated to high energy levels, creating electrons, gamma rays, neutrons and mesons when interacting with atmospheric nuclei. The flux of cosmic radiation highly depends on the altitude above the Earth's surface. The European cosmic-ray annual dose map has been developed and displayed, as well as a detailed description of cosmogenic radionuclides, using beryllium-7 (^{7}Be) as an example.

Chapter 9 – Annual effective dose from natural environmental radiation

The overall goal of the Atlas is to estimate the annual effective dose that the European population may receive from natural radioactivity. Indeed, this final chapter reports on the population-weighted average of the annual effective dose due to natural sources of radiation estimated for each European country as well as for all of them together, giving, therefore, an overall European estimate.

Chapter 10 – References and Appendices

References
Appendix 1 – The International System of Units (SI)
Appendix 2 – Country ISO codes
Appendix 3 – List of national competent authorities that provided data for the European Indoor Radon Map
Appendix 4 – Periodic Table of Elements

The authors tried to explain the scientific jargon at their best. However, for further terms or explanations, the reader may wish to consult standard references such as the IAEA Safety Glossary (IAEA, 2019: IAEA Safety Glossary: Terminology used in nuclear safety and radiation protection, 2018 edition. International Atomic Energy Agency, Vienna. ISBN 978-92-0-104718-2.)

Explanation of bold/coloured text

The bold/coloured text indicates that this text is repeated more than once in the Atlas, providing general information (see example below):

3.2 Thorium

Thorium is an actinide series element with an atomic number of 90 and an atomic mass of 232. It is radioactive with one main natural isotope, the primordial long-lived radionuclide ^{232}Th, which has the longest half-life (1.41×10^{10} years) of all known radioactive isotopes of thorium and comprises 99.98% of the total Th mass. Thorium decays through a long radioactive decay series ending with the stable lead isotope ^{208}Pb.

3.2.1 Thorium in rock minerals

Thorium (Th) is mainly present at minor to trace concentration levels (< 1 g/100 g) in accessory minerals such as zircon, sphene,

The parent reservoir of th which are (Cicchella et the soil profil concentrates and zircon. the cationic charged clay thorium is re transported in insoluble in su Thorium is taken up by

1.2 Legal basis and requirements on protection from exposure to natural radiation sources

Introduction

Radiation protection has a long tradition in Europe. Based on the Euratom Treaty (European Union, 2016), the European Atomic Energy Community has established a comprehensive set of legislation for the protection against the danger arising from ionising radiation. While in the early days, this protection focused on protection from exposure to artificial 'man-made' ionising radiations, recent developments propose to extend the protection system to cover coherently exposure to natural radiation sources, such as exposure to indoor radon, exposure to cosmic rays, exposure to natural radioactive substances in drinking water and in building materials, and exposure to naturally occurring radioactive material. The extension of the system makes particular sense, as exposure to natural radiation is one of the most important contributors to the overall total exposure of members of the public and can lead to significant exposure of workers in specific workplaces. The recently modernised and consolidated Basic Safety Standard (BSS) Directive (European Union, 2013b) contains detailed provisions on the protection from all natural radiation sources, including radon, cosmic rays, natural radionuclides in building materials, and naturally occurring radioactive material. These provisions are complemented by the Drinking Water Directive (European Union, 2013a), laying down requirements on the protection of the health of the general public with regard to radioactive substances in water intended for human consumption, which addresses radioactive substances of both artificial and natural origin.

History and development of the Basic Safety Standards Directive

Articles 2 and 30 of the Euratom Treaty (European Union, 2016) empower the Community to establish uniform basic safety standards to protect the health of workers and the general public against dangers arising from ionising radiations. Article 31 of the Treaty stipulates the procedure to develop such basic safety standards, which includes the consultation of a group of scientific experts in the public health area. Already in 1959, the first Euratom Basic Safety Standards (BSS) Directive was adopted and has subsequently been repeatedly amended (in 1962, 1966, 1976, 1980, 1984 and 1996, respectively), taking account of the latest scientific findings and recommendations, to ensure the highest level of protection for workers, patients and members of the public. The Basic Safety Standards Directive from 1996 (European Communities, 1996), which already contained first elements on protection from natural radiation sources but still focussed on the protection of workers and members of the public from artificial radiation sources, has been supplemented in 1997 by a Directive for the protection of patients from medical exposures (European Communities, 1997).

In 2014, the Community published the latest Basic Safety Standards Directive, namely Directive 2013/59/Euratom, laying down basic safety standards for protection against the dangers arising from exposure to ionising radiation (European Union, 2013b). The provisions in this Directive are based on the latest scientific findings and take account of technological progress and operational experience since 1996. At the same time, the Directive consolidates the previous set of Euratom radiation protection legislation by incorporating and repealing five Directives:

- the 1996 Basic Safety Standards Directive (European Communities, 1996);
- the Medical Exposure Directive (European Communities, 1997);
- the Outside Workers Directive (European Communities, 1990b);
- the Public Information Directive (European Communities, 1989); and the
- High Activity Sealed Sources Directive (European Union, 2003).

In addition, the Commission recommendation on indoor radon exposure (European Communities, 1990a) has been incorporated to become legally binding.

The main driver for the revision of the Basic Safety Standards Directive was the publication of The 2007 Recommendations of the International Commission on Radiological Protection (ICRP), ICRP Publication 103 (ICRP, 2007). In these recommendations, ICRP modifies the underlying radiation protection philosophy and proposes to categorise exposure situations in planned, existing and emergency situations. ICRP maintains the set of principles of radiation protection, justification of exposure, optimisation of protection and application of dose limits, emphasising their importance. Further to this ICRP recommends the consistent integration of natural radiation sources into the radiation protection system.

Following this ICRP philosophy, the 2013 Basic Safety Standards Directive applies to any planned, existing or emergency exposure situation, which involves a risk from exposure to ionising radiation, which cannot be disregarded from a radiation protection point of view. With this, the BSS applies to all relevant radiation sources with no distinction made between artificial 'man-made' radiation sources and natural sources of radiation.

The scope of the consolidated Basic Safety Standards Directive

As provided for in Article 2 of Directive 2013/59/Euratom (European Union, 2013b), the scope of the Directive has been extended to apply now to all human activities, including those which involve the presence of natural radiation sources and lead to a significant increase in the exposure of workers or members of the public. The human activities involving the presence of natural radiation sources include, inter alia, the operation of aircraft and spacecraft, in relation to the exposure of crews, the processing of materials with naturally occurring radionuclides, and workplaces involving exposure to indoor radon, the exposure of workers or members of the public to indoor radon, the external exposure from building materials, and cases of lasting exposure resulting from the after-effects of a past human activity.

Naturally occurring radioactive material

The 2013 BSS Directive introduces a graded approach to regulatory control of practices by way of notification, authorisation and appropriate inspections commensurate with the magnitude and likelihood of exposures resulting from the practice, and commensurate with the impact that regulatory control may have in reducing such exposures or improving radiological safety. Justified practices, if not exempted, need to be notified prior to the practice commencing and, if so decided, authorised. Authorisation can take the form of a registration or a license.

Following the above-mentioned philosophy, this system of regulatory control now equally applies to activities involving naturally occurring radioactive material (NORM). In a first step, the Member State shall identify, based on an indicative list given in Annex VI of the Directive, industrial sectors involving NORM which may lead to exposure of workers or members of the public which cannot be disregarded from a radiation protection point of view (Article 23). For identified sectors, a graded approach applies introducing exemption levels and decision criteria such as doses to workers and effluent releases to the environment.

Occupational exposure in NORM practices

Article 35 of the 2013 BSS Directive provides for the requirements on arrangements in workplaces introducing a graded approach. Paragraph 1 requires that radiation protection arrangements are made for all workplaces where workers are liable to exceed one of the dose limits for the public. The arrangements shall be appropriate to the nature of the installations and sources and to the magnitude and nature of the risks. It is worth noting that this requirement applies to all workplaces involving natural radiation sources extending a similar requirement which had been included in 1996 BSS Directive.

Exposure to radon

The exposure of members of the public or of workers to indoor radon is now explicitly taken up in the scope of Council Directive 2013/59/Euratom (Article 2 (2d)) (European Union, 2013b). Based on this, the Directive introduces, for the first time, legally binding requirements on protection from exposure to radon.

As major provision with regard to the radon protection strategy, the 2013 BSS Directive requires in Article 103 that Member States establish a national radon action plan addressing long-term risks from radon in dwellings, buildings with public access and workplaces for any source of radon ingress, whether from

soil, building materials or water. Annex XVIII offers a detailed list of items to be considered in preparing the national action plan. Further to this, Article 103 requires specifically that appropriate measures be in place to prevent radon ingress into new buildings. These measures may include specific requirements in national building codes. Finally, Article 103 requires Member States to identify areas where the radon concentration (as an annual average) in a significant number of buildings is expected to exceed the relevant national reference level.

Indoor exposure to radon

Article 74 of the 2013 BSS Directive requires that Member States establish national reference levels for indoor radon concentrations. For the annual average activity concentration in air, the reference level shall not be higher than 300 Bq/m^3. Member States can choose more challenging reference levels and have the possibility to define different reference levels for existing buildings and for newly built ones (of maximum 300 Bq/m^3).

Member States have to promote actions to identify buildings with radon concentrations exceeding the national reference level. This can be done by establishing a radon measurement campaign. For buildings exceeding the national reference level, radon-reducing measures shall be encouraged. This encouragement can mean that technical measures are promoted or that financial support is offered to those building owners investing in these radon-reducing measures.

At the same time, Member States need to ensure that the population is informed, on a national level and even more on a local level in radon-prone areas, about indoor-radon exposure, the associated health risks, and the importance of performing radon measurements, as well as on the technical means available for reducing existing radon concentrations. An important stakeholder in these activities is the building industry, e.g. architects, and construction companies.

Radon in workplaces

Article 54 of the 2013 BSS Directive contains specific requirements on radon in workplaces. It requires the establishment of a national reference level for indoor radon concentration in workplaces. The reference level for the annual average activity concentration in air shall not be higher than 300 Bq m^{-3}, unless it is warranted by national prevailing circumstances. Member States are free to establish different reference levels for workplaces and for buildings, as long as they are not higher than 300 Bq m^{-3}.

Member States are requested to establish programmes to carry out radon measurements in workplaces within the areas identified under the national radon action plan (see also Article 103(3)), and in specific types of workplaces also identified in the national action plan (see point 3 of Annex XVIII). Workplaces with radon concentrations above the reference level shall undergo appropriate remedial actions. If, despite all actions to optimise, the radon concentration in a workplace remains above the national reference level, this workplace needs to be notified to the competent authority (according to Article 25 (2)) and the relevant occupational radiation protection requirements may apply (see Article 35(2)).

In this context, is it worth noting that Article 31 paragraph 3c clearly recognises the responsibility of the employer or the undertaking to protect workers who are exposed to radon at work, in the situation specified in Article 54(3).

Article 35 paragraph 2 sets out the graded approach for workplaces with exposure to indoor radon as specified in Article 54(3). Workplaces where the exposure of workers is liable to exceed an effective dose of 6 mSv/a or a corresponding time-integrated radon exposure value shall be managed as a planned exposure situation, and the Member States shall determine which requirements set out in Chapter VI Occupational Exposure of the 2013 BSS Directive are appropriate. For workplaces where the effective dose to workers is less than or equal to 6 mSv/a or the exposure less than the corresponding time-integrated radon exposure value, the competent authority shall require that exposures are kept under review.

Finally, it should be noted that for workplaces where workers are exposed to authorised practices and radon, Article 9 stipulates that the dose limits for occupational exposures apply to the sum of annual occupational exposures from all authorised practices, occupational exposure to radon in workplaces requiring notification in accordance with Article 54(3), and other occupational exposure from existing exposure situations in accordance with Article 100(3).

Cosmic radiation

Already the 1996 BSS Directive (European Communities, 1996) introduced with Article 42 the protection of aircrew from exposure to cosmic radiation and requested that undertakings operating aircraft assess the exposure of the crew concerned, optimised through the organisation of working schedules, information of the crew of the health risks, and the application of special protection during pregnancy. The 2013 BSS Directive (European Union, 2013b) took these requirements with Article 35 (3) up and embedded them coherently in the overall system of protection from natural radiation sources. Recital (26) specifies 'The exposure of air crew to cosmic radiation should be managed as a planned exposure situation. The operation of spacecraft should come under the scope of this Directive and, if dose limits are exceeded, be managed as a specially authorised exposure.' Provisions on specially authorised exposures are laid down in Article 52 of the 2013 BSS Directive.

It is worth noting that the 2013 BSS Directive explicitly excludes exposure of members of the public or workers other than air or space crew to cosmic radiation in flight or in space from the scope of the Directive.

Building materials

All building materials contain various amounts of natural radioactive nuclides. Materials derived from rock and soil contain mainly natural radionuclides of the uranium (^{238}U) and thorium (^{232}Th) series, and the radioactive isotope of potassium (^{40}K). In the uranium series, the decay chain segment starting from radium (^{226}Ra) is radiologically the most important and, therefore, reference is often made to radium instead of uranium.

The 2013 BSS Directive (European Union, 2013b) introduces, for the first time, binding requirements on building materials. In Article 75 (1), it establishes a reference level of 1 mSv/a applying to indoor external exposure to gamma radiation emitted by building material in addition to outdoor external exposure.

Member States will have to identify building materials, which are of concern from a radiation protection point of view with regard to their emitted gamma radiation, taking into account the indicative list of materials which is set out in Annex XIII of the Directive. The annexed list contains natural materials and materials incorporating residues from NORM industries, which may require a link to the requirements on NORM industries. For identified building materials, Member States need to ensure that before these materials are placed on the market, the activity concentrations of certain radionuclides (^{226}Ra, ^{232}Th, and ^{40}K) are determined and the results of these measurements together with the corresponding activity concentration index, as defined in Annex VIII of the Directive, are communicated to the competent authority. Member States may also need to decide on an appropriate labelling of the materials before placing them on the market. For types of building materials which were identified and are liable to give doses exceeding the defined reference level of 1 mSv/a, the Member State needs to decide on appropriate measures on the further use of these materials – e.g. through specific requirements in building codes or restrictions on the use of these materials.

It should be noted that the provisions of the 2013 BSS Directive should be without prejudice to the provisions of Regulation (EU) No 305/2011 laying down harmonised conditions for the marketing of construction products (European Union, 2011), in particular on the declaration of performance, the establishment of harmonised standards or the means and conditions for making available the declaration of performance or with regard to CE marking.

Drinking water

Water is one of the most comprehensively regulated areas of the EU environmental legislation. Early European water policy began in the 1970s with the adoption of political programmes as well as legally binding legislation. Council Directive 98/83/EC, namely the EC Drinking Water Directive (European Communities, 1998), lays down the essential standards at EU level for the quality of water intended for human consumption. Its objective is to protect human health from adverse effects of any contamination of water by ensuring that it is wholesome and clean. Forty-eight microbiological, chemical and indicator parameters must be monitored and regularly tested.

In order to account for the potential presence of radioactive substances in drinking water, the EC Directive has been supplemented by Council Directive 2013/51/Euratom (European Union, 2013a), establishing requirements relating to the protection of the health of the general public against radioactive substances in water intended for human consumption.

The Council Directive 2013/51/Euratom (European Union, 2013a) applies to tap water and to water in bottles or containers intended for human consumption; it does not apply to natural mineral waters and to small private supplies. It lays down parametric values for radon, tritium, and – covering many other naturally occurring and artificial radionuclides – the indicative dose (ID). It is worth noting that the values given have an indicative function and are not meant to be limits. The Directive also lays down general principles for monitoring, including technical details (frequencies of sampling, analysis methods, measuring methods, etc.).

In its annexes, the Directive proposes as parametric values an indicative dose of 0.1 mSv/a over one year consumption of drinking water, and activity concentrations of 100 Bq/l for radon and tritium.

For the monitoring of radioactive substances in drinking water samples, the Directive proposes a graded assessment methodology: All drinking water samples shall undergo an initial screening for gross-alpha and gross-beta activity. If the measured activity concentrations are below the screening levels of 0.1 Bq/l for gross-alpha activity and 1 Bq/l for gross-beta activity, no further action is required. If either of the screening levels is exceeded, the concentrations of individual radionuclides should be determined and compared with the guidance levels provided in the annexes of the Directive. The outcome of this further evaluation may indicate that no action is required or that further assessment is necessary before a decision is taken on the need for remedial measures.

Résumé

Natural sources of ionising radiation are amongst the most important contributors to the overall total exposure of members of the public and can lead to significant exposures of workers in specific workplaces. Europe has established a comprehensive set of legislation for the protection against the dangers arising from ionising radiation, which, in its recent development, coherently covers the protection from exposure to natural sources of ionising radiation. This system of protection includes, in particular, protection from exposure to indoor radon, exposure to cosmic rays, exposure to natural radioactive substances in drinking water and in building materials, and exposure to NORM.

Clockwise from top-left:

Borkum sand island, North Sea coast, Germany
Source: Peter Bosew

Tõrvajõe variegated limestone in blocks fallen from klint escarpment, Tõrvajõe, Estonia.
Source: Ivns Saadre

The Aurora Borealis, or Northern Lights, shines above Sauðárkrókur, Iceland
Source: Vincent Guth on Unsplash

Folded limestone flysch, San Rocco, Liguria, Italy
Source: Reinaud Stiegler

Chapter 2
General background information

This chapter provides the background information necessary to understand how ionising radiation works, why it is present in our environment, and how it can be represented on a map.

The ionising radiation discussed in this chapter consists of alpha, beta and neutron particles as well as gamma rays. Each interacts with matter in a specific way, causing biological effects that can be hazardous. Health risk from radiation is described by the absorbed dose, equivalent dose and effective dose, calculated using specific weighting factors. The effects of ionising radiation on humans can be deterministic and stochastic. All this information leads to the general principles of radiation protection. Natural ionising radiation is emitted by a variety of sources, both cosmogenic and terrigenous, and can be primordial (existing since the origin of the Solar System) or secondary (created by the interaction of radiation with matter). The most important terrestrial primordial radionuclides are uranium (^{238}U and ^{235}U decay series), thorium ^{232}Th decay series and potassium ^{40}K. One particular descendant from uranium and thorium is radon gas, having a particular impact on human health. As radon forms by radioactive decay inside mineral grains, part of it escapes into the pore-space (emanation), and migrates to the atmosphere (exhalation). Once present in indoor air, radon becomes a potential source of hazardous exposure to the occupants. Being radioactive, it produces progeny that partly attaches to aerosol particles, leading to an attached fraction and an unattached fraction. The relation between radon gas, aerosol particle size and concentration and those attached and unattached fractions determines the health risk (by inhalation) to humans. In this way, scientists can estimate the different sources and contributions to radiation doses to humans, presented in a dose pie-chart. A case study about Ukraine shows how the highest radiation exposure to the population comes from natural radiation sources. Due to the radiation protection measures imposed, the exposure due to the Chernobyl accident is less.

The composition and structure of the sub-surface, described by geology, has a strong influence on the local level of natural background radiation, along with other conditions such as altitude and climate. Looking at the geology of Europe, one can already form a general and large-scale idea of the level of natural radioactivity that can be expected. For instance, young and mobile unconsolidated sediments (like clay or sand) that are found in many regions in northern and northwestern Europe contain generally fewer radionuclides than certain magmatic or metamorphic rocks found in for example Scandinavia (Fennoscandian Shield), Central Europe (Bohemian Massif), France (Bretagne and Central Massif) and in Spain (Iberian Massif). The more recent alpine mountain belts are composed of many different types of rocks, leading to strong spatial variations in radiological signature and radiological background. Some types of volcanic rocks have a higher radionuclide content and can lead to increased indoor gamma dose rates and radon or thoron concentrations. Another specific case are karstic limestone areas, where the radiological risk varies locally, leading to strong hot-spots of natural radioactivity. Organic-rich shale and slate can also be enriched in uranium leading to an increased radiological risk. Other geological factors like fractures such as faults can favour radionuclide concentration and radon migration to the surface. The topmost layer of the Earth's surface is often covered by a soil layer, which can influence the local content in radionuclides and affect the natural radioactivity presented in this Atlas.

The final section of this chapter describes the process of generating a map based on available knowledge and experimental data. Statistical analysis is the tool used to interpret the data and knowledge and the principles are illustrated and described in detail in this part. Concepts like accuracy and precision have very specific meanings in statistical terms, and it is important to appreciate them when dealing with data. Measurement uncertainty, sample bias, choice of scale and resolution are other examples, just to mention a few of the considerations going into the design of a survey or map. Without data there could be no map but without a detailed knowledge of the quality, the limitations and the different ways in which data could be sampled and interpreted, one cannot hope to create a useful map. The complexity of the process is demonstrated, and it concludes with a case study on designing a soil-gas survey.

General background information

2.1 Radiation physics

Ionising radiation (hereafter called radiation) is radiation that carries enough energy to liberate electrons from atoms or molecules, thereby ionising them. Ionising radiation is made up of energetic subatomic particles (alpha particles, beta particles and neutrons), ions or atoms moving at high speeds (usually greater than 1 % of the speed of light), and electromagnetic waves on the high-energy end of the electromagnetic spectrum. The ability of atomic nuclei to convert spontaneously (without exterior action) under emitting ionising radiation is called radioactivity.

The following section briefly describes radiation, together with its biological effects on humans, and the general principle of radiation protection.

2.1.1 Different kinds of radiation

Alpha

Alpha radiation is the emission of an alpha particle from the nucleus of an atom, changing the originating atom to one of an element with an atomic number 2 less and mass number 4 less than it started with. An alpha particle consists of two protons and two neutrons, essentially the nucleus of a helium-4 atom, and gets out from the nucleus by tunnel effect.

The alpha decay equation may be described in general terms as follows:

$$ {}^{A}_{Z}P \rightarrow {}^{A-4}_{Z-2}D + {}^{4}_{2}He \qquad (2\text{-}1) $$

where ${}^{A}_{Z}P$ is the parent nucleus of atomic number Z and mass number A, ${}^{A-4}_{Z-2}D$ is the daughter nucleus of atomic number Z-2 and mass number A-4, and ${}^{4}_{2}He$ is the alpha particle. The total energy released is shared between the alpha particle, recoil daughter nucleus, and gamma-radiation from the daughter nucleus when it is left in an excited energy state and decays to its ground state. The energy of the alpha particles typically ranges between 2 and 10 MeV and its value is characteristic of the emitting nucleus. Radionuclides emitting alpha particles of low energy decay with long half-lives, whereas those emitting alpha particles of high energy have short half-lives. The shorter half-lives exhibited by radionuclides with high alpha decay energies compared to the longer half-lives of nuclides with lower decay energies is explained on the basis of the nuclear potential barrier that the alpha particle must overcome to penetrate or escape from the nucleus.

The least penetrating alpha particle is positively charged and quite massive in comparison to the more penetrating negatively charged beta-, and the most penetrating, gamma and neutron radiations. Due to its charge and mass:

- an alpha particle interacts strongly with matter and stops within 100 µm in most materials. In air, alpha particles may travel only a few centimetres, e.g. an 5.5 MeV alpha particle travels 4 cm in air and 48 µm in water.
- travel distance depends on several variables including the energy of the alpha particle, the atomic number and atomic weight of the absorber and the density of the absorber.
- an alpha particle dissipates its energy in matter mainly by two mechanisms, ionisation and electron excitation.
- direct collisions with an atomic nucleus are few and far between.

Double positive charge of alpha particles allows ionisation within a given substance (solid, liquid, or gas) by the formation of ion pairs due to coloumbic attraction between a traversing alpha particle and atomic electrons of the atoms within the material the alpha particle travels. The two neutrons of the alpha particle give it additional mass, which further facilitates ionisation by coulombic interaction or even direct collision of the alpha particle with atomic electrons. Thus alpha particle produces thousands of ion pairs until its kinetic energy has been completely dissipated within the substance it traverses. It is the most ionising radiation emitted by natural sources, with the extremely rare exception of the spontaneous fission of uranium.

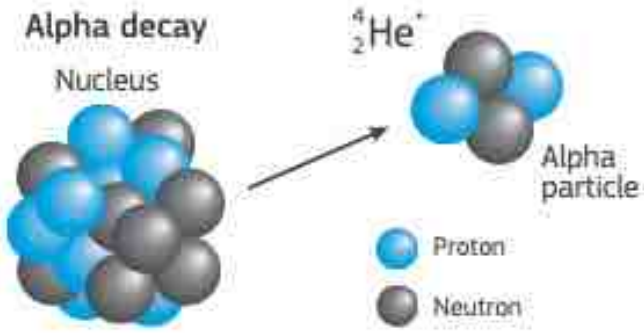

The amount of energy required to produce ion pairs is a function of the absorbing medium. For example, air absorbs an average of 35 eV, argon gas absorbs approximately 25 eV, and a semiconductor material requires only 2-3 eV to produce an ion pair. This gives semiconductor materials an important advantage as radiation detectors compared to gases when energy resolution in radioactivity analysis is an important factor.

Gamma

After an alpha or beta decay, the daughter nuclei are frequently in an excited energy state and decay by gamma emission into their ground state. In this situation, photons with energies up to 10 MeV can be produced. The nuclide in this excited energy state is called nuclear isomer, and the transition, or decay, from a higher to a lower energy state is referred to as isomeric transition, since neither the mass number, A, nor the atomic number, Z, of a nuclide (${}^{A}_{Z}P$) changes in the decay process, the nuclides are considered to be in isomeric energy states. Gamma rays emit discrete energies corresponding to the energy state transitions a nuclide may undergo when in an excited state. The gamma-ray energy is the difference in energy states of the nuclear isomers:

$$ E_{\gamma} = h\nu = E_1 - E_2 \qquad (2\text{-}2) $$

where $h\nu$ is the energy of the electromagnetic radiation (h is the Planck's constant and ν is the photon frequency), and E_1 and E_2 represent the energy levels of the nuclear isomers.

The lack of charge and rest mass of gamma radiation hinders its interaction with, and dissipation of its energy in matter. Accordingly, gamma radiation has greater penetration power and longer ranges in matter than the massive and charged alpha and beta particles with the same energy. Three typical interactions of gamma radiation (0.005–10 MeV) with matter, are the photoelectric effect, the Compton effect and the pair production.

For example, air absorbs an average of 35 eV, argon gas absorbs approximately 25 eV, and a semiconductor material requires only 2-3 eV to produce an ion pair. This enables an important advantage of semiconductor materials as radiation detectors compared to gases when energy resolution in radioactivity analysis is an important factor.

Neutron

The **neutron** is a neutral particle with a mass approximately 1850 times larger than the electron mass and one fourth of the alpha particle mass. Its mass is like that of the proton, is equivalent to 1 u (atomic mass unit). **A neutron is only stable within the confines of the nucleus of an atom**. Outside the nucleus, the neutron decays with a mean lifetime of about 15 min. Unlike the particulate alpha and beta nuclear radiation, neutron radiation is not emitted in any significant quantities from radionuclides that undergo the traditional nuclear decay process. Significant quantities of neutron radiation occur when neutrons are ejected from the nuclei of atoms following reactions between the nuclei and particulate radiation. Due to the lack of charge, the neutron cannot directly produce ionisation in matter. Neutrons can pass through the otherwise impenetrable coloumbic barrier of the atomic electrons and actually collide with nuclei of atoms and be scattered in the process or be captured by the nucleus of an atom. Its penetration depth depends on its energy. Scattering of neutrons and recoil nuclei occurs with conservation of momentum (elastic scattering) or loss of kinetic energy of the neutron as gamma radiation (inelastic scattering). The capture of a neutron by a nucleus of an atom may result in emission of other nuclear particles (alpha or proton) from the nucleus (nonelastic reactions) or the fragmentation of the nucleus into two (nuclear fission).

Radioactivity is the ability of atomic nuclei to convert themselves spontaneously by emitting ionising radiation.

Radioactive decay is a stochastic process in which the decay rate is proportional to the number of radioactive nuclei of a particular type present at any time t. The constant of proportionality (λ), termed the decay constant, is the probability of decay per unit time interval. It is related to the half-life ($T_{1/2}$) of a radionuclide (Equation 2-3), which is the time required for the decay of one half of the original number of its nuclei present. The activity is the number of decays per unit time interval.

$$ \lambda = \frac{\ln 2}{T_{1/2}} \qquad (2\text{-}3) $$

The unit of the activity is becquerel (Bq), named after the French physicist Henri Becquerel (1852–1908), one of the discoverers of radioactivity. One Becquerel is one transformation per second on average ($1\,Bq = 1\,s^{-1}$). Formerly, the unit Curie was used, representing the activity of 1 g ^{226}Ra, or $3.7 \cdot 10^{10}$ Bq.

The Electromagnetic Spectrum

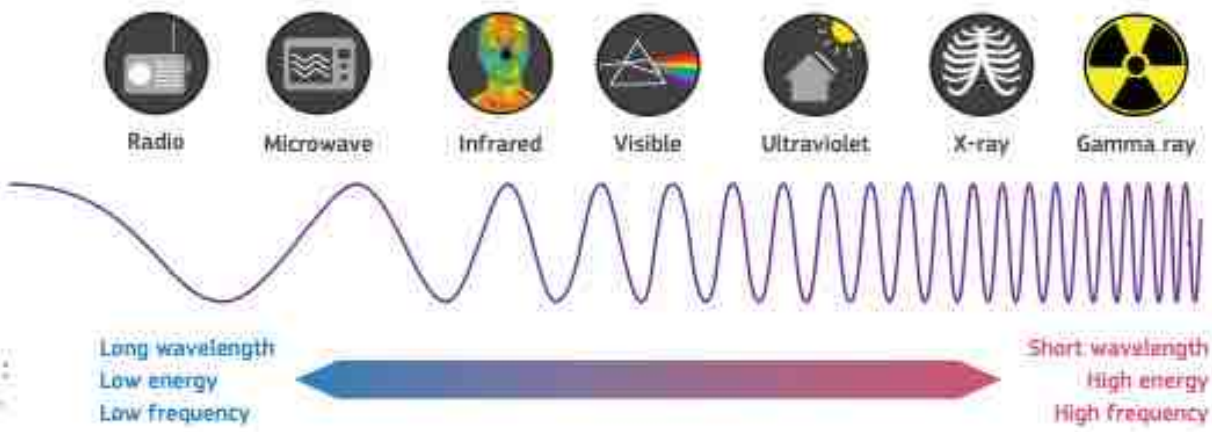

Figure 2-1.
The electromagnetic spectrum.
Source: http://www.atomic-energy.com/radiation/2011/02/28/284/1541.htm

What is an atom?

An atom is the smallest unit of any chemical element, consisting of a positive nucleus surrounded by negative electrons. The nucleus is made of protons and neutrons, called nucleons.

The **atomic number** (represented by the letter Z) of an element is the number of protons in the nucleus and it defines the chemical element.

The **mass number** (represented by the letter A) is defined as the total number of protons and neutrons (N) in an atom and it defines the isotope of the element.

Isotopes are variants of a particular chemical element which differ in neutron number. All isotopes of a given element have the same number of protons (same Z) but different numbers of neutrons in each atom (different N).

In quantum mechanics, an **excited energy state** of a system (such as an atom or nucleus) is any quantum state of the system that has a higher energy than the ground state (that is, more energy than the absolute minimum). Excitation is an elevation in energy level above an arbitrary baseline energy state.

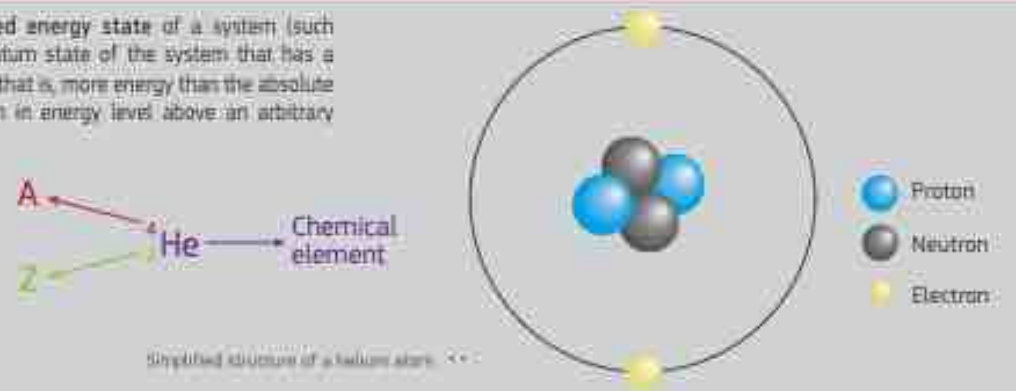

Simplified structure of a helium atom

Beta

Beta radiation is a term used to describe three types of decay in which a neutron (proton) transforms into a proton (neutron), differing in charge by +1 or −1. The beta decay modes are β^-, β^+ and electron capture (EC). During β^- emission a negative beta particle or negative electron is emitted from the nucleus. β^+ emission means the emission of a positive beta particle or positively charged electron from the nucleus (positron). Beta particles have the same mass and charge as electrons and differ from them only by their origin.

In a nucleus with excess neutrons, the neutron changes into a proton:

$$ {}^{A}_{Z}P \rightarrow {}^{A}_{Z+1}D + e^- + \bar{\nu} \qquad (2\text{-}4) $$

where ${}^{A}_{Z}P$ is the parent nuclide of atomic number Z and mass number A, ${}^{A}_{Z+1}D$ is the daughter nuclide of atomic number Z+1 and the same mass number as the parent, e^- is the electron or negative beta particle (β^-), $\bar{\nu}$ is the electron-antineutrino. The total kinetic energy released is shared between the beta particle, electron-antineutrino, recoil daughter nucleus, and any gamma radiation that may be emitted by the daughter nucleus, but most of the energy emitted in the decay appears in the rest and kinetic energy of the emitted beta particle and electron-antineutrino. Gamma-ray emission does not occur in all cases of beta decay. There are some nuclides, e.g. ^{3}H, ^{14}C, that decay with the emission of beta particle directly to the stable ground state without the emission of gamma radiation. Contrary to alpha particles, which have a discrete energy, beta particles are emitted from radionuclides with a broad spectrum of energies. Thus all beta-emitting radionuclides will display a wide spectrum of energies between zero and a maximum energy.

Nuclei with excess protons are β^+ emitters. In this case, a proton decays into a neutron by emitting a positron (β^+), which is a positively charged electron, and an electron-neutrino.

$$ {}^{A}_{Z}P \rightarrow {}^{A}_{Z-1}D + e^+ + \nu_e \qquad (2\text{-}5) $$

where ${}^{A}_{Z}P$ is the parent nuclide with atomic number Z and mass number A, ${}^{A}_{Z-1}D$ is the daughter nuclide with atomic number Z-1 and the same mass number as the parent, e^+ is the positron or positive beta particle (β^+), ν_e is the electron-neutrino, and K_β is the total kinetic energy released in the beta decay process.

Decay by positron emission can occur only when the decay energy is significantly above 1.022 MeV. This is because two electrons of opposite charge are produced (β^+, β^-) within the nucleus, and the energy equivalence of the electron mass is 0.51 MeV. The positive electron is ejected from the nucleus and the negative electron combines with a proton to form a neutron.

Electron capture (EC) does not result in emission of any beta particle, but an orbital electron is captured by a nuclear proton changing it into a nuclear neutron with the emission of an electron-neutrino:

$$ {}^{A}_{Z}P + e^- \xrightarrow{EC} {}^{A}_{Z-1}D + \nu_e \qquad (2\text{-}6) $$

where ${}^{A}_{Z}P$ is the parent nuclide with atomic number Z and mass number A, e^- is an orbital electron captured by the nucleus of the parent nuclide, ${}^{A}_{Z-1}D$ is the daughter nuclide of atomic number Z-1 and the same mass number as the parent, ν_e is the electron-neutrino, and K_β is the total kinetic energy released in the beta decay process. The change in atomic number is the same as occurs with positron (β^+) emission. EC competes with positron emission, and most radionuclides that decay by positron emission also decay by EC to the same daughter nuclide. In addition to positron emission, an unstable nucleus can increase its neutron/proton ratio by EC, via the capture by the nucleus of a proximate atomic electron, e.g. K-, or L-shell electron. A neutrino emitted from the EC decay process does not share the transition energy with another particle, and therefore it is emitted with a single quantum of energy equal to the transition energy less the atomic electron binding energy. The EC decay may compete with β^+ emission; that is, some radionuclides may decay by either EC or β^+ emission. Positron emission will predominate when the transition energy is high (above 1.022 MeV) and for nuclides of low atomic number, while the EC decay process will predominate for low transition energies and nuclides of higher atomic number. EC is the preferred decay mode for proton-rich heavy nuclei.

There are several radionuclides that decay via all beta decay modes, to varying degrees, yielding two daughter nuclides that differ by two units of atomic number. One of these radionuclides is ^{40}K which decays by the three β^-, β^+ and EC modes with 89 %, 0.3 % and 10.7 %, respectively, producing ^{40}Ca and ^{40}Ar.

A beta particle interacts with matter via ionisation and electron orbital excitation as it dissipates its kinetic energy. Its ionisation power is a factor of 1 000 lower than that of an alpha particle of equivalent energy, and it dissipates energy also by bremsstrahlung and Cherenkov Radiation. For example, a 1 MeV beta particle travels approximately 334 cm in dry air and 0.40 cm in water and a 5.5 MeV beta particle travels approximately 2 400 cm in air. Hazardous bremsstrahlung radiation can be significant when high-energy beta particles interact with shields of high atomic number (e.g. lead).

Beta-minus decay

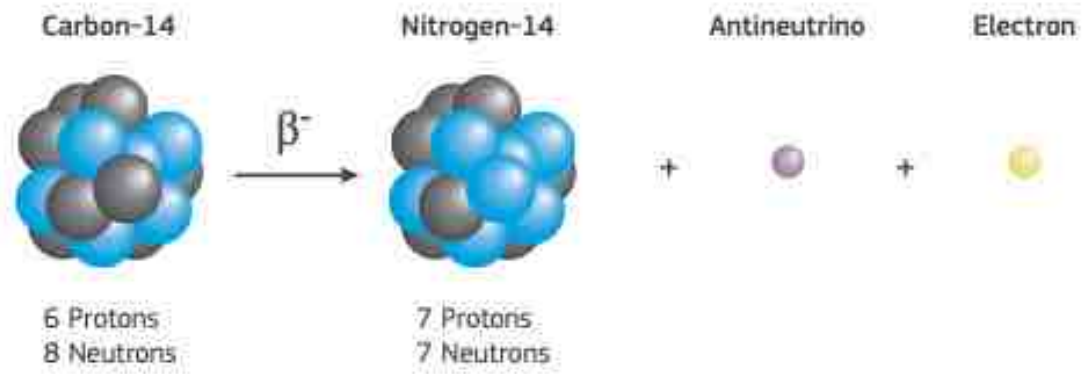

Beta-plus decay

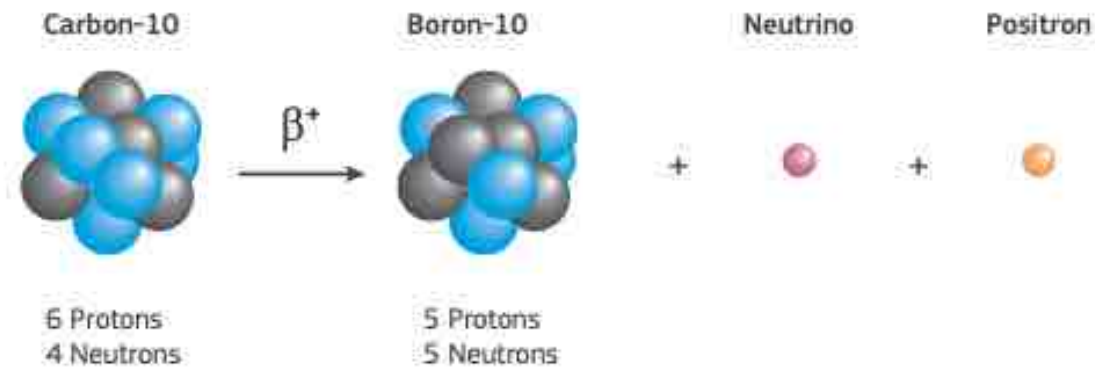

Electron capture

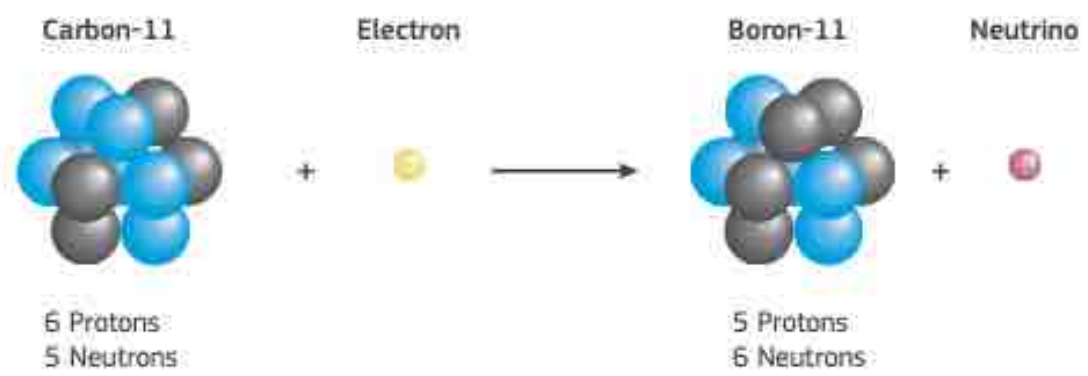

2.1.2 Biological effects of ionising radiation

In daily life, we are exposed to various sources of radiation, for example natural radiation sources, medical applications, industrial practices, effluents from nuclear installations (which are generally controlled and negligible), fallouts from nuclear weapons testing and the impact of nuclear accidents (historical events). Exposure to increased levels of ionising radiation can be harmful to human health. Indeed, radiation can ionise or excite atoms while passing through tissue.

There are various quantities to specify the dose received and the biological effectiveness of that dose:

Absorbed dose (D): the energy absorbed per unit mass $D = d\varepsilon/dm$ where $d\varepsilon$ is the mean energy imparted by ionising radiation to the matter in a volume element and dm is the mass of the matter in this volume element. It is expressed in gray (Gy=J/kg).

The **absorbed dose rate** is the rate at which an absorbed dose is received (Gy/s).

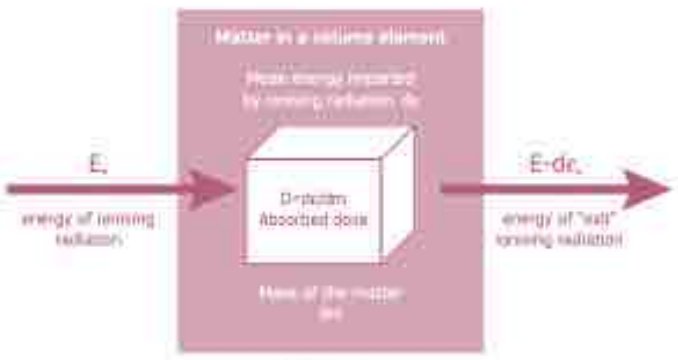

Figure 2-2.
Simplified schema for defining the absorbed dose.
Source: EAN, EC-JRC, 2019.

The biological effect of radiation depends not only on the energy deposited by radiation in an organism, but in addition on the type of radiation and the way in which the energy is deposited along the path of the radiation. So therefore the linear energy transfer (LET) is defined. It describes the mean energy deposited per unit path length in the absorbing material. The unit of the LET is keV/µm. So for the same absorbed dose, the biological effect of alpha particles or neutrons (high LET) is much greater than of beta or gamma rays (low LET). To characterise this difference in biological effects of various types of radiation, the radiation weighting factor w_R was established (Table 2-1) and has been published in ICRP Recommendation 103 (ICRP, 2007).

Radiation type	Radiation weighting factor, w_R
Photons	1
Electrons, and muons	1
Protons and charged pions	2
α particles, fission fragments, heavy ions	20
Neutrons	A continuous function depending on neutron energy (see Equation 2-7)

Table 2-1.
Radiation weighting factors.
Source: ICRP 2007, adapted by the Basic Safety Standards Directive (EU, 2013).

To calculate radiation weighting factors for neutrons, a continuous function in neutron energy, E_n (MeV), is used (Equation 2-7).

$$w_R = \begin{cases} 2.5 + 18.2e^{-(\ln(E_n))^2/6}, & E_n < 1\,\text{MeV} \\ 5.0 + 17.0e^{-(\ln(2E_n))^2/6}, & 1\,\text{MeV} < E_n < 50\,\text{MeV} \\ 2.5 + 3.25e^{-(\ln(0.04E_n))^2/6}, & E_n > 50\,\text{MeV} \end{cases} \quad (2\text{-}7)$$

The equivalent dose (H_T) represents the radiation dose to tissue and thus makes the link between absorbed dose and its biological effect. H_T is calculated as absorbed dose multiplied by the weighting factor (w_R) of the radiation. If there are several types of radiation (R) present, the equivalent dose in the tissue (T) is the weighted sum over all contributions. Equivalent dose is also expressed in joule per kilogram, because of the dimensionless weighting factor. For differentiation the unit of the equivalent dose is named sievert (Sv) after the Swedish doctor and physicist Rolf M. Sievert (1896–1966). The relation with the former unit, roentgen equivalents man (rem), is 1 Sv = 100 rem.

$$H_T = \sum_R w_R D_{T,R} \quad (2\text{-}8)$$

The equivalent dose rate is the rate at which an equivalent dose is received, expressed for example in Sv/s or Sv/h.

The equivalent dose is always related to a defined tissue or organ. Different tissues and organs show different sensitivities to radiation, depending on their cell cleavage frequency and their cell renewal frequency. To take these effects into account, the equivalent doses in different tissues must be weighted (Table 2-2; ICRP, 2007.

The equivalent dose (H_T) in tissue or organ T multiplied by this tissue weighting factor (w_T) reported in Table 2-2, is called the **effective dose (E)**.

$$E = \sum_T w_T H_T = \sum_T w_T \sum_R w_R D_{T,R} \quad (2\text{-}9)$$

The sum of the relative weighting factors is one; this means that the sum of the weighting risks for the organs is numerically equal to the risk for the whole body.

Calculating doses from intakes of radionuclides

Irradiation by ionising radiation outside the body causes only a dose during the period of irradiation. But by an intake through ingestion or inhalation some radionuclides can remain inside the body and irradiate the tissues for years. In these cases, the total radiation dose depends on the half-life of the radionuclide, its distribution in the body, and the rate at which it is excreted from the body. On the basis of mathematical models, doses can be calculated with consideration of the radionuclides intake each year. The resulting total effective dose delivered over a lifetime is called the **committed effective dose**.

ICRP develops **effective dose coefficients** to simplify the calculation of equivalent dose and effective dose for inhaled or ingested radionuclides: values for committed doses following the intake of 1 Bq of a radionuclide via ingestion and inhalation.

These coefficients have been calculated for members of the public at six standard ages and for intake by adult workers. The unit of the effective dose coefficient is Sv/Bq. The received dose via ingestion or inhalation of a radionuclide can be calculated as a product of the incorporated activity and the effective dose coefficient. Choosing the right dose coefficient depends on:

- The radionuclide
- Whether it is inhaled or ingested
- The particle size (for inhalation)
- The chemical form
- Population group
- The time since intake (if using bioassay data)
- Activity Median Aerodynamic Diameter (AMAD).

Deterministic and stochastic effects

Radiation can affect people's health in two different ways, called deterministic effects and stochastic effects.

Deterministic effects are characterised by a threshold (Figure 2-4); below it, no damage is recognised; and above it, the damage increases with dose. Deterministic effects are the acute radiation syndrome, which occurs immediately after an irradiation with high doses and damages, which occur at a later time, but induce no cancer (opacity of lens, vitiation of fertility). Immediate symptoms after a whole body irradiation can be recognised above a dose between 0.5 and 1 Gy. For doses between 2–6 Gy mortality is between 5–95% without treatment and 5–50% with treatment. These are estimates and recovery potential depends on treatment. If the whole body dose goes up to 10 Gy, the mortality would reach 100% (Eisenbud & Gesell, 1997).

Stochastic effects of ionising radiation are chance events, with the probability of the effect increasing with dose, but the severity of the effect is independent of the dose received. Primarily cancer risk, but also hereditary disorders are stochastic effects (ICRP Publication 103; ICRP, 2007). Stochastic effects are assumed to have no threshold (Figure 2-4). However it is not yet known what the curve looks like for small doses (i.e. <0.1 Sv), and several hypothesis have been considered, including homeostatic (positive effect for very small doses) and the existence of a threshold (i.e. limit below which there is no effect). However, for regulatory purposes, simplicity and conservatism, the most prevalent assumption is linear-no-threshold.

An approach is called 'conservative' if, according to the state of knowledge, it likely represents an unfavourable situation, i.e. it is pessimistic, or in other words, most likely the expected true effect is less severe. Its purpose is to be on the safe side.

Tissue or organ	Tissue weighting factor
Bone marrow (red)	0.12
Colon	0.12
Lung	0.12
Stomach	0.12
Breast	0.12
Gonads	0.08
Bladder	0.04
Liver	0.04
Esophagus	0.04
Thyroid	0.04
Skin	0.01
Bone surface	0.01
Salivary gland	0.01
Brain	0.01
Sum of remainder tissues or organs	0.12

Table 2-2.
The sum of w_T is equal to 1.
Source: ICRP 103, Annals of the ICRP, volume 37, pp 1-332, 2007.

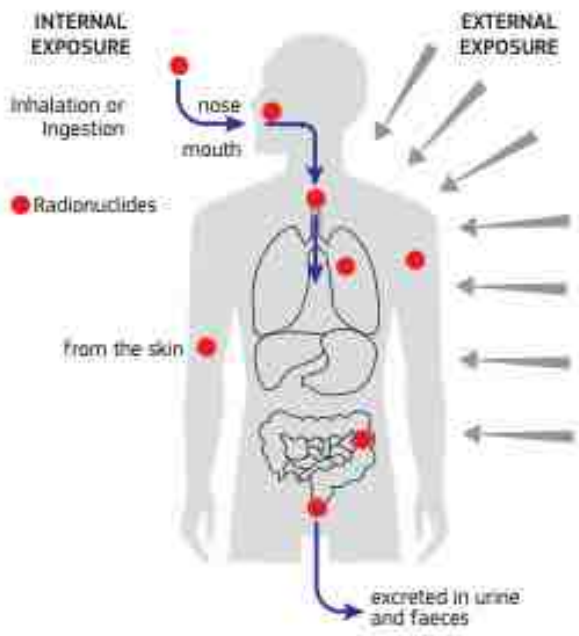

Figure 2-3.
Schematic representation of the modes of exposure to ionizing radiation.
Source: EAN, EC-JRC, 2019.

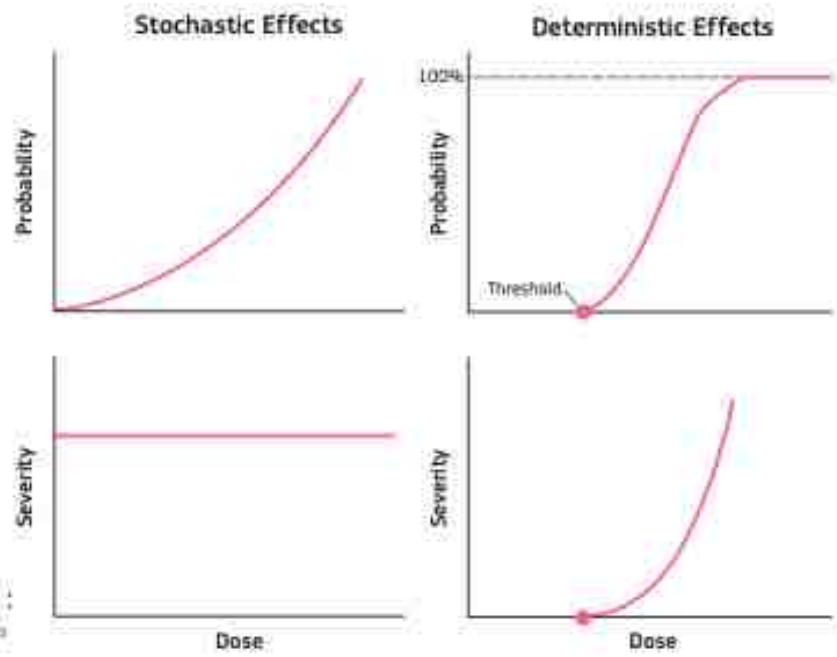

Figure 2-4.
Stylised probability dose and severity dose relationships for stochastic and deterministic effects.
Source: modified from Cardona et al., 2016.

General principles of radiation protection

The system of radiation protection is based on the following principles of justification, optimisation and dose limitation:

a. **The Principle of Justification**: Any decision that alters the radiation exposure situation should do more good than harm. Decisions introducing or altering a radiation source, an exposure pathway or actual exposures shall be justified in the sense that such decisions shall be taken with the intent to ensure that the individual or societal benefit resulting from them offsets the detriment that they may cause;

b. **The Principle of Optimisation**: In all exposure situations, radiation protection shall be optimised with the aim of keeping the magnitude and likelihood of exposure and the number of individuals exposed as low as reasonably achievable, taking into account economic and societal factors, whereby optimisation of the protection of individuals undergoing medical exposure shall be commensurate with the medical purpose of the exposure as described in Article 56 of the Basic Safety Standards Directive (European Union, 2013). This principle shall be applied in terms of Effective Dose as well as organ doses, as a precautionary measure to allow for uncertainties as to health detriment below the threshold, for deterministic effects;

c. **The Principle of Dose Limitation**: In planned exposure situations, the sum of doses to an individual from all regulated radiation sources may not exceed the dose limits laid down for occupational exposure or public exposure. See Section 1.2 for more details on dose limits. Dose limits shall not apply to medical exposures (EU, 2013).

Radiation protection (also called radiological protection) is defined as the protection of people from the effects of exposure to ionising radiation, and the means for achieving this (IAEA, 2007).

2.2 Sources of radiation

2.2.1 Natural sources of radiation

Living organisms are exposed to radiation from several natural sources, and, to a large extent, this exposure is unavoidable. Some natural radiation sources are affected by human activity, in which case it is possible to control the amount of radioactivity released. Remedial measures during construction of new buildings or remedial measures taken to reduce the exposure to the population are examples of possible control of natural radiation sources.

Natural radioactivity comes from extraterrestrial sources, as well as from radioactive elements in the Earth's crust.

About 340 nuclides have been found in nature, of which about 70 are radioactive. All elements with atomic number above 80 have radioactive isotopes (Eisenbud, 1997).

First, there is radiation that comes from space, called cosmic or **cosmogenic**. This type of radiation gives rise to the external radiation dose and depends on altitude and location. Second, there is radiation caused by **natural radionuclides**, mainly in the Earth's crust.

Units for U, Th and K

In Geoscience, contents of the naturally radioactive elements K, U, and Th in rocks are reported in conventional units of %K, mg/kg U and mg/kg Th (Adams and Gasparini, 1970; IAEA, 1976; ICRU, 1994; IAEA, 2003; IAEA, 2010), where K means the total natural potassium, in which the radioactive isotope ^{40}K occurs as 0.0118 percent of K. Since U and Th are indirectly estimated using field gamma-ray spectrometry, through gamma rays of their decay products, an abbreviation for the equivalent 'e' is added, and data and maps based on field gamma-ray spectrometry are reported in mg/kg eU and mg/kg eTh. In the SI system, mass concentration of principal naturally radioactive elements in rocks K, U, and Th are reported in mass of the radioelement per kilogramme. The relationship between conventional geological units and the SI units used in this Atlas are: 1 %K = 10 g/kg K, 1 ppm U = 1 mg/kg U, 1 ppm Th = 1 mg/kg Th, respectively.

Cosmogenic radiation

Cosmogenic radiation is one of the major components of natural radiation. It affects crew on aircraft and spacecraft as the dose received depends on altitude. In general, the dose rate from cosmic radiation doubles for each 2 000 m of altitude (Eisenbud, 1997). Only three components of cosmic radiation are important from the point of view of possible human radiation exposure: galactic cosmic rays representing the high-energy radiation coming from outside the solar system; solar cosmic rays are primarily ejected from solar flares; and coronal mass ejections and radiation from the Van Allen radiation belt (Klener et al., 2000). **Galactic cosmic rays** originate from distant galaxies outside the solar system. It is primarily composed of protons (84 %), helium nuclei (12 %), heavy nuclei of almost all the existing elements (1 %) and electrons (3 %). The radiation field of galactic cosmic radiation in the interstellar space changes little in the time horizon of millions of years. The solar wind and its associated magnetic field affect the cosmic radiation in the vicinity of the Earth and obstruct their entry into the atmosphere; in other words, an increase in solar cosmic rays results in a decrease in galactic cosmic rays. In contrast, the extent of solar cosmic radiation and its time variations are unpredictable and quick. **Solar cosmic radiation** consists mainly of protons (99 %). The last component of cosmic radiation, the Van Allen radiation belt, is a zone of protons and electrons captured by and held around the Earth by its magnetic field. The Earth has two such belts: an outer radiation belt at an altitude of roughly 20 000 km; and an inner belt at an altitude of 3 000 km. The radiation effect of this belt on the Earth is negligible.

Natural radionuclides

Natural radionuclides can be divided into three groups, based on where the radionuclides come from: cosmogenic, primordial and secondary.

Cosmogenic radionuclides are continuously created when cosmic rays interact with stable elements; this mainly occurs in the atmosphere. The most important isotopes are ^{3}H, ^{14}C and ^{7}Be. For human radiation exposure, the most important is ^{14}C, which is produced in the upper atmosphere through reaction with ^{14}N (Klener et al., 2000). Another important cosmogenic radionuclide is tritium (^{3}H), which is formed when cosmic rays react with nitrogen and oxygen in the upper atmosphere. The major part of tritium is incorporated into water molecules.

Primordial nuclides have existed since before the solar system was formed. They are classified as non-series and series depending on the decay pathway. Thanks to their very long half-life (more than 10^{8} years), they are still present in significant quantities on the Earth. The primordial radionuclides that now exist are those that have half-lives at least comparable to the age of the universe. Radioisotopes with half-lives of less than about 10^{8} years have become undetectable after about 30 half-lives since their creation. On the other hand, radionuclides with half-lives greater than 10^{10} years have decayed very little up to the present time (Eisenbud, 1997). Non series primordial radionuclides lighter than lead are listed in Table 2-3. U^{238}, ^{235}U and ^{232}Th are the parent radionuclides for the three naturally occurring decay series called the uranium (Figure 2-5), actinium (Figure 2-6) and thorium series (Figure 2-7). The uranium, thorium and potassium isotopes are described in more detail in the following text. A fourth chain of radioactive elements, the neptunium series, existed only for a short time. This series originated with ^{241}Pu, an isotope with a very short half-life of 14 years. The only isotope from the neptunium series still existing today is the almost stable ^{209}Bi with a half-life of 2×10^{18} years.

Secondary nuclides formed by radioactive decay of primordial nuclides are the last group of natural radionuclides. Since primordial and secondary nuclides originate directly from the Earth, they are called **terrestrial**.

Traces of former sulphur mining, Milos Island, Greece
Source: Peter Bossew

Table 2-3.
Non series Primordial Radionuclides lighter than lead
Source: Eisenbud, 1997

Radionuclide	Half-life (a)	Major radiations	Typical crustal concentration (Bq/kg)
^{40}K	$1.26 \cdot 10^{9}$	β, γ	630
^{50}V	$6 \cdot 10^{15}$	γ	$2 \cdot 10^{-5}$
^{87}Rb	$4.8 \cdot 10^{10}$	β	70
^{113}Cd	$8.04 \cdot 10^{15}$	β	$< 2 \cdot 10^{-5}$
^{115}In	$6 \cdot 10^{14}$	β	$2 \cdot 10^{-5}$
^{123}Te	$1.2 \cdot 10^{13}$	X rays	$2 \cdot 10^{-5}$
^{138}La	$1.12 \cdot 10^{11}$	β, γ	$2 \cdot 10^{-5}$
^{142}Ce	$> 5 \cdot 10^{16}$	Not reported	$< 1 \cdot 10^{-5}$
^{144}Nd	$2.4 \cdot 10^{15}$	α	$3 \cdot 10^{-5}$
^{147}Sm	$1.05 \cdot 10^{11}$	α	0.7
^{152}Gd	$1.1 \cdot 10^{14}$	α	$7 \cdot 10^{-5}$
^{174}Hf	$2.0 \cdot 10^{15}$	α	$2 \cdot 10^{-5}$
^{176}Lu	$2.2 \cdot 10^{10}$	e⁻, γ	0.04
^{187}Re	$4.3 \cdot 10^{10}$	β	$1 \cdot 10^{-3}$
^{190}Pt	$6.9 \cdot 10^{11}$	α	$7 \cdot 10^{-4}$
^{192}Pt	$1 \cdot 10^{15}$	α	$3 \cdot 10^{-5}$
^{209}Bi	$2 \cdot 10^{18}$	α	$< 4 \cdot 10^{-5}$
^{128}Te	$7.7 \cdot 10^{24}$	double β	

Uranium

(For more details see Section 3.1.)

Uranium is a heavy actinide series element (atomic number 92) with two main, natural, primordial long-lived radionuclides, including the more abundant ^{238}U (half-life of 4.5×10^9 years, 99.274% of U total mass) and the less abundant ^{235}U (half-life of 7.0×10^8 years, 0.72% of U total mass). Both decay separately through long and complex radioactive decay series ending with stable lead ^{206}Pb and ^{207}Pb respectively (Figures 2-5 and 2-6 respectively). Another natural uranium isotope ^{234}U (half-life of 2.4×10^5 years, 0.0056% of total natural uranium) is the third decay product in the ^{238}U radioactive decay series. This uranium isotope is generally considered to be in equilibrium (to slightly deficient) with its progenitor ^{238}U. Differentially, the $^{238}U/^{235}U$ ratio has increased over time due to faster radioactive decay of ^{235}U (Wedepohl, 1978a).

In nature, uranium is found with four possible valences, +3, +4, +5, +6, the most important being +4 and +6. The first is typical of its reduced form and is common in known ore deposits as the stable uraninite (UO_2) oxide, and in anoxic water. The second is typical of its oxidised form and is found in highly mobile ions and complexes (e.g. uranyl ion, UO_2^{2+}, and uranyl hydroxyl complex, UO_2OH^+) and some U-bearing minerals (De Vivo et al., 1984, Hinck et al., 2010). The chemical speciation of U depends strictly on the redox potential (Eh) of the environment.

In the **Goldschmidt classification** scheme (see the explanation below), uranium, together with other elements such as sodium (Na), potassium (K), calcium (Ca) and aluminium (Al), is geochemically defined as a lithophile element, i.e. with an affinity for silicates (Goldschmidt, 1937). The lithophile elements are typically partitioned into silicate minerals or oxides, depending on their affinity with oxygen, rather than sulphides or metal alloys.

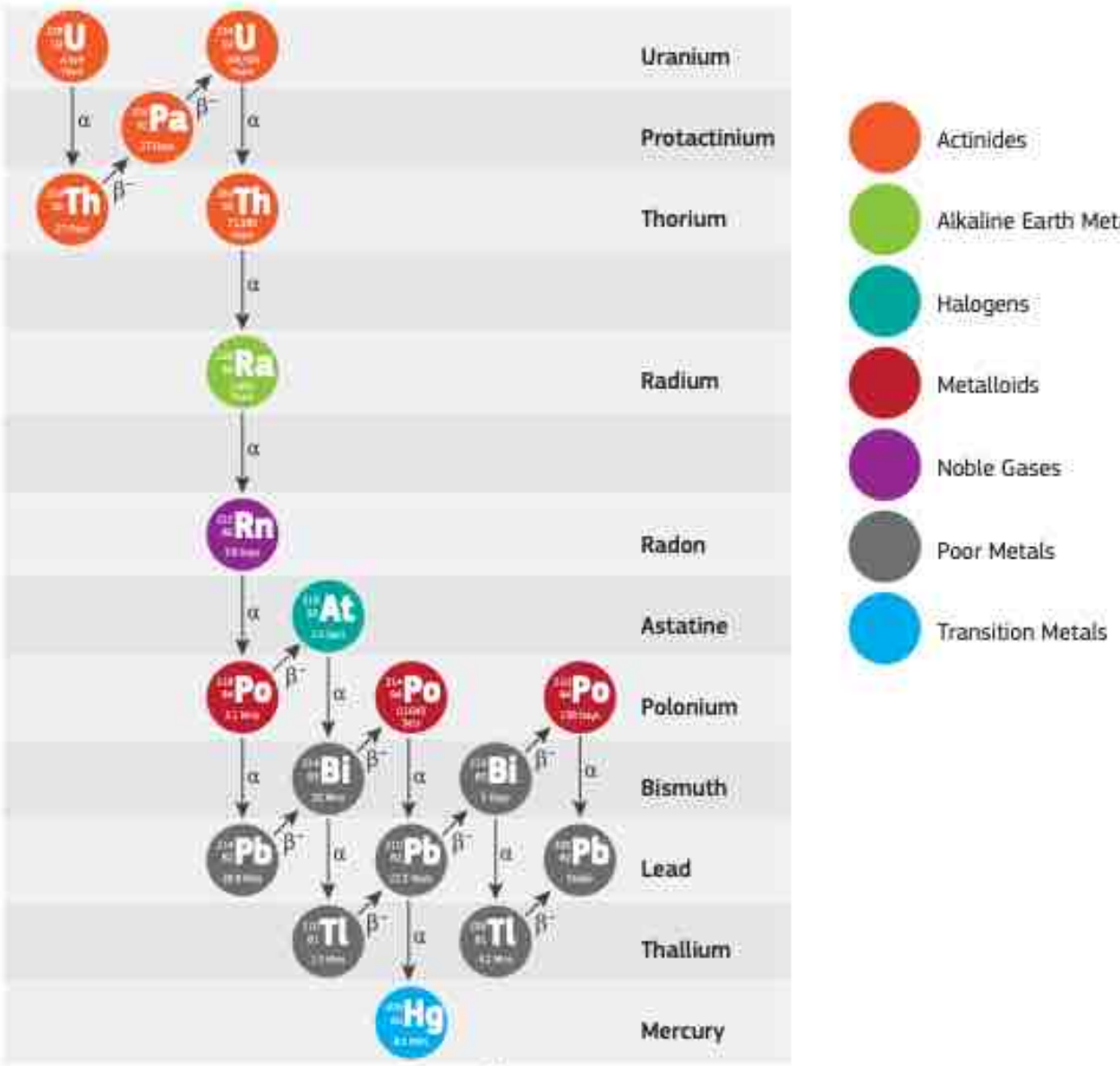

Figure 2-5
Natural ^{238}U radioactive series
Source: UNSCEAR 2000, Vol.1, ANNEX B Table 5

Goldschmidt classification

The geochemical classification of the elements, also called the **Goldschmidt classification** (after the work undertaken in the 1920s by the chemist Victor Goldschmidt), provides an understanding of the origin of the various proportions of chemical elements in the Earth's minerals and rocks, and more generally in the rocks of planets and meteorites.

It comes from the analysis of the various mineralogical phases in the crystallisation of a magma. It has been found that elements have a tendency to collect together in the various phases.

Goldschmidt introduced four classes of element:

- lithophiles, which have a dominant affinity for oxygen and consequently occur with aluminates and silicates;
- chalcophiles, which have a dominant affinity for sulphur (literally 'having an affinity for copper' due to an error by Victor Goldschmidt on originally giving the name which he thought meant 'having an affinity for sulphur');
- siderophiles, which have a dominant affinity for iron. This explains why metals such as gold and platinum are rare in the Earth's crust, having migrated with iron during the formation of the Earth's core;
- atmophiles, which have a dominant affinity for fluid phases. Thus hydrogen is an atmophile because it essentially occurs on Earth in sea water. The same is true for nitrogen and the inert gases.

Source: http://www.futura-sciences.us

Meta-autunite, a hydrated uranium phosphate. Origin: Hallmann Quarry, Kirchberg, Zwickau, Saxony, Germany.
Dimensions: 22 × 17 × 13 mm.
Source: Samples and photograph courtesy of Rolanda Sebastian Olivares

While the first isotopes of the U series are isotopes from the actinide series (U, Th, Pa and Ac), a change of the geochemical behaviour causes ^{226}Ra to be an alkali metal. The parent isotope of ^{222}Rn (^{226}Ra) displays a geochemical behaviour markedly different from that of U, by being less mobile in oxidising conditions, which can lead to U removal, whereas Ra remains in situ upon surface weathering (IAEA, 2014). Further contrasts in geochemical behaviour between U-series isotopes are observed when ^{226}Ra decays to ^{222}Rn, an atmophile element according to Goldschmidt's classification (i.e. an element that occurs as a liquid or gas at surface pressure and temperature ranges), and ultimately through the decay of ^{222}Rn to ^{210}Po and ^{210}Pb, which are classified as chalcophile elements, i.e. elements with an affinity for sulphur (IAEA, 1990). One of the most important forms of disruption of the U decay series corresponds to migration by diffusion or advection of ^{222}Rn as a noble gas (IAEA, 1990). U-series disequilibria can also be favoured by the alpha-recoil mechanism, which can enable the release of ^{230}Th, ^{226}Ra and ^{222}Rn from mineral grains. See Section 2.2.2 and Chapter 5 for more details about radon.

Due to its high ionic charge-to-radius ratio, U is a highly incompatible element, being classified as a High Field Strength Element (HFSE). (In petrology and geochemistry, an incompatible element is one that is unsuitable in size and/or charge to the cation sites of the minerals of which it is included (Wikipedia)). As an incompatible element, U partitions preferentially to the melted portion in a magmatic system, which increases its content during fractional crystallisation. Therefore, U tends to be incorporated in late-magmatic accessory minerals, such as monazite and zircon. These minerals, as well as xenotime and thorite, contain up to tens of mg/kg of U.

Most of the U present in crustal rocks is, however, found forming loose bonds with inter-crystal boundaries, adsorbed on mineral surfaces or dissolved in fluid inclusions and intergranular fluids, usually being labelled as labile U, and can readily be solubilised entering the hydrological cycle (De Vivo et al., 1984; Suksi, 2001). The contents and distribution of labile U are contingent upon alteration processes which may also cause radioactive disequilibria in the U series through selective leaching, diffusion, sorption and/or precipitation of U-series isotopes (Osmond & Ivanovich, 1992; Suksi, 2001). The susceptibility of U to leaching depends on the distribution and binding forms of U in the rock matrix, particularly on the oxidation state of U (Suksi, 2001). U is less susceptible to weathering when found in U-bearing weathering-resistant minerals, e.g. monazite and zircon, or adsorbed in Fe-oxyhydroxides, clay minerals and/or organic matter (Chabaux et al., 2003).

The incompatibility of uranium implies that highly differentiated felsic rocks (igneous rocks that are rich in feldspar and silicon) tend to have higher contents of U; granitic rocks contain an average of 2–5 mg/kg of U, depending on the magma source and the differentiation path. Metamorphic and sedimentary rocks deriving from felsic materials will inherit the U concentration of their parent rocks, as the most abundant U-bearing minerals are typically resistant to weathering processes. A significant enrichment of U in sedimentary rocks can be achieved by density-driven accumulation of these minerals, typical of placer deposits, as well as by absorption and/or adsorption of U in organic matter (Cumberland et al., 2016).

For these reasons, the upper crust is highly enriched in uranium, with a concentration value of 2.7 ±0.6 mg/kg (Rudnick & Gao, 2003), that is 10 times the value estimated for the lower crust, 0.2 mg/kg (Rudnick & Fountain, 1995), and 100 times the estimate for the primitive mantle, 0.02 mg/kg (Hofmann, 1988).

Extreme uranium concentrations have been found in phosphate rocks and bituminous shales (120 mg/kg, respectively 50–80 mg/kg) (Eisenbud, 1997). The decay products of uranium, ^{226}Ra and ^{222}Rn released from rocks and soils, are the source of the major fraction of dose originating from the natural internal emitters.

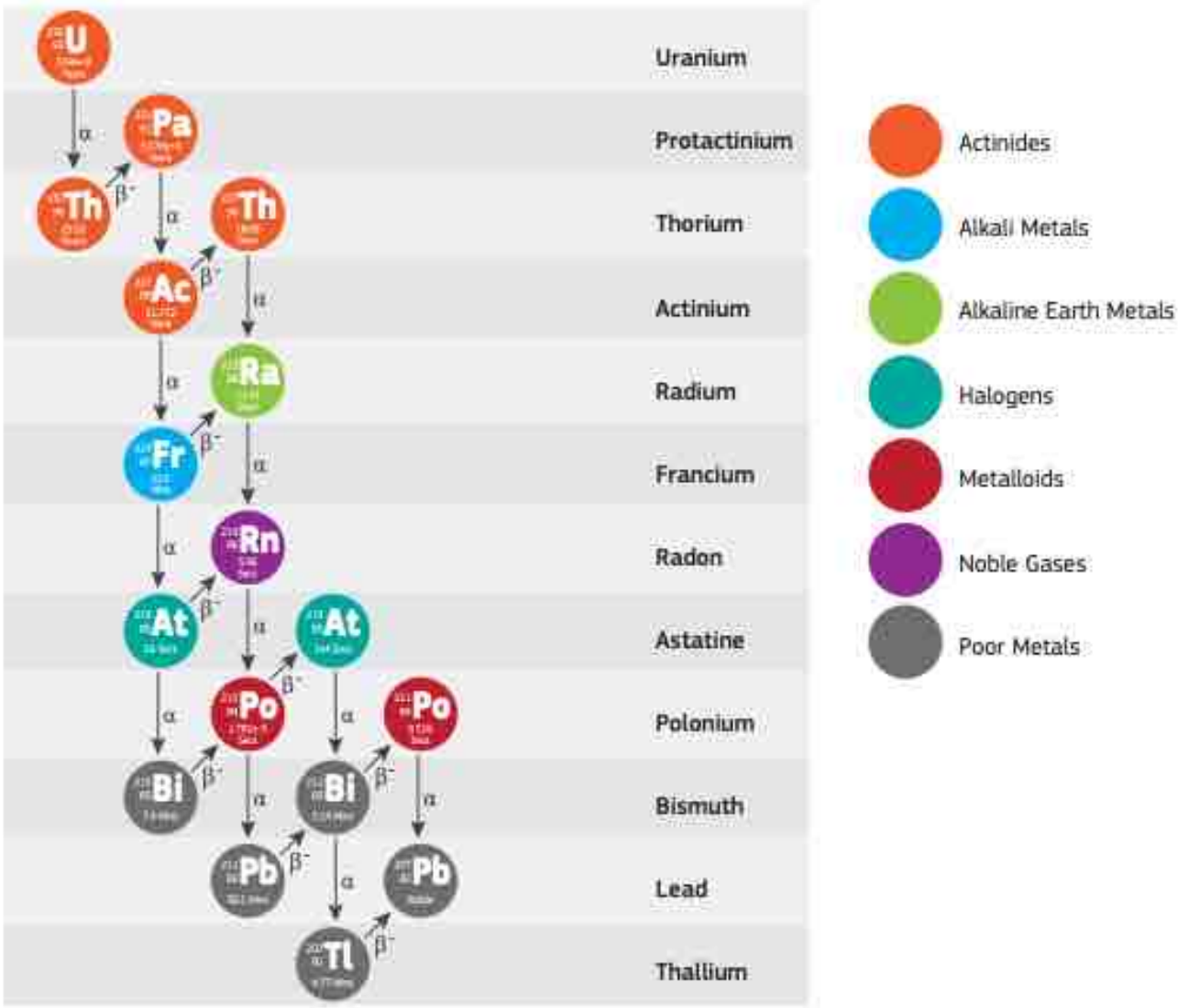

Figure 2-6.
Natural ^{238}U radioactive series.
Source: UNSCEAR, 2000, Vol. I, ANNEX B Table 1

Columnar lava (locally known as 'the church organ'), Aeolian islet near Stromboli, Italy
Source: Tom Gilfillan

Thorium

(For more details see Section 3.2.)

Thorium is an actinide series element with an atomic number of 90 and an atomic mass of 232. Thorium is radioactive with one main natural isotope, the primordial long-lived radionuclide ^{232}Th, which has the longest half-life (1.41×10^{10} years) of all known Th radioactive isotopes and comprises 99.98 % of Th total mass. Thorium decays through a long radioactive decay series (Figure 2-7), ending with the stable lead isotope ^{208}Pb.

The Thorium series includes actinium, radium, radon, polonium, bismuth, thallium and lead (Figure 2-7). Thorium is relatively insoluble, and is therefore present in biological materials only in small amounts. The principal source of human exposure is through inhalation of soil particles with suspended thorium (Eisenbud, 1997).

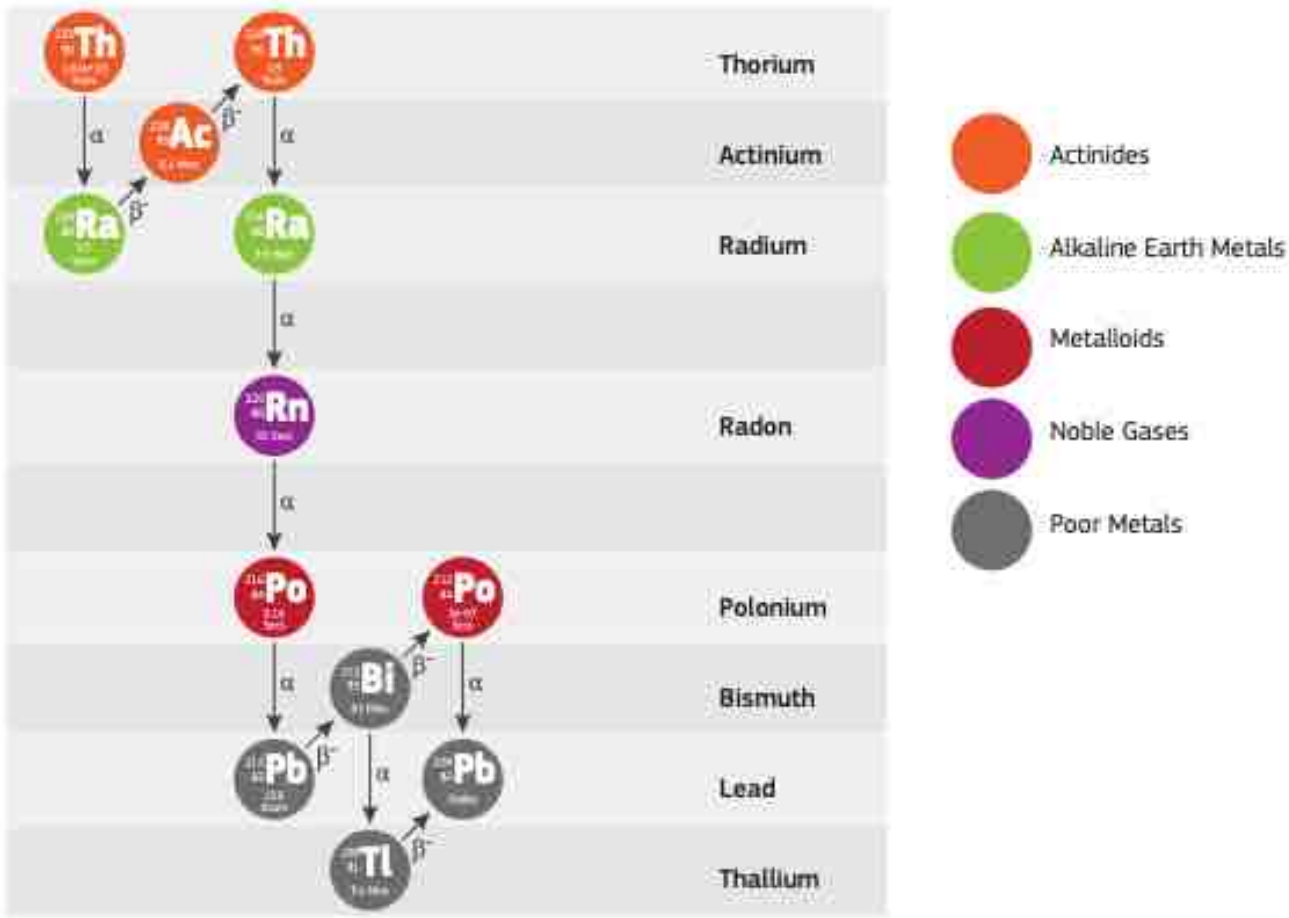

Figure 2-7.
Natural ^{232}Th radioactive series.
Source: UNSCEAR, 2000, Vol.1 Annex B Table 3.

Similarly to U, thorium is geochemically defined as a lithophile element (Goldschmidt, 1937). Thorium has only one important valence (+4) which, together with its ionisation energy and redox potential, implies that its geochemical behaviour is comparable to those of zirconium, cerium and hafnium, besides uranium (Martin et al., 1974).

Thorium is almost immobile in all near-surface conditions, except for very acidic environments, and its main host minerals are generally resistant to weathering. Additionally, Th is efficiently adsorbed by Fe-hydroxides, clay particles and organic matter (Chabaux et al., 2003). Thus, the solubilisation of Th present in bedrock or soil is unlikely, unless it enters surface waters as ThO_2 in suspended particles or colloidal state. Alkaline waters and the presence of humic matter in the fluid can, however, increase Th solubility and mobility (Hinck et al., 2010).

Thorium is a trace element in the Earth's crust (5.6 mg/kg; Rudnick & Gao, 2003), with a relative enrichment in the upper crust (10.5 mg/kg; Rudnick & Gao, 2003) due to its strong lithophile metallic character. Concentrations in common rock types range from 1.6 to 20 mg/kg. Monazite sands are one of the main sources of thorium, containing about 6% thorium. Consequently, monazite sand deposits are one of the areas with unusually high natural radioactivity (Aliyu, 2015). At present, thorium has a major use in nuclear power as a potential source of fissile material.

This yellow monazite crystal from Wanniglitscher (Switzerland) is 2 mm across. Monazite is the main Th repository in the Earth's crust.
Source: Sample courtesy of Pierre Grand. Photograph by Orlando S. Oliveira.

Amongst the daughter products of ^{232}Th, the major radiological hazards come from the radium, radon and polonium isotopes:

Radium (Ra) is a highly reactive alkaline Earth metal. ^{228}Ra has a half-life of 5.7 years;

Radon (Rn) is a colourless and odourless noble gas. The ^{220}Rn isotope, called **thoron**, derives from the ^{232}Th series and has a half-life of 55 seconds. It decays to a polonium isotope by emitting an alpha particle;

Polonium (Po) is a rare metal, or metalloid, of the 16th group, with a geochemical behaviour very similar to that of selenium and tellurium. The ^{216}Po isotope derives from the ^{232}Th series and has a half-life of 0.14 seconds. It decays to a lead isotope by emitting an alpha particle.

Potassium

(For more details see Section 3.3.)

The last primordial isotope discussed in detail is potassium.

Potassium (K) is an alkali metal (with one main oxidation state: +1) with 39 as atomic mass and three natural isotopes, including two stable ones, ^{39}K (93.3% of K total mass), ^{41}K (6.73% of K total mass), and the long-lived (half-life of 1.248×10^9 a), radioactive ^{40}K (0.0117%), which decays either to ^{40}Ca (89.3%) by emitting a beta particle, or, to gas ^{40}Ar (10.7%) by emitting a gamma ray of energy 1.46 MeV after electron capture.

Potassium is geochemically defined as a lithophile element (Goldschmidt, 1937). Furthermore, K is an incompatible element classified in the Large Ion Lithophile Elements (LILE) group, because of its low ionic charge-to-radius ratio. Like the other alkali metals, potassium has only one possible valence (+1). As for U and Th, due to its incompatibility, K enrichment increases with the progress of magmatic differentiation.

Potassium is found in several rock-forming minerals such as K-feldspar, micas (e.g. biotite and muscovite) and clay minerals (e.g. illite). The K concentration in rocks is usually expressed as an oxide percentage (K_2O). K_2O content in granitic rocks is 5 wt% on average, but may vary widely, while basaltic rocks have contents averaging 1-2 wt% of K_2O depending on their magmatic source (Rudnick & Gao, 2003). K content of 0.04 wt% is found in sea water; the increase of these contents due to evaporation may lead to precipitation of potassium salts such as sylvite (KCl) and carnallite ($KCl.MgCl_2.6(H_2O)$), which form the main K ore deposits.

Geological weathering of felsic rocks removes K from feldspars ($KAlSi_3O_8$) and micas ($X_2Y_{4-6}Z_8O_{20}(OH,F)_4$), in which X is K, Na, or Ca or less commonly Ba, Rb, or Cs; Y is Al, Mg, or Fe or less commonly Mn, Cr, Ti, Li, etc.; Z is chiefly Si or Al, but may also include Fe^{3+} or Ti allowing its transfer to the fluid phase. K is easily adsorbed by clay minerals and organic matter and enters the soil, which contains an average of 2 wt% of K_2O.

Potassium is the seventh-most abundant element in the Earth's crust and the sixth in the upper crust (K_2O is about 2.8%, Rudnick & Gao, 2003) and shows a lithophile / biophile character.

^{40}K is expected to follow the chemical behaviour of the two natural stable isotopes, so that their abundance proportions are expected to be preserved over different environments.

The potassium content, distributed uniformly in the human body, is about 0.18%. The radioactive isotope ^{40}K is 0.0117% of total potassium, while the rest is stable ^{39}K and ^{41}K. The average ^{40}K content in a human body weighing 70 kg is 4400 Bq, meaning that it undergoes 4400 radioactive decays within the body per second. Out of 4400 radioactive decays/per second, 470 are gamma rays, part of which come out of the body due to their higher penetrating power, and 3930 are beta radiations most of which are absorbed in the tissues. Potassium in the human body is homeostatic, a property of the system to regulate potassium content to equilibrium or constant value. However, its content depends on body height and weight, and a large number of studies have already been conducted to establish a kind of correlation between the body size and food habits (Rao, 2012).

Gamma-ray spectroscopy (see Section 2.5) is used to detect minute amounts of radioactive ^{40}K present in the human body; see an example in the figure below.

Argon (Ar), whose concentration is relatively high in the atmosphere (0.934%, third after nitrogen and oxygen) stems from ^{40}K decay in the Earth.

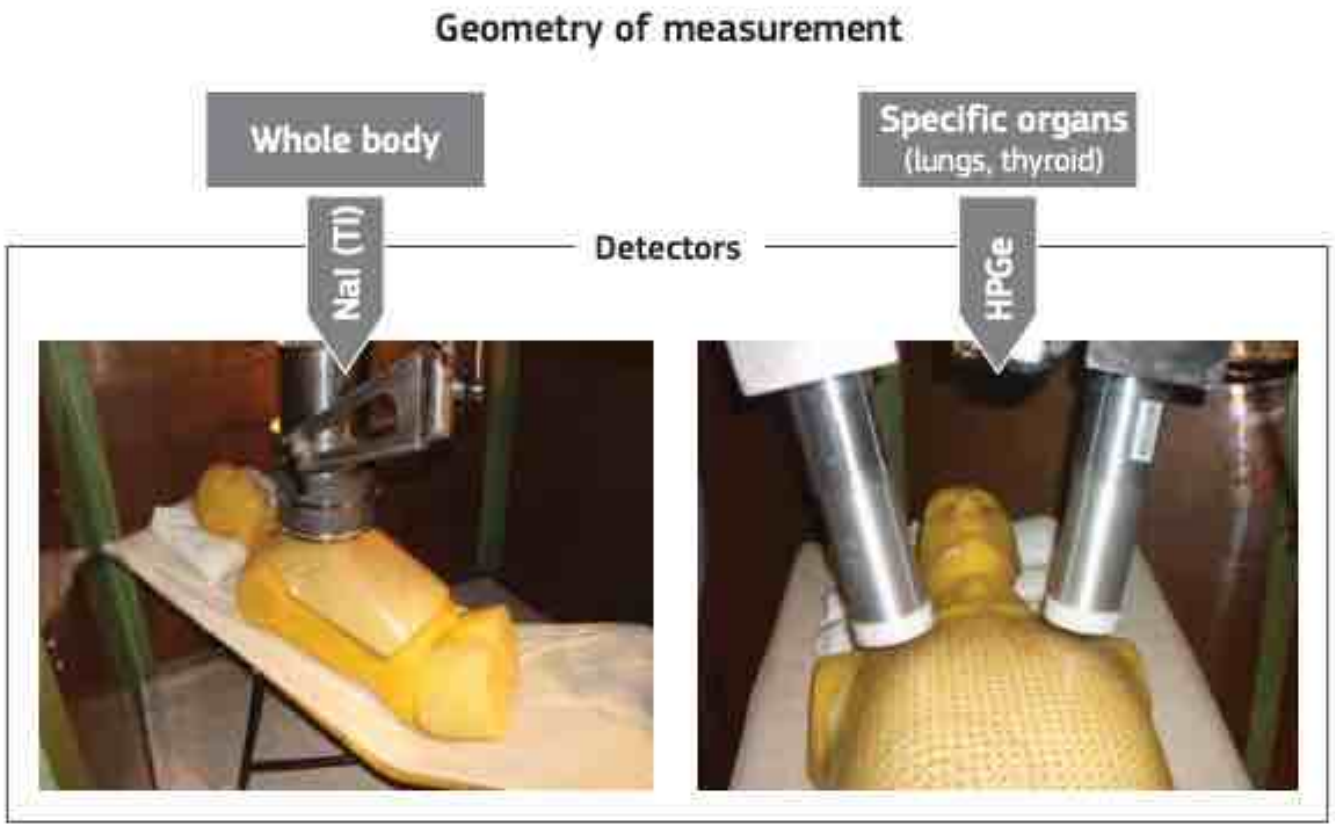

Measurement geometry : example with a Livermore phantom.
Source: JRC Ispra Whole Body Counter Laboratory

The hexagonal basal section of this white mica from Premia (Antigorio Valley, North Piedmont, Italy) is about 8 mm across. White mica is one the main rock-forming minerals with a high K content.
Source: Sample courtesy of Piero Gianti (Bologna), photograph by Orlando S. Olivari.

Radionuclides in water

Natural radioactivity in continental waters generally results from weathering of rocks and dissolution of the primordial radionuclides that they contain (mainly ^{40}K, ^{238}U, ^{232}Th, ^{226}Ra and ^{222}Rn). Therefore, their concentration essentially depends on the nature of the substratum and on the water aggressivity (pH, reduction potential (Eh) and complexing agent content). In most continental waters, the uranium concentration ranges from less than 0.1 to 10 µg/l (approximately from < 2.5 to 250 mBq/l). However, in some regions of the world, where natural radioactive minerals are particularly abundant, U concentration can reach much higher values, up to several mg/l. Although ^{234}U and ^{238}U should be in secular equilibrium, the energetic recoil associated with the disintegration of ^{238}U, different chemical properties of intermediate products (^{234}Th and ^{234}Pa) in the decay chain and differences in oxidation states between ^{234}U and ^{238}U often lead to a relative enrichment of ^{234}U in water.

^{226}Ra and ^{228}Ra are the most important radium isotopes found in water. Produced by the decay of ^{238}U and ^{232}Th respectively, their concentration depends on the content of their respective parent in the substratum. Since thorium is about three times more abundant than uranium in the lithosphere and a has a decay constant roughly three times higher, the global inventories of ^{226}Ra and ^{228}Ra should be roughly equal; however, locally specific geological structures of terrains lead to a great variability in the ratio between these two isotopes. In general, the Ra concentration in surface waters is low (0.4 – 40 mBq/l), and less than in most ground waters. Some mineral and thermal waters exhibit ^{226}Ra concentration values up to several Bq/l. ^{226}Ra, the daughter of ^{230}Th, is generally found in excess of its parent in most natural waters due to the greater solubility of Ra over Th. In freshwater, the highest concentrations of radium are found in limestone regions where it is more soluble in HCO_3 waters.

^{228}Ra is also found in excess of its parent ^{232}Th in natural waters. Products of radioactive decay in the U and Th series include radon (Rn) gas of which three isotopes exist. ^{222}Rn is the longest-lived and most abundant one. Loss of radon will cause disequilibrium between members of a decay chain.

Radon is a gaseous decay product of radium that can be found in rather high concentrations in well water (up to several hundred Bq/l) and in thermal springs (up to several kBq/l), but in negligible concentrations in surface water.

^{210}Po is largely insoluble. In the hydrological cycle, ^{210}Po generally follows its precursor ^{210}Pb. ^{210}Po is generally more readily adsorbed onto particulate matter than ^{210}Pb.

^{231}Pa is relatively insoluble when compared to uranium and radium.

2.2.2 Radon

Radon is a colourless, odourless, and radioactive noble gas, and is found in nature in three isotopes: ^{222}Rn, ^{220}Rn and ^{219}Rn (Nazaroff et al., 1998).

When ^{226}Ra, a descendent of the ^{238}U series, decays by alpha emission, it transmutes to its decay product ^{222}Rn, hereafter called radon, with a half-life of 3.8 days.

Similarly, ^{224}Ra, which is a descendant of the ^{232}Th chain, decays by alpha emission to ^{220}Rn, which is historically known as thoron and has a half-life of about 55.6 seconds.

^{219}Rn, historically called actinon, is a member of the ^{235}U chain and decays most rapidly, having a half-life of about 3.92 seconds.

Radon gas has a density of 9.73 g/l at 0 °C and 1 atm, which is 7.5 times higher than that of air. It is very soluble in water, with its solubility decreasing with increasing temperature (510 cm³/kg at 0 °C, 230 cm³/kg at 20 °C and 169 cm³/kg at 30 °C), but also very easily removable from it. Together with He, Ne, Ar, Kr and Xe, radon belongs to the family of noble gases, also known as inert gases. These are characterised by an absence of natural chemical compounds since they are essentially not chemically active.

Inhalation of radon gas is the second leading cause of lung cancer after cigarette smoking, and it is classified as a carcinogen agent by the World Health Organization (WHO, 2009), with the risk of lung cancer increasing 16 % per 100 Bq/m³ (Darby et al., 2005; WHO, 2009). The main risk of radon is not the gas itself, but its short-lived decay products, which are also alpha emitters. They attach to aerosol particles, thus increasing the chance of inhalation, and are easily trapped by lung tissues. There is a great concern to assess radon gas exposure in living and working environments and to reduce it to the lowest possible levels. In order to establish a level for indoor radon concentration, the European Union has considered 300 Bq/m³ as a reference level for all buildings (European Union, 2013).

A number of publications deal with the epidemiology of radon gas (e.g. Darby et al., 2005; Barros-Dios et al., 2002). Darby et al. (2005) carried out a collaborative analysis of individual data from 13 European countries where they showed that the estimated excess relative risk per 100 Bq/m³ increased to 0.16 (95 % confidence interval; see Figure 2-8).

Other important conclusions are the absence of a threshold and that the dose–response relation is linear even for those analyses for homes with measured indoor concentration below 200 Bq/m³. The relation between smoking, radon and lung cancer has also been studied. For life-long non-smokers, the absolute risk of developing lung cancer by the age of 75 years at radon concentrations of 0, 100 and 400 Bq/m³ is about 0.4 %, 0.5 % and 0.7 %, respectively. For smokers, the absolute risk of developing lung cancer by that age is about 25 times greater: 10 %, 12 % and 16 %, respectively. In the work carried out in Spain about radon and lung cancer (Barros-Dios et al., 2002), it was shown that radon is a risk factor for the general public even at concentrations below 37 Bq/m³. In the same way as the European study in 13 countries (Darby et al., 2005), the Spanish work showed that even at concentrations below 200 Bq/m³, radon may lead to a twofold or greater increase in lung cancer risk.

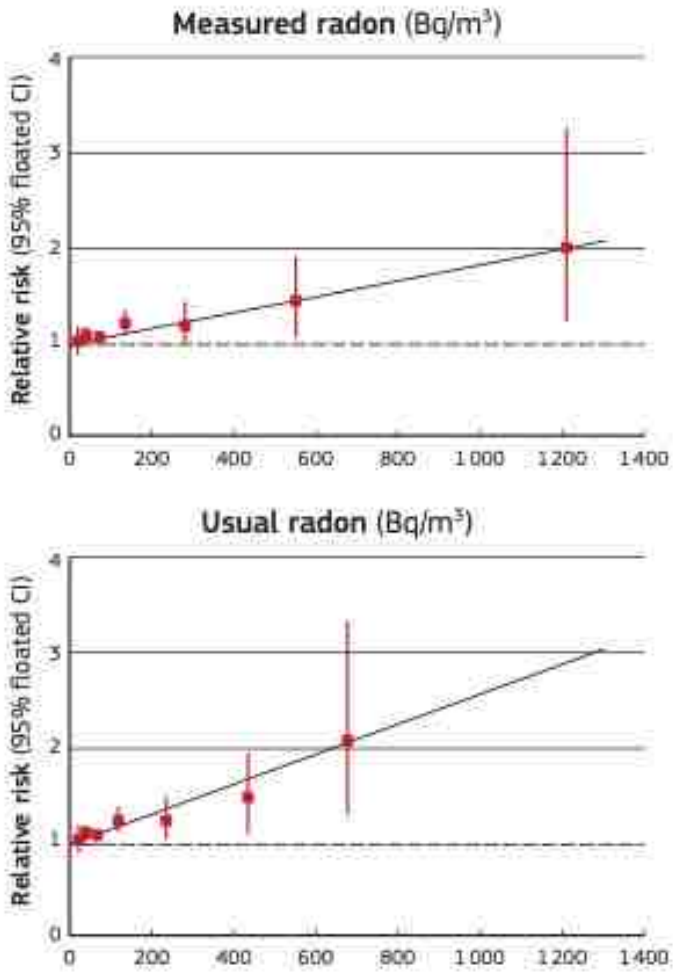

Figure 2-8.
Relative risk of lung cancer according to measured residential radon concentration and usual residential radon concentration, with best fitting straight lines (risks are relative to that at 0 Bq/m³). Usual radon takes into account random uncertainties in estimates of radon concentration over a period of 5–34 years.
Source: Darby et al., 2005.

Radon migration process

Radon gas is continuously produced in rock and soil mineral grains containing uranium and/or radium. Each radium atom decays by ejecting an alpha particle composed of two neutrons and two protons from its nucleus. As the alpha particle is ejected, the newly-formed radon atom recoils in the opposite direction. Alpha recoil is the most important factor that affects the release of radon from mineral grains (USGS, 1992) (Figure 2-9).

As shown in Figure 2-10, releases of radon from soils, rocks or building materials to the atmosphere take place through the following series of processes (Moed et. al., 1988):

a. **Emanation** – radon atoms formed from the decay of radium escape from the grains into the interstitial space between the grains.
b. **Transport** – diffusion and advective flow cause the movement of the emanated radon atoms through the residue or soil profile to the ground surface.
c. **Exhalation** – radon atoms that have been transported to the ground surface and then exhaled to the atmosphere.

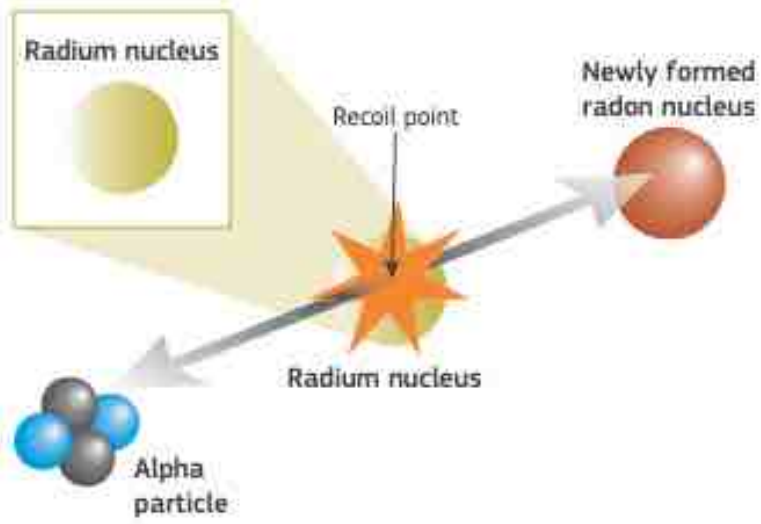

Figure 2-9
A radium atom decays to radon by releasing an alpha particle from its nucleus
Source: Modified from USGS, 1992

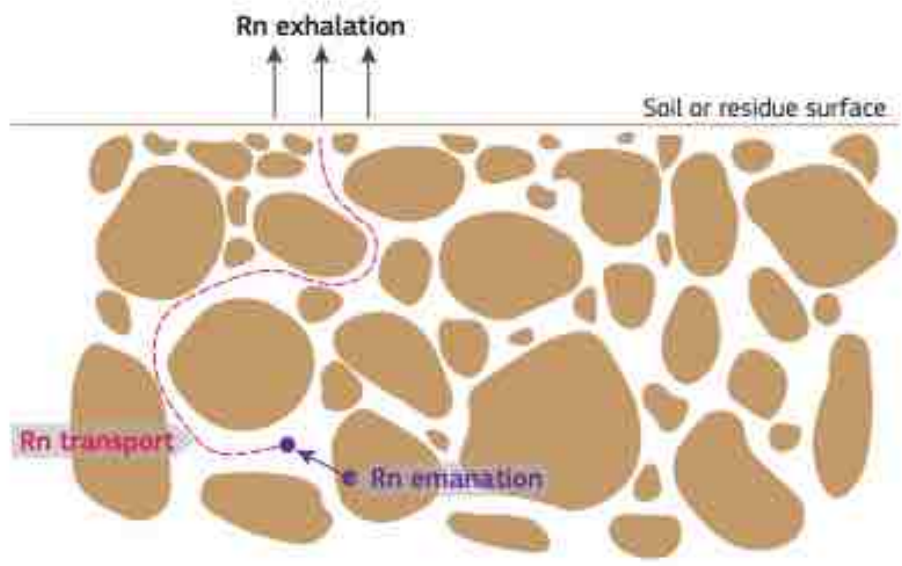

Figure 2-10
Processes leading to radon release into the atmosphere
Source: Ishimori et al. (2013)

Depending on the location of the radium atom in the mineral grain, the newly-formed radon atom enters the pore space between mineral grains (Figure 2-11). Radon atoms located within solid grains are unlikely to become available for release into the atmosphere, owing to their very low diffusion coefficient in solids. However, if they are located in the interstitial space between grains, they may escape the mineral to the pore space, from where they may travel through gaps, cracks and fractures up to the surface.

Most of the radon produced within a mineral grain remains embedded in the grain, while only 10 to 50 percent escapes to enter the pore space. The fraction of radon atoms that escapes from a medium into the interstitial space is known as the 'emanating power' or 'emanation coefficient', being the fraction of emanating radon atoms to total radon atoms; this quantity is dimensionless.

For soils, Tanner (1964 and 1980) describes that upon creation of a radon atom one of the following three things are likely to occur, as shown in Figure 2-11:

- Because of the energy of the recoil, the atom will travel a short distance inside the grain. If it does not encounter a surface, it remains within the grain (C).
- If the radon atom escapes from the grain, it might have enough energy to penetrate another grain and be trapped in it (G & D). If the ejected atom has low energy and encounters water between the grains, it might remain trapped or dissolved in the water (B).
- It is released into the pore space where diffusion and transport mechanisms migrate the radon (A & E).

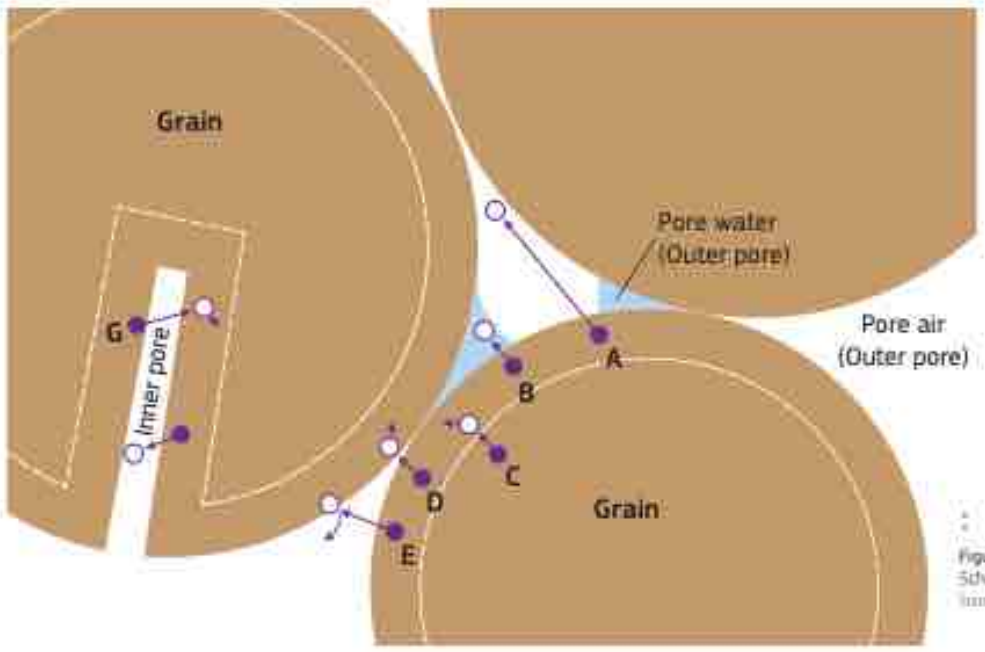

Figure 2-11
Schematic diagram of radon emanation
Source: Sakoda et al. (2011)

The distance that recoil radon can travel in a grain relies on the density and composition of the material (Sakoda et al., 2011). The recoil range of a radon atom after disintegration of radium is given as 30–50 nm for solids, 95 nm in water and 64 000 nm in air (Tanner, 1980; Greeman & Rose, 1995).

The emanation coefficient is affected by many factors related to the solid grain properties and the pore space properties such as radium distribution inside solid grains, solid grain size, moisture content and soil temperature.

	Rocks	Soils	Building materials
Emanation coefficient (%) **(Hassen et al., 2009)**	2.1–32	0.14–80	0.1–58

The relationship between radon emanation and the distribution of radium in soil grains has been investigated in several studies (Greeman & Rose 1995; Semkow, 1990; Schumann & Gundersen, 1996; Morawska & Jefferies, 1994; Morawska & Phillips, 1992; Nazaroff & Nero, 1988; Sakoda et al., 2010 and 2011). Radium distribution is concentrated over the surface layer of the grain (Nazaroff, 1988; Morawska & Phillips, 1993). It has been observed that radium concentration increases as the grain size decreases, and consequently the emanation coefficient increases as the radium content is more concentrated at the surface layers of the grains (Hassan et al., 2009). On the other hand, the emanation coefficient decreases as the solid grain size increases (De Martino et al., 1998; Markannen & Arvela, 1992; Hosoda et al., 2008). This is because the ratio of the grain surface area to its volume decreases. Therefore, the directed recoil radon atoms will decrease. Also the defused radon atom through the solid matrix will be decreased. For example, when the radius of the grains increases from 0.5, 1, to 8 μm, the emanation coefficient decreases from 40, 20, to 2 %, respectively (Morawska & Phillips, 1993).

Moisture content is well known to have a strong effect on the emanation coefficient (Markannen & Arvela, 1992; Breitner et al., 2010; Strong & Levins, 1982; Bossew, 2003). The stopping power of water is much greater than that of air which reduces loss of emanation of recoil radon atoms that results in penetrating a pore and embedding into another grain (Nazaroff et al., 1988; Nazaroff, 1992). Following emanation, for radon to reach the atmosphere, it must be transported through the pores of material so that a fraction of it reaches the surface before it decays. Radon movement in soil takes place with diffusion and convective (advective) flow. Radon emanation from soil is proportional to temperature (Stranden et al., 1984; Markkanen & Arvela, 1992; Iskandar et al., 2004; Goh et al., 1991). This may be due to a reduction in physical adsorption of radon onto grains that occurs during the diffusion through the porous material, as well as an increase of the transport coefficient with temperature. (Stranden et al., 1984).

Diffusion is always present, but is normally not a very efficient mechanism. Diffusion is migration from high concentration pores towards low-concentration pores governed by Fick's law.

Convective flow, induced by pressure differences, can be characterised by Darcy's law which relates the flow rate per unit cross-sectional area to the pressure gradient. Convective flow may be much more efficient, but not only in high-permeability materials. Note that in case of fractures, high-permeability pathways may exist in low-permeability materials (macroscopic or microscopic).

The release from the surface into the atmosphere is referred to as radon exhalation, and is characterised by the exhalation flux density Bq/(m^{2}s) (Ishimori et al., 2013). The amount of activity released per surface and time unit is called the exhalation rate (Porstendörfer, 1994). The radon exhalation rate is influenced by the geology of the study area, porosity and texture of the soil, humidity, temperature of the soil and physical properties of

building materials (intrinsic factors). The atmospheric temperature, atmospheric humidity, rainfall and pressure (extrinsic factors) will also affect the radon exhalation rate.

Radon levels can be very different according to the environmental compartment, namely outdoor, indoor, soil and ground water.

Radon released from rock and soil is quickly diluted in the atmosphere. Concentrations in the open air are normally very low and probably do not represent a hazard.

Radon concentration in outdoor air is generally low (2 – 20 Bq/m³), but may be as high as 100 Bq/m³ in some valleys when measured in the early morning. In indoor air, however, radon concentrations have been found to range from below 20 Bq/m³ to a maximum of 110 000 Bq/m³, but with a population-weighted world average of 40 Bq/m³. Averages per country range from 9 in Egypt, 20 in the UK, 22 in New Zealand, 44 in China, 46 in the United States, 108 in Sweden, 120 in Finland to 140 Bq/m³ in the Czech Republic (UNSCEAR, 2008; HPA, 2009). In the UK, radon concentrations in indoor air in dwellings range from less than 10 Bq/m³ to over 17 000 Bq/m³ (Rees et al., 2011), whereas those for outdoor air are generally low, on average 4 Bq/m³. Radon concentrations in soil air range from less than 1 to more than 10 000 kBq/m³; most soils in the United States contain between 5 and 55 kBq/m³ radon in soil air. The amount of radon dissolved in ground water ranges from about 3 to nearly 80 000 kBq/m³.

Radon concentration in ground water is generally much higher than in surface stream waters. This is because all ground water flows through rocks, in which uranium and radium are always present in different concentrations. At the surface, on the contrary, water tends to release radon, namely from natural aeration.

Since building materials derive from natural resources, namely rocks, they emit radon, both ^{222}Rn and ^{220}Rn isotopes, as well as gamma radiation.

Figure 2-12 shows how radon can enter a typical house: through cracks in solid floors, construction joints, cracks in walls, gaps in suspended floors, gaps around service pipes, cavities inside walls, the water supply.

There are three main sources of elevated indoor radon levels:

- **The underground soil**. Radon belongs to the decay chain of primordial ^{238}U. It is the direct product of ^{226}Ra; therefore wherever radium is present, there is a possibility of having high radon values. Uranium and radium are found in almost every soil type although in very different concentrations. Hence, in most cases the rocks and soil underneath and in the surroundings of a house are the reason for having significant indoor radon levels.
- **Building materials**. This is the second cause of radon concentration indoors. In some cases, the building materials may be the main reason for having high indoor levels. This is the case for the so-called blue concrete and other building materials that may increase indoor radon concentrations (Del Claro et al., 2017).
- The third cause is the **radon content in water**. It is very rare to find water as the source of having high radon values inside dwellings. Nevertheless, there are places where this source is not negligible, such as in thermal spas (Moreno et al., 2018).

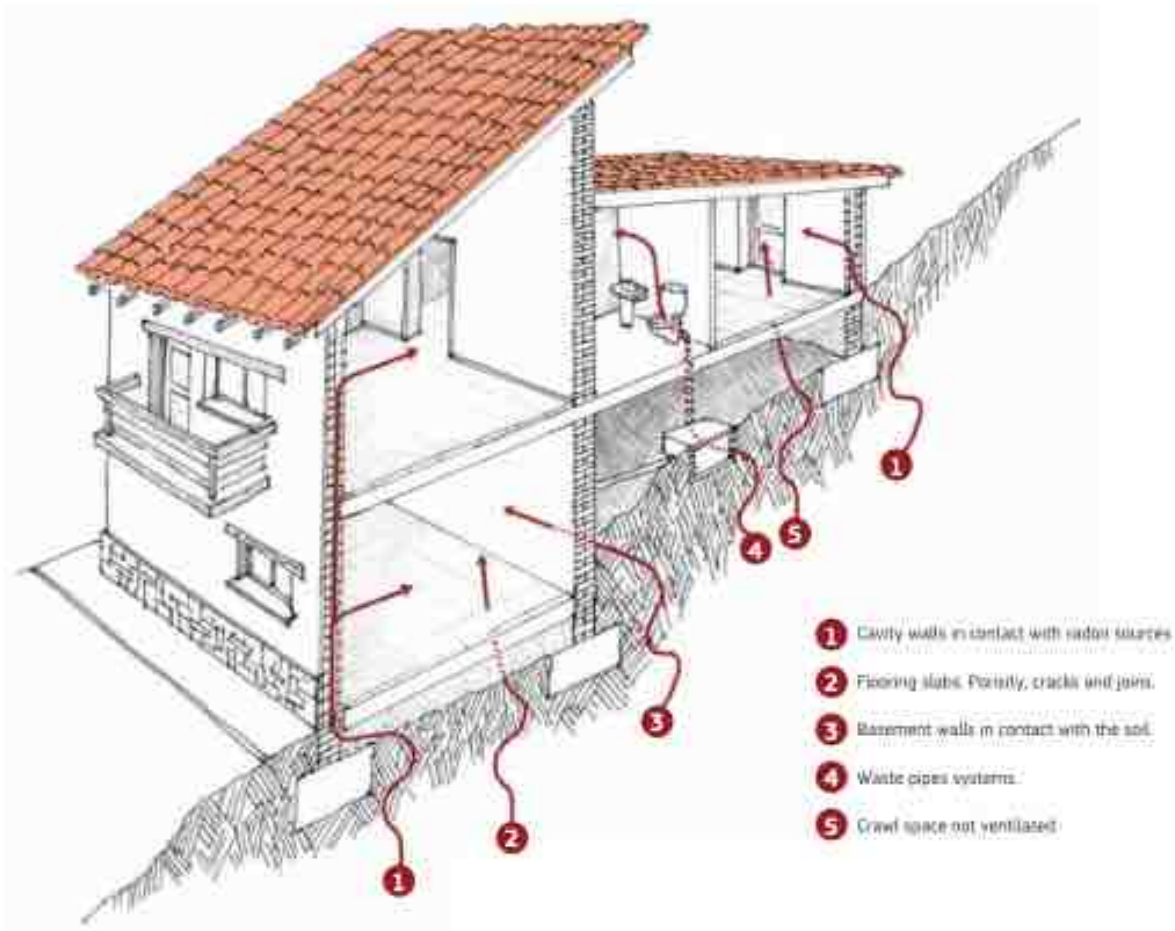

Figure 2-12.
Main sources of radon gas entry into a house
Source: Figure revised by Borja Frutos Vázquez

Radon progeny

For human beings, the problems with indoor radon are linked to inhalation of radon progenies. This problem is complex because many factors affect the amount of radon progeny, their entry into the human respiratory track, and their deposit on lung tissues, which increases the risk of triggering cancer growth. Radon progeny (Figure 2-13) is solids rapidly attached to the aerosols of indoor air.

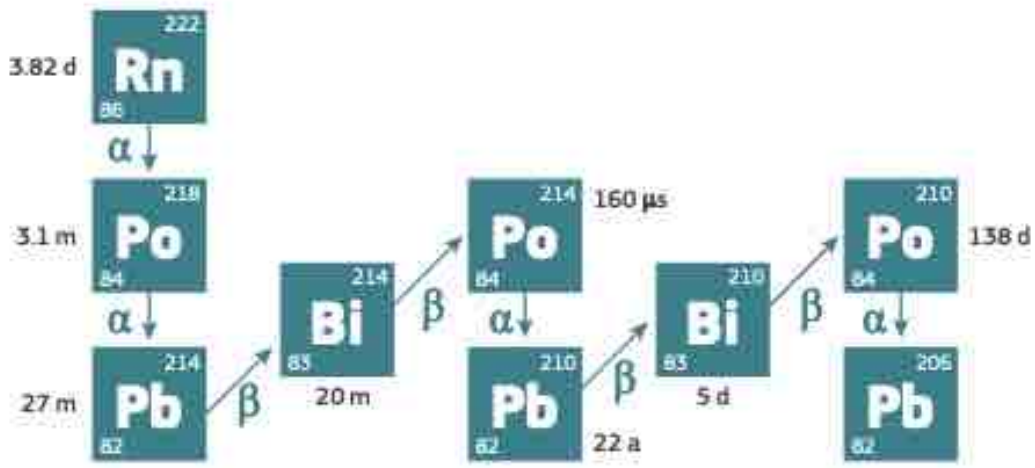

Figure 2-13.
Radon progeny
Source: Modified from UNSCEAR, 2000, Vol.1 ANNEX B Table 3

The ^{210}Pb isotope, with a much longer half-life of 22.3 years, and its decay products are called long-lived radon progenies, which contribute to creating cancer in humans since ^{210}Pb is deposited on the surface of the respiratory track.

Radon progeny produced by radon entry indoors reacts very fast (< 1 s) with trace gas and air vapours of the indoor air and becomes small-aerosol particles with a diameter of 0.5 – 5 nm, called clusters or 'unattached' radionuclides. Besides the cluster formation, radon progenies attach to the existing aerosol particles with a diameter of 10 – 1 000 nm, during 1 – 100 s, called 'attached' radionuclides. The aerosol particles, which now carry the radon progenies, diffuse in the indoor atmosphere and deposit on any available room surface. Moreover, radon progenies attached to aerosol particles can be detached due to recoil effect after mainly an alpha decay (Jacobi, 1972; Porstendörfer, 1984; Swedjemark, 1983). The above decay of radon progeny indoors is illustrated in Figure 2-14.

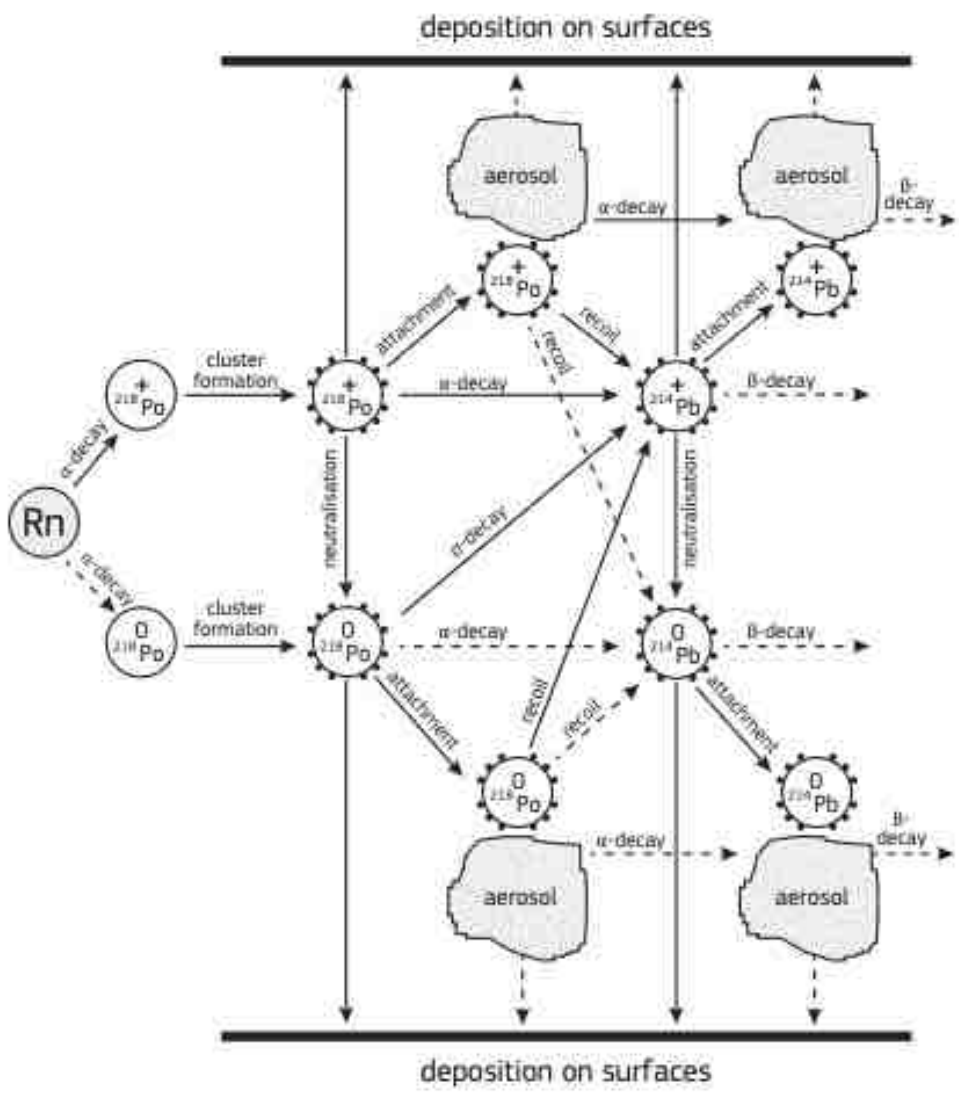

Figure 2-14
Radon progeny behaviour in indoor air – unattached-free and attached to aerosol particle
Source: modified from UNSCEAR, 1993

The following differential equations express the decay of indoor radon progenies (C, Bq/m³) in terms of free (f) and attached (a) nuclei:

$$\frac{dC_i^f}{dt} = kC_{0,i}^f + \lambda_{i-1}C_{i-1}^f + r_i\lambda_{i-1}C_{i-1}^a - (k + \lambda_i + q^f)C_i^f \quad (2\text{-}10)$$

$$\frac{dC_i^a}{dt} = kC_{0,i}^a + \lambda_{i-1}(1 - r_i)C_{i-1}^a + XC_i^f - (k + \lambda_i + q^a)C_i^a \quad (2\text{-}11)$$

where λ is the decay constant, k is the room ventilation rate, X is the attachment rate, q is the deposition rate and r is the recoil factor of each radon progeny, i = 1, 2, 3 corresponding to ^{218}Po, ^{214}Pb and ^{214}Bi, respectively, and C_0 is the indoor radon concentration.

Most of the newly-formed radon progenies in cluster formation (unattached mode) are positively charged and have high mobility. This mobility is characterised by the diffusion coefficient (cm²/s) that chiefly controls the formation of radioactive aerosols by attachment and also by the deposition velocity (cm/s) on room surface and human lungs. Diffusion coefficients for radon progenies range from 0.025 up to 0.085 cm²/s, depending on water vapour and the content of trace gases (NO_x, NH_3, SO_2) in the air. This also influences the neutralisation process of the positively charged clusters, especially in the case of polonium isotopes and so the production of attached nuclei (Porstendörfer & Reineking, 1992). Moreover, diffusion coefficients strongly depend on the aerosol particles diameter (Figure 2-15). Small aerosol particle (clusters-unattached mode) have high diffusion coefficients (> 0.01 cm²/s), while major aerosol particles (attached mode) have very low diffusion coefficients (< 0.0001 cm²/s).

The process by which radon progenies attach to indoor aerosol particles is characterised by attachment coefficient β (cm³/h), which is also influenced by the water vapour and trace gases in indoor air. The attachment coefficient is determined by pure diffusion according to the equations:

$\beta = 2\pi D_0 d$, for aerosol particle diameters (d > 1 μm), where D_0 is the diffusion coefficient;

$\beta = \pi v_0 d^2/4$, for aerosol particle diameters (d < 0.1 μm), where the coefficient is controlled by pure kinetic theory and it is proportional to the particles surface, and v_0 is the mean thermal velocity (Knutson et al., 1984; Porstendörfer & Reineking, 1992). The attachment coefficient also strongly depends on the aerosol particle diameter (Figure 2-16).

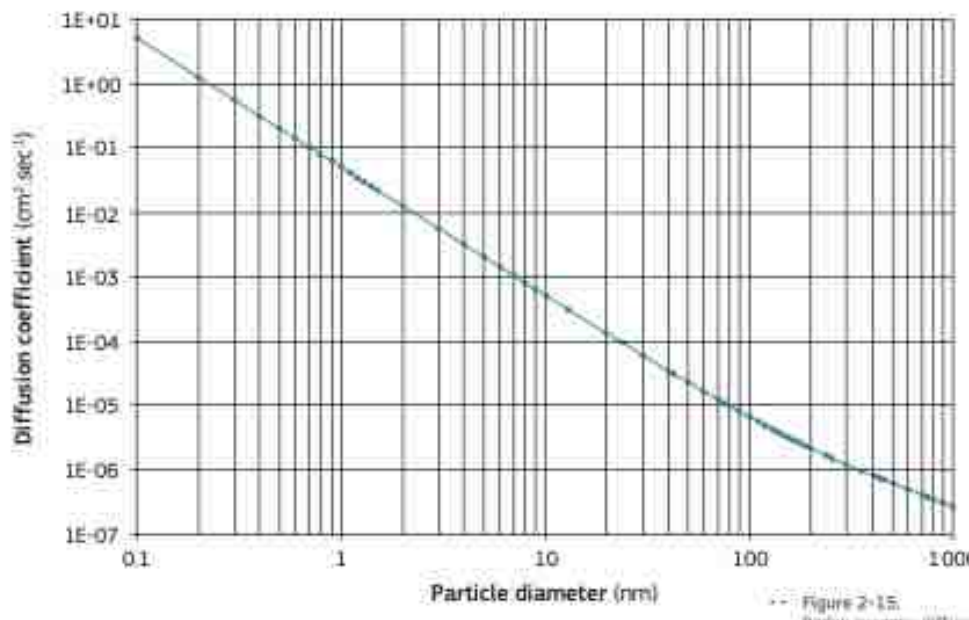

Figure 2-15
Radon progeny diffusion coefficient correlated to aerosol particle diameter
Source: Porstendörfer, 1991

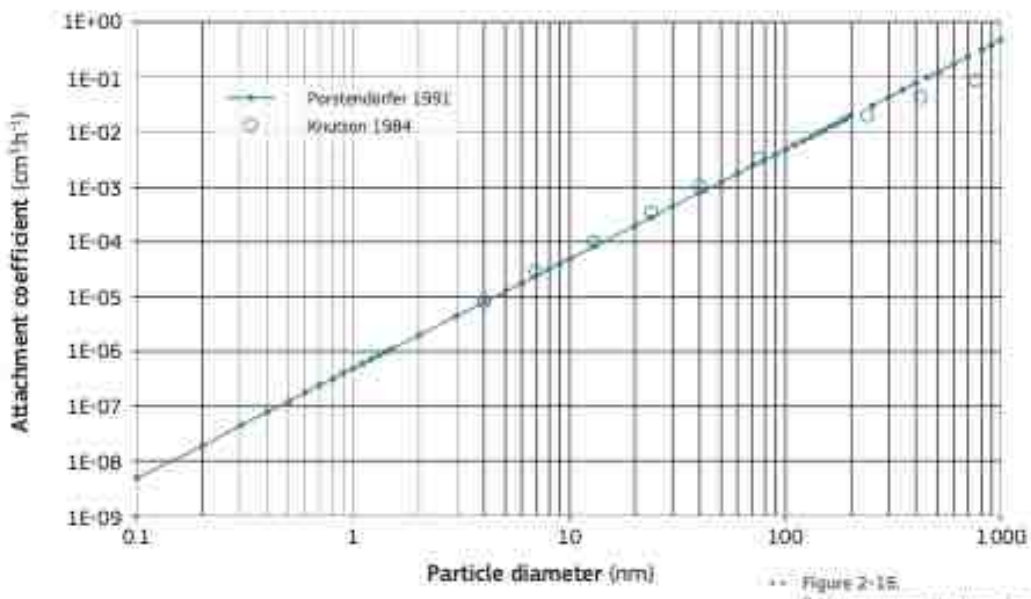

Figure 2-16
Radon progeny attachment coefficient correlated to aerosol particles diameter
Source: Knutson et al., 1984; Porstendörfer 1991

Aerosol particles in more detail

Small aerosol particles (clusters–unattached mode) have very low attachment coefficients (< 0.0001 cm^3/h), while major aerosol particles (attached mode) have high attachment coefficients (> 0.01 cm^3/h). The average indoor attachment coefficient is $\sim 5 \times 10^{-3}$ cm^3/h, while for outdoor it is $\sim 2 \times 10^{-3}$ cm^3/h. The attachment rate X (h^{-1}) is related to the attachment coefficient though the following integral:

$$X = \int_{0}^{\infty} Z(x)\ \beta(x)\ dx \qquad (2\text{-}12)$$

where Z(x) is the aerosol particle concentration (cm^{-3}). The attachment rate dependence on the aerosol particle concentration and diameter (nm) is presented in Figure 2-17 (Porstendörfer & Reineking, 1992; Porstendörfer et al., 2005). A high attachment rate (>100 h^{-1}) is associated with a high aerosol particle concentration and diameter, like outdoor. Indoor, the low aerosol particles concentration and diameter yield a low attachment rate (<10 h^{-1}).

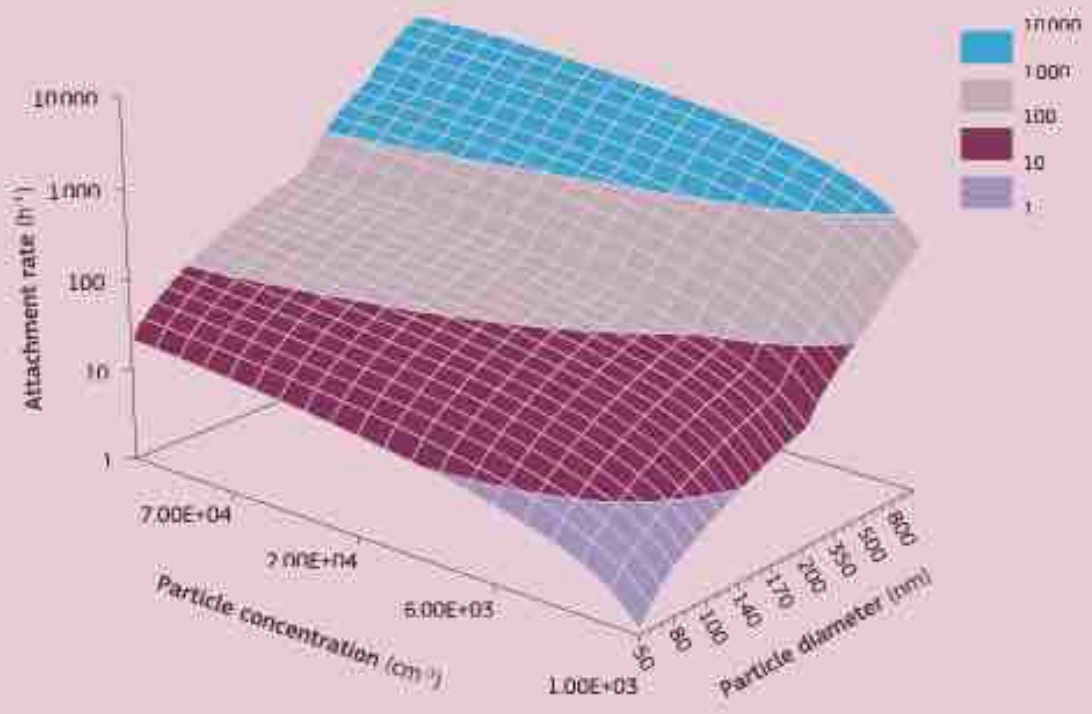

Figure 2-17.
Radon progenies attachment rate as a function of aerosol particle diameter and indoor concentration.
Source: Porstendörfer & Reineking, 1992; Porstendörfer et al., 2005.

The aerosol particles carrying radon progenies can be removed from the indoor atmosphere by transport towards any available surface (eddy diffusivity, D_T) and by precipitation of aerosol particles on surfaces (dry deposition). The aerosol particle number deposited per unit surface and time depends on particle diameter and texture of the surface, and is expressed as follows:

$$\Phi(d) = \left[D_T(z) + D_B(d)\right] \frac{dZ(z,d)}{dz} + v_s(d)\, Z(z,d) \qquad (2\text{-}13)$$

where Z(z,d) is the indoor aerosol particle concentration with diameter d and at height z above the surface. The turbulence-eddy diffusivity ($D_T(z)$) is much higher than Brownian diffusion ($D_B(d)$) and sedimentation ($v_s(d)$). The dry deposition rate can be characterised by introducing the depositional velocity, $v_g = \Phi(d) / Z(z,d)$. The deposition velocity is usually normalised by the friction velocity ($u^* = 40$ cm/s) due to eddy diffusivity, as follows: $v_g^+ = v_g/u^*$, and it is strongly influenced by the aerosol particle diameter (Figure 2-18) (Porstendörfer, 1991). Small aerosol particles (clusters-unattached mode) have high deposition velocity (>1 cm/s), while major aerosol particles (attached mode) have very low deposition velocity (<0.01 cm^2/s), assuming surface textures like filter paper. In well-mixed room air, the radon progenies deposition rate q (h^{-1}) depends on the deposition velocity and the room-surface-to-volume ratio S/V (m^{-1}) through the formula:

$$q = v_g\,(S/V) \qquad (2\text{-}14)$$

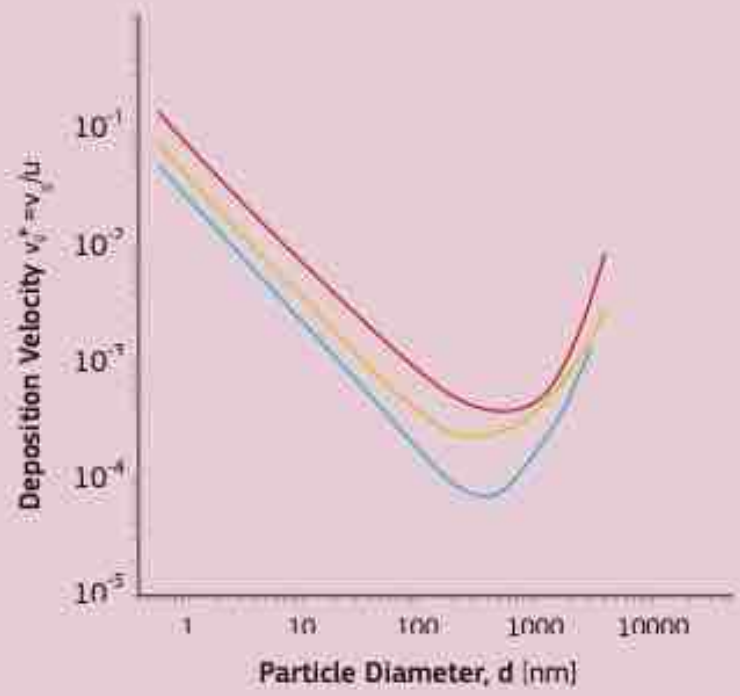

Figure 2-18.
Radon progenies deposition velocity normalised to friction velocity (40 cm/s) as a function of aerosol particle diameter. The lines correspond to simulated results on filter paper, Al-foil and grass.
Source: Wicke et al., 1984; Porstendörfer, 1991.

In residential rooms, high ratios of S/V ~5 m^{-1} should be attributed to room furniture. Small aerosol particles (clusters-unattached mode) have high deposition rates (>10/h), while major aerosol particles (attached mode) have very low deposition rates (<0.4 cm/s) (Knutson et al., 1984; Porstendörfer & Reineking, 1992).

Aerosol particles which are carriers of ^{214}Pb and ^{214}Bi (^{214}Po) in attached mode, have a mean activity size distribution ($dC_i / (d(\log d_{ae})\, C_i$) due to their aerodynamic equivalent diameter, d_{ae} (nm), as presented in Figure 2-19. The activity mean aerodynamic diameter (AMAD) of aerosol particles carrying ^{214}Pb nuclei indoors is ~200 nm, while ^{214}Bi attaches to aerosol particles with higher AMAD of ~280 nm. Outdoor, the AMAD increases up to 400 nm, since the surfaces available for aerosols to deposit are small, thus giving time for larger aerosol particles to form (Reineking et al., 1988). In case of ^{214}Po nuclei, another peak should be included at low AMAD of ~1 nm, corresponding to the unattached radon progenies during the clustering process. The indoor radon progenies total concentration (Bq/m^3) is the sum of the unattached (f) and attached (a) mode concentrations. The ratio of unattached-to-total radon progenies is defined as the unattached fraction (f_p) and refers mostly to ^{218}Po nuclei (Tu & Knutson, 1988; Reineking & Porstendörfer, 1990).

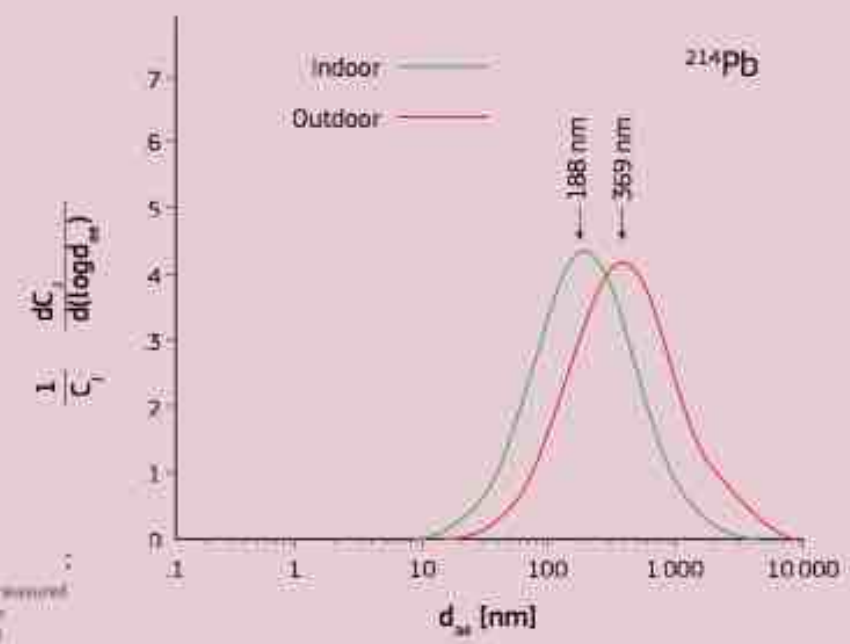

Figure 2-19.
Mean activity size distributions measured inside a closed room and outdoor.
Source: Reineking & Porstendörfer, 1990.

Health hazard due to radon progenies

Alpha particles and electrons emitted by deposited radon progenies are registered in lung tissues and so form the source of lung cancer. Short-lived radon progenies are the main contributors because two alpha particles (6.00 and 7.96 MeV) and two electrons (1.02 and 3.27 MeV max) can be absorbed by the tissue within hours, while long-lived radon progenies decay and produce one electron (0.017 MeV) and one alpha particle (5.3 MeV) over years. The amount of energy that potentially irradiates the lung-tissues and the duration determine the health effects, like cancer and other chronic pulmonary diseases (UNSCEAR, 1993). The crucial amount depends on the equilibrium achieved between radon and its progenies inhaled by the inhabitants indoor, and is called the **equilibrium factor,** F (Swedjemark, 1983). Mixtures of radon and its short-lived progenies exist in air inhaled that is not in equilibrium, so the potential alpha particle energy registered in lung tissues varies considerably. As a result, a new quantity has been introduced as the **equilibrium equivalent concentration of radon** (EEC), which is the activity of radon in equilibrium with its progenies that register the same potential alpha particle energy (Jacobi, 1972). The **equilibrium factor** is therefore defined as:

$$F = EER / C_0 = (0.105\, C_{Po} + 0.505\, C_{Pb} + 0.380\, C_{Bi}) / C_0 \quad (2\text{-}15)$$

where the constants are the fractional contributions of each radon progeny to the total potential alpha energy registered to the lung-tissues (UNSCEAR, 1993, 2000). The equilibrium factor is also strongly influenced by the air quality and the available deposition surfaces and their texture as well as the volume of the room. The indoor air quality includes both toxic and radioactive specimens entering from outdoor, foundation ground, building materials, water and oil-gas supply (Nero & Nazaroff, 1984). Indoor atmospheric conditions are mostly governed by the life style of the residents (room ventilation, heating, showering, washing, smoking) and their preferences about the volume and the available room surfaces (small/large room, heavy decoration with furniture, carpets, textures and plants) (Porstendörfer & Reineking, 1992).

Equilibrium factor, unattached fraction, aerosol concentration and attachment rate

In Figure 2-20, the equilibrium factor (F) and the unattached fraction (f_p) are correlated with aerosol particles concentration (cm^{-3}) and attachment rate X (h^{-1}). Various scenarios of the deposition rate q (h^{-1}) of the unattached (f) radon progenies are illustrated, while the attached deposition rate is constant $q^a = 0.2 h^{-1}$. Other constant input parameters, such as radon concentration (C_0 = 3.7 Bq/m³), radon entry rate indoors (e = 5 Bq/m³/h), attached fraction (F_a = 0.55), polonium-to-radon ratio (R_f) and room ventilation rate (v = 0.2 h^{-1}), are also presented.

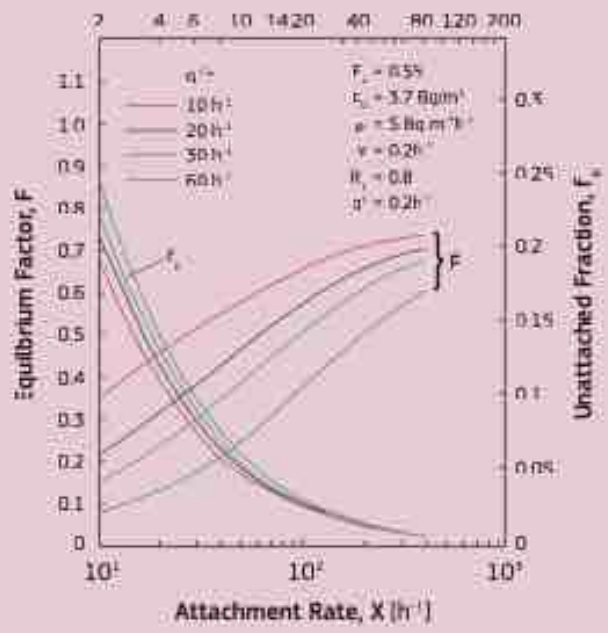

Figure 2-20
Equilibrium factor (F) and unattached fraction (f_p) for radon daughters as a function of attachment rate (X) and aerosol concentration (Z)
Source: Porstendörfer, 1994

The equilibrium factor (F) and the unattached fraction (f_p) are negatively correlated with aerosol particle concentration (cm^{-3}) and attachment rate X (h^{-1}). The equilibrium factor varies more than the unattached fraction due to unattached deposition rate (qa) variation from 10 up to 60 h^{-1}. A high aerosol particle concentration always increases the attachment rate, and so the unattached fraction is reduced to 0.01, while the equilibrium factor increases to 0.7. The above conditions are similar to the outdoor atmosphere, while the situation is opposite for indoor. A low aerosol particle concentration decreases the attachment rate, and so the unattached fraction increases up to 0.25, while the equilibrium factor decreases down to 0.1. Data presented in Figure 2-20 are based on constant ventilation rate of the room, although room ventilation is the most effective factor to control indoor radon and its progenies concentration.

The room ventilation rate is influenced by natural factors such as the indoor-outdoor temperature difference and wind speed. Moreover, the ventilation rate is most influenced by the habits of the residents, such as window opening and air-condition applied. A high ventilation rate caused by natural factors should be avoided, since high radon entry indoor due to sub-ground is expected. However, frequent windows' opening is a habit that definitely reduces the equilibrium factor indoor (and also radon concentration itself). A normally ventilated room (0.5 h^{-1}) corresponds to an equilibrium factor of ~0.5, low ventilation (0.1 h^{-1}) to a factor of ~0.7 and high (>1 h^{-1}) to a factor of ~0.2 (Mowris & Fisk, 1988).

The health hazard due to radon progenies is expressed through the effective dose rate received by the lung tissues by following the formula (ICRP 65, 1994):

$$E(Sv/a) = f_{P\text{-}eq} \cdot D_C \cdot B \cdot C_{EER} \quad (2\text{-}16)$$

where C_{EER} is the Equilibrium Equivalent Radon concentration defined as C_{Rn}*F, while $f_{P\text{-}eq}$ is the conversion factor from equilibrium equivalent radon concentration to potential alpha energy concentration, PAEC ($5.56*10^{-9}$ J/m³ per Bq/m³), D_c is the conversion factor from potential alpha energy concentration to the effective dose (2 Sv/J), F is the equilibrium factor (Equation 2-14 and Figure 2-20) and B is the annual breathing rate (7 013 m³/a).

So for dosimetric purposes, measuring this equilibrium factor F is highly important. There are several ways to measure F, and a large variability in the value of F has been reported (Chen, 2018). Another important fact related to F is that, while it is known that indoor radon concentration shows a large diurnal variability, the value of F is more constant due to the fact that radon and its daughters increase and decay altogether. It is very common to adopt an equilibrium factor of 0.4 (ICRP Publication 65, 1993; ICRP Publication 137, 2017), even if this value can be easily modified by processes such as cooking, space heating, smoking or ultrasonic humidification.

2.2.3 Environmental and exposure pathways

Humans are continuously exposed to ionising radiation from natural sources of radioactivity. Natural radionuclides, both terrestrial and cosmogenic, migrate in the environment through different pathways: air, water, rock, soil and the food chain. Then, radionuclides may enter the human body through ingestion (food and drinking water) and inhalation, giving the so-called internal exposure. Indeed, external exposure is due to cosmic radiation and radiation from terrestrial radionuclides present in soil, rocks and building materials.

Figure 2-20 gives a simplified description of the pathways of natural radioactivity through the environment and the different exposure pathways.

Pathways through the environment

Atmosphere:

Natural radionuclides present in the atmosphere, both having terrestrial or cosmogenic origin, can be inhaled directly by humans or removed from the air following other pathways. These particles can be removed from the atmosphere when air currents cannot keep them suspended or after rain and snow events. When particles are removed from the atmosphere, they may land in water, on soil, or on any kind of surface. These particles may return to the atmosphere by resuspension, which occurs when wind or some other natural or human activity generates clouds of dust containing radionuclides or through water evaporation.

Water:

There are several ways in which natural radionuclides can end up in water. They may be deposited by air, or released from the ground through erosion. Once in the water, some radionuclides will move with it while others will be deposited on the surrounding soil or rocks. Factors affecting their mobility in water are the solubility in water and the ability to adhere to the surfaces of rocks and soil through which the water flows.

Food Chain:

Natural radionuclides in soil, water and air may enter into the food chain. Plants are capable of absorbing radionuclides in the same way as other minerals are absorbed. Animals drink water and eat plants, and some of the radionuclides present in water and food will remain in their bodies. Airborne radionuclides deposited on the surface of the plants can be ingested by animals as well.

Subsequently, water, plants and animals will become food for humans by which natural radionuclides enter the organism causing internal exposure.

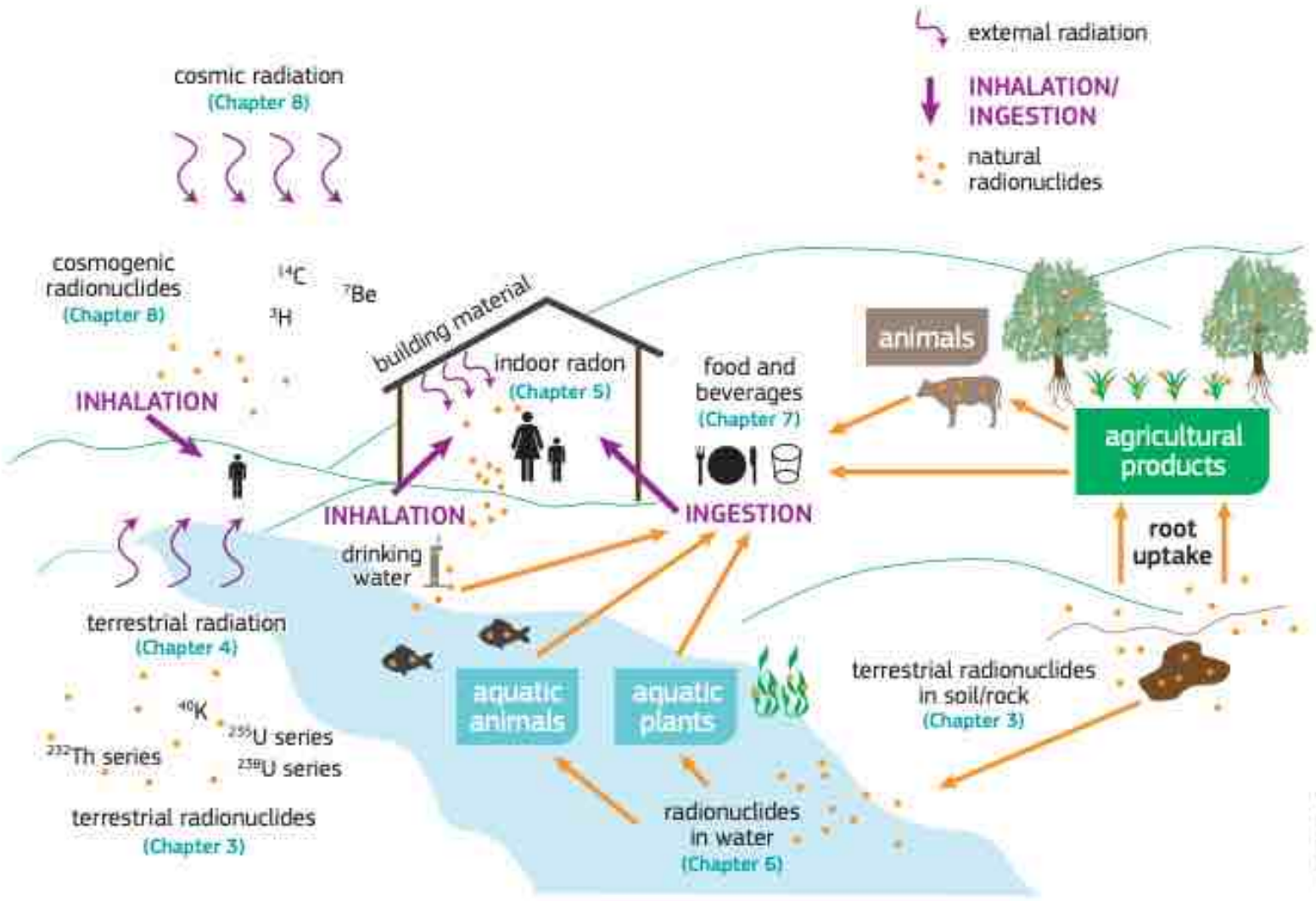

Figure 2-21.
Simplified pathways of natural radionuclides through the environment and different exposure pathways for humans. (The Atlas chapters that show the natural radioactivity in different media are indicated in parentheses).
Source: GMR, CC-JRC, 2010

2.2.4 Radiation dosage chart

Figure 2-22 shows the different contributions to the total dose of ionising radiation for the global population. The geographical distribution of total dose depends mostly on geology, altitude, life style and the use of radiation medicine both for diagnostic and therapeutic use. Some population groups are exposed to natural radiation doses one to two orders higher than the global mean value. Although public concern for radioactivity is mainly directed towards artificial sources of radiation, especially nuclear facilities, by far the largest contribution to public exposure (about 80%) is natural in origin.

There are two principal types of radiation exposure: internal and external.

Internal exposure occurs when the source of ionising radiation is located inside the organism, usually as a consequence of ingestion or inhalation of radioactive substances. Only some natural radionuclides are important in terms of population exposure. With the exception of inhalation of radon and its decay products causing highest internal exposure to the population (more details in Chapter 5), the most common way for natural radionuclides to penetrate into the human organism is generally through ingestion (Table 2-4). Another important example of internal radiation is radiation originating from medical sources, when radioactive tracers are used for a diagnostic or therapeutic purpose.

External exposure to radiation takes place when the radioactive source is located outside the body.

The proportion of effective dose for individual components of natural radiation due to external and internal radiation is shown in Figure 2-22. The natural sources of external radiation have terrestrial and cosmic origin. The terrestrial sources are mainly due to ^{40}K and radionuclides in the ^{238}U and ^{232}Th series (more details in Chapters 3 and 4).

Figure 2-23 intends to explain the exposure that humans may receive during their lifetime. It is possible to compare exposure resulting from natural and artificial sources. Doses due to natural background radiation, to radiology and nuclear medicine in diagnosis and treatment, and related to past nuclear accidents (e.g. Chernobyl and Fukushima) are reported.

Radionuclide	Committed effective dose (μSv)	
	Inhalation	Ingestion
^{238}U	0.021	0.25
^{234}U	0.026	0.28
^{230}Th	0.051	0.64
^{226}Ra	0.026	5.3
^{210}Pb	4	21
^{210}Po	1.2	70
^{232}Th	0.091	0.38
^{228}Ra	0.019	11
^{228}Th	0.29	0.22
^{232}U	0.001	0.012

Table 2-4.
Annual effective dose from inhalation and ingestion of uranium and thorium series radionuclides for adults, except radon.
Source: UNSCEAR, 2000

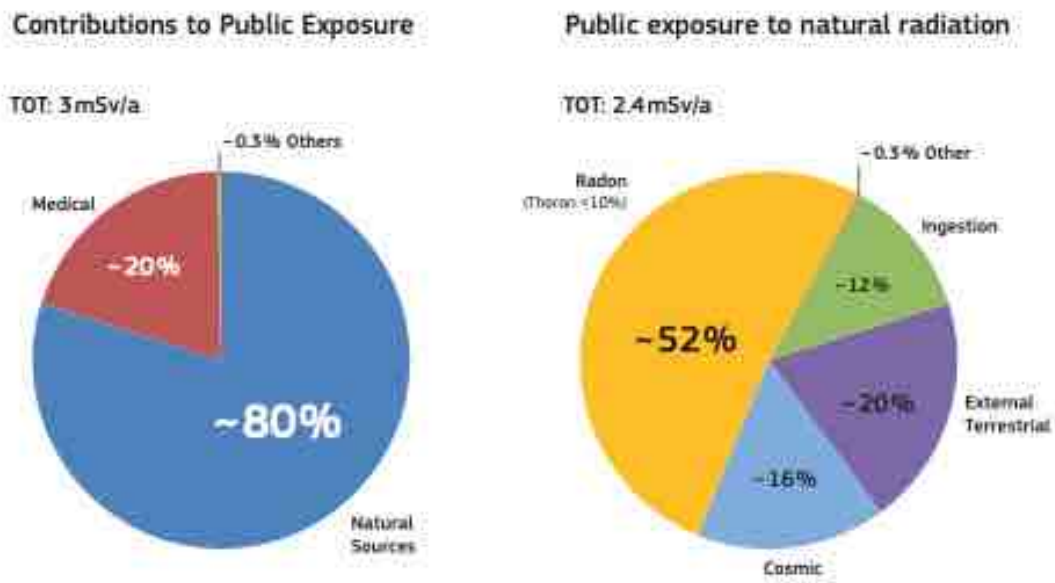

Figure 2-22.
Contribution of different sources of radiation to the dose forming ionising radiation.
Source: UNSCEAR, 2008

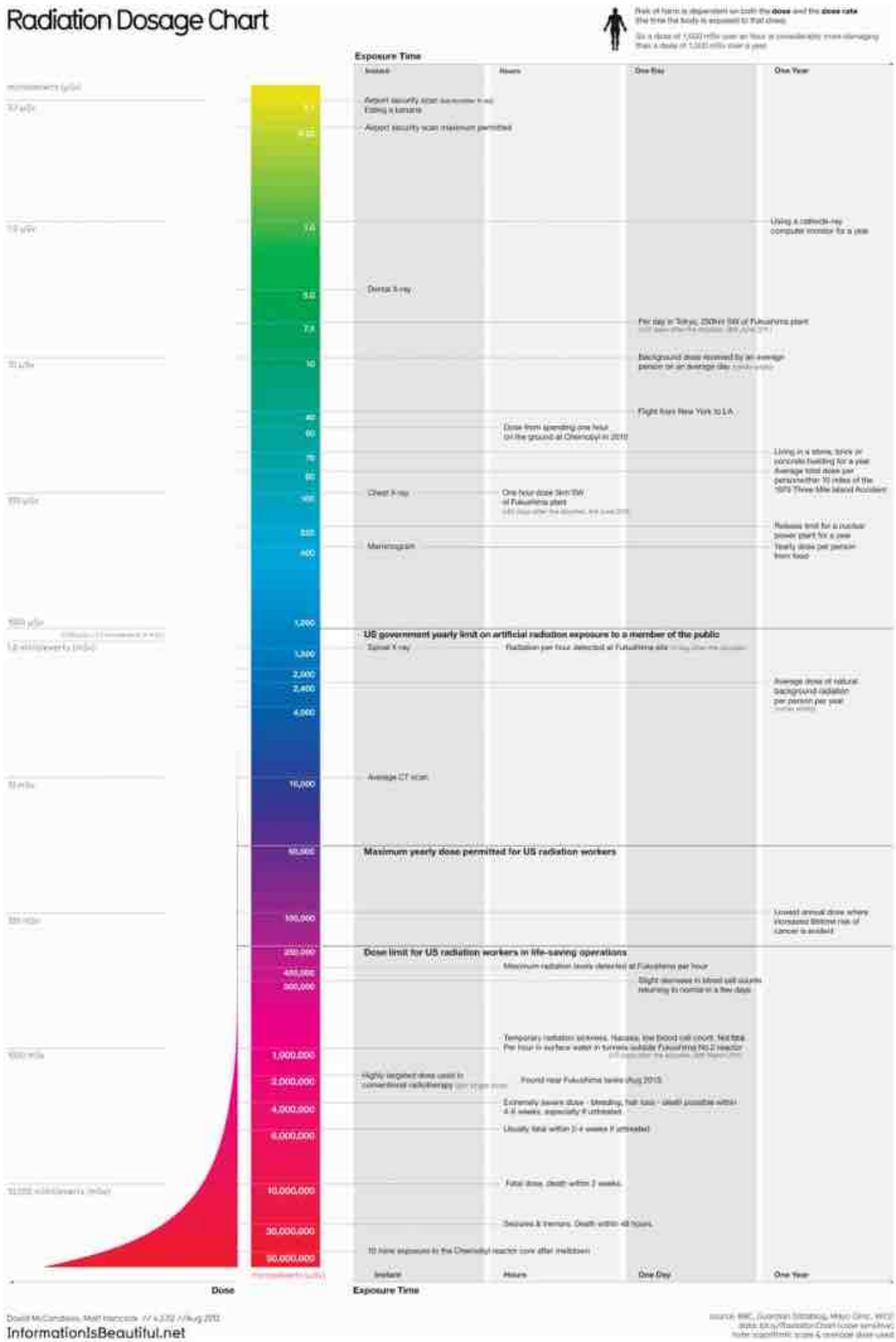

Figure 2-23.
Doses due to natural background radiation, radiology and nuclear medicine in diagnosis and treatment, and past nuclear accidents.

Case study: Ukraine

The major part of the average radiation dose received by Ukrainians comes from natural radiation sources including cosmic radiation, terrestrial radiation (soil and construction materials), and ingestion/inhalation of natural radionuclides present in air, food and water. Radon is the main source of the average annual effective dose of radiation from inhalation.

For the majority of people living in Ukraine, individual radiation doses received from natural sources vary relatively little. However, when radiation exposure from natural sources is considered for an individual, it appears that some individuals are exposed to radiation doses that are much higher than average.

Apart from that, some people are additionally exposed to man-made radiation from technogenic sources. Unlike exposure to radiation from natural sources that remains relatively stable over the years, the impact of radiation coming from technogenic sources may vary significantly. In order to protect people against adverse effects of ionising radiation, the Ukrainian law 'On the Protection of People against Ionising Radiation Effects' limits the individual occupational exposure to radiation from technogenic sources to 1 mSv/a.

In addition to the individual dose which is a measure describing the relative health impact caused by a particular activity, the collective dose is an equally important indicator. It is calculated as the sum of all individual doses caused by a particular source and characterises the total health effects of a source/process. It is used to compare various sources and processes in terms of their health impacts due to ionising radiation.

External exposure to cosmic radiation

Considering the geographic location of Ukraine and prevailing types of residential buildings, the average annual equivalent exposure dose from cosmic radiation is estimated to be 360 µSv, which is equal to the average annual dose experienced in Ukraine at the sea level.

External exposure to radiation from naturally occurring radionuclides

Considering that the Crimean and Carpathian mountains, Trans-Carpathian and Polissia regions occupy a relatively small part of Ukraine and that population densities in these regions are relatively low, it can be assumed that the average annual effective dose of external radiation from naturally occurring radionuclides is 360 µSv, and that the annual total average effective dose that takes account of the radiation shielding of buildings is 720 µSv.

Internal exposure to radiation from naturally occurring radionuclides

Cosmogenic radionuclides

The contribution of cosmogenic radionuclides to the internal exposure dose is very minor, with ^{3}H, ^{7}Be, ^{14}C and ^{22}Na being the major contributors.

The annual effective doses for ^{3}H, ^{7}Be, ^{14}C and ^{22}Na are 0.01, 3, 12 and 0.2 µSv, respectively, with their annual total effective dose amounting to about 15 µSv.

Primordial radionuclides

The primordial radionuclides are isotopes of ^{235}U, ^{238}U, ^{232}Th and some other radionuclides, with only ^{40}K and ^{87}Rb being considered as significant radiation sources.

The annual effective doses from internal exposure due to ^{40}K and ^{87}Rb are 180 and 6 µSv, respectively.

The annual equivalent dose of ^{238}U (without radon and its decay products) is ~154 µSv (^{238}U (10 µSv), ^{230}Th (7 µSv), ^{226}Ra isotopes (7 µSv) and ^{210}Pb/^{210}Po (130 µSv)).

The ^{232}Th isotopes (without thoron and its decay products) produce an annual equivalent dose of ~16 µSv (^{232}Th (3 µSv) and ^{228}Ra (13 µSv)).

Internal exposure to radiation from radon, thoron and their decay products

^{222}Rn (radon) and ^{220}Rn (thoron), along with their short-lived decay products inhaled with the ambient air, are the major sources of exposure to background radiation.

The average annual effective dose from exposure to radon in homes in Ukraine is 3.2 mSv, with the annual exposure dose varying from 2.2 to 5.5 mSv. The average annual effective dose from exposure to radon outdoors is 0.067 mSv at a radon concentration of 10 Bq/m^{3}.

Radon enters the human body through the water we drink and partly through the air we breathe. For a radon concentration in water of 10 kBq/m^{3}, the annual effective dose is 0.020 mSv. For indoor and outdoor radon concentrations of 180 Bq/m^{3} and 10 Bq/m^{3}, respectively, the effective dose from radon dissolved in blood is 0.220 mSv/a.

The total annual dose from internal exposure to radon and its decay products is about 3.5 mSv.

The total effective dose from natural radiation

The total effective dose from natural radiation is calculated as a sum of all effective doses resulting from external and internal exposure to natural radiation sources. In Ukraine, this dose is about 4.7 mSv (Kovalenko, 2013), being significantly higher than the worldwide average effective dose from natural radiation, which is 2.4 mSv (Bennett, 1995).

Exposure to technogenic sources of radiation

The technogenic sources of radionuclides contaminating the environment and causing human exposure to radiation include:

- Development and testing of nuclear weapons;
- Nuclear accidents;
- Radiation technology developments and projects not associated with nuclear fuel.

Human exposure to radiation from nuclear weapons tests

If we assume that no nuclear weapon tests will be conducted in the future, the effective dose is estimated to be about 4.5 mSv, which is approximately equal to the value of the annual effective dose from exposure to natural radiation in Ukraine. By 2012, the estimated annual effective dose from nuclear weapons tests was about 1.478 mSv, accounting for about 33 % of the total effective dose (Kovalenko, 2013). The estimated collective dose for the Ukrainian population is about 1.0×10^{5} **manSv**.

manSv: is the unit for the collective dose. The collective dose is the total radiation dose incurred by the population.

Human exposure to radiation released during the Chernobyl accident

External exposure

To estimate the effective dose from external exposure, we will use a method based on the relationship between the ground contamination by ^{137}Cs and radionuclides contributing most significantly to the external exposure dose (^{103}Ru, ^{106}Ru and ^{134}Cs). With this method, we can use available measurement data on the concentrations of ^{137}Cs which were collected for many years after the Chernobyl accident to derive information on the ground contamination by short-lived radionuclides.

An optimistic approach would lead us to assume that the average ^{137}Cs contamination density in those Oblasts that were hardest hit by the Chernobyl accident (Zhitomyr, Kyiv, Rivne, Cherkasy, and Chernihiv) is 18.5 kBq/m^{2}. In other Oblasts, the average ^{137}Cs contamination density due to Chernobyl accident is close to zero. For this scenario, the collective dose from external exposure to radiation is 111 000 manSv. In practice, the most reliable data on the external exposure levels can only be provided for those people who live in the areas where the density of ground contamination by ^{137}Cs is higher than 37 kBq/m^{2}. The collective dose for this part of the Ukrainian population is 85 800 manSv.

Internal exposure

The external exposure estimates have been produced by applying the dose conversion coefficient to convert the ^{137}Cs contamination densities to dose. It should be noted that the estimated exposure dose received during the first year after the accident takes into account contributions made by ^{131}I, ^{134}Cs, ^{137}Cs and ^{90}Sr, while only ^{134}Cs, ^{137}Cs and ^{90}Sr are taken into account for subsequent years.

The collective doses from internal exposure to ^{137}Cs and ^{90}Sr are 53 manSv and 4 070 manSv, respectively.

These estimates assume that there are no regulations setting limits on the content of ^{137}Cs and ^{90}Sr in food, and are therefore 5 to 30 times higher than the estimates produced based on data on the caesium content in the human body. If we apply the limits set on the amount of Cs and Sr in food, the internal exposure estimates would not take into account exposure from the ground contamination by Cs and Sr and would only consider the content of these radionuclides in food.

The total collective dose from exposure to radiation released during the Chernobyl accident has been estimated at 89 900 manSv over a 70-year period.

Thyroid gland exposure to radiation from iodine ^{131}I

The collective absorbed dose for Ukraine's population is 5.7×10^{5} Gy and the average dose per capita is about 0.012 man Gy. In Kyiv city and Oblast, the collective absorbed dose from the thyroid gland exposure is 1.5×10^{5} Gy, accounting for about 26 % of the total nationwide collective dose. The average absorbed dose in Kyiv city and Oblast is about 0.04 Gy. The estimated absorbed doses for the population living in Kyiv and Zhitomyr Oblasts could be as high as 1.8, 1.4 and 0.5 Gy for children under 1 year of age, children under 5 years of age and adults, respectively. The age structure of Ukraine's population is: children under 1 year of age (1.4 %), children between 1 and 5 years of age (5.3 %) and older children and adults (93.3 %).

Human exposure to radiation from nuclear fuel facilities and nuclear power plants

- The collective 70-year dose from emissions released by uranium mines is 6.6 manSv with ^{222}Rn and its short-lived decay products accounting for 90 % (6.0 manSv).
- The collective 70-year dose from emissions released by the uranium processing facilities is 3.8×10^{1} manSv.
- The collective 70-year dose from emissions released by nuclear power plants is 31 manSv.
- The collective 70-year dose from natural radionuclide emissions released by thermal (coal-fired) power plants is 1.6×10^{1} manSv.
- The total collective 70-year dose from technogenic sources of radiation is about 2×10^{5} manSv, which is significantly lower than the collective dose from natural background radiation of 1.67×10^{7} manSv (Kovalenko, 2013).

2.3 Geology

The composition and structure of the sub-surface has a strong influence on the local level of natural (background) radiation, along with other parameters such as altitude and climate. Geology and soil science describe and explain these variations in composition and structure of the sub-surface based on the history (over thousands to millions of years) and the physicochemical conditions of the region considered. This implies that by looking at the geology of Europe, one can already form a general and large-scale idea of the level of natural radioactivity that can be expected. For instance, young and mobile unconsolidated marine sediments (like clays, loams and sands) that are found in many coastal regions in northern and north-western Europe generally contain less radionuclides than certain magmatic or metamorphic rocks found in for example Scandinavia (Fennoscandian Shield), Central Europe (Bohemian Massif), France (Bretagne and Central Massif) and in Spain (Iberian Massif). The former regions have been periodically and geological-recently (during the last few million years) part of a shallow sea, whereas the latter are the result of very old mountain building processes that allowed hard rocks to form and radionuclides to migrate and concentrate, either homogeneously in specific parts of a magma chamber or in discrete fractures and veins. The more recent alpine mountain belts are composed of many different types of rock (magmatic, sedimentary/carbonate, metamorphic etc.) varying relatively locally and thus leading to strong spatial variations in radiological signature. As for volcanic rocks, generally speaking acidic materials like tuff and rhyolite have a higher radionuclide content and can lead to increased indoor gamma dose rate and radon or thoron concentrations, when present in the building foundations or when used as building materials. Another specific case are karstic limestone areas, where the radiological risk, mainly due to radon emanation, varies locally, leading to strong hot-spots of natural radioactivity. Organic-rich shale and slate can also be of particular importance to the radiological background due to their sometimes increased content in uranium or thorium in combination with a strong fracture permeability, allowing radionuclides (mainly radon or radium and sometimes uranium in water solution) to migrate and concentrate at specific locations. That leads to another important geological factor playing a role in the radiological background, namely fractures and faults. These structures can form pathways for radionuclides to migrate, concentrate and emanate, thus affecting locally or more widely (depending on their geometry and extent) the natural radiological background. Another specific situation exists in the Baltic region and northern Germany to Denmark, where glacial processes transported debris material from the Baltic Shield with increased radionuclide content over large distances, leading to deposits with increased natural radioactivity. Finally, the topmost layer of the Earth's surface is often covered by a soil layer, resulting from the *in situ* weathering of the local rocks, or deposited by transport processes like river flooding/meandering. The permeability and composition of these soils will again influence the local content in radionuclides and affect the natural radioactivity presented in this Atlas. For these reasons, the Atlas makes use of the geological and pedagogical information available to predict, determine or fine-tune the specific radiological maps collected herein.

2.3.1 Geological influence on radiation

Outdoor natural background radiation is mainly determined by the activity concentrations of the natural terrestrial radionuclides ^{238}U, ^{232}Th and ^{40}K and their decay products found in the Earth's crust. Radioactive decay of these nuclides occurs in all rocks (level 1 in Figure 2-24). However, the activity concentration of radioisotopes depends on the processes that control the mobilisation, precipitation, concentration and/or leaching of radionuclides (Langmur, 1978). Soil, formed by weathering of the rock and pedogenic biochemical processes, is a second source of natural radioactivity (level 2 in Figure 2-24). The soil-forming processes can cause further mobilisation and concentration of radionuclides, as for example accumulation of uranium which can be favoured in reducing conditions. The migration of radionuclides towards the surface and to the atmosphere further depends on physical properties such as permeability, soil-gas composition, water-table dynamics and tectonics (level 3 in Figure 2-24). Moreover, natural stone and raw materials (clay, marlstone, sand) that are used to produce building materials (e.g. bricks, cements, mortars) also contain radionuclides, leading to human exposure that, in some cases, may cause health risks (level 4 in Figure 2-24). Finally, raw materials used in a wide range of industrial processes (like mineral ore, oil and gas, rock) can lead to environmental pollution at various levels, causing human exposure to natural radionuclides artificially introduced in the environment, so-called naturally-occurring radioactive material (NORM). However, this Atlas does not address the occurrence of natural radionuclides originating from anthropogenic sources such as building materials or NORM.

Lithology

The natural radioactivity in rocks depends on their type and on how they were formed (Langmur, 1978; Maxwell et al., 2015). Rocks can be classified into igneous, sedimentary or metamorphic ones according to their formation process. Igneous rocks are formed from magma, either inside a magma chamber (thus forming magmatic rock like granite or diorite), inside intrusions (forming intrusive rock like dolerite), or from lava flows (forming volcanic rock such as basalt or rhyolite).

** Uniru limestone with characteristic texture. Uniru, Estonia.
Source: Kalle-Mart Suuna

Sedimentary rocks are formed by transport and deposition of rock forming substances such as clastic particles or chemical and biochemical precipitation. If they occur as unconsolidated and un-cemented formations, they are called sediments, like sand or clay. To various degrees, they can also undergo compaction, diagenesis or lixiviation during weathering, thus forming different types of sedimentary rocks like shale, limestone or sandstone. Metamorphic rocks are re-crystallised *sub-solidus* from protoliths of pre-existing sedimentary, igneous or other metamorphic rocks. Typical examples are gneiss and slate (schist).

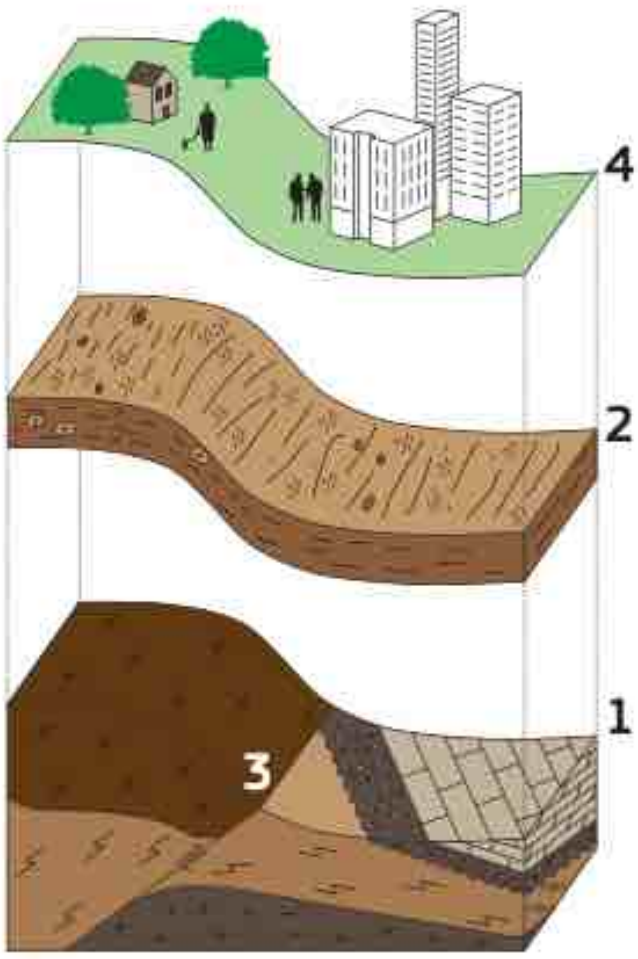

** Figure 2-24.
Sources of the principal natural radionuclides from the ^{238}U, ^{232}Th and ^{40}K decay series. Primary source: bedrock (level 1); secondary source: soil (level 2); additional sources: discontinuities (e.g. tectonics, level 3); anthropogenic source: building materials and environmental pollution (level 4).
Source: Graph created by Chiara Cuccia

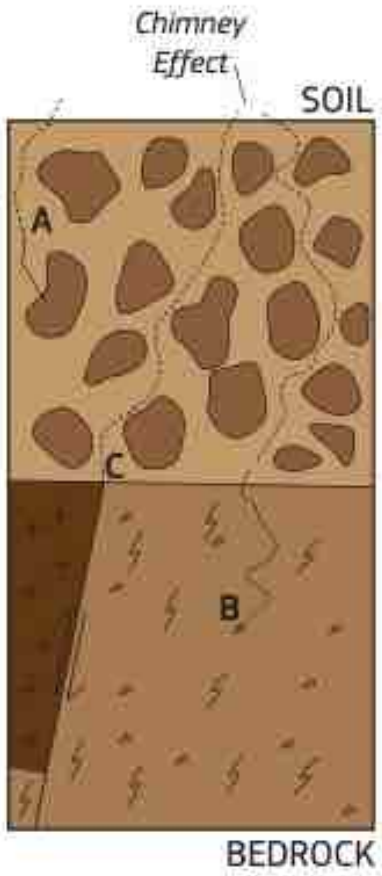

** Figure 2-25.
A. Radon atom emanation from within the solid grains into the free spaces of material;
B. Radon atom diffusion in the pore spaces between rock and soil particles;
C. Radon atom exhalation through preferential fluid flow pathways, 'chimney effect'.
Source: Graph created by Chiara Cuccia

High activity concentrations of radionuclides can be found in many different rock types, but they essentially originate from igneous rock-forming processes. U and Th are incompatible elements strongly partitioned into the initial melts formed by partial melting in a magma chamber. Because of their large ionic radius and high valence, they are strongly incompatible in major rock-forming minerals and show greatest affinity to other M^{4+} elements such as Ce and Zr. Therefore, uranium and thorium are generally enriched in granitoid rocks and their corresponding volcanic products, and are mainly incorporated into accessory minerals such as zircon ($ZrSiO_4$), titanite ($CaTiSiO_5$), apatite ($Ca_{10}(PO_4)_6(OH,F,Cl)_2$), and epidote ($Ca2Al_2(Fe^{3+},Al)(SiO_4)(Si_2O_7)O(OH)$) in which they are less incompatible, or in monazite ($(Ce,La,Th,U)(PO_4,SiO_4)$), allanite ($(Ce,Ca,Y,La)_2(Fe^{2+},Fe^{3+},Al)_3(SiO_4)(Si_2O_7)O(OH)$) and in specific U and Th minerals such as uraninite (UO_2), brannerite ($(U,Ca,Ce)(Ti,Fe)_2O_6$), carnotite ($K_2(UO_2)_2(VO_4)_2 \cdot 3H_2O$), coffinite ($USiO_4$), thorite ($ThSiO_4$) and thorianite ($ThO_2$), where they even become compatible (Blundy & Wood, 2003; Sakoda et al., 2010; Cuney, 2014). Hydrothermal and weathering processes may cause U and Th leaching from accessory minerals with subsequent ore crystallisation and adsorption on secondary hydrated Fe-oxide, Mn-oxide and clay minerals (Taboada et al., 2006).

Sedimentary rocks are, in general, significantly poorer in U and Th. Most U-ore deposits in sedimentary rocks are either detrital accumulation of Th-bearing uraninite in Archean and Palaeoproterozoic siliciclastic sediments under anoxic surficial conditions, or related to selective uranium leaching. This can be caused by oxidising hydrothermal fluids or ground water, which produce and transport highly soluble uranyl $(U^{6+}O_2)^{2+}$ complexes. They precipitate as uranyl minerals, or uraninite low in Th at reduction fronts. Uraninite and coffinite may also precipitate when uranyl-bearing solutions come across sediments rich in organic matter produced by sulphate-reducing bacteria (Hazen et al., 2009), leading for example to the typical 'black shale' or 'alum-shale' radioactive rocks. This difference in behaviour of U and Th results from the different possible oxidation states of uranium, mainly 4+ or 6+, or more rarely 5+, while Th is only present in the 4+ form. Significant Th mobilisation should therefore occur at high temperatures only in the presence of fluorine (F), forming Th^{4+}-F complexes, such as in magmatic environments forming alkaline and/or peraluminous granites (Keppler & Wyllie, 1990). Leaching of uranium from other accessory minerals, such as monazite or apatite, is possible only in the presence of exceptional conditions, e.g. when in contact with highly saline, acidic and oxidised diagenetic fluids. Radium,

which is the heaviest alkaline Earth metal, with ^{226}Ra as the most abundant and long-lived isotope (half-life of 1 600 years), can be incorporated into biogenic carbonates, such as those secreted by molluscs and corals, or in hydrocarbon compounds; but it is also found in inorganic carbonate deposits, such as in speleothems or travertines, and in high-temperature hydrothermal carbonates (Schmidt & Cochran, 2010). U-rich deposits in travertine, calcrete and calcite tufa may form when redox-sensitive elements, including U, are originally mobilised, possibly during weathering of crystalline rocks, pre-concentrated in black shale or bituminous marls, remobilised by alkaline lake waters (Cole et al., 2004) or in the presence of hyperalkaline hydrothermal systems (Khoury et al., 2014), and precipitated either by a variation in U/Ca ratio due to mixing with ground water, or the activity of hydrogen ions (pH), variation after water discharge, rapid uptake of atmospheric CO_2 and travertine formation. Moreover, uranium can be transported in hydrothermal solutions as uranyl-carbonate complexes [$UO_2(CO_3)_3^{4-}$], and precipitate in veins when fluids experience a decreasing concentration of CO_2 and rapid change in reduction potential (Eh) and pH due to localised reactions with the host rocks (Ruzicka, 1993). Thorium in sedimentary rocks is poorly leached because its host minerals, such as monazite and zircon, are highly resistant to both chemical and physical weathering, and due to low solubility in the 4+ form. Clay minerals in shales may contain some Th, although in small amounts in comparison with U. Nevertheless, in some specific cases such as monazite-rich sand deposits (Dawood & Abd El-Naby, 2007; Iyer, 2015; Chen et al., 2017), Th can be exceptionally enriched. Limestone, conglomerate and sandstone are normally very low in U and Th.

Metamorphic rocks reflect fairly well the geochemical features of their igneous and sedimentary protoliths. Nevertheless, mobilisation and redistribution of metals (and radionuclides) may take place during metamorphism by migration of hydrothermal fluids along fractures surrounding granitic plutons, or shear zones causing concentration of uranium minerals, typically uraninite and coffinite (Ruzicka, 1993). Generally, a decrease in the Th/U ratio is observed with increasing metamorphic grade, suggesting that Th becomes more easily mobilised than U under conditions of high pressure and temperature.

Soils

The weathering of rocks exposed on the Earth's surface can lead to soil formation. The associated chemical and physical processes can promote a redistribution of the radioactive elements included in the original rock, at a level proportional to the thickness and degree of evolution of the soil. The concentrations in different horizons depend on the mineralogy in the parent rock as well as on the typology and intensity of the weathering processes (driven by factors such as climate, tectonics, volcanic activity, etc.). The presence and type of minerals in the rock containing natural radionuclides control the degree of remobilisation. For example, the presence of U and Th-bearing minerals resistant to weathering, as in the case of zircon or monazite, leads to the concentration of these radioactive elements in horizons composed of parent material aggregates generally of coarse and medium grain size (boulders to sands). Within the presence of minerals less resistant to chemical weathering, such as uraninite, feldspars or biotite, the leaching potential of the radioactive elements can be increased depending on the geochemistry of the water, in particular pH and the Eh.

The change from an oxidising to a reducing environment favours the transition to the valence state U^{4+}. Under these conditions U becomes insoluble and precipitates in the form of uranium-bearing minerals (e.g. autunite or torbernite), or is incorporated into the structure of other minerals, as goethite, or adsorbed in clay minerals or organic matter. The influence of humic substances in the precipitation of U is still poorly understood (e.g. Lamas, 2005). The presence of other elements, such as Fe^{2+}, leads to the precipitation of U compounds in an oxidising environment. K is usually concentrated in horizons where clay minerals dominate.

Micro-organisms also play an important role in U mobility in soils. Bone et al. (2017) suggest a model that points to the importance of pyrite as a source of electrons that could be used by bacteria to promote the reduction of U^{6+} to U^{4+}, inducing U precipitation. Specialised bacteria may also be able selectively to extract U dissolved in ground water (Chung et al., 2014). In some cases, human activity can slightly increase the natural radioactivity of the top soil on a broad scale, mainly by the use of uranium-bearing fertilisers applied on large scale in agricultural areas.

Radon, a special radionuclide

Radium, the direct parent nuclide of radon, is bound to mineral structures, while radon gas can escape from the crystal structure and migrate through the material. The main phenomenon that allows radon atoms to leave the mineral grains is the recoil of a nucleus owing to alpha-particle emission during decay of radium to radon, resulting in the displacement of the radionuclide from its original location (Tanner, 1978; Figure 2-25, A).

Radon release to the atmosphere takes place through the combination of emanation, transport and exhalation processes. Emanation is the process that controls release of radon atoms from solid grains into free spaces of material (internal defects, pores, cracks). Transport is the movement of the emanated radon atoms by diffusion and advective flux through the pores (Figure 2-25, B), whereas exhalation is the process by which radon atoms migrate to the ground surface and exhale to the atmosphere (Hassan et al., 2009).

During emanation, the recoiled atoms can be ejected from the mineral. Cracks and fissures on the surface of the grain caused by previous radioactive decay and chemical or physical weathering can increase the specific surface area of the grain, thus increasing the emanation coefficient. This is the ratio of the number of radon atoms leaving the microstructure of the mineral to the total number of radon atoms generated (Eakin et al., 2016). Moreover, internal defects in the crystal lattice create conduits through which radon may escape. If the recoil ends outside the grain, radon is released into pores or textural discontinuities either filled with soil gas or aqueous solution (Tanner, 1978), from where it can exhale to the ground surface (Figure 2-25, B). Indeed, different pore systems and textures in different rock types control radon diffusion and transport.

The efficiency of radon release from mineral grains (emanation) flow to the atmosphere (exhalation) depends on the chemical and physical weathering, and on the porosity and permeability of the rock (Tuccimei et al., 2015; Domingos & Pereira, 2018).

Radon can migrate through the soil by diffusion, by advective flow of moving soil gases, or by a combination of both mechanisms. The rate of radon movement by diffusion in the pore space between the soil particles depends on the porosity (interstitial spaces), tortuosity (flow path around particles), soil moisture, humidity, compactness, permeability and climate. At high moisture contents, for example, free water appears in the interstitial space between the particles, and radon must either take a longer route through the air-filled pore space or else diffuse partially through the water. Advective flow of radon carried by a flux of other soil gases, such as underground water, carbon dioxide or methane can transport the radon gas over long distances determined by the carriers flow rate (Ioannide et al., 2013). Local discontinuities such as fractures and faults or contact zones between different geological formations can form high permeability pathways facilitating radon flux (Figure 2-25, C). These structural discontinuities can act as preferential fluid-flow pathways as chimney and cause important anomalous gas flow, revealed by locally high radon exhalation. In karstic regions, despite their overall low radionuclide content in carbonate and limestone, local hotspots of indoor radon often occur, due to local weathering and concentration of radionuclides and due to the very high and localised permeability of karst (sinkholes, dolines, galleries, caves, etc.), thus allowing transport of important air volumes over long distances, leading to an increased radon flux.

Further details about radon may be found in Section 2.2 and Chapter 5.

Building materials

Natural rocks can be used directly as building materials (wall stones, floor or roof tiles), or as raw materials for derived products such as brick, mortar, cement, concrete or plaster. All these building materials contain natural radionuclides exposing the population to a certain level of external gamma radiation and to internal radiation due to inhalation of radon gas and its decay products.

The radiological risk of building materials depends on the activity concentrations of U, Th and K (Radiation Protection 112; Stoulos et al., 2003) and on the exhalation potential of radon and thoron (Rafique et al., 2011; Kovler, 2017). The internal and external exposure due to the building materials has to be taken into account in radiological risk evaluation, but falls outside the scope of this Atlas.

Table 2-5 gives an overview of some typical activity concentrations of ^{226}Ra, ^{232}Th and ^{40}K in common rocks and derived building materials found in Europe. It is based on a compilation carried out by Nuccetelli et al. (2017) and Trevisi et al. (2018), and integrates data from Marocchi et al. (2011), Capaccioni et al. (2012) and Tositti et al. (2017). In general, granites and derived products have higher radionuclide concentrations, as well as high radon gas exhalation potential. Sedimentary rocks and their derived products generally have a lower radionuclide content, particularly marls and limestones. Acidic volcanic rocks, such as tuffs or rhyolites, can have high uranium concentrations (and high radon gas exhalation). Conversely, basic volcanic rocks have much lower radionuclide concentrations. In metamorphic rocks, anisotropy tends to increase the exhalation potential of radon, as is the case of gneisses formed from igneous acidic protoliths.

Table 2-5
^{226}Ra, ^{232}Th and ^{40}K activity concentration (Bq/kg) in natural stones, raw materials, and derived products (in the lighter shaded rows).

	^{226}Ra (Bq/kg)	^{232}Th (Bq/kg)	^{40}K (Bq/kg)	Source
Limestone	15	15	160	Tositti et al., 2017; Nuccetelli et al., 2017
Travertine	7	20	3	Nuccetelli et al., 2017
Marlstone	35	11	273	Nuccetelli et al., 2017
Granite	79	93	1 076	Marocchi et al., 2011; Nuccetelli et al., 2017
Syenite	146	106	971	Marocchi et al., 2011; Nuccetelli et al., 2017
Gabbro	17	20	324	Marocchi et al., 2011; Nuccetelli et al., 2017
Rhyolite	69	84	1 239	Marocchi et al., 2011; Tositti et al., 2017
Trachyte	96	126	1 338	Marocchi et al., 2011; Tositti et al., 2017; Nuccetelli et al., 2017
Basalt	81	117	892	Tositti et al., 2017; Nuccetelli et al., 2017
Schist	36	42	668	Nuccetelli et al., 2017
Gneiss	123	61	962	Marocchi et al., 2011; Nuccetelli et al., 2017
Slate	49	66	617	Nuccetelli et al., 2017
Tuff	147	224	1 506	Capaccioni et al., 2012; Nuccetelli e al. 2017
Clay	51	49	555	Nuccetelli et al., 2017; Trevisi et al., 2018
Chalk	15	15	112	Nuccetelli et al., 2017; Trevisi et al., 2018
Gypsum	18	16	105	Nuccetelli et al., 2017; Trevisi et al., 2018
Lime	19	11	109	Nuccetelli et al., 2017; Trevisi et al., 2018
Pozzolana	187	253	1 397	Nuccetelli et al., 2017
Pumice	269	66	1 073	Nuccetelli et al., 2017
Shale	174	131	493	Nuccetelli et al., 2017
Brick	51	49	555	Nuccetelli et al., 2017; Trevisi et al., 2018
Concrete	59	85	340	Nuccetelli et al., 2017; Trevisi et al., 2018
Cement	50	35	235	Nuccetelli et al., 2017; Trevisi et al., 2018
Aggregates	23	23	388	Nuccetelli et al., 2017; Trevisi et al., 2018

2.3.2 Simplified description of European geology

Introduction

The European continent, as we know it today as part of the Eurasian plate, is the result of multiple geodynamic and related rock-forming processes. These processes can be related to several mountain-building events caused by episodic subduction of oceanic crust and collision of continental plates. As a consequence, the European geology varies a lot, both in age and complexity. Simply put, European geology can be divided into the following periods: the Precambrian (ca. 4.6 Ga – 541 Ma before present (BP)), the Paleozoic era (541 Ma – 251 Ma BP), the Mesozoic era (251 Ma – 66 Ma BP) and the Cenozoic era (66 Ma BP – present). Every era is characterised by specific geodynamic processes which led to the development of five structural geological units that form the present European land mass: the Eastern European Platform, the Caledonides, the Variscides, the Mesozoic overburden and the Alpidic system (Figure 2-26). The geological setting is complemented by rock of all ages, overlying the bedrock in varying thicknesses (Labhart, 2004; Walter, 2007).

The Precambrian (~4.6 Ga – 541 Ma BP)

The Precambrian orogens

During the Precambrian, several orogenetic cycles took place (Frisch & Meschede, 2009). Over time, the originally sedimentary and magmatic rocks turned into gneisses and crystalline schists through folding and metamorphism. They are now known as cratons, which are stable parts of the Earth's lithosphere that have not been deformed significantly for millions, even hundreds of millions of years. Welded together, these cratons form the Eastern European Platform. This platform extends from the Barents Sea to the Black and Caspian Sea and from the Urals to the Scandinavian mountains, and thus comprises large parts of eastern and northern Europe (Faupl, 2003; The Great Soviet Encyclopedia, Third Edition, 1970 – 1979). Nowadays this basement, aged between 1.6 Ga and 3.5 Ga BP, is exposed in the Ukrainian Shield in the southwest and in the Baltic Shield in the northwest. The oldest rocks can be found on the Kola Peninsula. The remaining, larger area of the basement, i.e. the Russian Plate, is covered with sedimentary deposits up to 10 km thick.

The Paleozoic era (541 Ma – 251 Ma BP)

The Caledonian orogeny

From early Precambrian to Ordovician times, the Gondwana supercontinent united almost all continents present at that time on the southern hemisphere (Figure 2-27a, 480 Ma BP). Along the northern edge of Gondwana a broad magmatic arc was located and caused the development of several independent micro-continents or terranes (Nance et al., 2010). Some of these micro-continents, like Avalonia, Saxo-Thuringia, Bohemia, Armorica, Iberia and the Proto-Alpine terrane, nowadays form the basis for significant parts of the present European land mass. The South Pole was located in northern Africa at that time. Further north, at middle southern latitudes, the Baltica (Northern Europe), Siberia and, close to the Equator, Laurentia (North America and Greenland) continents were located (Figure 2-27b, 420 Ma BP).

Around 450 Ma BP (late Silurian period), the Avalonia micro-continent, due to north-up shift, collided with Baltica (Tait et al., 1997; Cocks et al., 1997; Torsvik & Rehnström, 2003). This collision made the Tornquist Ocean close, while the Rheic Ocean opened in the South. Around 420 Ma BP (Figure 2-27b), Baltica, now together with Avalonia, finally united with Laurentia by closing the Iapetus Ocean, forming the Laurussia supercontinent (e.g. Trench & Torsvik, 1992; Murphy et al., 2010). At this stage the Caledonian Orogeny was completed.

Matterhorn, Switzerland, one of the highest peaks in the Alps, is mainly composed of gneisses.
Source: Tom Tübrhan

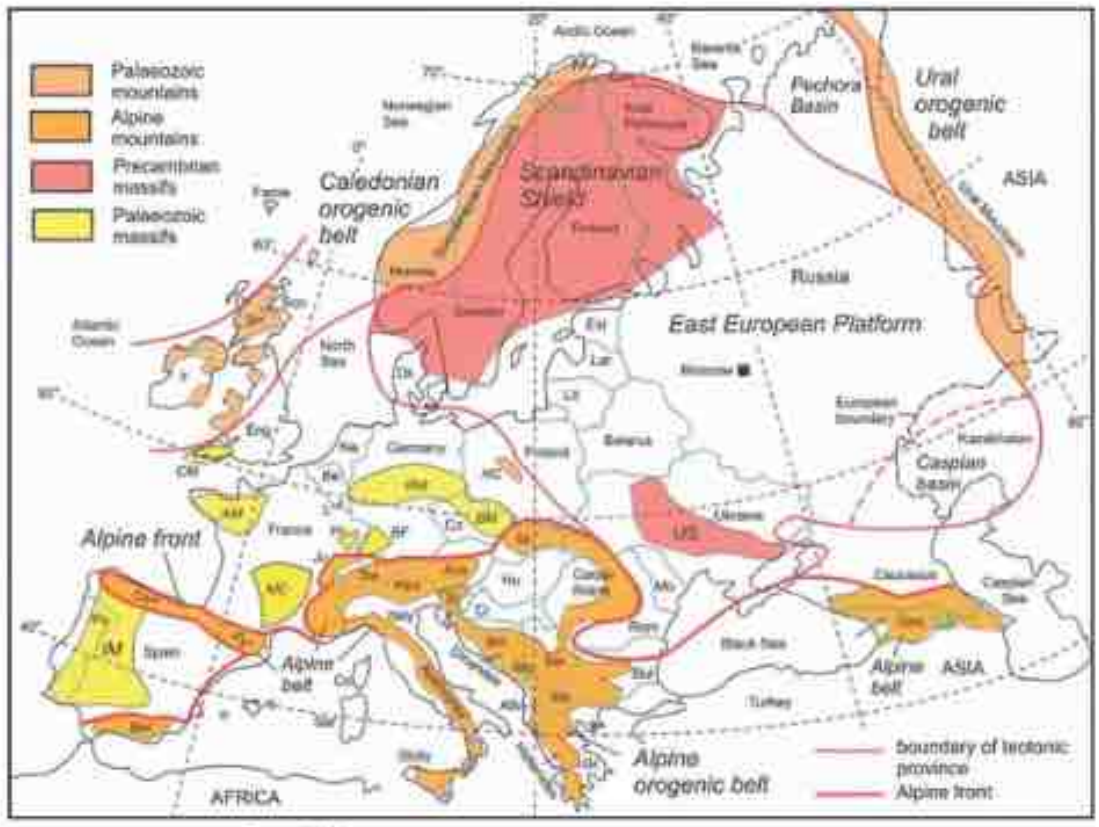

Figure 2-26.
Orogenic domains in Europe. Lowland plains are left blank. Countries: Alb, Albania; Aus, Austria; Be, Belgium; BH, Bosnia-Herzegovina; Bul, Bulgaria; Co, Corsica; Cr, Croatia; Cz, Czech Republic; Dk, Denmark; Eng, England; Est, Estonia; Geo, Georgia; Hu, Hungary; Ir, Ireland; L, Luxembourg; Lat, Latvia; Lit, Lithuania; Ma, North Macedonia; Mo, Moldova; Ne, Netherlands; Po, Portugal; Rom, Romania; Sar, Sardinia; Sco, Scotland; Ser, Serbia; Sk, Slovak Republic; Sl, Slovenia; Sw, Switzerland. Mountain ranges: Bet, Betic Cordillera; Can, Cantabrians; Ju, Jura; Pyr, Pyrenees; Sh, Scottish Highlands; Upland massifs: BF, Black Forest; BM, Bohemian Massif; CM, Cornish Massif; HC, Holy Cross Mountains; IM, Iberian Massif; MC, Massif Central; RM, Rhenish Massif; US, Ukrainian Shield; Vo, Vosges.
Source: Pohl, 2014 & 2016

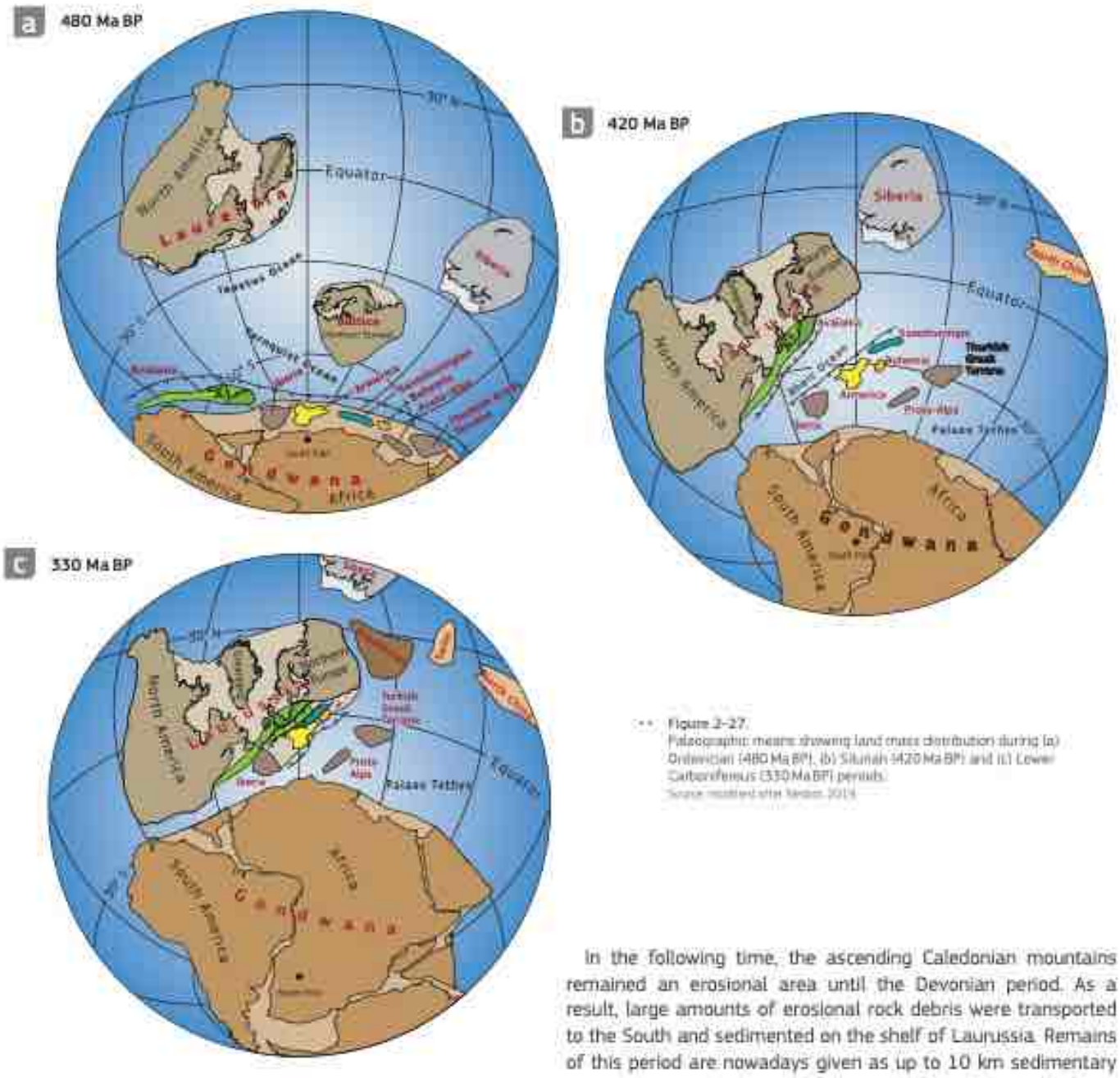

Figure 2-27.
Palaeographic means showing land mass distribution during (a) Ordovician (480 Ma BP), (b) Silurian (420 Ma BP) and (c) Lower Carboniferous (330 Ma BP) periods.
Source: modified after Torsvik, 2014

In the following time, the ascending Caledonian mountains remained an erosional area until the Devonian period. As a result, large amounts of erosional rock debris were transported to the South and sedimented on the shelf of Laurussia. Remains of this period are nowadays given as up to 10 km sedimentary succession, covering the crystalline rocks of the Russian platform in Eastern Europe.

The Variscan orogeny

The Variscan orogeny was the most extensive and defining orogeny for Central Europe. It was the result the Gondwana supercontinent in the South (consisting of the present South America, Africa, Antarctica, Australia and India) colliding with the above-mentioned Laurussia supercontinent (consisting of the present Northern Europe, Greenland and Northern America). This orogeny started most likely in Central Spain during the Upper Devonian period (Pastor-Galán et al., 2013) and reached its peak in the Upper Carboniferous period (Figure 2-27c, 330 Ma BP). The collisional processes were characterised by folding and metamorphism, accompanied by multiple magmatic intrusions. At the same time compression and stacking of rock formations led to a significant thickening of the crust of up to 60 km, which is comparable to the thickness of the crust beneath the present Alps. This suggests that the Variscan Mountains may have reached a maximum height of 4 000 – 5 000 m. While the crust thickened, a strong uplift (crust re-equilibration) and erosion took place, whereby the Variscan Mountains were mainly flattened again at the turn of the Carboniferous to the Permian period. The mountain remnant represents today's bedrock, mainly exposed in the shape of low mountain ranges, which have been lifted again in post-Variscan times. Remains clearly describe large-scale thrust sheets and lateral displacements with transfer distances ranging from less than hundred kilometres to several hundreds of kilometres (Bender & Nesbor, 2017), causing a spatially complex geologic setting. Originally the orogenic belt was 500 – 1 000 km wide and spread over Southern, Western and Middle Europe to the western margin of the Russian Plate.

According to the degree of metamorphism in Europe, the Variscides can be subdivided into the Internal Variscides, dominated by crystalline rocks, and the external Variscides, dominated by less metamorphic fold-and-thrust belts (McCann et al., 2006). For Central and Western Europe, Kossmat (1927) further subdivided the Variscides into four main zones, according to the degree of metamorphism, the rock age and the tectonic setting. The Moldanubian is the former core area of the Variscides and is nowadays exposed e.g. in the Bohemian Massif, the Black Forest, the Vosges, the Massif Central, the Armorican Massif and the Iberian Central Zone. These areas are mainly characterised by high metamorphic rocks such as gneisses, migmatites, amphibolites and granites. To the north the Saxothuringian is following, built up of carbonates, clastics and vulcanites of young Precambrian to young Paleozoic age as well as Carboniferous granites, which faced low to high metamorphosis and have been folded, foliated and deformed. Nowadays, rocks are exposed at the northern margin of the Bohemian Massif, the Spessart and the Odenwald. Further north follows the Rhenohercynian zone, which is represented by the Rhenish Massif (including the Ardennes), the Harz and parts of south-western England, southern Ireland and southern Portugal (South Portuguese Zone). The Rhenohercynian zone describes the passive continental shelf of south-east Laurussia and related rocks, i.e. coastal, shelf and deep sea sediments (clay, sand, turbidites) of Devonian to Carboniferous age, which got impacted by low-grade metamorphism, folding and foliation (forming argillaceous schists and slate, quartzites etc.). In addition, submarine lava developed. The Subvariscan zone finally describes the northern margin of the central European Variscides, running from western Poland, northern Germany, over southern Netherlands, Belgium and northern France to South Wales and South Ireland. Even if rocks of that period, i.e. sand- and claystones of Upper Carboniferous age, are exposed only in small portions at the northern margin of the Rhenish Massif, they have a great geological importance since they host the major European hard coal regions.

At the end of the Variscan orogeny, during the late Carboniferous period, the thickened Variscan orogenic crust collapsed. The resulting re-equilibration of the crust, together with alternating transpressional and transtensional tectonic forces, led to the development of around 70 basins in western and central Europe within just 10 million years (300 – 290 Ma BP) (McCann et al., 2006; Henk, 1993). Major structures are the Southern Permian Basin, located within or to the south of the Variscan orogenic belt, and the Northern Permian Basin, located to the north of the Variscan orogenic belt. These major structures host a number of smaller basins, such as the North German Basin (e.g. McCann, 1998; Kockel, 2002), the Polish Basin (e.g. Dadlez, 2006; Nikishin et al., 1996), the Oslo Rift (e.g. Olaussen et al., 1994; Torsvik et al., 1998) and the Saar-Nahe Basin (e.g. Henk, 1993; Schäfer & Korsch, 1998). Along with the basin, thick sequences of fluviatile-lacustrine and Aeolian sediments of Rotliegend age developed, partly accompanied by volcanic rocks (McCann et al., 2006). While the first period of sedimentation took place under arid and desert-like conditions, since Late Permian times both the Southern and Northern Permian Basins as well as the Danish Basin, the Peribaltic Depression, the Hessian Basin and partly the Variscan folding area have been repeatedly flooded by the so-called Zechstein Sea, forming successions of carbonates, sulfates, rock salt and potassium salt with thickness ranging from 1 000 – 2 000 m (Walter, 2007). Later, from the Triassic period onwards, diapirism took place, leading to the salt pillows, domes and walls in the northwest European Depression. Nowadays, Zechstein salt is exposed only in small areas, e.g. at the margins of the Hessian Basin.

The marine environment has been dominated by the Panthalassa single world ocean as well as the semi-enclosed Tethys Ocean.

During Late Carboniferous to Triassic/Jurassic times, the Siberian and Kazakhstanian Continents collided with Laurussia, forming today's eastern geological boundary of Europe, i.e. the Ural Mountains (Ivanov et al., 1977). These united landmasses formed the Pangea supercontinent, which almost stretched from pole to pole, with most of Europe emerging above sea level and located near the equator.

The Mesozoic era (251 Ma – 65 Ma BP)

The Mesozoic overburden

From the Upper Triassic epoch onwards (ca. 237 Ma BP), the Pangea supercontinent began to break up again because a continental rift system developed that first separated Southern Europe from Africa, and then, from the Middle Jurassic period onwards (ca. 174 Ma BP), North America from South America (Stanley, 2001). The rift system gave way to the Tethys Ocean, which gradually expanded westward and thus traced the rifting process that finally gave origin to the North Atlantic Ocean. Ongoing tectonic processes also caused graben structures and troughs, such as the Viking Graben, the Central Graben, the Horn Graben, the Danish-Polish Trough and the Hessian Depression, which subsequently captured deposits up to 6 000 m thick (Walter, 2007). While the beginning of the Triassic, i.e. the Lower Triassic epoch, was characterised by a continental depositional environment which resulted in the formation of sandstones (Lower and Middle Bunter Sandstone), in the Upper Bunter Sandstone the so-called Rhöt Sea transgression, coming from the Polish Trough, also led to the development of clay and salt deposits. During the Middle Triassic, the marine depositional environment caused the development of limestone, lime marl and marl clay as well as, in the Middle Muschelkalk (Anisium), evaporates and in the Upper Muschelkalk partly continental red sediments. The Upper Triassic (Keuper) is then generally characterised by a falling sea level and resulting regression, with only a few episodic transgressions that found their way from South to Central Europe. Deposits from this time are mainly clastic sediments and subordinate, salt rocks and carbonates. The most prominent Triassic outcrops are located in large areas to the east and the west of the Upper Rhine Graben, central Germany, the Northern and the Southern Alps (Figure 2-30).

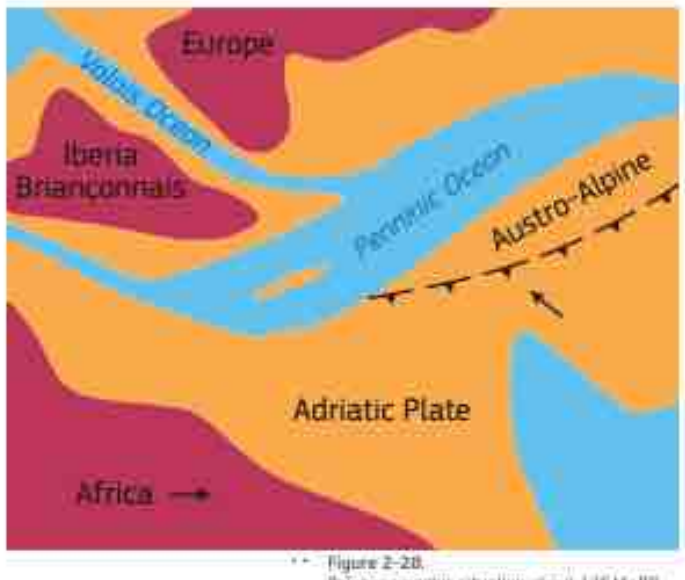

Figure 2-28.
Paleogeographic situation about 125 Ma BP
Source: modified after Stüwe & Homberg, 2011

A eustatic sea level rise, combined with regional subsidence and the opening of the central Atlantic Ocean due to ongoing plate tectonic processes (break-up of Pangea), caused flooding of large parts of Central and Northwestern Europe during the Jurassic period. However, significant portions remained mainland, i.e. the London-Brabant Massif, Rhenish Massif, Bohemian Massif, the Vindelician Barrier and most of Scandinavia. While the mainland got shaped by erosional processes, huge subsidence areas such as the Central Graben, the Sole Pit Basin, the Broad Fourteens Basin, the West and Central Netherlands Basin and the Lower Saxony Basin accommodated these erosion products in addition to the marine deposits (Walter, 2007; Rohl et al., 2001). The largest Jurassic outcrops nowadays occur in the French Jura Mountains, Southeast France, the eastern Paris Basin, southern Germany and southern Poland nowadays (Figure 2-32).

During Lower Cretaceous times, the marine depositional environment was still widespread on the European continent, but increasingly narrowed to smaller areas due to uplift of geologic features such as the Rhenish Massif. In addition to marine sediments, the accumulation areas gathered clastic sediments, e.g. the Danish Trough. The Upper Cretaceous period then showed another sea-level rise which caused extensive flooding and chalk deposition. From the geodynamic point of view, the Upper Cretaceous period is described by the opening of the North Atlantic Ocean and the Norwegian-Greenlandic Sea as well as the beginning of the Alpine orogeny, starting with the collision of the Middle Pennine Plate with the Adriatic Plate, causing subduction of the Penninic Ocean under the European Plate (Eo-Alpine orogenic episode; Pfiffner, 1992). Cretaceous outcrops can be found all over Europe, e.g. in France (Paris Basin), southeast England, Poland, Lithuania, Ukraine and Belarus (Figure 2-32).

Tectonic and geologic framework preceding the Alpidic Orogeny

The Alps consist of four zones in tectonic terms, the Helvetic, Penninic, Austro-Alpine and South Alpine zones (Froitzheim et al., 2008). The development of these structural zones had already started during the Triassic. Accompanied by the development of the Tethys Ocean from 237 Ma BP onwards (see above) a marginal basin formed at the most western part, i.e. the Meliata-Hallstatt Ocean (Schuster & Stüwe, 2010; Schmid et al., 2004). Ongoing spreading was guided by the development of new oceanic crust which caused both a further opening of the sea and cooling of the crust with increasing distance to the heat source and resulting decrease of crust thickness at the same time. This slow thermal subsidence together with the tropical climate gave rise to the development of up to 3 000 metres thick carbonate reefs between 245 Ma – 199 Ma BP which nowadays form the Northern Carbonate Alps and the Dolomites (Handy et al., 2010).

The continued opening of the Penninic Ocean and resulting compressional forces initiated a subduction zone in the western part of the Tethys Ocean (the Meliata-Hallstatt Ocean) around 170 Ma BP, where lithosphere that carried the Adriatic Skit was subducted under another lithospheric plate carrying oceanic crust. Partly oceanic crust was overthrusted onto the Adriatic Skit (e.g. Vardaz Zone, Meliata Zone) from 160 Ma BP onwards. The continuation of tectonic movements caused the vertical stacking of rock formations and the development of Jurassic coral reefs which developed on top in this area, while deep sea sediments and submarine debris flows developed as well. At the same time calcareous sediments were deposited to the north of the Penninic Ocean unaffected by tectonic forces (Froitzheim et al., 2008; Schuster & Stüwe, 2010).

From about 145 Ma BP onwards, the Adriatic Skit was detached from Africa and turned into an independent plate, the Adriatic Plate. Due to the eastwards drift of Africa relative to Europe the Adriatic Plate moved north towards Europe. This event marks the beginning of the convergence between Africa and Europe and thus the development of the Alps we know today. Tectonic movements during Lower Cretaceous times caused the enlargement of the Penninic Ocean to the north (Valais Ocean) which in turn led to the separation of an island, the Iberia-Brianconnais microcontinent (Schmid et al., 2004; Handy et al., 2010). At the same time, a new subduction zone originated within the Adriatic Plate along which material, coming from north, was subducted under the southern part of the Adriatic Plate (Figure 2-28).

As a result, parts of the crust have been peeled off the lithosphere and accreted to the southern part of the Adriatic Plate developing into nappes. Additional pressure caused internal folding (Schuster & Stüwe, 2010). The oldest remnants of this period are the Austro-Alpine nappes (135 Ma BP, Figure 2-29). The passive continental margin of the subducting Adriatic Plate turned

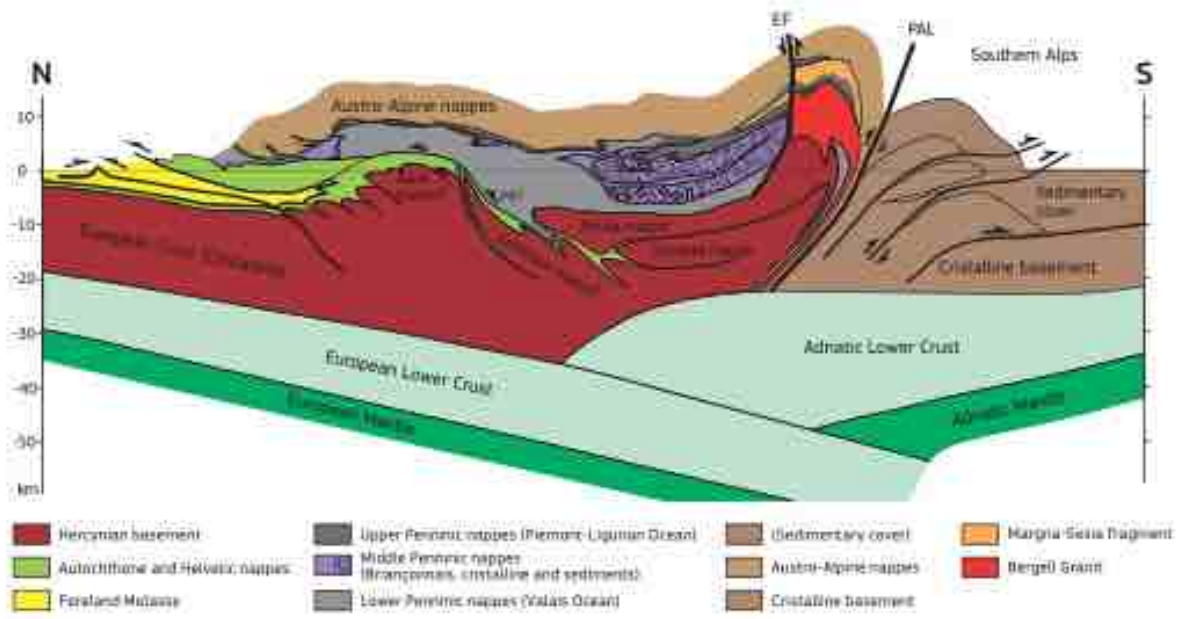

Figure 2-29.
Geologic cross section through the European Alps, running N-S from approximately the Bodensee (Lake Constance) to Bergamo (see Figure 2-28), showing the nappe pile that originated as a result of the collision between Africa and Europe.
Source: modified after Gisler & Hetenergi, 2011.

into an active margin about 80 Ma BP. Thereby, it started to shear material from the Penninic Ocean leading to the development of the Penninic nappes stack. Other geologic features were generated in the process, i.e. the Piedmont-Liguria Ocean, the Valais Ocean and the Iberia-Brianconnais Microcontinent (Figure 2-28). The development of nappes was also accompanied by deep subduction (up to 80 km) of lithospheric material which was metamorphosed (as well as folded) corresponding to depth-dependent temperatures and pressures. Later on (from 92 Ma BP onwards) those rocks were uplifted back to the surface, e.g. the Koralpe-Wölz nappe system (Froitzheim et al., 2008; Schuster & Stüwe, 2010).

The Cenozoic era (65 Ma BP – present)

The Alpine region

When the subduction of the Penninic Ocean was completed at about 50 Ma BP, the southern margin of the European continent became incorporated into the subduction zone. Sheared-off crust (Variscan rocks, Carboniferous granites and Permian sediments) is represented in the Helvetic nappes which are internally folded (Figure 2-30). As before, the subducted parts of the lithosphere underwent metamorphosis, folding and uplift, e.g. the external massifs (von Raumer et al., 2013). Between 40 and 30 Ma BP magmatism occurred (e.g. Rensen-Pluton), mainly along the Periadriatic line, which describes both the initial subduction zone and, beneath the Alps, the contact between the Adriatic and the European Plates (Figure 2-30).

The direction of overthrusting switched from northward to southward from 35 Ma BP onwards (Handy et al., 2010), resulting in the development of the Southern Alps (Schuster & Stüwe, 2010). Due to increased crustal thickening in association with a slab break-off, dynamic uplift occurred creating a high mountain region (von Blanckenburg & Davies, 1995; Schlunegger & Kissling, 2015). Erosional processes increasingly deformed the landscape. Erosional products accumulated to the North and South, forming the Northern and Southern Molasse Zones. The Eastern Alps were affected by E-W extension between 20 and 10 Ma BP, while plate movements caused their narrowing in the N-S direction at the same time. In combination with this movement, the resulting network of normal faults uncovered older strata which are exposed in tectonic windows (e.g. the Tauern window and the Engadin window, Figure 2-30). Dewatering channels and basins developed along normal faults at the same time (e.g. the Lavanttal Basin or the Vienna Basin), thereby accumulating huge quantities of sediments. Since the ongoing narrowing in the Central and Western Alps could not be sufficiently compensated by lateral extension, rocks continued to pile up and fold (e.g. in the external massifs). Even if strong tectonic activities ceased around 7 Ma BP, vertical movements continued and lifted the Alps locally up to 1 000 metres within the last 5 million years (Schuster & Stüwe, 2010). At about 5.3 Ma BP the Mediterranean Sea almost dried out for about 0.5 M years. However, the high topographical gradient provided significant erosional power to streams flowing towards the Mediterranean Sea, enabling them to carve the canyons that later, during the Pleistocene, became basins which nowadays host the large Italian lakes, such as Garda, Como and Maggiore (Schuster & Stüwe, 2010). The present shape of the Alps is the result of glaciations during the Quaternary which shaped the landscapes resulting from the pre-glacial processes (Litt et al., 2008).

Even though the Alps are the most prominent representative of the Alpidic orogeny, there are lesser Alpine chains, such as the Betic Cordillera, the Pyrenees, the Apennines, the Dinarides, the Carpathians, and the Caucasus, respectively.

The region north of the Alpidic system

The tectonic forces described above also impacted the area north of the Alps, causing the development of huge tectonic faulting systems (e.g. Bresse Graben, Upper Rhine Graben) and the uplift of the nowadays low mountain ranges (e.g. Black Forest, Vosges, Odenwald, Rhenish Massif) (Reicherter et al., 2008; Behrmann et al., 2005; Berger et al., 2005). The ongoing opening of the North Atlantic Ocean caused the development of Iceland, while at the same time Greenland increasingly moved away from Europe. Also, the North Sea Basin developed at that time and acted as an accumulation area from the Paleogene onwards (Rasser et al., 2008). During the Middle Oligocene, the North Sea was connected to the Tethys Ocean through the Hessian Basin and the Upper Rhine Graben. After this transgressional peak, a continuous retreat of the sea led to increasing land areas (Rasser et al., 2008). As a result, the depositional environment during the Tertiary in Europe is generally divided into onshore and offshore conditions. While the North Sea received glauconitic sands and clayey fine sands mainly from the Fennoscandian landmass, in the Hessian Basin and the Upper Rhine Graben carbonates, gypsum and salt deposits were also deposited. Due to subtropical conditions onshore, lateritic weathering covers developed which were redeposited and turned into clays and carbonate-free quartz sands. The majority of these sediments were not lithified (Walter, 2007).

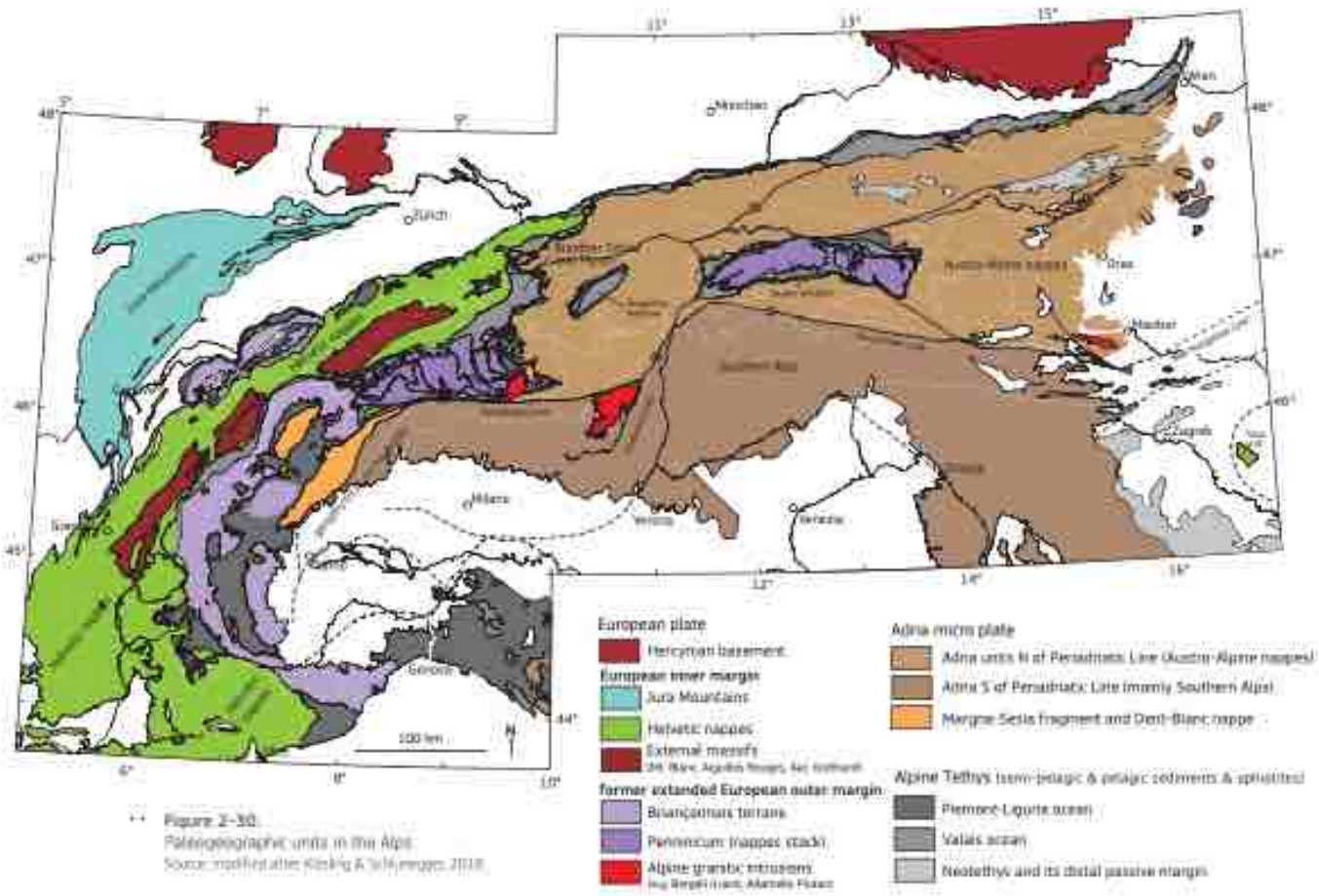

Figure 2-30.
Paleogeographic units in the Alps.
Source: modified after Kissling & Schlunegger, 2018.

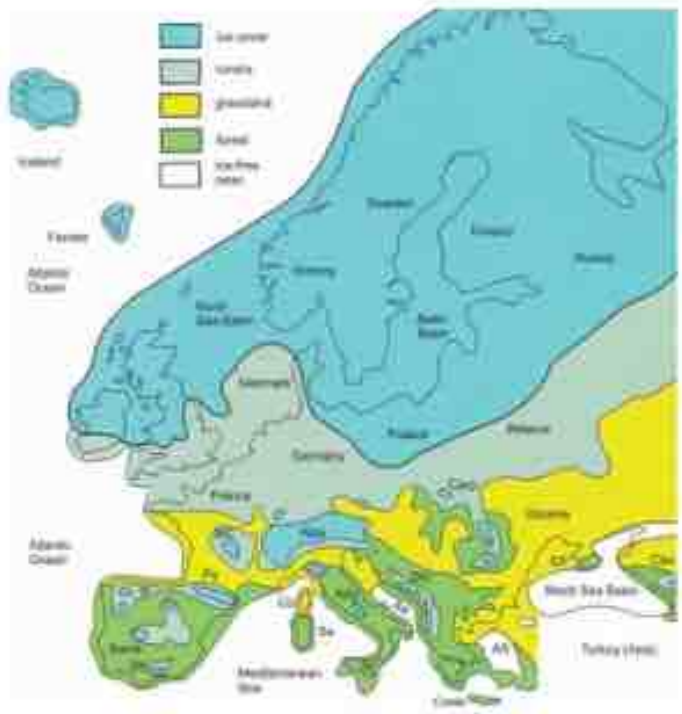

Figure 2-31.
Maximum ice cover during the Weichselian (~ 20 ka BP). Ad, Adriatic Sea; AS, Aegean Sea; Be, Betic Range; Carp, Carpathians; Cau, Caucasus; Co, Corsica; CP, Crimean Peninsula; Din, Dinarides; MC, Massif Central; Py, Pyrenees; Sa, Sardinia; Si, Sicily. Due to the Mercator projection, the area in the northern part of the map is exaggerated.
Source: Ehlers, 2011 & 2015.

Towards the end of the Neogene epoch, during the Pliocene, a significant temperature drop preceded the Quaternary period, around 2.6 Ma BP. Quite a few glaciations occurred and caused ice fields of different size that repeatedly covered large parts of Europe (Eissmann et al., 1995; Litt et al., 2008; Penck, 1879). The largest of these was the Elster Glaciation at about 400 – 320 ka BP, which completely covered northern Europe as well as the Alps and their surroundings. U-valleys developed due to ice flow and related erosional effects in mountainous regions. Other main advances of ice shields were the Saale Glaciation (ca. 300 – 120 ka BP) and the Weichselian Glaciation (115 – 11.6 ka BP, Figure 2-31) (Litt et al., 2008). More moderate climate conditions

caused the end of this last glaciation and led to the Holocene development until present. Even if tectonic processes at that time did not much impact the landscape, glaciations did. Large areas of Scandinavia were levelled down to the bedrock, and huge quantities of sediments were deposited south of the ice shields, e.g. in the North German and Polish Basins (Fjeldskaar et al., 2000). The present drainage system developed, along with terraces at the same time which document the intensity of material erosion, transport and deposition, mainly sand and gravel (Litt et al., 2008).

Glacial loess deposits developed in periglacial areas, e.g. in the northern Upper Rhine Graben, Northern France, South Poland, Ukraine and Hungary (Litt et al., 2008; Frechen et al., 2001 & 2003). Isostatic adjustment since the last glaciation led to an ongoing uplift of Scandinavia and the Baltic region, while the former glacial foreland was affected by moderate subsidence (Riis & Fjeldskaar, 1992; Milne et al., 2001). The depositional history to the present is completed by Holocene sediments which are mainly associated with fluvial dynamics, e.g. high flood loam. Nowadays, Quaternary sediments are exposed all over Europe, especially in the North European lowlands (Figure 2-30).

Volcanism

The tectonic processes during the Cenozoic era described above also led to significant magmatism/volcanism. The collision processes in the Mediterranean subduction of crust caused the development of volcanic arcs like the Calabrian Arc (hosting the Vesuvius, the Etna and the Stromboli) and the Hellenic Arc (hosting e.g. the historically active volcanoes Methana, Milos, Nisyros and two in Santorini). In central Europe the stress state due to plate tectonic movements led to the development of intra-plate volcanism (e.g. Kaiserstuhl, Vogelsberg, Rhenish Massif, Massif Central, Bohemian Massif, Eifel) (Reicherter et al., 2008; Rasser et al., 2008; Wilson & Downes, 2007). The most prominent region, however, is the North Atlantic Igneous Province (NAIP). Due to the opening of the North Atlantic Ocean, large amounts of lava spread over an area of 2500 km length and up to 2000 km width from east Greenland to Iceland and further to north Ireland, forming the Faroe-Iceland Ridge, the Rockall Plateau, and the Faroe Islands (Park, 2014 & 2015).

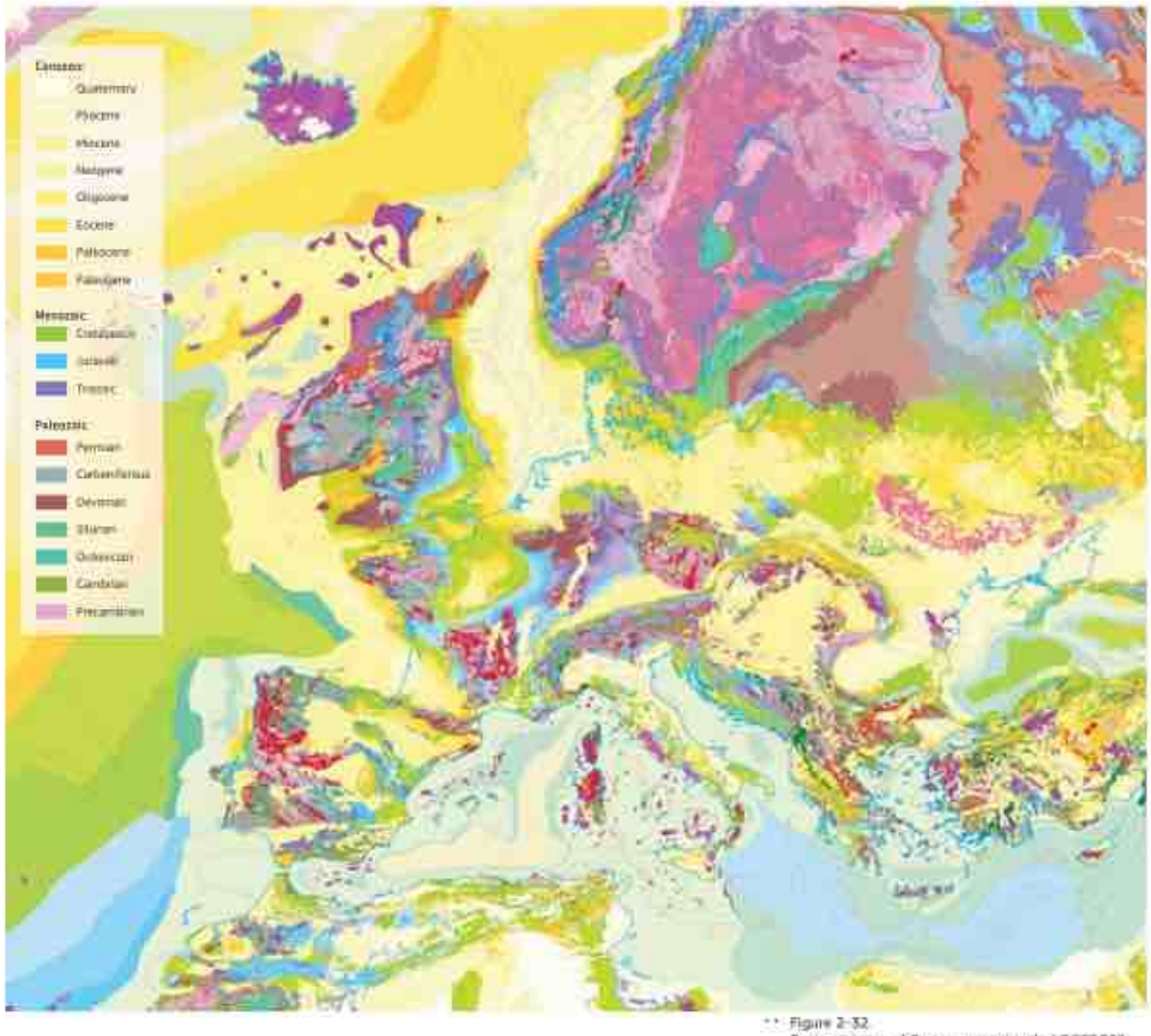

Figure 2-32
Geological map of Europe, original scale 1:5 000 000
Source: modified after Asch, 2005

Case study: Simplified description of the Ukrainian geology

The general features of the geological structure of Ukraine are determined by its location within: 1) the Eastern-European Pre-Riphean Platform; 2) the Scythian Epipaleozoic Plate; 3) the folded belt of the Ukrainian Carpathians and Crimean mountains, which is a part of the Alpine-Himalayan belt of Eurasia, formed during the Alpine orogeny in the Cenozoic era.

The geostructural axis of the whole Ukraine is the Ukrainian Shield, extending from north-west to south-east through the entire country with a stripe of about 1 000 km length and 250 km width. It has a long and complex history, spanning an interval more than three billion years, during which geological structures evolved, ranging from granulite-gneiss and granite-greenstone terrains in the Early and Late Archaean to intracratonic basins and troughs and zones. Inside the Ukrainian Shield, there are notably the folded Precambrian basement and the overlaying Phanerozoic sedimentary cover of irregular distribution and total thickness up to 120 m.

The Ukrainian Carpathians are represented with an area of young (Alpine) orogeny that commenced in the Neogene period, and it still continues. The Crimean Mountains emerged in the Mesozoic era, and then collapsed; their rejuvenation occurred in Alpine time, resulting in their fold-block patterns. The Donetsk folded structure arose under Hercynian orogeny.

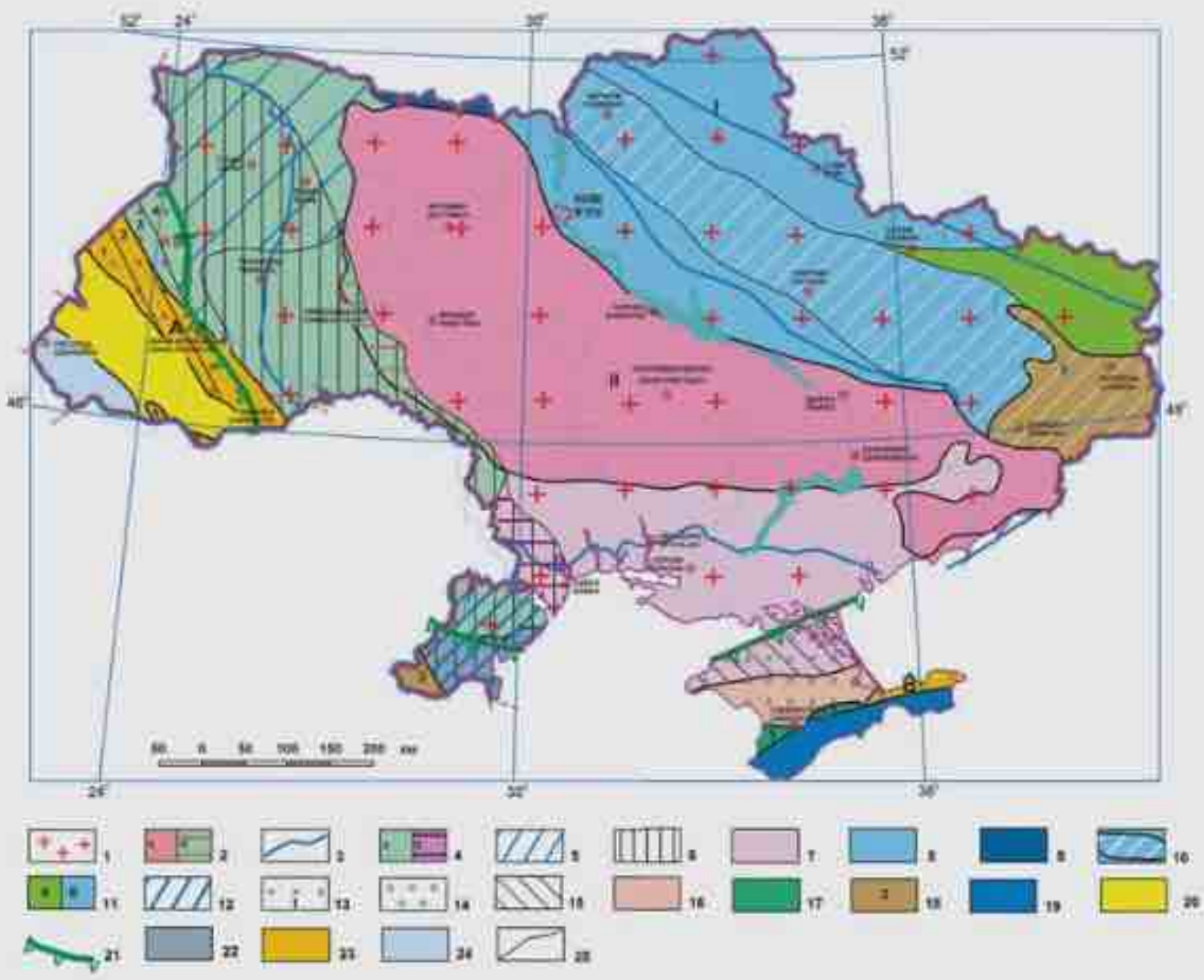

Figure 2-33.
Geological structure of the Ukraine.
1 - Eastern-European Pre-Riphean Platform; 2 - Ukrainian Shield: a - in contours of isohypse of basement 5 km; b - under formations of Volyno-Podolska Plate; 3 - Slopes of Ukrainian Shield and Voronezhskyi massif in contours of isohypse of basement -1 km; 4 - Volyno-Podolska Plate and fragments of Moldovska Plate (a) under formations of Prychornomorska Depression (b); 5 - Volyno-Podolsky Riphean Trough; 6 - Dnistrovskyi Late Vendian Early Devonian Paleotectonic Trough; 7 - Prychornomorska Cretaceous-Paleogene Depression; 8 - Dniprovsko-Donetska Mesozoic Depression; 9 - Pripyatskyi Late Devonian-Carboniferous Trough; 10 - Dniprovsko-Donetskyi Riphean-Devonian paleorift; 11 - South-Western limb of Voronezhska Anteclise (a) under formations of Dniprovsko-Donetska Depression; 12 - Prydobrudzhska Jurassic Depression; 13 - Western-European Epipaleozoic Platform and structural elements of its basement: Lemaskyi massif (1) and Rozhnitska zone (4) of Baikatska consolidation, Kokhanivska (2) and Bava-Ruska (3) zones of Caledonian consolidation; 14 - Scythian Epipaleozoic Plate; 15 - Kerkinitska - Northern Crimean Triassic and Early Cretaceous Trough; 16 - Kalamitske Central Crimean Cretaceous-Paleogene Uplift; 17 - Aimitska (1) and Biloporska (2) Cretaceous Depressions, Folded Structures; 18 - Hercynian-Marmaroshskyi massif, altered with Alpine folding (1), Northern Dobrudzha (2), complicated with Cimmerian folding, and Donetskyi Basin (3); 19 - Cimmerian-Alpine - Mountainous Crimea and Kerch Peninsula; 20 - Alpine - Carpathian Mountains; 21 - external border of Galician-Crimean Riphean-Triassic Paleorift, Foreland Basins; 22 - Pre-Dobrudzha Foredeep (Carboniferous-Early Triassic); 23 - A: Procarpathian Foredeep (Miocene), B: Indoto-Kubanskyi Foredeep (Oligocene-Miocene); 24: Inner-Eastern Carpathian Trough (Miocene-Pliocene); 25: borders of tectonic structures.
Source: Vikulenko & Sakevich, 2005

2.3.3 Simplified description of European soil

Soil is defined as the uppermost layer of the Earth's crust and is the interface between the ground, air and water. Soil performs many vital functions: food and other biomass production, storage, filtration and transformation of many substances including water, carbon, nitrogen. Soil has a role as a habitat and gene pool, serves as a platform for human activities, landscape and heritage and acts as a provider of raw materials.

It is a natural substance composed of weathered rock particles (minerals), organic matter, water and air. A typical sample of mineral soil comprises 45% minerals, 25% water, 25% air and 5% organic matter – however, these proportions can vary. The organic matter can include living organisms, the decaying remains of plants or excretions by plants and animals. It is an extremely complex, variable and living medium.

Soils are the result of six main factors: parent material (rocks and sediments), climate, position in the landscape, vegetation, living creatures, time and the effect of people. The patterns shown on the map reflect variations in the intensity of the various soil forming factors from one region to another and explain why there are so many different types of soils in Europe.

Soil-forming processes tend to be slow and occur over long periods of time — typical rates of soil formation under permanent grasslands in temperate climates are in the order of only 1 – 2 cm per 100 years. Soil that is lost due to degradation processes (e.g. erosion, pollution) would need hundreds or thousands of years to recover naturally. Compared to the lifespan of human beings, soil loss is not recoverable which means that soil must be regarded as a non-renewable resource.

From the photographs in this section, it is clear that soils have distinct colours, which are due to the varying proportions of organic and mineral matter. If the soil is rich in organic matter then the soil is dark and vice versa. If the soil is rich in a specific mineral, such as iron oxide (red) or calcium carbonate (white), then the soil will reflect that colour.

The soil resources of Europe are diverse. The map in Figure 2-34 below is derived from the 1:1 000 000 scale Soil Geographical Database of Eurasia. The database is the result of a collaborative project involving all the European Union Member States and neighbouring countries. The map shows a simplified representation of the diversity and geographical variability of the soil cover across Europe. The underlying database has been processed to extract the most dominant soil type for a particular unit of landscape. Each colour represents a specific type of soil as recognised by the World Reference Base System.

Relatively young soils dominate northern and central Europe. Soils in northern Europe tend to have higher organic matter content than those in the south. Poorly developed soils or soil with accumulations of calcium carbonate characterise the Mediterranean basin.

Figure 2-34.
The major soil types of Europe
Source: EC-JRC

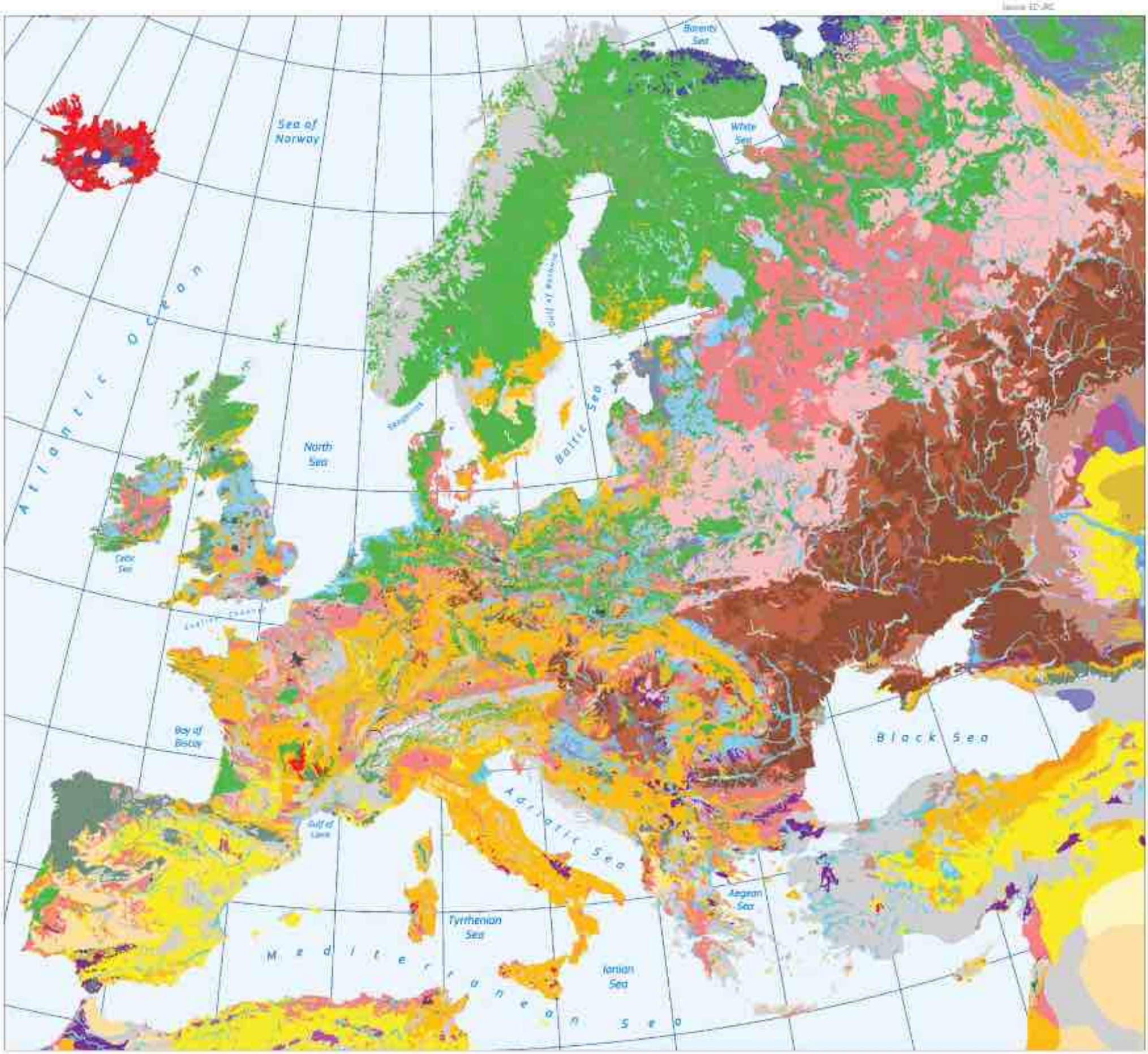

Soil and gases

Gases are found in spaces between soil particles. The amount of gas contained by soil is directly related to the bulk density of the soil and the amount of water held in the soil profile at a particular moment in time. In turn, this is governed by the texture and structure of the soil. Structure is conditioned by the amount of organic matter in the soil.

There is a strong link between the gas and water content of the soil, in most cases they are inversely related. As water drains or is removed from a soil pore by drainage, evaporation or root absorption, the space is filled by gases. The network of pores within the soil facilitates the movement of gas and is responsible for aerating or ventilating the soil.

The main gases found in soil are nitrogen, carbon dioxide, oxygen, methane and radon. Oxygen is critical because it allows for respiration of both plant roots and soil organisms. In most cases, the concentration carbon dioxide is higher in soil than the atmosphere at ground level.

In soil, gases move by diffusion along a gradient from high concentration to low concentration.

Soil structure

The structure refers to the natural arrangement of soil particles (also called aggregates) and the space between them.

Soil structure has a major influence on root growth and the movement of water and air within the soil. It depends on factors such as the parent material, the chemistry and structure of minerals, biological activity and environmental conditions (such as shrinking the presence of swelling clays or freezing and thawing).

Soil structure is affected and damaged by different land management practices such as tillage, wheel traffic and animal stocking densities. Structure can be improved through the addition of organic matter (such as compost), crop rotations or avoiding tillage, especially in wet conditions.

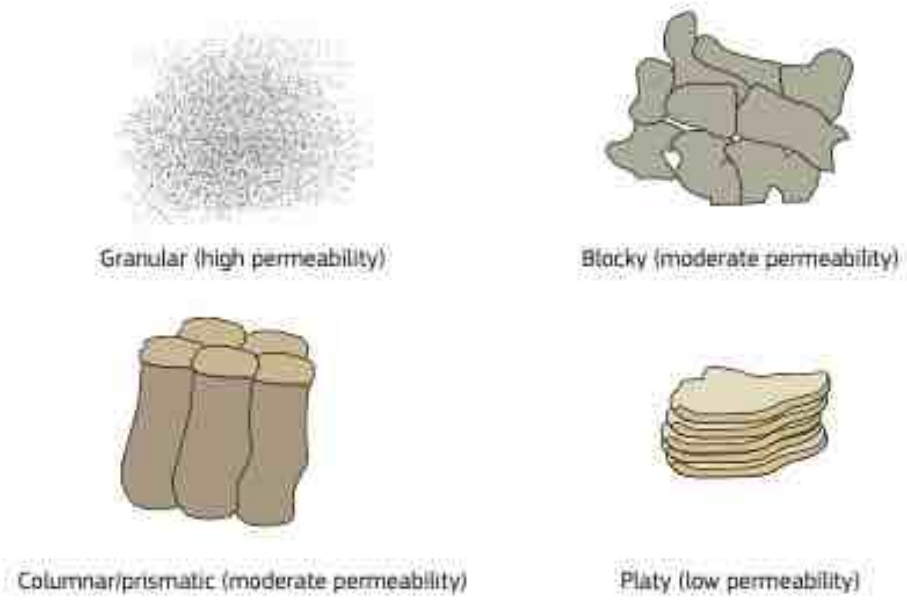

Figure 2-35
Examples of soil structure (clockwise from top left: granular or crumb, blocky, platy, prismatic or columnar.
Source: FAO

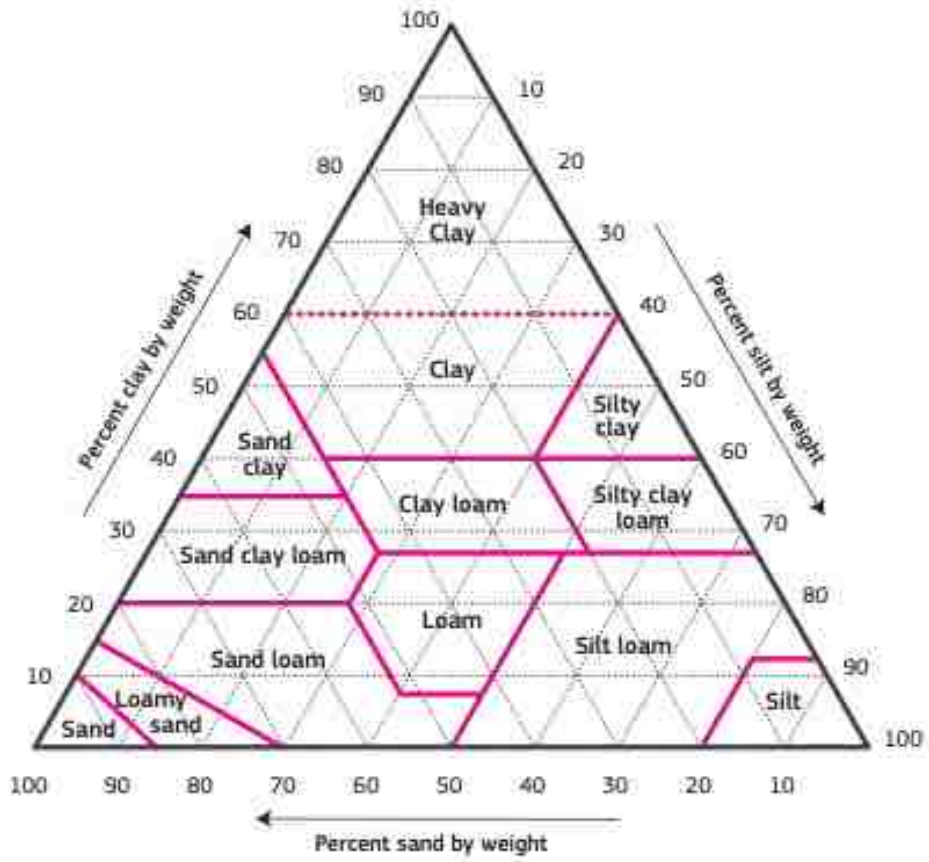

Figure 2-36
Soil texture triangle – soils can be categorised according to their texture following particle size analyses in a laboratory. Thus a soil with 40% sand, 40% silt and 20% clay fractions will be a loam.
Source: FAO

Figure 2-37.
Profiles of sand (left) and clay (right) soils.
Source: Erika Michael

Soil structure is usually described in terms of the degree of aggregation (from structureless to strong), size (very fine to very thick) and shape of aggregates (e.g. granular or crumb, blocky or subangular, prismatic or columnar, platy).

Soils with a good structure will have lots of spaces or pores between aggregates. Soils with few pores and fissures are said to be compacted.

Soils with a high clay or organic matter content tend to have a more stable soil structure than those that are mostly sand or silt. The presence of sodium salts in the soil can cause the structure to collapse.

Soil texture

Texture describes the proportion of different sized mineral particles that are found in a soil (Figure 2-36).

The main particle size classes are clay (< 0.002 mm), silt (0.02 – 0.63 mm) and sand (0.063 – 2.0 mm). Furthermore, large sand particles can be described as coarse, medium and fine.

Texture is measured by sieving or by feeling the grains by rubbing the soil between your fingers. Particle size classifications may vary between different countries.

Soil permeability and erodibility

The greatest obstacle to soil erosion modelling at larger spatial scales is the lack of data on soil characteristics. One key parameter for modelling soil erosion is the soil erodibility, expressed as the K-factor in the widely used soil erosion model, the Universal Soil Loss Equation (USLE) and its revised version (RUSLE). The K-factor, which expresses the susceptibility of a soil to erode, is related to soil properties such as organic matter content, soil texture, soil structure and permeability. The K-factor is a lumped parameter that represents an integrated annual value of the soil profile reaction to the process of soil detachment and transport by raindrops and surface flow (Renard et al., 1997). Soil erodibility is best estimated by carrying out direct measurements on field plots (Kinnell, 2010). However, since field measurements are expensive and often not easily transferable in space, researchers investigated the relation between 'classical' soil properties and soil erodibility.

Soil erodibility combines the influence of texture (silt, sand, clay), soil organic carbon, soil structure, permeability, coarse fragments and stone cover. At European scale, those attributes are available in the Land Use/Cover Area frame Survey (LUCAS) Topsoil database (Orgiazzi et al., 2018). In the 2009 LUCAS survey, topsoil samples (0–20 cm) were collected from 19 969 locations (approximately 10% of the total LUCAS observations) from 25 out of 28 EU countries, except for Romania, Bulgaria and Croatia. In the 2012 LUCAS survey, a further 2 034 topsoil samples were collected from Bulgaria and Romania following the standard procedure of 2009. In total around 22 000 soil samples of the LUCAS topsoil have been used to develop a high-resolution soil erodibility dataset (Figure 2-38).

Since data on soil permeability are not available at European scale, the textural classes were used to derive the soil permeability. The effect of stone cover is important both on the soil permeability and the shielding of rain splash. The majority of the samples had a moderate permeability class which means that their texture is loam or silty loam (Saturated hydraulic Conductivity: 5.1 – 20.3 mm/h). However, if we take into account the coarse fragments, the permeability of soils decreases. In future analysis, data analysis of the fraction of very fine sand and hydraulic conductivity would certainly improve the textural and permeability calculation factors, and lead to more precise estimations of soil erodibility.

Surface stone content, which acts as protection against soil erosion was for the first time included in the K-factor estimation. This correction is of great interest for the Mediterranean countries, where stoniness is an important regulating parameter of soil erosion (Panagos et al., 2014).

The soil erodibility dataset (Figure 2-38) is reverse to the permeability, which means that low permeability contributes to high erodibility values (also high erosion ones), while fast permeability has an influence in lower erodibility values. The soil erodibility dataset is also an index for the vulnerability of ecosystems.

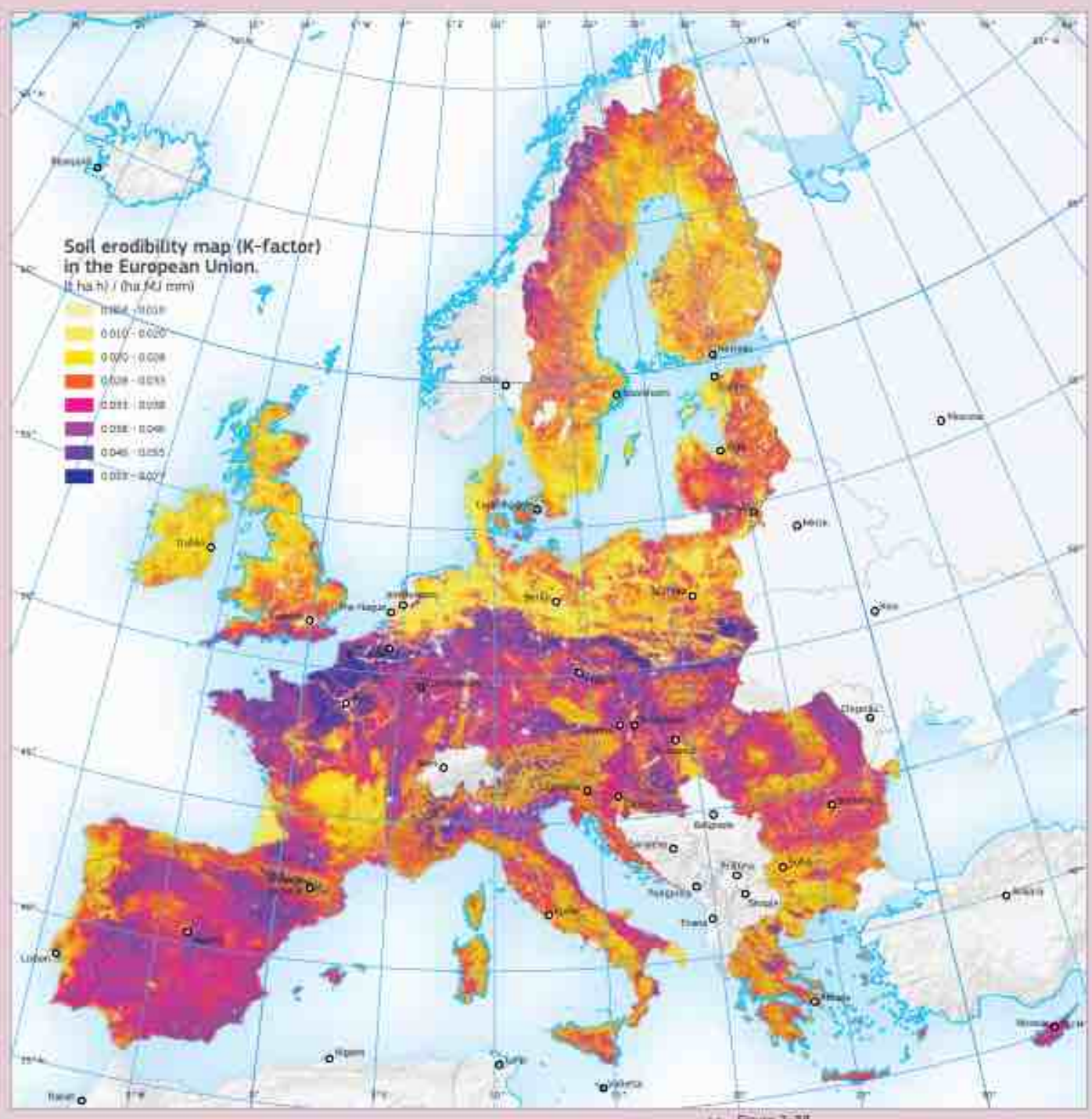

Figure 2-38.
Soil erodibility map (K-factor) in the European Union (EU).
Source: Panagos et al., 2014

2.4 Statistics, measurement, mapping

This section intends to address some basic concepts which should be kept in mind when generating a map of an environmental quantity. Since this is a large subject, we concentrate on point-type quantities, such as concentrations of radon or some element, sampled on individual locations (houses or spots in the field).

2.4.0 From sampling to mapping

Generating a map of a quantity, e.g. indoor radon concentration, is a procedure that consists of several stages. A flowchart is shown in Figure 2-39. Most importantly, the objective must be well defined for designing an experimental strategy which takes into account previous knowledge and possible constraints. Typical objectives are contour level maps, which show the geographical distribution of the levels of a quantity of interest; or class maps, which show whether a criterion regarding the quantity is fulfilled in an area, or not, for example, whether a reference level is exceeded on average or not.

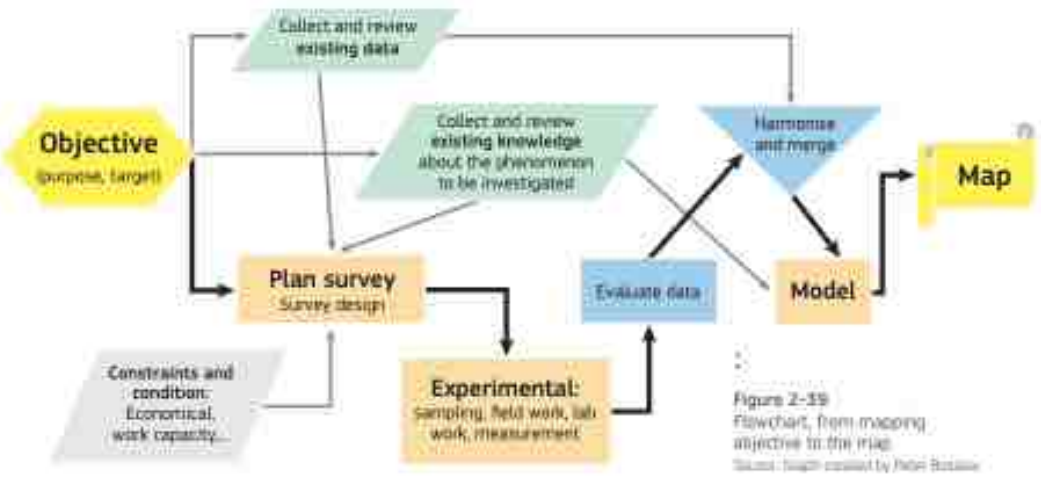

Figure 2-39
Flowchart, from mapping objective to the map
Source: Graph created by Peter Bossew

Only then would experimental (field and lab) work start, followed by data analysis; modelling (if required), leading to the final result which is the map. The individual steps should be quality assured, which means selecting adequate methodology and controlling for uncertainty as far as achievable. It can happen that designing the survey requires input which is not available from previous work; in this case a pilot study may be necessary in order to acquire the necessary information. A typical example in radon studies is the assumed dispersion within the investigated area, quantified e.g. by the geometrical standard deviation (GSD), which is a crucial quantity for estimating the sample size.

2.4.1 Observed and observation process

In a physical experiment, one always deals with two processes. One is the process which one wants to assess, the other one the processes which does that assessment, e.g. measurements. After all, measurement instruments are also physical systems. The observation process is tailored such as to allow statements about the observed process, or about a quantity which is its state variable.

The observed process is subject to temporal or spatial variability, or both. The observation process shall respond to this variability, sufficiently, exactly and sensitively.

The observation process, i.e. the procedure including sampling and measurement and the physical behaviour of the devices and instruments used for these purposes, must therefore be well understood and kept under control as far as achievable. For example, for field measurements, it must be known how a measurement instrument reacts to outdoor temperature or humidity.

In any case, the observed value that has been read from the display of the measurement instrument (or more common in these times, has been retrieved from a data log file produced by an instrument) is not the true value of the observed quantity (measurement uncertainty). Instead, it is the true value under the action of the measuring device (see the paragraph on calibration below).

2.4.2 Accuracy, precision and representativeness

Quality-assured measurements are preconditions for valid survey results and, finally, for valid maps. Key concepts are accuracy, precision and representativeness. In the best case, these should be validated before actually engaging in an experiment or measurement series. If existing data are used, which is less optimal, but inevitably often the case, one should try to verify them at least in the aftermath, or investigate possible deviations from the optimal case.

Repeated observations

a. Known true value

Repeated observations of the same quantity, for example dose rate measurements of a constant source performed with one instrument, form a data sample. If the mean of this sample equals the true value of the measured quantity (within given tolerance), the measurement is **accurate** and the bias low. In general, the measured values that constitute the sample are dispersed around the mean. The measurement is called **precise** if the spread around the mean is below a given tolerance. This concept is visualised in Figures 2-40 and 2-41 (upper graph).

The purpose of repeated measurements is to check the quality or the validity altogether of the observation process or the measurement instrument.

b. Unknown true value

In this case, accuracy cannot be determined, only precision. However, if the size of the measured effect is not known, but its constancy is known or assumed from physical knowledge, repeated series of measurements with the same instrument can at least inform about the constancy of bias, because the mean must remain the same (up to statistical tolerance).

Repeatability quantifies whether an observation or experiment, performed under the same conditions, i.e. with the same instrument, by the same person, in the same lab, under the same meteorological conditions, etc., yields the same result (up to statistical tolerance).

Calibration

An instrument is called well calibrated if its bias is tolerably low under all measurement conditions, for which calibration has been declared valid (to be specified in the calibration procedure). For a specified range, its readings should also be precise.

Calibration means to relate the reading of an instrument to a known true value. The assumption is that the readings are repeatable. Correct calibration is the most important issue in metrological quality assurance.

Parallel observations

a. Known true value

Parallel observations of the same quantity with several instruments, for example comparative dose rate measurements of a constant source with different instruments, also form a data sample. Its mean and dispersion informs about accuracy and precision of a certain class of instruments. The concept is visualised in Figure 2-41 (lower graph).

The purpose is to compare the performance of different instruments in **intercalibration** exercises, also called round robin tests.

b. Unknown true value

If the true value of a quantity is difficult to determine, one may apply different measurement methods, all of which are assumed to be able to yield repeatable results. In an **intercomparison** exercise, an estimate of the true value is established from the different methods or participants. Outlier analysis points to possible inadequacy of particular methods.

The setting can be further relaxed by allowing different observation conditions in general (i.e. not only different instruments, but also at different times).

Reproducibility quantifies whether the same result (up to statistical tolerance) is achievable or has been achieved by different methods. Reproducibility is a stronger condition than repeatability, for which variability between observation conditions is excluded.

Intercalibration and intercomparison exercises also inform about the practicability of different methods.

Some important statistics basics

Given a sample $(x_1 \ldots x_n)$ of a population X (which can be finite or infinite).

Arithmetic mean: $AM = \frac{1}{n}\sum_{i=1}^{n} x_i$

The AM is an unbiased (accurate) estimate of the expectation of X, $E(X) = \int x f(x)dx$ where f(x) is the probability distribution of X. The precision of the AM depends on the sample size n.

Distribution: The probability density function f(x) says that the probability that the quantity X lies in the interval (x, x+dx), equals f(x) dx. Therefore, the $prob(x_1 \le X \le x_2) = \int_{x_1}^{x_2} f(x)dx$. The cumulative distribution function F(x) = prob $(X \le x) = \int_{-\infty}^{x} f(x')dx'$. The complement, 1-F(x) probability to exceed x, is called the exceedance probability or survival function.

Variance: Empirical variance $Var = \frac{1}{n-1}\sum_{i=1}^{n}(x_i - AM)^2$

Var-hat is the unbiased estimate of the variance, $E(Var) = Var(X) = \int (x - E(X))^2 f(x)dx$.

Standard deviation: Empirical standard deviation $SD = \sqrt{Var}$.

This is not an unbiased estimator of $\sigma = \sqrt{Var}$, because the square root is not a linear function. Generally, for any statistic $E(g(stat)) \neq g(E(stat))$ for non-linear g.

Coefficient of variation: empirical $cv = SD/AM$. Also not an unbiased estimator of $\sigma/E(X)$.

This is used as dimensionless dispersion measure.

Geometrical mean: empirical $GM = [\prod_{i=1}^{n} x_i]^{1/n} = e^{AM(\ln x)}$.

$GM \le AM$. GM is not an unbiased estimate of EX. Sometimes it is used instead of the AM because it is less sensitive against extremes which can distort the AM, i.e. more precise (=less uncertain).

Geometrical standard deviation: Another useful dimensionless dispersion measure: $GSD = \exp(SD(\ln x))$.

Standard error SE or standard deviation of the mean: The AM calculated from a sample of size n (n data) from a population is again a random variable which has uncertainty. Its size is $SE = SD/\sqrt{n}$.

Covariance: Measure of association between two quantities X and Y. $Cov(X,Y) = E((x - E(X))(y - E(Y))$.

$Cov(X,X) = Var(X)$.

The Pearson's **correlation coefficient** when applied to a population is given by: $\rho(X,Y) = \frac{Cov(X,Y)}{\sigma_X \sigma_Y}$.

The **Spearman correlation coefficient** is defined as the Pearson correlation coefficient between rank variables. For a sample of size n, the n raw scores Xi, Yi are converted to ranks x(i), y(i), and r_s is computed from:

$$r_s = \rho(X_{(i)}, Y_{(i)}) = \frac{Cov(X_{(i)}, Y_{(i)})}{\sigma_{X_{(i)}} \sigma_{Y_{(i)}}}$$

where

rho $(X_{(i)}, Y_{(i)})$ denotes the usual Pearson correlation coefficient, but applied to rank variables;

$Cov(X_{(i)}, Y_{(i)})$ is the covariance of the rank variables;

$\sigma_{X_{(i)}}$ and $\sigma_{Y_{(i)}}$ are the standard deviations of the rank variables.

Autocovariance and autocorrelation: For a spatial variable Z(x), x – the location (coordinates), r(Z(x),Z(x')) is the autocorrelation between points x and x'. Under certain conditions, this depends only on the distance between x and x'. For a temporal variable Z(t), r(Z(t)=r(Z(t),Z(t-D(t)). These statistics indicate how spatially neighbouring values depend on each other or temporal values depend on preceding ones.

The **median** (MED) is the value separating the higher half from the lower half of a data sample. For a dataset, it may be thought of as the 'middle' value.

The **median absolute deviation** (MAD) is a non-parametric measure of variability. For a univariate sample, the MAD is defined as the median of the absolute deviations from the data's median:

$MAD = MED(|X_i - MED(X_i)|)$

A relative, dimensionless measure would be MAD/MED.

Quantile: The quantile Q_p to percentile p is the value, so that 100*p% of values are below and 100*(1-p)% of values above Q_p. $Q_{0.25}$ and $Q_{0.75}$ are called lower and upper quartiles. The Median equals $Q_{0.5}$.

Confidence interval (CI): Imagine that from a population X, n data $(x_1 \ldots x_n)$ are picked randomly, and the AM is calculated. This is repeated many times. The AMs will be different every time, in general. The p-confidence interval is the interval between $Q_{0.5-p/2}$ and $Q_{0.5+p/2}$ of all AMs, which means that 100*p% of the calculated AMs lie in this interval. The AM of all AMs converges to the true mean, which is the expected value of X. The same applies to any statistic Θ instead of AM: the AM of all estimated Θs converges to the true value of Θ. However, this is not always an operable definition, because normally, only one sample $(x_1 \ldots x_n)$ exists, so that the $Q_{0.5-p/2}$ and $Q_{0.5+p/2}$ cannot be calculated. Instead, if one knows the sampling statistics of a statistic Θ, i.e. the distribution of estimated Θ, one can calculate a CI associated to the estimated statistic Θ of one particular measurement or experiment, represented by $(x_1 \ldots x_n)$. This is the CI which is often given associated to a result.

Important: The CI to level p calculated from one experiment is often wrongly understood as the interval in which the true value is located with probability p. *But this is not the case!* Instead, if hypothetically the experiment is repeated many times, the CI to level p of the estimated parameter Θs includes the true value of Θ in 100*p% of cases. In spite of the more complicated correct interpretation, the CI can still be qualitatively understood as a measure of reliability of the estimate of statistic Θ.

Definitions

Repeatability: same method, same lab, same person, same conditions (ideally).

Reproducibility: different methods, different labs, different conditions.

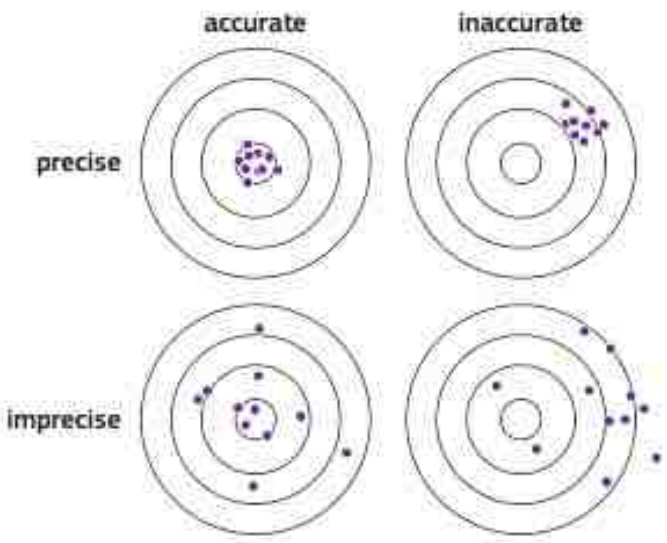

Figure 2-40.
Accuracy and precision.
Source: Graph created by Peter Bossew.

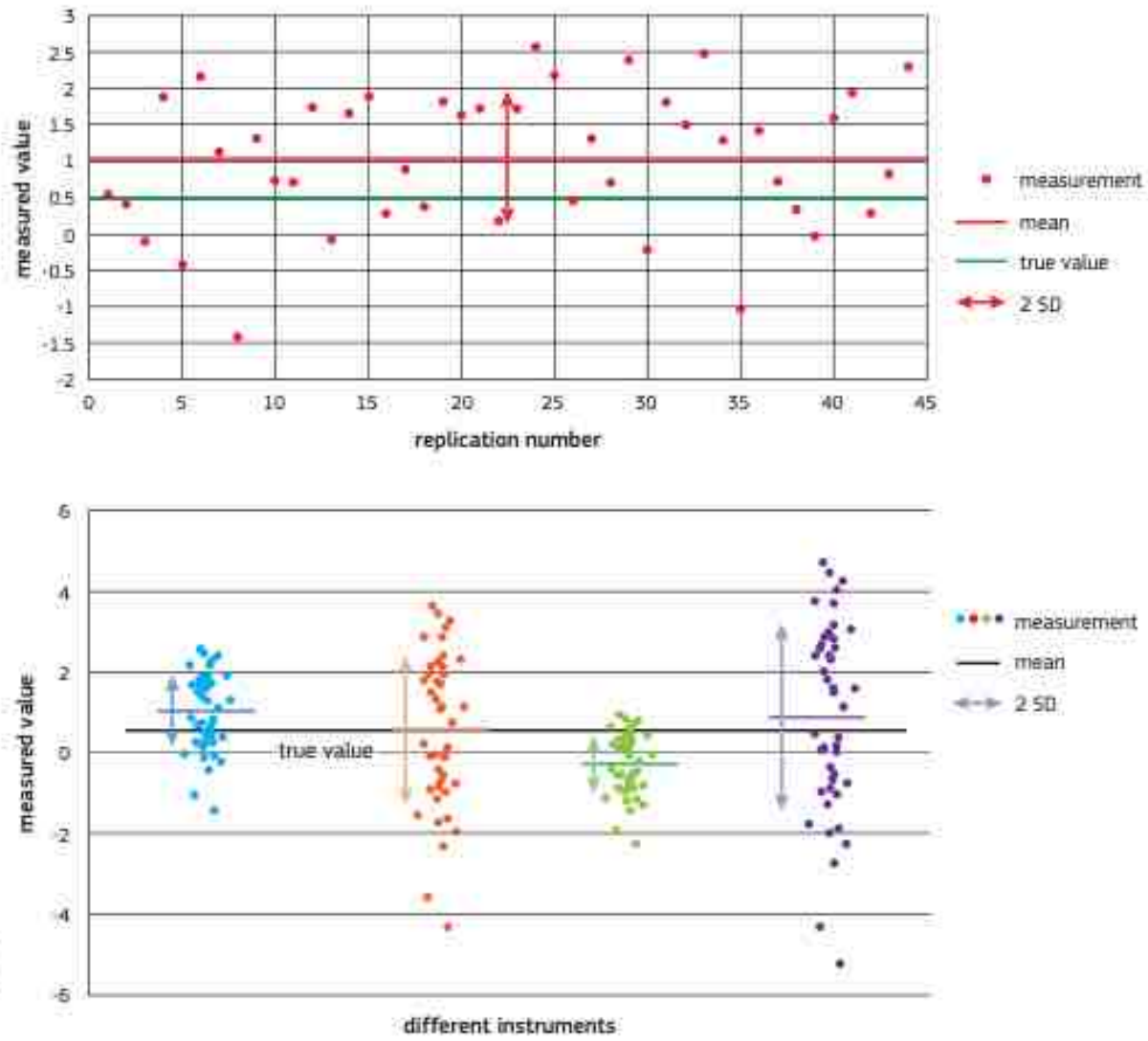

Figure 2-41.
Accuracy and precision.
Upper graph: replication with one instrument;
lower graph: parallel observation with different instruments.
Source: Graph created by Peter Bossew.

Survey data and representativeness

For survey data, accuracy has an additional meaning, which is essential for interpreting survey results.

Survey data can be understood as a sample taken from a true (but unknown) distribution of a quantity. The survey is called representative if the statistical parameters of the sample are equal to the ones of the population (within given tolerance). A statistic - in particular the mean - of the sample is called accurate if it is equal to the same statistic of the population (within given tolerance). The deviation between sample and population statistic is called bias. Very importantly, non-representative sampling schemes generally lead to biased results. Therefore, assuring representativeness (within defined tolerance) is perhaps the most important quality assurance issue in environmental surveying. In particular, for indoor radon surveys, representativeness is the biggest challenge.

In addition, the individual measurements which form the sample must also be quality-assured, i.e. accurate and precise individually.

Data are:

1. Numbers or items or instances which should be accurate and precise individually. This concerns metrological quality assurance.
2. A sample from a population which should represent the population accurately and precisely, i.e. be representative for the population. This concerns quality assurance of the survey design and its implementation.

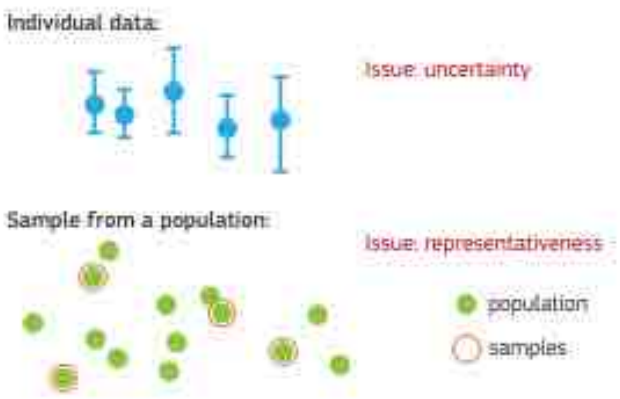

Figure 2-42.
Data as individual values and as sample: main quality-assurance issues.
Source: Graph created by Peter Bossew.

2.4.3 Scale, coverage, resolution and precision

Choice of scale

The map scale is defined as the ratio between a distance on the map and the distance on the ground which is represented on the map. A scale of 1:1 000 000 (or 1:1M) means that 1 mm on the map corresponds to 1 km in reality. Please note: a scale of 1:10 000 is deemed larger than one of 1:100 000 because the same distance is represented by a larger distance on the map in the former case.

The choice of scale depends mainly on two related factors: details of which minimal size shall be visible on the map? In which size shall the map be printed or visualised? Additionally, availability of data, from which the map is constructed, may play a role.

Coverage, scale, resolution and precision

a. Point samples

Intuitively, one would say that an area is well covered by samples if their distribution is nearly uniform over the area. The smallest distance (in space or time) over which variation or difference of level of a quantity can be observed reliably (after some criterion) is called the resolution of the observation process. In most practical cases, coverage is not entirely uniform, i.e. sampling density varies regionally; then also resolution varies regionally.

In regional surveys applying point sampling, for example dose rate or soil radon surveys, only a finite and therefore limited sample size (statistically) or a limited number of point samples (physically) can be achieved. Hence, by default resolution is limited by sample spacing. Details smaller than the space between two observations cannot be recognised by the monitoring network. A useful measure of resolution is the mean nearest-neighbour distance. However, this is a gross measure which may not be adequate for sampling schemes with variable sampling density; see Section 2.4.4 below on point density.

b. Aggregation or interpolation

By applying data aggregation or interpolation (Section 2.4.6), values are assigned to mapping units, which can be grid cells or other spatial units such as municipalities or geological units. Depending on the method, the map units will cover the domain of interest to different extent. For aggregation, non-empty mapping units can only be achieved if data exist within these units. Therefore, for example the European Indoor Radon Map, which consists of 10 km × 10 km grid cells as mapping units, has blank regions. These consist of empty cells, in which no data are available.

If interpolation or geostatistical tools are applied (Section 2.4.6), statements about the probability of finding a certain value at unsampled points (i.e. between sampling stations) can be made. This is schematically visualised in Figure 2-43. One can recognise that in this artificial example (lower graph) the true process is mostly contained within the confidence limits, but some of its details are badly covered by the interpolation. Precision of the estimated process therefore increases with sampling resolution. Methods relying on simulation do not generate one single smooth, interpolated estimate, but many 'realisations' that are compatible with data. Each realisation can be rough, depending on the covariance model assumed. In practice, estimates are made for grid cells or grid nodes. In the former case, the value represents the mean over the cell. In the latter case, the value at the node is assumed to represent an area of cell size around the node. In case of interpolation, larger parts of the domain can be covered by non-empty cells, depending on uncertainty that is tolerated.

For aggregated or interpolated maps, resolution is given by the size of the mapping units, for example 10 km × 10 km for the European Indoor Radon Map (see Section 5.4).

Note that estimates for grid cells achieved by different methods – aggregation or various interpolation methods – are not necessarily identical. Aggregation considers only data points within the cell, whereas for interpolation, also data outside a cell influence the result attached to a cell.

What is a sample?

In physical parlance, a sample is what is called a draw in statistics. This can be a single measurement or an object to be submitted to measurement (such as a soil sample). In statistics, the term sample denotes a set of draws from a population, i.e. a collection of measurements or physical samples.

Figure 2-43.
Schematically, upper graph: true process (green) which is to be assessed and sampling (measurement) points with bars indicating measurement uncertainty; middle graph: interpolation (pink) gained from the measured data and confidence limits (dashed curves); lower graph: process estimated on grid cells (blue).
Source: Graph created by Peter Bossew

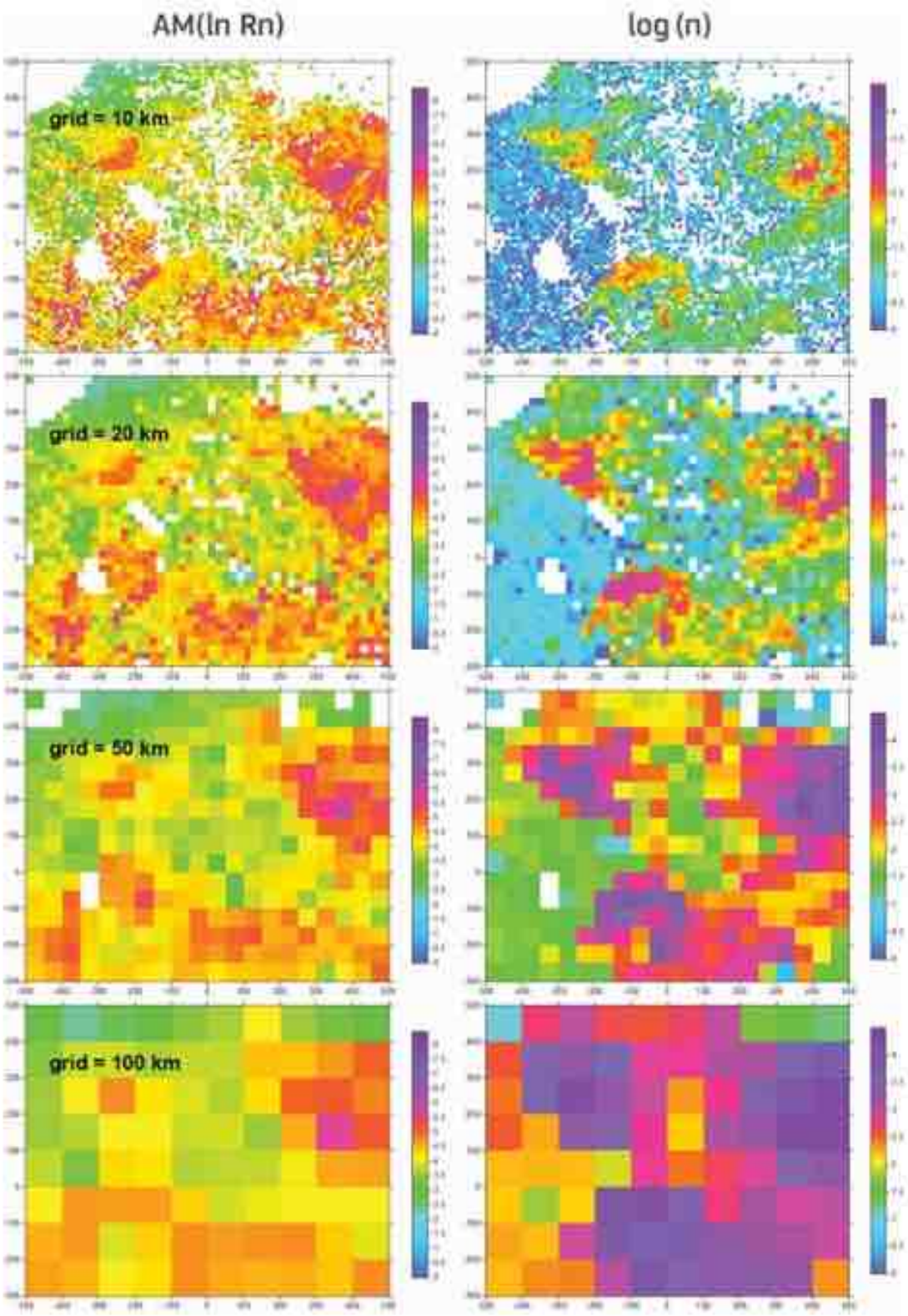

Figure 2-44.
Section of the European Indoor Radon Map. Left column: arithmetic mean (in cells) ln(Rn concentration), right column: log (number of data per cell). Top row: original data as shown in the European map; subsequent rows: re-aggregated into larger cells, size as indicated. Axis units: km.
Source: Graph created by Peter Bossew

c. Exhaustive sampling

Remote sensing measurements often produce exhaustive coverage of an area. A typical example is airborne gamma spectrometry, which can be performed so that gamma rays originating from every possible point of the surveyed areas are registered. In order to cover an area exhaustively, it is necessary that the sensor have a sufficiently wide field of view, so that a finite number of observations will register gamma rays from all points. While coverage is then 100% and sample spacing zero, the achievable resolution is deliberately still not high. This is because each observation represents a weighted average over a ground area. Therefore, such a method generates a smoothed picture of the investigated process, in spite of infinitely high sampling resolution. Certain methods attempt 'deconvolution' of the smoothed surface, but this procedure introduces uncertainty.

d. The resolution-precision dilemma

A particular problem arises for the minimum size of a physical sample. While, as discussed above, increasing resolution also increases precision of the estimate, this is not valid infinitely. In particular, time series assessment is affected by this problem.

Importantly, resolution and precision generally cannot be optimised independently. Radiation is usually measured by counting pulses, which arrive randomly due to the stochastic nature of radioactive decay. The precision of a measurement increases with the number of registered pulses, i.e. with observation time. On the other hand, faster changes of the source intensity require shorter measurements. Hence, with an instrument with given sensitivity, the tolerated lower limit of precision defines the maximally achievable temporal resolution of the measurement.

As a spatial example, consider soil samples (in a physical sense), taken to explore the small-scale variability of radionuclide concentration in soil. These samples need a minimal size to be able to measure the concentration with required precision with a given device. Variability within lower distance than the minimal sample size thus cannot be assessed.

e. Map scale and uncertainty

As addressed above, the map scale limits the size of detail that can be visualised on the map. Particular cases are geological and similar maps, which represent, technically speaking, an exhaustive partition (or tiling) of the investigated domain into non-overlapping polygons. Not only the availability of geological samples, but also the map scale limits the size of detail which is displayed on the map. In a larger scale (finer) map, a polygon of a coarser map may disintegrate into different units; borders of polygons will generally be rougher than the corresponding ones on the coarser map. Therefore, assigning a geological unit to a sampling point using a geological map, is affected by uncertainty due to the scale of the geological map. See Section 3.5 in Cafaro et al. (2014) for more details on this subject.

f. Map resolution and coverage

As explained in b., aggregation and interpolation lead to a certain coverage of the domain by mapping units such as grid cells. While the cell size defines resolution, it is also related to map scale, as discussed in this section.

For an aggregation map, based on a given a set of point data, coverage increases with cell size, i.e. with decreasing resolution. This is because smaller cells are more likely to contain no data than larger cells. As an example, Figure 2-44 shows a region of the European Indoor Radon Map; the original based on 10 km × 10 km grid cells shown on top (left the mean ln(Rn), right log(n), n – number of data per cell) and re-aggregations into 20 × 20, 50 × 50 and 100 × 100 sized cells. One recognises that with the original resolution, the map contains many empty cells, while with lower resolution, the region is completely covered (Figure 2-45). With lower resolution, not only the degree of detail decreases, but also maxima and minima are smoothed away (Figure 2-46), while on the other hand, precision increases. In Figure 2-47, precision is indicated by 1/uncertainty, where uncertainty is approximately proportional to $1/\sqrt{n}$. The graph shows the mean of $\sqrt{n}$ over all cells.

Summing up, by aggregating data into larger cells, one loses detail (the picture becomes 'blurred'), while one gains precision, because each cell value relies on more data. This has been called the resolution-precision dilemma or uncertainty principle of sampling.

	Coverage	Resolution
Point map	– uniformity of sampling density	Distance between points
Aggregation or interpolation	Fraction of non-empty cells	Cell size

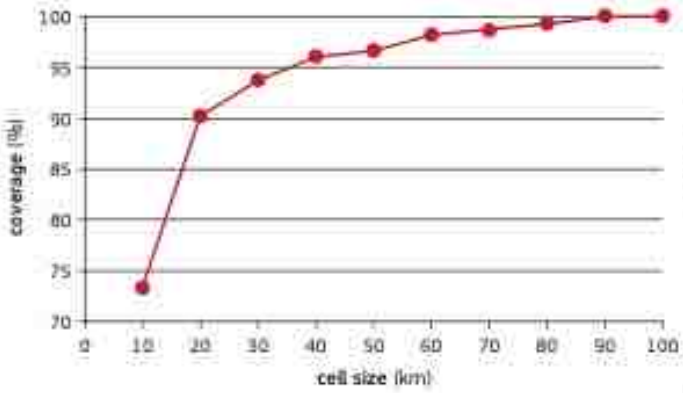

Figure 2-45.
Coverage of region shown in Figure 2-44, in dependence of cell size (side length of quadratic cells) in which the data are aggregated.
Source: Graph created by Peter Bossew.

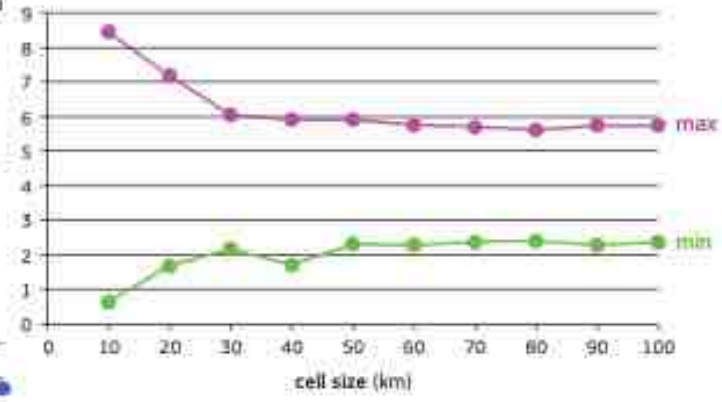

Figure 2-46.
Maxima and minima of mean (in cells) ln(Th concentration), in dependence of cell size.
Source: Graph created by Peter Bossew.

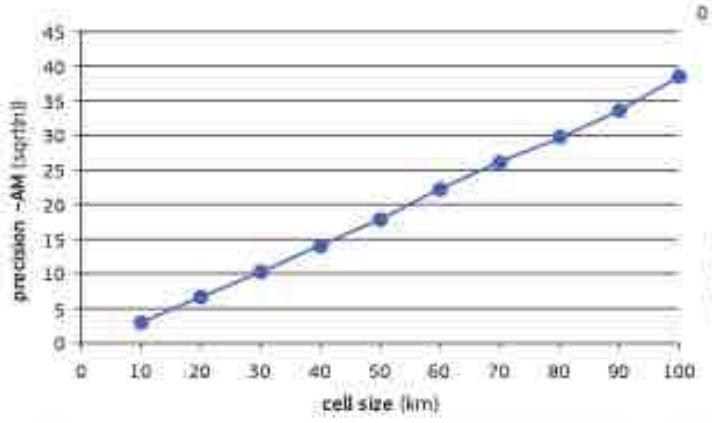

Figure 2-47.
Maxima and minima of mean (in cells) ln(Th concentration), as a function of cell size.
Source: Graph created by Peter Bossew.

Figure 2-48.
Screenshot showing the monitoring stations of the EURDEP network.
Source: http://eurdep.jrc.ec.europa.eu/Frontpage/DefaultPage

2.4.4 Geometry of point samples

Quantification of point patterns

Monitoring locations in a country can be understood as points in a domain. As an example, Figure 2-48 shows how the spatial design can be very different between countries (e.g. the geographical distribution of monitoring stations within a country participating to the European Radiological Data Exchange Platform (EURDEP) network; more details about EURDEP are given in Chapter 4). This reflects the different policies underlying the networks, as discussed in Section 2.4.6.

Since the first half of the 20th century, numerous studies have been performed about quantification of point patterns. Most were motivated by studies in vegetation ecology, for example the distribution of tree species.

Readers interested in the theory and quantification of spatial point patterns are referred to Cressie (1993), Chapter 8.

Analyses shown here were made with CrimeStat 3.3 (Levine 2010), Past 3.20 (Hammer 2001 - 2018) and homemade software.

Most popular statistics are based on distances between sample points or between random points in the domain and sample points. For a comparison of methods, see e.g. Cressie (1993) or Liu (2001). For the purpose of this Atlas, two statistics will be addressed here.

Point density

The density of points x_i at a target location x_0 (e.g. a grid node) can be estimated by counting the points x_i in the neighbourhood of x_0 and dividing the number by the area of the neighbourhood. These can simply be squares (grid cells) or circles around x_0. More advanced approaches are kernel density estimates: here points are counted in a weighted manner, where the weighting function is called the kernel. The estimated density at location x_0 equals:

$$\rho(x_0) = \sum_i k(d_{i0}) \qquad (2\text{-}16)$$

where d_{i0} is the distance (normally Euclidean) between point x_i and target location x_0, and k(.) is the kernel function. A function which simply equals 1 within a radius, 0 otherwise, is called uniform kernel. Commonly used is the Gaussian kernel.

$$k(x) = \frac{1}{h^2 \pi} \exp\left[-\frac{x^2}{2h^2}\right] \qquad (2\text{-}17)$$

where h is called the bandwidth. The resulting density map is 'noisier' for small and 'smoother' for large h values. A rule of thumb (used here) for an optimal bandwidth (in the sense of minimising the error) seems to be $h = \max(s_x, s_y)\, 0.7\, n^{-0.2}$, where n is the number of points, and s_x and s_y are standard deviations of x- and y- coordinates of the points. An alternative is *adaptive* bandwidth, which is tailored so as to account for local density. However, its implementation is more computationally expensive.

The effect of the bandwidth on the kernel density is shown in Figure 2-49 for the Austrian stations of the early warning dose rate network contributing to EURDEP. Gaussian kernel was used, and a bandwidth of h = 30 km is about optimal in this case. In the extreme case of high resolution, each sampling point would be represented by its individual 'bullseye' in the density map. Apparently, such a map would not convey useful information. On the other hand, a resolution that is too low leads to a grossly 'blurred' or 'smeared' picture, which is equally uninformative. Information-theoretical arguments have been proposed for determining the optimal bandwidth.

Figure 2-49.
Kernel density estimates of the Austrian stations of the EURDEP network. Gaussian kernel, bandwidths: h = 15 km (left), 30 km (centre) and 50 km (right). Density unit: $1/m^2$.
Source: Graphs created by Peter Bossew.

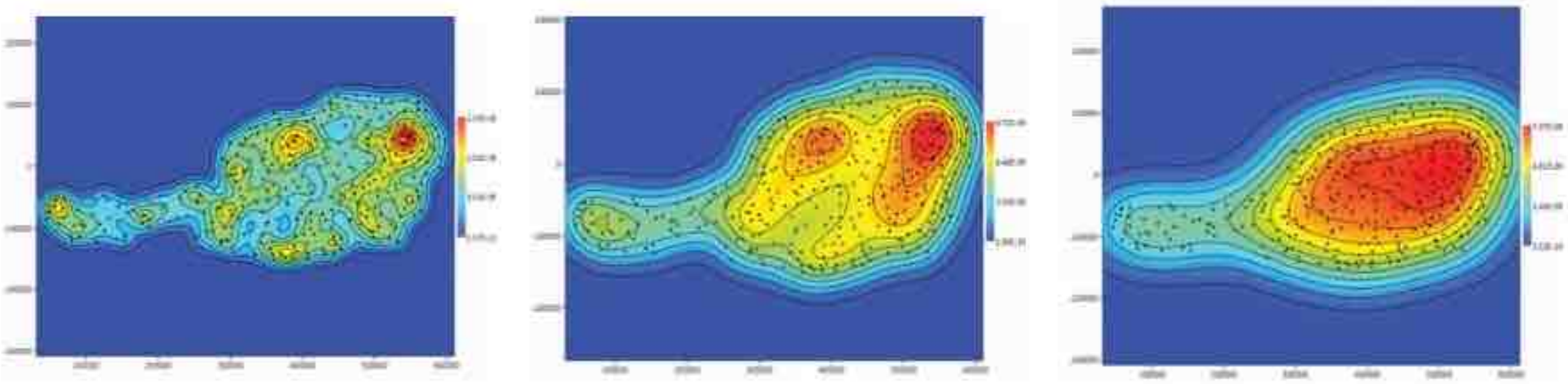

Measure of dispersion

a. Spatial randomness and Clark-Evans index

Monitoring points are chosen according to a defined network policy (Section 2.4.5). The resulting pattern can be quantified according to its relation to a random pattern, i.e. points in the domain chosen randomly.

The classical test to decide whether a 2-dimensional set of points is randomly distributed (mathematical speaking, following a Poisson process), has been designed by Clark & Evans (1954). They showed that under the assumption of complete spatial randomness (CSR, the null hypothesis), the expected mean distance between nearest neighbours equals:

$$d_{CSR} = \frac{1}{2}\sqrt{\frac{A}{n}} \qquad (2\text{-}18)$$

where A is the area of the domain, and n is the number of points.

The Clark-Evans index,

$$CE := d_{NN} / d_{CSR}, \qquad (2\text{-}19)$$

where d_{NN} is the empirical mean nearest neighbour distance, and is distributed approximately ~N(1, s),

$$s = \sqrt{\frac{4-\pi}{n\pi}}$$

which can be used to calculate the false acceptance probability of the null hypothesis.

CE > 1 indicates that points are, on average, more dispersed as would be expected for a random pattern, while CE < 1 indicates clustering. Regular patterns have CE > 1.

The histogram of nearest neighbour distances d_{NN} for Austrian EURDEP stations is shown in Figure 2-50. One can see that larger d_{NN} are more frequent than would be expected for a theoretical random distribution (black curve; based on convex hull as area estimate, no border correction), indicating overdispersion, CE > 1.

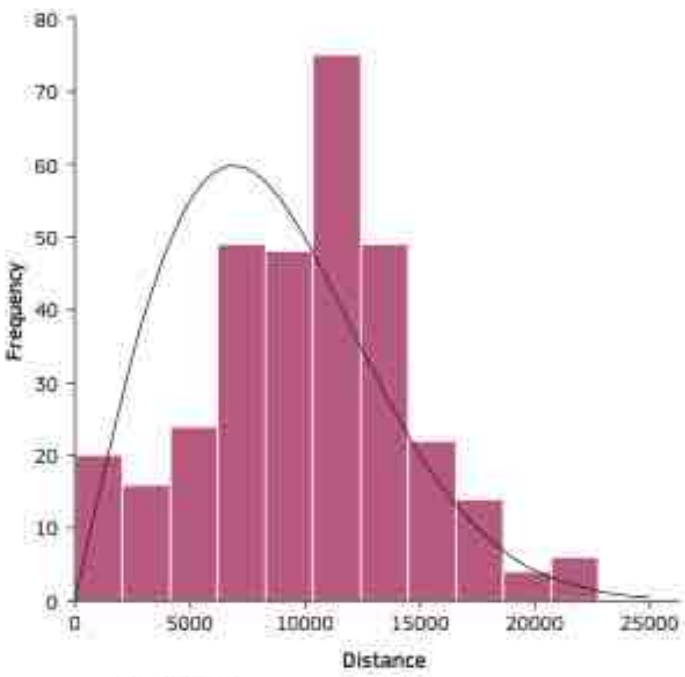

Figure 2-50.
Histogram of nearest neighbour distances, Austrian EURDEP stations. Curve: theoretical distribution.
Source: Graph created by Peter Bossew.

b. Pielou index

Pielou (1959) proposed an index based on a statistic derived from distances between random and sample points, instead of between-sample points, as for the Clark-Evans index. The Pielou index is defined as

$$PI := \pi\rho \frac{1}{K}\sum_{k=1} dNN_k^2 \qquad (2\text{-}20)$$

where K is the number of random points, and dNN_k is the distance between the random point and its nearest neighbour among the points of the sample and ρ is the density.

For a random pattern, PI ~ N(1,1/K) for large K, which can be used for testing. Low values of PI indicate clumped or aggregated, high PI to dispersed patterns.

c. Multiscale dispersion

Evidently, the CE and PI analyses (and others of that kind) capture only average behaviour. As the example of the EURDEP monitoring stations in France shows (Figure 2-48), stations can be overall dispersed but showing clusters that form themselves a certain pattern (in this case, they are clustered around nuclear plants).

Among several options, we shall shortly address the common Ripley K or L function. Imagine a circle of radius r around each sample point (or any point in the domain). For a regular or random point pattern, the mean number of points inside the circle increases with r^2, because with constant point density ρ the number of points in a circle with radius r equals $\rho r^2 \pi$. Deviation from this behaviour points to clustering or overdispersion at a certain scale (r). This scale effect is captured by the transformed Ripley's K statistic,

$$L(r) = \sqrt{\frac{1}{\pi}\frac{1}{\rho n}\sum_{i=1}^{n}\sum_{i\neq j}\Theta(r-d_{ij})} - r \qquad (2\text{-}21)$$

with d_{ij} is Euclidean distance between points i and j and the Heaviside function $\Theta(x) = I(x>0) = 1$ if $x>0$, $=0$ otherwise (indicator function). For CSR or regular patterns, E[L(r)]=0. The null hypothesis can be tested by simulation.

This function plays about the same role as the variogram for continuous quantities (Section 2.4.5).

Fractal measures

Fractal methods investigate – qualitatively speaking – the dependence of statistics on scale or resolution. Here we concentrate on geometrical properties of point sets. The concept can be extended to study the geometric properties of the value levels attached to the observation points, or to a random field as a whole, leading to multifractal theory.

a. Correlation dimension

Draw circles of radius r around a point of the network and count the number of other points that lie inside this circle. Repeat this for all points and compute the arithmetical mean, N(r), of the counts per circles. N(r) is essentially the double-sum term in the definition of Ripley's L(r) function above, also called point correlation function. N(r) × sample points is the number of pairs with distance below r.

Repeat this for several radii r and graph N(r) versus r. For a fractal pattern, log N(r) is a linear function of r, or $N(r) \sim r_{D2}$. The exponent D2, which equals the slope in the log-log plot, is called the correlation dimension.

For regular or random patterns, D2 = 2, because the number of points enclosed in a circle increases with its area, i.e. with r^2. D2 < 2 indicates that there are 'holes' in the pattern, so that fewer points are enclosed in increasing circles than expected, if the points would cover the domain uniformly.

A more rigourous treatment starts with the so-called correlation integral,

$$C(r) := \frac{2}{n(n-1)}\sum_{i=1}^{n}\sum_{j>i}\Theta(r-d(x_i,x_j)) \qquad (2\text{-}22)$$

where d is a distance (normally Euclidean) between points i and j. The classical reference is Grassberger and Procaccia (1983), estimation aspects e.g. in Theiler (1990).

Figure 2-51 shows the correlation functions (in terms of log N(r) vs. log r) of the EURDEP networks for four countries. For Germany (DE) and Turkey (TR), the relationship is reasonably linear over a long range, indicating fractal behaviour over those ranges. France (FR) and Switzerland (CH) show a deviation for lower ranges due to the station clustering around nuclear installations. These networks are better described as multifractals.

b. Box dimension

If the domain is covered by 'boxes' (squares) of side length δ, one can count the number of boxes that contain sample points.

The box dimension is defined as

$$D_0 = -\lim_{\delta\to 0}\frac{\log(N)}{\log(\delta)} \qquad (2\text{-}23)$$

where n is the number of occupied boxes, δ is the box side length and 1/δ is the resolution. This can be estimated by calculating the ratio for several δ and extrapolating to zero (or 1/δ to the highest achievable). The theoretical value for a uniform (regular or random) pattern is D_0=2, because the number of occupied boxes increases linearly with the inverse of their area (as long as the boxes do not become so small that most fall into the voids between the points) or with 2nd power of their inverse side length or resolution.

However, if there are 'holes' in the pattern, smaller boxes are less and less able to cover the points, and consequently their number will increase with lower than 2nd power of resolution. The deviation of D_0 from 2 is therefore a measure of the 'patchiness' of the pattern. In Figure 2-52, the regression is shown for the set of non-empty 10 km × 10 km grid cells, which constitute the European Indoor Radon Map. The Box fractal dimension D_0 of this set equals 1.73, according to the analysis, plausibly, given the large 'holes' in the dataset and in the map (more details on the European Indoor Radon Map are given in Section 5.4.4).

Box and correlation dimension are members of a family of fractal dimensions, called Renyi dimensions D_q (e.g. Wikipedia: Fractal dimension). Of particular interest is the case q = 1, called information dimension (Renyi, 1959). The term fractal dimension was coined by Mandelbrot (1967).

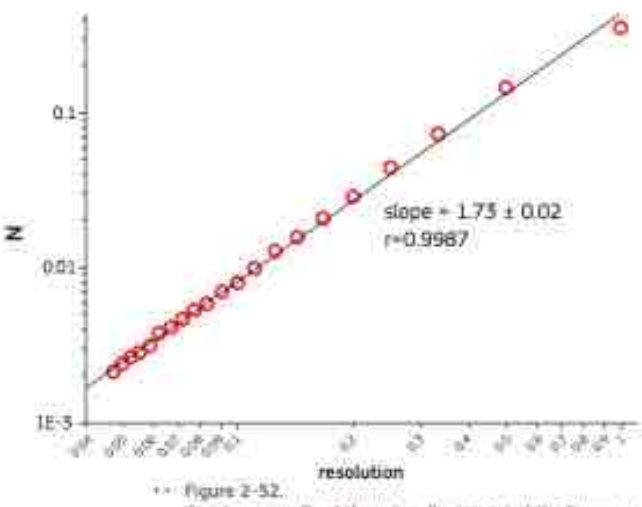

Figure 2-52.
Box dimension D_0 of the indoor Rn dataset of the European Indoor Radon Map (Section 5.4). Resolution = 10km/linear box size (km). N = relative number of non-empty boxes.
Source: Graph created by Peter Bossew.

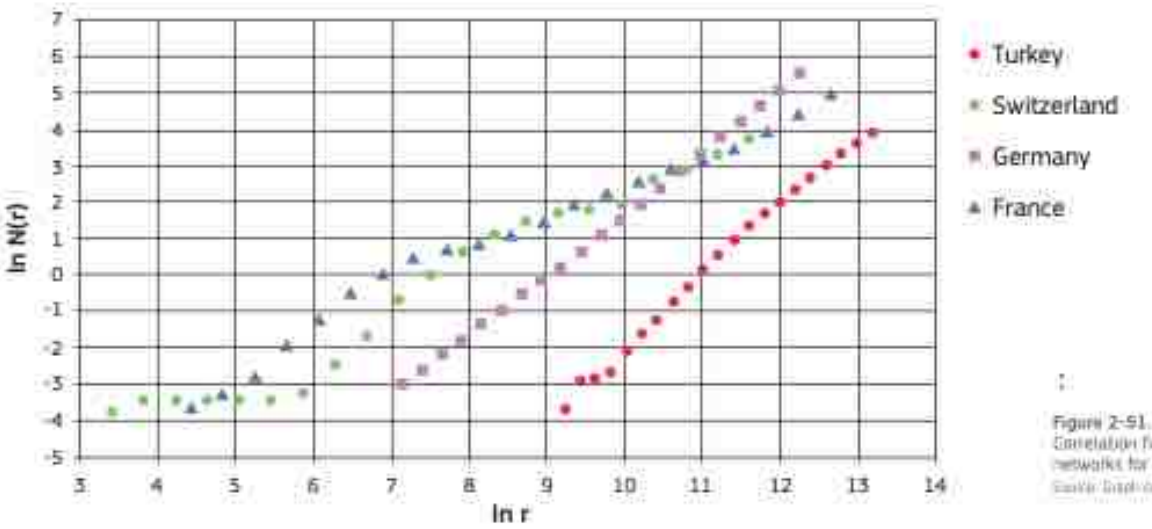

Figure 2-51.
Correlation functions of EURDEP networks for 4 countries.
Source: Graph created by Peter Bossew.

c. Lacunarity

Evidently, patterns cover or fill their domain to different degrees. Some networks provide more or less uniform coverage, while others leave "holes" or "gaps". The differences are quantified by the lacunarity function,

$$\Lambda(r) := CV^2(N(r)), \qquad (2\text{-}24)$$

where where CV is the coefficient of variation (CV = standard deviation / arithmetic mean) and N(r) is the number of sample points in a box of size r. (The boxes can be contiguous squares or rectangles or sliding boxes or circles, leading to slightly different definitions.)

Qualitatively speaking, lacunarity captures the differences in point density (Section 2.4.4), estimated with kernels of different sizes. For references, see Allain & Cloitre (1991), Plotnick (1993, 1996) or Reiss et al. (2016).

Figure 2-53 shows the Λ(r) functions of the automatic ambient dose rate stations that contribute to the EURDEP network, for a dozen European countries. One can recognise that the lacunarities (i.e. the CV) differ between countries, but also that the shapes of the functions differ, reflecting different heterogeneity at different spatial scales.

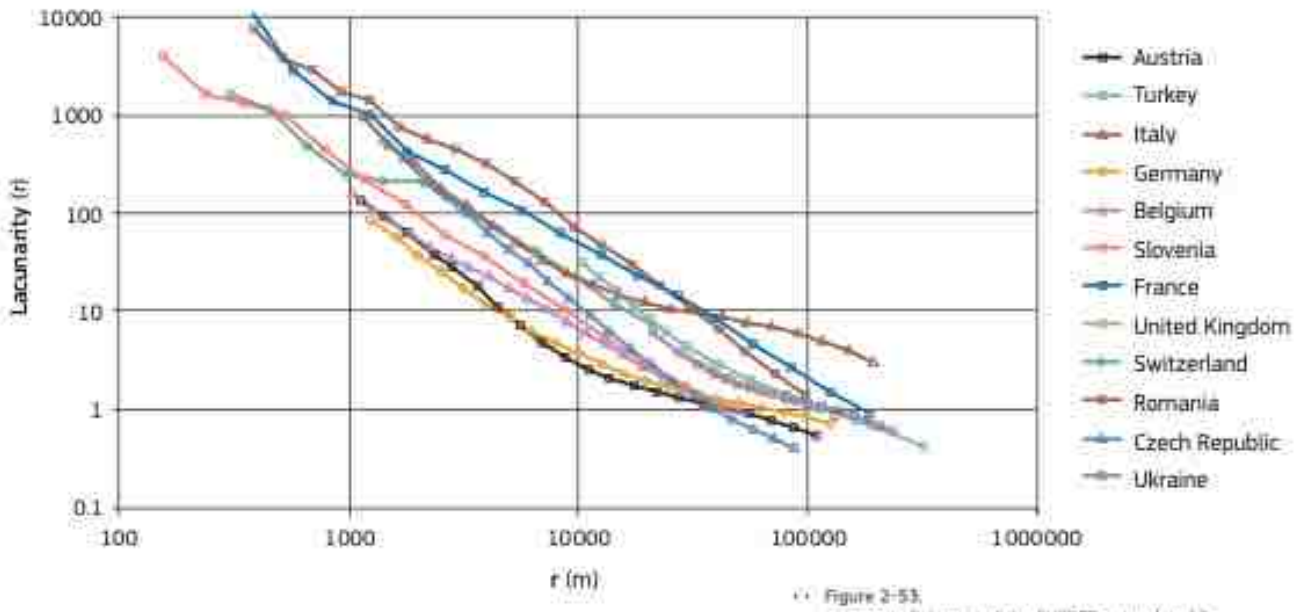

Figure 2-53.
Lacunarity functions of the EURDEP network in 12 European countries.
Source: Graph revised by Peter Bossew.

Estimation relies on the moving window approach. Uniform kernels of different radius r were attached to grid nodes. The estimate is biased because it assumes a rectangular domain, thus unrealistically including void areas inside the rectangle but outside the actual territory. Coordinate rotation, which results in different bounding rectangles, leads to up to 25% variability of absolute Λ, but the shape of the functions is preserved.

Edge effects

All methods suffer from so-called edge effects. Since the domains are necessarily limited, performing analyses close to domain borders introduces biases if one assumes that in reality the pattern extends across the border, but has not been observed. In software, this is often compensated by introducing edge corrections based on assuming rectangular or at least convex domains (estimated as the convex hull of the points). On the other hand, if the pattern of interest is truly limited, as is the case for stations of one particular country, one may argue that edge effects are not statistical biases (because of deliberately cutting out an analysed domain from a larger, but unobserved u realm) but true effects which do not need to be corrected. This latter approach is followed here. On the other hand, the effect, true or induced by domain cropping, can in particular invalidate analyses such as Ripley K and fractal dimension.

Another problem with interpreting point pattern statistics appears for fractured territories, e.g. Greece, where in large parts of the domain stations cannot be located even hypothetically because they would lie in the Aegean Sea. Analysis would then require detailed modelling of the domain and possibly computationally expensive simulations.

Clustering

Very often, measurement locations of environmental spatial datasets are spatially clustered. Reasons can be that the dataset results from merging several sets with different sampling policy; that a survey has been preceded by a regional pilot study whose data were then integrated into the main dataset; or that preferential sampling has been performed on purpose.

Reasons for intentional preferential sampling can be:

- Areas with anticipated higher levels are considered more important and should therefore be sampled more intensively;
- Areas with higher population density are considered more important than less-inhabited regions;
- Particular information is sought for certain geological areas.

Statistics derived from clustered data are biased if the sampling density is correlated with the level of the surveyed quantity. In this case, data points with high levels would be over-represented and distort the mean upwards. To some degree, this can be remedied by data declustering or by geostatistical methods. For the latter, see Section 2.4.5 below.

Various methods are available for declustering. For example, one can divide the domain in cells of fixed size and draw one or several random points from each cell. Then the wanted statistic is calculated from these points. This can be repeated many times and a mean per cell size of the statistic calculated. Then the cell size is modified and the procedure is repeated. In the end one has a plot of the mean of the statistic in question versus cell size. A reasonable choice for the appropriate size of the declustering cells is the one at which the graph approximately levels in.

2.4.5 Network and survey design

Network policy

Monitoring stations (e.g. for radiation early warning systems, EURDEP) or sampling points (e.g. for radon surveys) will be selected according to criteria derived from the purposes of the networks.

For EURDEP, network policies have been distinguished in the AIRDOS project:

- Uniform coverage of the territory, to be able to achieve a comprehensive picture of the radiation situation in the case of a large-scale nuclear event;
- Preferential siting along borders, as early warning against airborne contamination from outside the territory;
- Preferential siting around nuclear facilities, as early warning in case of emissions;
- Preferential siting in populated areas, because this is where most of the dose would occur, and therefore finer spatial resolution is striven for.

Of course, networks can be designed to serve different purposes. For EURDEP, see further discussion in Chapter 4.

Sample schemes of environmental quantities such as pollution surveys are often designed to account for areas in which high variability or high gradients are anticipated (sometimes based on previous knowledge, such as pilot studies or known properties of the emission characteristic and/or of the environmental compartment in which emission took place). Population density or vulnerable ecosystems are also common, and obviously important factors which motivate intense sampling.

For radon studies, one strives to achieve representative sampling, if the purpose is estimation of doses. However, one objective can also be to explore areas with known or anticipated (e.g. based on geological information) high radon concentration, which is an example of preferential sampling.

Geochemical surveys are often motivated by resource exploration. Sampling schemes will preferentially be directed towards areas in which higher concentrations of the sought mineral is expected. On the other hand, background studies will establish sampling schemes that are representative for a certain geological unit.

Survey planning

a. Establishing a sampling plan

In many instances, the most demanding part in conducting a survey is to develop its design, in particular its sampling scheme, suited to meet its purpose. This is particularly true for indoor radon surveys. Its success depends on the validity of the sampling procedure. Because this subject is particularly complicated, this section is restricted to indoor radon surveys.

Sampling means to take a representative portion from the whole of the buildings or the population for testing in order to evaluate the exposure or to define an area where high radon concentration could be found. The aim of sampling is to reveal information and to enable measurement results to be related to the whole population with confidence. There is no single optimal approach to sampling. For that reason, the sampling or observation should be designed carefully, because sampling is central to the accurate estimation or prediction of properties of areas. Poorly designed and inadequate sampling can lead to biased predictions with large errors which, in turn, can have consequences for decision-making. An optimal sampling design is one which allows the best possible estimation of the target quantity, while at the same time accounting for constraints related to economical limits and logistical constraints such as difficult accessibility or non-availability.

The keyword here is representativeness. As a reminder, a representative sample is one which has the same statistical properties (up to tolerance) as the population (in statistical sense) from which it has been drawn. In most cases, the target of a survey is to assess the mean concentration or exposure; thus the empirical arithmetical mean of the sample must be the same as the true (but of course unknown) population mean; other characteristics of the statistical distribution are less relevant in such a case.

b. Validation of representativeness

When an indoor radon survey is conducted, as a matter of rule, questionnaires are distributed. These are intended to acquire information on the building and room characteristic and on sociological factors. Provided that the questionnaires are filled correctly (deviation, errors or intentional wrong information, which are generally difficult to recognise, are a source of uncertainty), statistics derived from them, e.g. about the frequency of certain types of buildings, can be compared with independent statistical sources, e.g. census data. Coincidence is a necessary condition for accepting the representativeness hypothesis. (Sufficient conditions are probably impossible to meet, and checks of the type indicated will usually do.)

c. Design- and model-based approaches

Two types of approaches are often distinguished: Design-based and model-based.

If a sampling design is chosen in such way that the derived results can be derived directly from the data one speaks of a **design-based approach**. For example, if the objective of a radon survey is mean exposure in a certain municipality, one would distribute detectors representatively, i.e. such as to represent all sources of variable radon controls according to demographic reality, and measure over a long period. The wanted quantity is then, simply, the arithmetical mean over samples.

Design-based sampling is the classical statistical approach to sample design, which aims to estimate the population parameters, such as the mean and the variance, without bias. The population is

the set of all units of interest. The probability of selecting any site is determined by the sampling design. In order to obtain a sample that is representative of the population exposure, it is sufficient to select a random sample from the list of all the dwellings or inhabitants in a country or region. This is called a simple random sampling. Randomness of dwelling (inhabitant) selection and completeness of dwelling (person) list are the key elements to selecting a representative sample (IAEA, 2013). In simple random sampling, the units are chosen with equal probability from the target population. The determination of the sample size (number of sample) for simple random selection is directly proportional to the dispersion and guaranteed probability, and vice versa with maximum allowable error rate. Typically, there is a pre-orientation for the accuracy with which we need to evaluate the characteristics we are interested in.

Often, however, a representative design is not achievable. This is particularly true if evaluation shall be based on an existing, non-representative dataset, which may be a compilation of previous data or partial surveys, possibly having had different purposes. In this case, the design-based approach, relying on an appropriate sample, is not possible. The situation can still be remediated by applying models. In indoor radon surveys, for example seasonal correction can be applied if measurement periods are not uniform (e.g. all spanning one year, or all 3 months in the transition periods of spring or autumn, etc.). Deviation from spatial representativeness, which means that spatial sampling density is not strictly proportional to population density everywhere, as it should be in a design-based approach if the survey target is to assess the population exposure, can be fixed by applying geostatistical means (Section 2.4.6). In any case, the **model-based approach** introduces additional uncertainty. Hence, while the model-based approach is more flexible, it is technically more challenging.

	Representativeness	Evaluation
Design-based	essential	simple statistics of data
Model-based	relaxed	modelling: models must be available, introduces additional uncertainty

Guidelines for establishing correct sampling plans and statistical considerations can be found in WHO (2009) (Section 6), IAEA (2013), Bossew (2014), and references therein. A useful document on design- (or probability sampling) vs. model-based sampling is Hansen et al. (1983).

An indoor radon survey where much care has been invested in representativeness, is the first Austrian survey (Friedmann, 2005).

Optimisation of monitoring networks

In reality, monitoring networks often grow according ad-hoc true or assumed needs, and their patterns are thus historical products, so to say. Sometimes one realises that they are not optimally adapted to a purpose: a too dense monitoring network in a region may produce redundant information, while a too scarce network may lead to missing information, which may however be needed for generating an overall picture.

As said, the pattern reflects network policy. There may be several possible conflicting criteria underlying a design. For example, high resolution (dense network) conflicts with economy (monitoring stations is expensive), comforting public concern (many stations in a densely populated area) may lead to unnecessary redundancy; and so on.

Treating the problem formally, a loss function is defined which is built from the criteria which define the network policy. The network is arranged, or an existing network rearranged such as to minimise the loss function. Rearranging means inserting, deleting or relocating stations. Among criteria are:

- the spatial resolution (or the degree of detail) with which one wants to be able to assess an anticipated phenomenon (a pollution scenario, variability of indoor radon concentration due to geological variability, etc);
- the uncertainty of estimates at unsampled locations, if interpolation or other modelling is applied (Section 2.3.6);
- public demand for a denser sampling network;
- costs of building, operating and maintaining a network.

Evidently, the weights given to different criteria are a political decision. Formal minimisation of a loss function may be computationally demanding, although theory and practical examples exist. References include the textbook by Müller (2007).

2.4.6 Mapping

Types of maps

Geographical quantities can be displayed in different ways. The simplest way to display georeferenced data is as *post maps*, where symbols are set on the data location. The value is coded by means of a different symbol, different symbol size or different symbol colour. Values can be ordinal (such as real numbers) or categorical ('good', 'bad', 'ugly').

In *level maps*, the mapping units (grid cells or pixels from the map perspective) of interpolated or aggregated data are colour coded. An alternative is to display as a 3D map, where the elevation of a 'mountain' stands for the level. Hence, this requires ordinal quantities.

For class maps, mapping units can also be assigned to categories, such as 'limestone', 'granite', etc. Usually mapping units are polygons in which the category takes the same value, but this is also possible on a grid base: regions where cells contiguously represent the same category substitute the polygons.

A particular case of a class map is the *contour map*. In a level map with continuous response, points with the same value can be connected, forming contours or isolines. The spacing of contour levels is specified by the mapper. The area between contours that represent subsequent contour levels, is assigned one level code, usually a colour. Effectively, the level map is thus transformed into a class map of ordinal classes. Such maps are very popular, but have the weak point that contours suggest an accurate reality, although in fact they are estimates whose uncertainty (i.e. where the contour line 'really' runs) is difficult to display.

Clearly, the visual appearance of a map depends strongly on the chosen resolution and map scale (see also Section 2.4.3).

Projection

A map is a flat object with Euclidean geometry, while the surface of the Earth is a spherical object. Gauss' *theorema egregium* (1828) states, '*Si superficies curva in quamcumque aliam superficiem explicatur, mensura curvaturae in singulis punctis invariata manet. Manifesto quoque quaevis pars finita superficiei curvae post explicationem in aliam superficiem eandem curvaturam integram retinebit*', from which follows that surfaces with different curvature (such as planes and spheres and their respective topological identicals) cannot be projected on each other without distortion. Any projection of the Earth to a plane is therefore a compromise, and one tries to select the best one for a given purpose. An immense body of geodetic literature exists about this problem. Compendia of map projections include Snyder (1987) and Annoni et al. (2003).

For maps encompassing the entire European continent, the INSPIRE Directive recommends using the Lambert azimuthal equal area (LAEA) projection, a version of which has also been applied for the European Atlas of Natural Radiation. INSPIRE (2007) is a Directive of the European Parliament and of the Council about infrastructure for spatial information in Europe. Among the relevant documents is INSPIRE (2014; p.11).

Aggregation

Point data can be aggregated into spatial units such as grid cells, municipalities or geological units. Typically, arithmetic or geometrical means or medians of data located within a unit are calculated. Other statistics are also common, such as exceedance probability (the probability that in a unit, a reference level is exceeded) or measures of dispersion (coefficient of variability, CV, or geometrical standard deviation, GSD, and others), if one is interested in the variability of the quantity within a unit. Clearly, the precision (and for some statistics also the accuracy) of an aggregated quantity depends on the sample size.

As an example, the European Indoor Radon Map consists of grid cells of size 10 km × 10 km, into which the following statistics have been aggregated by participating countries: number of data (i.e., sample size), the arithmetic mean (AM), standard deviation (SD), arithmetic mean and standard deviation of the natural logarithm (AML, SDL), median, minimum and maximum. Original data remain with the participating countries for data protection and are not communicated to the JRC.

From this information, other quantities can be derived, such as exceedance probability or expected maximum, assuming that the process (indoor radon concentration, in this case) can be adequately described by some model; in radon studies, the lognormal (LN) model is particularly popular.

As examples, assuming the LN model with GM and GSD from data one can obtain:

- Quantiles to percentile p, $Q_p := \exp(\Phi^{-1}(p|GM,GSD))$, to be estimated:

$$\hat{Q}_p = \exp(t_{p,n-1}SDL + AML) \qquad (2\text{-}25)$$

- Exceedance probability: prob(Z>z) := Φ((ln GM − ln z)/ln GSD), estimator:

$$\hat{p}_p = t_{n-1}\left[\sqrt{\frac{n}{n+1}}\,\frac{(\ln z - AML)}{SDL}\right] \qquad (2\text{-}26)$$

- Quantiles of the expected maximum in a cell: see $Q_p(Y_n) = F_Z^{-1}(p^{1/n})$, where $Y_n := \max\{z_1, \ldots, z_n\}$, F_Z the distribution of the underlying population, e.g. LN. For the estimated median maximum, p=0.5. The expected maximum, $E(Y_n)$, is mathematically more complicated.

More sophisticated (unbiased) estimators can be developed.

Filling grid cells or other geographical units by aggregation is a simple method. However, it is sensitive to deviations from representativeness of the individual data (for example, if they result from preferential sampling within the unit, which can produce bias) or to low sample size (which results in low precision of the statistics). Additionally, it treats the input data as independent individuals, i.e. not spatially correlated (see next paragraph).

Spatial correlation and interpolation

If mapping is supported by modelling that accounts for the statistical association between observations within a vicinity, the problem of uncertain data or statistically poor cells is alleviated to an extent. The physical reason is similarity between adjacent values of the observed quantity for continuous variables; Tobler's First Law of Geography states: '*Everything is related to everything else, but near things are more related than distant things*' (Tobler, 1970).

Consequently, estimating the quantity at a point or in a grid cell, considering neighbouring points or cells, takes advantage of the information contained in the ensemble of points or cells in the neighbourhood, even if the point data may be uncertain or the cells poorly populated. An example is given in Figure 2-54, which shows the auto-correlogram of the variable AM(ln of radon concentrations in ground-floor living rooms) within 10 km × 10 km grid cells, as used in the European Indoor Radon Map. One can see a correlation of 0.6 between neighbouring cells (lag = 10 km), decreasing with distance.

For cell data, for example means of individual data within grid cells as done for the European Indoor Radon Map, measures of reliability that correspond to uncertainty of individual measurements may simply be the number of data points included. Also relative standard errors CV/√n or confidence intervals of the mean or the geometrical standard error GSE=exp(SDL/√n) can serve this purpose. In variogram-based interpolation, as in kriging, this uncertainty is included as the nugget effect, estimated by extrapolating the variogram to lag=0 or by including replicate observations (i.e., lag=0 exactly) into the analysis. The latter option is not available for cells which exist only once at each cell location by default. (Bootstrapping could circumvent this, i.e. by generating random replicates of cells, but it is rarely used in this context probably due to the high computational effort.)

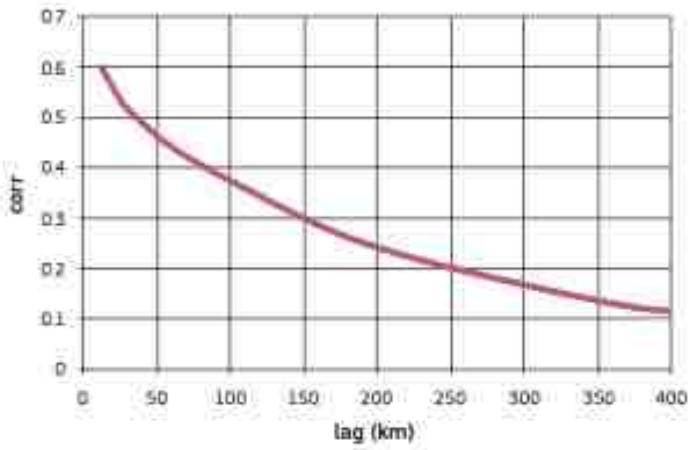

Figure 2-54.
Auto-correlogram of AM (natural logarithm of radon concentration in ground-floor rooms, dataset of the European Indoor Radon Map, Section 5.4).
Source: Graph created by Peter Bossew.

Interpolation methods

Interpolation means estimating values of a quantity at locations where it has not been measured.

A very simple and popular method is Inverse Distance Weighting (IDW), which calculates the value on the target point at location x_0 as the weighted mean of all (or a fraction of) measured values at locations $x_i \neq x_0$. The weights are defined as $w(x_0, x_i) = 1/d(x_0,x_i)^p$, where d is the distance (usually Euclidean) between x_0 and x_i and p an exponent. Most common is p=2, but adaption is possible by optimising e.g. through cross-validation. Implementation is simple and fast, but there is no guarantee that the method minimises the estimation error. It also does not respect the auto-correlation structure of the variable (see previous section).

A very frequently used method that minimises estimation errors and accounts for autocorrelation is kriging (which is actually a family of methods). Under certain, but relatively rigid conditions, kriging yields local uncertainty. However, for estimating uncertainty, confidence intervals and local exceedance probability, mostly simulation-based methods are used (which at some stage also use kriging). In general, these methods are computationally more demanding. For more information, the reader is referred to standard geostatistical textbooks, such as Cressie (1993), Goovaerts (1997), Chilès & Delfiner (2012), Bivand et al. (2013).

Due to their computational demand, machine-learning methods are relatively new, among them support vector machines, regression trees and random forests, etc. Often (but not always) they yield superior results, in particular if predictors are included to improve estimation (such as geology or uranium concentration in the ground when estimating geogenic or indoor radon), and for classification problems. See, for example, Kanevski et al. (2009).

Classification

Often the main purpose of a map is to display where a condition is met or not. Typical examples are radon priority area (RPA[1]) maps, which indicate whether an area is labelled RPA or not, in case of binomial RPA definition, or to which priority class it belongs, in case of multinomial definition. The resulting map can be understood as a class map.

A class map can be generated from a level map by assigning uniform level codes between level thresholds, e.g. blue below a reference level and red above (technically speaking, performing an indicator transform on the levels). The procedure is similar to creating a contour map, with only one contour line in the bivariate case which divides the area into two (possibly topologically complicated, i.e. non-connected) areas, one in which a condition is fulfilled, the other, where it is not.

Estimation methods which yield class membership of a mapping unit directly are also available, i.e. without previous estimation of the full level map, which contains more information than necessary for a class map. A relatively difficult problem is uncertainty of classification. In contrast to uncertainty of a level value (which can be expressed as a confidence interval), this requires assessment of misclassification probabilities. Key terms are first- and second-kind error: If it is estimated that a condition – e.g. to be RPA – is fulfilled, while in reality it is not, one speaks of a first-kind error or false alarm. Conversely, if a condition is fulfilled in reality but this is missed by the estimate, this is called second-kind error or false non-alarm.

A classification-type RPA map which visually divides a domain into neatly separated classes can be criticised on the same grounds as a contour map. This can lead to severe misunderstandings and misinterpretation, if naively used as a decision tool.

The topology of areas which represent classes strongly depends on map resolution and to some extent on map scale. The higher the resolution, the more likely it is that a contiguous area disintegrates into disconnected areas, in particular for underlying quantities which have high geographical variability by their nature, such as typically geogenic and indoor radon concentrations.

1 The term has been coined to express that there are areas in which preventive or remedial action should be applied with priority. The frequently used term radon prone area has been criticised as suggesting that in an area not labelled RPA, no radon problem exists and no action would be required. Due to the high variability of radon, also non-RPA can have high radon concentrations, but with lower frequency and therefore lower priority might be assigned.

2.4.7 Interpretation, documentation, quality assurance

Interpretation and documentation

Data need to be interpreted adequately to be meaningful. Thus, advanced statistical tools are necessary to extract relevant information from the data. Observations can be affected by many sources of uncertainty which may even conceal the wanted information behind 'noise'.

It goes without saying that proper documentation is a prerequisite for repeatability of an investigation, as another essential element of quality assurance.

Statistics from spatial data

Global statistics refer to the entire dataset within a domain, while local statistics may refer to neighbourhoods or grid cells. Literature on the subject is ample.

a. Basic univariate global statistics

Perhaps the most important statistic is the mean, whose unbiased estimator is the empirical arithmetical mean of data. Also the geometrical mean and the median can be useful, but should be used with consideration. For relative dispersion, the coefficient of variation CV is often used, as is the geometrical standard deviation GSD.

CV := standard deviation / arithmetical mean = SD/AM.

GSD := exp(SD(ln data))

Other dispersion measures are based on quantiles, such as Qdev95 = (Q95-Q05)/(Q95+Q05), where Q95 is the 95th and Q05 the 5th percentile of the data, respectively.

Variability must not be confused with uncertainty of the mean, or relative standard error. The former quantifies the dispersion of the data, from which a mean may be estimated. The latter is the uncertainty attached to that mean.

Also important is the univariate data distribution, as histogram (empirical probability distribution function) or as quantile plot (empirical cumulative distribution function).

Statistics derived from clustered data (Section 2.4.4) are, in general, biased. This may be remediated by data declustering or applying geostatistical methods. Clustering with respect to the surveyed population is a special case of deviation from representativeness, which is the general source of bias.

b. Global two-point statistics

For certain purposes, such as kriging interpolation, important information is the association between data at different locations. See Section 2.4.6.

c. Multivariate statistics

Often several quantities are reported, such as uranium concentration in the ground, ambient dose rate and geogenic radon concentration. These may have been measured on the same points (collocated data) or at different points (non-collocated data). Of particular interest is the correlation between the quantities. For non-collocated data recovering correlation can be a difficult problem.

In analogy to the univariate case, multivariate distributions and multivariate two-point statistics can be investigated.

d. Statistics over aggregates

Like point data, aggregates (cells which carry a value or other area units such as municipalities) can themselves be subjected to statistics. However, one should be careful not to confuse statistics performed on aggregated data with the ones on the data. For example, correlation between aggregates of two quantities is generally higher than the one between the data themselves, because the aggregates are less affected by noise (uncertainty) than the data. For example, it may be difficult to reveal the correlation between uranium concentration in the ground and indoor radon concentration. However, if both quantities are aggregated into cells or other areal units, the correlation may become visible.

e. Anomalies, outliers, extremes, hot spots

There is no standard terminology here.

Outlier: a value that differs significantly from other observations in the same sample. Reasons can be:

- observation error or uncertainty;
- an accidentally isolated extreme of the population;
- an instance which belongs to a different population.

A multivariate outlier is not necessarily an outlier of any individual univariate distribution involved. Be aware that whether a value is an outlier depends on the assumed distribution.

Extreme: The highest or lowest value of a set. It does not say anything about its nature, i.e. whether it is a data error, a statistical artefact or representing a true phenomenon.

Anomaly: a point or a region in which the variable behaves differently from most of the data domain or of its neighbourhood, or simply being 'too large' (or too small) than is considered typical for that part of the field. An anomaly may be an outlier, but does not necessarily need to be one.

The concept of anomaly cannot be separated from the one of background, as an anomaly is a value distinct from the background. Among methods for identifying spatial anomalies are:

- Establish a background model and find data which significantly deviate from the background;
- Estimate the bivariate distribution of values and their neighbours in a given (small) distance, and find outliers from the bivariate distribution (e.g. by Mahalanobis analysis).
- Compare values with the ones in their vicinity and find the ones which lie in the critical region of the distribution of a null hypothesis (H_0: no deviation). One interesting method, based on fractal considerations, is the local Hölder exponent (Cheng, 1999).

Hot spot: seems to be mostly used for points, or a cluster of points, or small regions, where the variable takes anomalously high values. Reasons can be:

- A region in which the background process takes high levels;
- A region which is the domain of a separate process.

Distinguishing these can be quite complicated. In environmental studies, isolated extremes should not be discarded as outliers without careful consideration. Sometimes they contain most important information, depending on the purpose of an analysis.

The terms anomaly and hot spot mostly seem to denote 'true' effects, i.e. not related to observation; 'outlier' seems to be neutral in this respect, i.e. can also denote observation effects.

A summary of outlier detection and problems involved can be found in Ben-Gal (2005).

f. Data transforms

It may be useful to use transformed instead of original data. Right-skew data are often log-transformed because certain relationships become visible which are otherwise hidden by data noise or by the presence of very high values. For procedures which require normally distributed data, log-transform can help when lognormality (LN) is assumed, or Box-Cox or normal score (z-score) transforms. In these cases, the sample is transformed such as to generate a normally distributed sample.

Data transforms must be applied with care. Back-transform of results attained with transformed data may not be easy. Beware also that the multivariate distribution of quantities transformed to normal individually is not multivariate normal, in general.

Quality assurance

We may distinguish between three levels of quality assurance (QA).

1. **Design QA**: sampling such that the purpose or target of a study (e.g. AM of the population in an area) can be met with a given tolerance; this implies sample size and provision for representativeness of the sample.
2. **Data QA**: This concerns 'classical' metrological QA, i.e. correct experimental procedures, in particular calibration and measurement, proper consideration of uncertainty that occurs in different stages of the procedure and of detection limits.
3. **Evaluation QA**: This part deals with selecting a proper evaluation methodology, selecting adequate models and correct statistics, while considering model-induced uncertainty whenever possible.

Implementation of proper QA can be demanding, but is a prerequisite for a valid end product. However, one has to recognise that it is often difficult to achieve a complete uncertainty budget, in particular in special studies which may include a rather long chain of aggregation and modelling steps.

A part of proper QA (level 3) is *adequate and correct* statistical treatment. Also this can require advanced methods, just to name the missing data problem (including measurements below detection limit), bias correction of statistics (typical: standard deviation), or respecting the composite nature of certain quantities (typical: geochemical data).

Case study: Soil-gas survey design

Soil gas radon has been found to be used in a wide range of geoscientific applications (e.g. tectonics, earthquakes, volcanic fluids, surface ground waters, environmental risk, etc.), and soil-gas sampling is a screening tool used to rapidly and cost-effectively study radon distribution in the shallow environment, especially where soil-gas concentrations appear to be noticeably different from those produced in the soil grains by the decay of its parent nuclides. This technique may be used at any stage of the exploration phases, both in unexplored areas and during further detailed prospections. A specific Sampling and Analysis Plan (SAP) should be prepared by considering all procedures and techniques used for soil-gas sample collection and analysis. The sampling design (in terms of sample distribution and sample-to-sample distance) should be constructed to obtain all necessary and required information with a minimal expenditure of time and resources. The development of the design should be based on background information from previous studies and data provided by the conceptual model of the site. All this information should be used to design a sampling strategy specific to the characteristics of the site.

Soil-gas surveys may be designed as regional, detailed, or local and must be focused to the exploration objectives. Soil gas sample density per unit area determines whether a soil gas survey is of regional, detailed or a local type. Regional soil-gas survey is in general a preliminary reconnaissance activity that should be very inexpensive and should involve few soil gas samples (1 to 10 samples/km^2), while detailed sampling may be designed with dense spacing of soil-gas sample sites (10–30 samples/km^2). Special high-density soil-gas spacing has been used in local surveys, with more than 30 samples/km^2 commensurate with the extension of the study area. The spatial dependence among samples (i.e., Tobler's First Law; Tobler, 1970) strictly depends on the pattern used for the spatial distribution of sampling points within a defined grid (e.g., sampling design). Classical sampling theory is based on probability sampling (Dixon & Leach, 1977) and more recently in Deimelle (2008). It includes methods for sample selection and estimation that provide, at the lowest costs, precise estimates (Cochran, 1977).

The most important criterion for choosing a method should be to obtain a representative sample of the population distribution and of the housing stock for a region or country.

- The sample should not be biased.
- The sample size should ideally be equal to the housing stock, but this is impractical, so the sample size should be appropriate to determine the population exposure to radon with certain accuracy.

Samples can be selected with an **equal** or an **unequal probability sampling**. Equal probability sampling is often approximately feasible for sampling in practical surveys. Simple random sampling (SRS) and systematic sampling within grids (SSG) serve as the starting point for an understanding of sampling. In SRS or SSG, sample units are drawn independently from each other with equal probability. These two main sample patterns can also be used if the population is divided into two or more homogeneous subgroups, i.e. stratified sampling (SS). SRS is the most straightforward probability sampling method. It is also the most popular method for choosing a sample among population, samples are taken from random locations across the study area (without gridding); thus each member of population has equal probability to be chosen as part of the sample. It is assumed that the population is independent and identically distributed. The advantage of this method is that the sample will represent the target population and eliminate sampling bias, but the disadvantage is that it requires a list of all potential respondents, and this can be problematic for large studies. Furthermore, it completely neglects prior knowledge for the object and leads to relatively large gaps in the sampled area and a marked clustering caused by difficult to find access to locations.

Soil-gas sampling, Ciudad Rodrigo 2016 exercise, Spain
Source: Sara Tejedor

The most common sampling schemes are based on sampling points located within regular grids of different size according to the objective of the work. Grid sampling is an effective way to provide data over a large area at a low cost. The SSG ensures relatively even spatial distribution of samples across the site and is generally easier to implement in the field. It shows a set of regularly spaced sample points in a sample square region. Systematic sampling of this type suffers from two major problems: (i) the sampling interval may coincide with some periodicity in the data being studied (or a related variable), resulting in biased data; and (ii) the set of fixed sampling distance causes important distance-related effects (such as dispersal, contagion etc.) to be missed. A compromise approach is the random sampling within a grid, defined as uniform sampling (US) that includes elements of both simple random and systematic sampling. It consists of locating a fixed number of samples within the grid thus maintaining a uniform sampling distribution (i.e., sampling density).

SS is a probability sampling method in which the population is divided into two or more sub-groups or strata based on some similar attributes. The random sampling method is then applied to every stratum and the obtained samples are representative for each sub-group. The advantage of this method is that it will produce a representative sample of the population with a correct size. The disadvantage of this method is that its application requires a good knowledge of the sample in order to select the right members of each stratum.

In addition to fixed sampling schemes, adaptive schemes can be applied which may offer improvements in terms of estimating mean values and reducing uncertainty (providing lower variances). Typically, an adaptive scheme will involve four steps: apply a coarse resolution fixed scheme to the study area and extend sampling in the neighbourhood of locations where a pre-defined threshold is exceeded. Then additional samples might be taken radially around the initial threshold locations. Alternatively, the initial values at each location might be used to compute an experimental variogram, from which estimate values and variances of these values can be computed using kriging methods. Locations with high kriging variance (i.e. poorly represented) could then be identified and additional sampling designed to reduce this uncertainty.

Soil-gas sampling and measurements

Soil-gas sampling is a screening tool used to rapidly and cost-effectively identify gas content in the subsurface and delineate their spatial distribution at surface. It is also used to ascertain the source and movement of some trace species (i.e. Rn, He, H_2, and pollutants) in different environmental scenarios. The sampling method allows the collection of a large number of samples that statistically minimises sampling/analytical error and bias caused by individual samples (Lombardi et al., 2010; Ciotoli et al., 1998, 1999, 2007; Beaubien et al., 2002; Annunziatellis et al., 2003; Hinkle, 1994; Reimer, 1990).

Soil-gas sampling consists of the collection and analysis of the gas contained in the interstitial spaces of the soil from the unsaturated or vadose zone (Roberts, 1975; Brady & Rice, 1977; Ciotoli et al., 2007; Beaubien et al., 2013).

In the study reported samples were collected using a 6.4 mm, thick-walled, stainless-steel tube onto which two steel cylinders are welded to act as pounding surfaces when installing and removing the probe with a co-axial hammer (Beaubien et al., 2013; Ciotoli et al., 1998). The bottom end of the probe is fitted

Instruments for collecting soil-gas samples, Ciudad Rodrigo 2016 exercise, Spain
Source: Sara Tejedor

with a sacrificial tip to prevent blockage of the tube when inserted into the soil. The probe is pounded down to the desired depth, a small aspirator bulb is attached to the upper end, evacuated, and then the probe is gently tapped upwards until the bulb fills with air (indicating that the probe bottom is free and within a gas permeable horizon). The aspirator bulb is pumped twice to clean the probe of atmospheric air, and then the probe is sampled for field or laboratory analysis, as described below. The probe is driven into the ground to a depth between 0.7 and 0.9 m, depending on the soil consistency and thickness. Collecting samples at this depth determines levels of equilibrated soil gas with the surrounding soil air, therefore measurements tend to be more accurate than shallower sampling. Furthermore, it is sufficient to avoid the influence of infiltrating atmospheric air and then below the major influence of meteorological variables (Hinkle, 1994; Segovia et al.,1987).

Field analyses of some gas species (i.e., CO_2, O_2, CH_4, H_2 and H_2S) were carried out *in situ* by using portable gas analysers attached directly to the sampling probe; an internal pump was used to draw soil gas, at a rate of about 0.5 l/min, into the instrument for analysis. All field instruments were calibrated prior to shipping to the field site and then re-checked upon their return; calibration was found to be stable over the survey periods. Radon (^{222}Rn) and thoron (^{220}Rn) were also measured on site using active detectors (±5% absolute accuracy, and a sensitivity of 0.0067 cpm/(Bqm^{-3})) (Reimer et al., 1990; Ciotoli et al., 2016; Valente et al., 2018). Dried soil air is delivered to the radon monitor by pumping. The pump runs for just 1 min in every 5 min until the end of the cycle. The flow rate of the pump is 1 l/min. The instrument is equipped with a solid-state alpha detector that allows measuring ^{222}Rn using the activity of its daughter ^{218}Po that reaches equilibrium with the parent about 15 minutes. A single measurement has an average duration of 25–30 minutes, with partial readings every five minutes (cycles), and ends when the relative difference between the last two cycles (starting from the fourth, when equilibrium conditions are reached) is lower than 15%. In this case, the final result is the average value of the last two readings.

In general, soil-gas samples were also collected and shipped to the laboratory for gas chromatography (C1-C3 alkanes and C_2H_4, and permanent gases, N_2, O_2 + Ar, and CO_2) and spectrometry (He) analyses. A plastic syringe was used to transfer approximately 50 ml of soil gas from the probe into pre-evacuated, 25 ml volume, stainless-steel sample canisters, with a brass valve and a secondary septum.

Discussion of used statistical, geostatistical, mapping methods, defined grid

Different statistical and geospatial analysis techniques were applied to the soil-gas data to construct estimated maps of soil gas concentration in an area, according to the following steps: Exploratory Data Analysis (EDA), Exploratory Spatial Data Analysis (ESDA), and Geostatistical Analysis (GA).

Exploratory Data Analysis (EDA) evaluates the basic characteristics of the raw data and their statistical distribution by using numerical (i.e., calculation of summary statistics) and graphical methods (i.e., histograms, box plots, etc.) that summarise the data in a diagrammatic or pictorial way (Tukey, 1977; Good, 1983; Sinclair, 1991; Reimann & Filzmoser, 2000). EDA was conducted to evaluate the basic characteristics of the data (i.e., summary statistics and statistical distribution of each variable) that can be referred to different geochemical processes and to compare data with other available database (Ciotoli et al., 2007, 2014; Zhang et al., 2005; Rantitsch, 2004). Normal Probability Plots (NPP) and Quantile-Quantile (QQ) plots were used to determine the occurrence of different geochemical populations and to define anomaly 'threshold' values (Sinclair, 1991), particularly when the study area was characterised by a large variety of factors such as soil types, geologic units, fractured zones, etc. Some papers report the analysis of the radon statistical distribution both in soil gas and indoor and generally agree that Rn shows a log-normal distribution (Cinelli et al., 2015; Daraktchieva et al., 2014; Bossew, 2010; Hamori et al., 2006; Andersen et al., 2001).

Exploratory Spatial Data Analysis (ESDA) consists in the application of statistical techniques to examine the data in the spatial context to gain a deeper understanding of the investigated phenomena (i.e., sampling pattern, post and classed post maps, spatial outliers, presence of trends, etc.). In particular, it is focused on spatial autocorrelation and spatial heterogeneity, i.e., the correlation of a single variable between pairs of neighboring observations by using indexes of spatial autocorrelations (Local Moran's I and Getis-Ord Gi* statistics) (Bailey & Gatrell, 1995; Anselin, 1998; Moran, 1950).

Geostatistical Analysis (GA) compares individual spatial features to their nearest neighbors (i.e., variogram maps, experimental variograms, models, etc.) for the study of spatial autocorrelation and the construction of final prediction maps by using spatial interpolation. Geostatistical analysis also allows to investigate the presence of phenomena acting along specific directions (e.g., fault-related anisotropy effect) according to the following tasks: (1) construction of experimental directional variograms to investigate the spatial dependency of gas concentrations (i.e., calculate the main variogram parameters: nugget, range, and sill) for the variables that showed normal or lognormal distributions; (2) determination of the anisotropy (where present) which is important for defining parameters for the kriging estimation (i.e., directions and anisotropy ratio); and (3) construction of contour maps by using variogram model parameters in the kriging algorithm.

Spatial interpolation and mapping techniques

Spatial interpolation methods are techniques that predict the value of a regionalised variable (ReV) at a given location by using values of the same variable sampled at neighboring points (Matheron, 1963; Journel & Huijbregts, 1986). There are many spatial interpolation methods and all work under the assumption that the ReV is spatially dependent, indicating that the values closer to the interpolated location together are more likely to be similar than the values farther apart and therefore will influence the interpolated value more strongly than sample points which are further away (Tobler's first law of geography; Tobler, 1970).

The most common interpolation techniques calculate the estimates for a ReV at any given location by a weighted average of nearby data according to the general formula:

$$\hat{z}(x_0) = \sum_{i=1}^{n} \lambda_i z(x_i) \qquad (2\text{-}27)$$

where, $\hat{z}$ is the estimated value of ReV at the point x_0, z is the observed value at the sampled point x_i, λ_i is the weight assigned to the sampled point, and n represents the number of sampled points used for the estimation. The main difference among all the interpolation techniques is the criterion used to weight the values of the sample points, i.e., simple distance relations, minimisation of curvature, minimisation of variance. Weights are assigned either according to deterministic or probabilistic criteria. The goal is to create a surface to best represent empirical reality, but as a number of factors affect map quality (i.e., statistical distribution of the studied variable, sampling density, the applied interpolation method, etc.), the selected method must be assessed for accuracy.

Interpolation includes deterministic and geostatistical techniques, depending on the type of the function used to interpolate the values of the ReV. Deterministic interpolation techniques (e.g., Inverse Distance Weighting, IDW; Radial Basis Function, RBF, etc.), uses mathematical formulas to calculate the weight for each measured value to estimate the unknown values of the ReV at any point across a given area. The weight depends only on the distance between sample point and location of the estimation point. Geostatistical interpolation techniques, i.e., kriging techniques, use a generic family of generalised least-squares regression algorithms, which are based on the theory of ReV (Matheron, 1963; Journel & Huijbregts, 1978; Goovaerts, 1997).

Kriging techniques are increasingly preferred because they capitalise on the spatial correlation between neighbouring observations to predict attribute values at unsampled locations. These methods are not only a function of the distance, but in addition, they implement the function of unknown spatial autocorrelation between the values of the sample points by using experimental variogram calculation and modelling. The variogram γ(h) displays the degree of spatial dependence of a spatial random variable Z (x, x+h) at locations (x) and (x+h). The experimental variogram is defined as:

$$\gamma(h) = \frac{1}{2N(h)} \sum_{N(h)} \left[Z(x_i) - Z(x_i+h) \right]^2 \qquad (2\text{-}28)$$

where N(h) is the number of pairs of sample points x(i) and x(i+h) separated by distance h, and γ(h) is the variogram (Webster & Oliver, 2001). It is commonly represented as a graph which shows the increase in the variance of the random variable of interest as a function of distance between all pairs of sampled locations. The graph is then fitted with a mathematical model that describes the variability of the ReV with location.

The experimental variogram displays several important features:

a. the 'nugget', a positive value of γ(h) at h close to 0, which is the residual reflecting the variance of sampling errors and the spatial variance at shorter distance than the minimum sample spacing;
b. the 'range' is a value of distance at which the 'sill' is reached. Samples separated by a distance larger than the range are spatially independent because the estimated semivariance of differences will be invariant with sample separation distance. If the ratio of sill to nugget is close to 1, then most of the variability is non-spatial. The range provides information about the size of a search window used in the spatial interpolation methods.

Geostatistical kriging-based techniques include monovariable estimation by using simple kriging (SK), ordinary kriging (OK), universal kriging (UK), empirical bayesian kriging (EBK, for non-stationary phenomena (Krivoruchko & Gribov, 2014). For geostatistics see the following specific literature: Matheron (1963); Journel & Huijbregts (1978); Isaaks & Srivastava (1989); Cressie (1990); Goovaerts (1997); Raspa et al. (1997); Clark & Harper (2001); Webster & Oliver (2001); Johnston et al. (2001); Li Jin et al. (2011).

Multivariate spatial techniques

The geogenic radon potential (GRP) mapping is a multivariate problem that can be addressed through the construction of a conceptual model based on the selection of the variables that most influence the presence of radon in the shallow environment. Such a geochemical model should be based on available and/or ad hoc measured geological, geochemical, structural and geomorphological data. These environmental data are more suitable to construct GRP maps because they are characterised by: (i) higher spatial autocorrelation; (ii) mostly lower variability than radon data; (iii) and do not depend on anthropogenic factors with respect to the indoor radon data mainly affected by the building parameters.

As soil-gas radon is the direct measure of radon that potentially can enter the buildings, the spatial relationships between this quantity of available radon and the other environmental data, can be modelled by using global (Ordinary Least Squares, OLS) and spatial (Geographically Weighted Regression, GWR, Fotheringham et al., 2002; Ciotoli et al., 2017) multivariate regressions. Furthermore, multivariable kriging techniques can be used: simple cokriging (CoK, Goovaerts, 1997; Deutsch, 2002), kriging with external drift (KED, Journel & Rossi, 1989; Raspa et al., 1997) or regression kriging (RK, Hengl et al., 2007). Machine learning methods appear to be increasingly popular for addressing multivariate problems (e.g. Kanevski, 2009). All these models include a response variable (i.e., the radon concentration in soil gas) and some explanatory variables (i.e., the radium content of the rocks, the rock permeability, the presence of faults and fractures, etc.). The final spatial model is used to estimate the response variable at unknown locations.

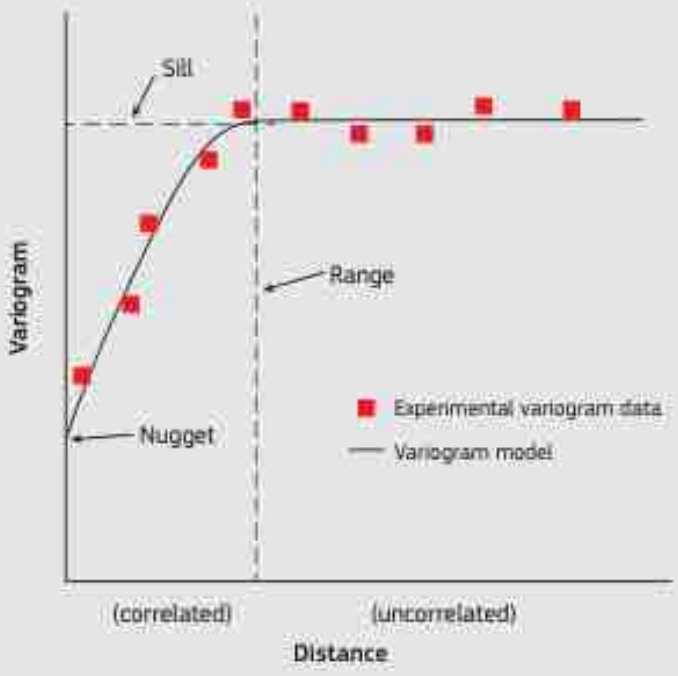

Figure 2-55.
Example of a variogram model demonstrating the variogram parameters.
Source: https://[illegible] (accessed on [illegible]) [illegible]

Field measurements of radon in soil gas, RM 2018 exercise, Cetyně, Czech Republic.
Source: Tom Tolofus

2.5 Measurement methods

2.5.1 Introduction

The detection and measurement of natural radioactivity are a fundamental step for studying the distribution of natural radioactivity sources and for assessing the doses received by humans. Because of the need to provide a qualitative and quantitative analysis of natural radioisotopes in different environmental matrices (i.e. rock, soil, air, water, etc.) a large number of different detectors have been used and are described in this session.

Ionising radiation is rarely detected directly; instead, detectors usually measure the secondary products arising from the interactions of the radiation with the detector material. For example, as an alpha or beta particle traverses a detector's sensitive volume, electric charges in the form of electron-ion pairs or electron-hole pairs are created and the subsequent movement and collection of these charges gives rise to an electrical pulse or current which can be measured. Indirectly ionising radiation such as gamma photons and neutrons must first undergo interactions in the detector material that produce secondary charged particles, recoil atoms or electrons that, in turn, produce charged pairs as they slow down.

The rate of generation of radiation-induced pulses can then be used to measure the rate at which radiation particles traverse the detector. Such detectors are termed **radiation counters**. In some detectors, the magnitude of the radiation induced pulse is related to the type of radiation particle and its energy. By measuring both the number of pulses and the distribution of pulse sizes produced by a given type of radiation, one can determine both the number and energy distribution of the incident radiation. These detectors can then be used as **energy spectrometers**. In some detectors the average current can be used as a measure of the amount of ionisation or energy deposition, per unit mass of detector material, caused by incident radiation. These detectors can then be calibrated to measure radiation absorbed (or equivalent) doses and are thus called **rate meters** (McGregor, 2007; Knoll, 2000).

The measurement systems mainly used in the field of natural radioactivity can be divided in three main groups according their uses to:

- detect and count gamma, alpha and beta particles;
- perform spectrometry analyses (gamma, alpha and beta);
- measure radon concentrations.

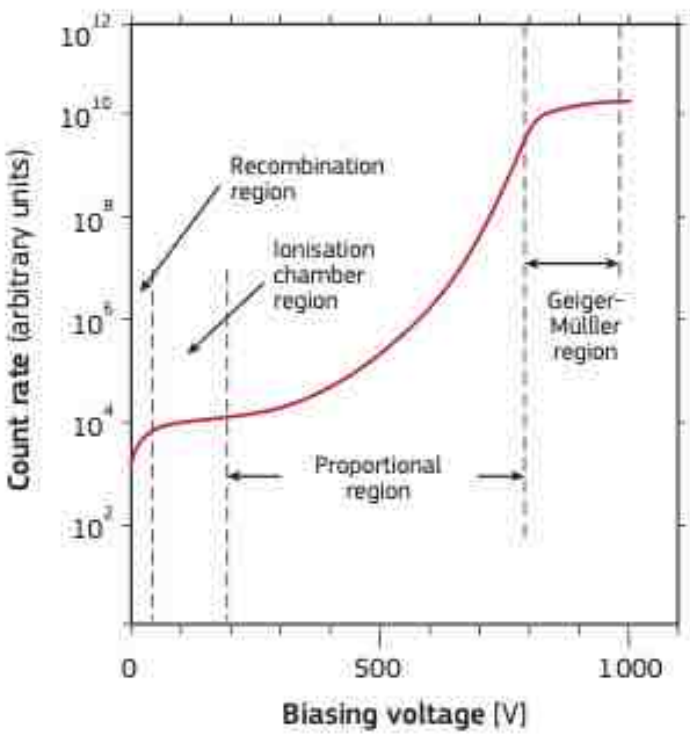

Figure 2-57.
Qualitative plot of the response of a gas detector.
Source: modified from https://physicsworldlab.org/2017/07/2/the-rise-proportional-counter-2

2.5.2 Gamma, alpha and beta particles detection

Gas-filled detectors

Gas-filled detectors are conceptually the simplest devices, and have been used since the beginning of radiation sciences. The basic structure is as follows: a conductive enclosure (most often cylindrical) with a thin metal component (mostly a wire) electrically insulated from the enclosure; the enclosure is filled with a gas; between the two metal parts (i.e., two electrodes) a voltage difference, known as the biasing voltage, is maintained and a circuitry is attached to measure either the current that flows through the device or the voltage surge that this current produces flowing through a resistor. The schematic drawing of a generic gas detector is shown in Figure 2-56.

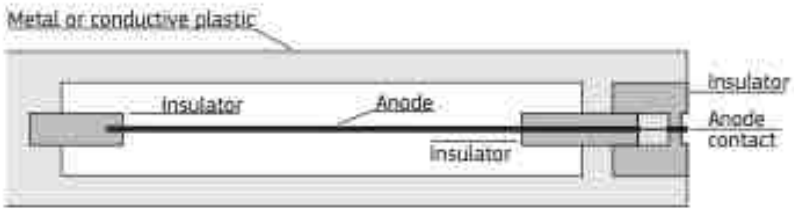

Figure 2-56.
Schematics of a gas detector.
Source: graph created by Dominikos Mollaco

Normally the circuit is open, insofar as the gas between the electrodes insulates them; however, if ionisation is produced in the gas (as is the case when the detector is traversed by radiation), the ions and electrons produced are attracted towards the cathode and anode, respectively, and charge is collected. Circulating in the circuitry this charge is formed into an electric signal that can be visualised in one of many possible ways, to be read by the operator.

If a detector is placed in a radiation field, its reading can be modified by acting on the biasing voltage. A qualitative plot of the response (in count rate) vs. the biasing voltage is shown in Figure 2-56.

Several regions can be seen to exist as voltage is varied; for very low voltage ions and electrons are attracted very weakly to the electrodes, and have thus time to recombine. At zero voltage they all recombine, but as the voltage is applied and slowly increased less and less ions and electrons manage to recombine, while more and more do reach the electrode, so that an increasing current is measured. This is the region known as '**recombination region**'. At some value of the biasing voltage (usually of the order of 100 V) one sees that the current reaches a value that does no longer grow, increasing (moderately) the voltage: a plateau appears in the current-voltage characteristic. The region of existence of this plateau is know as '**ionisation chamber region**'. This mode is exploited in the ionisation chamber (to be described below). Increasing the voltage further and further the plateau is left behind and the characteristic starts rising again, and a region can be recognised where the growth is almost linear, termed '**proportional region**': this is the region where proportional counters (see below) operate. Finally increasing even further the voltage a new plateau is attained, where increasing the voltage no longer produces an increase in the reading: this is the '**Geiger-Müller region**' where Geiger-Müller counters (see below) function.

Beyond the Geiger-Müller region the counter ceases to function: when such high voltages are applied the electron cascade becomes incontrollable and produces a continuous discharge that can only be stopped by switching the power supply off. Needless to say, this region must be avoided, since the continuous discharge will damage - and possibly destroy - the counter.

We will now examine separately the three functioning modes mentioned above.

Ionisation Chamber

In the ionisation chamber (IC) regime, the voltage is set so that essentially all charges produced by ionisation are collected. ICs are used in current mode, since the charge generated by a single event (be it a gamma ray, or a beta or whatever ionising radiation is being measured) is too small to be detected singularly. ICs are suited to investigate things like dose rate, by measuring the current produced by a steady flow of radiation, or to measure the overall dose due to a fluence received in a limited lapse of time, e.g., the dose delivered by a discharge of an X-ray tube.

Proportional counter

As the voltage is raised further, electrons produced by ionisation are accelerated to higher energies before they are collected on the anode, and thus acquire sufficient energy to produce, in turn, further ionisation, increasing the number of electrons collected: this effect is called a cascade. In a wide range of voltages the number of electrons collected is strictly proportional to the number of electrons initiating the cascade, and the number of the latter, in turn, is proportional (on average) to the energy deposited by the initial radiation event. As a result, the number of electrons collected is proportional to the energy of the incoming radiation event. The proportionality factor is controlled by the biasing voltage: the higher the voltage the larger the multiplication factor. Given the proportionality of the signal to the energy of the incoming radiation event, they can be used to determine the count rate and at the same time allocate the events to different energy bins; in other words, they permit spectrometry. The obvious problem is that, since the proportionality factor depends strongly on the voltage, the latter must be kept extremely stable, unlike the case of the IC and, as we will see presently, that of the Geiger Müller, instruments, both, rather insensitive to small fluctuations in the biasing voltage.

Proportional counters are no longer commonly used.

Geiger-Müller counters

Finally, as the voltage is raised to even higher values the Geiger-Muller (GM) region is entered. In this region, electrons get sufficiently accelerated by the electric field to produce new ionisation, and the new generation of electrons in turn gets enough acceleration to produce more electrons and so forth: the result is the so-called 'avalanche'. The avalanche, once started, continues to build up until the charge spreads to the entire length of the anode and the space charge field masks completely the anode stopping the process. It is worth stressing that any event starts the avalanche, regardless of the energy of the radiation producing the initial ionisation, so that all radiation events produce the same charge collected at the anode.

Also, in these conditions, the electric charge collected is rather high and, once collected, produces a signal strong enough to be detected even without being amplified. Since the avalanche is always the same, GM counters have no way of distinguishing the energy of the seeding radiation: the only information returned is the count rate.

Summarising, GM tubes are useful, cheap and robust, they basically detect the presence and intensity of radiation in terms of count rate and cannot determine the type, energy, or vectors of the radiation detected. They have high sensitivity, versatility with various types of radiation, wide variety of shapes and windows, large output signal and reasonable cost.

Finally, an oscilloscope, LED screen, or other display conveys the particle count to the user.

Albeit that the direct reading from a Geiger counter provides the either the count of particles detected during the exposure time, or the count rate, often it can provide several standard units of measurement, with the understanding that the readings apply only to the types of radiation that particular model is able to accurately detect. Quite typically they are calibrated with ^{137}Cs, i.e. if the source is indeed ^{137}Cs gammas, then the dose rate displayed is the actual value, which means that they provide the actual dose rate for gamma rays of this energy (661 keV). Dose rates due to gamma rays from other sources (hence difference energies) will be an approximate assessment.

Scintillation detectors

Scintillation counters are radiation detectors based on materials (named scintillators or phosphors) that emit light flashes when struck by radiation. As, for instance, a gamma ray photon interacts in the scintillation material, it transfers its energy to a number of bound electrons proportional to the energy of the original photon; every excited electron then deexcites by emitting a photon; the same type of process happens for all types of particle-scintillator interaction. The photons are emitted in the visible spectrum.

To convert the light into an electric signal, scintillation counters are coupled to a light-sensitive photomultiplier tube. Figure 2-58 shows an example scheme of a scintillation counter using a thallium-activated sodium iodide crystal.

A schematic cross-section of one type of photomultiplier tube is shown in Figure 2-59.

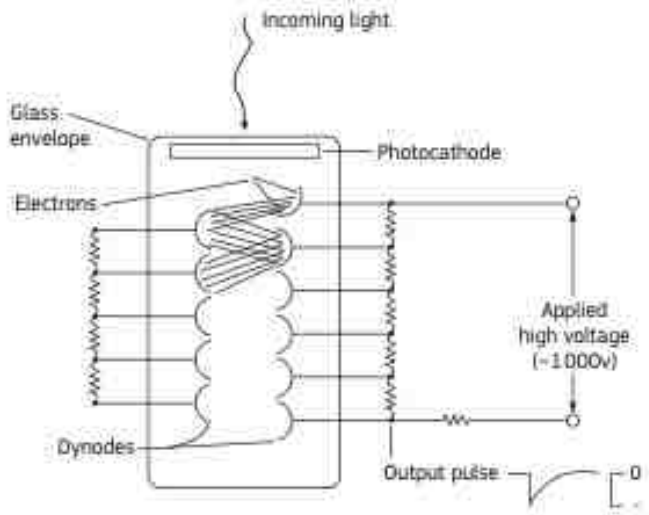

Figure 2-59.
Photomultiplier tube
Source: IOE, 1993

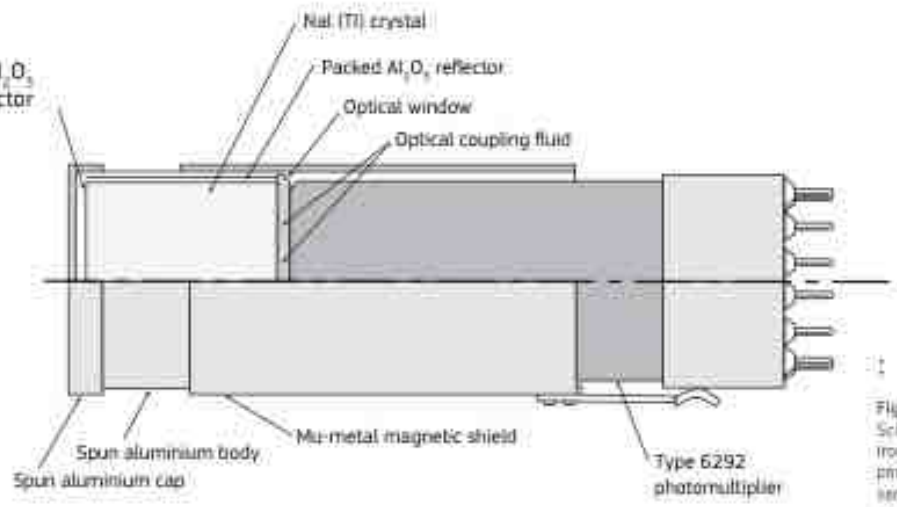

Figure 2-58.
Scintillation counter. (Mu-metal is a nickel-iron soft ferromagnetic alloy with very high permeability, which is used for shielding sensitive electronic equipment against static or low-frequency magnetic fields (Wikipedia).)
Source: IOE, 1993

There are three classes of solid-state scintillation phosphors: organic crystals, inorganic crystals, and plastic phosphors, and then there are a number of liquid scintillators. Solid-state scintillators are usually used for gamma spectrometry, liquid scintillators are mostly used for beta spectrometry.

Inorganic crystals include lithium iodide (LiI), sodium iodide (NaI), cesium iodide (CsI), and zinc sulfide (ZnS). Inorganic crystals are characterised by high density, high atomic number, and pulse decay times of approximately 1 µs. They possess high efficiency for gamma ray detection and can handle high count rates. Organic scintillation phosphors include naphthalene, stilbene, and anthracene. The decay time of this type of phosphor is approximately 10 ns. Plastic phosphors are produced adding scintillation chemicals to a plastic matrix. The decay constant is the shortest, approaching 1 or 2 ns. The characteristics of a number of phosphors are shown in Table 2-6.

Scintillator	Density (g/cm³)	Wavelength of maximum emission (Å)	Relative pulse height	Decay time (µs)
NaI (Tl)	3.67	4100	210	0.25
CsI (Tl)	4.51	Blue	55	1.1
KI (Tl)	3.13	4100	50	1
Anthracene	1.25	4400	100	0.032
Trans-Stilbene	1.16	4100	60	0.0064
Plastic	-	3550–4500	28–48	0.003–0.005
Liquid	-	3550–4500	27–49	0.002–0.008
p-Terphenyl	1.23	4000	40	0.005

Table 2-6
Scintillating materials
Source: R. Swank, 1954

Light flashes from the scintillator hit a photocathode liberating electrons.

The photomultiplier is a vacuum tube with a glass envelope containing a photocathode - a material sensitive to light that emits electrons by the photoelectric effect when struck by photons with a wavelength characteristic for the phosphor - and a series of electrodes called dynodes. A light flash from the scintillation phosphor, upon hitting the photocathode liberates electrons. These electrons are not numerous enough to form a signal sufficient to be detected reliably. However, in the photomultiplier tube, they are attracted by a voltage drop of about 50 volts to the nearest dynode. Each photoelectron that strikes the first dynode with sufficient energy liberates a number of new electrons. The second-generation electrons are, in turn, attracted to the second dynode where a larger third-generation group of electrons is emitted and so forth. This amplification continues through 10 to 12 stages. At the last dynode, sufficient electrons are available to form a good current pulse, that will be then processed through appropriate electronics.

The advantages of a scintillation counter are its efficiency and the high precision and counting rates that are possible. The latter attributes are a consequence of the extremely short duration of the light flashes, from about 10^{-9} to 10^{-11} seconds.

As mentioned, the intensity of the light flash, and hence the amplitude of the output voltage pulse, are proportional to the energy of the radiation event responsible for triggering the phenomenon. Consequently, scintillation counters can be used to determine the energy, together with the number, of the exciting particles (e.g., gamma photons), thus permitting spectrometry.

2.5.3 Spectrometric analysis

Gamma spectrometry

Gamma-ray spectrometry is the quantitative study of the energy spectra of gamma-ray sources allowing the identification and quantification of radionuclides. Indeed, most radioactive sources produce gamma rays, which are of various energies and intensities. When these emissions are detected and analyzed with a spectrometry system, a gamma-ray energy spectrum can be produced.

Gamma and X-ray transfer energy that is stored in their electromagnetic field and the individual wave packets of this radiation are called photons. Apart from the energy carried by gamma and X-ray photons, the main difference between gamma rays and X-ray is their origin; while X-ray are produced by atomic excitations, gamma rays are emitted by transitions from excited states in the nucleus. An X-ray or gamma-ray photon is uncharged and creates no direct ionisation or excitation on the material through which it passes. Only the fast electrons created in gamma-ray interactions provide any clue to the nature of the incident gamma rays. These electrons have a maximum energy equal to the energy of the incident gamma-ray photons and will slow down and lose their energy in the same manner as any other fast electron such as a beta particle. In order to serve as a gamma-ray spectrometer, a detector must carry out two distinct functions:

a. act as a conversion medium in which incident gamma rays have a reasonable probability of interaction to yield one or more fast electrons,
b. act as a conventional detector for these secondary electrons.

The devices most typically used for gamma spectrometry are high-purity germanium (HPGe) detectors and scintillator detectors (NaI-sodium iodine), while a new solid-state detector known as cadmium-zinc telluride (CZT) has been gaining more and more attention in recent years. Scintillator detectors were discussed earlier, and CZT are not yet used in the field of radon measurements. Hence we limit the discussion to Germanium devices.

Germanium semi-conductor detectors (HPGe)

A Germanium detector contains a Ge-crystal across which a large electric field is applied so that it is totally depleted. When a photon interacts in the depleted region of the crystal, electron-hole pairs are created. The number of produced charge pairs is proportional to the energy deposited by the photon. The charge pairs drift to the electrodes of the detector under the influence of the electric field. The drift of charges produces an output pulse with an amplitude proportional to the energy deposited by the photon. Thus, the higher the energy deposited in the detector, the bigger the pulse height. Pulses from the preamplifier are then amplified once more and sorted according to their size by a multichannel analyser as long as the gamma rays are. A spectrum is finally built by adding the pulses into the corresponding energy channels.

Ge-detectors:

a. allow non-destructive measurements, i.e. no radiochemical separations are necessary,
b. provide information about both the energy and the rate of photons reaching the detector, i.e. they provide a spectrum; photons with different energie can be recorded simultaneously in the same spectrum,
c. their resolution is much better than other photon detectors such as scintillators, which allows differentiating photons with quite similar energies.

A disadvantage of the semiconductor detectors is the need to keep them cold, generally at liquid nitrogen temperature.

Alpha spectrometry

Alpha spectrometry is the quantitative study to measure the energy of alpha particles emitted in the decay process, allowing the identification and quantification of alpha-emitting radionuclides. Because of the limited penetrating power of alpha particles, preparation of the sample for counting is often a critical step. Gross alpha measurements can be made using small sample sizes with a gas-flow proportional counter, but self-absorption of the alpha particles results in a relatively high detection limit for this technique. Liquid scintillation spectrometers can also be used to measure alpha-emitting radionuclides. Most alpha-emitting radionuclides are measured in a vacuum (to limit absorption by air) using alpha spectrometry. This method requires that the sample is prepared as a virtually weightless amount in a specific geometry. Electrodeposition is the traditional method for preparing samples for alpha counting. This technique provides the highest resolution, but it requires a significant amount of training and expertise on the part of the analyst to produce a high-quality sample. Precipitation of the radionuclide of interest on the surface of a substrate is often used to prepare samples for alpha spectrometry. While this technique generally produces a spectrum with lower resolution, the preparation time is relatively short compared to electrodeposition, and personnel can be trained to prepare acceptable samples relatively quickly (EPA, 2000).

Alpha-emitting radionuclides are typically measured using alpha spectrometry. Alpha spectrometry produces a spectrum of alpha particles detected at different energies, but because the sample is purified prior to counting, all of the alpha particles come from radionuclides of a single element. This simplifies the process of associating each peak with a specific radionuclide, but the lower resolution associated with alpha spectrometry increases the difficulty of identifying the peaks. Although commercial software packages are available for interpreting alpha spectrometry results, an experienced operator is required to ensure that the software is working properly (EPA, 2000).

Beta spectrometry

Beta spectrometry is the quantitative study to measure the energy of beta particles emitted in the decay process allowing the identification and quantification of beta emitting radionuclides.

Beta-emitting radionuclides are usually prepared for a specific type of counter in a specified geometry. The solid material is usually precipitated and collected on a filter in a circular geometry to provide a homogeneous sample. Liquid samples are typically converted to the appropriate chemical form and diluted to a specified volume in preparation for counting. Measurements of solid samples are typically performed using a gas-flow proportional counter. Because the total beta activity is measured, it is important that the purification step is performed to remove any interfering radionuclides (EPA, 2000). Liquid samples are usually diluted using a liquid scintillation cocktail and counted using a liquid scintillation spectrometer (LSC). Liquid scintillation spectrometers can be used for low-energy beta emitting radionuclides, such as ^{3}H and ^{90}Sr. They also have high counting efficiencies, but often have a high instrument background as well. Gas-flow proportional counters have a very low background (EPA, 2000).

a

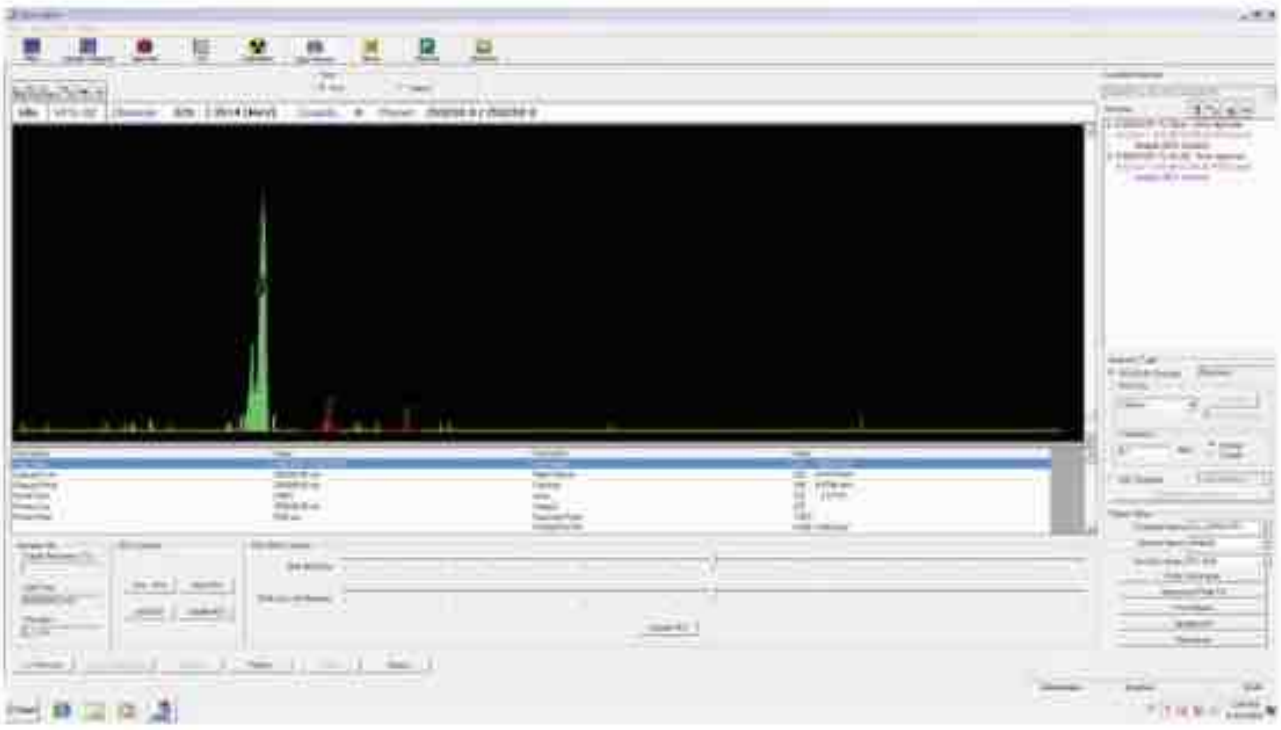

b

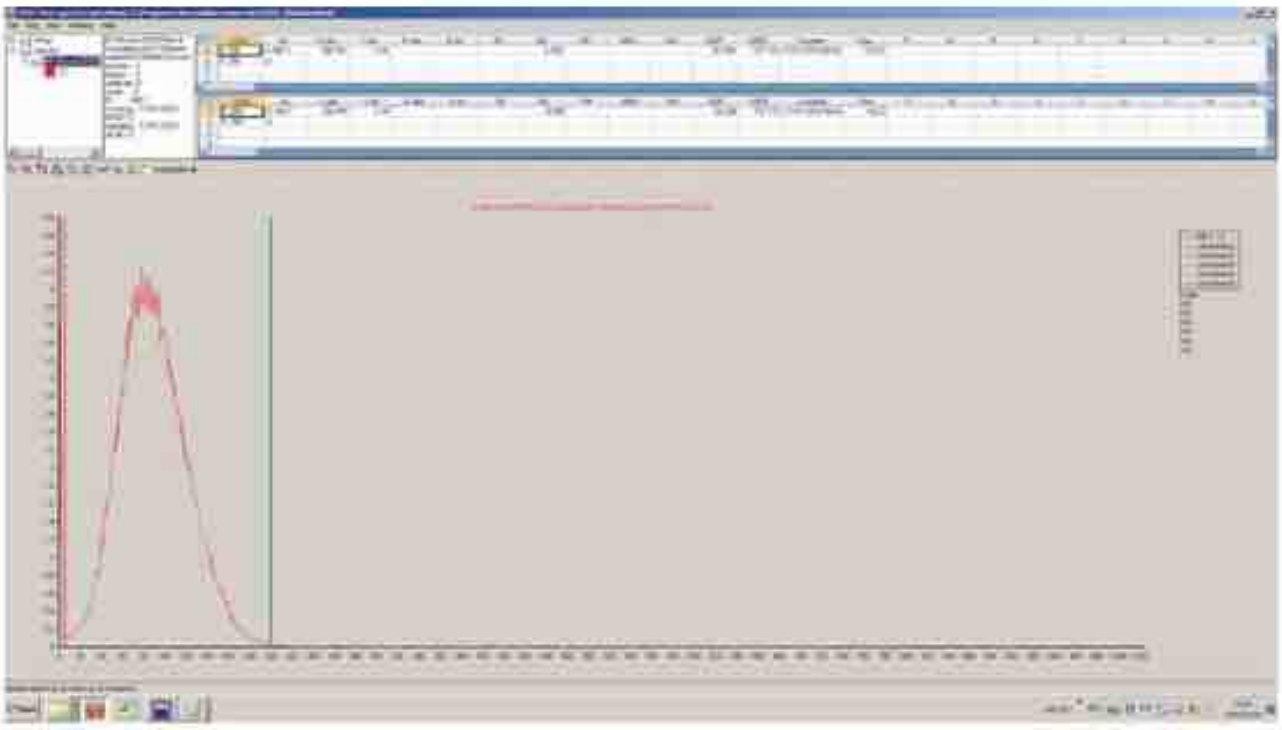

c

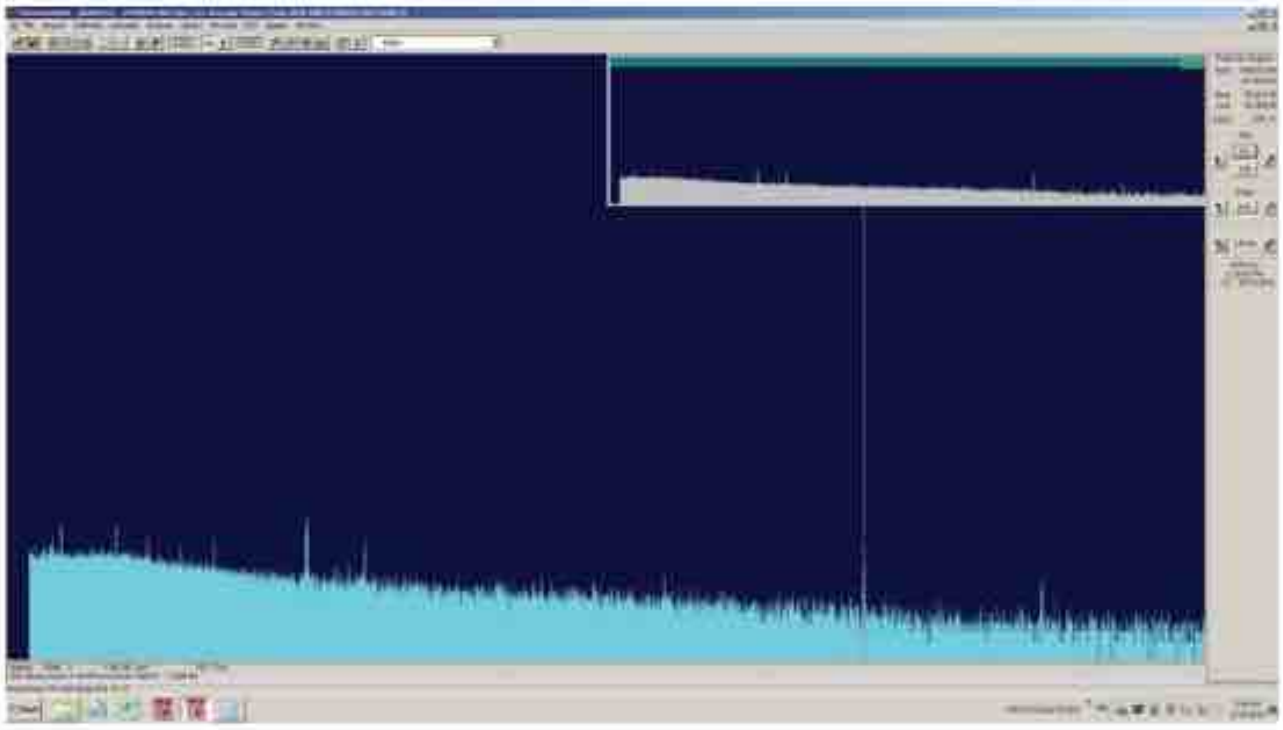

Figure 2-50:
a) Typical alpha spectrum of environmental soil samples. The peak is due to the ^{209}Po radio-trace
b) Typical beta spectrum of Tritium using a Liquid Scintillation Counter
c) Typical gamma spectrum of lake water sample
Source: JRC Ispra Site Laboratory for Radioactivity Measurements

2.5.4 Radon measurements

Many detector techniques have been established to measure the concentration of radon and its decay products in indoor air or in soil gases. Methods requiring an electric source are termed active, otherwise they are called passive.

The measurement techniques can be classified into 3 classes, based on the timing of the measurements:

i. **Grab sampling**: or spot measurement. It is quick: the entire measurement is completed within minutes or a few tens of minutes. In the radon case it produces the value of radon or radon progeny concentration at a given time instant; it is of limited interest for determining long-term mean concentration, given the wide fluctuations typical of radon concentration: it may serve the purpose of categorising generally the location (high, medium, low radon concentration). Considering the potential variability of concentration with time, this does not give a useful measure of the average exposure rate in a home.

ii. **Continuous active sampling**: an extended, uninterrupted sequence of spot measurements (see point i. above), or a sequence of grab samplings repeated numerous times at short time intervals (from several minutes to an hour). It is a very demanding practice only justified by special needs, like, e.g., identifying radon entry points. For radon decay products it is based on grab-sampling methods, with modifications to permit automatic sampling, counting, and, in some case analysis.

iii. **Integrative sampling**: sums up data collected over a period of time. Mostly done with passive devices. The duration of the measurement can be a short-time average (days) or long-term average (weeks or months). Typical integrative devices are charcoal canisters, alpha track film dosimeters and Electret Ion Chambers; all are quite simple to use. Except for charcoal canisters, they are the appropriate devices for evaluating radon risk in a house and ideally measure over a whole year.

Active measurement methods

Measurement systems, in turn, are subdivided into two classes:

i. **Active systems**: those based on detectors requiring electric power. Some in common use are: ionisation chambers; proportional counters; GM tubes; lucas cells; scintillators; solid state detectors; and more.

ii. **Passive systems**: those based on detectors not requiring a power supply. Typical examples are: all kinds of film, of particular interest track film (ATD: alpha track dosimeters); active carbon canisters; electret chambers; and more.

An overview of the most common measurement systems follows.

Active systems

Lucas cells: they are comprised of a hermetically sealed container lined with an alpha-sensitive scintillator, with a transparent window and a photomultiplier device. Air is introduced through an absolute filter and then measured by alpha spectrometry. Air can be introduced in one of the following methods:

- The cell is vacuumed: an inlet valve permits to suck in the desired quantity of ambient air
- A pump maintains a continuous flow of air through the cell
- Radon flows in spontaneously by diffusion, through an appropriate filter (note: this entails a delay connected to the diffusion time which must be small compared to the half-life)

Solid-state detectors: air diffuses through a filter to the sensitive chamber of the device. A solid-state detector, sensitive to alpha rays, collects the signal. Here too diffusion time must be kept in mind.

In some devices radon progeny isotopes are collected on the detector and a quick alpha spectrometry is processed measuring, e.g., ^{218}Po, ^{214}Po, ^{216}Po. Radon and thoron are easily discriminated.

Ionisation chambers: here too air diffuses inside the sensitive volume through a filter. Again diffusion time needs to be considered.

Passive systems

Active charcoal canisters: the canister is a tin box filled with active carbon. The can is only opened on location to be measured. Ambient radon diffuses and is captured inside the carbon. After the desired time the can is sealed and sent to the laboratory for counting. Counting is mostly done by gamma spectrometry, counting the gammas emitted by ^{214}Pb and ^{214}Bi (see decay chain in Section 2.2.2).

Alpha-track films are comprised of a film substrate that suffers damage along the track of an incoming alpha particle. After exposure the film is treated with a 'developing' chemical that renders the tracks visible and hence countable under a microscope. From the surface density of tracks exposure is then determined. Three materials are generally used for this kind of radon measurements: LR-115 (a thin film of coloured cellulose nitrate on an inert backing), polycarbonate, and CR-39 (poly allyl diglycol carbonate, PADC). Two operation modes are possible for alpha track detector: the closed detector, in which the film is enclosed by a container allowing ^{222}Rn to diffuse into it; and the open detector, i.e., film exposed naked to the ambient atmosphere. Closed detectors exclude radon decay products present in the ambient air, recording only those alpha particles generated by the radon entering the container and the decay products formed from it. It also discriminates against ^{220}Rn (thoron) whose half-life is too short to enter the chamber through the diffusion barrier. This mode of detection provides a result related to the true average radon gas concentration during the time of exposure. Open detectors, instead, record alpha particles originating from both ^{222}Rn and ^{220}Rn and their decay products in the ambient atmosphere: their response to radon and its decay products depends on equilibrium factors. Alpha-track detectors are generally used over periods of time ranging from a month to a year. In order to obtain representative results from a building, the duration should be as long as possible.

Electret ionisation chambers: The system is based on an electret, a plastic disk charged to a very stable known potential difference (e.g., around 450 V when factory-new) mounted inside a chamber of conducting plastic. The most common model is used here to describe the concept (Figure 2-61).

The electret is both the source of the electric field and the sensor. The volume inside the chamber is put in contact with ambient air through a filter designed to block all aerosol, and radon enters the chamber volume through passive diffusion. Ion pairs generated inside the volume are collected and discharge progressively the electret. The ensuing voltage reduction is a known function of the chamber volume and of the overall ionisation occurred inside the chamber during the exposure time. The residual voltage is measured at the end of the exposure and the voltage drop converted, with the appropriate algorithm, into radon (average) concentration. Depending on the choice of electrets and chambers, measurements can last from a few days to several months.

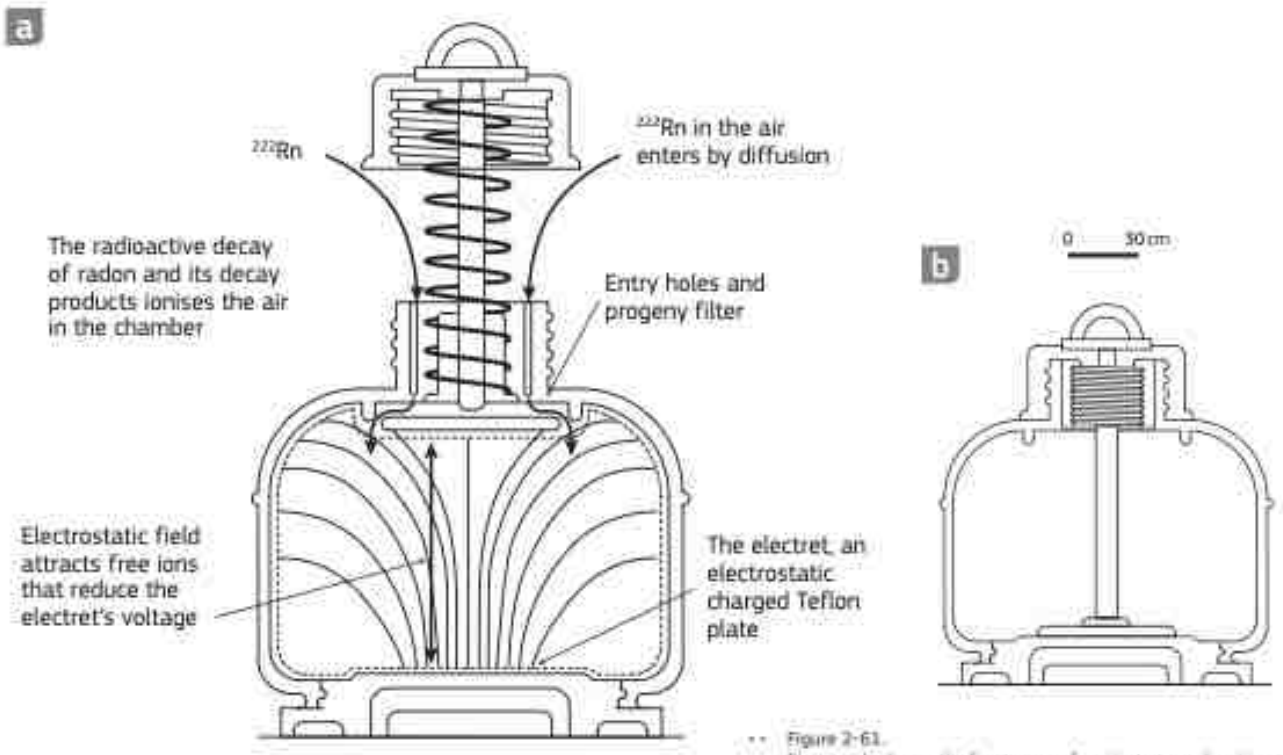

Figure 2-61.
Diagram displaying the functioning of an electret ion chamber: open (a) and closed (b)
Source: modified from Nulliec & Pern, 2008

Charcoal canister used to measure indoor radon concentration
Source: Peter Bossew

CR-39 track etch passive radon detector
Source: EAN, JCGC, 2019

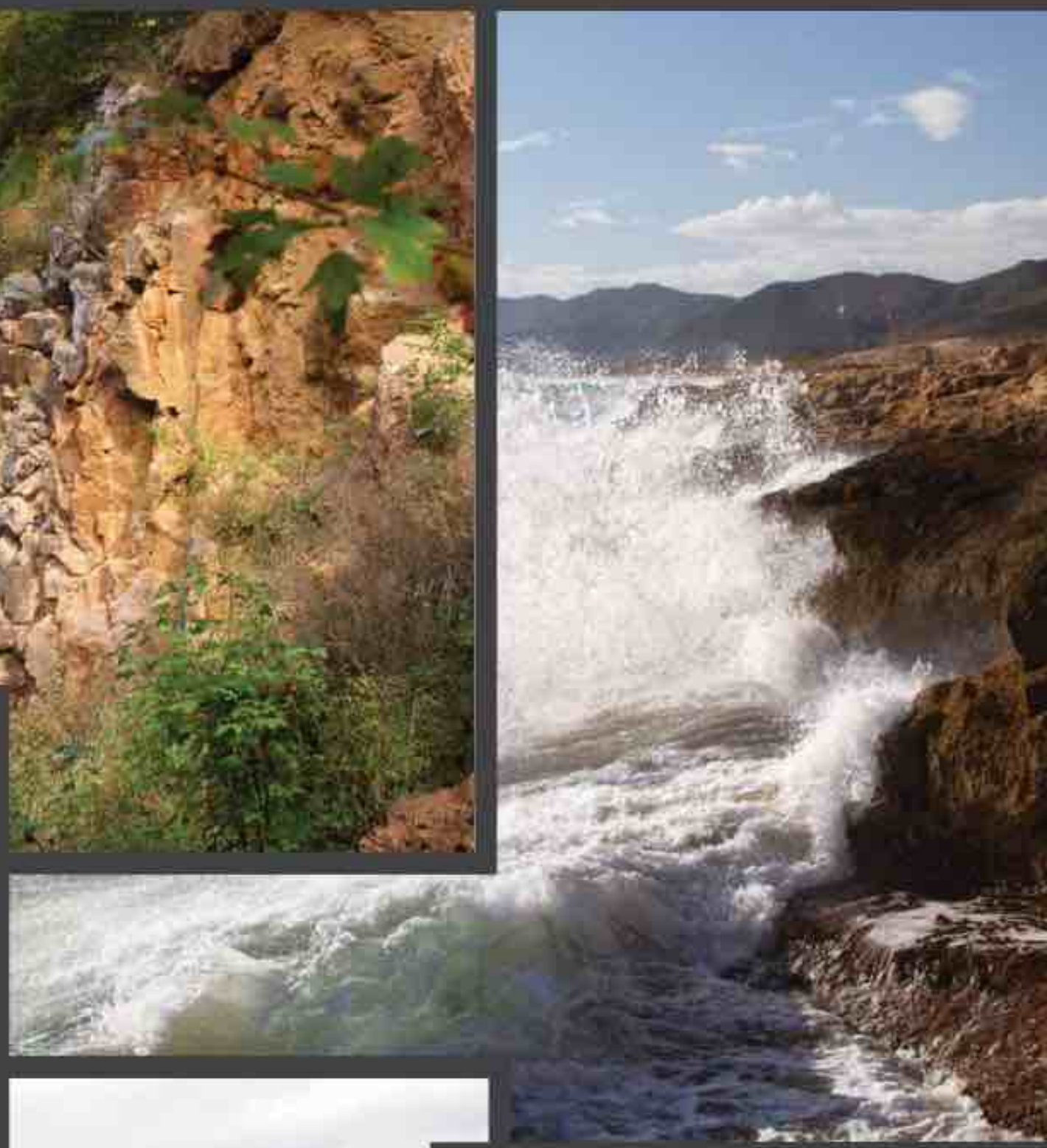

Chapter 3
Terrestrial radionuclides

Radioactive decay of radionuclides found in the Earth accounts for more than 50% of the total dose received by the population.

This chapter describes the characteristics, materials and methods used to produce European maps of uranium (U), thorium (Th) and potassium (K) concentration in, respectively, soil and bedrock. The maps of U, Th and K concentration in soil are based on data from two geochemical projects carried out at the European level: FOREGS (topsoil data) and GEMAS. After tests for the possibility to harmonise the databases, it was realised that the best solution was to merge the two databases without any correction-harmonisation. Areas characterised by the highest values for all the elements considered are found in Central Italy, Northwest Spain, East Sweden, South Finland and Central France.

At present, mapping U, Th and K_2O concentration in bedrock is extremely difficult due to the scarcity of data available, whereas maps of U, Th and K_2O concentrations in soil have been completed. For mapping U, Th and K_2O concentration in bedrock for this Atlas, a simple methodology has been developed on a country-by-country basis. The methodology consists in mapping the arithmetic mean of U, Th and K_2O over geological units. The arithmetic means of the radionuclides concentration are estimated from geochemical and radiological data compiled from scientific literature. Maps of U, Th and K_2O concentration in bedrock are displayed for Italy, Spain and Portugal as examples.

Clockwise from top-left:

Limestone formation, Karlstein region, Czech Republic
Source: Tore Tollefsen

Waves crashing against cliffs, Cabliarque Regional Park, Spain, one of the few undeveloped shorelines along the Mediterranean Sea.
Source: Tore Tollefsen

The Giant's Causeway, County Antrim, Northern Ireland, is an area of about 40 000 interlocking basalt columns, the result of an ancient volcanic fissure eruption.
Source: Peter Bossew

Danube, Vienna forest, Austria marks the northern end of the Alps
Source: Peter Bossew

Pebbles, Danube river, Austria. The Danube flows through many different geological zones, reflected by the diversity of the pebbles found along the river.
Source: Peter Bossew

Terrestrial radionuclides

In the context of natural radioactivity, one of the main contributors to the total dose received by the population corresponds to the terrestrial one caused by the radioactive decay of radionuclides present in the Earth; this accounts for more than 50% of the total dose received by the population (UNSCEAR, 2010). This contribution is mainly due to the radioactive families of thorium (Th) and uranium (U) and to the radioactive isotope of potassium (K).

Since its birth in the 1930s, geochemical mapping has been almost entirely dedicated to mining exploration (Garrett et al., 2008): the objects of sampling campaigns have been soil, water or stream sediments rather than bedrock, because of the difficulty of retrieving representative data from the latter. Through the analysis of soil, water and stream sediments, it was possible to estimate the contents of bedrock from which the soil or sediment derived (Webb et al., 1964). This implied that bedrock sampling and characterisation only rarely became the aim of the study. Large-scale surveys of bedrock geochemistry have therefore been scarce.

At present, mapping U, Th and K_2O concentrations in bedrock is extremely difficult due to the scarcity of data available, whereas maps of U, Th and K_2O concentrations in soil have been completed. Because this lack of data hinders the development of geochemical maps, only a few European countries, e.g. Austria (Berka et al., 2014) and France (Ielsch et al., 2017), have created and published maps of U, Th and/or K_2O concentration in bedrock on their own. However, different methodologies have been used to develop these maps thanks to the growing demand for estimating environmental risks.

3.1 Uranium

Uranium (U) is a heavy actinide series element (with atomic number 92) with two main natural, primordial long-lived radionuclides, including the more abundant ^{238}U (half-life of 4.5×10^9 years, 99.3% of U total mass) and the less abundant ^{235}U (half-life of 7.0×10^8 years, 0.72% of U total mass). Both decay separately through long and complex radioactive decay series ending respectively with a stable isotope of lead, ^{206}Pb and ^{207}Pb. Another natural uranium isotope ^{234}U (half-life 2.4×10^5 years, 0.0056% of total natural uranium), is the third decay product in the ^{238}U radioactive decay series. This uranium isotope is generally considered in equilibrium (to slightly deficient) with its progenitor ^{238}U. The $^{238}U/^{235}U$ ratio has increased over time due to faster radioactive decay of ^{235}U, now being 137.5 ± 0.5 (Wedepohl, 1978a).

3.1.1 Uranium in rock-forming minerals

In igneous and metamorphic rocks, uranium is mainly present as a trace element (concentrations <0.1 g/100 g) in major minerals such as biotite, hornblende, muscovite, K-feldspar, calcite and quartz. In these rocks, the uranium budget is controlled by accessory minerals such as zircon, apatite, allanite, monazite and xenotime. It is the main component in some minerals, such as uraninite UO_2, brannerite $(U,Ca,Ce)(Ti,Fe)_2O_6$ and carnotite $K_2(UO_2)_2(VO_4)_2$ and is often present in complexes with organic matter and phosphatic ironstone. As uranium is sensitive to magmatic differentiation behaving incompatibly, it concentrates in the late stages of crystallisation, becoming enriched in felsic silicic igneous rocks and showing the lowest concentration in the silica-poor igneous rock types.

Uranium concentration in acid igneous rocks, such as granites, granodiorites, rhyolites and trachytes, is generally above 2 mg/kg, with some uraniferous granites reaching 50 mg/kg; intermediate rocks (e.g. diorites, andesites, syenites and phonolites) generally show uranium concentrations between 1 and 6 mg/kg, while basic igneous rocks (e.g. gabbros, basalts) show U concentrations generally lower than 1 mg/kg (Alloway, 2013) and ultrabasic rocks (e.g. peridotites, komatiites) most often show concentrations below 0.1 mg/kg (Wedepohl, 1978).

Uranium concentration in sedimentary rocks is highly variable. Two of the major factors that influence the uranium content are: (i) the detrital source mineralogy, and (ii) the redox chemistry of uranium, which is strongly influenced by the geochemical processes operating during weathering of source rock and sediment transport, within the depositional environment, and during subsequent burial diagenesis. Uranium is redox-sensitive, and although it can exist in oxidation states from +2 to +6, only the tetravalent (+4) and the hexavalent (+6) forms are significant in nature. Consequently, uranium concentrations can be significantly higher in sedimentary rocks than in the parent igneous rocks (Cumberland et al., 2016). Sandstones typically contain between 0.5 to 4 mg/kg U; shales and mudrocks typically between 1 to 5 mg/kg U; limestones are generally low in uranium – about 2 mg/kg (Wedepohl, 1978a), although some more uraniferous limestones have been reported (e.g. Basham & Kemp, 1993; Milodowski et al., 1989); and pure evaporites are typically very low in uranium, <0.1 mg/kg U (Wedepohl, 1978a). In general, much of the uranium in siliciclastic sedimentary rocks (sandstones, shales, mudrocks) is contained within resistate (i.e. resistant to weathering) detrital heavy minerals (e.g. zircon, xenotime, apatite, sphene, monazite), which occur as trace components, or as inclusions preserved in major detrital minerals such as quartz, feldspars and micas (e.g. Wedepohl, 1978a; Milodowski & Hurst, 1989; Hurst & Milodowski, 1976). In carbonate rocks, the uranium trace concentration is considered to substitute calcium in the lattice. Organic-rich and phosphatic sediments and sedimentary rocks often host significantly higher concentrations of uranium. Phosphorites are often enriched in uranium, with up to 700 mg/kg reported in some formations (cf. Wedepohl, 1978a; Bowell et al., 2011; Cumberland et al., 2016). Black shales and organic sediments (coals, lignites, peats) display a large variation in uranium content (1 to 6000 mg/kg) with very high concentrations of uranium reported from some formations (e.g. Wedepohl, 1978a; Bowell et al., 2011; Cumberland et al., 2016).

Pink granite with a rounded inclusion made of black tourmaline and grey quartz. This granite is used as a decorative slab on buildings. Field of view: 60 cm across.
Source: Roberto Braga

In summary, considering the geochemical peculiarities of uranium, high concentrations of this element are expected in the following types of bedrock:

a. Highly differentiated volcanic and plutonic felsic rocks;
b. Metamorphic and/or sedimentary rocks derived from a);
c. Ore deposits of uranium related to placers, veins or other tectonic/hydrothermal structures;
d. Organic matter-rich sedimentary rocks.

In Europe, there are several areas that are known for their above-average uranium content (De Vivo et al., 1984), namely:

- The Variscan massifs, especially the Iberian Meseta (Spain), the Massif Central (France), the Bohemian Massif (Czech Republic) and the Lysa Gora zone (Poland);
- Some regions of the Alpine orogeny located in the eastern Alps and in the Dinarides-Balkan area;
- Sporadic uranium enrichments are observed within Tertiary and Plio-Quaternary volcanic activity, as in the Tyrrhenian region (Italy) and in North Macedonia.

On the contrary, low concentrations of uranium are expected in the following bedrock exposures:

a. Mafic and ultramafic igneous rocks;
b. Carbonate rocks;
c. Metamorphic and/or sedimentary rocks derived from a);
d. Metamorphic rocks derived from b).

Fumaroles, Vulcano Island, Italy.
Source: Sara Tolomeo

Strongly deformed augen gneiss derived from the metamorphism of a former granitoid.
Source: Roberto Braga

3.1.2 Uranium in the soil – plant system

Soil is a complex and evolving entity consisting of a mixture of minerals, organic matter, living organisms, water and air, with depth extension and composition varying from place to place. The mineral component is frequently composed of weathered rock, mineral fragments, different clay minerals, Fe, Mn and Al oxi-hydroxides, secondary carbonates and sulphates, all derived from the parent materials under weathering, in most cases the bedrock. Organic matter originates from living organisms, namely plants and soil biota decay. Water and air are mainly obtained from the atmosphere, but also from chemical, physical and microbial reactions permanently taking place. Soil also contains pollutants derived from anthropogenic activities such as urbanisation, energy generation, transportation, waste disposal, agriculture, mining and industry (FitzPatrick, 1986; White, 2006; Kabata-Pendias, 2011).

The parent material (most often the bedrock) is the main reservoir of the natural uranium radionuclides (^{238}U and ^{235}U) and their decay products, which are released into the soil through weathering processes (Cicchella et al., 2014). The mobility of uranium during weathering processes highly depends on the host minerals (Kabata-Pendias, 2011). Uranium contained in the resistate mineral fraction, such as monazite and zircon, tends to be retained in the soil profile after bedrock weathering. On the contrary, uranium minerals may not resist to weathering and thus may be progressively removed by dissolution from the rock / soil profile, namely as uranyl (UO_2^{2+}). Still, the dissolved uranium may remain in the soil as it may form relatively stable hydrolysates, organic complexes, or may co-precipitate with (iron) oxides, carbonates, phosphates, vanadates and arsenates (Drever, 1988, 2002; Kabata-Pendias, 2011), depending on the prevailing redox potential (Eh) and pH conditions. The affinity of uranium to be absorbed by organic matter and bioconcentrated by microorganisms may explain how it often accumulates in significant amounts in coal and peat (Kabata-Pendias, 2011).

Uranium has no known biological function, but plants may rarely take it from the soil in very small amounts that preferably accumulate in their roots (Chen et al., 2005; Roivainen et al., 2011). Uptake amounts for uranium are generally much higher than those for thorium and lower than those for radium (Chen et al., 2005). Notably, the ^{226}Ra isotope has a half-life sufficiently long to allow some separation from its parent ^{238}U, since radium shows an Eh-pH chemical behaviour in the surface environment different from that of uranium. This may yield environmental radium concentrations which do not coincide with those observed for uranium, for example in soils formed over some limestones and argillaceous limestones (Kabata-Pendias, 2011). The chemical behaviour of radium is sufficiently similar to that of barium, strontium and calcium to allow it to replace calcium in carbonate minerals, make a solid solution with barium in radiobarite ($(Ba, Ra)SO_4$), or easily be taken up by plants (Kabata-Pendias, 2011) since calcium is an essential element for life and one of the most soluble and important cations in soil solutions (Kabata-Pendias, 2011).

3.1.3 Natural exposure to uranium by biota

The natural ionising radiation in the environment caused by uranium varies from place to place, mainly according to geology, that is, depending on uranium concentration in rocks and soils (UNSCEAR, 2000).

Uranium is a chemotoxic and radiotoxic carcinogen, although its harmfulness is mainly considered to be its radioactive character and that of its decay products, rather than to its chemistry. Isotopes of ^{238}U and ^{235}U are the progenitors of complex radioactive decay series emitting alpha, beta and gamma radiation until a stable isotope of lead is produced (more details in Section 2.2). Three types of ionising radiation to which humans and other life forms are exposed derive from uranium: they are external, essentially from uranium and its decay products present in rocks and soils; internal from ingestion of food and drinking water (with trace amounts of uranium and/or radium); and inhalation of dust particles containing ^{238}U decay products (namely radon and its decay products). In case of ingestion, uranium and radium isotopes tend to concentrate in the skeleton (UNSCEAR, 2000), replacing calcium in bones and teeth, as it has chemical behaviour similar to that of calcium. Inhalation is mainly due to ^{222}Rn, as this ^{238}U decay product has the unique property of being a radioactive gas. This increases the risk of internal exposure to ionising radiation mainly from alpha particles of ^{222}Rn decay products, since its half-life of 3.8 days is long enough to allow it to travel from its production site to the immediate environment of human beings, namely indoors (UNSCEAR, 2000). It is estimated that ^{222}Rn is responsible for about 43 % of the total ionising radiation to which, on average, the world population is exposed.

Exposure to uranium by ingestion and/or inhalation is enhanced by several anthropogenic activities, including those related to uranium mining and processing, nuclear energy production; production and use of phosphate fertilisers (these often contain much higher concentrations of uranium than does soil); and coal burning (its resulting fly ash may show high uranium concentrations) (UNSCEAR, 2000; Cicchella et al., 2014).

Environmental radiation from ^{238}U can be measured using gamma-ray spectrometry related to its progeny or estimated from the concentration of uranium in soil and rocks.

FOREGS

A project aiming at producing a first 'Geochemical Atlas of Europe' covering most of Europe, was carried out by 26 countries under the auspices of the Forum of European Geological Surveys (FOREGS, now EuroGeoSurveys). One of the main drivers was the need for environmental geochemical baselines to assist decision-making, and to monitor future changes in the near-surface environment of the European continent (De Vos et al., 2006; http://weppi.gtk.fi/publ/foregsatlas/articles/Abstract2.pdf). With a target sampling density of ca. 1 site / 5 000 km² (5 samples on each 160 km × 160 km square), samples from more than 800 drainage basins across 26 countries were collected between 1997 and 2001, using the standardised methods established by Darnley et al. (1995) and Salminen et al. (1998). Samples of topsoil, subsoil, stream water, stream sediment, floodplain sediment and humus were collected, whenever available, from each drainage basin. Chemical analysis of the samples was completed in 2004, and data subsequently collated and examined for error by the Geological Survey of Finland. A two-volume 'Geochemical Atlas of Europe' has been published: 'Part 1: Background Information, Methodology and Maps' (Salminen et al., 2005) and 'Part 2: Interpretation of Geochemical Maps, Additional Tables, Figures, Maps and Related Publications' (De Vos et al., 2006). Both volumes are available online from http://www.gtk.fi/publ/foregsatlas/. The FOREGS/EuroGeoSurveys 'Geochemical Atlas of Europe' was officially launched to European Commission officers and other interested parties at the DG Environment headquarters in Brussels on 21 September 2006.

Sampling and analysis

As mentioned above, two soil samples (each made of 3 to 5 grabs) have been collected at each FOREGS sampling site: a topsoil sample corresponding to the top 0 – 25 cm of the soil (excluding organic layer) and, when feasible, a subsoil sample corresponding to a 25 cm thick section collected from 50 to 200 cm deep in the soil profile (Salminen et al., 2005; Sampling, http://weppi.gtk.fi/publ/foregsatlas/article.php?id=10). Sampling sites were located in forested and unused lands, greenland, pastures and non-cultivated parts of agricultural land.

Soil samples were dried at 40°C, disintegrated and homogenised and passed through a 2 mm sieve. A portion was pulverised to a grain size <0.063 mm, homogenised and submitted to the analytical laboratories for analysis. (Sandstrom et al., 2005, Sample Preparation and Analysis, http://weppi.gtk.fi/publ/foregsatlas/article.php?id=3).

Total concentrations for a range of rare Earth and other trace elements, including thorium and uranium, were determined on soil samples using a Perkin-Elmer Sciex Elan 5000 inductively coupled plasma mass spectrometer (ICP-MS). Samples were digested with a nitric / hydrofluoric / perchloric acid attack: the residue was further dissolved in nitric acid and 30 % hydrogen peroxide and fused with a mix of lithium metaborate and sodium perborate followed by dissolution in nitric acid. The digested solutions were finally combined and analysed. The quality of sampling and analysis was controlled and assessed by using internationally recommended procedures. At concentrations with an order of magnitude above the limit of quantification (0.1 for both thorium and uranium), the uncertainty of the method is better than 10 % (Sandstrom et al., 2005, Sample Preparation and Analysis, http://weppi.gtk.fi/publ/foregsatlas/article.php?id=3).

GEMAS

A project named Geochemical Mapping of Agricultural and Grazing Land Soil in Europe – GEMAS, involving 33 European countries, was carried out as a cooperation between the Geochemistry Expert Group of EuroGeoSurveys and the Eurometaux (the European Association of Metals). GEMAS aimed at characterising soil in two types of land use, namely, agricultural soil (arable land, Ap) and grazing soil (grassland, Gr) to meet requirements under Registration, Evaluation, Authorisation and Restriction of Chemicals (REACH) Regulations (Verougstraete & Schoeters, REACH and GEMAS, Chapter 2 in Reimann et al., 2014a, Part A). These two types of soil represent the majority of land used for agricultural food production in Europe (Reimann, Chapter 3 in Reimann et al., 2014a). With a target sampling density of ca. 1 site / 2 500 km² (1 sample on each 50 km × 50 km square), a total of 2 108 samples of agricultural soil and 2 023 samples of land under permanent grass cover were collected between 2008 and 2009, making use of standard methods established by the EU REACH regulation (European Union, 2006; ECHA, 2008). Many soil properties have been determined, including pH, effective cation exchange, total carbon and sulphur, total organic carbon, loss on ignition, grain size, mid-infra-red (MIR) spectra, concentrations of 55 elements after mobile metal ion extraction, concentrations of 53 chemical elements after aqua regia extraction, total concentrations of 41 elements by X-ray fluorescence, magnetic susceptibility and lead and strontium isotopes. The GEMAS project (http://gemas.geoloa.ac.at/) results, entitled 'Chemistry of Europe's agricultural soils', were released in 2014 as a set of two volumes and a DVD with all the analytical data, maps, diagrams and tables: 'Part A: Methodology and interpretation of the GEMAS data set', and 'Part B: General background information and further analysis of the GEMAS data set', both edited by Reimann, Birke, Demetriades, Filzmoser & O'Connor, and published by Schweizerbart Science Publishers in Hannover (https://www.schweizerbart.de/publications/detail/isbn/9783510968473/Geologisches_Jahrbuch_Reihe_B_Heft_B103_Chemistry).

Sampling and analysis

Two different types of soil have been collected across Europe with a sampling density of 1 sample per 50 km × 50 km: (i) a soil sample corresponding to the top 0 - 20 cm of agricultural soil (Ap), that is, arable land or regularly ploughed land; and (ii) a soil sample corresponding to the top 0 - 10 cm of grazing land (Gr), that is, under permanent grass cover (Reimann, Chapter 3 in Reimann et al., 2014a).

Soil samples were air-dried, disaggregated and sieved through a 2 mm mesh. Ten portions were prepared from each soil sample. One portion was pulverised to a grain size < 0.063 mm, homogenised and submitted to the laboratory (Mackovych & Lucivjansky, Chapter 4 in Reimann et al., 2014a).

Determination of total element concentrations, including U, were obtained by wavelength dispersive X-ray fluorescence spectrometry (WD-XRFS), hereafter referred to as XRF (Birke et al., 2014, Chapter 5 of GEMAS book, Part A). Data quality was optimised by randomisation of samples before being sent for analysis, and estimated by including project standards for accuracy assessment and project replicates for precision assessment. Uranium analysed by XRF is reported with a high detection limit (3 mg/kg) and low precision values above 25 % (Demetriades et al., Evaluation of GEMAS Project Quality Control Results, Chapter 6 in Reimann et al., 2014a). Samples reporting a value below the detection limit were assigned half of the detection limit, that is, 1.5 mg/kg.

The datasets described (FOREGS, GEMAS Gr, GEMAS Ap) can be considered representative of the main types of topsoil prevailing across Europe. Also, the analytical methods provide near 'total' concentrations, thus taking into account uranium in all types of minerals in the soil, including those more resistant to weathering, such as quartz, feldspar, micas, zircon, monazite, etc. This method gives a clear advantage over partial extraction methods (e.g. aqua regia digestion), particularly when intended to be used as a proxy for the overall radioactivity originating from uranium and its decay products in the natural environment.

3.1.4 European map of uranium concentration in topsoil

This Section aims to provide information on the variation in background concentrations of the naturally occurring radionuclide uranium (U) in topsoil across Europe.

The European map of uranium concentration in soil (as U in mg/kg) shown here is a proxy for the ionising radiation caused by ^{238}U and ^{235}U and their decay radioactive products found in the surface environment. Apart from its value for outlining natural radioactivity levels in Europe, the map can also be used as an input parameter for the European Geogenic Radon Map.

Materials and methods

The map of uranium concentration in soil for the purposes of the EANR is based on two European datasets (FOREGS and GEMAS) containing information about topsoil geochemistry at continental level.

Data overview

A total number of 4653 topsoil samples containing total concentrations of uranium (as U in mg/kg) was compiled in a new EANR dataset, in order to produce a new European map of uranium in topsoil. The values included in the EANR dataset collate 839 (by ICP-MS) from FOREGS, 1864 (by XRF) from GEMAS Gr and 1950 (by XRF) from GEMAS Ap (Figure 3-1).

Neolithic tombs of granite slabs, Central-Eastern Portugal
Source: Peter Bossow

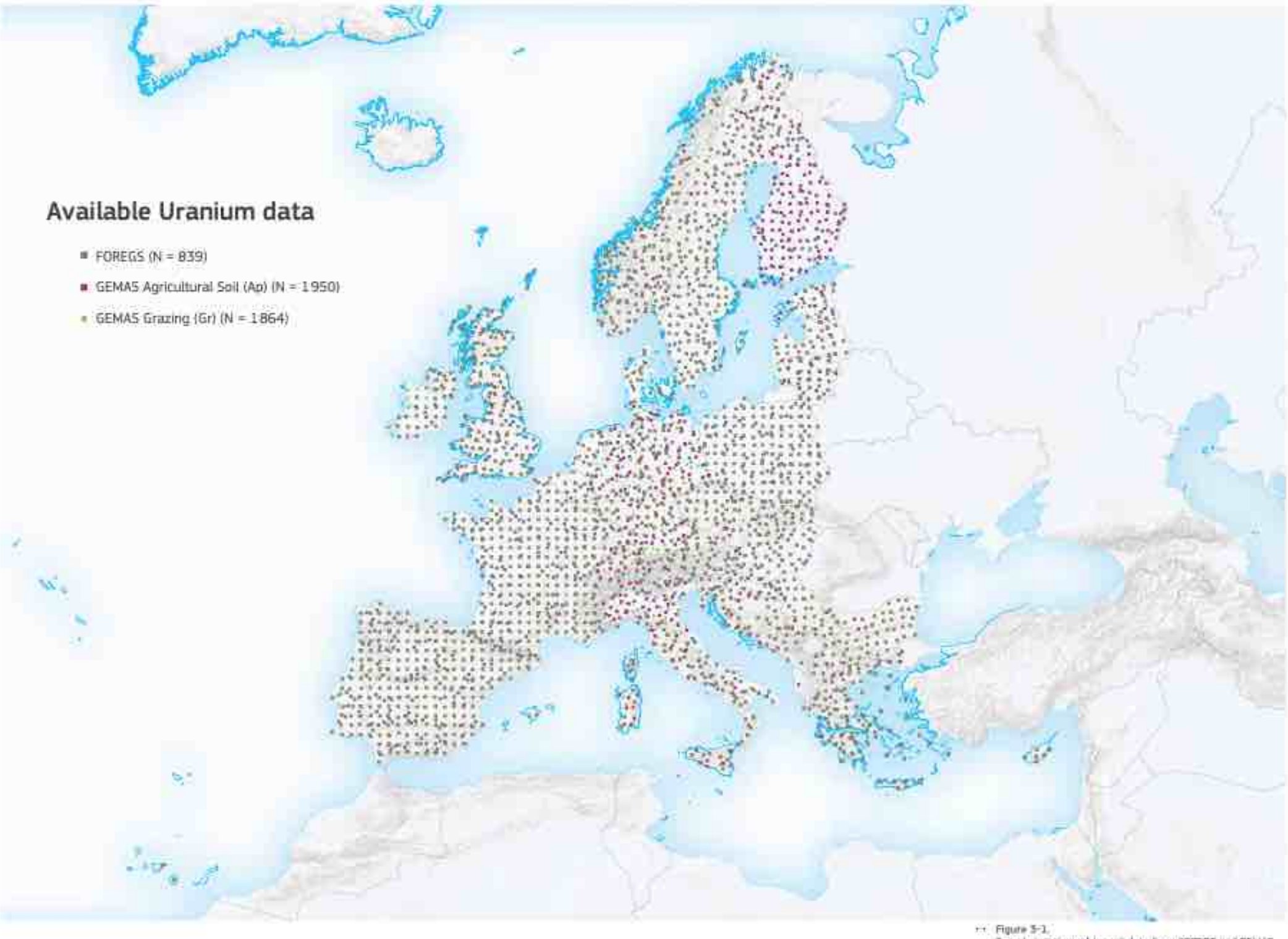

Figure 3-1.
Sample locations of topsoil data from FOREGS and GEMAS reporting total concentration of uranium.
Source: Map created by A. Ferreira, T.B. Lister, P.S. Lawley and A.M. Tye

A preliminary overview of the uranium EANR topsoil dataset and the three corresponding subsets (FOREGS, GEMAS Ap, GEMAS Gr) is given in Table 3-1 and in the graphs of Figure 3-2.

	EANR	FOREGS	GEMAS Gr	GEMAS Ap
N	4653	839	1864	1950
DL	-	0.1	3	3
%<DL	-	0	75.6	62.1
Minimum	0.21	0.21	<3.0	<3.0
P25	1.5	1.31	<3.0	<3.0
Median	1.5	2.03	<3.0	<3.0
P75	3	2.82	<3.0	3
P95	6	4.83	5	6
P99	9.42	7.93	10	9.5
Maximum	94	53.2	94	25
MAD	-	1.13	-	-
CVR (%)	-	56	-	-
Mean	2.44	2.35	2.3	2.6
SD	2.43	2.34	2.8	2
CV%	99	100	124	76
GM	2.04	1.94	1.9	2.2
GSD	1.71	1.83	1.61	1.72
powers	2.7	2.4	1.8	1.2
skewness	15.52	13.31	20.17	3.41
U median concentration at the **Upper Continental Crust: 2.7 mg/kg***				

N: number of samples; DL: detection limit; P##: percentiles; MAD: median absolute deviation; CVR%: robust coefficient of variation; SD: standard deviation; CV%: coefficient of variation; GM: geometric mean; GSD: geometric standard deviation. MAD is a robust equivalent of the standard deviation (SD) measuring the average deviation from a central value, the Median in this case. The CV% is defined as the SD divided by the Mean, while the CVR% is defined as the MAD divided by the Median, both shown in % relative to the central value used. Powers show the orders of magnitude of the variation, being defined as the decimal logarithm of the ratio between the maximum and the minimum (Reimann et al., 2008). Skewness is a measure of asymmetry of the distribution, indicating whether the tails on both sides of the Mean balance out or not.
*Rudnick & Gao (2003).

Table 3-1.
U (mg/kg) statistics for the topsoil EANR dataset and corresponding subsets.
Source: A. Ferreira, T. B. Lister, R. S. Lawley and A. M. Tye.

The graphs shown in Figure 3-2 are a histogram, a Tukey boxplot (Tukey, 1977) and a cumulative probability plot (Sinclair, 1976) for the EANR dataset and for each of the subsets used, FOREGS, GEMAS Gr and GEMAS Ap. In the histogram plot, the distribution of each of the three subsets is represented by a density line, while the histogram bars refer to the overall EANR collated dataset.

For GEMAS samples, the detection limit (DL) for uranium (3 mg/kg) is above the estimated value for the Upper Crust (2.7 mg/kg, Rudnick & Gao, 2003), thus, not surprisingly, the number of GEMAS values for uranium reported as below its detection limit is also very high (62.1% for Ap and 75.6% for Gr, Table 3-1). This problem has a clear effect on the EANR dataset, as can be seen from Figure 3-2, namely (i) the histogram plot (very visible peak at half the DL value, 1.5 mg/kg, and a smaller one at the detection limit, 3 mg/kg); and (ii) the cumulative probability plot (a strong vertical break at half the uranium DL, from about 5% to >60% of probability). Also, the GEMAS results for total uranium are provided as integers, which explains the stair-like appearance of the same cumulative probability plot curves (Figure 3-2) and revealing a lack of sensibility of the analytical method. FOREGS, on the contrary, shows a low detection limit (DL = 0.1 mg/kg), so that all samples are reported above it, and thus the resulting cumulative probability curve (blue dots in the right plot in Figure 3-2) is set over a continuous line with no vertical breaks.

For the purpose of the EANR map of uranium total concentration in topsoil samples, it was decided not to take into account uranium data collated from GEMAS for which a value below the detection limit is reported. This implies that the EANR map of uranium in topsoil relies on the FOREGS subset for the delineation of the European areas where low values of uranium predominate, while areas dominated by high values are delineated from both the FOREGS and GEMAS (Ap and Gr) projects.

After removing GEMAS samples with uranium below the DL, the total number of valid EANR samples is 2034, with 839 (by ICP-MS) from FOREGS, 455 (by XRF) from GEMAS Gr and 740 (by XRF) from GEMAS Ap (Figure 3-3).

An overview of the uranium EANR topsoil dataset (and corresponding subsets), after removing samples reported as below the detection limit, is given in Table 3-2 and in the graphs of Figure 3-4.

As expected, removing GEMAS data points below the DL causes a general overestimation of the uranium statistics of the EANR dataset (compare the EANR column of Table 3-1 with that of Table 3-2), as areas of mean to low values are now under-sampled (relying on FOREGS only) relative to areas where high values dominate (relying on both FOREGS and GEMAS). This should not cause major problems in the uranium map production, on the contrary. By not using the data points below detection limit, the map benefits from the high-quality natural variability at the low values provided by the FOREGS subset, which otherwise would be hidden in a generalised flattening surface (map not shown).

From the above rationale, the best estimate for the statistics of uranium at European level is, most possibly, the one provided by the FOREGS subset (see Table 3-1 and Table 3-2).

Apart from removing samples below detection limit, no further corrections have been applied to the EANR topsoil uranium data.

	EANR	FOREGS	GEMAS Gr	GEMAS Ap
N	2034	839	455	740
Minimum	0.21	0.21	3	3
P25	2.37	1.31	3	3
Median	3	2.03	4	4
P75	4	2.82	5	5
P95	8	4.83	9	8
P99	12.4	7.93	14	14
Maximum	94	53.2	94	25
MAD	1.48	1.13	1.5	1.5
CVR (%)	49	56	37	37
Mean	3.66	2.35	4.7	4.5
SD	3.29	2.34	5	2.2
CV%	90	100	107	50
GM	3.03	1.94	4.1	4.2
GSD	1.85	1.83	1.52	1.44
powers	2.7	2.4	1.5	0.9
skewness	13.07	13.31	13.32	3.61
U median concentration at the **Upper Continental Crust: 2.7 mg/kg***				

N: number of samples; P##: percentiles; MAD: median absolute deviation; CVR%: robust coefficient of variation; SD: standard deviation; CV%: coefficient of variation; GM: geometric mean; GSD: geometric standard deviation.
*Rudnick & Gao (2003).
See explanations of the other statistical parameters below Table 3-1.

Table 3-2.
U (mg/kg) statistics for the topsoil EANR dataset and corresponding subsets showing total concentration of uranium above the corresponding detection limit.
Source: A. Ferreira, T. B. Lister, R. S. Lawley and A. M. Tye.

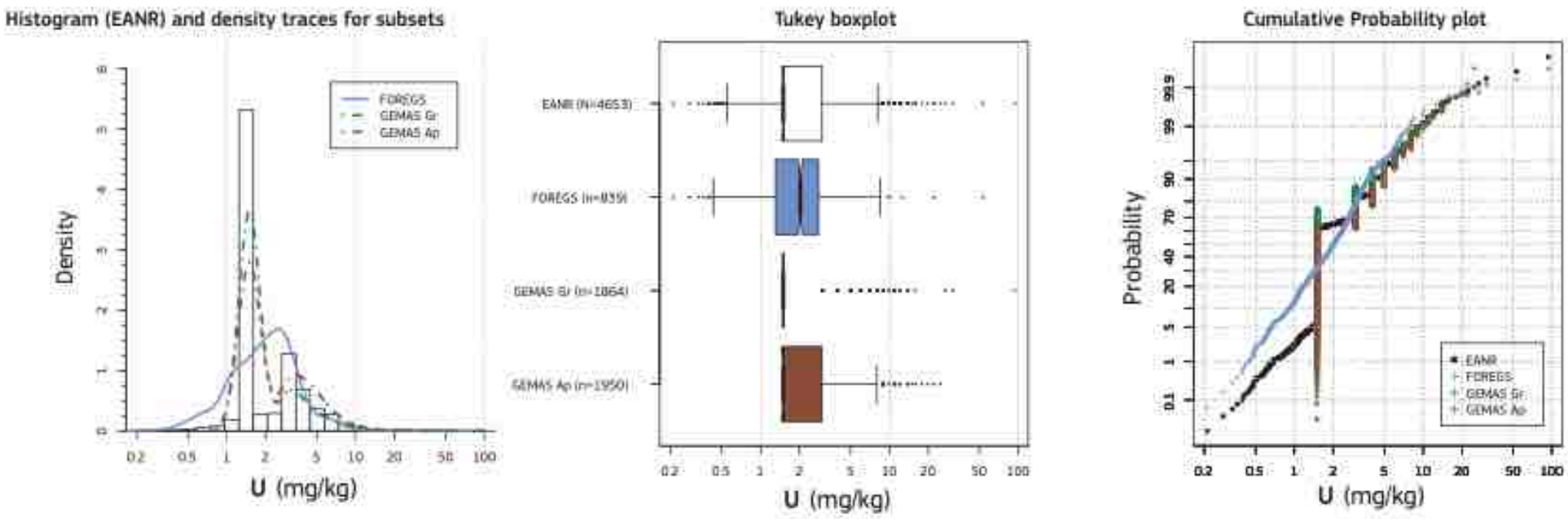

Figure 3-2.
Graphical representations of U (mg/kg) in the EANR dataset and the corresponding subsets.
Source: Graph created by A. Ferreira, T. B. Lister, R. S. Lawley and A. M. Tye.

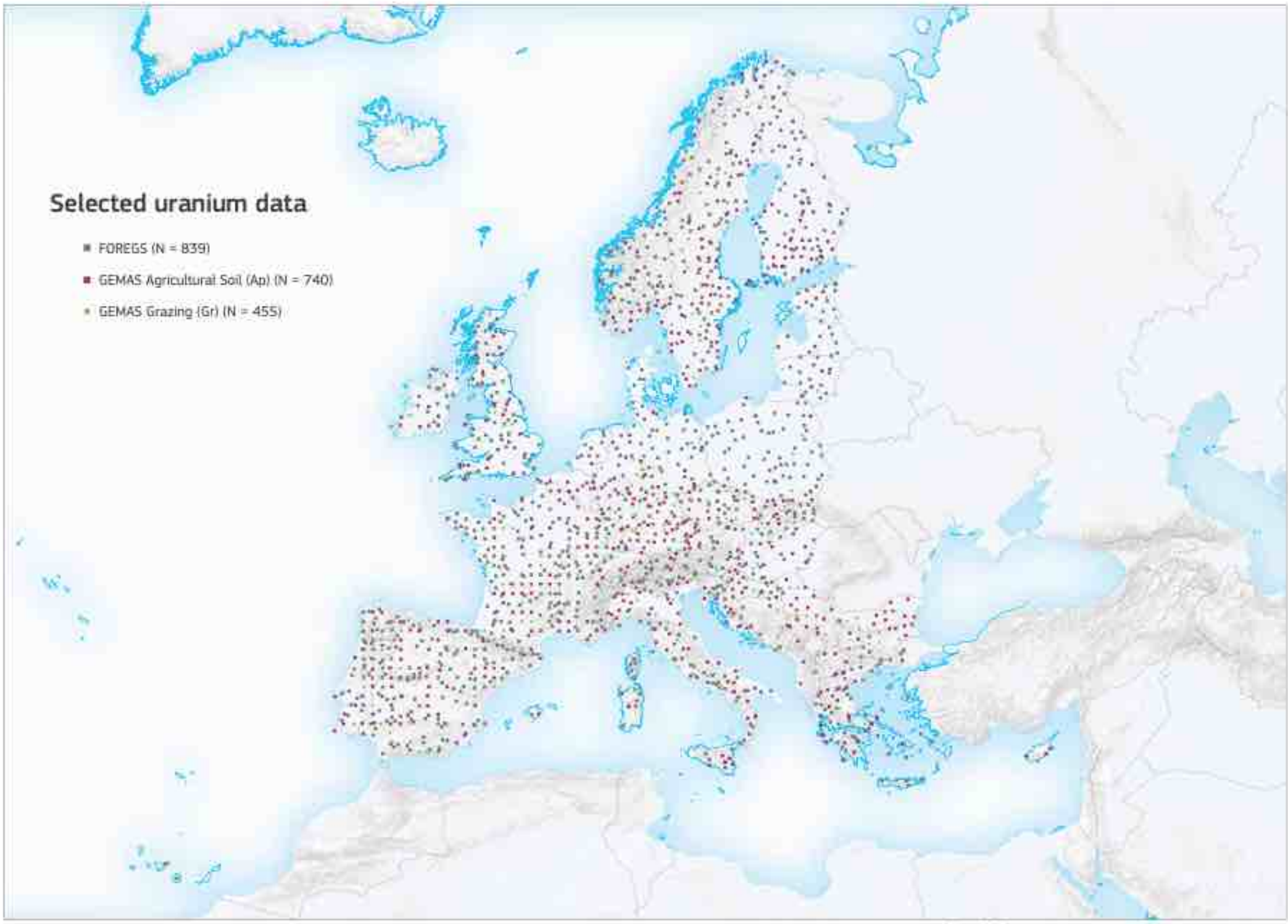

Figure 3-3.
Sample locations of topsoil data from FOREGS and GEMAS having total concentration of uranium above the corresponding detection limits
Source: Graph created by A. Ferreira, T. B. Lister, R. S. Lawrey and A. M. Fye

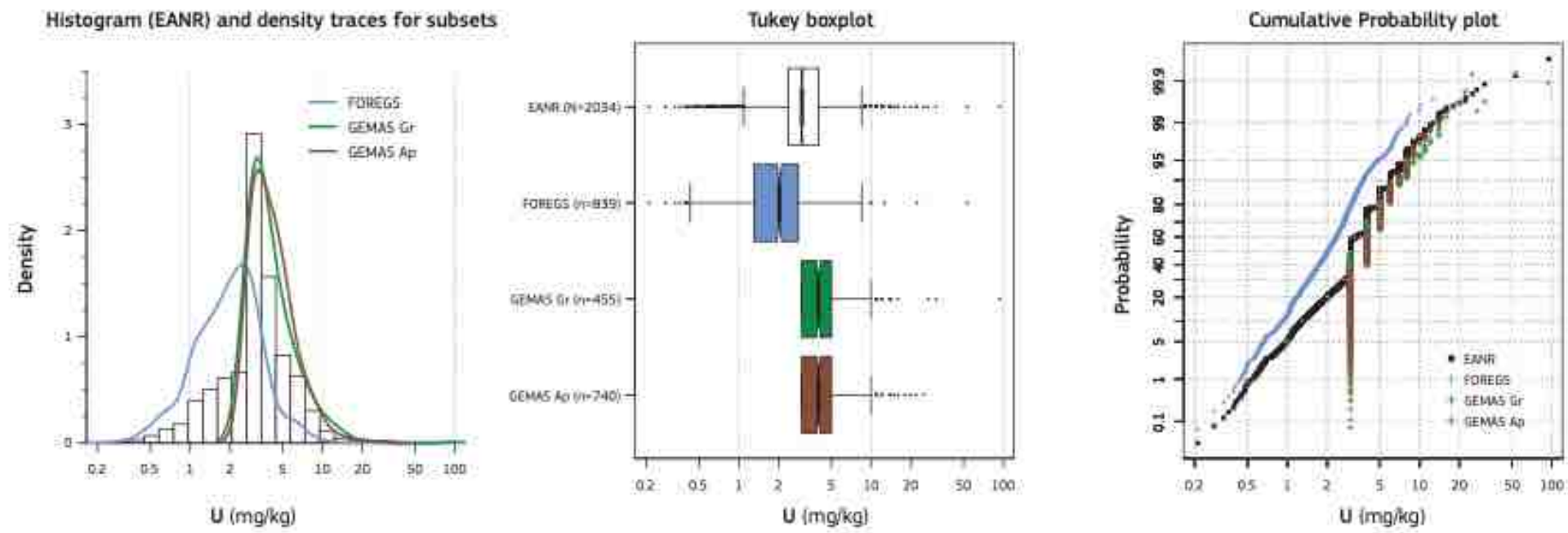

Figure 3-4.
Graphical representations of U (mg/kg) in the EANR dataset and the corresponding subsets showing total concentrations of uranium above the corresponding detection limits
Source: Graph created by A. Ferreira, T. B. Lister, R. S. Lawrey and A. M. Fye

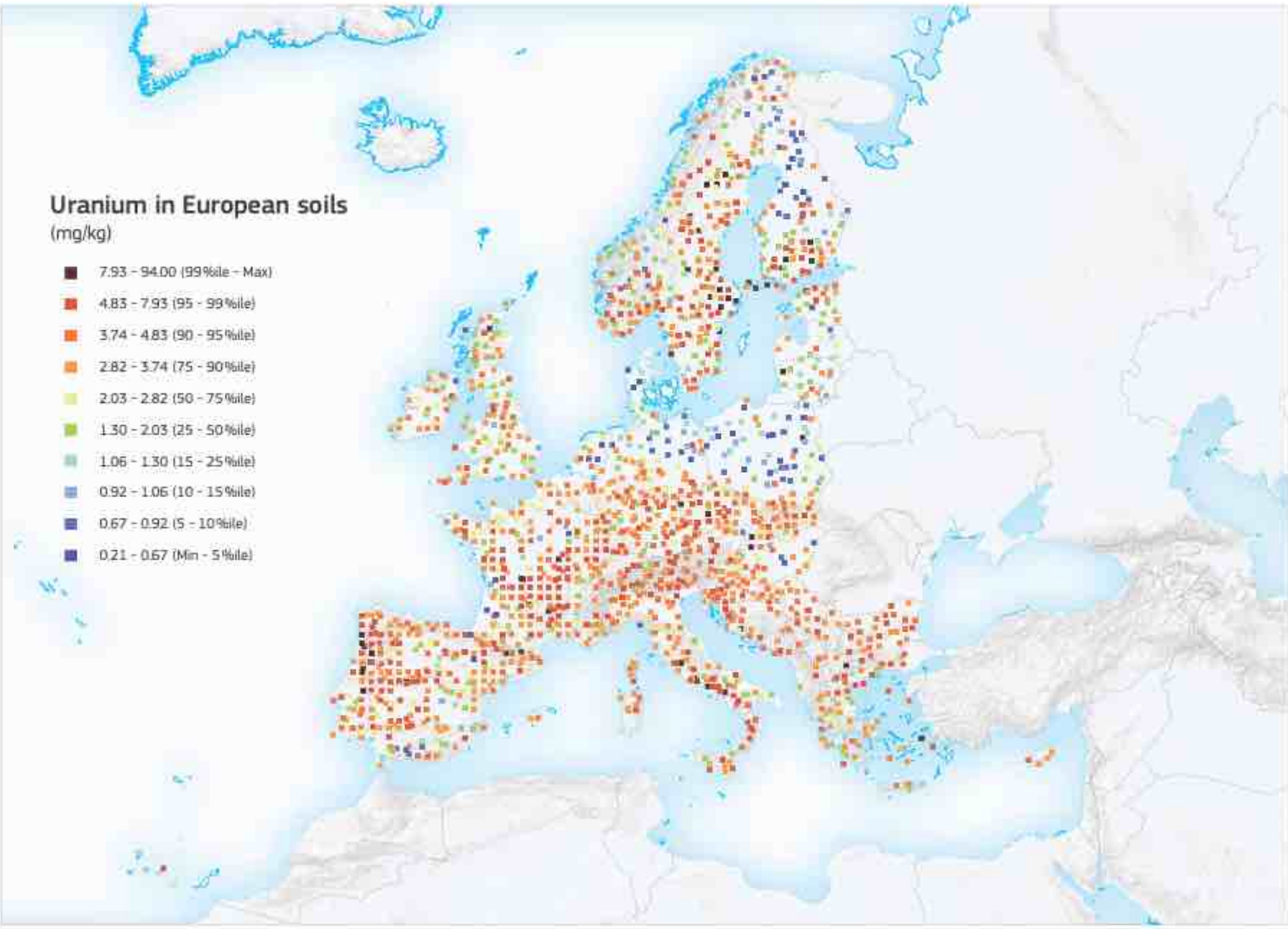

Figure 3-5
EANR total concentration of uranium in topsoil samples over Europe (N = 2 034), after removing values below the detection limit.
Source: Graph created by A. Ferreira, T. R. Lister, R. S. Lawley and A. M. Tye.

Map

The EANR map of total concentration of uranium in topsoil was produced using the 2 034 samples discussed and shown in Figure 3-3, Figure 3-4 and Table 3-2.

The total concentration of uranium in the EANR samples is shown in Figure 3-5, with colours attributed according to the percentiles of the FOREGS subset.

The data shown in Figure 3-5 were interpolated, using ordinary kriging, in order to obtain the required 10 km × 10 km regular grid image of the distribution of estimated uranium total concentrations in topsoil over Europe. The data were processed and maps were produced in R software environment, using several appropriate packages, such as 'sp' and 'gstat', and according to the following steps:

i. a variogram model for the log-transformed uranium data was produced (Figure 3-6);
ii. a value at each node of the 10 km × 10 km grid was computed after ordinary kriging, conditioned by the variogram model referred to in (i) and using a maximum of 13 neighbouring points in a maximum distance of 150 km radius;
iii. the values obtained in (ii) were back-transformed from logarithmic to regular total concentrations of uranium;
iv. and the data were plotted in a colour map with class boundaries based on the percentiles of the EANR dataset.

The resulting map of estimated total concentration of uranium in topsoil over Europe is shown in Plate 1.

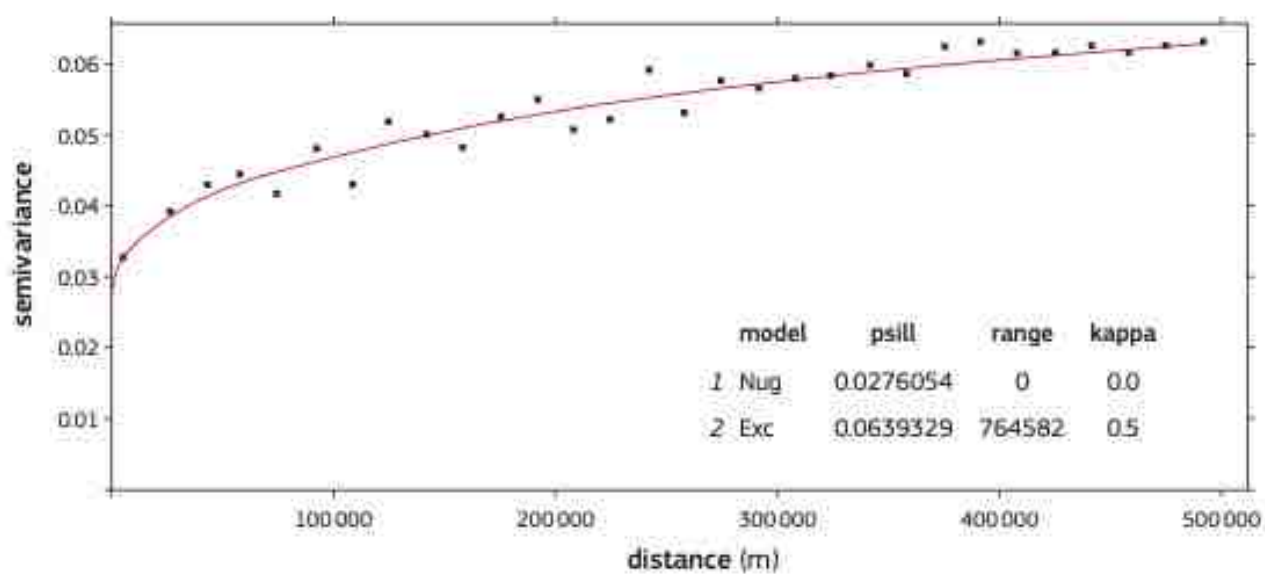

Figure 3-6
Variogram model for $\log_{10}$(U) in topsoil data collated from FOREGS (ICP-MS) and GEMAS (XRF) European datasets.
Nug: nugget; Exc: Exponential class.
Source: Graph created by A. Ferreira, T. R. Lister, R. S. Lawley and A. M. Tye.

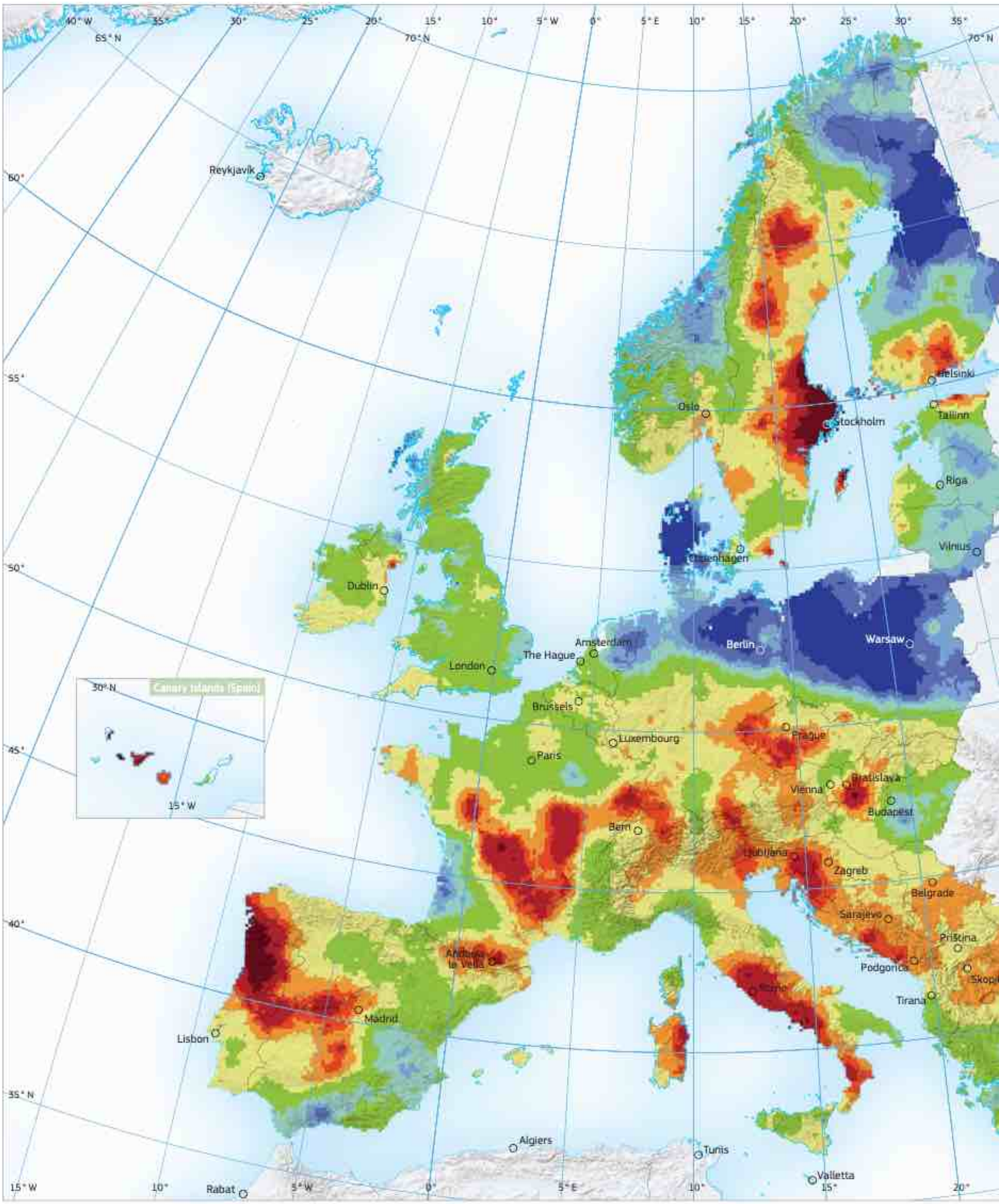
Reykjavik
Oslo
Stockholm
Helsinki
Tallinn
Riga
Vilnius
Copenhagen
Dublin
London
Amsterdam
The Hague
Berlin
Warsaw
Brussels
Luxembourg
Paris
Prague
Vienna
Bratislava
Budapest
Bern
Ljubljana
Zagreb
Belgrade
Sarajevo
Pristina
Podgorica
Skopje
Tirana
Rome
Madrid
Lisbon
Andorra la Vella
Algiers
Tunis
Valletta
Rabat
Canary islands (Spain)
70° N
65° N
60°
55°
50°
45°
40°
35° N
30° N
15° W
40° W
35°
30°
25°
20°
15°
10°
5° W
0°
5° E
10°
15°
20°
25°
30°
35°

copyright © European Commission, JRC, 2019

Plate 1:
Map of estimated total concentration of uranium in topsoil over Europe
(mg/kg)

- 6.27 - 94.00 (99%ile - Max)
- 4.58 - 6.27 (95 - 99%ile)
- 4.15 - 4.58 (90 - 95%ile)
- 3.56 - 4.15 (75 - 90%ile)
- 2.94 - 3.56 (50 - 75%ile)
- 2.10 - 2.94 (25 - 50%ile)
- 1.66 - 2.10 (15 - 25%ile)
- 1.43 - 1.66 (10 - 15%ile)
- 1.13 - 1.43 (5 - 10%ile)
- 0.21 - 1.13 (Min - 5%ile)

Plate 1: Map of estimated total concentration of uranium in topsoil over Europe, based on data collated from the FOREGS (ICP-MS) and GEMAS (XRF) European datasets as shown in Figure 3-3 and Figure 3-5. The colours are attributed according to the percentiles of the EANR-estimated map points.

Source: Map created by A. Ferreira, T. R. Lister, R. S. Lawley and A. M. Tye

Discussion and conclusions

Summary statistics for the FOREGS data, the EANR data and the resulting kriging-estimated map points are shown in Table 3-3.

The differences observed in percentiles between the FOREGS and EANR estimated map points (Table 3-3, Figure 3-7) have several causes. A first reason is the shift in the shape of the distribution towards high values caused by removing GEMAS values below its U detection limit (U = 3 mg/kg). Also, the areas covered by FOREGS and GEMAS do not perfectly match, with the latter covering more Balkanic countries, over which median-to-high values are observed, thus further increasing the referred shift. This shift can be roughly estimated from the differences observed in percentiles for the FOREGS and for the EANR data (Table 3-3 and Figure 3-4). A second reason is due to the data processing, as interpolation of data usually tends to overestimate low values and underestimate high ones; that is, it tends to smooth values towards the central ones. This bias can be roughly assessed from the differences observed in percentiles for the EANR data and for the EANR estimated map points (Table 3-3).

	Min	P5	P10	P25	Median	P75	P90	P95	Max
FOREGS	0.21	0.67	0.92	1.3	2.03	2.82	3.74	4.83	53.2
EANR data	0.21	0.99	1.28	2.37	3	4	6	8	94
EANR estimated	0.59	1.13	1.43	2.1	2.94	3.56	4.15	4.58	9.73

Table 3-3
U (mg/kg) percentiles for FOREGS (N = 839, as in Table 3-1 and Table 3-2) and for the EANR data (N = 20341 and the EANR estimated map points (N = 47095, map U)
Source: A. Ferreira, T. B. Lister, R. S. Lawley and A. M. Tye

Figure 3-7
Graphical representations of U concentration (mg/kg) in the EANR estimated map points and the subsets from which the map was produced.
Source: Graph created by A. Ferreira, T. B. Lister, R. S. Lawley and A. M. Tye

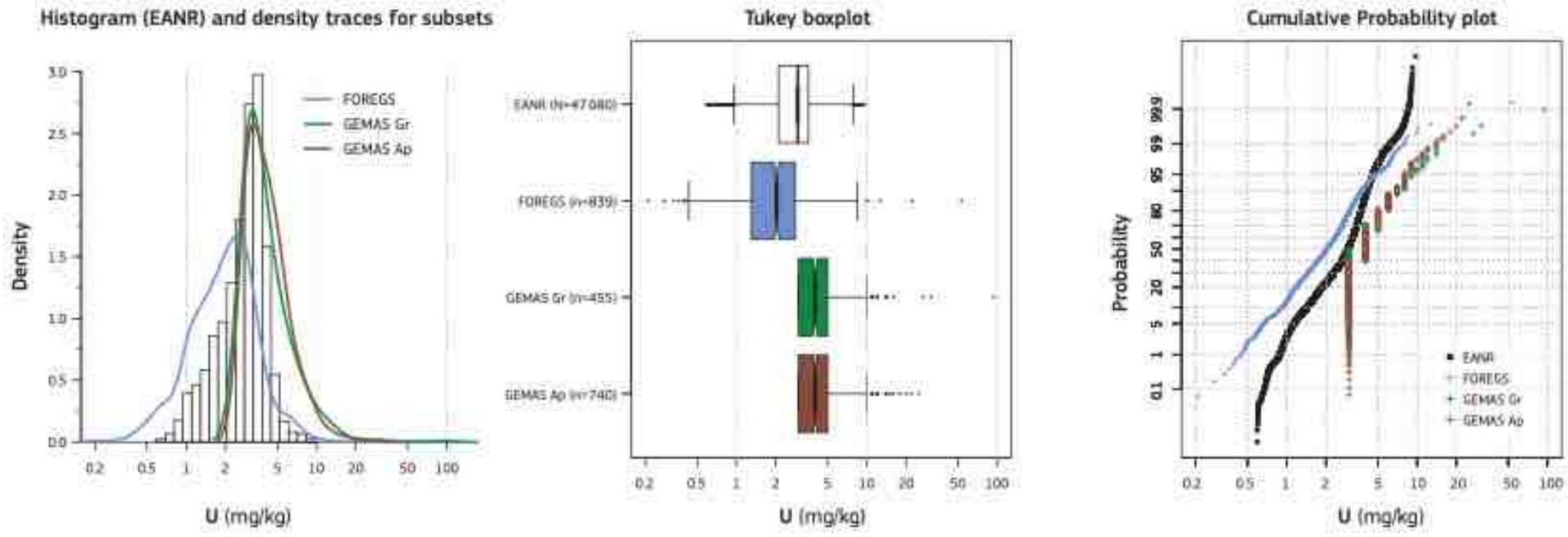

Uranium geochemical patterns

The FOREGS project already has provided a distribution map of uranium total concentration in Europe (http://weppi.gtk.fi/publ/foregsatlas/maps/Topsoil/t_icpms_u_edit.pdf), adding a short description of the geochemical patterns included in the element's factsheet (http://weppi.gtk.fi/publ/foregsatlas/text/U.pdf). Distribution patterns of uranium partial concentration (after aqua regia and MMI®) have been provided by the GEMAS project (Reimann et al., 2014) and discussed in Chapter 8 of Cicchella et al., 2014 et al. (2014), in Reimann et al. (2014) and in Negrel et al. (2018).

Uranium statistics for the EANR data are given in Table 3-2, Table 3-3 and Figure 3-4 and explained in the 'Data overview' section above. The uranium total concentration in the EANR dataset varies from 0.21 to 94 mg/kg, with a median of 3.0 mg/kg. As explained, this median value is most possibly an overestimation of the real median value over European topsoil, which is likely to be nearer to that reported for the FOREGS dataset (2.03 mg/kg). About 50 % of the mapped area shows uranium concentration values in the range of 2.10 – 3.56 mg/kg (areas in green and in yellow on the map) around a median value of 2.94 mg/kg; one quarter (25 %) of the map shows uranium concentration values below 2.10 mg/kg (areas in blue on map) and the remaining 25 % show uranium concentration values above 3.56 mg/kg (reddish areas on map).

The distribution pattern of total uranium across the EANR European countries is characterised by an extensive area of deep low values (often below 1.13 mg/kg), ranging from the Netherlands and Denmark to Eastern Poland, then extending north throughout the Eastern part of the Baltic countries up to Southern Estonia, where values are slightly higher (roughly above 1.66 mg/kg). This extensive area is characterised by a cover of unconsolidated glacial drift deposits over bedrock (Plant et al., 2003, quoted in Cicchella et al., 2014) on top of which sandy-like soils developed. Another two areas of low uranium concentration values are apparent: one in Central Norway, and one in Central to Northern Finland extending to the Northern part of Norway and Sweden; both areas are related to glacial deposits and peat cover. Other areas with low concentration of uranium are found in Southern to Eastern Spain (left margin of Guadalquivir basin and Segura and Jucar basins), Southwest France (Garonne basin) and Eastern Hungary (Tizsa basin in the left margin of Danube river), all related to sandy sedimentary basins, often including loess deposits as in the last example.

Areas with high values can be found a bit all over Europe. In many cases these high values are spatially related to outcropping Variscan terrains, particularly granite masses, such as in the Northwest Iberian Peninsula (from Galicia in the Northwestern-most of the peninsula, to as far South as Sierra Morena), France (Massif Central, Armorican Massif and Voges), Southwest England and the Czech Republic (Bohemian Massif). All these areas are known for occurrence of uranium mineralisation, whether related to granitic intrusions, derived hydrothermal fluids, vein-type deposits or karstic fillings (Negrel et al., 2018), some of which have been exploited in the past.

High values are also found over Alpinide terrains (often overprinting a Variscan core with granite), particularly along the karstic Eastern Adriatic coast and extending to Northern Greece and Bulgaria, where granitic rocks outcrop, as well as in the Pyrenees axial zone, some areas over the Alps, Calabria (Southern Italy) and Sardinia. Lazio and Campania Regions, on the Western Italian coast, also show anomalous U concentrations in topsoil over Cenozoic alkaline volcanic rocks (e.g. rhyolites and phonolites).

A main area of anomalous uranium areas is found in Sweden and Southern Finland, which is related to the Southern Svecofennian Province of the Baltic Shield (Lahtinen, 2012). This is dominated by Paleoproterozoic granites, pegmatites and volcano sedimentary rocks and includes uranium mineralisation associated with these rock types as well as with alum black shale and skarns. Another uranium anomaly in Central Northern Sweden coincides with the contact between the Caledonian front and the Central Svecofennian Province, along which the Cambrian - Ordovician organic matter-rich and uranium-rich alum black shale formation occurs (Lecomte et al., 2017). The uranium anomaly found in Northern Estonia is also explained by a similar occurrence of alum black shale (Lecomte et al., 2017).

3.2 Thorium

Thorium (Th) is an actinide series element with an atomic number of 90 and an atomic mass of 232. It is radioactive with one main natural isotope, the primordial long-lived radionuclide ^{232}Th, which has the longest half-life (1.41×10^{10} years) of all known radioactive isotopes of thorium and comprises 99.98% of the total Th mass. Thorium decays through a long radioactive decay series, ending with the stable lead isotope ^{208}Pb.

3.2.1 Thorium in rock minerals

Thorium is mainly present at minor to trace concentration levels (< 1 g/100 g) in accessory minerals such as zircon, sphene, epidote, allanite and apatite, and it is a major component (> 1 g/100 g) in monazite $(Ce,La,Nd,Th)(PO_4,SiO_4)$ and the rare minerals thorite $(ThSiO_4)$ and thorianite (ThO_2). Because of its affinity to replace other elements with the same dominant oxidation state (+4), e.g. Zr, Ce and U, thorium may form solid-solutions thorite-zircon and thorianite-cerite-uranite. As thorium is sensitive to magmatic differentiation, concentrating in the late stages of crystallisation, it is enriched in felsic, silicic igneous rocks and has the lowest concentration in the silica-poor ultramafic igneous rock types.

Granodiorite outcrop from Val Codera, Northern Italy. This intrusive igneous rock contains large alkali-feldspar with regular shape.
Source: Orlando Sebastian Olivieri

Its concentration in acid to intermediate igneous rocks, such as granites, granodiorites, rhyolites, trachytes, syenites and phonolites, is generally above 10 mg/kg, often reaching 50 mg/kg; in basic igneous rocks, including gabbros and basalts, thorium concentrations range from 0.1 to 4 mg/kg, and ultrabasic rocks generally show concentrations below 0.1 mg/kg (Wedepohl, 1978).

Thorium concentration in sedimentary rocks varies highly. Thorium is relatively immobile and tends to be geochemically-separated from mobile mineral fractions (e.g. uranium) during weathering and alteration of primary minerals from igneous parent rocks (Adams & Weaver, 1958, quoted in Tye et al., 2017). Thus, thorium concentrates in resistant detrital heavy minerals (e.g. zircons, monazite, apatite, xenotime, etc.); or if released during weathering, it is strongly adsorbed by clays and iron and manganese oxi-hydroxide minerals. In carbonate rocks the thorium concentration is very low (< 3 mg/kg) and concentrated in the non-carbonate fraction, namely in clays. Typical thorium concentrations in shales and mudrocks are around 12 mg/kg, while in sandstones typically vary from 1 to 7 mg/kg, but higher values may occur in heavy mineral-enriched sands. Residual deposits such as bauxites or bentonites may show thorium concentrations above 20 mg/kg (Wedepohl, 1978).

Most metamorphic rocks tend to keep similar thorium levels of its igneous or sedimentary protolith. Thorium concentrations usually range from < 0.1 ppm in marble to > 67 ppm in some high-grade feldspathic rocks. However, most metamorphic rocks have thorium contents close to the crustal average between 6 – 10 ppm Th (Wedepohl, 1978).

3.2.2 Thorium in the soil – plant system

Soil is a complex and evolving entity consisting of a mixture of minerals, organic matter, living organisms, water and air, with the depth extension and composition varying from place to place (see Section 3.1.2, first paragraph).

The parent material (most often the bedrock) is the main reservoir of the natural radionuclide ^{232}Th and its decay products, which are released into the soil through weathering processes (Cicchella et al., 2014). Most of thorium tends to be retained in the soil profile after weathering of the bedrock, as it essentially concentrates in the resistate mineral fraction, such as monazite and zircon. A small part released from minerals, namely as the cationic species Th^{4+}, is readily adsorbed by the negatively charged clay minerals (Shepard & Evenden, 1988). When thorium is removed from the bedrock and/or soil profile, it is transported in the solid mineral fraction as thorium is essentially insoluble in surface and ground water (Hem, 1992).

Thorium has no known biological function. Very little of it is taken up by plants (Shepard & Evenden, 1988), generally with transfer factors (plant/soil concentration ratios) of about one order of magnitude lower than that for uranium or radium. This is a consequence of the very low solubility of thorium relative to that of uranium and radium (Morton et al., 2001, quoted in Negrel et al., 2018), as the plant uptake of radionuclides depends more on their concentration in solutions than on their total concentration in the soil (Shepard & Evenden, 1988). If taken up by plants, thorium tends to accumulate in their roots, namely in their surfaces; thus, not surprisingly, root crops have higher concentration ratio values than cereal grain crops (Shepard & Evenden, 1988; Chen et al., 2005).

Notably, the ^{228}Ra isotope has a half-life sufficiently long to allow some separation from its parent (^{232}Th), since radium shows an Eh-pH chemical behaviour in the surface environment which differs widely from that of thorium. This may produce radium concentrations in the environment which do not coincide with those observed for thorium (and uranium). For instance, soils formed over some limestones and argillaceous limestones may accumulate significant amounts of radium (Kabata-Pendias, 2011). The chemical behaviour of radium is sufficiently similar to that of barium, strontium and calcium, so that radium can replace calcium in carbonate minerals, make a solid solution with barium in radiobarite $((Ba, Ra)SO_4)$, or be easily taken up by plants (Kabata-Pendias, 2011) since calcium is an essential element for life and one of the most soluble and important cations in soil solutions (Kabata-Pendias, 2011).

3.2.3 Natural exposure to thorium by biota

The natural ionising radiation in the environment caused by thorium varies from place to place, mainly according to geology, that is, depending on thorium concentration in rocks and soils (UNSCEAR, 2000).

Thorium is a chemotoxic and radiotoxic carcinogen, although its harmfulness is mainly considered to be its radioactive character and that of its decay products, rather than to its chemistry. The ^{232}Th isotope is the primordial progenitor of a complex radioactive decay series emitting alpha, beta and gamma radiation until a stable lead isotope is produced.

Humans and other life forms are exposed to three types of ionising radiation derived from ^{232}Th:

- external, essentially from thorium and its decay products present in rocks and soils;
- internal, from direct ingestion or air inhalation of dust particles containing ^{232}Th and its decay products; and
- from ingestion of food and water with trace amounts of thorium and/or radium.

Thorium in drinking water is generally not considered problematic as a consequence of its very low solubility, contrary to radium and uranium. In case of food ingestion, thorium is retained mainly in the skeleton, depositing on bone surfaces (UNSCEAR, 2000).

^{220}Rn is also a decay product with unique properties as it is a radioactive gas, thus it may escape the minerals to the breathing air, where it tends to concentrate in confined spaces, namely indoors. This creates a chance of internal exposure to ionising radiation mostly by alpha particles of its decay products, however to a lesser extent than that from ^{222}Rn. The reason for the different degree of exposure posed by ^{222}Rn (higher) and ^{220}Rn (lower) is mainly linked to their different half-lives, 3.8 days and 55.6 seconds respectively. The very short half-life of the latter constrains travel from its production site to the immediate environment of human beings (UNSCEAR, 2000).

Exposure to thorium by ingestion and/or inhalation is enhanced by several anthropogenic activities, namely those related with thorium (and uranium) mining and processing; nuclear energy production; production and use of phosphate fertilisers and coal burning (UNSCEAR, 2000; Cicchella et al., 2014).

The radiation in the environment from ^{232}Th can be measured mainly by gamma-ray spectrometry related to its progeny or estimated from the concentration of thorium in soil and rocks.

Coarse-grained gabbro, an intrusive igneous rock, cut by a basaltic dike, an effusive igneous rock. Both rock types have typically low U, Th and K_2O contents.
Source: Roberto Rinaldi

3.2.4 European map of thorium concentration in topsoil

This section aims to provide information on variation in background concentrations of the naturally occurring radionuclide thorium concentration in topsoil across Europe. The European map of thorium in soil (as Th in mg/kg) shown here is a proxy for the ionising radiation caused by ^{232}Th and its decay products present at the surface environment. The map is based on data from two geochemical projects carried out at European level, FOREGS and GEMAS. Besides its value for outlining natural radioactivity levels in Europe, the map can also be used as an input parameter for the European Geogenic Radon Map.

Materials and methods

For the purpose of the EANR, the map of thorium concentration in soil is based on two European datasets (FOREGS and GEMAS) containing information about Topsoil geochemistry at continental level.

FOREGS AND GEMAS

See page 61.

Data overview

In order to produce a European map of thorium in topsoil, a total of 4653 topsoil samples reporting total concentration of thorium was compiled into a new EANR dataset. The values included in the EANR dataset collate 839 (by ICP-MS) from FOREGS, 1 864 (by XRF) from GEMAS Gr and 1 950 (by XRF) from GEMAS Ap (Figure 3-8).

Karst limestone formations, Serbia.
Source: Peter Bonow

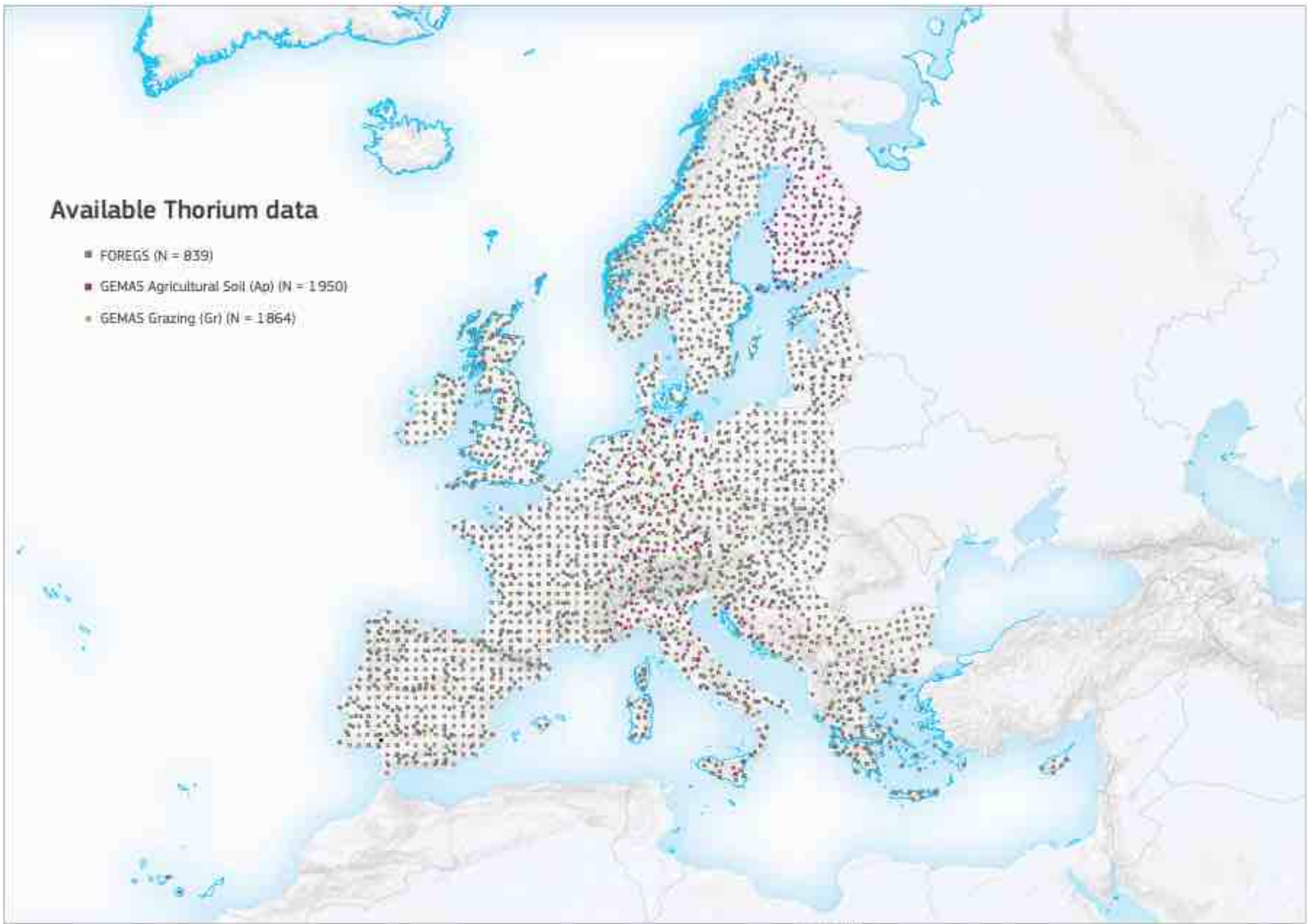

Figure 3-8
Sample locations of topsoil data from FOREGS and GEMAS reporting total concentration of thorium
Source: Map created by A. Ferreira, T. R. Lister, R. S. Lawley and A. M. Tye

A preliminary overview of the thorium EANR topsoil dataset and the three corresponding subsets (FOREGS, GEMAS Ap, GEMAS Gr) is given in Table 3-4 and in Figure 3-9.

The graphs shown in Figure 3-9 are a histogram, a Tukey boxplot (Tukey, 1977) and a cumulative probability plot (Sinclair, 1976) for the EANR dataset and for each one of the subsets used, namely FOREGS, GEMAS Gr and GEMAS Ap. In the histogram plot, the distribution of each of the three subsets is represented by a density line, while the histogram bars refer to the overall EANR collated dataset.

	EANR	FOREGS	GEMAS Gr	GEMAS Ap
N	4653	839	1864	1950
DL	-	0.1	5	5
%<DL	-	0	13.4	24.1
Minimum	0.3	0.3	<5.0	<5.0
P25	5.05	4.36	7	5
Median	9	7.16	11	9
P75	13	10.4	14	12
P95	19	17	21	18
P99	31	32.01	32	28
Maximum	84	75.9	80	84
MAD	5.93	4.42	5.9	5.9
CVR%	66	62	54	66
Mean	9.79	8.23	11.1	9.2
SD	6.49	6.16	6.5	6.4
CV%	66	75	59	69
GM	7.91	6.62	9.3	7.3
GSD	2	1.97	1.91	2.03
powers	2.4	2.4	1.5	1.5
skewness	2.64	3.73	2.12	2.99
Th median concentration at the **Upper Continental Crust: 10.5 mg/kg***				

Table 3-4
Th (mg/kg) statistics for the topsoil EANR dataset and corresponding subsets
Source: A. Ferreira, T. R. Lister, R. S. Lawley and A. M. Tye

N: number of samples; DL: detection limit; P##: percentiles; MAD: median absolute deviation; CVR%: robust coefficient of variation; SD: standard deviation; CV%: coefficient of variation; GM: geometric mean; GSD: geometric standard deviation. See explanations of the other statistical parameters below Table 3-1.
MAD is a robust equivalent of the standard deviation (SD) measuring the average deviation from a central value, the Median in this case. The CV% is defined as the SD divided by the Mean, while the CVR% is defined as the MAD divided by the Median, both shown in % relative to the central value used. Powers show the orders of magnitude of the variation, being defined as the decimal logarithm of the ratio between the maximum and the minimum (Reimann et al., 2008). Skewness is a measure of asymmetry of the distribution, indicating whether the tails on both sides of the Mean balance out or not.
*Rudnick & Gao (2003)

For GEMAS samples, the detection limit (DL) for thorium (5 mg/kg) is about half of the estimated value for the Upper Crust (10.5 mg/kg; Rudnick & Gao, 2003); even so, the number of GEMAS values for thorium reported as below detection limit is high (13.4 % for Gr and 24.1 % for Ap, Table 3-4). The effect of this problem in the EANR dataset is obvious, as can be seen from Figure 3-9, namely (i) the histogram plot (a notorious peak at half the DL value, 2.5 mg/kg) and (ii) the cumulative probability plot (a strong vertical break at half the uranium DL, from about 1 % to < 20 % of probability). Also, the GEMAS results for total thorium are provided as integers, leading to the stairs-like appearance of the same CPP curves (Figure 3-9) and revealing poor sensibility of the analytical method. The problems mentioned here are however less notorious than for uranium (described in Section 3.1). FOREGS, on the contrary, shows a low detection limit (DL = 0.1 mg/kg), such that all samples are reported above it, and thus the resulting cumulative probability curve (blue dots in the plot on the right of Figure 3-9) is set over a continuous line with no vertical breaks.

For the purpose of the EANR map of thorium total concentration in topsoil samples, it was decided not to take into account thorium data collected from GEMAS for which a value below the detection limit is reported. This implies that the EANR map of thorium in topsoil relies on the FOREGS subset for delineating the European areas where the lowest values of thorium are found, while areas with predominance of median-to-high values are delineated from both FOREGS and GEMAS (Ap and Gr) projects.

After removing GEMAS samples with thorium values below the DL, the total number of EANR valid samples is 3 934, with 839 (by ICP-MS) from FOREGS, 1 615 (by XRF) from GEMAS Gr and 1 480 (by XRF) from GEMAS Ap (Figure 3-10).

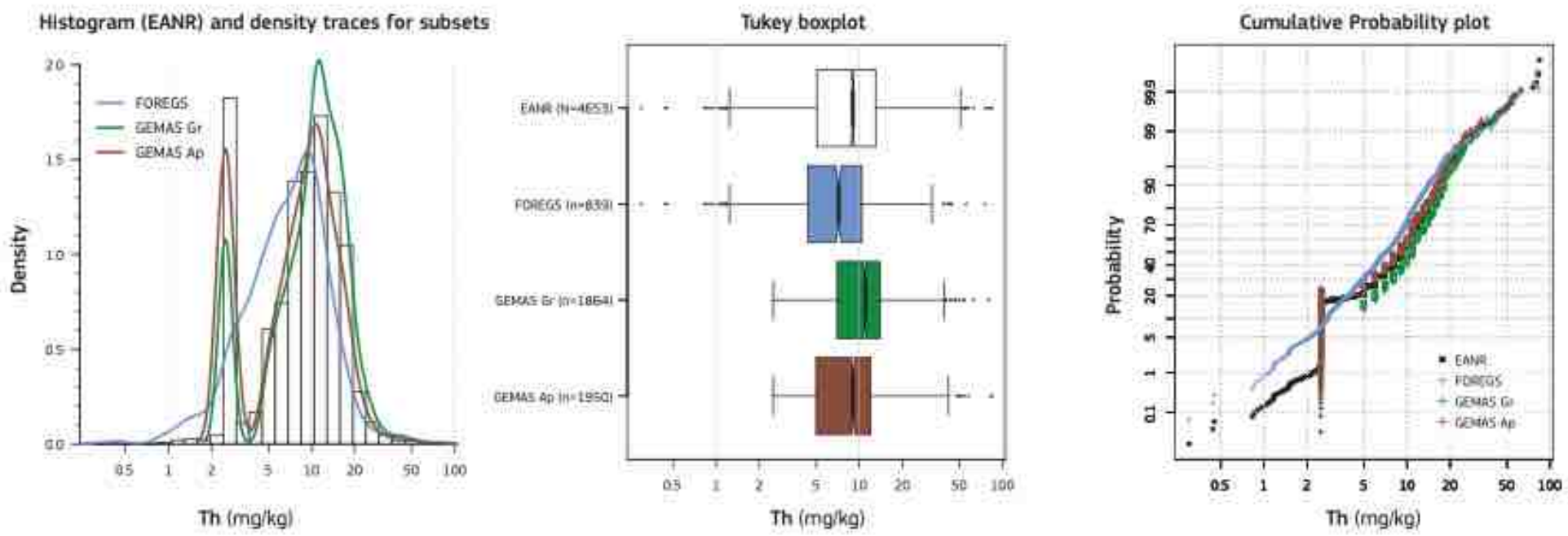

Figure 3-9.
Graphical representations of Th concentration (mg/kg) in the EANR dataset and the corresponding subsets.
Source: Graphs created by A. Ferreira, T. B. Lister, R. S. Lawley and A. M. Tye

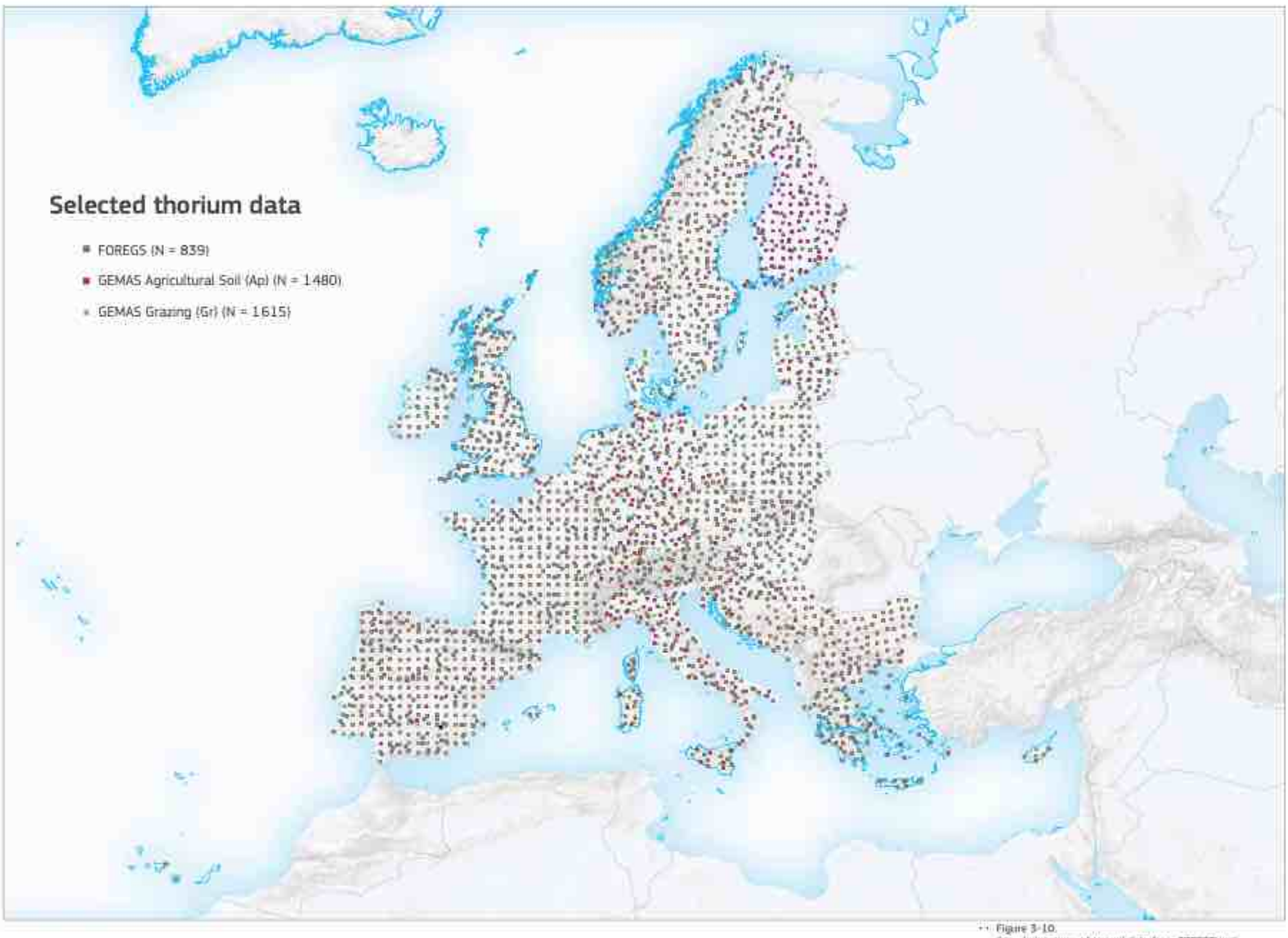

Figure 3-10.
Sample locations of topsoil data from FOREGS and GEMAS reporting total concentration of thorium above the corresponding detection limit.
Source: Graph created by A. Ferreira, T. B. Lister, R. S. Lawley and A. M. Tye

An overview of the thorium EANR topsoil dataset (and corresponding subsets), after removing samples reported as below the detection limit is given in Table 3-5 and in Figure 3-11.

As expected, the removal of GEMAS data points below the DL causes a general overestimation on the uranium statistics of the EANR dataset (compare the EANR column of Table 3-4 and Table 3-5), as areas of low values are now under-sampled (relying on FOREGS only) relative to areas where mean-to-high values dominate (relying on both FOREGS and GEMAS). This should not cause major problems in the thorium map production, on the contrary. By not using the data points below the detection limit, the map benefits from the high-quality natural variability at the low values provided by the FOREGS subset, which otherwise would be hidden in a generalised flattening surface (map not shown).

From the above rationale, the best estimate for the statistics of thorium at European level is, most possibly, the one provided by the FOREGS subset (see Table 3-4 and Table 3-5).

Apart from removing samples below the detection limit, no further corrections have been applied to the EANR topsoil thorium data.

	EANR	FOREGS	GEMAS Gr	GEMAS Ap
N	5934	839	1615	1480
Minimum	0.3	0.3	<5.0	<5.0
P25	7	4.36	9	8
Median	10.2	7.16	11	11
P75	14	10.4	15	13
P95	20	17	22	19
P99	32	32.01	32.9	31.2
Maximum	84	75.9	80	84
MAD	4.47	4.42	4.4	4.4
CVR%	46	62	40	40
Mean	11.12	8.23	12.4	11.3
SD	6.19	6.16	6	5.9
CV%	56	75	48	52
GM	9.77	6.62	11.4	10.3
GSD	1.69	1.97	1.52	1.51
powers	2.4	2.4	1.2	1.2
skewness	3.24	3.73	2.94	4.33
Th median concentration at the Upper Continental Crust: 10.5 mg/kg*				

N: number of samples; DL: detection limit; P##: percentiles; MAD: median absolute deviation; CVR%: robust coefficient of variation; SD: standard deviation; CV%: coefficient of variation; GM: geometric mean; GSD: geometric standard deviation. See explanations of the other statistical parameters below Table 3-4.
*Rudnick & Gao (2003).

Table 3-5
Th (mg/kg) statistics for the topsoil EANR dataset and corresponding subsets reporting total concentration of thorium above the corresponding detection limit.
Source: A. Ferreira, T. R. Lister, R. S. Lawley and A. M. Tye.

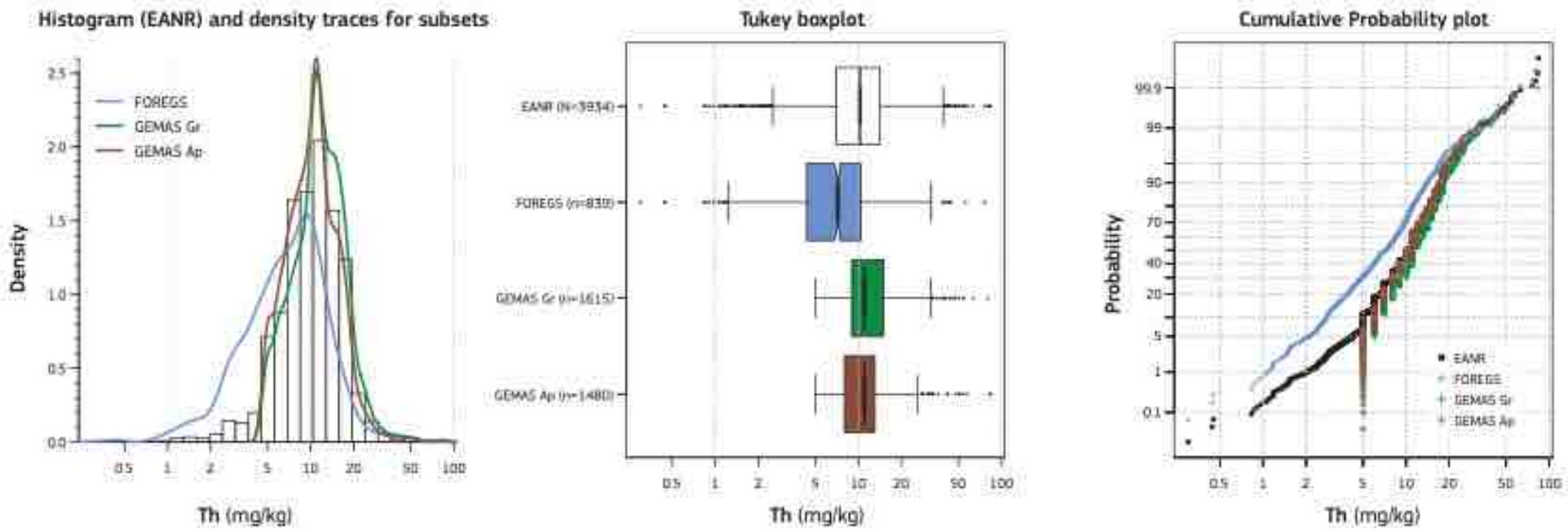

Figure 3-11
Graphical representations of Th concentration (mg/kg) in the EANR dataset and the corresponding subsets reporting total concentrations of thorium above the corresponding detection limit.
Source: Graph created by A. Ferreira, T. R. Lister, R. S. Lawley and A. M. Tye.

Lime kiln located at Lake Maggiore, Ispra, Italy. Since ancient times, lime has been the source for the manufacture of building materials, disinfectant and fertiliser.
Source: Peter Bossier (left) and Tore Tollefsen (right).

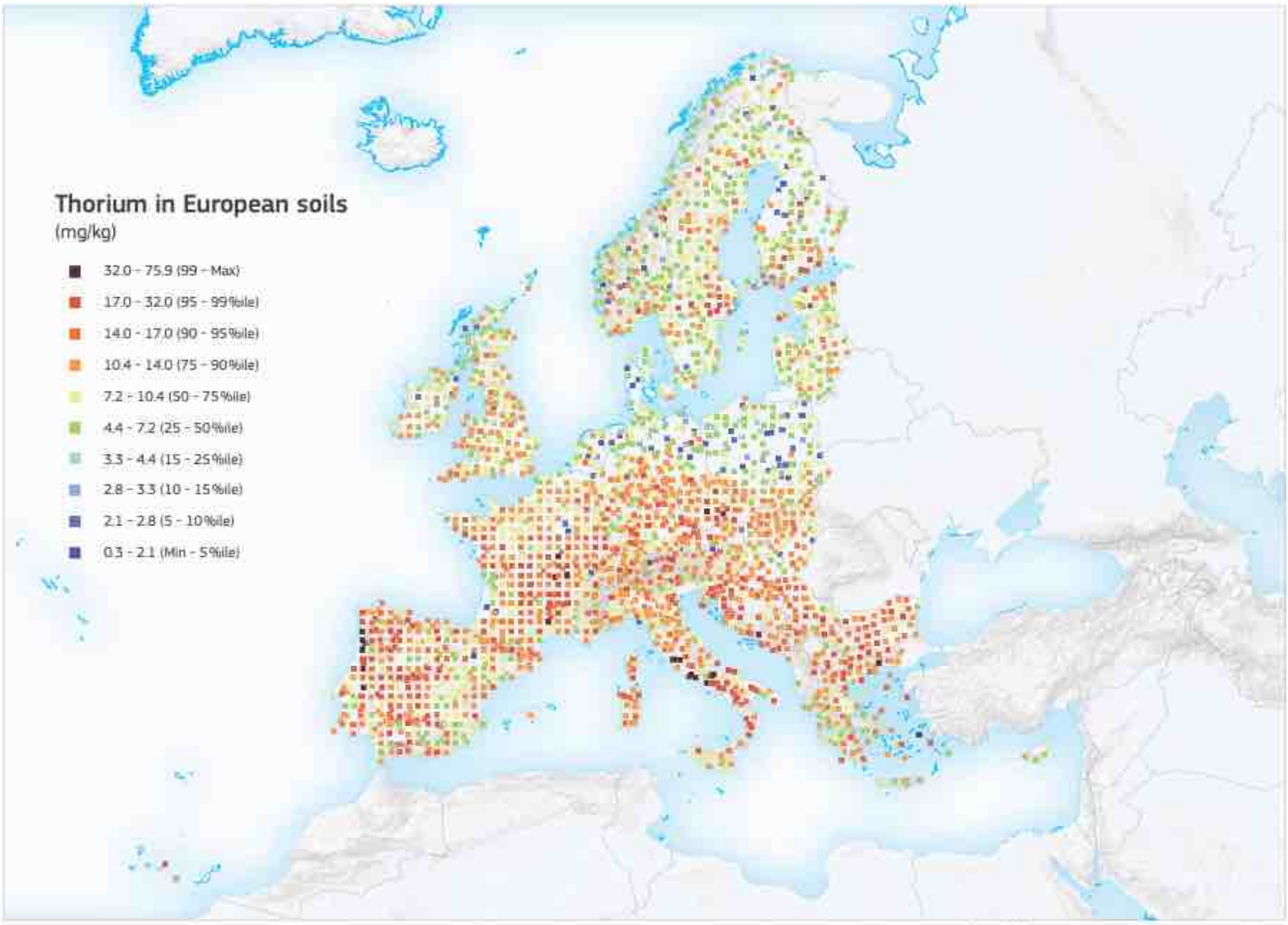

Figure 3-12
EANR total concentration of thorium in topsoil samples over Europe (N = 3 934), after removing values below the detection limit. Colours are according to FOREGS percentiles.
Source: Grunt created by A. Ferreira, T. R. Lister, R. S. Lawley and A. M. Tye

Map

The EANR map of total concentration of thorium in topsoil was produced using the 3 934 samples discussed and shown in Figure 3-10, Figure 3-11 and Table 3-5.

The total concentration of thorium in EANR samples are shown in Figure 3-12, with colours attributed according to the percentiles of the FOREGS subset.

The data shown in Figure 3-12 were interpolated, using ordinary kriging, in order to obtain the required 10 km × 10 km regular grid image of the distribution of estimated thorium total concentration in topsoil over Europe. The data were processed and maps were produced in R free software/environment using several appropriate packages, such as 'sp' and 'gstat', and according to the following steps:

i. a variogram model for the log-transformed thorium data was produced (Figure 3-13);
ii. an estimated thorium value at each node of the 10 km × 10 km grid was computed after ordinary kriging, conditioned by the variogram model referred to in (i) and using a maximum of 13 neighbouring points in a maximum distance of 100 km radius;
iii. the values obtained in (ii) were back-transformed from logarithmic to regular total concentration of thorium in mg/kg;
iv. and the data were plotted in a colour map with class boundaries based on the percentiles of the EANR dataset.

The resulting map of estimated total concentration of thorium in topsoil over Europe is shown in Plate 2.

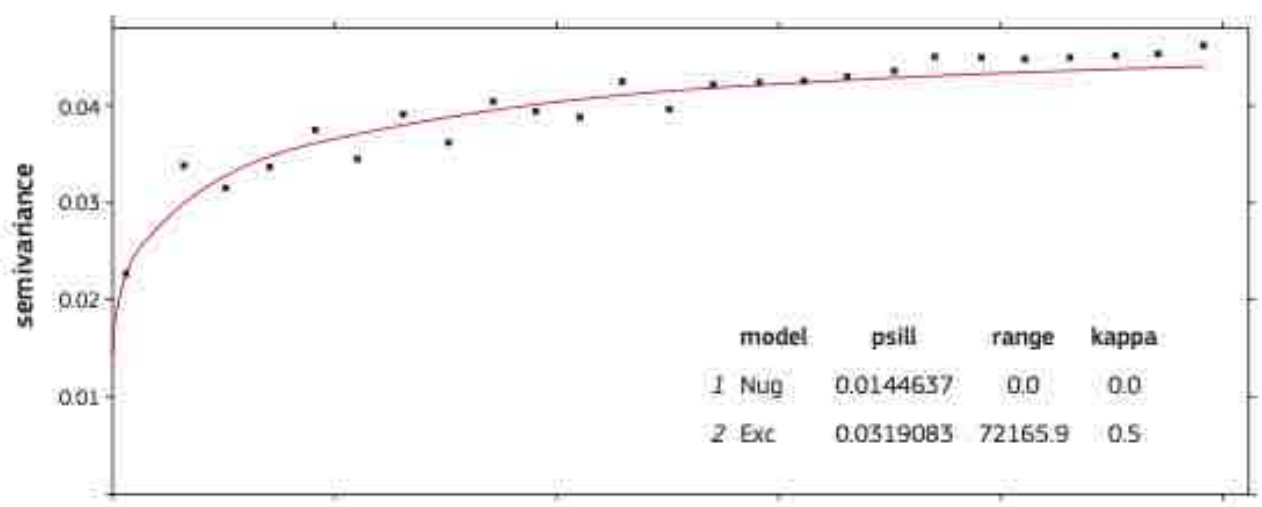

Figure 3-13
Variogram model for $\log_{10}$(Th) in topsoil data collated from FOREGS (ICP-MS) and GEMAS (XRF) European datasets.
Nug: nugget; Exc: Exponential class.
Source: Grunt created by A. Ferreira, T. R. Lister, R. S. Lawley and A. M. Tye

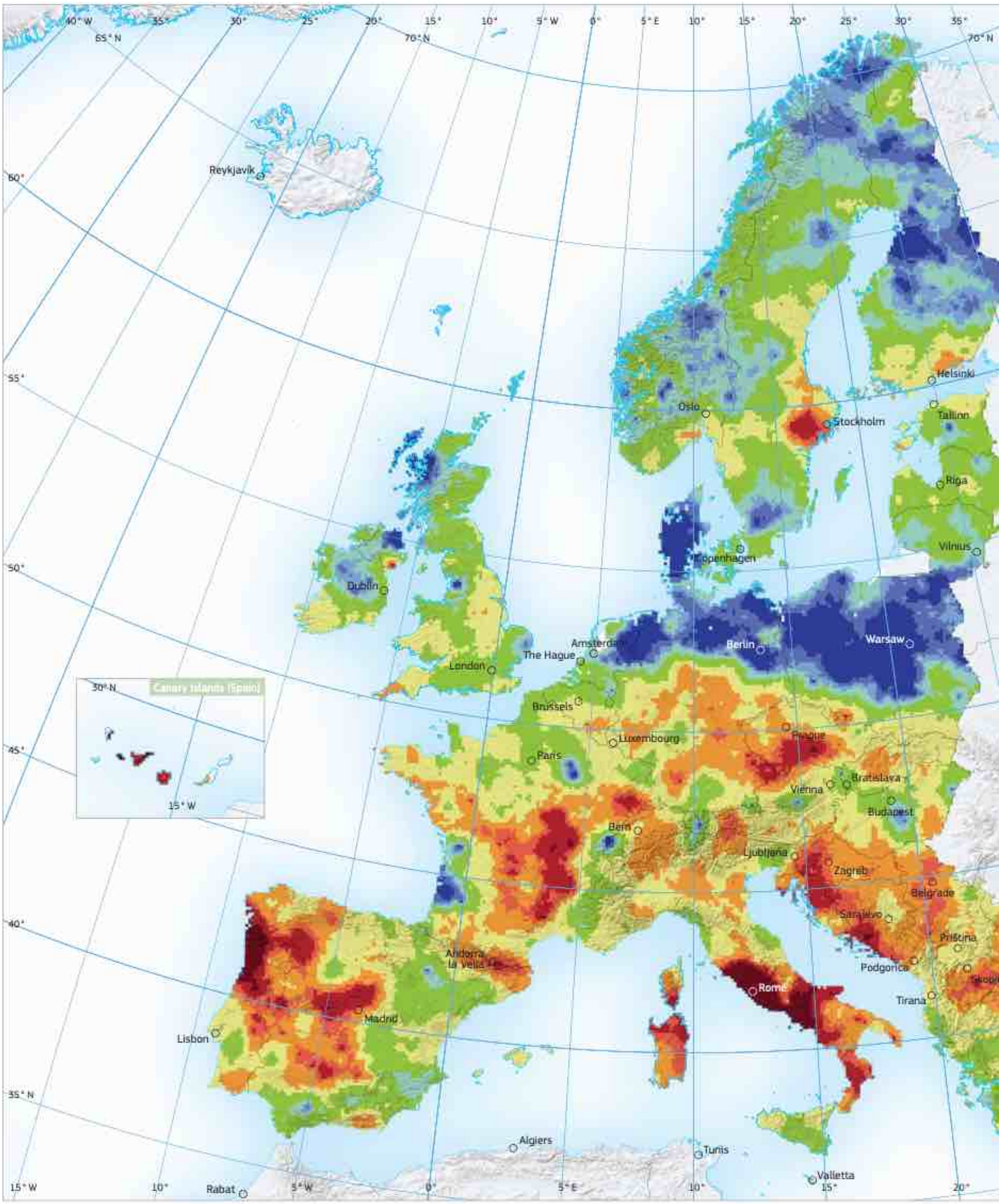
40° W
35°
30°
25°
20°
15°
10°
5° W
0°
5° E
10°
15°
20°
25°
30°
35°
65° N
70° N
70° N
60°
55°
50°
45°
40°
35° N
30° N
15° W
10°
5° W
0°
5° E
10°
15°
20°
Canary Islands (Spain)
Reykjavik
Oslo
Stockholm
Helsinki
Tallinn
Riga
Vilnius
Copenhagen
Dublin
London
The Hague
Amsterdam
Berlin
Warsaw
Brussels
Luxembourg
Prague
Paris
Vienna
Bratislava
Budapest
Bern
Ljubljana
Zagreb
Belgrade
Sarajevo
Priština
Podgorica
Skopje
Tirana
Andorra la Vella
Rome
Madrid
Lisbon
Algiers
Tunis
Valletta
Rabat

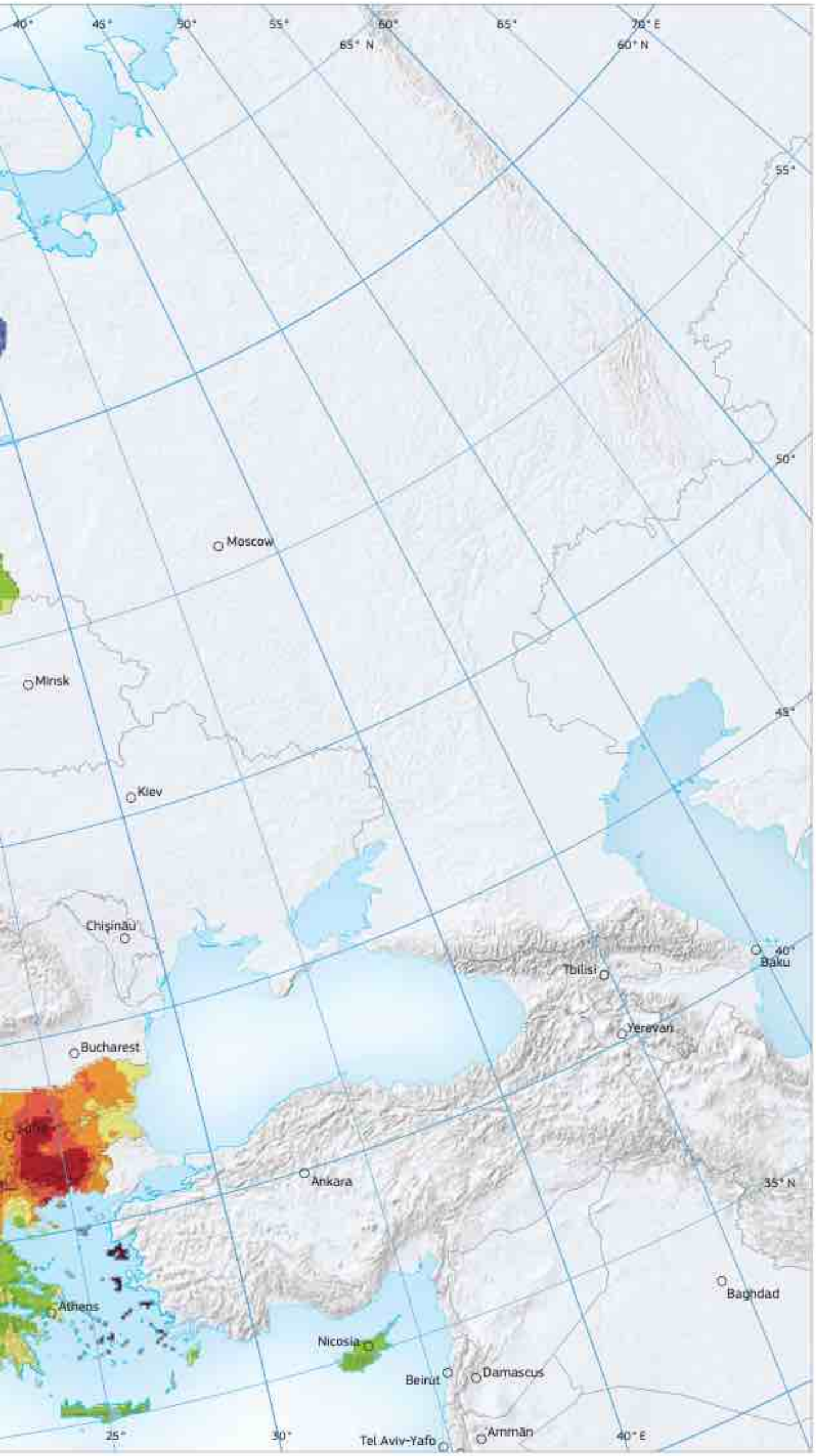

Plate 2:
Map of estimated total concentration of thorium in topsoil over Europe

(mg/kg)

- 20.3 - 84 (99%ile - Max)
- 15.8 - 20.3 (95 - 99%ile)
- 14.2 - 15.8 (90 - 95%ile)
- 11.8 - 14.2 (75 - 90%ile)
- 9.3 - 11.8 (50 - 75%ile)
- 7.0 - 9.3 (25 - 50%ile)
- 6.0 - 7.0 (15 - 25%ile)
- 5.5 - 6.0 (10 - 15%ile)
- 4.8 - 5.5 (5 - 10%ile)
- 0.3 - 4.8 (Min - 5%ile)

Plate 2: Map of estimated total concentration of thorium in topsoil over Europe, based on data collated from the FOREGS (ICP-MS) and GEMAS (XRF) European datasets as shown in Figure 3-8 and Figure 3-10. The colours are attributed according to the percentiles of the EANR-estimated map points.

Source: Map created by A. Ferreira, T. R. Lister, R. S. Lawley and A. M. Tye

copyright © European Commission, JRC, 2019

Discussion and conclusions

Thorium percentiles for FOREGS data, EANR data and the resulting kriging-estimated map points are shown in Table 3-6.

The differences found in percentiles between FOREGS and EANR-estimated map points (Table 3-6, Figure 3-14) have several causes. A first reason is a shift in the shape of the distribution towards high values caused by the removal of GEMAS values below the thorium detection limit (Th = 5 mg/kg). Also, the areas covered by FOREGS and GEMAS do not perfectly match, with the latter covering more Balkan countries, over which median-to-high values are observed, thus further increasing the referred shift. This shift can be roughly estimated from the percentiles difference observed for FOREGS and for EANR data (Table 3-6 and Figure 3-14). A second reason is due to data processing, as interpolation of data usually causes an overestimation of the low values and an underestimation of the high values; that is, it tends to smooth values towards the central ones. This bias can be roughly assessed from the percentiles difference observed for EANR data and for EANR-estimated map points (Table 3-6).

	Min	P5	P10	P25	Median	P75	P90	P95	P99	Max
FOREGS	0.3	2.1	2.8	4.4	7.2	10.4	14	17	32	75.9
EANR data	0.3	4.2	5	7	10.2	14	18	20	32	84
EANR estimated	2.1	4.8	5.5	7	9.3	11.8	14.2	15.8	20.3	44.4

Table 3-6
Th (mg/kg) percentiles for FOREGS (N = 839) and for EANR data (N = 3 934) and EANR-estimated map points (N = 47 108, Figure 13).
Source: A. Ferreira, T. B. Lister, R. S. Lawley and A. M. Tye

Figure 3-14
Graphical representations of Th concentration (mg/kg) in EANR-estimated map points and the subsets from which the map was produced
Source: Graph created by A. Ferreira, T. B. Lister, R. S. Lawley and A. M. Tye

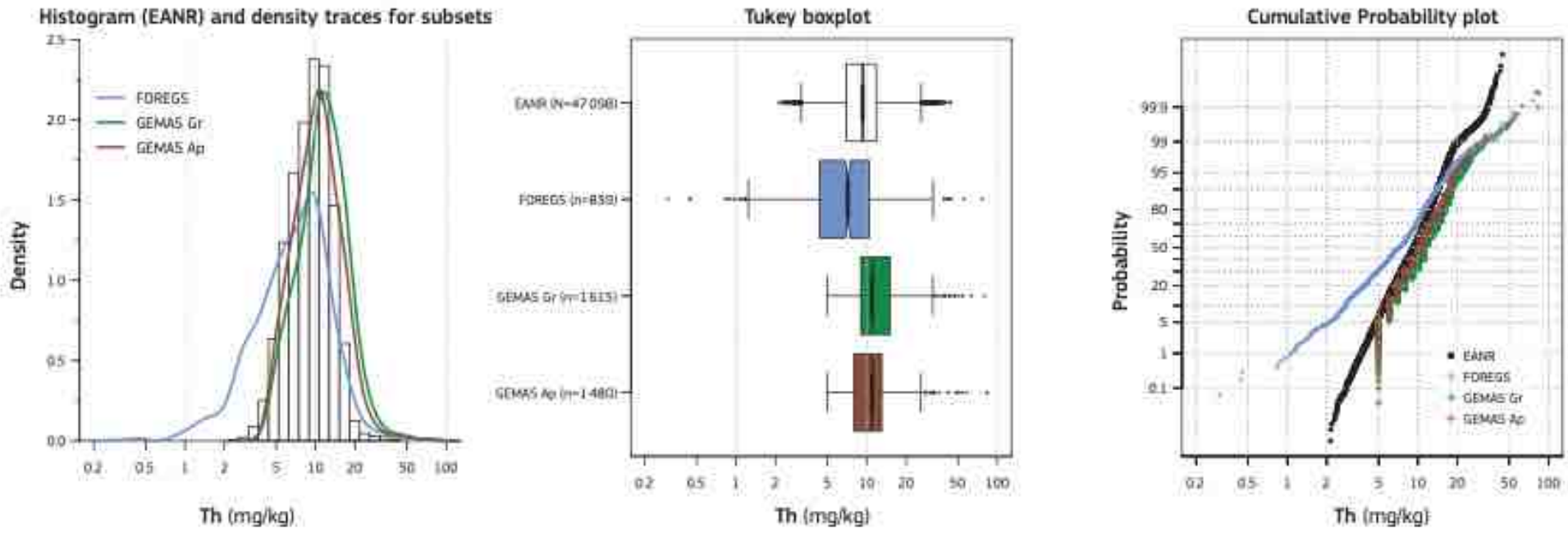

Thorium geochemical patterns

The FOREGS project has already provided a distribution map of thorium total concentration in Europe (http://weppi.gtk.fi/publ/foregsatlas/maps/Topsoil/t_icpms_th_edit.pdf), adding a short description of the geochemical patterns included in the element's factsheet (http://weppi.gtk.fi/publ/foregsatlas/text/Th.pdf). Distribution patterns of thorium partial concentrations (after aqua regia and MMI®) have been provided by the GEMAS project (Reimann et al, 2014) and discussed in Chapter 8 of Cicchella et al. (2014), in Reimann et al. (2014) and in Negrel et al. (2018).

The statistics of thorium for the EANR data are given in Table 3-5, Table 3-6 and Figure 3-14 and explained in the 'Data overview' section above. Thorium total concentrations in the EANR dataset vary from 0.3 to 84 mg/kg, with a median of 10.2 mg/kg. As explained above, this median value is most possibly an overestimation of the real median value over European topsoil, which is likely to be nearer to that reported for the FOREGS dataset (7.2 mg/kg). About 50% of the mapped area show estimated concentration values for thorium in the range of 7.0 – 11.8 mg/kg (areas in green and in yellow of the map) around a median value of 9.3 mg/kg; one quarter (25%) of the map shows thorium estimated concentrations below 7.0 mg/kg (areas in blue on the map) and the remaining quarter shows estimated thorium concentrations above 11.8 mg/kg (reddish areas on the map).

The distribution pattern of total thorium across the EANR European countries is characterised by an extensive area of deep low values (often below 4 mg/kg), ranging from the Netherlands and Denmark to Eastern Poland, similarly to that observed for uranium and many other elements, as shown in the FOREGS (http://weppi.gtk.fi/publ/foregsatlas/maps/Topsoil/) and GEMAS (Reimann et al., 2014) projects. This extensive area is marked by a cover of unconsolidated glacial drift deposits over bedrock (Plant et al., 2003, quoted in Cicchella et al., 2014 and Negrel et al., 2018) on top of which sandy-like soils developed. Another two areas of low thorium concentration values are apparent, one in Central Norway, Northern Scotland and Ireland, and one in Central to Northern Finland extending to the Northern part of Norway and Sweden; both areas are mainly related to glacial deposits and peat cover. Other areas of low-to-moderate values of thorium total concentration are found in Southern to Eastern Spain (left margin of Guadalquivir basin, Segura, Jucar and Ebro basins) and Southwest France (Garonne basin), related to sandy sedimentary basins.

Areas with high values can be found a bit all over Europe, often coinciding with high values for uranium. Similarly to uranium, in many cases these high values are spatially related to outcropping Variscan crystalline terrains, particularly granite masses, such as in the Northwestern Iberian Peninsula (from Galicia in the Northwestern part of the peninsula, to as far South as Sierra Morena), France (Massif Central, Armorican Massif and Vosges), Southwest England and from South Belgium (Ardennes-Rhenish Massif) to the Czech Republic (Bohemian Massif).

High thorium concentrations are also found over Alpinide terrains (often overprinting a Variscan crystalline core), particularly along the karstic Eastern Adriatic coast and extending eastwards to Serbia, Northern Greece and Bulgaria, where granitic rocks outcrop; as well as in the Pyrenees axial zone, some areas over the Alps, Calabria (Southern Italy) and Sardinia. Moreover, Lazio and Campania Regions, on the Western Italian coast, show anomalous thorium concentrations in topsoil over Cenozoic alkaline volcanic rocks (e.g. rhyolites and phonolites), with the anomaly extending to soils over other rock types, such as limestone.

Notably, the generalised high thorium concentration observed in Central Europe from the Pyrenees to the Slovak Republic, forms a rough, arc-like major pattern, delimited in the south by the valleys of the Rhone river (South of France) and by the Danube river (as far downstream as the South of Hungary), along which low thorium values can be found. This rough lineament grossly coincides with the northern delimitation of the Alps. This generalised high concentration of thorium extending over Central Europe is suddenly interrupted by the deep thorium lows extending from Poland to the Netherlands, and cut by several thorium lows related to other river valleys, such as the high Rhine, Seine and Garonne.

High thorium concentrations are also found in Central Sweden, extending to Southern Finland, which is related to the Southern Svecofennian Province of the Baltic Shield (Lahtinen, 2012). This area is dominated by Paleoproterozoic granites, pegmatites and volcano sedimentary rocks and includes uranium mineralisation associated with these rock types as well as with alum black shale and skarns. Thus, this thorium peak coincides with a more extensive uranium anomaly.

3.3 Potassium

Potassium (K) is an alkali metal (with one main oxidation state: +1) with an atomic mass of 39 and three natural isotopes, including two stable ones, namely ^{39}K (93.3% of K total mass), ^{41}K (6.7% of K total mass); and the long-lived (1.248 million years) radioactive ^{40}K (0.0117%), which decays either to ^{40}Ca (89.3%) by emitting a beta particle, or to gas ^{40}Ar (10.7%) by emitting a gamma ray of energy 1.46 MeV after an electron capture.

3.3.1 Potassium in rock minerals

Potassium is a major element in many igneous and metamorphic rocks and in some chemically-precipitated sedimentary rocks (e.g. evaporite deposits). By contrast, widespread carbonates such as limestones and dolomites may contain minor or trace amounts of potassium. As potassium is sensitive to magmatic differentiation, concentrating in the late stages of crystallisation, it is enriched in acid igneous rocks and in pegmatites and late-stage hydrothermal fluids, and has its lowest concentration in the silica-poor ultramafic rock types.

Its concentration in igneous rocks primarily reflects the abundance of major potassium silicate minerals, namely, alkali feldspars (orthoclase, sanidine, microcline), micas (biotite, muscovite, phlogopite, paragonite), feldspathoids (nepheline) and alkali-bearing amphiboles. K_2O concentration in acid to intermediate igneous rocks, such as granites, granodiorites, rhyolites, trachytes, syenites and phonolites, varies between 2.5 and 6%, whereas in diorites and andesites it varies between 1 and 2%. In basic igneous rocks, including gabbros and basalts, K_2O concentration ranges from 0.5 to 1.3%; ultrabasic rocks, including pyroxenites, dunites and peridotites are estimated to have an average concentration of about 0.6%, ranging from less than 10 mg/kg in some dunites and peridotites to about 1% in some anorthosites (Wedepohl, 1978).

White limestone with light red chert nodules, a biochemical sedimentary rock that forms from the deposition and recrystallisation of SiO_2 rich skeletons of marine organisms. Source: Roberto Rosa.

Potassium concentration in sedimentary rocks is highly variable and depends on detrital mineralogy, primary chemically-precipitated sedimentary minerals and chemical modifications during sediment diagenesis. Carbonate rocks and sediments may contain between <0.01 to 5% of potassium, concentrated in the non-carbonate fraction, that is, in detrital silicate minerals such as alkali feldspars, micas and clay minerals. Thus, potassium content is considered a good proxy for the terrigenous component in carbonate rocks, as pure limestones and dolomites contain only trace amounts of potassium (Wedepohl, 1978). In fine-grained sedimentary rocks, such as clays, shales, mudstones and siltstones, potassium is largely controlled by the clay mineralogy, with a secondary contribution from K-feldspar (Wedepohl, 1978). The most important carriers of potassium in these rocks are illite, smectites and clay-grade detrital micas. The potassium content of arenaceous sedimentary rocks and sediments is principally controlled by three main minerals, namely K-feldspar, mica and glauconite (Wedepohl, 1978). The amount of detrital K-feldspar and mica decreases with increasing sediment maturity. Glauconite is usually formed *in situ* as authigenic mineral during burial diagenesis and can also be an important source of potassium in some sedimentary sequences. The potassium content of evaporitic rocks is a function of the presence or absence of potassium-rich salts that are precipitated from highly-evolved brines during late-stage extreme evaporation, and the presence of detrital clay minerals. The most important potassium mineral in evaporate rocks are sylvite (KCl), carnallite ($KMgCl_3 \cdot 6(H_2O)$), and the sulphate salt polyhalite ($K_2Ca_2Mg(SO_4)_4 \cdot 2H_2O$).

Most metamorphic rocks tend to keep similar potassium levels of its protoliths. For example, pelitic rocks derived from metamorphism of fine-grained sedimentary rocks contain major mica and thus are expected to contain significant amounts of potassium, while a quartzite originating from metamorphism of a clean quartz-rich sandstone (paraquartzite) is expected to contain little or no potassium. Exceptions to this rule may occur when some rocks are subjected to high-grade metamorphism and anatexis: in this case after melt extraction, the residual rock may become depleted relative to its protolith (Rollinson & Windley, 1980).

Cross-bedded sandstone used as a block from a retaining wall. Source: Roberto Rosa.

Considering the geochemical peculiarities of potassium, the zones of exposed bedrock where high potassium concentrations are expected to be found include to the following:

a. Highly differentiated volcanic and plutonic acid rocks;

b. Metamorphic and sedimentary rocks derived from a);

c. Evaporitic sequences.

In Europe, the localities that show an enrichment in potassium content can be divided into two categories:

- The great evaporitic sequences, such as the Zechstein Permian evaporitic sequence in Germany and Poland (Vovnyuk & Czapowski, 2007) and the upper Eocene evaporitic basin of Navarra, Spain (Ayora et al., 1994);
- Potassic to ultra-potassic igneous rocks, such as those from Central Italy (Peccerillo, 2005), Spain (Benitoa et al., 1999) and the Pannonian Basin (Embey-Isztin et al., 1993).

On the contrary, zones of exposed bedrock where low potassium concentrations are expected include the following:

d. Mafic and ultramafic igneous and metamorphic rocks;

e. Carbonates;

f. Metamorphic and/or sedimentary rocks derived from a);

g. Metamorphic rocks derived from b).

3.3.2 Potassium in the soil – plant system

Soil is a complex and evolving entity consisting of a mixture of minerals, organic matter, living organisms, water and air, with the depth extension and composition varying from place to place. The mineral component is frequently composed of weathered rock, mineral fragments, different clay minerals, Fe, Mn and Al oxi-hydroxides, secondary carbonates and sulphates, all derived from the materials under weathering, in most cases the bedrock. Organic matter originates from living organisms, namely plants and soil biota, decay. Water and air are mainly obtained from the atmosphere, but also from chemical, physical and microbial reactions permanently taking place. Soil also contains pollutants derived from anthropogenic activities such as urbanisation, energy generation, transportation, waste disposal, agriculture, mining and industry (FitzPatrick, 1986; White, 2006; Kabata-Pendias, 2011).

Potassium is a major constituent of soil, as part of its mineral fraction. Thus, its concentration is essentially related to the bedrock from which the soil derives. In most environmental conditions, the K cations released from minerals through weathering are readily incorporated in the structure or adsorbed by clay minerals and/or readily taken up by plants.

Potassium is a key nutrient for plant growth. With long-term and continuous intensive farming, many soil types may have become depleted in available potassium, leading to the generalised use of potassium in fertilisers, which is currently its main use on a global scale. Despite being increasingly added to soil as fertilisers, the natural sources are still considered more significant (Saaltink et al., 2014; Reimann & de Caritat, 1998; Cicchella et al., Chapter 8 in Reimann et al., 2014), as potassium added as fertiliser is likely to be entirely taken up by plant crops.

3.3.3 Natural exposure to potassium by biota

Potassium is an essential nutrient for regular functioning of most plants and animals, including humans. As the radioactive ^{40}K isotope behaves in the same way as the non-radioactive, more abundant potassium isotopes, it is expected to be incorporated by organisms with an approximate rate of 0.0117 parts per 100. This means that all potassium present in rocks and soils, water, atmosphere and biota, is a source of two types of ionising radiation to which biota, including humans, are exposed, namely (i) gamma radiation from external origin, as a result of the potassium present in the surrounding environment; and (ii) both gamma radiation and beta particles from internal origin, as a result of the necessary intake of potassium by biota. In a healthy human body the amount of potassium is relatively constant, balanced by homeostatic processes which regulate how much of the ingested potassium is retained or eliminated (UNSCEAR, 2000).

The natural ionising radiation in the environment caused by potassium varies from place to place mainly according to geology, that is, depending on K concentration in rocks and soils, with the activity concentration of ^{40}K in soil being one order of magnitude higher than that of ^{238}U or ^{232}Th (UNSCEAR, 2000).

Environmental radiation from ^{40}K can be measured by using gamma-ray spectrometry or estimated from potassium concentration in soil and rocks.

3.3.4 European map of potassium concentration in topsoil

This Section aims to provide information on the variation of background concentration of the naturally occurring radionuclide potassium (K) in topsoil across Europe.

The European map of potassium concentration in soil (as K_2O in wt%) shown here is a proxy for the ionising radiation caused by ^{40}K found in the surface environment. The map is based on data from two geochemical projects carried out at the European level, FOREGS and GEMAS. Besides its value for outlining natural radioactivity levels in Europe, the map can also be used as an input parameter for the European Geogenic Radon Map.

Materials and methods

The map of potassium concentration in soil for the purpose of the EANR is based on two European datasets (FOREGS and GEMAS) containing information about Topsoil geochemistry at continental level.

FOREGS AND GEMAS

See page 61.

Data overview

In order to produce a European map of potassium concentration in topsoil, a total of 4659 topsoil samples reporting total concentration of potassium (K_2O in wt%) was compiled into a new EANR dataset. The values included in the EANR dataset collate 845 (by ICP-MS) from FOREGS, 1864 (by XRF) from GEMAS Gr and 1950 (by XRF) from GEMAS Ap (Figure 3-15).

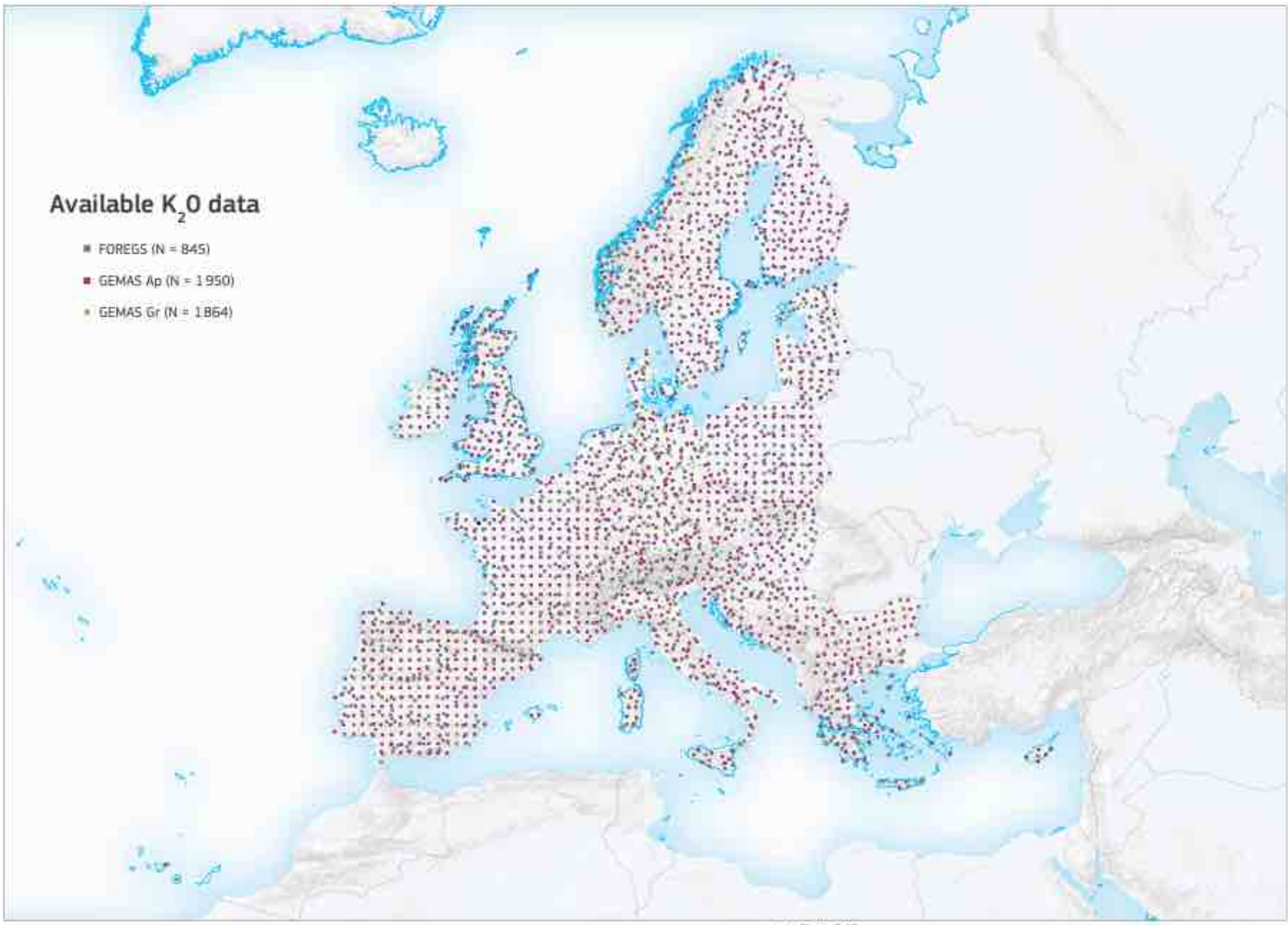

Figure 3-18.
Sample locations of topsoil data from FOREGS and GEMAS reporting total concentration of potassium.
Source: Spatial created by A. Ferreira, T. B. Lima, R. S. Lavado and A. M. Tye

A preliminary overview of the potassium EANR topsoil dataset and the three corresponding subsets (FOREGS, GEMAS Ap, GEMAS Gr) is given in Table 3-7 and in the graphs of Figure 3-16.

The graphs shown in Figure 3-16 are a histogram, a Tukey boxplot (Tukey, 1977) and a cumulative probability plot (Sinclair, 1976) for the EANR dataset and for each of the subsets used, FOREGS, GEMAS Gr and GEMAS Ap. In the histogram plot the distribution of each of the three subsets is represented by a density line, while the histogram bars refer to the overall EANR collated dataset.

The statistics from Table 3-7 show very similar results for the three datasets used. In fact, the absolute difference of each subset median value to the overall (EANR) median (1.86%) is 0.07 or lower, thus, representing less than 4% of the overall median K_2O concentration. Also, the graphs from Figure 3-16 confirm that the distribution shape of the three subsets essentially overlap. This indicates that the three datasets are highly compatible and thus merging them into a single dataset (EANR) does not seem to constitute a problem.

All values are above the reported detection limit (FOREGS: 0.01%; GEMAS 0.005%); N: number of samples; DL: detection limit; P##: percentiles; MAD: median absolute deviation; CVR%: robust coefficient of variation; SD: standard deviation; CV%: coefficient of variation; GM: geometric mean; GSD: geometric standard deviation. *Rudnick & Gao (2003).
MAD is a robust equivalent of the standard deviation (SD) measuring the average deviation from a central value, the Median in the case. The CV% is defined as the SD divided by the Mean, while the CVR% is defined as the MAD divided by the Median, both show in % relative to the central value used. Powers show the orders of magnitude of the variation, being defined as the decimal logarithm of the ratio between the maximum and the minimum (Reimann et al., 2008). Skewness is a measure of asymmetry of the distribution, indicating whether the tails on both sides of the Mean balance out or not.

	EANR	FOREGS	GEMAS Gr	GEMAS Ap
N	4659	845	1864	1950
Minimum	0.03	0.03	0.03	0.03
P25	1.31	1.33	1.25	1.37
Median	1.86	1.92	1.79	1.91
P75	2.45	2.57	2.37	2.47
P95	3.53	3.71	3.47	3.44
P99	4.64	4.9	4.71	4.62
Maximum	9.54	6.13	6.03	9.54
MAD	0.84	0.92	0.83	0.81
CVR%	45	48	46	42
Mean	1.94	2.02	1.87	1.97
SD	0.9	0.95	0.9	0.87
CV%	46	47	48	44
GM	1.7	1.77	1.62	1.76
GSD	1.77	1.76	1.84	1.7
powers	2.6	2.4	2.3	2.5
skewness	0.86	0.76	0.82	0.95
K_2O median concentration at the Upper Continental Crust: 2.80 wt%*				

Table 3-7.
K_2O (wt%) statistics for the EANR topsoil dataset and corresponding subsets.
Source: A. Ferreira, T. B. Lima, R. S. Lavado and A. M. Tye

The three subsets can be considered representative of the main types of Topsoil prevailing across Europe, as the samples were taken from their topmost, though different maximum depths were allowed (from 10 cm for Gr to 25 cm for FOREGS). Each GEMAS subset represents a unique type of farming use, while FOREGS represents a wider range of soil type including unused lands, forested soil, grassland, pastures but avoiding cultivated fields. From this we could expect higher variability in FOREGS relative to each GEMAS subset. This may explain the slightly higher MAD (a robust measure of the variability) observed for FOREGS (Table 3-7).

As the three EANR subsets are very similar (Table 3-7 and Figure 3-16), the overall EANR potassium data (N = 4 659) provide good estimates for the statistics of potassium total concentration in European topsoil. No corrections have been applied to the EANR topsoil potassium data.

Scandinavian coloured granite, deposited after retreat of glaciers. Hiddensee Geological Beach, near Stralsund, Germany.
Source: Peter Bierman

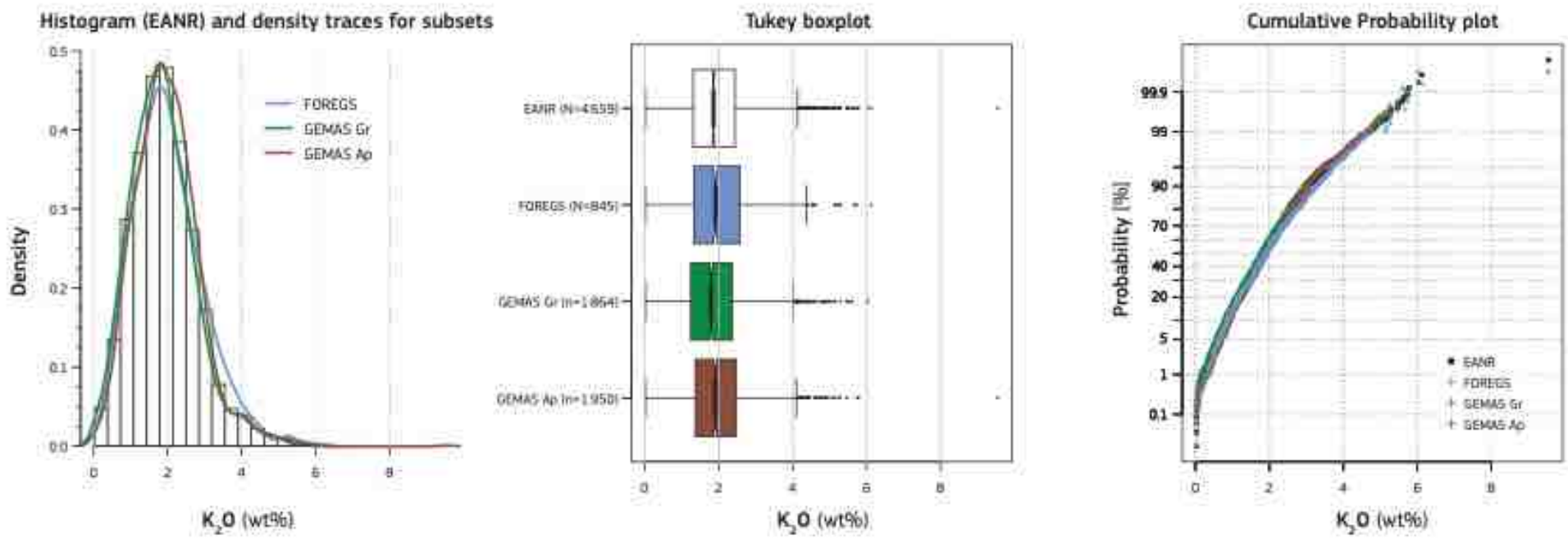

Figure 3-16.
Graphical representations of K_2O concentration (wt%) in the EANR dataset and the corresponding subsets.
Source: Graph created by A. Ferreira, T.B. Lopes, R.S. Lawley and A.M. Tye.

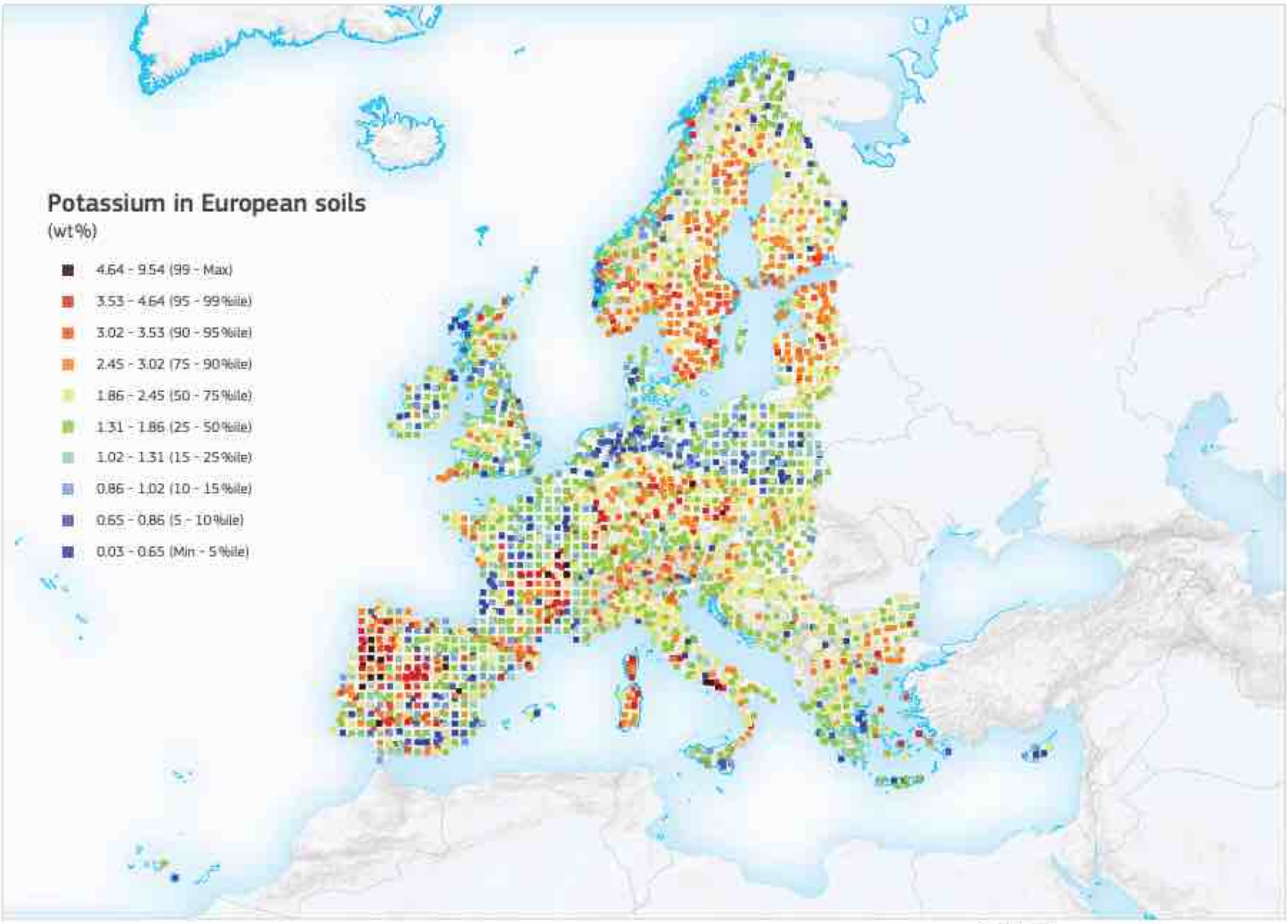

Figure 3-17.
EANR total concentration of potassium in topsoil samples over Europe (N = 4659).
Source: Graph created by A. Ferreira, T.B. Lopes, R.S. Lawley and A.M. Tye.

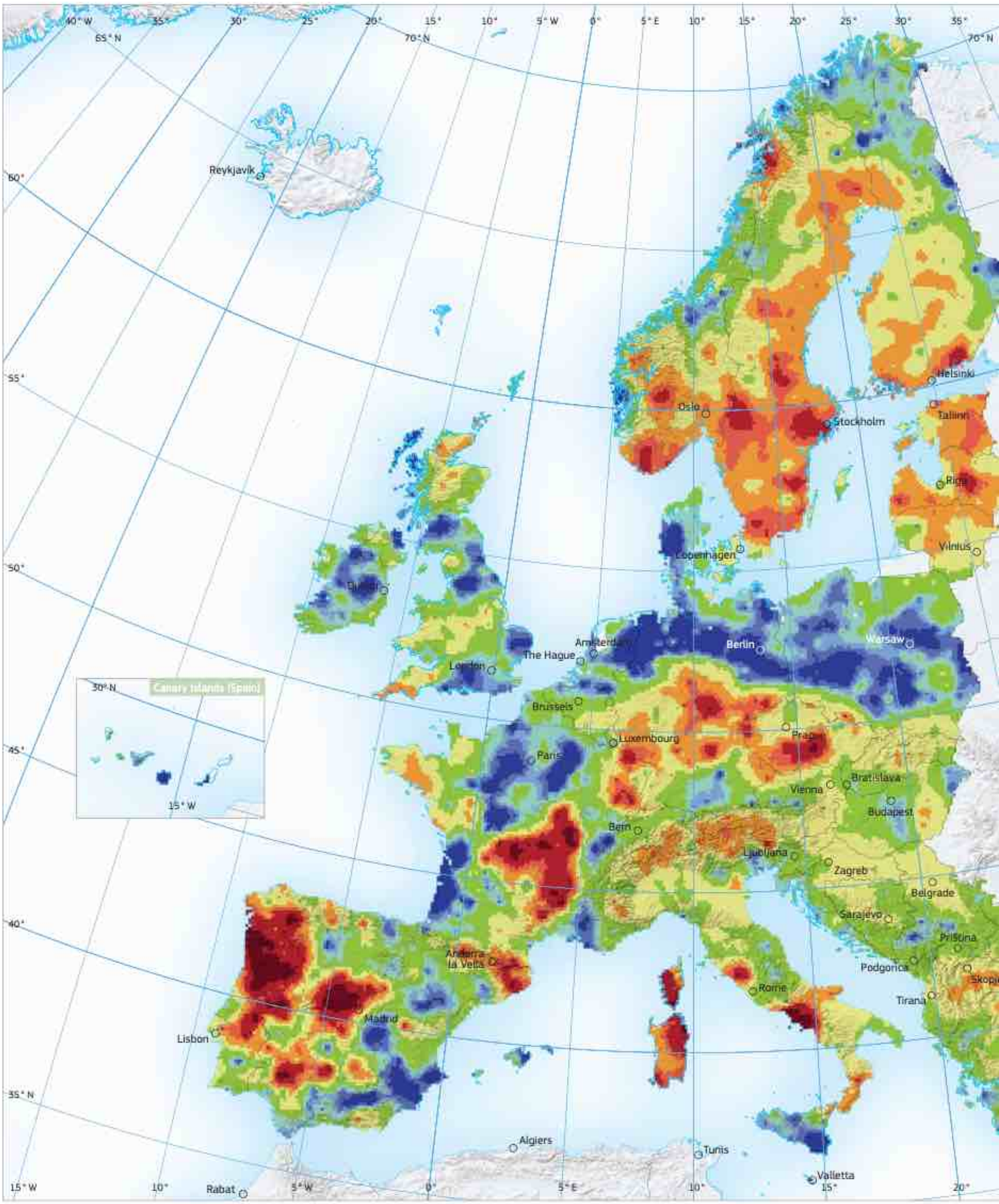
40° W
35°
30°
25°
20°
15°
10°
5° W
0°
5° E
10°
15°
20°
25°
30°
35°
65° N
70° N
70° N
60°
55°
50°
45°
40°
35° N
Reykjavik
Helsinki
Oslo
Stockholm
Tallinn
Riga
Vilnius
Copenhagen
Dublin
Amsterdam
The Hague
Berlin
Warsaw
London
Brussels
Luxembourg
Prague
Paris
Bratislava
Vienna
Budapest
Bern
Ljubljana
Zagreb
Belgrade
Sarajevo
Pristina
Podgorica
Andorra la Vella
Rome
Tirana
Madrid
Lisbon
Canary islands (Spain)
30° N
15° W
Algiers
Tunis
Valletta
Rabat
15° W
10°
5° W
0°
5° E
10°
15°
20°

copyright © European Commission, JRC, 2019

Plate 3:
Map of estimated total concentration of K_2O in topsoil over Europe

(wt%)

- 3.74 - 9.54 (99%ile - Max)
- 3.03 - 3.74 (95 - 99%ile)
- 2.76 - 3.03 (90 - 95%ile)
- 2.36 - 2.76 (75 - 90%ile)
- 1.90 - 2.36 (50 - 75%ile)
- 1.48 - 1.90 (25 - 50%ile)
- 1.30 - 1.48 (15 - 25%ile)
- 1.19 - 1.30 (10 - 15%ile)
- 1.03 - 1.19 (5 - 10%ile)
- 0.03 - 1.03 (Min - 5%ile)

Plate 3: Map of estimated total concentration of K_2O in topsoil over Europe, based on XRF data collated from the FOREGS and GEMAS European datasets as shown in Figure 3-15 and Figure 3-17. The colours are attributed according to the percentiles of the EANR-estimated map points.

Source: Map created by A. Ferreira, T. R. Lister, R. S. Lawley and A. M. Tye

Map

The EANR map of total concentration of K_2O in topsoil was produced using the 4659 samples discussed and shown in Figure 3-15 and Table 3-7.

The total concentration of potassium in EANR samples is shown in Figure 3-17.

The data shown in Figure 3-17 were interpolated, using ordinary kriging, in order to obtain the required 10 km × 10 km regular grid image of the distribution of estimated uranium total concentration in topsoil over Europe. The data were processed and maps were produced in R free software/environment using several appropriate packages, such as 'sp' and 'gstat', and according to the following steps:

i. a variogram model for the K_2O total concentration was automatically fitted to an experimental (sample) variogram (Figure 3-18);

ii. a value at each node of the 10 km × 10 km grid was computed after ordinary kriging, conditioned by the variogram model referred to in (i) and using a maximum of 13 neighbouring points in a maximum distance of 150 km radius;

iii. and the data were plotted on a colour map with class boundaries based on the percentiles of the EANR dataset.

The resulting map of estimated total concentration of K_2O in topsoil over Europe is shown in Plate 3.

Discussion and conclusions

Potassium percentiles for FOREGS data, EANR data and the resulting EANR kriging-estimated map points are shown in Table 3-8.

The negligible differences in the statistics observed between the FOREGS and GEMAS datasets (Table 3-7 and Figure 3-16) lead to a consistent EANR dataset, likely to be representative of the European topsoil potassium total concentrations. The difference between the EANR dataset and the EANR-estimated map points (Table 3-8, Figure 3-19) is a consequence of data processing, namely interpolation. Kriging, a geostatistical interpolator, like most other interpolation methods tends to overestimate the low values and underestimate the high ones, that is, to smooth values towards the central ones. This bias can be roughly assessed from the difference in percentiles found for the EANR data and for the EANR-estimated map points (Table 3-8) and from differences observed between the corresponding statistical graphs (Figure 3-16 and Figure 3-19). For instance, the cumulative probability plot for the EANR estimated map points is steeper (Figure 3-19) than that for the EANR dataset (Figure 3-16).

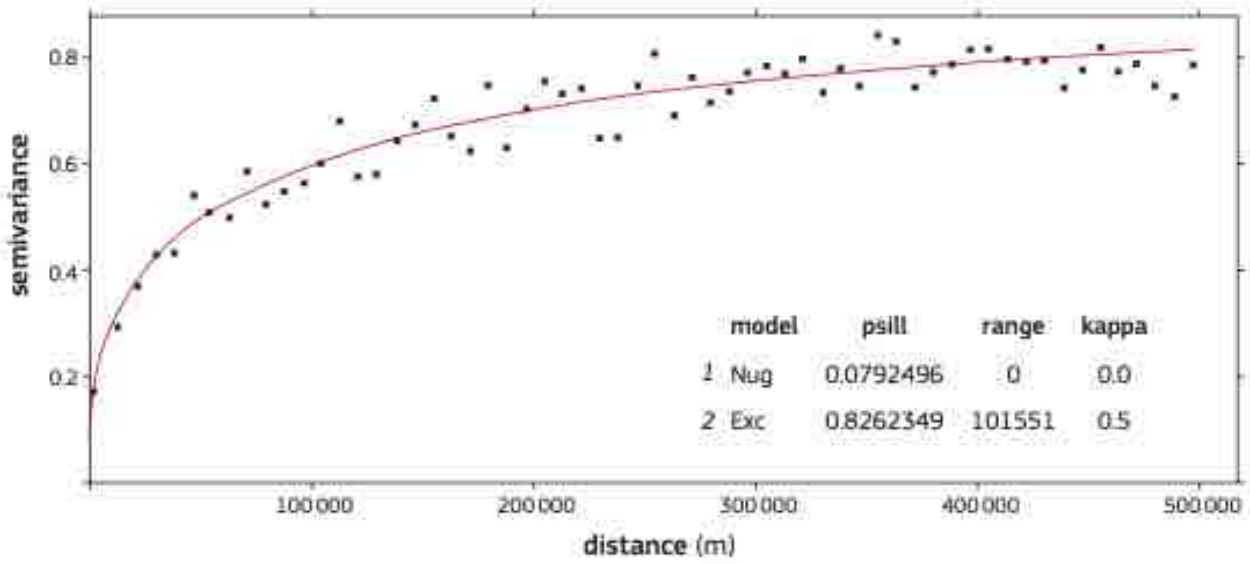

Figure 3-18.
Variogram model for K_2O in topsoil data collated from the FOREGS and GEMAS European datasets.
Nug: nugget; Exc: Exponential class.
Source: Graph created by A. Ferreira, T. R. Lister, R. S. Lawley and A. M. Tye

	Min	P5	P10	P25	Median	P75	P90	P95	Max
FOREGS	0.03	0.67	0.87	1.33	1.91	2.57	3.25	3.71	6.13
EANR data	0.03	0.65	0.86	1.31	1.86	2.45	3.02	3.53	9.54
EANR estimated	0.36	1.03	1.19	1.48	1.9	2.36	2.76	3.03	5.05

Table 3-8.
K_2O (wt%) percentiles for FOREGS (N = 845, as in Table 3-7) and for EANR data (N = 4659) and the EANR-estimated map points (N = 47 085, map).
Source: A. Ferreira, T. R. Lister, R. S. Lawley and A. M. Tye

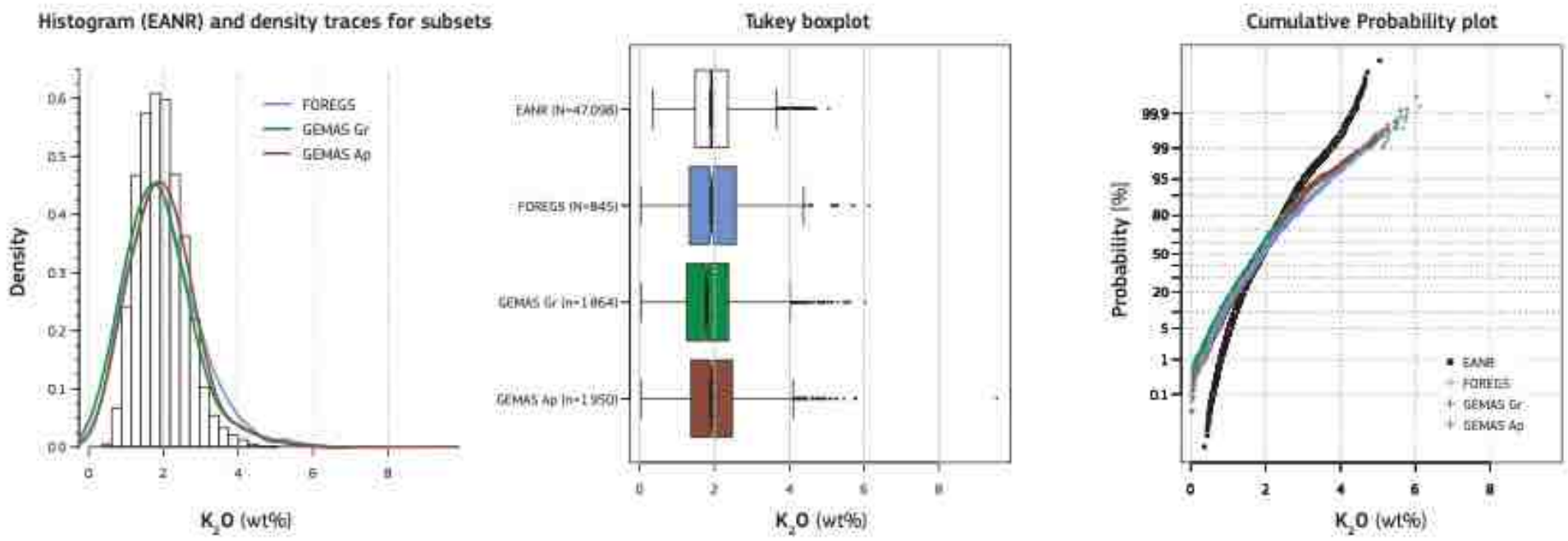

Figure 3-19.
Graphical representations of K_2O concentration (wt%) in the EANR-estimated map points and the subsets from which the map was produced.
Source: Graph created by A. Ferreira, T. R. Lister, R. S. Lawley and A. M. Tye

Potassium concentration

K_2O statistics for the EANR data are given in Table 3-7, Table 3-8 and Figure 3-16 and explained in the, Data overview, section. The potassium (as K_2O) total concentration in the EANR dataset varies from 0.03 to 9.54 wt%, with a median of 1.86 wt%. About 50% of the data show K_2O concentrations in the range of 1.31 to 2.45 wt% (areas in green and yellow on the map) around a median value of 1.86 wt%; about one quarter (25%) of the map shows K_2O concentrations below 1.31 wt% (areas in blue on the map); and the remaining quarter shows K_2O concentrations above 2.45 wt% (reddish areas on the map).

The K_2O medians observed for the overall EANR and for each of the subsets are lower than the median observed for the upper continental crust (UCC = 2.80%, Rudnick & Gao, 2003). The medians in topsoil are about 2/3 (or 6/9) of that for UCC, suggesting that soil has lost an average of about 1/3 of its K_2O provided by the parent bedrock. These values, however, cannot be directly compared, as the sum of the values for the 10 major elements as oxides (SiO_2 + Al_2O_3 + FeO + CaO + Na_2O + K_2O + MgO + TiO_2 + P_2O_5 + MnO) reported by the UCC is about 100%, while in our topsoil subsets this is not the case, summing up to between 83% for GEMAS Gr and 87% for FOREGS. This is most possibly due to the organic and/or volatile components of the soil. If these values are corrected to 100%, the median values for K_2O in the three subsets will become 2.21%, 2.16% and 2.22% for FOREGS, GEMAS Gr and GEMAS Ap, respectively (Figure 3-20), thus becoming more similar among each other and increasing to about 7/9 of that reported by UCC. Assuming that UCC and European topsoil values are accurate, this suggests that European topsoil has been depleted in K_2O relative to the UCC with about 2/9 (1 - 7/9). Weathering of bedrock and uptake from plants are likely to explain most of this depletion. The remaining difference between the UCC and the topsoil medians for K_2O shown in Table 3-7 (1/3-2/9 = 1/9) is possibly a dilution effect due to the *addition* of organic matter to soil, whether from natural biota decay or as organic fertilisers.

This simple exercise about the balance of K_2O in soil highlights the importance of the other elements in explaining a given element and in understanding the related processes, that is, the importance of taking into account the compositional nature of these geochemical datasets.

The median values for K_2O concentration as well as for other major elements, after correction to 100% in the FOREGS and GEMAS datasets, are compared with the UCC values (Figure 3-20), in a way similar to Negrel et al. (2015). P_2O_5 (in GEMAS only), SiO_2 and TiO_2 are on the left of the line X=Y, indicating an enrichment

for these elements in European topsoil relative to UCC. SiO_2 and TiO_2 are usually associated with the detrital resistate fraction of the soil, thus tend to remain in the soil. Other major elements, such as Ca, Mg, Na, may be leached (and/or taken up by plants) at a higher rate from the soil profile, thus not surprisingly positioned on the right side of the X=Y reference line (Figure 3-20). Thus, the relative enrichment of SiO_2 and TiO_2 is most likely a result of the higher leaching rate for the other major elements. Phosphorus (P_2O_5) shows a different behaviour in GEMAS, set on the left side of the X=Y line, and FOREGS, set over the X=Y line (Figure 3-20). This suggest that the higher median values observed for P_2O_5 in GEMAS datasets are perhaps a result of the generalised addition of phosphorus fertilisers to agricultural topsoil. In fact, P_2O_5 in non-agricultural topsoil types, here roughly represented by the FOREGS dataset, coincides with the value estimated for the UCC (0.15 wt%, Rudnick & Gao, 2003). At depth, the same non-agricultural soil is generally depleted relative to its topmost, as the median total concentration of P_2O_5 in FOREGS Subsoil (after correction to 100%) is only 0.11 wt% (about 0.75 of the UCC value). This suggests a general tendency for phosphorus concentrations in European natural topsoil to reach a kind of equilibrium, perhaps at the cost of a generalised depletion of the same soil at depth.

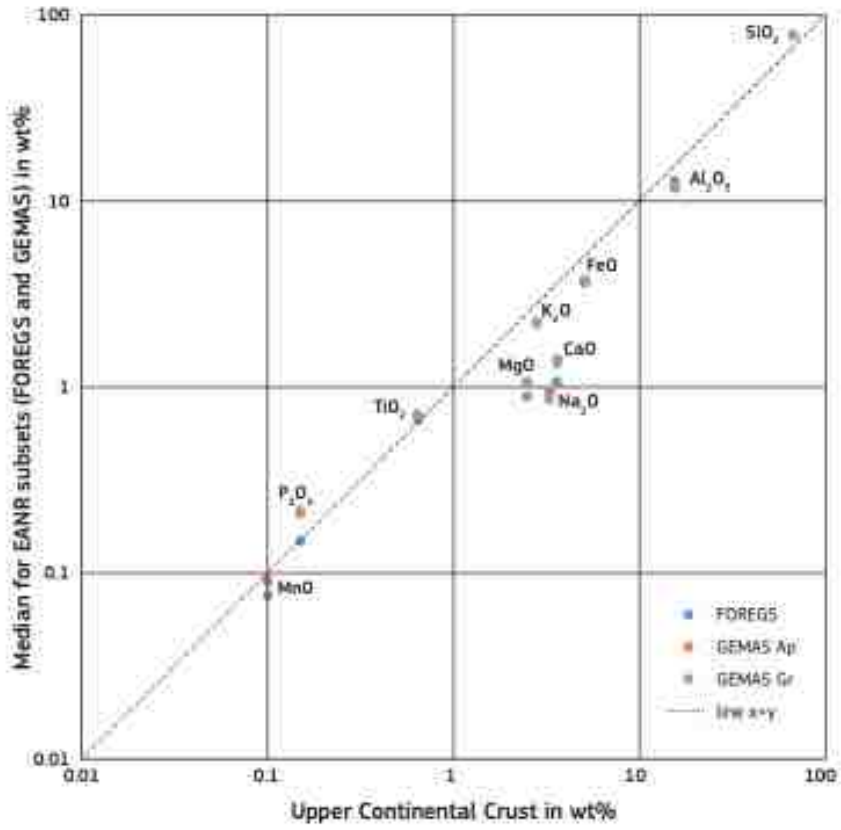

Figure 3-20.
Median total concentration of the 10 major elements (in wt%) in topsoil over Europe compared with the Upper Continental Crust average composition (Rudnick & Gao, 2003). The X=Y line is used as reference.
Source: Modified from Negrel et al. 2015

Potassium geochemical patterns

The FOREGS project has already provided a distribution map of potassium total concentration in European topsoil (http://weppi.gtk.fi/publ/foregsatlas/maps/Topsoil/t_xrf_k2o_edit.pdf), adding a short description of the geochemical patterns included in the element's factsheet (http://weppi.gtk.fi/publ/foregsatlas/text/K.pdf). Distribution patterns of potassium for both total and partial concentrations (after aqua regia and MMI®) have been provided by the GEMAS project (Reimann et al, 2014) and discussed in Chapter 8 of Cicchella et al., in Reimann et al. (2014).

An arc-like major pattern of generalised high K_2O total concentration is found in Central Europe from the Pyrenees to the Slovak Republic, delimited in the South by the valleys of the Rhone river (South France) and the Danube river (as far downstream as South Hungary), along which low K_2O values can be found. This rough lineament (arc-like) grossly coincides with the northern delimitation of the Alps. The generalised potassium high extending over Central Europe is suddenly interrupted by a generalised arc-like major pattern of low K_2O concentrations extending from Poland to Denmark, the Netherlands, Northern Belgium, Southeast England, Northern France and Southwest France. This large area of low K_2O concentrations is characterised by recent sedimentary deposits, such as (i) unconsolidated glacial drift deposits over bedrock (Plant et al., 2003, in Cicchella et al., 2014 and Negrel et al., 2018) on top of which sandy-like soils developed, namely from Poland to the Netherlands; and (ii) other sandy materials related to glacial and fluvial deposits. This low-high-low arc-like pattern is clearer on the map, and suggests a structural control for the distribution pattern of K_2O in European topsoil, somehow related to the uplift of the Alps.

In many cases the high K_2O values are spatially related to outcropping Variscan crystalline terrains, particularly granite masses, such as in the Northwestern Iberian Peninsula (from Galicia in the nortwestern-most part of the peninsula, to as far South as Sierra Morena), France (Massif Central, Armorican Massif and Vosges), Southwest England and from South Belgium (Ardennes-Rhenish Massif) to the Czech Republic (Bohemian Massif).

High K_2O concentrations are also found over Alpinide terrains (often overprinting a Variscan crystalline core), particularly North Macedonia, Northern Greece and Bulgaria, where granitic rocks outcrop, as well as in the Pyrenees axial zone, some areas over the Alps, Calabria (Southern Italy), Sardinia and Corsica. Moreover, Lazio and Campania Regions, on the Western Italian coast, show anomalous K_2O concentrations in topsoil over Cenozoic alkaline volcanic rocks (e.g. rhyolites and phonolites).

Other areas with high K_2O values can be found in other parts of Europe, e.g. an extensive anomaly over Sweden and Southern Norway, Finland, Estonia, Latvia and Lithuania, related to the Baltic Shield (Lahtinen, 2012). This is dominated by Paleoproterozoic to paleozoic granites, pegmatites and volcano sedimentary rocks.

The Haytor granite outcrop on Dartmoor, Devon, England. A tor is a large, free-standing rock outcrop that rises from surrounding smooth and gentle slopes.
Source: By Nickubica - Own work, CC BY-SA 3.0, https://commons.wikimedia.org/w/index.php?curid=28375418

Massif Central, France is a highland region formed during the Variscan orogeny. View from the highest point (Puy de Sancy) to the Pas de l'Âne.
Source: Hans-Jan Nijssen - Own work, CC BY 4.0, https://commons.wikimedia.org/w/index.php?curid=51470710

3.4 European maps of uranium, thorium and potassium concentration in bedrock

A simple methodology has been implemented to develop comprehensive maps of U, Th and K_2O concentration in bedrock (Braga et al., 2015). The methodology consists in mapping the arithmetic mean of U, Th and K_2O over geological units. The arithmetic means of the radionuclide concentrations are estimated from geochemical and radiological data compiled from scientific literature. Compiling data from literature has many advantages, such as the following:

a. a large amount of data is already available;

b. data published in scientific literature is seemingly valid and reliable with respect to the quality control (e.g. analysis of geological international standards, duplicates and/or replicates, minimisation of laboratory and/or field related contamination, among others);

c. the maps can be developed without the need for a sampling campaign and with limited resources;

d. the time-consuming procedures and expenses related to sampling design, sample collection, preparation and analysis are evaded;

e. the available data may allow a higher sampling density than that of national and/or international geochemical surveys (e.g. the compiled database for Portugal has a sampling density of approximately 1 sample per 30 km^2, whilst common sampling densities in national datasets are 1 sample per 1 000 km^2 or 1 sample per 10 000 km^2);

f. the growth of geochemical databases facilitates access to geochemical data and data-quality assessment (Greenhot & Dowsett, 2012);

g. continuous data collection for research and exploration purposes is expected, thereby increasing data availability in the future;

h. due to the simplicity of the methodology, the maps can be readily updated when new data become available;

i. and the maps developed may provide information useful to the general public as well as support further research.

Data from the OneGeology-Europe (OGE) project (Baker & Jackson, 2010) are chosen as the reference geological map to be used because they are freely available at the European level (at http://www.onegeology-europe.org/). However, the maps of radionuclide concentration in bedrock are developed on a country-by-country basis due to lack of uniformity of geological units between different countries.

OGE provides access to geological maps at the scale of 1:1 000 000 that comprise three distinct layers, namely, lithology, age and geologic structures. The lithology layer encompasses 118 different classes that constitute attributes to a given geological unit. The layer is subdivided into several datasets in order of decreasing predominance of the lithology within the geological units (e.g. umlitho_1, umlitho_2 and so forth). An example is given in Table 3-9. The age layer comprises information on the known limits of the lower and upper age of each geological unit, while the geological structures layer sets the location of faults, impact structures and fold belts, among others.

Due to the high number of geological units in the OGE map, it is necessary to simplify the OGE classification scheme in order to enable developing comprehensive geochemical maps of U, Th and K_2O concentration. The OGE classification scheme has been simplified by grouping geological units while maintaining geological coherence between the geological units. The grouping of geological units has been accomplished with expert knowledge supported by the litho-, chrono- and tectono-stratigraphic setting of each geological unit.

Upon the definition of a simplified classification scheme, geochemical and radiological data of the radionuclides studied are compiled from scientific literature and geochemical databases such as EarthChem (a database of compiled geochemical data at European level and available at: http://www.earthchem.org/portal) dealing with rock samples that belong to the geological units defined. Three types of samples are considered as valid observations:

i. individual analyses of individual samples;

ii. averages of individual samples' analyses;

iii. and analyses of composite samples.

code	ID	name	description	lowerAge	upperAge	um_litho1	um_litho2
IT033	32	GEO1MDB_32	Ophiolites: peridotites, gabbros, basalts, serpentinites and ophiolitic breccias with various grade metamorphism	Jurassic	Jurassic	Peridotite	Gabbro
IT034	33	GEO1MDB_33	Tectonic melanges, locally with low-grade metamorphism. Emplaced during Miocene	Miocene	Miocene	Clastic sedimentary rock	missing

Table 3-9
Example of OneGeology-Europe data
Source: Baker & Jackson, 2010

Measurements of U, Th or K_2O concentration by electron microprobe on single crystals and chemical and radiological analyses carried out on enclaves, xenoliths, veins or highly altered materials (such as fault rocks) are discarded due to their lack of representativeness of the geological unit sampled. Sample averages are treated statistically as individual samples.

For each observation of U, Th and/or K_2O concentration, the sample identification, location (latitude and longitude), the lithology and the analytical technique used to determine the radionuclide concentration are registered as attributes in the compiled database as (or if) stated by the authors. The radionuclide concentrations are then converted into a similar reference unit using appropriate conversion factors.

All observations are considered valid (regardless of the analytical technique used in the analysis) and representative of the geological units sampled by the authors. No corrections are applied with respect to loss on ignition or volatile content. Values stated by the authors as below the detection limit (DL) as well as zero values are either set to half of the DL value (if reported by the authors) or to an arbitrary small value.

The compiled data are assigned to the geological units based on the litho-, chrono-, tectono-stratigraphic and geographical setting of the samples. If the assignment of an observation to a geological unit is uncertain due to the lack of qualitative information, the observation is excluded from the compiled dataset.

Checking the compiled dataset for quality control involves evaluating the precision and accuracy of the data by comparing the compiled data to available datasets at the scale required (i.e. national and/or international geochemical or radiological datasets) using the geological units as reference units.

The size of the effects of the analytical techniques and the geological classification scheme are assessed and compared through the percentage of variation explained by those effects, calculated through an analysis of variance. If the effects of the analytical techniques are statistically significant, further investigations are carried out to evaluate the compatibility of the datasets acquired with the various analytical techniques. Normalisation of the datasets from different analytical techniques may be attempted; otherwise, the datasets that fail the compatibility tests are discarded from the compiled database.

After an adequate evaluation of data quality, the descriptive statistics and the distribution of the radionuclides are studied within each geological unit. Values lower than the first quartile minus 1.5 times the interquartile range (IQR) or higher than the third quartile plus 1.5 times the IQR are considered outliers and then discarded. The remaining data are used to estimate the arithmetic mean contents of U, Th and K_2O in bedrock.

The maps of U, Th and K_2O concentration in bedrock display the arithmetic mean concentration of the radionuclides for each geological unit defined.

The concentrations of U and Th are expressed in parts per million (mg/kg), while the concentration of K_2O are displayed in percentages (%). References to scientific literature used to compile the data are given as supplementary material at https://remon.jrc.ec.europa.eu/About/Atlas-of-Natural-Radiation.

Plane spraying fertiliser onto crops.
Source: Bryan Peterson, https://www.flickr.com/photos/bryanpeterson/6254915478/ (CC BY-NC-ND 2.0)

Silage harvesting in Clonard, Co. Meath, Ireland.
Source: Peter Mooney, https://www.flickr.com/photos/pmooney/2727513280/ (CC BY-SA 2.0)

copyright © European Commission, JRC, 2019

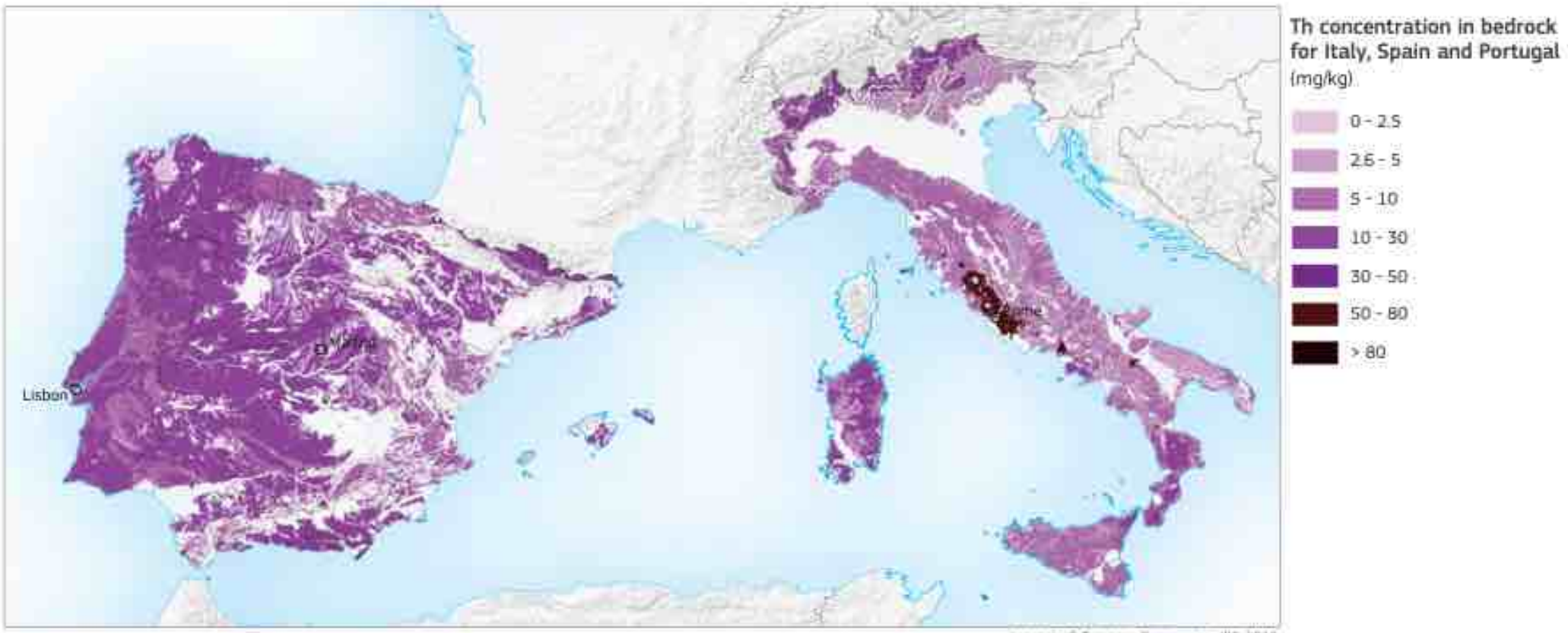

copyright © European Commission, JRC, 2019

Figure 3-21
As examples we show maps of uranium, thorium and potassium concentration in bedrock for Italy, Spain and Portugal.
Source EANR, EC-JRC, 2019

copyright © European Commission, JRC, 2019

3.4.1 Discussion and conclusions

Developing the maps of U, Th and K_2O concentration in bedrock for the EANR has proven to be a long and demanding task. A lack of comprehensive and homogeneous geochemical databases as well as mapping methods among different European countries forced implementation of a methodology that was economically sustainable and, at the same time, applicable in every country.

The maps provide useful information with respect to the distribution of the radionuclides in bedrock; however, the following limitations of the methodology must be taken into account:

a. the sampling methodology and sampling density is heterogeneous within and between different geological units;
b. the degree of alteration of the materials sampled is unknown and thus inconsistent between the surveys;
c. individual surveys may not be designed to represent the bedrock at the required scale;
d. the preparation of the samples prior to the chemical analyses is different as both destructive (e.g. total or partial digestion of the samples using various acids, preparation of fusion beads) and non-destructive (e.g. loose powders, pressed pellets) techniques can be used, depending upon the analytical technique chosen for the analysis;
e. the analyses are carried out at different laboratories with various instruments and different analytical techniques, thus the limits of detection and the precision of the analytical techniques are different between the various datasets;
f. information about data quality (e.g. instrument calibration, precision, etc.) often not provided by the authors;
g. the location of sampling sites may be unknown, inhibiting the use of geostatistical tools to estimate the radionuclides content in bedrock;
h. uranium and thorium contents are rarely acquired for sedimentary rocks, so the number of available data in scientific literature for them can be limited;
i. and the professional judgment involved in selecting and grouping the geological units conditions estimation of uncertainty and thus the use of the results in decision-making processes.

All these problems are difficult to deal with, and unfortunately there are no simple solutions.

Concerning the sampling methodology, density and data representativeness, there are several geological units that are extremely under-represented (Nogarotto, 2018), and the average concentration values found for them could be misleading. This is especially true for sedimentary units, since geochemical analysis is very rarely carried out in stratigraphic and sedimentologic studies. The only way to overcome this problem would be to improve the existing database by increasing the number of samples and their coverage; this can be done by funding new sampling campaigns and/or by complementing the databases with already existing data from inaccessible published articles and from well and boreholes data acquired during hydrocarbon exploration (through techniques such as gamma-ray log and neutron log). If more data become available, the accuracy of this method can obviously be improved.

The reliability of the data could be improved if detailed and precise information about the sampling location (with geographic coordinates), the geological background and the analytical technique were available, which would also allow the use of geostatistical tools to generate unbiased and reliable estimates of radionuclide concentration in bedrock. However, problems related to the different analytical techniques and instruments used to acquire the data cannot be solved; the effects of the analytical techniques have been estimated for Italy, on average being lower than 15 %, and much lower than the variance explained by geological factors, averaging more than 50 % (Nogarotto, 2018).

In the Portuguese project, the terrestrial gamma dose rate (TGDR) calculated from the compiled data was compared to the Radiometric Map of Portugal (Batista et al., 2013) that displays the TGDR across mainland Portugal. Despite the significance of the effects of analytical techniques, the arithmetic means contents were significantly correlated between the two datasets, and pairwise comparisons show that the differences between the datasets are not statistically significant. The differences observed were mostly due to the under- or overestimation of some units' average concentration due to a lack of data representativeness (most significantly in sedimentary units) and to limitations associated with estimating the TGDR from the radiometric data. Nonetheless, the variance explained by the analytical techniques was lower than 5 %.

The main problem regarding the methodology implemented to map U, Th and K_2O concentration in bedrock remains the huge geological variability within each geological unit, which is by far the major cause of variance between the data. This is implicit in the methodology, because the realisation of large-scale maps implies grouping heterogeneous material. The only solution to this problem would be to reduce the scale of the mapping processes; however, more data would be necessary to develop comprehensive maps. Given that the purpose of the EANR is to study natural radioactivity on a European scale, the use of large-scale units is justified considering the low number of data available for some geological units and the ease of processing a lower number of units.

The maps developed so far for Italy, Spain and Portugal show that there are areas that can be considered safer from the point of view of exposure to natural radiation. Ultramafic units have always extremely low contents of terrestrial radionuclides, averaging < 1 mg/kg of U, < 2 mg/kg of Th and <0.5 wt% of K_2O. Mafic units also have low contents of these elements, even though they are more heterogeneous. In Italy, mafic rocks have contents ranging from 0.9 ± 0.5 to 3.9 ± 1.6 mg/kg of U, from 2.6 ± 1.6 to 14.4 ± 6.4 mg/kg of Th and from 1.0 ± 0.5 to 2.5 ± 1.1 wt% of K_2O. In Spain, the mafic units have on average 0,4 mg/kg of U, 1.3 mg/kg of Th and 0.5 wt% of K20, while in Portugal, the mafic unit has on average 1.6 ± 2.2 mg/kg of U, 5.1 ± 4.9 mg/kg of Th and 1.4 ± 1.3 wt% of K_2O. Carbonate units may also have low contents of U, Th and K_2O, but this highly depends on the percentage of siliciclastic rocks found in them and on the proportion of collected data between the two types of rock. As a matter of fact, Mesozoic carbonates of Italy show average contents of 1.0 ± 1.1 mg/kg of U, 3.1 ± 2.7 mg/kg of Th and 1,4 ± 1,1 wt% of K_2O, while those of Portugal show higher average contents of 3.8 ± 2.3 mg/kg of U, 15.6 ± 7.4 mg/kg of Th and 3.1 ± 1.1 wt% of K_2O.

Furthermore, the maps of U, Th and K_2O concentration in bedrock are a viable option to point out the regions which are correlated with a higher risk of exposure to natural radiation, so that further studies can be commissioned. This is the case of the Latium Plio-Quaternary volcanic province in central Italy (which has already been subject to numerous studies, e.g. Beaubien et al., 2003; Cinelli et al., 2015), with average contents of 11.4 ± 7.5 mg/kg of U, 56.6 ± 38.5 mg/kg of Th and 5.8 ± 2.8 wt% of K_2O, and of the Paleozoic granitic rocks of Portugal, with average contents of 9.4 ± 5.8 mg/kg of U, 18.6 ± 19.6 mg/kg of Th and 4.7 ± 0.9 wt% of K_2O, with which a high risk of exposure to radon is also associated (e.g. Pereira et al., 2017). All the interpretations must take into account that these concentrations refer to mean values related to large-scale units and are not meant to be representative of medium to low-scale observations.

The results achieved so far demonstrate that this methodology can be reliable and allow a better understanding of bedrock contribution to natural radioactivity. While the maps developed here cannot be used in decision-making processes because the professional judgement involved in selecting and grouping the geological units inhibits a proper estimation of uncertainties, the results set the groundwork for further research.

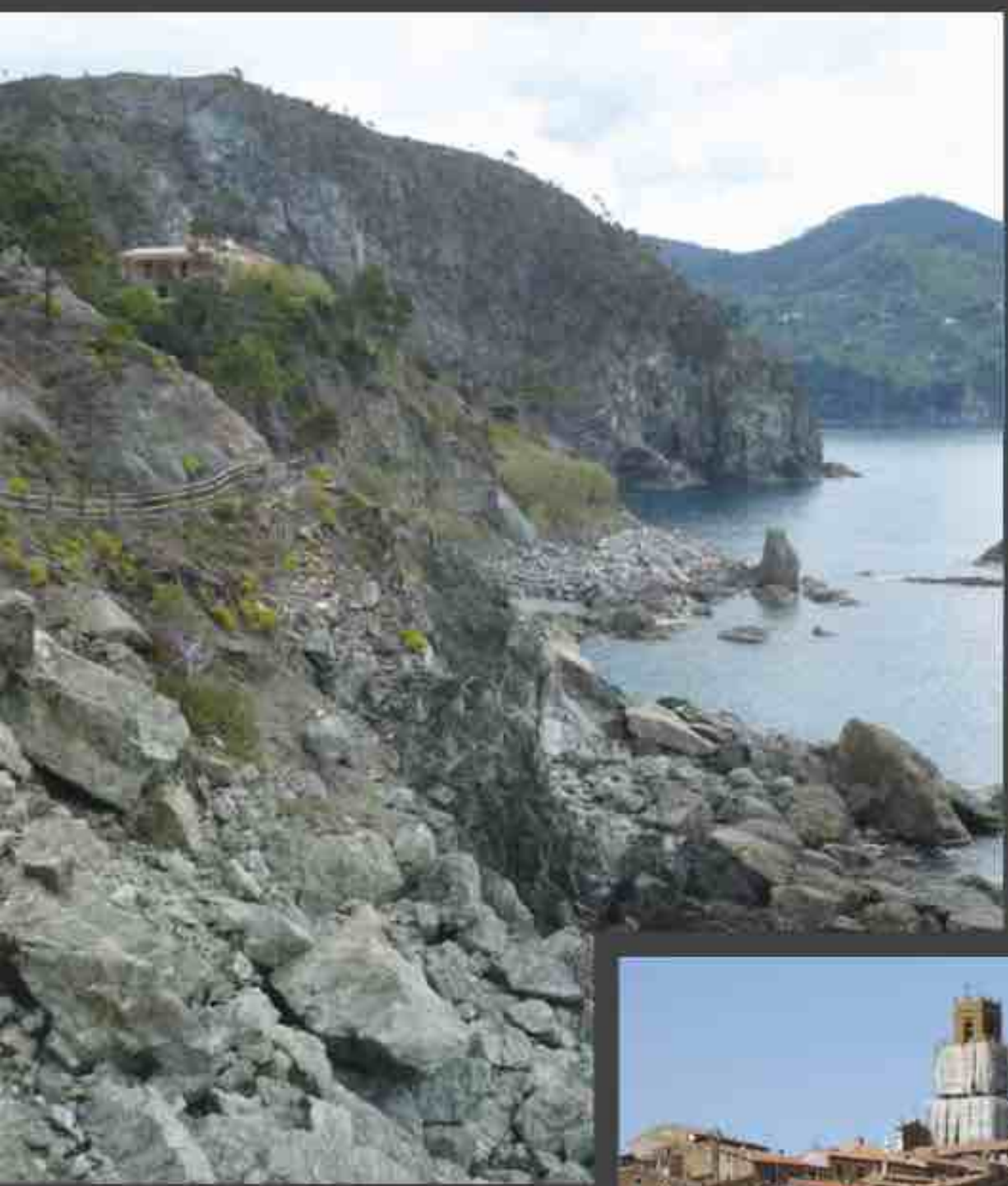

Chapter 4

Terrestrial radiation

Gamma radiation from terrestrial sources is an important component of the natural radiation environment. Natural sources of terrestrial gamma radiation are considered in the light of mapping the dose rate from gamma rays emitted by these sources. In this respect, the radioactivity properties of potassium (K), thorium (Th) and uranium (U) are of particular interest, because terrestrial gamma radiation is mostly caused by isotopes of the radioactive decay series of ^{238}U, ^{232}Th, ^{235}U and the radioactive isotope ^{40}K. With a half-life of 1 248 million years, ^{40}K is a long-lived isotope and represents 0.0117 % of the total mass of potassium. Since the presence of ^{235}U in natural uranium is only 0.72 %, a more significant source of gamma radiation is the ^{238}U decay series. In both the ^{238}U and ^{232}Th series, gamma radiation is mainly emitted by their daughter products, and not by the parent isotopes.

The radioactivity levels of rocks can vary considerably depending on their type. The presence of radioactive elements in soils is mostly governed by the parent rock and the climatic conditions in the region. Due to their interaction with matter, gamma rays rarely penetrate more than tens of centimetres in soil/rocks. Actually, about 95 % of terrestrial gamma radiation above the Earth's surface originates from the top 35 cm surface layer of the rock-soil medium.

This chapter discusses methods for mapping terrestrial dose rate, which is only component of gamma dose rate in the environment, as well as decomposition of signals from gamma detectors. Also addressed are the spatial and temporal variability of natural terrestrial dose rate and the variability of dose rate from nuclear fallout.

Terrestrial gamma dose rate can be determined by measurements or indirectly by using geochemical data. Experimentally, the dose rate can be determined either by total count rate measurements or by field gamma-ray spectrometry. In both cases, calibrating radiometric instruments is fundamental for correctly converting measurement data into dose rate. Opportunities for using measurement data generated by European countries and transferred to the European Radiological Data Exchange Platform (EURDEP) System are discussed. Prospects for using new types of spectrometric detectors and new monitoring techniques are outlined.

Within the indirect approach, TGDR is determined by using activity concentrations of ^{40}K, ^{238}U and ^{232}Th, respectively, in rock-soil medium (according to UNSCEAR, 2008). This approach has been used to create the European Terrestrial Gamma Dose Rate Map (in nGy/h). Furthermore, TGDR is converted to external effective dose to adults. The European Annual Terrestrial Gamma Dose Map shows the annual effective dose (in mSv) that a person would receive from terrestrial radiation, if she/he spends all the reference time in a location where the soil has fixed U, Th and K concentrations.

Clockwise from top-left:

Outcrops of dunite, serpentinised peridotite and clinopyroxene-rich coarse gabbro around Bonassola (Liguria, Italy). They are rocks with low activity concentrations of natural radionuclides.
Source: Giorgio Dinelli

Pyroclastic deposit in the Vulsini Volcanic District, an area characterised by a high natural background radiation (Latium, Italy).
Source: Giorgio Dinelli

A crop field in the Vulsini Volcanic District, an area characterised by a high natural background radiation (Latium, Italy).
Source: Giorgio Dinelli

In situ gamma spectrometry measurement in the Vulsini Volcanic District, an area characterised by a high natural background radiation (Latium, Italy).
Source: Giorgio Dinelli

View of Pitigliano, a town built on tuff with volcanic rocks (Latium, Italy).
Source: Laura Trotti

Terrestrial radiation

This chapter discusses natural sources of terrestrial radiation, their radiological properties as gamma radiation, and the relevance of mapping dose rate generated by gamma rays which are emitted by these sources. Moreover, the European Terrestrial Gamma Dose Rate Map is shown.

4.1 Source of terrestrial natural radiation

Terrestrial radiation, a significant component of the natural radiation environment, is generated by natural radionuclides in rocks and reflects the Earth's surface geological setting. More than twenty primordial natural radionuclides in rocks, formed during the origin of the Earth 4.6 billion years ago, are the sources of alpha, beta and gamma radiation in rocks. Due to their contents in rocks and their radiation intensity, primordial radionuclides of potassium (K), thorium (Th) and uranium (U) are the fundamental sources of radioactivity in rocks. The half-lives of prominent natural radionuclides are very long (e.g. for ^{40}K, $T_{1/2}$ = 1.3*10^{9} a; for ^{238}U, $T_{1/2}$ = 4.47*10^{9}; and for ^{232}Th, $T_{1/2}$ = 1.39*10^{10} a), and K, U and Th are permanent sources of terrestrial radiation (more details in Section 2.2 and Chapter 3). Uranium and thorium form natural decay series whose decay products contribute to overall terrestrial radiation. Radioactivity of rocks is predominantly determined by the detection of gamma rays and expressed as gamma dose rate (Gy/s, practically nGy/h), or as the contents of single radionuclides. The gamma dose rates generated individually by K, Th or U in rocks of the Earth's crust are of the same order of magnitude.

Among primordial gamma-radiating radionuclides which have no radiological importance in our context, are ^{50}V, ^{87}Rb, ^{138}La and ^{176}Lu (more details in Section 2.2).

4.1.1 Radioactivity properties of K, Th and U

Potassium (K) is an alkali metal (with one main oxidation state: +1) with an atomic mass of 39 and three natural isotopes, including two stable ones, ^{39}K (93.2581 % of K total mass), ^{41}K (6.7302 % of K total mass), and the long-lived (1248 million years half-life) radioactive ^{40}K (0.0117 %). The latter decays either to ^{40}Ca (89.28 %) by emitting a beta particle, or to gas ^{40}Ar (10.72 %) by emitting a gamma ray with energy of 1.46 MeV after electron capture (Figure 4-1a).

Figure 4-1 presents gamma-ray energy emission line spectra of potassium, uranium decay series and thorium decay series. Simplified gamma-ray spectra illustrate the most significant energy lines contributing to terrestrial gamma dose rate and are used for radioelement analyses. Since ^{40}K occurs as a fixed proportion of K, these gamma rays can be used to estimate the total amount of K present in analysed rocks. The determination of K by gamma-ray spectrometry is direct. The relationship between units of mass concentration of potassium and its specific activity is 10 g/kg K ~ 313 Bq/kg of ^{40}K (IAEA, 1989). By emitting ~ 3.1 gamma quanta/s per 1 g K, potassium contributes to terrestrial gamma dose rate.

Potassium is a widespread element in the lithosphere, with the highest concentrations occurring in magmatic and metamorphic rocks containing potassium: namely, feldspars, leucite, nepheline, biotite, muscovite, sericite and phlogopite. An increased concentration of potassium is common in pegmatites and clays and accompanies alterations at some deposits. Potassium is mobile in the geological environment. Potassium (K) is preserved in the Earth's upper crust in concentrations between 20 and 25 g/kg K.

Thorium (Th) is an actinide-series element with an atomic number of 90 and an atomic mass of 232. Thorium is radioactive with one main natural isotope, the primordial, long-lived radionuclide ^{232}Th, which has the longest half-life (1.405 × 10^{10} years) of all known radioactive isotopes and comprises 99.98 % of the total mass of Th. Thorium decays through a long radioactive decay series, ending with the stable lead isotope ^{208}Pb.

Energy emitted by gamma rays of isotopes of ^{232}Th decay series is in the range up to 2.615 MeV (Figure 4-1b). Since ^{232}Th is not a source of gamma rays, analysis of thorium in rock environment is performed by detecting gamma rays of suitably selected daughter products in the ^{232}Th decay series (see Section 2.1). The relationship between mass concentration of thorium and its specific activity is given by 1 mg/kg Th ~ 4.06 Bq/kg of ^{232}Th (IAEA, 1989).

Thorium, with many complex geochemical forms, occurs in increased amounts in accessory minerals such as zircon, monazite, allanite, sphene, xenotime and apatite. Thorium in tetravalent state exhibits low solubility. Thorium (Th) crustal abundance is 7 – 12 mg/kg Th.

Uranium (U) is a heavy actinide-series element (with an atomic number of 92) with two main natural, primordial, long-lived radionuclides, including the more abundant ^{238}U (half-life of 4.5 × 10^{9} years, 99.274 % of the total mass of U) and the less abundant ^{235}U (half-life of 7.0 × 10^{8} years, 0.72 % of the total mass of U), both decaying separately through long and complex radioactive decay series, ending with stable lead isotopes (^{206}Pb and ^{207}Pb, respectively). Another natural uranium isotope ^{234}U (half-life of 2.4 × 10^{5} years, 0.0056 % of total natural uranium), is the third decay product in the ^{238}U radioactive decay series. This uranium isotope is generally considered in equilibrium (to slightly deficient) with its progenitor ^{238}U. The ^{238}U/^{235}U ratio has increased over time due to faster radioactive decay of ^{235}U, being at present 137.5 ± 0.5 (Wedepohl, 1978a).

The ^{238}U and ^{235}U isotopes are mother elements of decay series, whose daughter elements are sources of alpha, beta and gamma radiation. The ^{238}U series is more important as a source of gamma radiation in rocks than is the ^{235}U series, since the presence of ^{235}U in natural uranium is low (0.72 %). The energy of emitted gamma rays of ^{238}U decay series is generally in the interval of 0 – 2.2 MeV, while single energy lines are typical for individual radionuclides (Figure 4-1c). Analysis of U in rocks is mostly carried out by detecting selected energy of gamma rays of daughter products of the ^{238}U decay series. Conversion between mass concentration of natural uranium and its ^{238}U specific activity is given by the relation: 1 mg/kg U ~ 12.35 Bq/kg of ^{238}U or ^{226}Ra (IAEA, 1989). Specific gamma-ray emission of U is approximately given as ~ 33 gamma quanta/s per 1 g U (Kogan et al., 1969).

Uranium in rocks has many complex geochemical forms and occurs in primary uranium minerals and secondary uranium minerals formed under oxydation. Minerals with uranium as a major constituent include uraninite (pitchblende), betafite, coffinite, while those with uranium as a minor constituent include zircon, xenotime, monazite, orthite, apatite and sphene. Uranium in tetravalent state is generally geochemically stable, while uranium in its hexavalent state is soluble and mobile in the geological environment, and as a result the radioactive equilibrium in ^{238}U decay series can be disturbed due to uranium mobility. Uranium has an average crustal abundance of 2 – 3 mg/kg U.

4.1.2 Radioactivity as a function of rock type (see also Chapter 3)

Natural radionuclide contents vary widely between and within different types of rock (magmatic, metamorphic, sedimentary). The radioctivity levels of magmatic rocks tend to increase with the acidity of the rocks. Granite, granodiorite and syenite are usually highly radioactive, while basic and ultrabasic magmatic rocks are characterised by extremely low radioactivity. The radioactivity of sedimentary rocks is mostly related to the composition of material undergoing sedimentation. Enhanced radioactivity has been observed in clays, phosphates, potassium salts and bituminous sediments. Limestones, gypsum and quartzites all belong to the least radioactive sediments. The radioactivity of the metamorphosed rocks corresponds mainly to the primary rock material. Some orthogneisses and composite gneisses (migmatites) display fairly high activity, whereas amphibolites and serpentinites belong to the least radioactive. Fluidal magma component penetrating crystalline rocks can be enriched by potassium or silicates which enhances or reduces rock radioactivity. The presence of radioactive elements in soil is mostly governed by the parent rock and climatic conditions of the region. Depending on the solubility of radioactive elements and the direction of water inflow or evaporation, the soil may either be enriched or depleted by single radionuclides. General trends show a 0 – 30 % relative decrease in radioactive elements in soils in comparison with the radioactive elements in the geological basement (Dickson & Scott, 1997; IAEA, 2003).

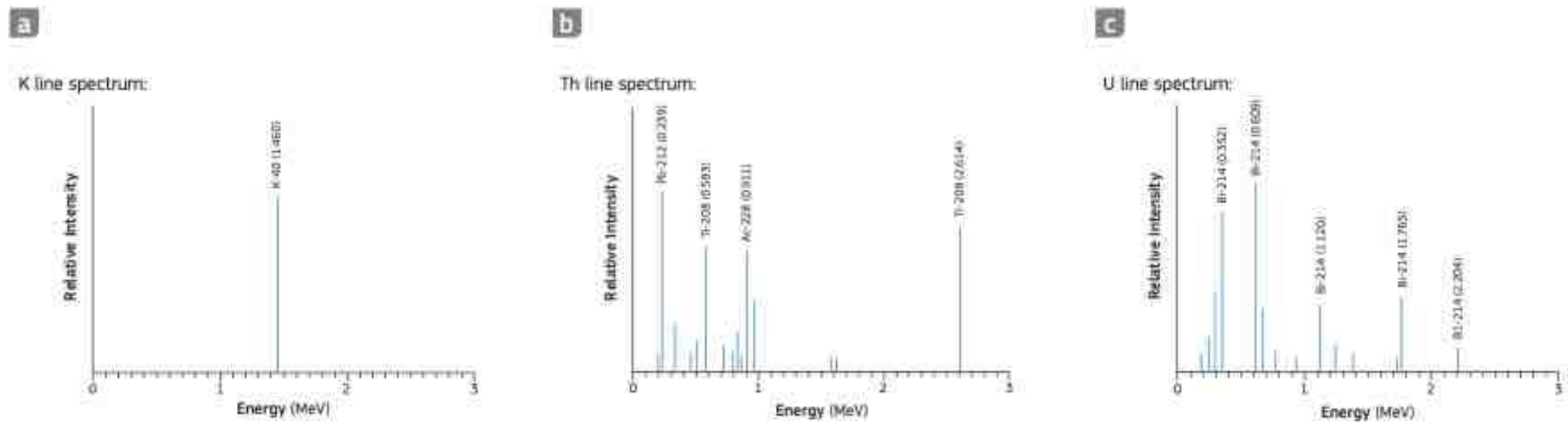

Figure 4-1
Gamma-ray energy emission line spectra of potassium, thorium and uranium
Source: IAEA, 2003

Example: Variability of K, Th and U concentrations in the Czech Republic

While the radioactivity of identical lithological types of rocks in single European countries varies, the current contents of radioelements in some rocks are illustrative. For example, Table 4-1 introduces typical low and enhanced contents of K, Th and U in rocks of the Bohemian Massif, Czech Republic, and corresponding terrestrial gamma dose rate. Data in Table 4-1 do not correspond to the extremely high radioactivity values found in Cambrian Alum shales in Scandinavia or those of local volcanic rocks found in southern Europe. Numerous illustrative data on radioactivity of rocks, their contents of K, Th and U and their research have been published (Matolín, 2017).

Figure 4-2
Index map of the Czech Republic with localities quoted in the Table 4-1.
Source: Data on field gamma-ray spectrometry from various projects on radioactivity of rocks in the Czech Republic (Matolín, 2017), modified by Lenka Mihalík.

Locality	Rock	K	Th	U	Dose rate
		g/kg	mg/kg	mg/kg	nGy/h
1 Adršpach	sandstone	1	2.1	0.6	9.9
2 Křucemburk	sandstone	9	4.2	1.8	33
3 Příbram	schist, graywacke	10	5.2	2.4	40
4 Dol. Rožínka	paragneiss	17	8.7	3.5	63.9
5 Říp	alkaline basalt	12	13.6	3.4	68.9
6 Příbram	granodiorite	20	13	3.4	78.5
7 Budíkov	durbachite	32	24	5.9	135.2
8 Bezděz	phonolite	51	32	8.6	195.5
9 Teplice - Cínovec	rhyolite	47	41	12	231.6

Table 4-1
Typical concentrations of K, Th and U in rocks of the Bohemian massif, Czech Republic, and the corresponding terrestrial gamma dose rate.
Source: Matolín, H. (dose rate based on spectrometry from various projects on radioactivity of rocks in the Czech Republic)

4.1.3 Terrestrial gamma rays in the environment

The gamma-ray field of a rock – soil medium (terrestrial radiation) is generated by the natural radionuclides in rocks–soils and is affected by the composition and physical state of rocks–soils. Gamma radiation is defined as electromagnetic radiation with wavelength on the order of 10^{-12} m and frequency on the order of 10^{18} Hz. Gamma rays emitted by natural radionuclides, in rocks primarily by K, Th and U, penetrate through matter. The photoelectric effect, Compton scattering and pair production are the fundamental processes by which gamma rays interact with atoms in matter. The cross section (probability of interaction) is a function of their energy and the elemental composition of the matter. The gamma rays are partly absorbed or their emission energy decreases gradually through Compton scattering.

The dispersion of gamma radiation above various geological sources depends on source radioelement, source physical dimensions, and on the detector – source geometry. Gamma radiation of a certain energy emitted by a point source (small geological surface object) is determined by the relation:

$$I_r = \frac{k * m}{r^2} e^{-\mu r} \qquad (4\text{-}1)$$

where:
k is the constant expressing gamma radiation of a particular radionuclide;
m (kg) is the mass of the radionuclide;
r (m) is the distance from source to detector; and
μ (m^{-1}) is the linear attenuation coefficient of gamma rays along their path.
The linear attenuation coefficient μ depends on the gamma energy and on the composition of the medium. The unscattered gamma-ray field of an infinite plane geological body at height h is attenuated at height h according to the relation:

$$I_h = I_0 * E_2(\mu h) \qquad (4\text{-}2)$$

where:
I_0 is the ground intensity of radiation; and
$E_2(\mu h)$ is the integral exponential function of the second kind for the argument μh.

While attenuation of gamma rays with distance r from a point source is significant, the gamma-ray field over an infinite rock source (the Earth's surface) at an altitude of h = 80 m is approximately one half of the ground value I_0.

Physical models of gamma-ray fields define sources of gamma radiation, its geometry, intensity and energy of gamma rays, elemental composition and geometry of absorbing media, distance between the source and point of gamma-ray field evaluation, and attenuation of gamma rays in the matter. Literature (e.g. Mares et al., 1984; Grasty, 1987; IAEA, 1989; ICRU, 1994; IAEA, 2003) introduces various mathematical models enabling estimates of gamma-ray fields of point sources, linear sources and three-dimensional sources of gamma radiation, the latter modelling geological environment. Specification of gamma-ray detectors is fundamental for estimating radiometric measurements and their precision and errors (more details about detectors in Section 2.5). Attenuation of gamma rays in the rock environment limits their penetration range. Theory and experiments show that gamma rays generated by natural radionuclides in rocks are nearly absorbed by any media having the area density 100 g/cm². Thus 95% of the gamma radiation recorded on the Earth's surface originates from the top 35 cm of the soil.

Various environmental effects change the gamma-ray field over rocks. The significant parameters are soil moisture, surface snow layer, mass of surface vegetation, precipitation of air radon (^{222}Rn) daughter products (^{214}Pb and ^{214}Bi) which leads to an instant increase of surface gamma radiation, changes of radon emanation power, temperature and pressure effects on the atmospheric air density and its gamma rays attenuation, and topography and its geometrical effects.

Terrestrial gamma dose rate (see below for definition) is just one component registered on the Earth's surface. A gamma radiometric instrument on the surface registers terrestrial radiation, cosmic radiation, gamma rays of daughter products of aerial radon, internal radioactivity of radiometric equipment and the platform and nuclear fallout (see Section 4.2.4). In geophysical rock radiometric mapping, radiation originating not from the rock environment is regarded as 'background', i.e. caesium-137 (^{137}Cs) contamination is removed during data processing.

4.2 Dose rate

4.2.1 Ambient dose rate

Ambient dose rate (ADR) is the generic term used for dose rate at a location, usually in free air.

a. Kerma and absorbed dose

The kerma ('kinetic energy released per unit mass' (acronym: kerma)), denoted K, is the total initial kinetic energy of all charged particles set free by uncharged particles (photons, neutrons) per unit mass of a medium. It is expressed in units of gray (Gy). 1 Gy = 1 J/kg. The energy which is actually deposited in and therefore absorbed by or imparted to the mass element, is called absorbed dose (D) in a medium, again expressed in Gy. The difference between kerma and absorbed dose lies in the fact that part of the energy set free in the mass (i.e. kerma) escapes and is deposited outside. Therefore K ≥ D. This effect is important for higher incident energy. For example, bremsstrahlung escapes and is not deposited in the mass element, but outside, and is not counted as absorbed dose. For exact definitions, see ICRU (2011). Environmental dose rates are frequently reported as kerma rates in nGy/h. While lower gamma energies are typical of most ambient radiation, kerma and absorbed dose rates in an instrument are almost equal.

b. Dose equivalent

In environmental monitoring the quantity generally reported is the **ambient dose equivalent rate (ADER)**, which denotes the energy deposited in a certain material per unit of time, such as tissue. It is calculated from absorbed doses by applying weighting factors. It is expressed in units of sievert (Sv), also 1 Sv = 1 J/kg. The difference between the two is that absorbed dose (Gy) quantifies a physical effect, while equivalent dose (Sv) a biological one. Since this generally cannot be measured, the ADER has been introduced as an 'operational quantity': the dose per unit time in the so-called ICRU sphere, which serves as human 'phantom', i.e., mimics the human body. The actual ADER quantity is dH*(10)/dt, in units of nSv/h, where (10) refers to the dose 10 mm deep within the ICRU sphere (ICRP, 2007):

> The ambient dose equivalent, H*(10), at a point in a radiation field, is the dose equivalent that would be produced by the corresponding expanded and aligned field in the ICRU sphere at a depth of 10 mm on the radius vector opposing the direction of the aligned field.

Detectors are calibrated to the ambient dose equivalent, which is believed to be a conservative estimate of the true (but non-measurable) dose in tissue caused by external radiation. Calibration means that given an exposure, the instruments show the dose value which the ICRU sphere would receive in 10 mm depth. Dose depends on the energy spectrum of the radiation to which matter or tissue is exposed. Since detectors do not react entirely uniformly to radiation of different energy, they are calibrated by irradiation with defined energy.

Additional information on calibration

For European ADR networks, irradiation with ^{226}Ra sources has been recommended for calibration. ^{226}Ra decay products, which contribute most to the gamma radiation of ^{226}Ra sources, simulate quite well the gamma ray spectrum of natural exposure and the one to typical reactor accident fallout. However, also ^{137}Cs and (rarely) ^{60}Co are used for calibration to ADER. For typical environmental radiation, a ^{226}Ra (+progeny) or ^{137}Cs source, kerma dose in air of 1 Gy corresponds to ADER approximately 1.2 Sv/h*(10), see also Yi et al. (1997). For further information on this subject, see e.g. IAEA (2000) and ICRP Publication 103, Annexes B3 and B4 (ICRP, 2007).

4.2.2 Components of the ambient dose rate signal and its decomposition

The recorded ADR signal has a number of components, schematically visualised in Figure 4-3.

1. Intrinsic background (also called self-effect) of the instrument: radioactivity of technical components and electronic noise;
2. Cosmic radiation; see Chapter 8;
3. Terrestrial natural radiation:
   a. Gamma rays emitted by primordial natural radionuclides and their progeny in the ground; see Section 4.1 and Chapter 3.
   b. Gamma-radiating radionuclides generated by induced nuclear reaction of cosmic rays.
4. Terrestrial artificial radiation: gamma rays emitted by artificial radionuclides in and on the ground. These are radionuclides from global fallout (from atmospheric nuclear bomb testing) and, concerning Europe, from fallout due to the reactor accident at the Chernobyl nuclear power plant on 26 April 1986. The radionuclide which contributed to ADR over long term is ^{137}Cs (with a half-life of 30 years), for both global and Chernobyl fallout (De Cort et al., 1998). Up to a few years after the Chernobyl accident, other radionuclides also contributed, such as ^{134}Cs (half-life of 2.1 years), ^{106}Ru (half-life of 372 days) and ^{131}I (half-life of 8 days).
5. Airborne natural radiation:
   a. ^{222}Rn and ^{220}Rn which are members of the ^{238}U and ^{232}Th decay series, respectively, are exhaled from the ground into the atmosphere, where they further decay, e.g. into gamma-radiating isotopes of lead and bismuth. These gamma rays are recorded by the ADR monitors. Their intensities depend on the vertical distributions of radon progenies in the atmosphere, which in turn depend on meteorological conditions. A ^{222}Rn concentration of 10 Bq/m³ in the near-ground atmosphere contributes approximately 2.5 nSv/h to ADER (details and references in Bossew et al. 2007; see also Section 2.2.4).
   b. During precipitation (rain, snow, fog), radon progenies are transported to the ground by scavenging and washout by raindrops. Concentrated on the ground surface, they can give rise to high ADR peaks, which last a few hours and can even trigger radiation alarms.
   c. Cosmic radiation can induce nuclear processes in atoms (mainly oxygen, nitrogen and carbon) present in the atmosphere and generate so-called cosmogenic gamma-radiating radionuclides such as ^{7}Be. Their contribution to ADR is small, far below pSv/h. It varies with the intensity of cosmic rays (see Chapter 5).
   d. In analogy with (b), the cosmogenic radionuclides can precipitate to the ground and thus enhance ADR. This is also a small effect, contributing fractions of nSv/h to ADER.
6. Airborne artificial radiation: After nuclear explosions and accidents, high concentrations of gamma radionuclides can be found. Shortly after the Chernobyl accident, up to several µSv/h were registered in Central Europe, i.e. two orders of magnitude above the usual background radiation.
7. Contamination of the monitor: Airborne natural and artificial radionuclides will be deposited on the housing of the detector and contribute to the ADR signal. Experiments have shown, however, that this effect is small and does not lead to undue bias.
8. Particular signals can arise from nearby activities involving nuclear methods, typically such as material testing using gamma-ray sources. Such cases have occurred, sometimes causing confusion to network operators who may suspect a radiation accident. Lightning may also induce noticeable detector response.
9. Spurious signals: Apart from signal loss, system malfunction may lead to spurious, highly anomalous readings. Usually, these are easy to identify and then to discard.

To estimate the terrestrial natural component, one should subtract all the components listed above except 3a from the ADR.

4.2.3 Variability of natural terrestrial dose rate

Terrestrial dose rate is subject to spatial (i.e. geographical) and temporal variability.

a. Spatial variability

The sources of natural terrestrial gamma radiation are the primordial radionuclides and progeny. Their geographical distribution is not uniform, but varies according to geology and geochemistry, as explained in detail in Section 4.1.

b. Temporal variability

At first glance, it may seem surprising that observed natural terrestrial ADR is not constant over time. The reason is that gamma rays from the source, which are the radionuclides in the upper few tens of centimetres of the ground are attenuated by the matter between emitter and monitor. This attenuation depends on soil humidity: in wet soil, gamma rays are attenuated more strongly than in dry soil.

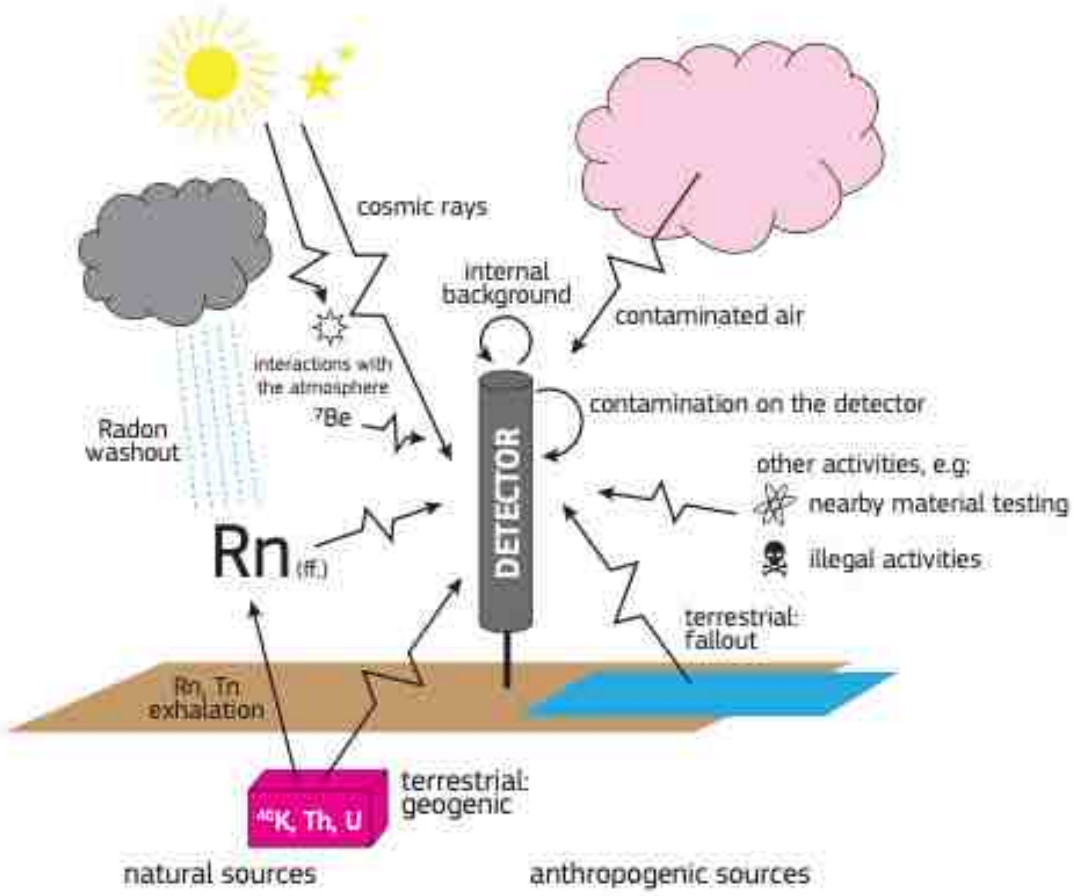

Figure 4-3
Contributions to the dose rate recorded by a detector. Rn = radon (^{222}Rn); Tn = thoron (^{220}Rn); see Section 2.2.2 for details.
Source: Graph created by Peter Bossew.

Case study: ADER 'rain peaks' due to radon progeny

After a hot and dry period in Vienna, heavy thunderstorms started in the evening of 2 May 2018. The ADER 'rain peak' due to radon progeny precipitated to the ground is clearly visible in Figure 4-4 to the right. The progeny are short-lived (half-lives of about half an hour) and decay within a few hours. ADR returned to background values, but slightly, about 5 nSv/h, lower than before rain, about 93 instead of 98 nSv/h. The reasons are attenuation by the now wet soil and the 'clean' atmosphere, comparatively devoid of radon progeny.

The effect shown in Figure 4-4 is thus a combination of soil humidity and decreased airborne radionuclide concentration. Identification of the individual contributions is rather complicated without dedicated measurements.

A similar effect is shown in Figure 4-5, an ADER series recorded over 4.4 years at a high-lying mountain station in the Austrian Alps. Here the attenuation effect by snow (up to several metres deep at that location) can be observed, which reduces the 'summer background', without snow, from about 80 to 20–50 nSv/h. The values are net ADER, i.e. contributions from cosmic rays and self-effect subtracted.

Figure 4-4
ADER recorded by a monitoring station in Vienna, Austria, around 2 May 2018. Timestamp: UT. The peak is caused by radon progeny deposited by heavy rain after a long dry period.
Source: Graph created by Peter Bossew.

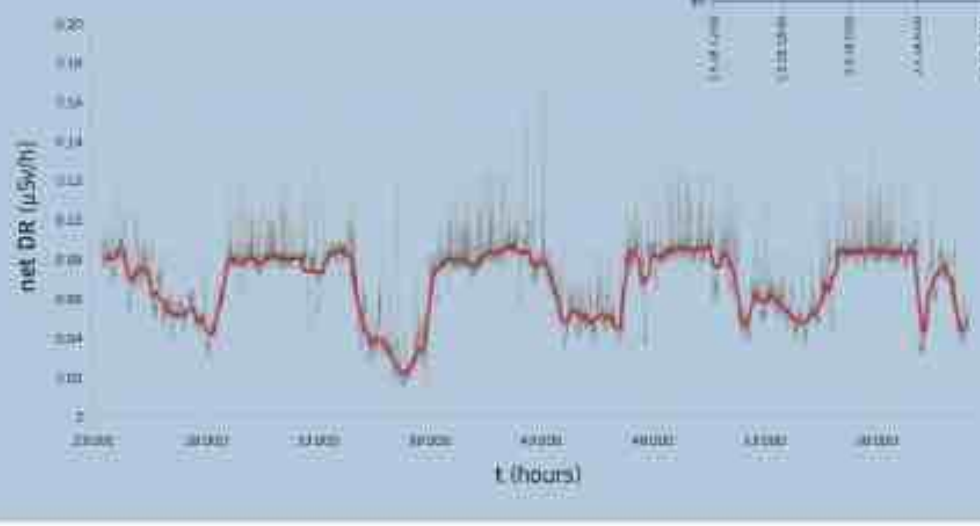

Figure 4-5
ADER series from a station in the Austrian mountains. Rain peaks and attenuation by snow are clearly visible. Red curve: background after removing the rain peaks.
Source: Graph taken from Bossew et al. (2017).

4.2.4 Variability of dose rate from nuclear fallout

Since this Atlas focuses on natural sources of radiation, the artificial ones, i.e. nuclear fallouts, are only briefly mentioned. Its spatial variability is due to geographically variable fallout density. Global fallout is mainly correlated with long-term precipitation and a latitude effect. The Chernobyl fallout was governed by the movement of the air, which was contaminated when passing the still emitting reactor, and deposition, which mainly depended on precipitation during passage of contaminated air. Maps of Chernobyl fallout can be found in De Cort et al. (1998).

Concerning temporal variability, fallout gamma-ray intensity above ground decreases with radionuclide physical decay; by migration of the contaminant into deeper soil layers and resulting higher attenuation by overlaying soil; and the attenuation effect described. Typically, caesium migrates downwards by a few millimetres per year (Bossew & Kirchner, 2004; Strebl et al., 2009).

The Compton scattered flux has been neglected in this simple model. Its contribution increases with the depth of the source in soil. The dose rate is constituted by scattered and unscattered flux.

Technical details:

Assume that ^{137}Cs (with energy 662 keV) is distributed in soil according to Equation 4-3, which approximates the solution of the diffusion-advection equation. The advection velocity v and dispersion constant D were set to v=0.2 cm/a and D=0.2 cm²/a, respectively, which is realistic. The unscattered gamma-ray flux is given by Equation 4-4, where φ_z denotes the flux from an infinitely thin disk at depth z. In Equation 4-5, C_a, set to unity, denotes the total inventory (Bq/cm²), Y the emission probability (=0.85 for ^{137}Cs), h the measurement altitude above ground (1 m), μ_a the attenuation constant of air (0.0093 m^{-1} for 662 keV), μ_s the attenuation constant of soil and ρ_s soil density, assumed to be 1 g/cm³. (μ_s/ρ_s)=0.075 cm²/g for 662 keV photons. E_1 is the exponential integral of first order.

$$f(z) = \frac{1}{\sqrt{Dt}} \exp\left[-\frac{(z-vt)^2}{4Dt}\right] \quad (4\text{-}3)$$

$$\varphi = \int_0^\infty \varphi_z f(z)\,dz \Big/ \int_0^\infty f(z)\,dz \quad (4\text{-}4)$$

$$\varphi_z = \frac{C_a Y}{2} E_1\left[h\mu_a + z\frac{\mu_s}{\rho_s}\rho_s\right] \quad (4\text{-}5)$$

Temporal changes in dose rate, ^{137}Cs concentration and gamma-ray flux after the Chernobyl accident

Figure 4-6 shows ADER values recorded at two Austrian monitoring stations after the Chernobyl accident on 26 April 1986. Except for the beginning, the dominant part of ADER is caused by radiation from radionuclides deposited on the ground, although airborne concentrations were also partly quite high. The peak in the Hainburg series at about t=150 h may have been caused by the passage of another contaminated cloud. The decrease in ADER reflects the decay of short-lived radionuclides such as ^{132}Te and ^{131}I.

Temporal change of the depth distribution of ^{137}Cs concentrations in soil at a location in Salzburg (Austria) is shown in Figure 4-7 (each curve represents the mean of 3 soil profiles). One can recognise decreasing ^{137}Cs concentration in the surface layer and the shift of the maximum towards deeper layer; both effects result from migration, typically in the order of a few millimetres per year. Also the total activity decreases (represented by the areas under the curves), due to physical decay and migration to deep soil layers that have not been sampled, and into ground water.

During the first days to weeks after the Chernobyl accident, dominant radionuclides, which contributed most to the ambient dose rate, were iodine and tellurium isotopes. Due to their short half-lives (for ^{131}I, 8 days) their contribution soon disappeared. For months to a few years, radionuclides such as ^{134}Cs, ^{106}Ru, ^{125}Sb and ^{144}Ce contributed to the dose rate. Today (2019), more than 33 years after the accident, only the long-lived ^{137}Cs (with a half-life of 30 years) can be detected. Long-lived radionuclides such as ^{90}Sr and plutonium isotopes are present and can be measured, but since they do not emit gamma rays, they do not contribute to ambient dose rate.

According to the changes of total inventory and depth distribution of the contaminant, the gamma-ray flux above ground also changes with time. An example is shown in Figure 4-8.

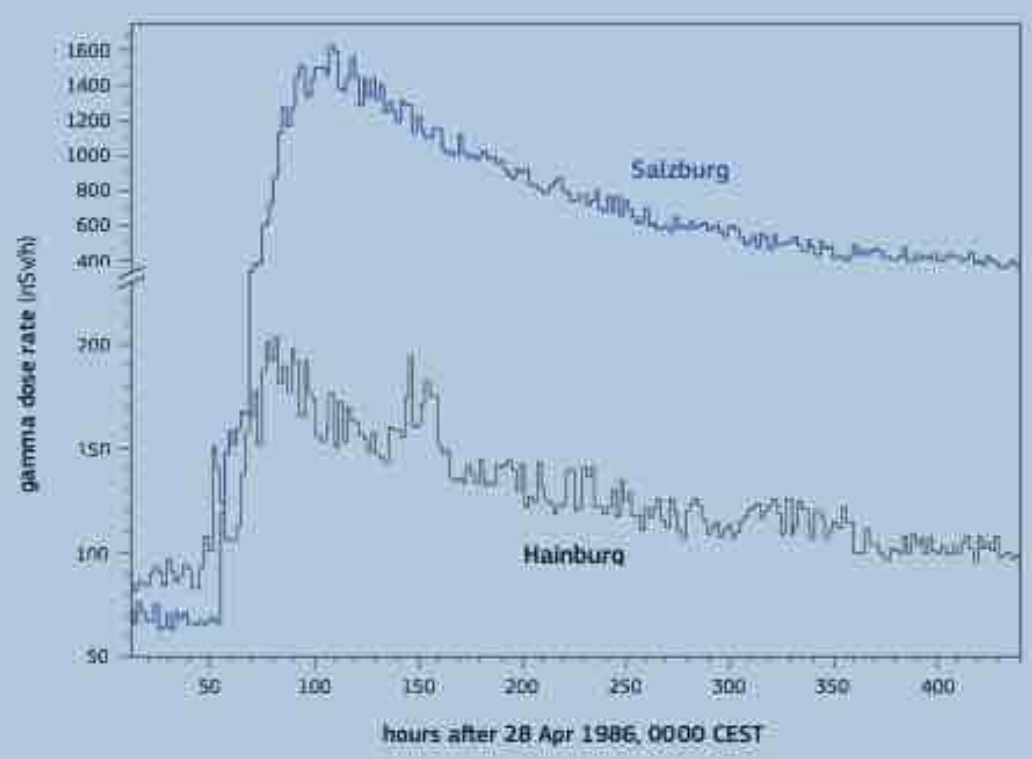

Figure 4-6.
Dose rate signal after the Chernobyl accident recorded by two stations of the Austrian early warning network. Temporal resolution: 2 hours. Please note the gap in the y axis.
Source: Graph created by Peter Bossew

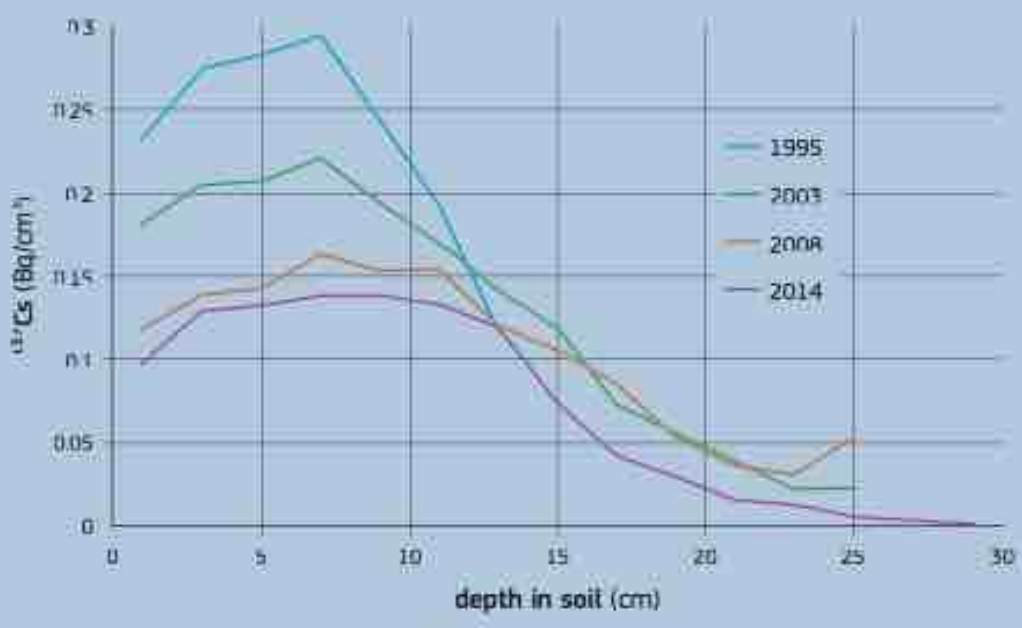

Figure 4-7.
Changes of the depth distributions of ^{137}Cs in Salzburg, Austria, from 1995 to 2014.
Source: Data provided by F. Lettner

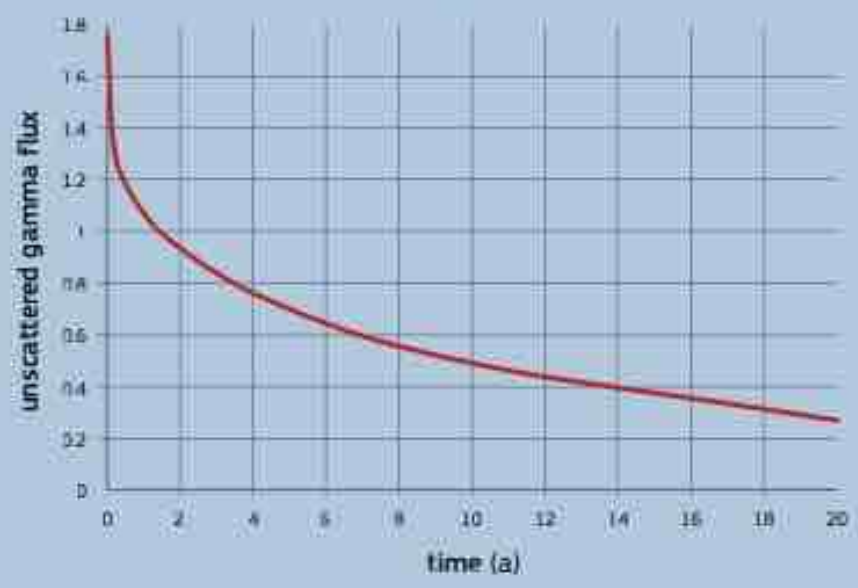

Figure 4-8.
Time dependence of the unscattered 662 keV gamma-ray flux, 1 m above ground over a normally distributed ^{137}Cs source in the soil.
Source: Graph created by Peter Bossew

4.3 Materials and methods

Terrestrial gamma dose rate can be determined experimentally by measurement or indirectly by using geochemical data.

Geophysical field radiometric measurements, focused on radioactivity of rocks and soils and backed with sophisticated specialised instruments, developed techniques of data acquisition and data processing, can provide reliable information on the dose rate and contents of radioactive elements in extensive areas. Geophysical radiometric gamma surveys are conducted as a total count measurement (TC) or gamma-ray spectrometry, both applicable for the airborne, car-borne and ground measurements with portable radiometric instruments.

4.3.1 Dose rate in geophysical research

Total count rate measurement

Total count (TC) surveys with count rate meters equipped with scintillation detectors or Geiger-Müller counters are mostly applied in ground measurements. The relationship between the recorded count rate, n_{TC} (counts per second or cps), and the concentration of K, U, and Th in rocks is given by

$$n_{TC} = s_K c_K + s_{Th} c_{Th} + s_U c_U + n_{BG} \qquad (4\text{-}6)$$

where:

s_K, s_{Th}, s_U are the sensitivities of a TC radiometric instrument (cps per unit concentration of relevant radionuclide) for K, Th and U, respectively; and

c_K, c_{Th}, c_U are K, Th and U element concentrations.

Sensitivities of the instrument can be estimated by measuring the TC response over calibration pads or over selected geological bodies that have different K, Th and U concentrations (IAEA, 2003). The background count rate, n_{BG}, is estimated by measuring over a large water plane. The count rate response of the TC instrument to gamma radiation of K, Th and U of specific energy fundamentally depends on the type of detector and its detection efficiency (IAEA, 1976), and on the energy discrimination threshold of the instrument. The results of a TC measurement can be expressed in dose rate (nGy/h), by converting count rates n_{TC} to dose rate using the instrument calibration constant. Since the response of a TC instrument significantly depends on its detector and energy discrimination threshold, the resultant dose rates of single instruments may deviate from correct values. Reference literature describes these effects and range of deviations over rocks having variable proportions of K, Th and U (e.g. IAEA, 1990; IAEA, 2003; IAEA, 2013; Matolin, 2017).

Gamma-ray spectrometry (see also Section 2.5)

Since the 1960s, gamma-ray spectrometry has been widely used for geological surveys and environmental monitoring since the 1960s. Field multichannel scintillation gamma-ray spectrometers record count rates (cps) in energy intervals which are centred on the 1 461 keV (^{40}K), 1 765 keV (^{214}Bi, decay product of ^{238}U) and 2 615 keV (^{208}Tl, decay product of ^{232}Th) photopeaks for estimating the K, Th and U concentrations, respectively (IAEA, 1989). The K, Th and U energy window count rates, n_i (cps), recorded in three selected energy windows i = 1, 2, 3, are linearly related to the K, Th and U concentrations c_j, j = K, Th, U such that

$$n_i = s_{iK} c_K + s_{iTh} c_{Th} + s_{iU} c_U + n_{iBG} \qquad (4\text{-}7)$$

The sensitivity constants, s_{ij}, are estimated from measurements on the four calibration pads of a calibration facility, or for the airborne gamma-ray spectrometer by flying over a calibration strip (Tauchid & Grasty, 2002). Background activity can be estimated by taking measurements over a large body of water. For a given count rate n_i that is corrected for background, the radioelement concentrations c_K, c_{Th}, c_U can be calculated using either a matrix or stripping method. More sophisticated methods based on the full gamma-ray energy spectra processing have also been developed (IAEA, 2003).

Scintillation detectors with NaI(Tl) crystals, having relatively high detection efficiency, are mostly used for airborne, car-borne and ground radiometric mapping. High-purity germanium (HPGe) semiconductor detectors (see details in Section 2.5.3), with high energy resolution but low detection efficiency resulting in long exposure times, are used for gamma-ray spectrometric identification of unknown radionuclides and investigation of already localised radiation sources.

Methods of field gamma-ray spectrometry

Airborne gamma-ray spectrometry is an efficient technique to cover extensive areas. Specific features of airborne gamma-ray spectrometry include large-volume scintillation detectors of 30–50 litres NaI(Tl), additional upward looking 4 l NaI(Tl) detector for atmospheric radon correction, a multichannel pulse amplitude analyser, an energy spectrum stabilisation and dead time correction unit. Additional instruments are radar altimeter and differential GPS. Measurements are carried out at constant heights above the ground, selected in the interval 30–120 m, along parallel flight lines, with flight speed between 25–50 m/s (90–180 km/h), and with a sampling interval of 1 s. The field of view (zone of influence) is usually related to the diameter, d, of a circular plane, which generates an assigned percentage (%) of radiation from an infinite source. The field of view is a function of the flying height h. Processing of airborne gamma-ray data requires a number of corrections (IAEA, 1991; IAEA, 2003).

A NaI detector placed one metre above the ground. Source: Lenka Tondl

Car-borne gamma-ray spectrometry is applicable in natural car-accessible terrain. Specific features of car-borne measurements are the use of 4–8 l NaI(Tl) scintillation detectors, car speeds of 15–30 km/h, and sampling intervals of 1–4 s. The field of view for a rooftop-mounted detector may be in the range of 14–36 m.

Ground radiometric measurements with portable total count instruments or portable gamma-ray spectrometers can be performed in stationary mode or dynamic mode. Portable gamma-ray spectrometers are equipped with 103–350 cm³ NaI(Tl) scintillation detectors, or recently also with BGO crystals, $LaBr_3$ and other crystals (see Section 4.3.4). Uniformity of ground radiometric measurements requires a fixed height of the detector over terrain. For a detector placed on the ground, the detected gamma radiation comes from the circular area with a diameter of about 1 m. As the detector is raised from the ground, the field of view increases progressively. Stationary gamma spectrometry measurements require sampling times of 2 minutes over rocks of enhanced radioactivity (granites) and 6 minutes over low-radioactivity rocks (limestone). With HPGe detectors, typical sampling times are in the order of several tens of minutes.

Calibration of radiometric instruments

Calibration of radiological radiometric instruments in open air is mostly performed by means of suitable point reference sources (standards), as are ^{226}Ra, ^{137}Cs, or others. Calibration of geophysical field radiometric instruments used for radiometric mapping and environmental studies is conducted by means of calibration pads. A calibration pad is a three-dimensional slab of concrete containing a known concentration of natural radioelements K, Th and U. A calibration pad should simulate a geological source by its geometry, radionuclides, matrix composition, density, humidity and generated gamma ray energy spectrum. The objective of the use of calibration pads is to analyse correctly natural radionuclides K, Th and U in rocks and control existing deviations between registered instrument count rate (cps) and existing dose rate. Only field total count radiometric instrument, having uranium equivalent of potassium equal to 2.30 and uranium equivalent of thorium equal to 0.44, reports correct values of the dose rate (Lavborg, 1984; IAEA, 1990). Three calibration pads individually enriched by potassium, uranium, or thorium, and one low radioactivity background pad have been recommended by the IAEA (1989). A calibration strip of known ground K, Th and U concentration serves for calibration of airborne gamma ray spectrometers. Calibration of gamma ray spectrometers results in determination of instrument sensitivities s_{ij}, stripping ratios, and background count rates n_{iBG} (IAEA, 2003). Calibration of radiometric instruments is a fundamental procedure for standardisation of radiometric data. The International Atomic Energy Agency under the concept of 'A Global Radioelement Baseline' supports uniformity of radiometric data through using the IAEA primary reference standards for laboratory gamma ray spectrometry (IAEA, 1987), construction and use of three-dimensional calibration pads (IAEA, 1989), calibration of radiometric instruments, and acquisition of field data and data processing by verified procedures (IAEA, 2003; IAEA, 2010). An excellent example of application of the IAEA concept 'A Global Radioelement Baseline' is the compilation of a uniform radiometric map of Australia (Minty et al., 2009). An appreciable assistance in calibration of field gamma-ray spectrometers was the introduction and manufacturing of portable calibration pads (Grasty et al., 1991) that enabled calibration of field radiometric instruments in more countries.

Calibration pads, concrete enriched with K, Th and U. Source: Peter Bossner

4.3.2 Dose rate calculation from geochemical data

Computation of terrestrial gamma dose rate (TGDR) using known concentration of natural radioelements K, Th and U in rocks and soils is based on the model of gamma radiation of the homogeneous infinite plane over the Earth's surface. Constants for converting the unit K, Th and U mass concentration in soil at an elevation of 1 m above the homogeneous soil surface cited in literature (IAEA, 2003; Will et al., 2003) differ negligibly, in dependence on selected density of rocks and applied radiation constants.

A possible approach for estimating the TGDR, i.e. the external doses due to natural radionuclides, is a theoretical calculation based on concentrations of natural radionuclides in the soil (UNSCEAR, 2008).

In particular, the TGDR is estimated from the concentrations of all the natural radionuclides in the soil, considering all their gamma emissions. In doing so, a fundamental assumption has to be made: the secular radioactive equilibrium (see Section 4.4.2). Apart from ^{40}K, the large majority of the terrestrial radionuclides in soil emitting gamma rays belongs to the uranium and thorium series, two large groups of radionuclides produced by the decay of uranium and thorium. The parents of these natural families, namely ^{232}Th ($T_{1/2}$=1.41·10^{10} years) and ^{238}U ($T_{1/2}$=4.47·10^{9} years), are very long-lived radioisotopes, with half-lives in the order of billions of years, much longer than those of all the other radioisotopes belonging to the series. As a consequence of that the so-called secular radioactive equilibrium condition is established between the members of the radioactive families: i.e. the activity of all the radionuclides have the same value, thus drastically simplifying the calculation issue. It is therefore possible to estimate the TGDR simply by knowing the concentration in soil of only three radionuclides: ^{40}K, ^{232}Th and ^{238}U.

Several methods can be used to calculate the gamma dose rate, starting from the gamma-ray flux produced by radionuclides. In most applications, the gamma-ray transport equation is solved by using Monte Carlo techniques. However, for the TGDR, a simplified semi-analytical approach, namely the point-kernel isotropic method, can be successfully used. In this case, the soil is modelled as a semi-infinite space, and the dose rate is evaluated at a receptor point, 1 metre above the ground. Each infinitesimal volume (dv) of soil, acting as a point source irradiating isotropically, gives at the receptor point an infinitesimal gamma-ray fluence dΦ whose expression is:

$$d\Phi = \frac{e^{-(\mu/\rho)_s \cdot \rho_s \cdot r_s - (\mu/\rho)_a \cdot \rho_a \cdot r_a} dS}{4\pi r^2} \qquad (4\text{-}8)$$

where:
dS is the intensity of the gamma source due to the presence of gamma-emitting radionuclides in the infinitesimal volume of soil dv;
$(\mu/\rho)_s$ and $(\mu/\rho)_a$ are the mass attenuation coefficients for the photons in soil and air respectively; and
ρ_s and ρ_a are the soil and air density while r is the length of the total path travelled in the medium (soil+air: $r=r_s+r_a$) by the gamma rays from soil to the receptor point.

The corresponding, absorbed dose rate at the receptor point can thus be evaluated integrating Equation 4-8 over the semi-infinite volume V, as follows:

$$\dot{D} = \int_V \frac{k \cdot E \cdot \left[\frac{\mu_{en}}{\rho}\right] \cdot B \cdot e^{-(\mu/\rho)_s \cdot \rho_s \cdot r_s - (\mu/\rho)_a \cdot \rho_a \cdot r_a} dS}{4\pi r^2} \qquad (4\text{-}9)$$

where:
E is the photon energy;
(μ_{en}/ρ) is the mass energy absorption coefficient in air at the point dose;
k is an appropriate conversion factor; and
B is the build-up factor, i.e. the parameter that quantifies the dose due to the scattered photons.

Another key element in Equation 4-9 is the quantity dS, which is directly related to the gamma-emitting radionuclides in soil. The explicit expression for dS is:

$$dS = \sum_j \left(\sum_k a_j \cdot y_{jk} \right) \cdot dv \qquad (4\text{-}10)$$

where:
a_j is the volumetric activity concentration (Bq/cm^3) of the generic radionuclide j;
y_{jk} is the yield of the j_k gamma emission of the radionuclide j; and
dv is the infinitesimal volume of soil.

Equation 4-10 is then inserted into Equation 4-9 and the TGDR can thus be computed. In doing so, Equation 4-9 has of course to be evaluated for each generic gamma line j_k, with given energy E_{jk} and with their corresponding values for the attenuation and absorption coefficients: $(\mu/\rho)_{sjk}$, $(\mu/\rho)_{ajk}$ and $(\mu_{en}/\rho)_{jk}$.

Operating in this way, in 1972 Beck and co-workers (Beck et al., 1972) were able to calculate the TGDR due to natural radioactivity. They proposed a very a simple formula:

$$TGDR(nGy/h)) = 0.0424 \cdot C_K + 0.668 \cdot C_{Th} + 0.431 \cdot C_U \qquad (4\text{-}11)$$

where:
C_K, C_{Th} and C_U are, respectively, the activity concentration of ^{40}K, ^{232}Th and ^{238}U in Bq/kg.

More recently, following a very similar approach, the UNSCEAR (UNSCEAR, 2008) has proposed a slightly different formula, based on newer data:

$$TGDR(nGy/h)) = 0.0417 \cdot C_K + 0.604 \cdot C_{Th} + 0.462 \cdot C_U \qquad (4\text{-}12)$$

The latter expression is used to calculate the European Terrestrial Gamma Dose Rate Map (see Section 4.4.2): the dose rate can be evaluated in each cell grid simply by inserting in the above equation the corresponding ^{40}K, ^{232}Th and ^{238}U activity concentration values (Bq/kg).

The use of expressions such as Equation 4-9 and its simplified forms (Equation 4-11 or 4-12) for evaluating the TGDR are based on some important underlying assumptions that are worth discussing in some detail. These fundamental assumptions are:

- The secular radioactive equilibrium condition between all the members of the radioactive families (Th and U), already mentioned in the introduction; this is a very important assumption, allowing the calculation of the TGDR from the simple knowledge of the activity concentration of only three radionuclides: ^{40}K, ^{232}Th and ^{238}U. It is almost everywhere a very good assumption, but some local exceptions generally cannot be ruled out.
- The complete homogeneity of the soil medium, characterised by a unique density value ρ_s, a unique mass attenuation coefficient $(\mu/\rho)_s$ and a standard composition, valid for all types of soils.

4.3.3 Dose rate in the EURDEP system

Motivation and history

a. Introduction

Many countries operate automatic systems, which continuously monitor radiometric quantities in the environment. Their purpose is to warn against effluents of large-scale radiological emergencies, which might have been caused by reactor accidents. Most monitoring stations measure ambient dose rate, while a smaller number collect air samples and measure activity concentrations of airborne radioactivity. While the systems are operated and evaluated nationally, a large part of data generated in European countries is transmitted to the European Radiological Data Exchange Platform (EURDEP), which makes radiological monitoring data from most European countries available in nearly real-time. While participation of the EU Member States is regulated by EU law, non-EU countries take part on a voluntary basis. As of mid-2019, 39 countries participate to EURDEP. In addition to EU Member States and non-EU countries, a few non-European countries have joined. Extensive information about EURDEP is available on its website, https://remon.jrc.ec.europa.eu/. The values are displayed as maps; see Figure 4-9 as an example.

More than 5 000 stations across Europe monitor ambient dose rate (ADR); and a few tens of stations, radionuclide concentrations in air. (Data transmission from the latter is currently poor.)

Large-scale nuclear accidents or events are fortunately rare. Indeed, since the Chernobyl accident (on 26 April 1986), no anthropogenic event extending beyond one station has been monitored. (Such events are usually material tests using gamma radiation sources.) The Fukushima accident (e.g. Masson et al., 2011; Bossew et al., 2012) did not lead to a detectable increase of ADER in Europe. Such events are only detectable by air monitoring.

A secondary use of dose rate monitoring stations is the assessment of natural radiation. Operating continuously, these monitors generate large amounts of 'background' data, which are being stored by national authorities as well as by the Joint Research Centre of the European Commission. The data can potentially be used to assess and map natural environmental radioactivity, which is why they are discussed in this Atlas.

Figure 4-9.
EURDEP screenshot. ADR stations, showing the arithmetic means of ADER (h*10), (nSv/h) over one day, ending on 1 August 2019.
Source: EURDEP (JRC, 2019)

b. Radiation background and signals

Except for the Austrian network that was operable during the Chernobyl accident, no new artificial contamination (i.e. on top of existing) has been observed by EURDEP. In Europe, the ADR due to contaminated air from the Fukushima accident was about three orders of magnitude smaller than typical detection limits of the dose rate monitors. Air contamination could be easily measured with high-volume laboratory-based air samplers, but not by automatic air sampling stations.

This means that the ADR readings represent natural radiation as well as existing residual fallout. Over most of Europe, the latter component contributes a few percent at most, with about 10% in regions highly affected by Chernobyl fallout (parts of Scandinavia, Austria, South Germany and others). An exception is one station in Southeast Belarus, where the signal is dominated by Chernobyl fallout.

In ADR readings, natural and artificial components cannot be distinguished. Estimating the latter depends on gamma-spectrometric measurements, which require instruments that are more complicated and expensive than the relatively simple ADR monitors.

As mentioned, although made for detecting large-scale accidental contamination, the systems constantly generate background signals, which however convey interesting radiometric information. Therefore, in recent years, effort has been made to better understand these signals and possibly exploit them for scientific and general radioprotection purposes.

Network policy and design

Radioactivity monitoring networks are usually designed for two main purposes: to detect anomalies for early warning and to manage accidents. In the first case, monitoring stations are located preferentially around nuclear installations and/or, if neighbouring countries have nuclear power plants, at country borders. The preferential siting of monitoring stations requires that the potential sources of radioactive releases are known in order to maximise the probability of detecting local anomalies and report these in the shortest possible time. Fixed station monitoring is therefore not capable of warning against, or monitoring small-scale nuclear events, in particular not malevolent criminal and terroristic activity.

History has shown, however, that large-scale disasters can occur and, should the radioactive release be atmospheric, that contamination can affect a whole continent. The management of such an accident would ideally require radiation levels to be reported anywhere at any time. Following the Chernobyl accident (on 26 April 1986), most countries have set up an additional number of automatic stations spread over their territories and/or at critical places (typically large cities), even when these places were distant from any nuclear power plant.

The map of monitoring networks shown in Figure 4-9 easily illustrates the above: while in some countries, a number of stations seems to be distributed randomly over the territory, aggregated stations will, in most cases, reflect sites of nuclear industry. Inversely, a lower density of stations will usually indicate regions with lower population density and regions where physical obstacles such as water bodies and mountains make it difficult to install and maintain a monitoring station.

Test probes at the BfS premises in Berlin, showing antennas in various stages of development. Each can be equipped with a pair of Geiger-Muller counters, one for low and one for high dose rate.
Source: Peter Bossew

Thus, the siting criteria for the monitoring stations, the density of the monitoring network and the spatial distribution of individual stations depend on many factors, including:

- The intensity of the nuclear activity within the country;
- The country's economic resources that are available for acquiring and maintaining a monitoring network;
- Environmental policies and regulations;
- Concern about nuclear activities of neighbouring countries;
- The importance which is attributed to a network's capability to provide a detailed geographical picture of an existing contamination situation;
- The geographical distribution of the population and of the main resources of the country; a certain relationship between network and population densities can be observed, see Figure 4-10.
- Topography.

What is shown here as stations of a national network is actually a collation of several networks, in some cases, where clustered stations around nuclear power plants are part of a network operated by an authority different from the one responsible for the sparse networks that cover much larger areas.

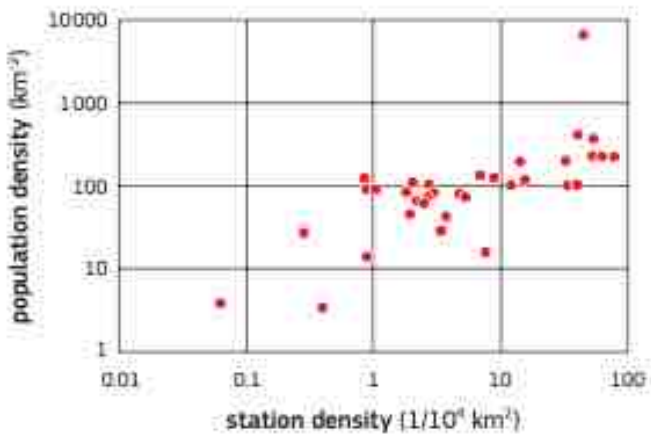

Figure 4-10
Scatterplot of station density vs. demographic density. The outlier in the upper right corner represents Hong Kong.
Source: Graph created by Peter Bossew

However, because of the need for managing the collected data for early-warning coherently and for the longer term, there is a trend in combining all networks under the umbrella of a single national authority to ensure better coordination (see e.g. Deurwaarder et al., 2001) in case of an accident. Here we consider all stations as part of a single network.

Figure 4-9 clearly shows that the geographical distribution of stations is not uniform between countries. This reflects different policies which underlie the networks, as discussed above. Some countries attempt to cover their territories more or less uniformly to be able to identify fallout levels as quickly as possible and to be able to follow dispersing contaminated air; examples are Germany, Austria, Belgium, Turkey or the UK. Others chose to locate stations more densely around nuclear plants (e.g. France and Spain). Yet others locate stations preferentially along borders to detect radioactive clouds intruding from abroad as efficiently as possible (the East coast of Ireland, Turkey). In Finland, the station density conforms approximately to the population density.

Apart from geographical configuration of the network, countries choose different station densities. This reflects the desired degree of precision of geographical information generated by the monitor readings. Evidently, higher precision conflicts with economic constraints and a suitable trade-off has to be found.

As a consequence of the geometrical heterogeneity, when used for mapping on European level, different degrees of precision between regions must be accepted.

Photo taken during a art 35 Euratom Verification visit in Croatia, September 2013, showing various types of detector for environmental radioactivity.
Source: Tom Tollefsen

Network design: Description of network geometries

Figure 4-9 shows the monitoring stations of the European network, excluding the Atlantic islands, that are transmitting data as of June 2019.

The network patterns, or 'geometries', are evidently different between countries, reflecting different policies, as discussed above. Basic statistics of network geometries are given in Table 4-2, where:

- CE is the Clark-Evans index of complete randomness. CE=1 indicates that the distribution of stations is compatible with a random distribution; CE<1 means that the pattern is aggregated or clustered; CE>1, that it is more dispersed that could be expected for a random pattern.
- D2 is the fractal correlation dimension that quantifies 'patchiness' of the network. A regular or random pattern has D2 = 2, i.e. the 'patchier' it is, the lower is D2. For instance, France and Switzerland have low values of D2, whilst the UK and Norway have high values. Turkey has a uniform pattern inland but clusters along her borders, which reduces D2 somewhat.
- CV is the coefficient of variation of estimated station density. A high coefficient of variation of the estimated station density points to presence of regions with low and high density, notably France, Switzerland and Italy. In France and Switzerland, the reason is a high degree of clustering around nuclear facilities, while in Italy the 'non-stationary' nature of the density function, because density in the North is much higher than in the South of Italy. (The two effects could be distinguished by spatial trend analysis.)
- CV (NND) is the coefficient of variation of the nearest neighbour density, is an indicator of station clustering. Within clusters, NND is smaller than outside, which leads to higher dispersion of the NNDs.

code	country	area (km²)[1]	number of stations	stations per 10 000 km²	km² per station	population density (km⁻²)[1]	AM(NND) (km)	CE index	CV (NND)	corr. dim. D2	SD(D2)	CV(density)[2]
AL	Albania	28 748				100						
AD	Andorra	468	0			165						
AM	Armenia	29 743				101.5						
AT	Austria	83 856	327	39	256	105	10.2	1.27	0.45	1.81	0.05	0.23
AZ	Azerbaijan	86 600				114						
BA	Bosnia and Herzegovina	51 126				74						
BE	Belgium	30 510	160	52.44	191	372	9.1	1.31	0.71	1.4	0.04	0.68
BG	Bulgaria	110 994	27	2.43	4111	64	45.6	1.42	0.49	1.67	0.08	0.4
BY	Belarus	207 600	40	1.93	5190	46	55.6	1.54	0.23	2.02	0.09	0.16
CA	Canada	9 984 670	63	0.06	158 487	3.92	172.8	0.87	1.97			
CH	Switzerland	41 290	132	31.97	313	203	10.2	1.15	1	1.07	0.09	1.23
CY	Cyprus	9 251	8	8.65	1156	126	29.4	1.73	0.6			
CZ	Czech Republic	78 866	54	6.85	1460	135	21	1.10	0.62	1.87	0.06	0.21
DE	Germany	357 168	1 853	51.88	193	232	9.7	1.40	0.48	1.76	0.01	0.53
DK	Denmark[3]	43 094	11	2.55	3918	132	71.1	2.27	0.51			
EE	Estonia	45 339	15	3.31	3023	29	61	2.22	0.34	1.68	0.29	0.26
ES	Spain[4]	505 992	45	0.89	11 244	92						
ES	Spain[5]	493 476	43	0.87	11 476		72.4	1.35	0.62	1.36	0.05	0.58
FI	Finland	338 145	256	7.57	1321	16	25.3	1.39	0.55	1.75	0.02	0.71
FR	France[6]	557 394	857	15.38	650	118	9.5	0.74				
FR	France[7]	643 801	873	13.56	737							
FR	France[8]	548 714	855	15.58	642		9.3	0.77	1.61	1.01	0.01	0.99
GB	United Kingdom[9]	248 532	93	3.74	2672		49	1.89	0.36	1.96	0.03	0.48
GE	Georgia	69 700				53						
GR	Greece	131 940	24	1.82	5498	85	64.2	1.73	0.63	1.9	0.09	0.3
GL	Greenland	2 166 086	2	0.01	1 083 043							
HK	Hong Kong	2 755	12	43.56	230	6 777	10	1.32	0.73			0.29
HR	Croatia	56 594	30	5.30	1886	73	39.1	1.80	0.61	1.3	0.05	0.55
HU	Hungary	93 030	112	12.04	831	105	12.3	0.85	1.08	1.32	0.07	0.82
IE	Ireland	70 273	15	2.13	4685	68	64.9	1.90	0.56	1.17	0.18	0.35
IS	Iceland	102 775	4	0.39	25 694	3.4						
IT	Italy	301 338	419	13.90	719	201	14	1.05	0.92	1.49	0.07	1.18
KZ	Kazakhstan	2 724 902				6.49						
LI	Liechtenstein	160	1	62.50	160	233						
LT	Lithuania	65 300	24	3.68	2721	43	25.6	0.98	0.69	1.24	0.04	0.4
LU	Luxembourg	2 586	20	77.34	129	228	9.2	1.62	0.45			0.36
LV	Latvia	64 589	22	3.41	2936	30	31.8	1.17	0.81	1.08	0.17	0.39
MC	Monaco	1.95	0	0		18 469						
MD	Moldova	33 846	0	0		103						
ME	Montenegro	13 812	0	0		45						
MT	Malta	316	3	94.94	105	1 410	17.6	3.42				
NL	Netherlands[10]	41 198	166	40.29	248	414	11	1.40	0.39	1.63	0.02	0.33
MK	North Macedonia	25 713	12	4.67	2143	81	68.8	2.97	0.27	1.99	0.35	0.2
NO	Norway[11]	384 801	34	0.88	11 318	14	122.9	2.51				
NO	Norway[12]	323 779	33	1.02	9811			1.26	0.27	1.8	0.09	0.29
PL	Poland	312 685	26	0.83	12 026	123	65.8	1.20	0.60		0.06	0.15
PT	Portugal	91 568				112						
RO	Romania	238 392	71	2.98	3358	82	31.7	1.10	0.86	1.01	0.08	0.71
RS	Serbia[13]	77 453	8	1.03	9682	91	100.4	2.04	0.26			
SM	San Marino	61	0	0		544						
RU	Russia[14]	3 972 400	111	0.28	35 787	28	62	0.66	0.67	1.2	0.03	0.36
SE	Sweden	449 964				22						
SI	Slovenia	20 273	67	33.05	303	102	9.6	1.10	0.74	1.3	0.03	0.61
SK	Slovak Republic	49 036	10	2.04	4904	111	35.7	1.02	0.42	1.06	0.08	0.18
TR	Turkey	783 562	211	2.69	3714	105	42.7	1.40	0.46	1.73	0.03	0.2
UA	Ukraine[15]	603 628	158	2.62	3820	73.8	45.2	1.46	0.3	1.87	0.05	0.31
VA	Holy See	0.44	0	0		2 273						
XK	Kosovo	10 908	0	0		175						
	Median			**2.98**	**2721**	**102.5**	**31.8**	**1.37**	**0.6**	**1.56**		**0.36**

1 From Wikipedia
2 Over cells by Gauss kernel estimate (lower 10% truncated
3 Excluding Faroe Islands (1 393 km²) and Greenland (2 166 086 km²)
4 Including Balearic Islands (4 992 km²), Canary Islands (7 447 km²), Ceuta (18.5 km²), Melilla (12.5 km²)
5 Only mainland, i.e. excluding islands, Ceuta and Melilla
6 Excluding overseas departments
7 Including overseas departments
8 Mainland France = (6) minus Corsica (8 680 km²)
9 Excluding overseas territories, including Jersey (116 km²), Guernsey (65 km²), Isle of Man (572 km²), Gibraltar (6.7 km²)
10 Only European territories, i.e. excluding Caribbean territories
11 Including Svalbard (61 022 km²), excluding Jan Mayen (377 km²)
12 Excluding Svalbard and Jan Mayen
13 Excluding Kosovo
14 European part
15 Including Crimea (27 000 km²)

Table 4-2:
EURDEP ADER stations. All European countries as well as Canada and Hong Kong, that contribute data to the network. Based on stations in operation end-May 2018. AM(NND) – Mean nearest neighbour distance; CE – Clark-Evans (see text); CV(NND) – coefficient of variation of nearest neighbour distances; corr. dim. – correlation dimension (see text); SD – standard deviation; CV(density) – coefficient of variation of estimated density over grid cells. CE: green: statistically not different from 1 (90% confidence); black: CE>1 (over-dispersed); red: CE<1 (aggregated).
Source: Table created by Peter Bossew

Station design

Between and even within networks, monitoring stations are designed differently, with different types and models of monitors and detectors utilised. As a consequence, the raw values sent to EURDEP are not entirely comparable, although all measure the same nominal quantity, namely ADER in nSv/h. The following factors control the measured value:

a. Station level

This concerns siting of the monitor. The standard protocol requires that it is located 1 m above even, regionally typical, natural ground without objects such as buildings, trees, waterbodies or roads in its surroundings. Ideally, this "object-free zone" should be a circle with a radius of about 100 m, reflecting the range of "view" of the detector (i.e. the area from which a high percentage of gamma rays originate) although this is often hard to realise in the field. A large proportion of EURDEP stations more or less conform to this protocol, however a number do not as monitors are sometimes mounted on roofs or close to buildings etc. A procedure has been developed to quantify the bias due to deviation of the actual station siting from the ideal (e.g. Zähringer & Sempau, 1996). For terrestrial dose rate, the issue is particulary significant because, for example, a monitor mounted on top of a roof may record the natural radioactivity of building materials rather than from the surrounding ground. Finding close-to-ideal sites is certainly more difficult in densely populated or mountainous regions.

b. Monitor level

The raw ADER value given by the monitor depends on its intrinsic background and on response to the different components of dose rate. Response depends on gamma-ray energy and on radiation type, as it is different for cosmic rays (mainly muons) and gamma rays. Conversion from count rate, which is the initial output into ADER, is made by applying a calibration factor. Depending on the reference gamma-ray energy used in the calibration facility, the same environmental gamma flux may be converted into different ADER values.

c. Detector types

ADR monitors often consist of two detectors, one for low and one for high dose rates. Different detector types are in use, typically Geiger-Müller and proportional counters. Increasingly, spectrometric detectors are being used, the main type currently employing a lathanum-bromide ($LaBr_3$) scintillator. In principle, these monitors allow discrimination between different sources of registered radiation. Different types of monitors are shown in the picture on the right.

d. Quality assurance

For monitoring networks, quality assurance (QA) focuses on monitor and detector level. On network level, design is subject to political conditions, i.e. the objective of the network, but also to economic constraints. There seem to be no procedures of QA for validating the degree to which the planned objective is met.

On monitor and detector level, QA efforts are intense. Detectors are calibrated at certified facilities and characterised in designated experiments and research projects. Important parameters are intrinsic background (self-effect), linearity of energy response and response to cosmic radiation. Literature about the subject is abundant; just to quote a few, we mention the long-term experiment for intercomparison of monitors under real ambient conditions INTERCAL (Bleher et al., 2014). In Europe, the key coordinator for QA is the EURADOS (European Radiation Dosimetry, http://eurados.org/) working group 3, e.g. Wissmann & Sáez-Vergara (2006), Sáez-Vergara et al. (2007), Dombrowski et al. (2009) and Neumaier & Dombrowski (2014). The most recent progress of this EURADOS working group is presented in Vargas (2018).

Data management

Again, data are processed differently and stored at the station by local electronics and transmitted to the network, where other data-processing steps may be performed. Processing steps include subtraction of the intrinsic background and of cosmic radiation, computing averages over several data counting cycles. These can be very short, in the order of seconds, allowing high temporal resolution of a dynamic radiation situation, but inevitably involving high uncertainty in counting. For transmission to EURDEP, 1 hour-averages are computed. For their own purposes, networks may use different aggregation periods. EURDEP performs simple statistics and plots the data. Time series of individual stations can be displayed. Data are being stored permanently.

Dose rate monitors used in European early-warning networks, installed for long-term intercomparisons at the intercalibration site in Schauinsland, Germany. Source: Picture taken from EURAMET (2017).

Heterogeneity of the EURDEP system

The previous sections showed the high degree of heterogeneity between and even within monitoring networks. Within-network heterogeneity is mostly caused by non-uniform station siting. Between networks, the main differences are due to detector types, calibration procedures and data processing.

Heterogeneity leads to reduced comparability of values. This is of concern if small geographical differences need to be detected, because methodical bias could show difference where there is none or obscure the existing ones. The within-network heterogeneity (mainly due to station siting) may induce a noise component into a geographical picture, which may again obscure true signals.

Therefore, attempts have been made since the early 2000s to harmonise EURDEP, in the sense of identifying and understanding the systematic differences and proposing methods of "top-down" harmonisation. This denotes standardisation procedures that "recalculate" reported values to standardised ones, for example by subtracting intrinsic detector background or the cosmic component, or by labelling stations which should not be compared with standard ones due to their non-standard siting. (This is to be distinguished from "bottom-up" harmonisation, which means having the same measurement conditions and instruments everywhere; evidently, this is not achievable.)

Several studies have been performed on the subject and numerous documents published. One project is AIRDOS (Evaluation of existing standards of measurement of ambient dose rate; and of sampling, sample preparation and measurement for estimating radioactivity levels in air); some documents can be accessed on the EURDEP site (registered users only).

4.3.4 New technical developments

a. Spectrometric detectors

As mentioned, spectrometric detectors are increasingly used for fixed and mobile (see below) monitoring, as new scintillators such as $LaBr_3$, $CeBr_3$, SrI_2 or $Bi_4Ge_3O_{12}$ (BGO) and semiconductors, notably CdZnTe (CZT), are becoming affordable. The appeal of these detectors consists in the possibility of energy resolved in addition to dose rate measurement, which allows gamma radionuclide discrimination, to some extent, but limited only by energy resolution. The recent European research project "MetroERM" has dealt with QA aspects of such detectors being employed in early-warning networks (EURAMET, 2017). To calculate dose rate from gamma spectra, see Dombrowski (2014) and Camp & Vargas (2014).

Apart from higher resolution, the advantages of CZT and new scintillator systems are light weights, which make them interesting for small, unmanned carriers. A drawback of $LaBr_3$ detectors is their internal background, due to the naturally occurring radioisotope ^{138}La (abundance 0.9%, half-life of 10^{11} years, gamma energies of 789 and 1436 keV, the former interferes with the 796 and 802 keV peaks of ^{134}Cs, the latter

Influence of site geometry

Figure 4-11 shows the fractions of dose rate originating from discs of different radii. The selected gamma energies are typical for natural terrestrial radionuclides. About 70 to 80% of gamma dose rate originates from the area within 10 m surrounding the monitor. (In this example radionuclides are assumed homogeneously distributed on the ground. This is approximately valid for natural radionuclides in most cases.) To capture 90%, a surrounding of 100 m is necessary. This implies that deviations from the standard site geometry within several 10 m around the monitor can introduce serious bias into the monitor response. Note that the dose rate is also generated by the part of the energy spectrum below the full energy photo peak due to Compton scattering in soil, air, and back-scattering (skyshine). For similar graphs, see Malins et al. (2015).

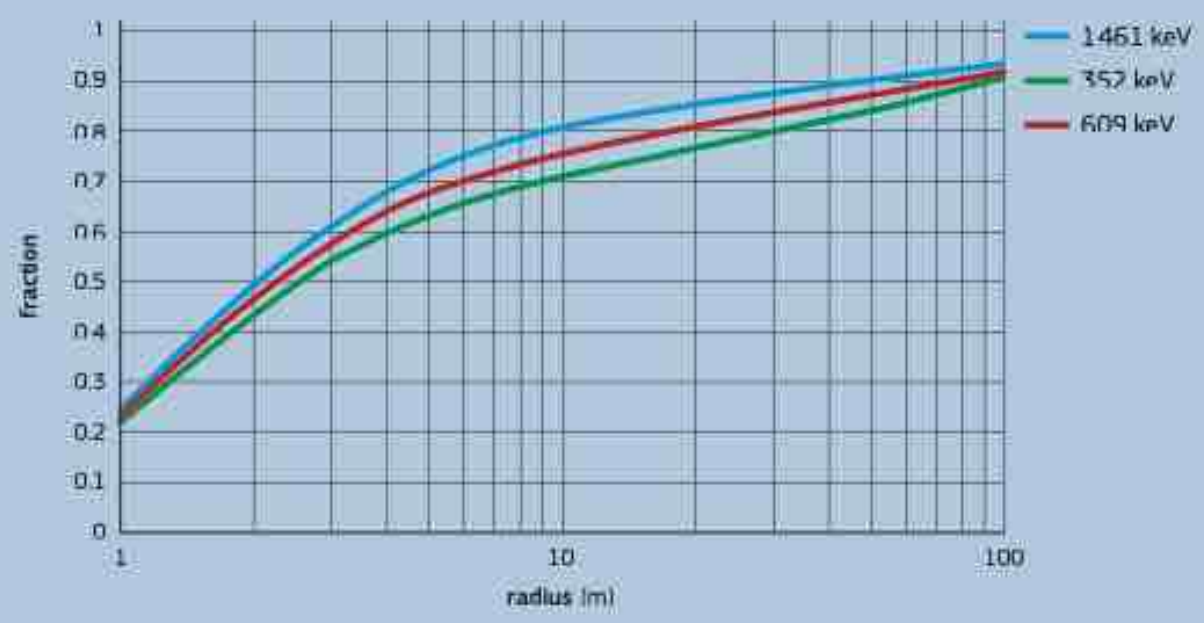

Figure 4-11
Fraction of the dose rate coming from a disc of given radius around the detector, for three gamma energies characteristic of geogenic radionuclides; source homogeneously distributed in the ground. The detector is located 1 m above ground. From data in Zähringer & Sempau (1997), Table 7.
Source: Tondeur et al. (2017).

with ^{40}K, 1.461 keV). Newly available $CeBr_3$ detectors do not have this disadvantage. On the other hand, CZTs, in their current state of development, are comparatively less sensitive. Therefore, they can only be used in situations of relatively high gamma flux, i.e. high levels of contamination.

It appears, up to now, that for airborne gamma-ray spectrometric routine mapping of natural radioactivity, the new systems cannot compete with the 'classical' NaI-detector-based ones. However, Martin et al. (2015) used an unmanned aerial vehicle (UAV; also called a drone) equipped with a CZT detector to map residues around former uranium mines.

b. New monitoring techniques

Fixed monitoring stations, as discussed here, have the advantage that QA is relatively easy, so that these stations yield reliable, reproducible and comparable results (the latter with regard to readings of the same monitor, but in principle also with those of other stations; see discussion above). Their disadvantage lies in their inevitably coarse spatial resolution. Local, 'small' events will likely go unnoticed unless they happen to occur in the immediate vicinity of the station; even if noticed otherwise, their development cannot be followed by fixed stations possibly far away. Moreover, locally high contamination gradients and complex contamination situations in spatial scale below the one of the monitoring network cannot be resolved by these means. As a complement to fixed-station networks, mobile monitoring of different kinds has gained importance, and QA of such systems has been intensively developed for some years. Among the available techniques are car-borne and 'backpack-borne' monitoring (picture below, right) and detectors carried by drones, as these are cheaply available nowadays (picture below, left), or light aircraft (Guastaldi et al., 2013; Albert et al., 2017).

A very important development is 'crowd-sourced' monitoring, as part of the Citizen Science movement: using quality-assured instruments and protocols, citizens roam the environment and measure dose rate (or other quantities) and transmit the data to a centre where they are further processed. This approach has gained momentum after the Fukushima accident (11 March 2011). The best-known platform seems to be Safecast (https://blog.safecast.org/), which collects dose rate data worldwide and has produced astonishing results. The European research project entitled 'Metrology for mobile detection of ionising radiation following a nuclear or radiological incident' deals with QA aspects of these new techniques, EURAMET (2018).

4.4 Terrestrial dose rate mapping

Natural radiation, composed of cosmic radiation, terrestrial radiation and of radionuclides in air and water sources, varies as a function of latitude and altitude. Terrestrial radiation varies according to the lithology of rocks, genesis and age of rocks and by absorption at the Earth´s surface. Indeed the radioactivity of rocks is widely studied since rocks are the prevailing material for house construction.

Due to physical properties of different types of radiation and their penetration, gamma rays are often detected as a measure of the terrestrial radiation. Gamma-ray fields of regional geological objects or areas can be specified by the dose rate and expressed in nGy/h, or by the rate of photon dose equivalent and expressed in nSv/h.

Dose rate maps provide fundamental knowledge of the natural radiation environment, an initial parameter for the radiation protection. Since rocks are the basic building materials, their radiometric signatures and contents of K, Th and U are studied for their applicability in building industry. Localisation of anomalies of terrestrial gamma dose rate is the fundamental technique for exploring radioactive raw materials, as has been described in numerous publications of the IAEA (1979).

Recently, the potential of terrestrial dose rate maps to serve on the regional scale as predictors of radon risk has been investigated (see Section 5.4).

4.4.1 General overview

As described in Section 4.3, different data sources of ambient dose rate data and measurement techniques are available:

a. Field measurement – dedicated surveys

Extensive radiometric measurements have been performed for geological mapping and surveys of the raw materials. More than fifty percent of the area of the Earth's continents have been covered by airborne and ground gamma-ray surveys, focused predominantly on uranium prospecting (IAEA, 2010). Extensive areas and inaccessible areas have been monitored by airborne surveys, local objects have been investigated by ground measurements. The output of these surveys are maps of natural radioelements in rocks and gamma dose rate of rocks. Since airborne and car-borne gamma-ray surveys produce thousands of registered data, compiled dose rate maps have the capacity to depict irregularities in monitored radiation fields.

Monitoring environmental radiation serves to estimate radiation levels and compare them with national reference standards. Resultant values of these investigations include cosmic radiation, terrestrial radiation and nuclear fallout dose rate. Since the nuclear fallout radiation levels vary over time, the year of measurement is significant.

Field airborne radiometric mapping with high-volume scintillation detectors (30–50 l of NaI(Tl)), at a standard height of 60–120 m, an airplane speed of 90–200 km/h, a field of view up to 400 m and 1 second scans provides numerous radiation data along the flight trajectory. The usual procedure for environmental radiation mapping is filter and aggregate data to a regular grid, corresponding to profile separation, before performing radiometric data contouring. Resultant radiometric dose rate maps (nGy/h) correspond to radiation of large geological bodies.

Mobile monitoring. Left: The experimental drone of the German Office for Radiation Protection (BfS), equipped with a CdZnTe detector. Right: 'Walking-borne' and 'Backpack-borne' ground monitoring. Data are automatically geo-referenced and transferred to the base station.
Source: Both pictures from an exercise in the Chernobyl exclusion zone, 2015.

Ground radiometric measurements, carried out along the profiles or irregular tracks over the area of interest, provides local dose rate data. Fundamental parameters affecting the reliability of the radiometric data are inhomogeneity of the geological basement, geometry of the terrain, change of the background and exposure time of single measurements. Dependence on portable instruments and their calibration results are introduced in dose rate (nGy/h), or in the rate of photon dose equivalent (µSv/h).

Basic references for evaluating airborne gamma-ray spectrometry are Beck et al. (1972), Miller & Shebell (1993), ICRU (1994), IAEA (1991) and IAEA (2003).

b. Monitoring networks

Systematic measurements focused on radioactive raw materials prospecting and localisation of radioactive anomalies are carried out in fixed-line separation, using airborne, car-borne and ground measurements, or rough terrain airborne contouring, while estimates of environmental radiation can also be based on observations at irregularly placed stations in the area of interest. An example of the latter on European scale is the EURDEP system, described in detail in Section 4.3.2.

c. Calculation from geochemical data

Computation of dose rate using known concentration values of natural radioelements K, U and Th in rocks and soils is based on the model of gamma radiation of the homogeneous infinite plane over the Earth´s surface. Constants for conversion of the unit K, U, and Th mass concentration in soil at a height of 1 m above the homogeneous soil surface cited in literature (IAEA, 2003; Will et al., 2003) differ negligibly, depending on selected density of rocks and applied radiation constants. The limiting parameter compiling a dose rate field is the source data. K, U and Th concentrations in surface rocks and soils can be effectively determined by *in situ* gamma-ray spectrometry, where the field of view and corresponding analyses depend on the detector elevation, while geochemical sampling represents local random samples of low mass.

Mapping uncertainty

Apart from the uncertainty of input data from which the maps are made, the mapping procedure itself is also prone to uncertainty. Maps made of sets of methodically different data, even if nominally measuring the same quantity, can therefore look different. This effect is inevitable by physical nature, but it can give rise to misunderstandings and miscommunication, and in consequence to credibility problems.

a. Point samples

'Point samples' of rock or soil have to be interpolated to generate a spatially continuous map. In this context, 'points' mean locations where individual pieces of material have been collected, or small areas from which several pieces have been collected and mixed. Inference to a contiguous map, or 'response surface', involves uncertainty.

Sampling 'points' may not be representative for the quantity which one attempts to assess. If the target is to establish a map of the radiometric background, i.e. the average or 'typical' level over an area, including anomalies that may be small in spatial extension, may distort the picture. Because of their small size, interpolation may yield misleading results, in particular if the samples were originally collected to search for anomalies (e.g. in the framework of mineral exploration), i.e. for a different objective. Such objectives usually result in preferential sampling schemes, which can introduce heavy bias if used for background mapping. The clear separation, conceptually as well as in practice, of background and anomaly is a non-trivial subject, to which large amounts of scientific literature have been devoted.

Interpolation between 'point' samples requires a model of how values at points in a neighbourhood are correlated. The model is usually estimated from available data and is therefore subject to systematic (see above) and random uncertainty, the latter as every estimation procedure. For more details on geostatistical procedures; see Section 2.4.

b. Area samples

Ground-based ADR measurement or *in situ* gamma-ray spectrometry, usually performed at 1 m above ground, generates values that represent a weighted mean over an area whose radius around the location of the instrument extends from several 10s, up

to 100 m, depending on the gamma-ray energies of the source and its distribution in the ground. The weighting function, called point spread function, can be quite complicated; in any case, the result is not a uniform mean over the detector 'horizon' or 'footprint'. The ideal measuring situation is an infinite, even, empty plane, which is evidently not realistic. Deviation from this ideal geometry introduces bias into the result, which is generally difficult to quantify in terms of gamma rays.

c. Remote sensing – airborne gamma-ray spectrometry

In analogy to (b), aerogamma data represent weighted means over rather large areas. Since the carrier (aircraft, helicopter or, more recently, drones) moves, the footprint is elongated along the flight direction.

Footprints overlap along the flight line (and data corresponding to subsequent footprints are therefore strongly correlated), but may be separated perpendicular to the flight line, depending on the distance between flight lines. The resulting anisotropic correlation structure is a challenge for mapping.

The weighting function is even more complex if the surveyed territory is orographically structured and covered by different vegetation or different type of land use. To some degree, correcting for these effects is possible but complicated. Evidently, they are a source of uncertainty that is difficult to quantify.

Also for the (unrealistic) ideal situation, i.e. the infinite even plane, it is not trivial to conclude from footprint-related data to the theoretic value at a point. Deconvolution of areal data is mathematically demanding as a discipline of inverse modelling (similar to generating tomographic pictures) (e.g. Billings et al., 2003; Druker, 2016).

However, if the objective of airborne survey is to detect anomalies and assess the general contamination pattern, these uncertainties matter little. But straightforward comparison with ground-based methods (a) and (b) is problematic.

Examples of national and regional ambient dose rate maps

An overview of some national and regional dose rate surveys is given in Table 4-3. Some of these countries appear to be active in regional surveying, but apparently did not assemble their data into a national database; a notable example is Turkey which has probably covered most of its territory by regional surveys. In many cases, dose rate surveys are not published in international literature, but remain in reports which are often difficult to access. Some of these maps report ambient dose rate, while the others, after subtracting the radiation background, report natural terrestrial radiation (radioactivity of rocks).

Table 4-3
Some national and regional ambient dose rate surveys in Europe
Source: Table created by Peter Bossew

Code	Country	Method	Map?	Reference
AT	Austria	ground measurements	no	Tschirf (1975)
BA	Bosnia and Herzegovina	calculated from samples	no	Pehlivanovic (2016)
BE	Belgium	calculated from samples, TLD, ground measurements	yes	Deworm (1988)
CH	Switzerland	airborne & ground measurements	yes	Rybach (2002)
CZ	Czech Republic	airborne, ground & carborne measurements, geochemical surveys	yes	Manová & Matolín (1995); Matolín (2017)
DE	Germany	ground measurements	yes	Will et al. (1997); Will et al. (2003)
ES	Spain	ground measurements	yes	Quindós Poncela et al. (2004); Garcia-Talavera et al. (2007, 2013)
IT	Italy / Aeolian Islands	ground measurements	yes	Chiozzi (2001, 2003)
PL	Poland	ground measurements	yes	Strzelecki et. al. (1994)
RS & ME	Serbia, Montenegro	calculated from samples	no	Dragovic (2006)
SK	Slovak Republic	ground measurements	yes	Daniel et al. (1997)
TR	Turkey / Adana	ground measurements	yes	Degerlier (2008)
TR	Turkey / Balikesir	ground measurements	yes	Kapdan (2012)
TR	Turkey / Kayseri	ground measurements	yes	Otsanev (2012)
TR	Turkey / Akkuyu	calculated from samples	no	Ozmen (2014)
TR	Turkey / Canakkale	car-borne measurements	yes	Turhan (2012)
TR	Turkey / Kutahia	calculated from samples	no	Sahin (2008)

4.4.2 European Terrestrial Gamma Dose Rate Map

Terrestrial gamma dose rate (TGDR) all over Europe has been estimated from geochemical concentration, according to the UNSCEAR formula, as described in Section 4.3.2.

The input data for the the concentrations of uranium, thorium and potassium in soil have been taken from the European maps (10 km × 10 km grid cells) developed using FOREGS and GEMAS databases. The maps are shown and described in Chapter 3.

The calculation is based on two fundamental assumptions: the secular equilibrium; and homogeneity and standard composition of the soil.

Using 0.7 as a factor to transform the absorbed dose in air to external effective dose to adults (UNSCEAR, 2008), the effective dose due to external exposure from terrestrial radionuclides can be estimated by applying the following formula:

$$D\ (mSv/a) = 0.7\ (Sv/Gy) * TGDR\ (nGy/h) * t * [(1 - OF) + SF * OF] * 10^{-6} \quad (4\text{-}11)$$

where:
TGDR (nGy/h) is the absorbed dose rate estimated in Section 4.3.2;
t is the time of exposure in hours (8 760 h = 1 year);
OF is the occupation factor, 0.8 (UNSCEAR, 2008);
SF is the shielding factors of buildings, 1.4 (UNSCEAR, 2000, Annex B).
As input data for TGDR, the values at 10 km × 10 km grid cells estimated for the European Terrestrial Gamma Dose Map have been used.

The European Annual Terrestrial Gamma Dose Rate Map shows the annual effective dose that a person would receive from terrestrial radiation, if she/he spends all the reference time in a location where the soil has fixed K, Th and U concentrations.

Secular radioactive equilibrium

The secular radioactive equilibrium condition is a very good and useful approximation but not strictly true, in particular for the uranium series, because of the presence of radon gas (^{222}Rn) in the middle of the chain. Actually, its relatively long half-life ($T_{1/2}$=3.82 days) allows radon to escape from the soil matrix, entering into the atmosphere. As a consequence, the most superficial layers of soil are partially depleted by radionuclides belonging to the lower part of the uranium chain, in particular the short-lived radon daughters ^{214}Pb and ^{214}Bi, both very strong gamma emitters. These gamma emitters, once produced in air by radon decay, are distributed along the whole atmospheric column, following more or less the concentration pattern of radon. Therefore a significant reduction of the dose rate is expected, as the gamma irradiation at the receptor point (conventionally, 1 m above the ground) due to the short-lived radon daughters is much weaker than it could have been if there were no radon emanation and all the radionuclides would remain trapped in the soil matrix. Anyway, the contribution of this component is very small (a few nGy/h), although during strong atmospheric inversion conditions it can increase somewhat, since radon and its short-lived daughters remain close to the ground. For that reason, no great errors are expected when assuming a standard value for radon emanation in the calculation, thus neglecting the irradiation coming from the radionuclides suspended in the atmosphere. The fraction of radon escaping from soil is difficult to estimate: values of the order of 20 %–30 % can be assumed for the most superficial layers, although in some special cases the radon emanation fraction can reach values up to 50 %. Moreover, the value of this parameter is not constant in time, being influenced by rain and changes in the soil humidity. The uncertainty regarding the real value of this fraction is probably one of the most important factors affecting the estimation of the gamma dose rate component due to the uranium series.

More rarely, in some particular soils a substantial break of the radioactive equilibrium conditions can also occur due to complex geochemical processes involving uranium and radium: in these cases the secular equilibrium condition between the upper part of the chain (^{238}U) and the lower part (^{226}Ra) can no longer be assured and therefore TGDR cannot be calculated using the simplified Equations 4-11 or 4-12.

In principle, similar considerations also apply to the thorium series: the presence in the radioactive family of another radon gas isotope, namely ^{220}Rn, can break the secular radioactive equilibrium conditions of the chain. However the much shorter half-life of ^{220}Rn (55.6 seconds) significantly limits the fraction of ^{220}Rn able to escape from the soil matrix. Therefore, for the thorium series, an almost perfect secular equilibrium condition can reasonably be assumed.

Soil homogeneity and composition

The assumption of soil homogeneity, characterised by a unique value for the density and by a unique mass attenuation coefficient $(\mu/\rho)_a$, could seem to be a rather crude approximation of reality. However, it can be shown that the variation of these parameters in the typical accepted ranges only slightly affects the dose rate values. Beck's calculations indicated that the differences in composition and moisture content for most plausible soils result in some variations of the TGDR of about 5 % or less. Moisture content is generally the most important factor influencing the $(\mu/\rho)_s$ values. In Beck's work, the $(\mu/\rho)_s$ values were given for a moisture content ranging from 0 to 25 %. Typical values are usually in the range of 10 %–20 %. In the calculation, a standard soil composition and moisture content were assumed for all soils: Al_2O_3 (13.5 %), Fe_2O_3 (4.5 %), SiO_2 (67.5 %), CO_2 (4.2 %), H_2O (10 %).

The TGDR, calculated as average values over the grid cells, span a wide range, varying from a minimum of 17 nGy/h (0.14 mSv/a) to a maximum of 189 nGy/h (1.53 mSv/a). These values are of course correlated to the highest uranium, thorium and potassium concentrations. Figure 4-12 shows the distribution of the TGDR values: it looks slightly asymmetrical, with a mean of 62 nGy/h

(0.5 mSv/a) and a median of 59 nGy/h.

The distribution pattern of the calculated terrestrial gamma dose shows a wide area (25 %) of low values (below 50 nGy/h or 0.4 mSv/a) from the Netherlands through Denmark and Northern Germany to Eastern Poland. This area corresponds to the Northern Lowland, which is characterised by a cover of glacial drift deposits related to advances and retreats of the Scandinavian Ice Sheet during the Pleistocene.

Other low-value areas are related to glacial deposits (Northern Finland, Sweden and Norway, and Central Norway) or to fluvial sedimentary basins (Tizsa basin in South-Eastern Hungary, Garonne basin and parts of the Rhone valley in France, the Guadalquivir basin and the Segura and Jucar basins in Spain).

The map shows a pattern of higher values forming a wide arc at the northern margin of the Alps, which seems to be due to high potassium concentrations, which in turn are related to fluvioglacial and fluvial sedimentary supply from the uplifted Alps.

High values occur in the mountain ranges related to the Alpine orogeny (Pyrenees, Alps, Apennine Mountains, Dinaric Alps, Hellenides Carpathians, Balkan Mountains), which incorporate several Cenozoic syn- and postorogenic magmatic bodies along with a metamorphic-overprinted Variscan granitic core.

Areas with the highest values (namely, above 99 nGy/h or 0.71 mSv/a) correspond to the mainly granitic Variscan massifs, relics of the late Paleozoic orogenic belt: North Western Iberian Peninsula; Massif Central, Armorican Massif and Vosges in France; Cornubian Massif in Southwest England; the Ardennes and Rhine Massif, Black Forest, Harz Mountains, Bohemian Massif.

In the Mediterranean areas, high values may be noticed also in Central Italy (Lazio and Campania magmatic areas), Northeast Sardinia (Variscan granitic rocks), Calabria in Southern Italy (a fragment of the Alpine chain), Rhodope mountains in Greece and Bulgaria (Early Cenozoic magmatism).

High values in Eastern Sweden and Southern Finland are connected to the Paleoproterozoic granites, pegmatites and volcano-sedimentary rocks of the Southern Svecofennian Province of the Baltic Shield (Lahtinen, 2012), including uranium mineralisation.

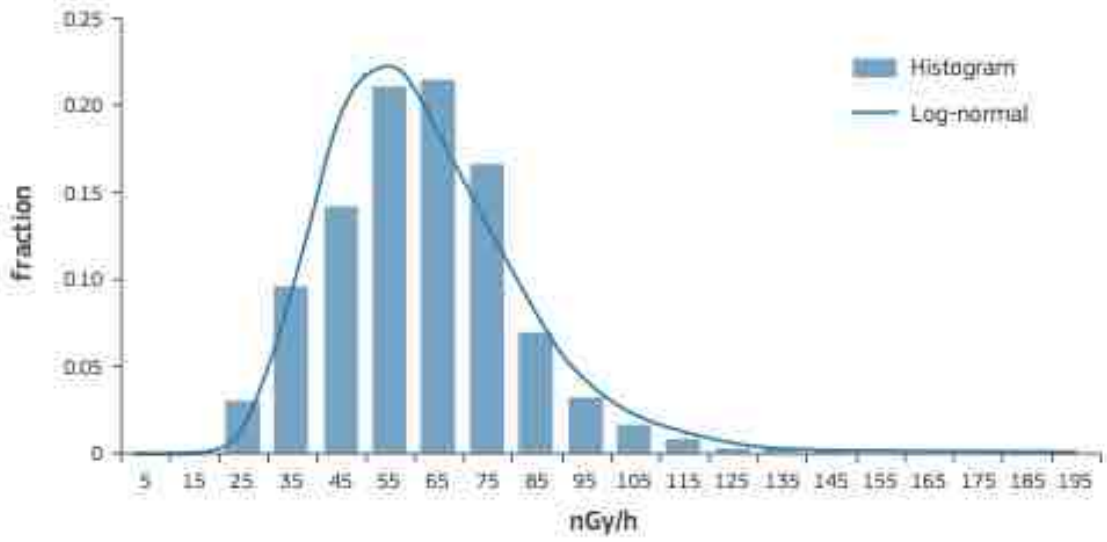

Figure 4-12.
Histogram of TGDR in Europe created with more than 47 000 cells. The distribution is slightly asymmetric and can be fitted with a log-normal function with a mean of 62 nGy/h and a median of 59 nGy/h. Maximum value 189 nGy/h, minimum 19 nGy/h.
Source: EAN, JC-JRC 2019

4.4.3 Work in progress: Using EURDEP data to map terrestrial gamma dose rate

Reflecting the geographical variability of external dose rate, the EURDEP network is a natural candidate of a data source for creating ambient dose equivalent rate maps.

In order to identify the contribution from terrestrial natural gamma sources, one has to estimate the contributions of cosmic rays and anthropogenic fallout, and subtract the corresponding dose rates from the total one recorded by the monitor. The different contributions depend on source strengths and on the sensitivity of the probes against these components, as well as on local set-up and mounting of probes. Often, not all factors are exactly known, so that decomposition of the total recorded ADR in order to retrieve the terrestrial natural gamma component is not simple, and problems are multiple:

- ADER is the sum of several components, which need to be disentangled if the objective is mapping of a particular component, notably the terrestrial gamma dose component. This aspect has been discussed in Section 4.2.2.
- Network heterogeneity (see Section 4.3.3):
  a. on network level: this affects precision which depends on station density and geometrical homogeneity;
  b. on station level: this affects comparability of data generated by individual stations.

In spite of large amounts of raw ambient dose rate data available in EURDEP, and many years of efforts to understand in detail and to harmonise the differences between national systems, which is necessary for correct decomposition of the signals, sufficient information is only available for a few countries, namely Austria, Belgium, Croatia, Germany and Hungary. For details, the reader is referred to more extensive discussions in Bossew et al. (2017).

Only for stations from the mentioned countries have the following standardisation steps been performed:

- selection of stations whose siting was deemed to conform sufficiently to the standard;
- calculation and subtraction of site-specific cosmic dose rate (see Section 8);
- subtraction of intrinsic detector background;
- airborne components were deemed of minor relevance;
- artificial fallout, which may locally contribute significantly, was not subtracted because of lack of site-specific information;
- "rain peaks" above and in the next section, were removed.

The value of terrestrial background was defined as the arithmetic mean over long measurement periods (at least 1 year) of the remaining signal. For technical details, the reader is referred to Bossew et al. (2017).

Ordinary kriging has been applied to interpolate the data coming from the above countries. The map, Figure 4-13, shows the gamma dose rate from terrestrial sources (natural plus ^{137}Cs fallout) to which a person would be exposed if she/he spends all the time outdoors. At this stage, ^{137}Cs fallout could not be separated, but in most locations it contributes little (see Bossew et al., 2017). The data do not include the contribution of so-called radon peaks, i.e. radiation of radon progeny deposited on the ground by precipitation. Dose rate generated this way can be quite high in the short-term (up to a few 100 nSv/h), but contributes only in the order of 2 - 5 % to the annual terrestrial gamma dose.

The mapping support is formed by the same 10 km × 10 km cells as for the European Indoor Radon Map (Chapter 5). In this figure, all countries have used nSv/h H*(10) as unit for ambient dose equivalent rate.

As a result, to date, the map of terrestrial ambient dose equivalent rate covers only parts of Europe. In principle, however, the methodology has been established and could be applied to other countries once sufficient technical information becomes available.

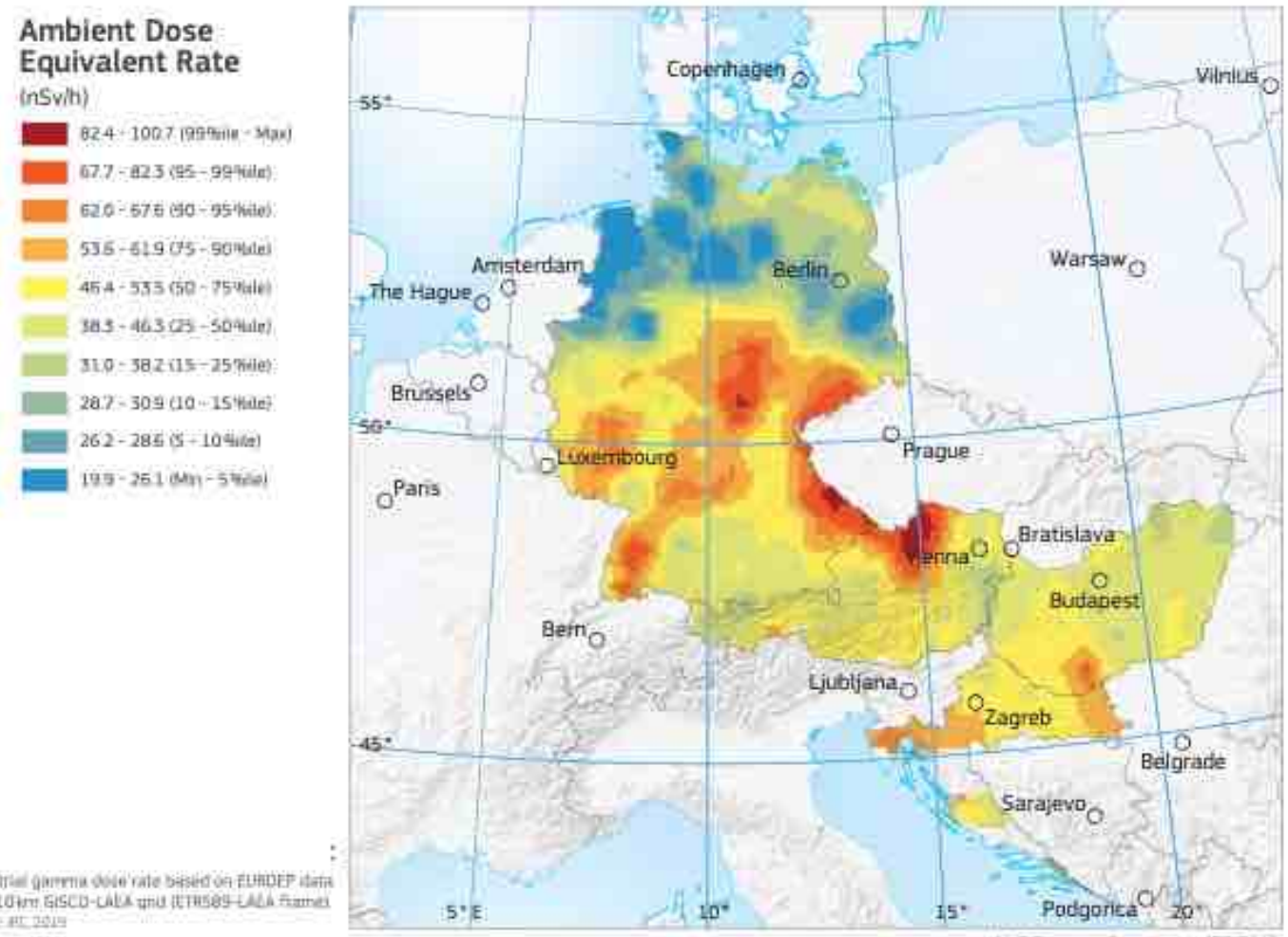

Figure 4-13.
Map of terrestrial gamma dose rate based on EURDEP data on a 10 km × 10 km GISCO-LAEA grid (ETRS89-LAEA frame).
Source: EAN, JC-JRC 2019

copyright © European Commission, JRC, 2019

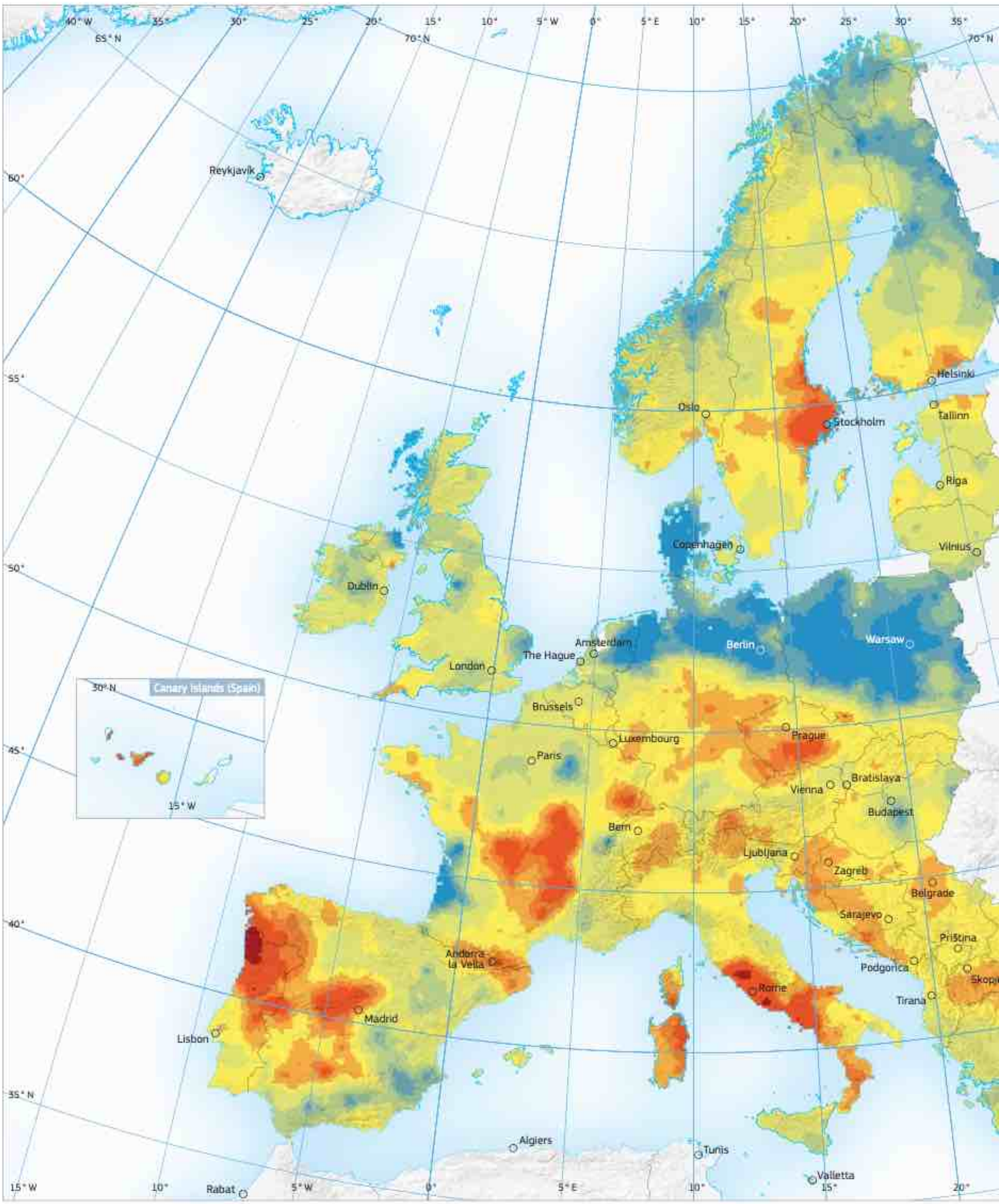
40° W
35°
30°
25°
20°
15°
10°
5° W
0°
5° E
10°
15°
20°
25°
30°
35°
65° N
70° N
70° N
60°
55°
50°
45°
40°
35° N
30° N
15° W
10°
5° W
0°
5° E
10°
15°
20°
Canary Islands (Spain)
Reykjavik
Oslo
Stockholm
Helsinki
Tallinn
Riga
Vilnius
Copenhagen
Dublin
London
The Hague
Amsterdam
Berlin
Warsaw
Brussels
Luxembourg
Paris
Prague
Vienna
Bratislava
Budapest
Bern
Ljubljana
Zagreb
Belgrade
Sarajevo
Priština
Podgorica
Skopje
Tirana
Rome
Andorra la Vella
Madrid
Lisbon
Algiers
Tunis
Valletta
Rabat

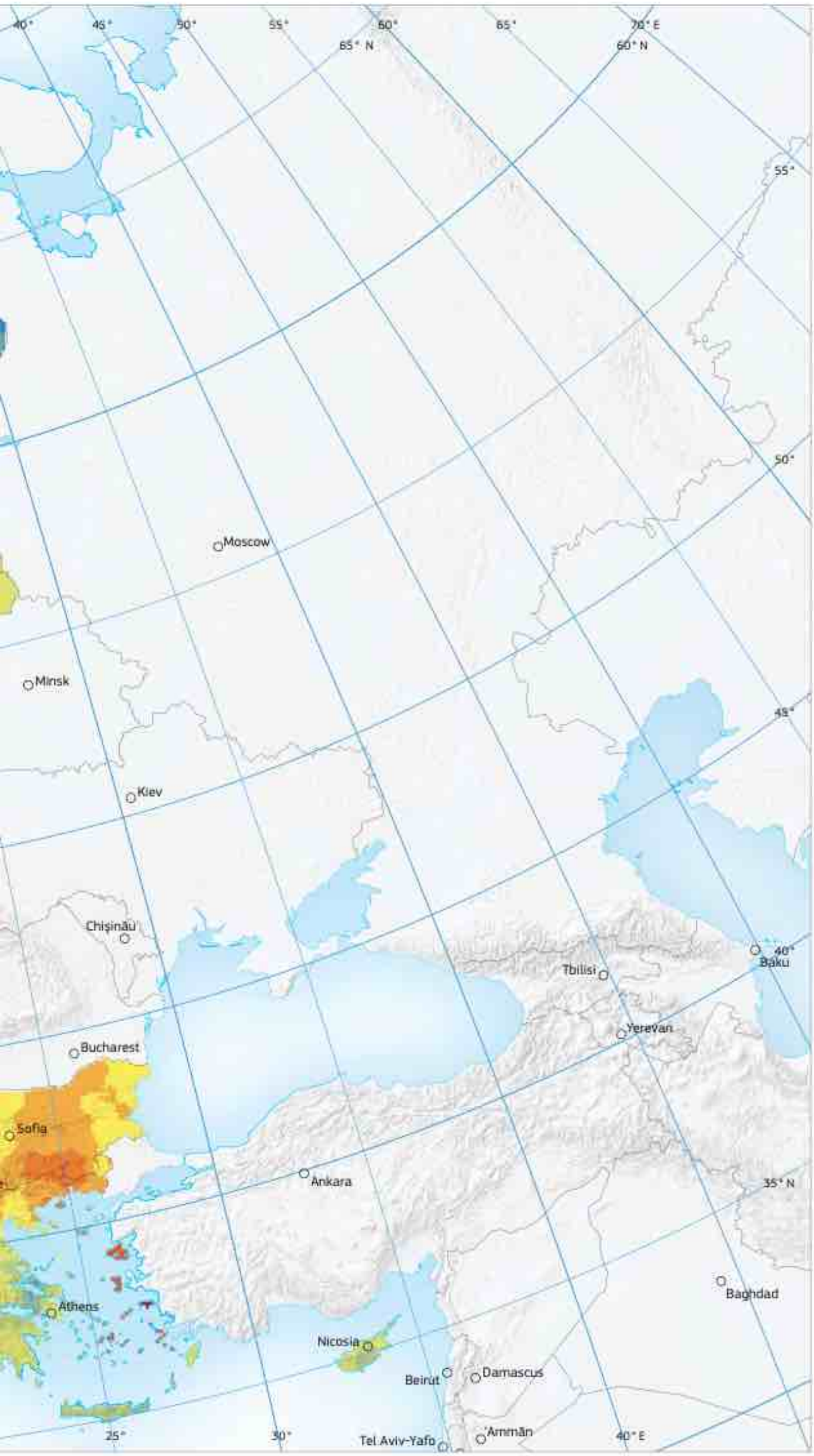

Plate 4: European Terrestrial Gamma Dose Rate Map

(nGy/h)

- 144.3 - 200.0 (99%ile - Max)
- 99.2 - 144.3 (95 - 99%ile)
- 88.5 - 99.2 (90 - 95%ile)
- 75.0 - 88.5 (75 - 90%ile)
- 62.3 - 75.0 (50 - 75%ile)
- 48.8 - 62.3 (25 - 50%ile)
- 41.4 - 48.8 (15 - 25%ile)
- 37.4 - 41.4 (10 - 15%ile)
- 32.0 - 37.4 (5 - 10%ile)
- 32.0 - 37.4 (Min - 5%ile)

Plate 4: European Terrestrial Gamma Dose Rate Map
The map shows the dose rate, in nGy/h, that a person would receive from terrestrial radiation, if she/he spends all the reference time in a location outdoor in which the soil has fixed U, Th and K concentrations.
Source: EANR, EC-JRC, 2019

copyright © European Commission, JRC, 2019

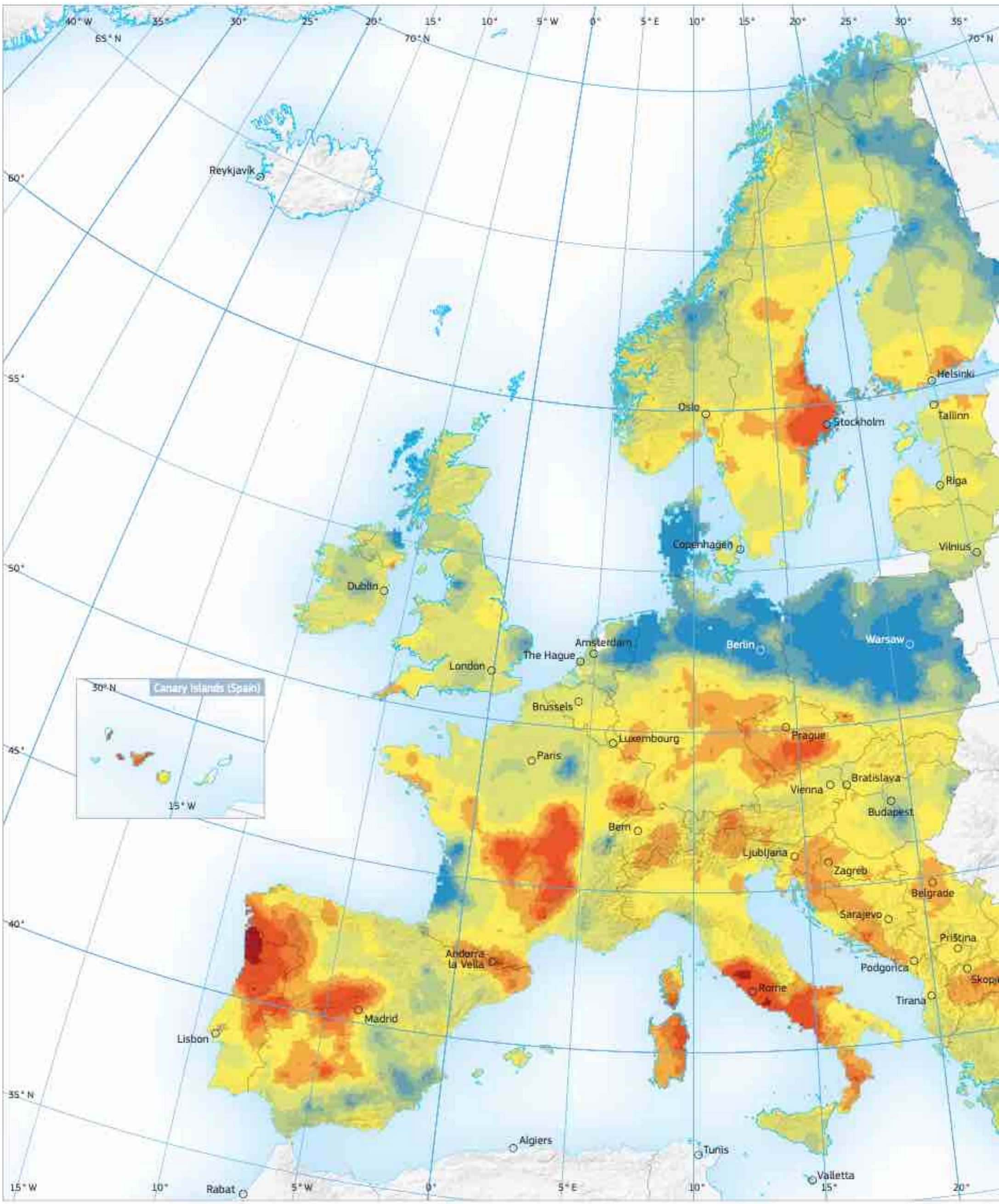
40° W
35°
30°
25°
20°
15°
10°
5° W
0°
5° E
10°
15°
20°
25°
30°
35°
65° N
70° N
70° N
60°
55°
50°
45°
40°
35° N
30° N
15° W
10°
5° W
0°
5° E
10°
15°
20°
Canary Islands (Spain)
Reykjavik
Oslo
Stockholm
Helsinki
Tallinn
Riga
Vilnius
Copenhagen
Dublin
London
The Hague
Amsterdam
Berlin
Warsaw
Brussels
Luxembourg
Paris
Prague
Vienna
Bratislava
Budapest
Bern
Ljubljana
Zagreb
Belgrade
Sarajevo
Priština
Podgorica
Skopje
Tirana
Rome
Andorra la Vella
Madrid
Lisbon
Rabat
Algiers
Tunis
Valletta

Plate 5: European Annual Terrestrial Gamma Dose Map

(mSv)

- 1.17 - 1.60 (99%ile - Max)
- 0.80 - 1.17 (95 - 99%ile)
- 0.72 - 0.80 (90 - 95%ile)
- 0.61 - 0.72 (75 - 90%ile)
- 0.50 - 0.61 (50 - 75%ile)
- 0.39 - 0.50 (25 - 50%ile)
- 0.33 - 0.39 (15 - 25%ile)
- 0.30 - 0.33 (10 - 15%ile)
- 0.26 - 0.30 (5 - 10%ile)
- 0.14 - 0.26 (Min - 5%ile)

Plate 5: European Annual Terrestrial Gamma Dose Map.
The map shows the annual effective dose in mSv that a person would receive from terrestrial radiation, if she/he spends all the reference time in a location in which the soil has fixed U, Th and K concentrations.
Source: EANR, EC-JRC, 2019

copyright © European Commission, JRC, 2019

Case study: Piedmont (Italy), soil and rock samples

While soil databases are convenient for their uniformity over Europe, in some regions concentrations of uranium, thorium and potassium in rocks are made available from gamma spectrometry. Comparison of data in rocks and soils, carried out by relating soil data to the bedrock in regions where both datasets are available, shows that soil data are strongly connected to the bedrock lithology.

Gamma spectrometry of rocks clearly displays a relation between uranium, thorium and potassium concentrations and different classes of lithologies, characterised not only by homogeneity of broadly defined rock types but also by common genetic processes. As an example, in the Alpine regions cenozoic intrusive rocks with upper crustal contamination and late Paleozoic (Variscan) acid igneous rocks show the highest concentrations of natural radionuclides, while mafic and ultramafic rocks and calcareous mesozoic rocks indicate the lowest. Radionuclide concentrations in detrital rocks and sediments reflect their petrographic compositions. In sediments, depositional environments may play a significant role, like high uranium concentration in lacustrine anoxic sediments.

The consistent number of gamma spectrometry measurements (HPGe) of rocks allows consolidating traditional geological units, identified by lithologic, stratigraphic and genetic criteria, into 'radiogeolithological' classes characterised by homogeneity of radionuclide content, yet preserving a defined geological singularity.

Following this approach, a more detailed work was performed in the Piedmont Region, an administrative district in Northwest Italy near the Alpine French border, covering about 25 400 km². Actually, in this area a large set of experimental radioactivity data were available: 154 topsoil samples and 239 rock samples were analysed by means of HPGe gamma spectrometry during several measurement campaigns conducted by ARPA Piemonte (Environmental Protection Agency of Piedmont), allowing for a quantitative determination of the activity concentrations (Bq/kg) of uranium, thorium and potassium.

It was then possible to assign activity concentration values for uranium, thorium and potassium to each of the 26 'radiogeolithological' classes in which Piedmont's geology was classified. The TGDR for Piedmont was then calculated for each cell grid ($TGDR_{cell}$) as a weighted mean of the $TGDR_{RC}$ radiogeolithological values of the RC_i classes present in each cell:

$$TGDR_{cell} = \sum_i w_i \; TGDR_{RC_i} \qquad (4\text{-}14)$$

where w_i are proper weights, calculated on an areal basis.

In Figure 4-14 two maps of the TGDR in Piedmont are displayed. The map on the left has been produced following the 'radiogeolithological' approach described in the previous paragraph, using the UNSCEAR formula for the calculation, while on the right the Piedmont TGDR map, simply taken from the European map is shown for comparison. It can easily be seen that in the 'radiogeolithological' map many local peculiarities and details, lost at the European level, appear: some high background areas (TGDR > 120 nGy/h), in particular located along the Alpine ridge, can easily be identified.

Similar, more detailed maps could also be produced for any other European region, provided that a convenient radiogeolithogical database is available.

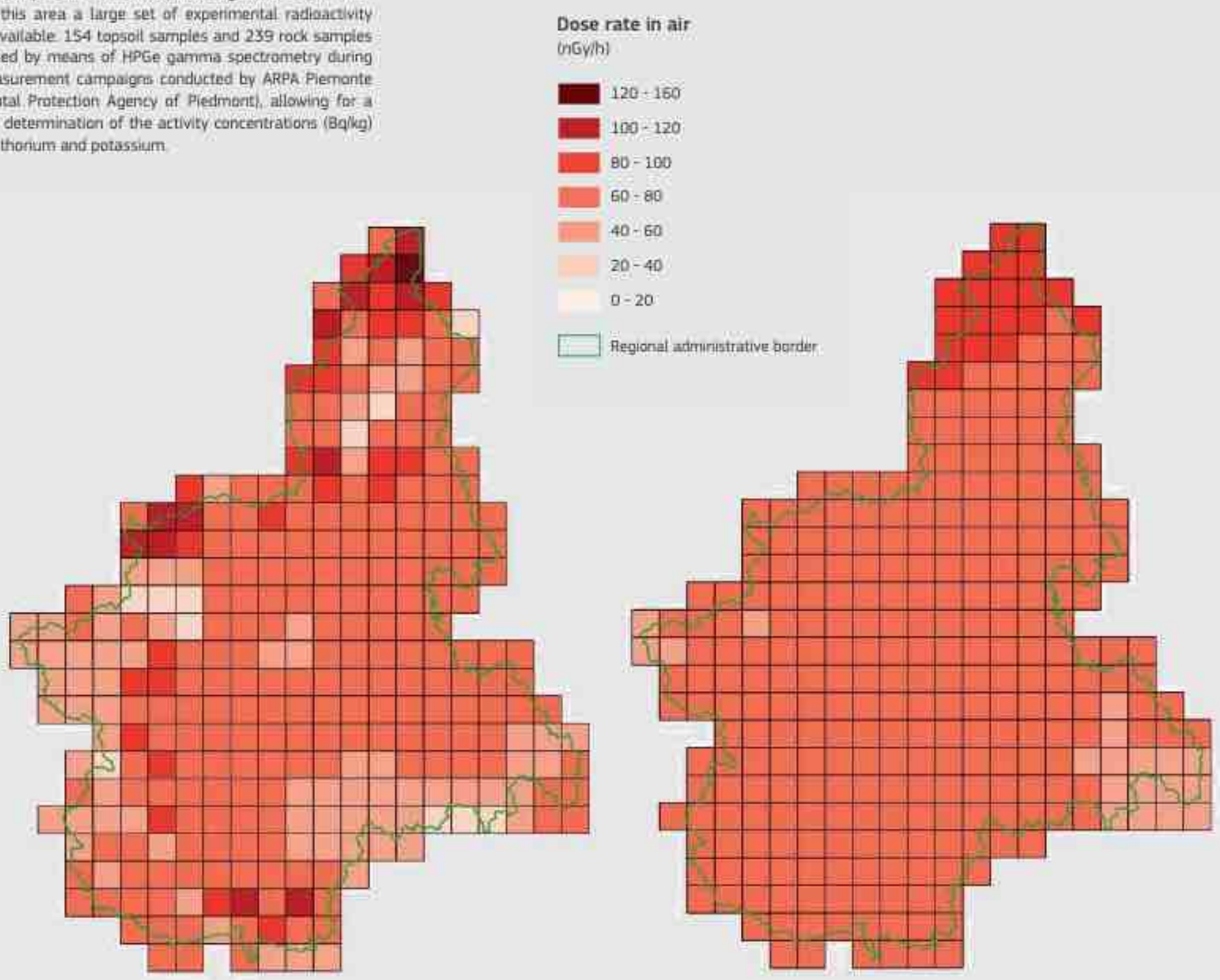

Figure 4-14
On the left, the 'radiogeolithological' Piedmont's map compared with the 'UNSCEAR map' (extracted from the European Terrestrial Gamma Dose Rate Map). It provides more detailed local radiological information that is lost at greater scale.
Source: Cinelli et al. 2018

Chapter 5

Radon

Radon isotopes (^{222}Rn, ^{220}Rn) are noble, naturally occurring radioactive gases. They originate from the alpha decay of radium isotopes (^{226}Ra, ^{224}Ra), which occur in most materials in the environment, i.e. soil, rocks, raw and building materials. Radon is also found in ground and tap water. The two radon isotopes are chemically identical, but they have very different half-lives: 3.82 days for radon (^{222}Rn) and 56 seconds for thoron (^{220}Rn). Thus, they behave very differently in the environment. Both isotopes are alpha-emitters; their decay products are polonium, bismuth and lead isotopes.

The main source of radon in air (indoor or outdoor) is soil, where radon concentrations are very high and reach tens of Bq/m^3. Radon release from soil into the atmosphere depends on radium (^{226}Ra) concentration in soil, soil parameters (porosity, density, humidity) and weather conditions (e.g. air temperature and pressure, wind, precipitation). Outdoor radon concentrations are relatively low and change daily and seasonally. These changes may be used to study the movement of air masses and other climatic conditions.

Radon gas enters buildings (homes, workplaces) through cracks, crevices and leaks that occur in foundations and connections between different materials in the building. This is due to temperature and pressure differences between indoors and outdoors. Indoor radon is the most important source of radiation exposure to the public, especially on ground floor. Radon and its decay products represent the main contributor to the effective dose of ionising radiation that people receive. Radon is generally considered as the second cause of increased risk of lung cancer (after smoking).

The only way to assess indoor radon concentration is to make measurements. Different methods exist, but the most common one is to use track-etched detectors. Such detectors may be used to perform long-term (e.g. annual) measurements in buildings. The exposure time is important because indoor radon levels change daily and seasonally. Moreover, radon concentration shows a high spatial variation on a local scale, and is strongly connected with geological structure, building characteristics and ventilation habits of occupants.

A European map of indoor radon concentration has been prepared and is displayed. It is derived from survey data received from 35 countries participating on a voluntary basis.

Clockwise from top-left:

Three radon passive detectors on a desk.
Source: José-Luis Gutiérrez Villanueva

Former uranium mine, Ciudad Rodrigo, Spain.
Source: Tore Tollefsen

Soil-gas sampling, RIM 2018 exercise, Cetyně, Czech Republic.
Source: Tore Tollefsen

Metamorphic Variscan plutonite. Contact zone between old metamorphic and newly intruded (Variscan) plutonite. This is the main uranium-bearing zone, Ciudad Rodrigo, Spain.
Source: Peter Bossew

Block of flats built on alum shale, Røyken, Norway. Røyken is one of the communities in Norway with the highest indoor radon concentration.
Source: Peter Bossew

Introduction

Radon, 'From Rock to Risk' – The geogenic compartment

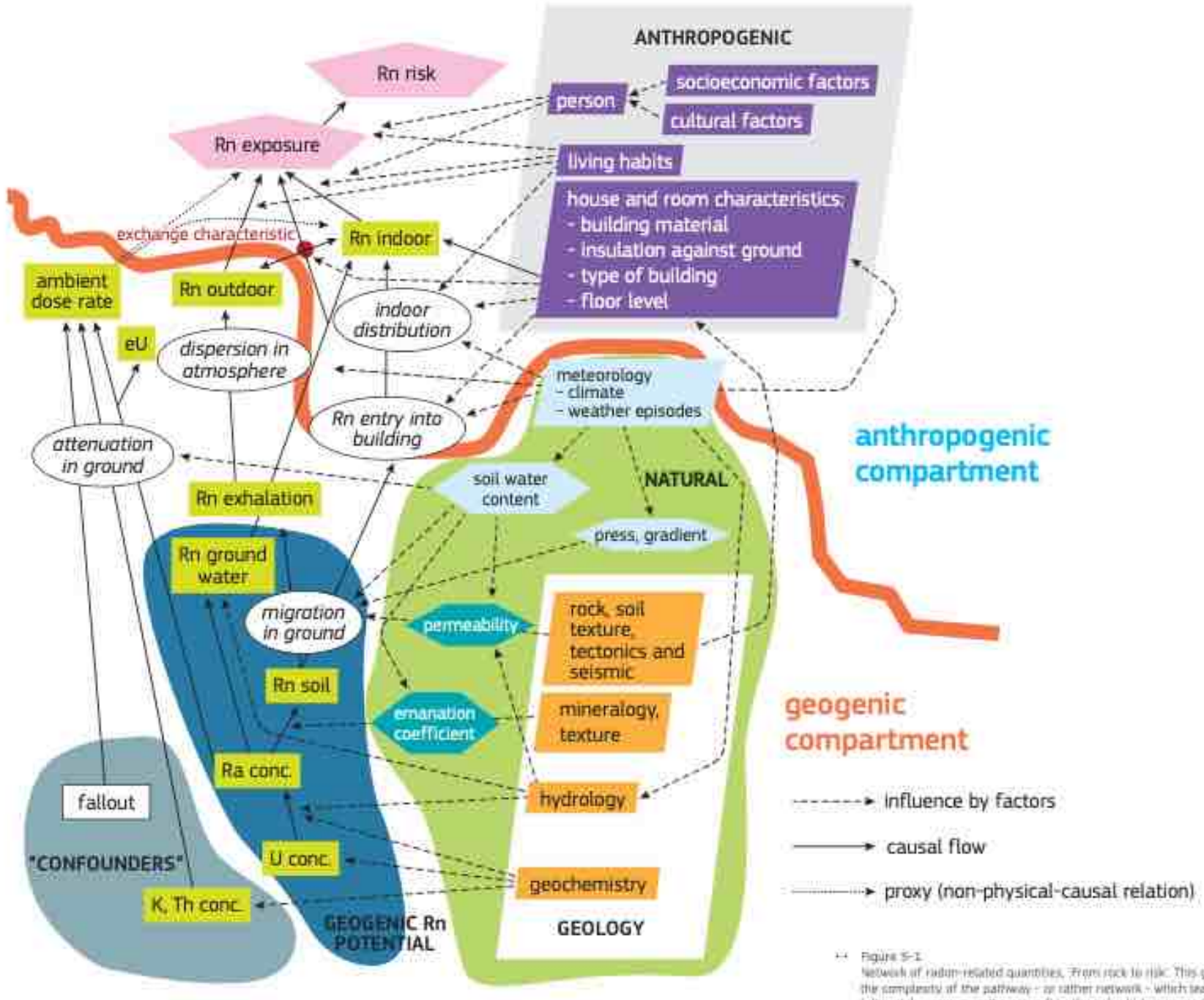

Figure 5-1
Network of radon-related quantities, 'From rock to risk'. This graph intends to visualise the complexity of the pathway – or rather network – which leads from radon sources (ultimately uranium in the ground) to the risk which is caused by radon, controlled by many factors and interactions. These are of many kinds, essentially natural and anthropogenic factors. They act on all levels of the network with different strength, again controlled by other factors.
Source: Graph created by Peter Bossew

Radon is a radioactive noble gas that exists naturally in the form of three isotopes: ^{222}Rn, ^{220}Rn and ^{219}Rn. The most stable and environmentally relevant one, ^{222}Rn, hereafter called radon (Rn), is formed by alpha decay of ^{226}Ra, and ultimately from ^{238}U; it has a half-life of 3.82 days. On the other hand, ^{220}Rn, hereafter called thoron (Tn), is a short-lived isotope with a half-life of 55.6 seconds.

Motivation

This chapter is devoted to describing the complex path of radon 'from rock to risk'. Some compartments are described in particular; they can be distinguished depending on whether they house natural or human-made or -induced phenomena, or depending on the medium (rock, soil, water, air) that dominates them. Emphasis is on the geogenic compartments.

Geogenic compartments

Radon source

The original sources of radon are uranium (^{238}U, for ^{222}Rn) and thorium (^{232}Th, for ^{220}Rn) in the ground. Due to their physical and chemical properties, the two radon isotopes are distributed in part similarly, and in part differently in the various environmental compartments. We distinguish between the geogenic and anthropogenic compartments.

The geogenic compartment comprises a number of connected and interacting 'sub-compartments'. These are the lithosphere (rocks); the pedosphere (soil) which is partly derived from rock, but soil can also have different origins (Aeolic – loess, alluvial / colluvial – by sedimentation of material transported by rivers); the hydrosphere (ground and surface water bodies); and the atmosphere.

All spheres are connected and interact through exchange of matter, technically speaking: material fluxes. For example, ground water is in contact with rock. Rock chemistry controls water chemistry and, reversely, substances dissolved in the water can precipitate into rock and modify its mineralogy, or if exhaled (such

Complexity in environmental sciences

Although it is difficult to define complexity, it is a keyword in environmental sciences. It may be characterised by the following features:

- Complex systems consist of many interacting 'players' (e.g. factors, controls, quantities);
- Factors may depend upon each other in different ways and even be nested. The factors may be 'coupled' in a way that is itself a function of other factors, or convoluted in structures which are not well known.
- Yet the underlying physical laws may be simple (such as, in radon science, radioactive decay, diffusion, advection, convection, dissolution etc.);
- Often such systems develop complicated temporal and spatial patterns, with regular components, but also show a tendency to seemingly erratic spatial or temporal variability;
- Complex systems have a tendency to extreme behaviour in temporal evolution or spatial pattern;
- Patterns often look similar when viewed on different scales or 'magnifications'. Self-similarity is a characteristic of fractal behaviour. On the other hand, results may depend on the scale or resolution under which the system is viewed;
- Often it is difficult to establish clearly defined 'laboratory conditions'. Consequently, input quantities of analysis are often 'noisy' or 'dirty' to some degree. Sometimes factors are only fuzzily defined or definable.
- This reality often makes modelling, and in particular prediction and forecasting, difficult and technically demanding. Simple regression models often perform badly, because they can hardly capture a high-dimensional space of convoluted covariates.
- Usually only statistical modelling is possible, i.e. finding statistical rules which describe the behaviour of the system.

Ecological modelling can be understood as reducing the complexity by focusing on key processes. A model should be simple (Ockham's razor), but fit for the purpose. Oversimplification is characterised by processes ill-captured, which leads to high uncertainty in terms of accuracy and precision. On the other hand, when too many components are present (which is conceptually similar to over-fitting in regression), too many uncertain and/or correlated (sensitive) model parameters may lead to a deteriorated prediction capability.

as radon), migrate within the ground according to its permeability.

Radon, in particular, is the direct decay product of two radium isotopes: ^{226}Ra (^{222}Rn) and ^{224}Ra (^{220}Rn). The radon isotopes are relatively long-lived (especially ^{226}Ra, with a half-life of 1 620 years), which is why they are not necessarily in equilibrium with their 'grandparents', ^{238}U and ^{232}Th. Mainly the action of ground water can lead to disequilibrium, due to different solubility of radium and uranium in water, resulting from their different chemical properties. This implies that the local radon production rate is not necessarily proportional to the uranium (thorium) concentration at the same point in the ground.

Radon (^{222}Rn) and thoron (^{220}Rn) (see Section 2.2)

Chemically, radon isotopes are identical, but due to their very different half-lives (Rn: 3.82 days vs. Tn: 56 seconds) their presence in the environment has different spatial and time patterns.

Concerning radiology and radon risk, geogenic thoron is mostly considered to be a practically negligible component, as infiltration into buildings is usually a 'slow' process that effectively removes thoron due to its short half-life. However, in (mostly old) buildings with unsealed interface to the ground, i.e. basement or ground floor directly exposed to exhalation, geogenic thoron can be a factor that should be considered. Otherwise, it seems that thoron is a problem if exhaled from thoron-containing building materials, typically raw clay, which can have a high radon exhalation rate. Close to exhaling surfaces (walls), exposure to thoron progenies can be a factor to consider.

Radon in soil gas (see Section 5.1)

Most radon that has been generated by radium decay in a rock or soil grain never leaves that grain. The fraction of radon actually being released into pore space, and available for further migration, is called emanation power. It depends on mineralogy and grain size. Mineralogy defines the crystal geometry, which in turn determines 'how easily' a radon atom generated within a crystal can escape. Grain size can be tectonically modified if strain leads to fracturation or the 'milling' of rock. Water content is controlled by meteorological conditions (how deep into the ground the impact of rain is effective, depends on soil type) and possibly by ground-water dynamics.

Radon movement in the pore space depends on water content (radon diffusive mobility is much lower in water than in air, and radon will decay in humid soil before reaching the surface, compared to dry soils), permeability at different scales, pressure difference and the presence of carriers, such as water or geogenic CO_2 or methane. Diffusion driven by concentration difference also contributes. *Permeability* is usually understood, e.g. in the sense of Darcy's law, as a summary quantity which comprises geometrical properties without specifying them.

Still, one sometimes distinguishes between micro- and macro-permeability. The former is related to the porous structure of the soil, while the latter, to fissures or cracks, up to caves and karst phenomena, or also to ducts created by plant or animal activity. Therefore, permeability depends not only on the presence of space between grains, but also on whether the spaces are connected, so that *percolation* over longer distance is actually 'geometrically' possible. Percolation theory has many important applications in analysing the behaviour of networks of all kinds in nature or in the social sphere. The distribution of soil grains and spaces between them can be understood as a network. Apart from the availability of pathways in a network, quantified by connectivity, their length is also relevant. *Tortuosity* quantifies how bent or convoluted migration paths are.

As a summary, the effective path length between the point of Rn generation and a target point (e.g. soil surface or the interface with a building) which radon together with its carrier fluids have to travel, not only depends on the straight distance between the two points, but on the geometrical properties of the medium in which migration takes place.

• • Soil-gas sampling drill, RM 2018 exercise, Cetyne, Czech Republic
Source: Tom Tokehan

Radon exhalation and radon outdoor (see Sections 5.2 - 5.3)

Once exhaled from the soil or rock surface, radon spreads in the atmosphere by diffusion, convection and advection carried by air movement. This phenomenon is being extensively studied because radon and its progeny generated in the atmosphere can serve as tracers of atmospheric processes.

In the context of this section, this behaviour is relevant only as far as outdoor radon contributes to dose and is a minor source of indoor radon.

Radon in ground water (see Chapter 6)

Radon is soluble in water. The air/water distribution coefficient depends mainly on temperature. Ground water is important, being an efficient carrier of radon and possibly a significant secondary source of indoor radon. It can be taken up by water through dissolution from its point of generation, or after some migration with other carriers, transported over quite large distances and released if the solubility conditions change. Other, but minor sources of radon in water are radium dissolved in the water and uptake from the atmosphere. Because uranium and radium have different chemical properties, no equilibrium exists between them in water (Skeppström & Olofsson, 2007).

In terms of radiological relevance, radon in drilled well water can be an important source of exposure. Pathways are ingestion and inhalation of dissolved radon.

Radon in ground-water serves as an important tracer of hydrological processes, e.g. in karst studies and speleology.

Interface to buildings (see Sections 5.2 and 5.4)

Radon may enter from the ground into a building. This process is controlled by driving forces and by the nature of the interface between the soil and the building. Physical mechanisms for migration are diffusion, convection and advection. The driving forces are the concentration gradient for diffusion and the pressure difference for convection and advection. In the presence of a barrier, such as a concrete slab as foundation or insulating layers, advection through small fissures is usually the dominant mechanism. The pressure gradient is generated by temperature and pressure differences indoors – outdoors.

Synthesis

In a 'taxonomy' of compartments, we may distinguish between:

The **geogenic compartment**, which consists of:

- The *geosphere*, in which reside:
  - original sources of Rn and Tn; ^{238}U and ^{232}Th decay series;
  - geochemical fractionation, secondary mineralisation;
  - emanation from Ra bearing mineral;
  - transport in the geosphere: diffusion, advection.
- The *hydrosphere*, which characterises:
  - Rn solution / dissolution;
  - Rn transport with ground water;
  - Rn transport in the porous ground via influence on emanation factor and permeability.
- The *outdoor atmosphere*:
  - dispersion and transport of Rn.

The **anthropogenic compartment**, which is addressed only marginally in this chapter, may be divided into:

- The '*domosphere*' (house ecosystem), treating:
  - building construction type;
  - building materials: exhalation;
  - physics of the indoor atmosphere;
  - attachment of Rn progenies to aerosols, adhesion to surfaces;
  - influence of house usage.
- 'Type of work':
  - speed and amount of air pumped by the lungs.
- The '*pneosphere*' (the human respiratory system), including:
  - physiology;
  - radiation biology.

5.1 Radon in soil gas

5.1.1 Introduction

Radon atoms, generated in the soil or rock within the solid mineral grains, can escape into the air or water-filled pores and further migrate by diffusion, convection and/or advection towards the surface.

In most cases, radon in soil gas is considered to be the main source of enhanced indoor radon concentrations compared to two other sources: water and building materials. (Only where the contribution from geogenic radon is small can building materials be the dominant contributor.) Research on radon behaviour and release from soils or parent rocks might have the advantage of identifying areas where indoor radon levels are expected to be high or enhanced over the existing limits. Hence, appropriate remedial actions can be taken for existing houses, or soil-gas radon can be prevented from entering newly-built houses. In addition, soil-gas radon has been found to be used in a wide range of geoscientific applications, such as tectonics, in studies of earthquakes, volcanic fluids, and surface ground water.

Several factors control radon concentration in the soil, both on daily and seasonal scales. Precipitation and temperature appear to control mainly soil-gas radon levels on a seasonal scale, whereas other climatic factors, such as barometric pressure, temperature, soil moisture and wind, affect radon concentration and behaviour on a daily scale. In order to use soil-gas sampling results to predict long-term radon concentration (e.g. over different seasons), it is necessary to know the interaction between these climatic variables and perform robust statistical analyses. Furthermore, as soil gas surveys generally cover large areas with different rock and soil characteristics, it is necessary to have a deep knowledge of the geological and soil processes affecting radon generation and transport.

Factors influencing radon concentration in soils

Geological factors

a. Uranium concentration in rocks and soils

Radon (^{222}Rn) is a member of the uranium (^{238}U) decay chain. ^{238}U is present in all genetic rock types (sedimentary, metamorphic and magmatic) in varying concentrations. Generally, it can be stated that this sequence of genetic rock types also describes average uranium concentrations from the lowest (sedimentary) to the highest (magmatic). However, anomalous uranium concentrations can be found in all rock types in the form of impregnations in sedimentary deposits or vein-type deposits in metamorphic or magmatic rocks. The current methods to determine uranium concentrations are usually based on gamma-spectrometric measurements in the form of airborne measurements for large-area coverage, field or laboratory gamma spectrometry on solid samples (soils, rocks) or liquid (water) samples for detailed studies or calibration of airborne measurements. After periods of extensive uranium exploration and environmental mapping, these data are usually available in many countries and can contribute to efficient radon risk mapping (Matolin, 2017; Smethurst et al., 2017; Szabó et al., 2017; Cinelli et al., 2017; Ielsch et al., 2017). The use of radiometric data has some limitations which may be summarised as follows:

1. differences between airborne and ground gamma spectrometric data;
2. differences in regional and detailed geological mapping; and
3. the presence of factors influencing the radon migration and diffusion from deeper soil horizons to the surface and subsequently to dwellings.

b. Permeability

Soil permeability characterises the ability of the geological environment to transport radon and other soil gases from the source (parent solid or weathered rock) to the target surface or dwelling (Nazaroff & Nero, 1988; Nazaroff, 1992). Mineral grains, containing U, produce radon in a quantity characterised by the emanation coefficient. The radon escapes from the mineral grains into a pore space through diffusion, at distances of millimetres or a few centimetres. From the vicinity of a mineral grain, radon is transported into the surrounding pore spaces, and its mobility is controlled by space connections between pores and physical conditions such as temperature, pressure gradients or soil moisture. This process is called convection and propagates to distances of metres or tens or hundreds of metres. The diffusion can be both vertically and laterally oriented. The vertical convection can be limited by the presence of sub-horizontally oriented mineral particles (like micas) or layered clay intercalations in soils or clayey weathered rocks. On the other hand, these vertical barriers close to the surface layers can trigger lateral transport under the impermeable barrier into the basement of houses, especially when the process is supported by pressure or thermal gradient. As the permeability for gases varies vertically and horizontally even in a small area of a building site, it is necessary to characterise this parameter for several points of the studied area, namely in the ground plan of the future house and its close vicinity. At present, permeability is usually determined through:

1. *in situ* measurements by permeameters;
2. soil texture analysis; and
3. data from soil permeability maps (generally available at regional level, so cannot be used for local estimation).

c. Geological inhomogeneities

Different types of geological and man-made inhomogeneities can influence soil-gas radon concentrations at a specific local site of interest. These inhomogeneities are usually more permeable, subvertically oriented and they intersect more rock types with different radon potential. The geological inhomogeneities are mostly represented by faults of different types. The soil-gas radon convectivity of faults could depend on the position of the faults in geodynamically active or passive regions (Pereira et al., 2010; Ciotoli et al., 2007, 2016). Specifically, the proximity to the fault plane and the bedrock lithology are the main factors controlling the soil-gas radon migration velocity and concentration in the shallow soil.

According to the literature, radon anomalies above a fault vary in intensity (in particular when there is a thick sediment layer over the rock with several aquifers and no radon anomalies) and shape, and radon peak values can assume different spatial positions within the fault zone; therefore the spatial distribution of soil-radon concentration is affected by the fault geometry and activity, as well as by the volume of fractured rock involved (Ciotoli et al., 2016; Seminsky et al., 2014; Pereira et al., 2010; Kolke et al., 2009; Annunziatellis et al., 2008; King et al., 1996).

In fact, the distribution of radon anomalies in faulted areas is strictly linked to the evolution of the fault zone that at first stage is generally characterised by stepwise developments of different densities of fault segments, and fractures within the fault zones across and along their strike (Fossen, 2010). Usually the faults have a thin core (Childs et al., 2009), which serves as a convective pathway for radon flux upwards. The damage zone surrounding the fault core has a wider extent for radon release, namely when the fault core is impermeable (Ciotoli et al., 2015, 2016; Seminsky et al., 2014; Pereira et al., 2010; Kolke et al., 2009; Annunziatellis et al., 2008; King et al., 1996). Especially in the geodynamically active regions, the faults can express the unexpected radon variations, which depend mainly on changes in tectonic stress and strain (Ciotoli et al., 2007, 2014).

In karstic areas (Kropat et al., 2017), the radon flow strongly depends on the convective characteristics of open spaces (such as cave systems, chimneys) in karstic bedrock.

The presence of rock types with different levels of natural radioactivity changes the average radon concentrations in areas with low radon risk. Silurian black shales in low-radon limestones, black shales in metasedimentary sequences of Neoproterozoic (Barnet & Pacherová, 2013) or alum shales in Scandinavia (Sundal et al., 2004) serve as typical examples. For instance, the underlying rocks characterised by high soil-gas radon concentrations (e.g. magmatic rocks) can influence the radon level in surface layers in geodynamically stable areas of Quaternary fluvial sediments of the Czech Republic (Barnet & Pacherová, 2011), or glaciofluvial sediments like Scandinavian eskers (Watson et al., 2017).

The man-made inhomogeneities can be widely found in areas influenced by old mining activities, where the soil-gas geodynamic regime of underground spaces can be copied to surface layer through the pits, abandoned adits (even if backfilled with inert material) or through fissures in case of subsidence areas.

Differences in natural soil-gas radon concentrations can also be found between arable soils (mostly lower radon concentrations than in the parent rock due to atmospheric release) and their intact rock equivalents.

Due to the convection of soil-gas radon, increased concentrations may also appear on the rims of artificial flat barriers such as asphalt and concrete covers, where radon accumulated under the barrier can be released in the form of anomaly levels not corresponding to the surrounding bedrock. During building activities for levelling building grounds, huge amounts of soil and rock material are often transported, and this process can change the natural radon concentration of building sites.

Variations in radiation concentration with depth

Radon concentrations increase with depth (Clavensjö & Åkerblom, 1994). At the surface layer, when disturbed by disintegrated soil particles, roots of vegetation or the presence of the soil rock structure, the radon concentration is diluted in contact with atmospheric air. The trend of increasing radon concentration with depth is not generally defined for all rock types, since local differences at soil layers and bedrock lithological types influence the radon variations with depth at a sampling site (Neznal et al., 1994, 1996). Radon concentrations measured in soils usually range between 5 and 100 kBq/m^3 (with extremes up to some 10 000s) for different rock types, while concentrations in the atmosphere directly above the soil surface only reach levels of tens of Bq/m^3 (with extremes up to hundreds). Therefore, representative soil-gas samples must be taken from deeper soil horizons. At present, steel-hammered probes with lost tip or drilled probes with packers are used to make sure that the undersurface cavity is opened and that the soil gas is sampled directly from the predefined depth horizon. Usually, a depth of 0.8 - 1 m is recommended for correct and economically efficient radon concentration measurements (Ciotoli et al., 1998, 2007; Neznal, 2004). These sampling devices are widely used in EU countries.

Climatic variations

Seasonal variations affect the physical processes of radon generation in the soil gas, due to the combined effect of geological and meteorological parameters. From different sites, geological and soil factors (e.g. rock type, mineralogy, structure, etc.) may affect radon concentration at the level of a single geological unit. Furthermore, radon concentrations measured in summer cannot be used to predict radon levels in winter; this is the reason why soil-gas surveys are usually carried out in a short time and during stable weather conditions (Kraner et al., 1964; Taipale & Winqvist, 1985; Fukui, 1987; Schumann et al., 1992; Ciotoli et al., 2007).

In order to predict soil-gas radon values at different timescales (i.e., seasonal, daily), one should consider the climatic factors controlling soil-gas concentrations. In fact, a meteorological signal is generally characterised by short-term fluctuations (daily) superimposed on longer, seasonal changes (year). According to literature, the main factors affecting radon concentration in soil gas are essentially the following: soil moisture retention characteristics (e.g. permeability, porosity, grain size, and the number of consecutive rainy days); barometric pressure; soil temperature; hydrometeors occurrence (mainly snow and ice); and wind velocity (Washington & Rose, 1990; Schumann et al., 1989; Lindmark & Rosen, 1985; Clements & Wilkening, 1974).

Soil moisture and precipitation

Studies of temporal variations of meteorological parameters show a marked effect of soil moisture on radon concentration in the soil pore. An increase in soil moisture content reduces the soil permeability and availability of soil air, thus increasing the radon content of the soil by the double effects of partitioning and reduced diffusivity. In fact, radon has a non-negligible solubility in water, the partition coefficient of radon between water and air being approximately equal to 0.25 at standard conditions (Clever, 1979). Since radon also has less diffusive mobility in water than in air, it can accumulate in the water surrounding the grains of soil and consequently in the same air pores of the soil, reducing the radon flux toward the atmosphere (Arvela et al., 2016; Alharbil & Abbady, 2013; Voltaggio et al., 2006).

Radon variability due to soil moisture is probably related to the condition of water saturation and moisture retention characteristics of the terrain. This phenomenon can occur especially in highly permeable soil, where a rapid decrease of shallow soil permeability can be associated with increased moisture content (reduction of air in the pores, expansion/hydration of clays etc.). This inhibits advective and diffusive transport of radon escaping from the soil (i.e. capping effect), yielding an increase in the soil-gas radon concentration within the diffusion/advection zone (Pinault & Baubron, 1996; King & Minissale, 1994). In highly permeable and homogeneous soil, a good correlation between soil-gas radon concentration, permeability and soil moisture can be obtained, while in areas with medium or low permeable environment the correlation can often be very weak (Kraner et al., 1964; Kovach, 1945).

Effective rainfall (i.e. water saturation grade, which can be directly measured or inferred from the number of consecutive rainy days) makes the soil radon concentration increase just after the rainfall (Pinault & Baubron, 1996). During the rainy winter/spring, radon concentration may seasonally increase in soil gas, when radon tends to be trapped in the soil under a layer of water-saturated horizon characterised by reduced gas permeability (i.e. the capping effect), while during the sunny summer/autumn, it exhales more easily as the soil becomes drier and more permeable. For sites characterised by relatively high permeability, the water-saturated layer quickly extends below the sampling depth, thus resulting in minimum radon concentration during the rainy season (King & Minissale, 1994). For sites that had relatively low permeability, the wet layer was thinner than the sampling depth, and the capping effect caused higher radon values during the rainy season (Arvela et al., 2015; Rose et al., 1990). In addition, the presence of snow and ice on the soil causes accumulation of radon in the soil due to the capping effect (Lindmark & Rosen, 1985; Hesselbom, 1985; Jaacks, 1984; Kovach, 1945).

Barometric pressure

Barometric pressure is another important parameter. Even when not associated with precipitation, large-scale barometric pressure changes show an inverse correlation with soil-gas radon concentration. The magnitude of changes in radon values in response to barometric pressure changes is generally lower than that caused by soil moisture (i.e. precipitation) alone. Decreasing barometric pressure tends to draw soil gas out of the ground, increasing the radon concentration in the near-surface layers. This phenomenon is particularly pronounced in highly permeable soils, where near-surface radon-bearing soil gas escapes more rapidly into the atmosphere, generally causing a decrease in radon concentration at the 0.6 – 0.8 m sampling depth. Conversely, increasing barometric pressure forces atmospheric air into the soil, diluting the near-surface soil gas and driving radon deeper into the soil (Lindmark & Rosen, 1985; Kraner et al., 1964; Kovach, 1945). Clements & Wilkening (1974) noted that pressure changes of 1 – 2 % associated with the passage of weather fronts could produce changes of 20 – 60 % in the radon flux, depending on the rate of pressure change and its duration.

Soil and air temperature

Temperature shows a contrasting effect with barometric pressure. The effect of temperature on soil-gas radon concentrations appears to be minor compared to those of precipitation and barometric pressure. Some studies suggest that a decrease in air temperature is correlated with high concentrations of soil-gas radon, but this correlation is no longer evident from a depth of 0.6 m. Temperature gradients between soil and air could induce thermal convection that would cause soil gas to flow in a vertical direction (Jaack, 1984; Kovach, 1945).

Soil temperature variations can cause rapid increase in soil radon concentrations due to the enhanced radon convection that increases the mobility of radon in soil gas and the radon concentration ratio between gas and water (Washington & Rose, 1992; Memugi & Mamuro, 1973). Otherwise, increasing temperatures may also increase production of some gas carriers (CO_2 and H_2O vapour), which again may increase radon transport from depth (Pinault et al., 1996). Arvela et al. (2015) reported that high soil temperatures in summer increased calculated soil-gas radon concentration by 14 % with respect to winter values. Furthermore, temperature changes may play a significant role in radon accumulation during winter months, due to capping effects caused by the freezing of water in shallower soil layers. Beneath frozen layers, the soil is likely to be unfrozen and relatively permeable, so at that depth radon can concentrate to elevated levels. This phenomenon can have an important effect in producing elevated indoor radon levels during winter months in many areas.

In general, temperature and barometric pressure can have a synergistic action; for example a temperature increase and/or a barometric pressure decrease favour the flux of radon from soil to atmosphere, causing a transient disequilibrium between the flux from the deeper level of soils and the shallower levels, resulting in a non-stationary radon content.

Wind

High wind velocities cause local depressurisation and, therefore, decreasing radon concentration in soil (Voltaggio, 2012), because the gas is diluted by atmospheric air and/or removed at surface. Wind effects have been observed up to a depth of 1.5 m (Kovach, 1945; Kraner et al., 1964). However, in addition to wind velocity, soil permeability, soil moisture and ground cover (i.e., snow, ice, etc.) may affect the magnitude and the depth to which wind can influence soil-gas radon levels. Strong wind turbulence and the Bernouili effect across an irregular soil surface can draw soil gas upward from depths caused by alternating pumping between pressurisation and depressurisation of the soil, similarly to that caused by barometric pressure (Kovach, 1945; Jaacks, 1984; Hesselbom, 1985; Lindmark & Rosen, 1985).

5.1.2 Measurement methods

Indirect and direct methods can be used to estimate the soil-gas radon concentration.

Indirect methods are based on measuring the radioactive parent isotopes and, through calculation, result in a derived maximum level of radon activity concentration. Uranium and radium are analysed as parent isotopes for radon (more details in Section 2.2.1). The underlying assumption of this method is that there is a balance between uranium and radium.

eU is defined as the ^{238}U concentration in radioactive equilibrium with ^{226}Ra.

For example, a gamma spectrometer could be used to calculate the *in situ* eU concentration in soil or rock. Using this concentration, one may use the following formula to calculate the maximum concentration of radon activity forming in soil (Andersson et al., 1983; Clavensjö & Åkerblom, 1994):

$$C = A \cdot e \cdot \beta \cdot (1 - p)\, p^{-1} \qquad (5\text{-}1)$$

where

C is the maximum concentration of radon capable of migrating in soil (in kBq/m³), forming at the expense of ^{226}Ra (eU) in soil;
A is the eU concentration (1 ppm U = 12.35 ^{238}U Bq/kg);
e is the emanation factor (coefficient) of the lithotype;
β is the compact specific weight (relative density) (in kg/m³); and
p is porosity (as a fraction).

Unfortunately, indirect methods cannot give an indication about the inflow of radon from deeper sediments or rocks, from karst cavities or from fault zones that can sometimes increase radon content by a factor of ten (Neri et al., 2016; Tähti-Kok et al., 2012).

Direct methods are based on measuring the concentration of radon and its progeny decay products in a sample of soil gas (more details in Section 2.5). Since radon and its decay products emit alpha and/or beta particles as well as photons, in principle a whole range of detectors can be used for measurements in combination with a suitable sampling technique.

Direct measurement methods, whether active or passive, are recommended by the ISO11665-11:2016 international standard, 'Test method for soil gas with sampling at depth'.

In active sampling, one considers a certain soil-gas volume at a certain moment or period of time representative of the soil under investigation. The sample is transferred into the detection chamber, and activity concentration is measured with a semi-conductor or a scintillation detector. With passive methods, a detection chamber must be placed below the ground for a certain time interval, during which the transfer of the soil-gas sample into the detection chamber occurs by diffusion and the activity concentration is estimated.

Sampling

Choosing locations

Choosing the number and locations of sampling points depends on the task at hand and on the available resources, but it is highly recommended to study geological and topsoil maps of the target area first. Since samples taken from a very limited area must aim to represent a larger area than just their immediate surroundings, a sound geological knowledge is especially relevant in areas where uranium-rich rocks occur in sections of bedrock. When compiling a radon risk map for larger areas or regions, it becomes even more delicate to choose locations for sampling points, and thus a good knowledge of the existing geological context is equally essential.

Soil-gas sampling

A relatively easy way to measure radon concentration in soil gas is to use a soil-gas probe coupled with a measuring instrument. This probe can be operated anywhere above the water table and is often used in conjunction with a drying unit.

Either sucking or pumping soil gas directly into the measurement chamber or extracting soil gas from the surface using syringes are both delicate operations in the sampling procedure, because there is always a risk that environmental air may leak through the probe into the radon measuring instrument.

The entire system must be perfectly sealed. If the sampling system is not perfectly sealed or does not reach a sufficient level of underpressure to collect gas samples in soils of low permeability, the soil-gas radon concentration may be underestimated. Measurement results that indicate a radon activity concentration lower than 1 - 2 kBq/m³ are usually considered to be failures. The internal volume of the cavity, which is created at the lower end of the sampling probe, must be large enough to enable sample collection. The soil-gas samples are collected from a depth of about 1.0 m below the ground surface; for instance a depth of 0.8 m is used in the Czech Republic, Sweden, Estonia and in many other countries (Neznal, 2015), which corresponds to the ISO 11665-11:2016 international standard mentioned above, 'Test method for soil gas with sampling at depth'.

Soil-gas sampling sequence, RIM 2018 exercise, Cetyně, Czech Republic.
Source: Tiec Tolefson

In soils with high permeability, such as coarse-grained gravel, sampling succeeds better during a rainy period or during winter, when the upper ground is frozen. In clay, on the contrary, better measurements are obtained during the dry season. In these cases, indirect methods can give reliable results.

In conditions of high ground-water saturation, soil gas can also be measured during a dry period. However, if peat forms the upper layer of the soil, no radon sampling method can give reliable results; then, only geological data can provide some hypotheses about radon concentration.

If there are homogenous hard rock or layered bedrock outcrops on the surface, indirect methods can be used. However, in case the interlayers of bedrock differ much from each other, indirect methods cannot be used. In North Estonia, for instance, uranium-rich graptolite argillite is covered with limestone, and the topsoil is thin or almost absent, which creates a situation where radon emitted by uranium-rich graptolite argillite only flows freely from a depth of tens of metres to the surface through cracks in the limestone. Thus, only probes used in the limestone cracks will yield results. In Sweden and Norway these uranium-rich argillites are known as alum shale; in other countries, as black shale.

Simultaneous sampling

In Sweden and Estonia, but also in many other countries, direct and indirect methods are used simultaneously to have a reference value. When the Atlas of Radon Risk and Natural Radiation in Estonian Soil (Petersell et al., 2017) was compiled, this practice was also used. There, it was discovered that indirect methods complement the direct methods and provide a mutual check on the plausibility of the results of the measurements, and thereby help to avoid making large mistakes.

Porosity and permeability

Porosity and permeability are terms related to the measurement of intrinsic characteristics of rocks and soils.

Porosity or void fraction is a measure of the void (i.e. 'empty') spaces in a material, and is a fraction of the volume of voids over the total volume. It is expressed either as a figure between 0 and 1, or as a percentage between 0 and 100.

Permeability is a measure of the ability of a porous material, such as rock or soil, to allow fluids to pass through it. Permeability is represented using Darcy's Law. The SI unit for permeability is m^2. A practical unit for permeability is the darcy (d), or more commonly the millidarcy (md) (1 darcy = 10^{-12} m^2). Permeability is a decisive parameter for classifying potential radon (risk). In case the contact zone between buildings and soil has high permeability, even low soil-gas radon concentrations can cause significant indoor radon levels. In addition, parameters such as soil moisture, the degree of water saturation, compactness, texture, occurence of macro- and micro-fissures, the degree of inhomogeneity of the fine (clay) fraction, content of the coarse fraction fragments, cobbles, stony debris etc. have a significant impact on the final permeability. Thus, all of these parameters should be taken into account when measuring the gas permeability, and should – also including effects from the wider environment, such as the presence of faults, anthropogenic impacts in soil layers and the presence of various paths or barriers – describe the potential of soil gas movement at a given place. By measuring permeability, one may estimate the ability of soil gas to flow from deeper ground and up to the surface level.

Radon potential

For decades, there have been attempts to define a quantity called **radon potential (RP)**, which is intended to be a standardised quantity that 'factors out' the anthropogenic contributions. It shall measure the availability of radon, for natural (geogenic) reasons, to exhale from the ground into the atmosphere, or to infiltrate a building. In colloquial terms, the RP measures 'what Earth delivers in terms of radon'.

Knowledge of the radon potential in an area can support decisions on whether further local measurements are necessary in areas of planned development.

The **geogenic radon potential (GRP)** is a bottom-up approach of the radon potential, since it starts from geogenic quantities, which measure geogenic radon sources and transport in the ground.

Soil-gas radon concentration can be used to estimate the geogenic radon potential of an area (Bossew, 2014; Cosma et al., 2013; Gruber et al., 2013; Neznal et al., 2004; Szabó et al., 2014). In most European countries, however, data on soil-gas radon concentration are rather sparse; hence no European-wide geogenic radon map could be based on them alone. Thus soil-gas radon is often one of many input variables (e.g. uranium content of soil) for different methods (categorical, multivariate etc.) (Bossew et al., 2008; Bossew, 2014; Cinelli et al., 2011; Ielsch et al., 2010; Kemski et al., 2001; Neznal et al., 2004; Schumann, 1993; Zhu et al., 2001).

Several classification methods have been developed to estimate the geogenic radon potential based on radon activity concentration in soil and soil permeability-porosity (e.g. Åkerblom et al., 1988; Gundersen et al., 1992).

Equation 5-2 gives a method to quantify the radon potential of the building site as a continuous variable (Neznal et al., 2004):

$$RP = \frac{C_\infty}{(-\log_{10}(k) - 10)} \qquad (5\text{-}2)$$

where:

C_∞ is the equilibrium concentration of ^{222}Rn in soil air, in kBq/m^3; and

k is the effective soil-gas permeability, in m^2.

Three categories have been identified to determine the radon index (Neznal et al. 2004), see Figure 5-2. The parameters C_∞ and k can best be assessed by direct field measurements over the given homogeneous rock type. However, when direct field measurements are lacking, it seems possible that the GRP can be estimated based on the rock and soil types (i.e. based on their physical and chemical characteristics such as soil air permeability, porosity, arithmetic mean particle diameter and bulk density). Moreover, it can be prohibitively costly to perform all the required measurements, or direct field observations may not be possible due to harsh field conditions and lack of accessibility. Assuming geological homogeneity of the target area and by understanding the relationship between the geological characteristics and GRP, one may theoretically assign representative 'default' values to the spatial units.

Indeed there is no unanimous definition of the RP, as this concept has evolved over time, in different contexts. When using the term radon potential, one should always indicate the definition to which it refers. For instance, in the UK and Ireland, RP denotes the exceedance probability of indoor radon concentration (C) over a reference level (RL), within an area, RP= prob (C>RL). A similar 'top-down' approach has been proposed by Friedmann (2005), developed for the Austrian radon survey (ÖNRAP) in the early 1990s. Measured indoor radon concentration is standardised according to the anthropogenic factors that are considered most influential, such as floor level. If anthropogenic factors are thus 'factored out', the remaining values should reflect only the geogenic influence.

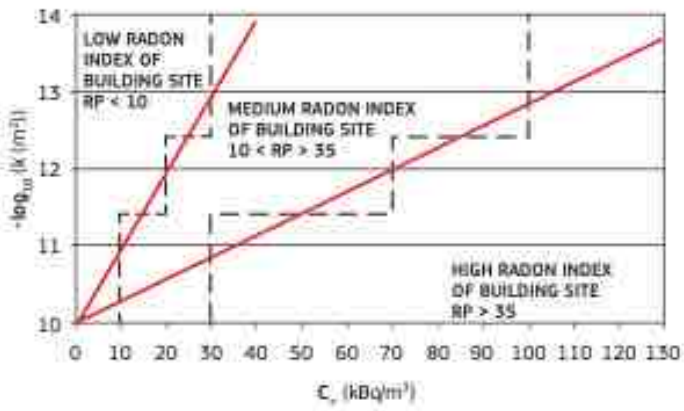

Figure 5-2.
Radon potential of the building site
Source: Neznal et al., 2004

Tanner (1988) proposed a radon availability number (RAN), defined as source times migration distance of radon in the ground under standard pressure difference. Alonso et al. (2010) proposed using radium concentration times emanation power, because it can quantify the 'potential radiological hazard' of a porous material.

Among schemes based on combined scoring of factors, there is:

- The one introduced by the U.S. EPA (Schumann, 1993b): classes of indoor radon concentration, eU, geology, soil permeability, prevalent basement type;
- The approach proposed by Kemski et al. (2001, 2009) and similarly, the Czech Radon Index (Neznal et al., 2004), are based on joint classification of soil Rn concentration classes and permeability classes;

The geogenic radon hazard index

The geogenic radon hazard index (GRHI) has been conceived as a possible alternative or complement to the GRP. It shall quantify the hazard originating from geogenic radon on a deliberate scale, for example from 0 to 1 or from 0% to 100%, etc. The underlying idea is that in most European countries, quantities have been surveyed, or are available as databases, which are physically and statistically related to the GRP. These include:

- Geological maps;
- Maps or datasets of soil properties (soil type, texture etc.);
- Hydrogeological maps (Elio et al., 2017c);
- Tectonic (faults, volcanism) and seismic maps. (Recent European studies of the relation between these phenomena and radon include Piersanti et al., 2015; Ciotoli et al., 2017b; Giammanco et al., 2017; Barnet et al., 2018; Crowley et al., 2018);
- Geochemical maps or datasets, including airborne gamma-ray spectrometry (Ferreira et al., 2016);
- Dose rate maps or datasets (Garcia-Talavera et al., 2013);
- Soil radon maps or datasets;
- Standardised indoor radon maps.

However, the availability of databases varies between European countries. At European level a possible approach could be to generate a GRHI based on whatever quantities are available in the various countries. It would constitute a harmonised measure which does not rely on a harmonised dataset. It can be understood as a top-down or *a posteriori* harmonisation method, which takes advantage of all the available data, contrary to bottom-up or *a priori* harmonisation, which is based on harmonised input data.

The common concept is a weighted mean of transformed geogenic quantities, as regionally available (Cinelli et al., 2015b; Bossew et al., 2017; Ciotoli et al., 2017a). Weights are the strength of statistical association with the GRP, found by individual correlation analyses or analysis of variance (ANOVA for categorical quantities) or through principal component analysis or related techniques.

An earlier proposal was made by Friedmann in 2011. Here, the RH is defined as a combination of soil radon concentration and permeability. If not available, soil radon is estimated from uranium concentration or ambient dose rate via 'transfer functions'.

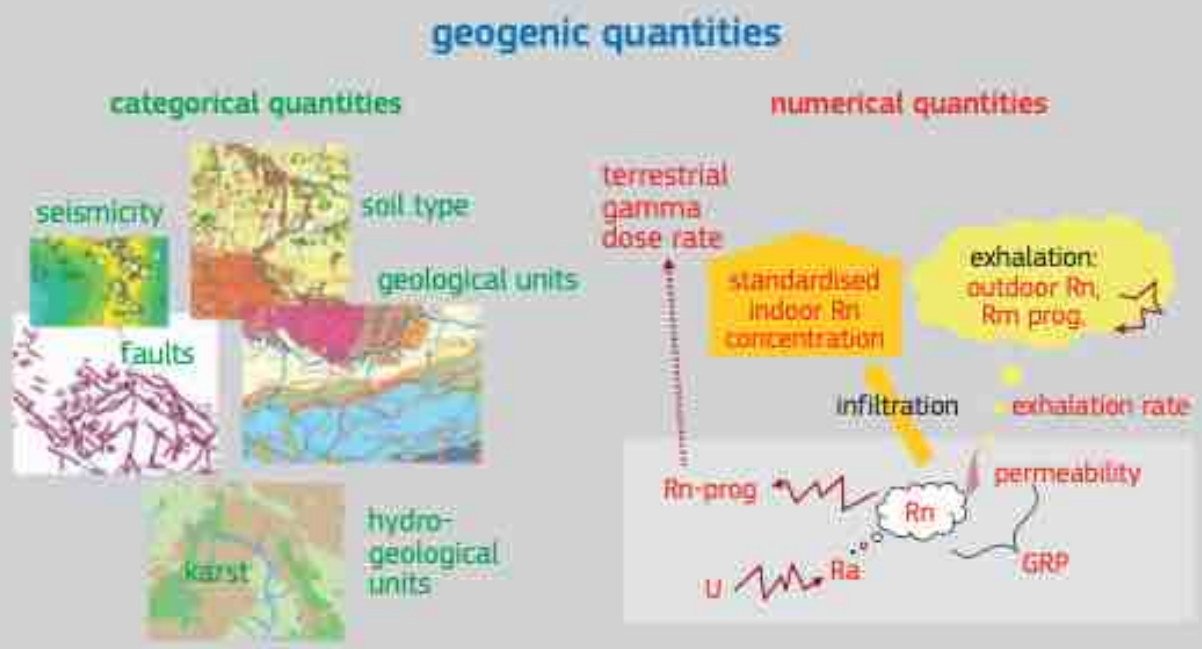

- Wiegand (2001, 2004) suggested a '10-point system' based on scoring categorical variables such as lithology, topography and land cover. Tung et al. (2013) used this system;
- In Sweden, schemes for regional classification and for characterisation of building sites based on lithology, permeability, texture, radium and soil radon concentration have been introduced;
- Guida et al. (2010) combined scoring of permeability, geology, radium concentration, vegetation cover, morphology, tectonics and karst features;
- Ielsch et al. (2010) proposed to aggregate classes of radon source potential, factors which enhance transport, 'aggravating' factors

5.1.3 Applications

a. Indoor radon risk estimator

Soil-gas radon is the main source of indoor radon (UNSCEAR, 2000). Knowing the soil-gas radon concentration gives information about the potential risk, without considering artificial effects such as building characteristics or living habits. Moreover, in areas where no indoor radon measurements are available (e.g. uninhabited areas), knowing the soil-gas radon concentration and soil permeability could give an indication for characterising the radon hazard (or potential risk).

A number of European countries have performed soil-gas measurements, including the following (note that this list may not be exhaustive):

- In the **Czech Republic**, starting in the 1980s, more than 300 000 measurements have been carried out throughout the country. The Czechs have gained a long experience in describing radon transfer from building ground into houses and in mapping soil-gas radon (Barnet, 1994; Barnet et al., 1998, 2000; Jiranek, 2000; Neznal et al., 1994, 1996).
- **Germany** started soil-gas radon measurements in 1989 (Kemski et al., 2000). They studied approximately 4 000 sites throughout the country (Kemski et al., 1996, 2000, 2001, 2005, 2009; Siehl et al., 2000). Surveys are ongoing, with currently more than 5 000 sites sampled.
- The **United Kingdom** has also performed soil-gas radon measurements at several thousands of locations since the 1990s and reviewed soil-gas radon survey and measurement procedures (Appleton & Ball, 1995; Appleton et al., 2000).
- **Sweden** investigated more than 2000 locations from 1979 onwards (Mjönes et al., 1984). They used these measurements to establish radon risk maps in almost every municipality, but did not produce a national map (Åkerblom & Wilson, 1980, 1981; Åkerblom, 1986; Åkerblom et al., 1988).

To our knowledge, these are the only European countries that have performed soil-gas radon surveys at national level. In most other countries, soil-gas radon measurements have been performed locally, usually in areas known *a priori* to have elevated indoor radon concentration, and the number of measurements has been below 1000. It is also well known that in some countries (e.g. Hungary), thousands of soil-gas radon measurements were performed in connection with oil exploration, or for remediation processes near uranium mines, but those data are neither public nor have they been published.

- Between 2000 and 2004, **Austria** performed soil-gas radon measurements at 60 sites in regions where high levels were expected (crystalline rocks, glacial (ice-age) deposits) (Maringer et al., 2001). Following other regional projects, results from a few hundred sites are currently available.
- De Heyn et al. (2017) made 113 soil-gas radon measurements in **Belgium**.
- In **Croatia**, 823 locations were studied from 2001 onwards (Planinić et al., 2002; Radolić et al., 2014, 2017).
- **Estonia** studied 566 locations between 2001 and 2004 (Petersell et al., 2005, 2015, 2017).
- In **France**, 230 locations were studied between 1997 and 2002. Maps have been produced on a regional scale, but not for the whole French territory (Ielsch & Haristoy, 2001; Ielsch, 2003; Ielsch et al., 2002).
- In **Hungary**, 192 sites were studied between 2010 and 2011, and maps were compiled for the central region of the country (Szabó et al., 2014).
- In **Ireland**, soil-gas radon measurements were recently started, and 55 locations have been studied (Elío et al., 2017a, 2017b).
- In **Italy**, 70 locations were investigated (Cinelli et al., 2015) and 7 625 measurements made in one region of Italy (Ciotoli et al., 2017), with additional, local measurements for seismological purposes (Sciarra et al., 2017).
- Abromaitytė et al. (2003) studied 70 locations in **Lithuania**.
- **Luxembourg** has soil-gas radon measurements from 1994–2005, but their number is not known. Maps have been published in internal reports and linked to geological studies (Dubois, 2005).
- The **Netherlands** performed 475 soil-gas measurements on a national level between 1995 and 1996 (Stoop et al., 1998).
- Soil-gas radon measurements do not exist in significant numbers in **Norway** (Watson et al., 2017).
- In **Poland**, 228 locations were investigated between 1996 and 2004. Surveys have been made in regions with anticipated high levels, such as: 1) regions with faults, in areas of surface disposal of mining and industrial waste materials, and 2) local, disjunctive tectonic zones (Malczewski & Zaba, 2007; Swakon et al., 2000, 2004; Wysocka et al., 1995).
- In **Romania**, 1 081 measurements were made in 5 counties (Cucos et al., 2017).
- In the **Slovak Republic**, soil-gas radon measurements were performed at 5 sites of a tectonic zone (Mojzes et al., 2017).
- In **Slovenia**, 70 locations distributed over the whole country were investigated (Kovács et al., 2013), and 1 site of a tectonic zone was studied in detail (Vaupotic et al., 2010).
- **Switzerland** performed soil-gas radon measurements at 49 locations to improve indoor radon prediction (Surbeck, 1993; Johner & Surbeck, 2001).

A major application of soil-gas measurements is the assessment of radon risk in building sites (Appleton et al., 2000; Matolin & Prokop, 1991; Neznal et al., 2004).

b. Radon as a natural tracer

Radon in soil gas is generally employed to infer indoor radon accumulation, but it is also used as a natural tracer of different geological processes, such as the dynamics of volcanic activity, earthquake precursor, tracer of buried faults, tracer of non-aqueous phase liquid (NAPL) contamination and to study relationships between ground water and surface water, as well as estimate ground-water residence time. These will be described below.

Radon as a tracer of volcanic activity dynamics

Radon in soil gas is widely used to investigate the dynamics of volcanic activity. Most of the active volcanoes monitored around the world are characterised by continuous injections of magma that stall at very shallow levels or feed complex dyke networks, even at a few metres below the ground surface. Thermal gradients due to magma dynamics may affect the emanating power of the substrate at subvolcanic conditions (Scarlato et al., 2013) or in geothermal areas, modifying the background level of the radon signal (Ricci et al., 2015). Nonetheless, radon emission from the warm host rock is controlled not only by the dependence of the gas diffusion coefficient on temperature (Beckman & Balek, 2002; Voltaggio et al., 2006), but also by the intense hydrothermal alteration and/or weathering processes that affect the substrate, forming hydrous minerals, such as zeolites able to store and release great amounts of water at relatively low temperatures. This thermally-induced devolatilisation strongly enhances the radon signal from the degassing host rock material, giving important information on the ascent of small magma batches from depth (Mollo et al., 2017).

Radon as a tracer of buried fault geometry

In the literature, ^{222}Rn is considered as a convenient fault tracer in geosciences, because of its ability to migrate over comparatively long distances from host rocks and/or deeper sources (if the media is filled with air and until the first water layer), as well as the availability of efficient instruments that can detect it at very low levels. Measuring ^{222}Rn concentration in soil gases is used as a technique to detect and localise active geological faults, as well as to define their shallow geometry and spatial influence, even if they are buried beneath an unconsolidated sedimentary cover (e.g. Baubron et al., 2002; Fu et al., 2008; Walia et al., 2009; Ciotoli et al., 2007, 2014, 2016; Seminsky et al., 2014).

The theoretical correspondence between active faults and radon leaks at surface level is linked to the hypothesis that faults and fractures provide enhanced pathways for fluid flows, even in basins filled by unconsolidated cover that can mask the fault trace at surface (Ciotoli et al., 1998, 1999, 2007, 2014). In particular, enhanced ^{222}Rn release from active faults frequently occurs during the stress/strain changes related to seismic activity, whereas crustal fluids are forced to migrate up, thereby altering the geochemical characteristics of the faults and surrounding zones, composed of highly fractured rock materials, gouge and fluid (Annunziatellis et al., 2008; Baubron et al., 2002; King, 1986).

Local increases in radon emanation along faults could be caused by a number of processes, including precipitation of parent nuclides caused by local radium content in the soil (Tanner, 1964; Zunic et al., 2007), increase of the exposed area of faulted material by grain-size reduction (Holub & Brady, 1981; Kolke et al., 2009; Mollo et al., 2011), and carrier gas flow around and within fault zones (e.g., King et al., 1996; Annunziatellis et al., 2008). Therefore, active fault types, permeability, geometry and fracturing area can affect the presence of radon (and other gases) geochemical anomalies in the soil pores in terms of magnitude and distribution pattern at surface (Annunziatellis et al., 2008; Seminsky et al., 2014; Ciotoli et al., 2016). By contrast, fluids (i.e. gases) may have an impact on the strength of a fault by controlling the faulting processes during the deformation stages; therefore faults may result in structures that prevent fluid flow (i.e. cementation, pore collapse, pressure solution), and structures that represent enhanced fluid pathways (i.e. extension fractures) (Caine et al., 1996; Shipton & Cowie, 2003; Shipton et al., 2005; Berg & Skar, 2005; Johansen et al., 2005; Faulkner et al., 2010; Fossen, 2010).

In general, the evolution of the fault zone is characterised by the initial spatiotemporal heterogeneity, which results in a stepwise development and irregular patterns of fracturing across and along their strike, with alternating segments with denser and rarer faults. At early stages, there are few large faults within the fault zone, whereas at the final stages, the fault zone is dominated by a single main fault (Rotevatn & Fossen, 2011; Fossen, 2010; Seminsky, 2003) (Figure 5-3). In these complex structural scenarios, radon anomalies at surface level can provide reliable information about the location and the geometry of the shallow fracturing zone, as well as about the

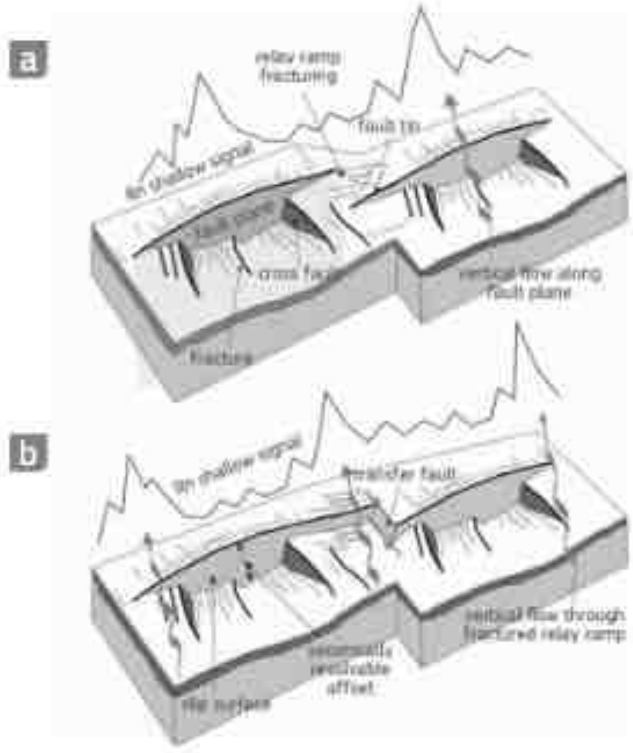

Figure 5-3
Evolution of a fault. Development of damage zone within and around overlapping fault segments during fault growth (a); the join of two faults segments that resolves in a transfer fault (b)
Source: Cowie et al., 2000

Example of radon distribution in a tectonic depression

Figure 5-4 shows an example of radon distribution in soil gas in the Fucino plain (Central Italy), a tectonic depression filled by lacustrine and alluvial sediments (max thickness ~ 900 m) (Ciotoli et al., 2007). The plain is bordered and crossed by a complex network of buried and/or exposed faults characterised by a high seismic activity (the plain was struck by the Avezzano earthquake, Mw 7.0, on 13 January 1915). Linear gas anomalies occur in correspondence of the exposed San Benedetto-Gioia dei Marsi Fault (SBGMF), as well as provided clear indication of the presence of buried Ortucchio Fault (OF) and Trasacco Fault (TF) in the middle of the plain, and Avezzano-Celano Fault (ACF) to the north.

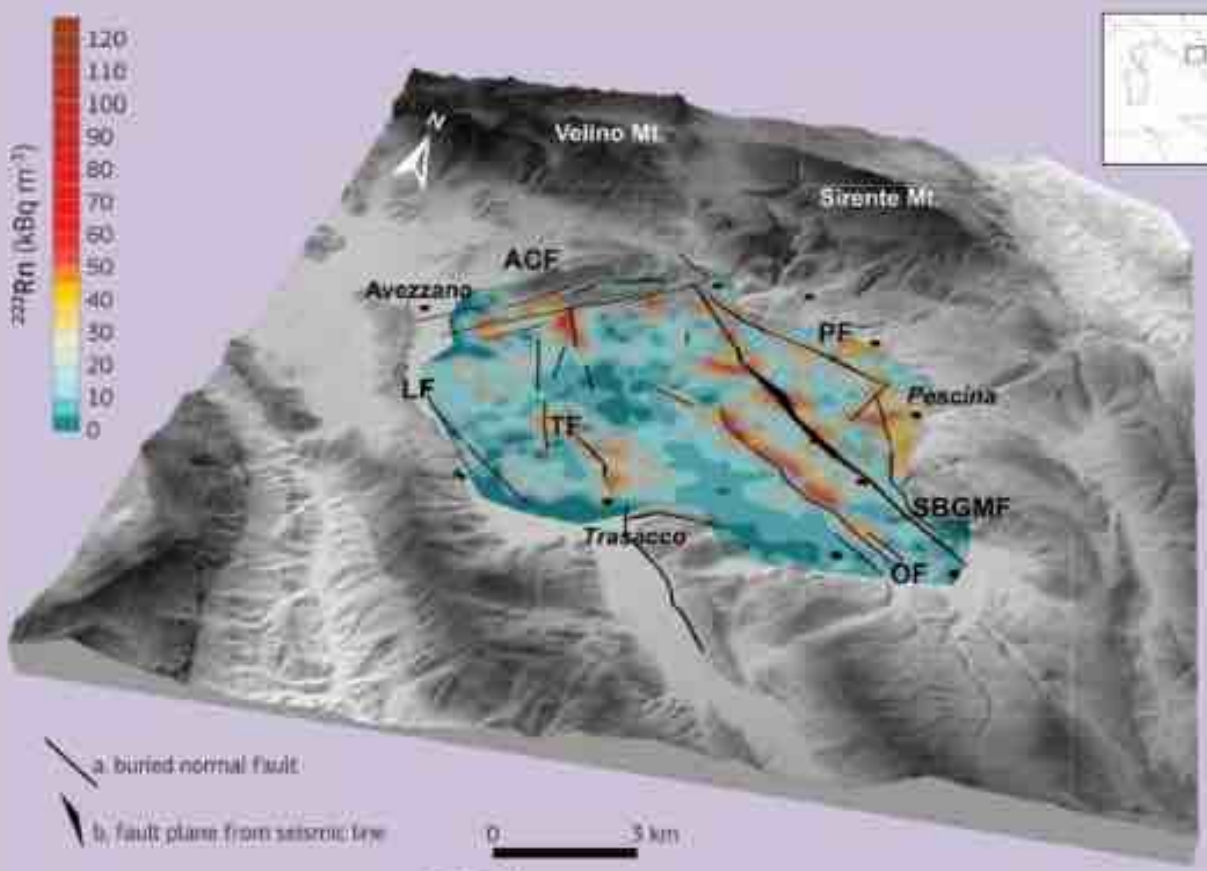

Figure 5-4
Radon distribution in the Fucino plain (Central Italy). The highest concentrations of radon highlight linear anomalies in correspondence of the main faults of the plain: exposed faults (San Benedetto-Gioia dei Marsi Fault, SBGMF; Avezzano-Celano Fault, ACF; Paterson Fault, PF), and buried faults (Ortucchio Fault, OF; Trasacco Fault, TF; Luco dei Marsi Fault, LF).
Source: modified after Ciotoli et al., 2007.

Example of anomalous radon values in a tectonic depression

Figure 5-5 shows the distribution of the highest radon values measured along the strike of the main buried (TF and OF) and exposed (SBGMF) faults of the basin in the Fucino plain (Central Italy). The distribution of anomalous values (>26 kBq/m^3, red dots) shows parallel displacement zones that separate different fault segments; peak values generally decrease in correspondence to the fault tips (blue dots). The spatial distribution of peaks (i.e. their shifting along the fault strike) may indicate the presence of junction zones probably related to dense fracturing with a typical geometry, e.g. relay ramps or real transfer faults, causing the fault displacement.

Furthermore, variations in the offset along the strike of the fault suggests that the linkage process is not completed; if this is the case, the faults of the Fucino basin may still be formed by a series of major segments.

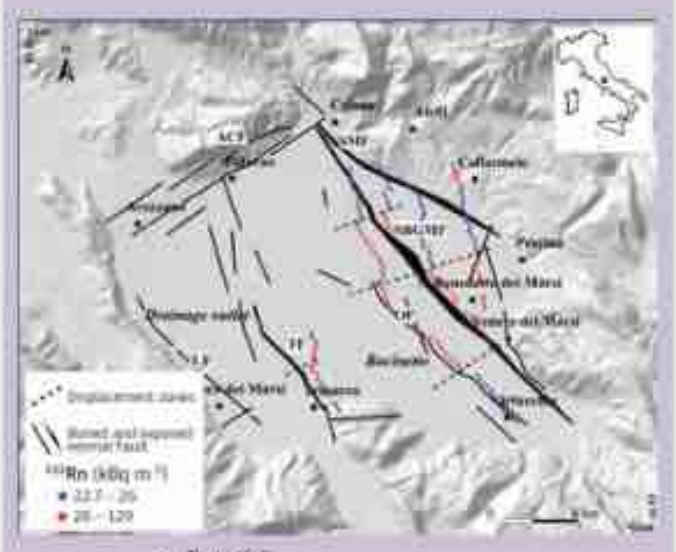

Figure 5-5
Closed post map of radon peak values (blurred circles). Radon values below the anomaly threshold occur in correspondence of the displacement zones along the radon peak alignments.
Source: Ciotoli et al., 2017.

permeability within the fault zone (King et al., 1996; Baubron et al., 2002; Annunziatellis et al., 2008; Ciotoli et al., 2007, 2016). According to literature data, radon anomalies above active faults show concentrations significantly higher than background levels above the main fault line; then radon concentrations decrease laterally up to background (King et al., 1996; Baubron et al., 2002; Ioannides et al., 2003; Font et al., 2008; Ciotoli et al., 2007, 2015, 2016).

However, as radon migration does not necessarily occur in the same way through all faults, radon anomalies vary widely in magnitude, shape and position within the main fault zone that can be affected by plastic and brittle deformations related to the stage of formation of the main fault. Seminsky & Bobrov (2009) proposed that soil-gas anomalies depend on the fault type (i.e. reverse or normal faults). Different fault types impose particular fracture patterns, and according to the origin of fluids may lead to a range of different patterns of the anomalies at surface (Ciotoli et al., 2015, 2016; Annunziatellis et al., 2008; Toutain & Baubron, 1999).

These structural features and their different geodynamic activity predetermine the existence of radon anomalies according to two possible scenarios (Figure 5-6):

1. in correspondence of faults, with low permeability core gauge bounded by damage zones, high soil-gas concentrations should occur laterally above the fracture zones (twin-peak anomaly) (Annunziatellis et al., 2008; Seminsky et al., 2014; Ciotoli et al., 2016); and
2. in correspondence of localised and not healed fault zones, the open fracture network provides interconnected gas migration pathways, resulting in sharp peak anomalies (Seminsky et al., 2014; Annunziatellis et al., 2008).

In the first case, the presence of fault gouge leads to a low-permeability zone; the gouge is thought to alter soil-gas composition as it is usually enriched with trace elements and radionuclides (Lyle, 2007; Sugisaki et al., 1980). King et al. (1996) visualise a twin-peak pattern of ^{222}Rn anomalies in soil gas across a creeping fault; they suggest that this pattern could be caused by the presence of a low permeability zone in correspondence of the fault core (i.e. filled with gouge material) and by the presence of an adjacent, fractured zone. This behaviour was also observed by Annunziatellis et al. (2008).

This could be a reason for elevated radon concentrations observed in some cases, i.e. geochemical conditions in which radium leaches on the walls of a fault or cracks, resulting in high levels of radon emanation. Changes in permeability and porosity characteristics of the faulted zone due to self-sealing of fractures or weathering processes influence the geochemical signal. Furthermore, small strains induce geochemical anomalies along pre-existing faults that may amplify the anomalies if former stresses were near the critical levels and pore fluids were abundant (King, 1996).

c. Radon versus tectonic stress

Radon emanation from rocks under effective stress variation was investigated using laboratory experiments to detect the evolution process of induced fracturing (Zhang et al., 2016; Mollo et al., 2011; Holub & Brady, 1981). Results reported radon anomalies before rock failure under uniaxial stress, probably correlated with decreasing radon emanation when the acting stress is too low to produce microcracks. When the load exceeded the limit strength of the rock samples, radon concentrations significantly increased, reaching maximum values during the fall, and finally tended to be stable (Zhang et al., 2016; Holub & Brady, 1981) (Figure 5-7).

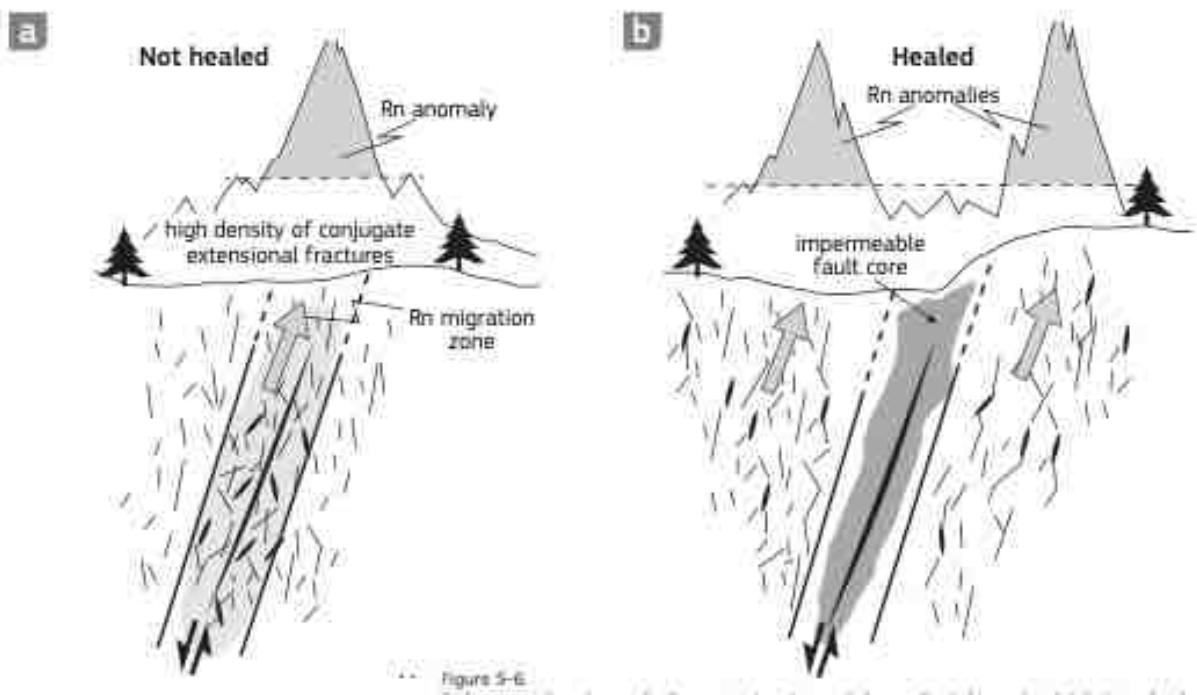

Figure 5-6
Radon anomalies above a fault vary in intensities and shapes. Spatial irregular distribution of soil-radon concentration is predetermined by the complex architecture (i.e., fault geometry) not healed and healed faults, as well as by the volume of fractured rock involved: (a) open fault network, interconnected gas migration pathways; (b) mature fault with a very low permeability core, bounded by damage zones.
Source: modified after Annunziatellis et al., 2008.

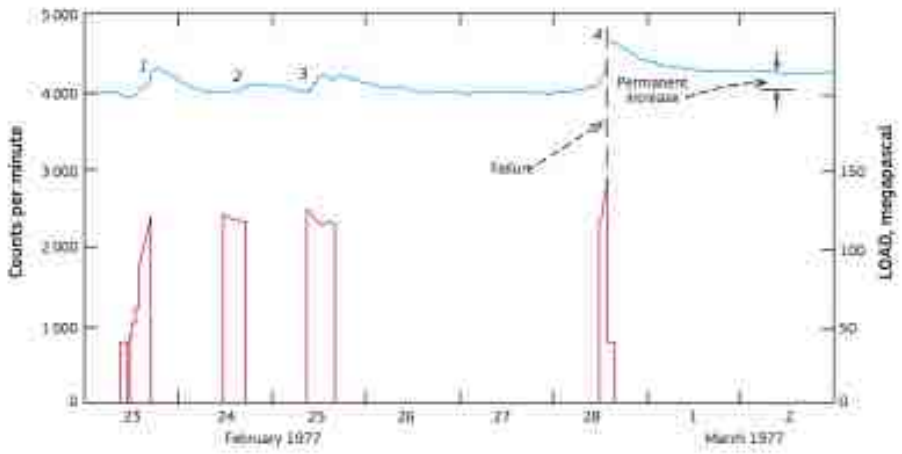

Figure 5-7.
Radon anomalies from uranium-bearing rocks under uniaxial stress. The graph shows the recorded radon emanation during the formation of microcracks. Results seem to be correlated with decreasing radon emanation when the acting stress is too low to produce microcracks.
Source: from Holub & Brady (1981)

Although literature describes some experiments, the mechanism of radon release during rock failure and their connection to earthquakes is still unresolved (Mollo et al., 2011; Ramola et al., 1990). Before an earthquake, stress in the Earth's crust builds up, causing a change in the strain field and the formation of new cracks and pathways under the tectonic stress. During this change, volatiles play a widely recognised role in controlling the strength of the fault zones. Anomalous changes in radon concentration are closely linked to changes in fluid flow and, therefore, also to highly permeable areas along fault zones.

d. Radon as an earthquake precursor: an overview

Over the past decades, radon in soil gas and dissolved gases has received considerable attention as an earthquake precursor (Wakita et al., 1980; Reddy et al., 2004; Walia et al., 2009; Ghosh et al., 2009; Hashemi et al., 2013; Petraki et al., 2015; Riggio & Santulin, 2015; Hatuda, 1953; Ulomov & Mavashev, 1971; Hirotaka, 1988; Virk & Singh, 1994; Igarashi et al., 1995). According to Cicerone et al. (2009), the term 'earthquake precursor' is generally used for phenomena that anticipate some earthquakes. Among the broad spectrum of geophysical and geochemical precursors, radon provides signals of high quality, because, due to its great mobility, it can easily be forced to migrate up by the stress/strain changes related to seismic activity, especially along active faults, thereby altering the physical (i.e. increased permeability) and the geochemical characteristics of the fault zone at surface (Rice, 1980; Sibson, 2000; Collettini et al., 2008). This phenomenon favours intense degassing and may cause formation of radon anomalies on the ground surface with concentrations significantly higher than background levels (King et al., 1996; Toutain & Baubron, 1999; Ciotoli et al., 2007; Annunziatellis et al., 2008; Bigi et al., 2014; Sciarra et al., 2017).

The link between radon anomalies and seismic events has been explained by different models all referring to the dilatancy process (Scholz et al., 1973; Sibson, 2000). The opening of cracks before an earthquake increases the movement of fluids (i.e. gas transport) within the pores and the newly formed fractures and, together with the modified strength and pore pressure, may cause variations in the chemical-physical characteristics of the rocks. As a result, anomalous concentrations of radon can occur at shallow soil depth up to the final stage of the dilatancy process when the emission of radon stabilises and decreases just before the earthquake. However, the distribution of radon anomalies at surface during the preparation of an earthquake does not justify observing precursory phenomena at long distances from the epicentre area.

In general, the width of the zone affected by the stress loading is proportional to the magnitude and to the depth of the occurring earthquakes (i.e. strong earthquakes involve a wide area). Consequently, the problem is rooted in the definition of the area to investigate. In fact, the first problem regarding the use of radon as an earthquake precursor is that the radon decay time does not allow the gas to migrate over long distances. However, even if the monitoring sites are located very far from the earthquake epicentre, the stress propagation may cause some local precursory phenomena (i.e. local radon anomalies) (Riggio & Santulin, 2015).

Several authors have studied the occurrence of anomalous temporal changes of radon concentration in soil gas (King, 1986; Kuo et al., 2010; Mogro-Campero et al., 1980; Planinić et al., 2001; Ramola et al., 1990, 2008; Reddy & Nagabhushanam, 2011; Walia et al., 2009; Yang et al., 2005; Zmazek et al., 2005) and ground water (Barragán et al., 2008; Favara et al., 2001; Gregorič et al., 2008; Heinicke et al., 2010; Ramola, 2010; Singh et al., 1999; Zmazek et al., 2003, 2006). Toutain & Baubron (1999) analysed 15 cases of geochemical precursors reported in the scientific literature. Taking into account the very high heterogeneity of such datasets, they suggest that the magnitude of gas anomalies is independent of magnitudes and epicentre distances of related earthquakes, suggesting that local conditions may control amplitudes. However, radon anomalies are not only controlled by seismic activity, but also by meteorological parameters such as soil moisture, rainfall, temperature and barometric pressure (Ghosh et al., 2009; Stranden et al., 1984). The influence of these parameters on radon behaviour at surface level makes it complicated and, for small earthquakes, often impossible to distinguish anomalies caused by seismic events from those by meteorological parameters (Choubey et al., 2009; Ramola et al., 2008; Torkar et al., 2010; Zmazek et al., 2003).

e. Radon as tracer of NAPL contamination

Soil radon is also used as a naturally occurring tracer for assessing residual non-aqueous phase liquids (NAPLs) contamination of unsaturated aquifers, because it is extremely soluble in these substances (oil, gasoline, petroleum products and chlorinated solvents) and produces a concentration deficit compared to nearby unpolluted areas. The mapping of this process, known as radon-deficit technique (Semprini et al., 2000), permits identifying the contamination affecting the vadose zone. A review of that process with an exhaustive list of related references has been published by Schubert (2015). Based on equations reported by Schubert (2015), who correlates soil radon activity concentration with NAPL fraction in the pore space ($NAPL_{Pr}$), De Simone et al. (2017) developed a new formula (Equation 5-3) to quantify the residual fraction of kerosene in the subsoil of a site in the Latium Region in Italy.

$$NAPL_{Pr} = \frac{-J \pm \sqrt{J^2 - 4CH}}{2H} \qquad (5\text{-}3)$$

where J, C and H are site-specific polynomials which depend on soil radon deficit (radon concentration in the polluted site compared to soil radon in close unpolluted areas), soil water content, soil density, radon partition coefficients water/soil gas and NAPL/soil gas and NAPL saturation in the pore space.

For further details on this calculation, the reader is referred to De Simone et al. (2017) and to Castelluccio et al. (2018). This approach has also been extended to a couple of areas in India where gasoline spills were assumed (Castelluccio et al., 2018). The joint application of geophysical methods based on soil electrical resistivity and induced polarisation strongly improves this kind of investigations, also giving information about residual NAPL configurations in porous media (Johansson et al., 2015; Castelluccio et al., 2018).

f. Radon as tracer of interaction between ground water and surface water

Radon gas has also been used to study the discharge of fresh or saline ground water into coastal zones or into other low-radon surface water bodies. This kind of application (Burnett et al., 2006) works because ground water often has ^{222}Rn concentration orders of magnitude greater than surface water, having a half-life on the same order as many coastal and environmental processes. In addition, improvements in automated monitoring systems have made continuous measurements of radon at environmental activities possible. Estimating ground-water discharges using radon is based on a mass balance approach. Inventories are measured, either as a snapshot or continuously over time, and are converted into input fluxes after making allowances for losses due to decay, atmospheric evasion, and other net 'mixing' terms, such as for example advective transport of radon-rich ground water (pore water) through sediment. Thus, if one can measure or estimate these radon fluxes, the water discharge may be estimated (Burnett & Dulaiova, 2003; Tuccimei et al., 2005).

Radon may also be used to determine ground water infiltration velocity in river bank areas (Van Giap, 2003) and to measure river–ground water exchange at the riparian margins of fluvial systems (Close et al., 2014). The radon concentrations measured in rivers are actually very low and tend to grow in shallow ground water with increasing distances from the river. This is consistent with radon ingrowth processes to determine equilibrium radon values and ground-water velocities near rivers.

Examples of radon anomalies

The first evidence of anomalous radon concentrations in soil gas was reported by Hatuda (1953) before the Tonanke earthquake in Japan (magnitude M=6, December 1944). Changes in radon concentrations were also observed during the spring before the 15 April 1966 earthquake of M=5.3 in Tashkent, Figure 5-8 (from Ulomov & Mavashev, 1971).

Another important example has been reported by Igarashi et al. (1995), who monitored radon concentrations in a well at a depth of 17 m between November 1993 and March 1995 (Figure 5-9). The radon concentration increased from October to November 1994, reaching 60 Bq/l (up to three times the background value). Furthermore, a sudden increase was recorded on 7 January and followed by a sudden decrease on 10 January, 7 days before an earthquake of magnitude 7.2. In India, Singh et al. (1991) measured radon anomalies before different earthquakes (April 1986, M=5.7; March 1987, Kangra earthquake, M=7; June 1988, M=6.8). Recently, radon pre-seismic anomalies in subterranean cave and soil air in Korea, Nepal, and Taiwan have been reported by Oh et al. (2015), Deb et al. (2016) and Fu et al. (2017), respectively.

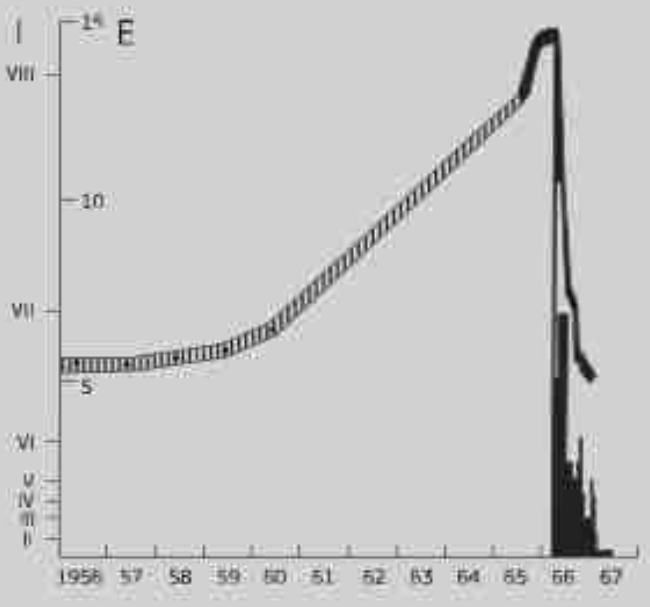

Figure 5-8.
Evidence of radon anomaly in ground water as a precursor of earthquakes before the 1966 Tashkent earthquake of magnitude M=5.3.
Source: from Ulomov and Mavashev (1971)

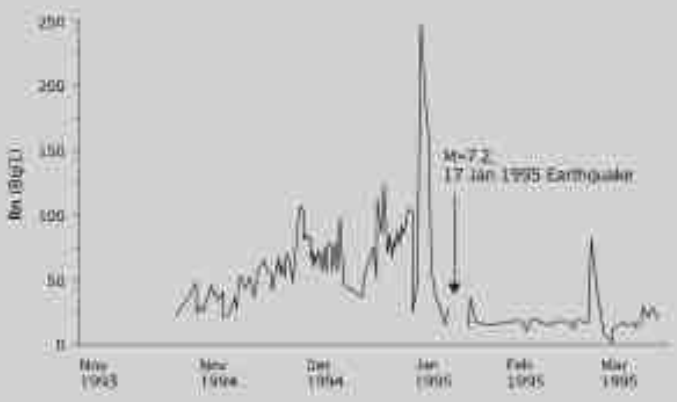

Figure 5-9.
Radon concentration measured in a well in the southern part of Nishinomiya city, Japan.
Source: adapted from Igarashi et al. (1995)

5.1.4 Challenges to developing a European map

As seen in Section 5.1.3, nationwide soil-gas radon surveys have been performed in some European countries, such as the Czech Republic, Germany, Sweden, the Slovak Republic and the United Kingdom. In several other countries, only local or regional data exist, and elsewhere there are no soil-gas radon data at all. If one were to develop a European map, a harmonised dataset would be needed since countries designed different surveys in the past. For instance, in some countries (e.g. the Czech Republic, Germany) a site is characterised by more than single measurements in an effort to minimise the error caused by heterogeneity, but in other countries instantaneous measurements are made with no repetition. Another example is the difference in the measurement depth. There are also limitations on soil-gas radon measurements: they are time-consuming and expensive, and a lot of environmental factors cause temporal and spatial variability in the concentration. Thus a properly implemented measurement protocol is indispensable, e.g. preventing soil air from mixing with outdoor air during the measurements or taking into account its temporal variations. Nowadays it can be said that there is a recognised and commonly used standard for measuring soil-gas radon at measurement depths of at least 0.8 - 1 m.

In order to create a European soil-gas radon concentration map, only comparable data should be collected and mapped. To verify field measurements of soil-gas radon, it is necessary to perform intercomparison exercises.

When harmonising datasets from different sources, one has to be aware that estimation – in the physical sense, i.e. physical sampling and measuring – is made according to protocols. In the good case, that is, if quality assurance is in place, these protocols are well-defined and codified. However, they may differ between institutions, authorities and countries, depending, inter alia, on legal or regulatory constraints, or the natural situation in which the quantities are sampled. (For instance, in predominantly rocky regions, soil radon will be sampled differently than in thick, humic soils.)

This means that the same nominal, or theoretical, quantity, translates into different operational quantities. Here is an example: the concentration of radon in soil gas, as estimated in the Czech Republic and Germany. In the former, at least 15 samples have to be taken from an area the size of building ground (up to 800 m^2), soil air taken from a depth of 0.8 m, and the 75 % percentile of the measurement results (Neznal et al., 2004). In the latter, 3 samples located at the corners of an equilateral triangle with side length 3 – 5 m are taken from a depth of 1 m, and the maximum value of the measurements is retained as the operational variable (Kemski et al., 2001, 2009). The influence of the different protocols has been studied. The result was that the difference of results is quite small.

As a consequence, when attempting to integrate datasets, one must first harmonise operational variables; that is in practice, to 'recalculate' tabulated values. In some cases, this is not trivial and requires additional studies and intercomparisons, modelling steps including model assumptions and estimation of model parameters. In any case one must expect to introduce additional uncertainty, which we may call 'harmonisation uncertainty', another non-trivial source which one has to take into account when trying to establish an uncertainty budget.

5.2 Radon exhalation rate

5.2.1 Introduction

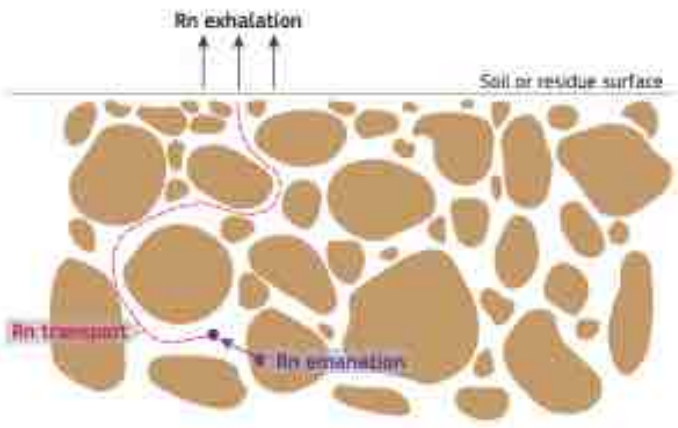

Figure 5-10.
Processes leading to radon release into the atmosphere.
Source: Sherier et al. (2013)

Radon (^{222}Rn) is generated by radium (^{226}Ra) decay and can then migrate into soil pores depending on the size of the grain and location of the radium atom close to the surface of the grain (Nazaroff & Nero, 1988) (see Section 2.2.2). This process is called radon emanation. Once radon atoms reach soil pores, they escape into the air in a process known as radon exhalation. Radon movement in soils is driven by diffusion and convective flow. It depends on several factors such as soil moisture content, soil temperature, porosity etc. (Figure 5-10). Finally, other factors, such as flow mechanisms, temperature difference, pressure etc., can influence radon transport into air (more details in Section 2.2.2).

Ranges of radon exhalations rates (mBq m^{-2} s^{-1}) (Hassan et al., 2009)	
Rocks	0.11 - 80
Soil	2.0×10^{-3} - 5.0×10^{4}
Building materials	4.0×10^{-3} - 5.0×10^{2}

Table 5-1.
Typical radon exhalation rates of geological materials.
Source: Hassan et al. (2009)

Radon enters the atmosphere (or indoor air) mainly by crossing the soil-air or building material-air interface. Because soil and most earth-building materials (see Section 5.1) have higher radon concentrations than the atmosphere (see Section 5.3), there is a large radon concentration gradient between such materials and open air. This gradient is permanently maintained by the generation of the ^{238}U and ^{232}Th series from their long-lived mother nuclides, and is responsible for a continuous flux of radon isotopes into the atmosphere.

The release from the soil/building materials into the atmosphere is referred to as the radon exhalation rate (or exhalation flux density), and is measured in radon exhaled per surface unit (m^{-2}) and per time unit (s^{-1}) (Porstendorfer, 1994; Ishimori et al., 2013). Thoron (^{220}Rn) follows the same mechanisms for exhalation as radon (^{222}Rn).

Several studies (Strong & Levins, 1982; Stranden et al., 1984; Megumi & Mamuro, 1974) have demonstrated that the exhalation rate from materials increases when water content in the sample increases until it reaches a certain saturation level; then the exhalation rate generally decreases if the moisture content is above the saturation level. When decreasing it could also reach values lower than those for dry samples (Megumi & Mamuro, 1974). Schery et al. (1989) and Hosoda (2007) estimated that the radon exhalation rate, in dry soil with very low water content (nearly 0 %), increases steadily with increased water content until it reaches 8 %. Then the exhalation rate will decrease with increasing water content.

The soil's ability to retain moisture primarily depends on the soil porosity. The radon exhalation rate increases steadily with increasing porosity of the medium. This can be explained as follows: At low porosity, soil grains are close to each other, whereas at high porosity, radon atoms can easily find their way to the atmosphere (Lee et al., 2001; Shweikani et al., 1995; Hosoda et al., 2007).

As explained in Chapter 2 with regard to emanation, in general variations in grain size appear to be inversely proportional to the radon exhalation rate; i.e. when the grain size increases, the radon exhalation rate will decrease.

Many researchers investigated the dependence of radon exhalation rate on soil temperature (Schery et al., 1989; Stranden et al., 1984). When the soil temperature increases, the exhalation rate will also increase. This is because the thermal expansion of soil air enhances convection.

Atmospheric pressure has been described as the most important meteorological condition affecting radon exhalation and soil-gas concentration (Tanner, 1964, 1980). Several studies have shown that when atmospheric pressure decreases, the exhalation rates decreases and soil-gas concentrations increase, while the opposite is observed for a decrease in atmospheric pressure (Wilkening et al., 1974; Fleischer et al., 1980; Schery & Gaeddert, 1982; Clements & Wilkening, 1974; Chen et al., 1995; Koarashi et al., 2000).

The extrinsic factors affecting the radon exhalation rate are the meteorological parameters. The radon exhalation rate increases with increasing wind velocity. Wind velocities up to 7 m/s enhance the exhalation rate by about 15 % (Schery et al., 1984; Kojima & Nagano, 2005). The radon exhalation rate does not change significantly with light rainfall (13 mm), but it decreases dramatically with heavy rainfall (93 mm) and remained low for several days after heavy rainfall (Megumi & Mamuro, 1973; Schery et al., 1984; Kojima & Nagano, 2005).

5.2.2 Measurement methods

Radon (^{222}Rn) and thoron (^{220}Rn) exhalation rates from soil can be obtained using three main approaches:

a. direct *in situ* measurements (Grossi et al., 2011);

b. estimation of radon flux density using models based on theoretical equations and on proxy data;

c. laboratory measurements of soil samples.

The first two approaches will be outlined below, followed by a description of how to determine exhalation rates from soil samples.

a. Direct *in situ* measurements

Radon exhalation rate measurements, Ciudad Rodrigo, Spain.
Accumulation method using active monitors and charcoal cartridges (inside the plastic glass).
Source: Luis S. Quindós

Direct *in situ* measurements of radon (^{222}Rn) and thoron (^{220}Rn) fluxes from soil are problematic because they are strongly affected by changes in environmental (meteorological) parameters. For the same reason they represent the 'true' picture of what is happening during measurement (which may not be representative for the site), rather than ideal conditions in the laboratory. In addition, physical properties of the soil, such as water content, have a significant effect on radon and thoron release from soil (see Section 5.2.1). The basic approaches for measuring the radon exhalation flux density are accumulation, including both the diffusion measurement and circulation (flow through) methods (ISO 11665-7:2012, 2012).

The accumulation method is commonly used to measure the exhalation flux densities of ^{222}Rn, ^{220}Rn and also of stable trace

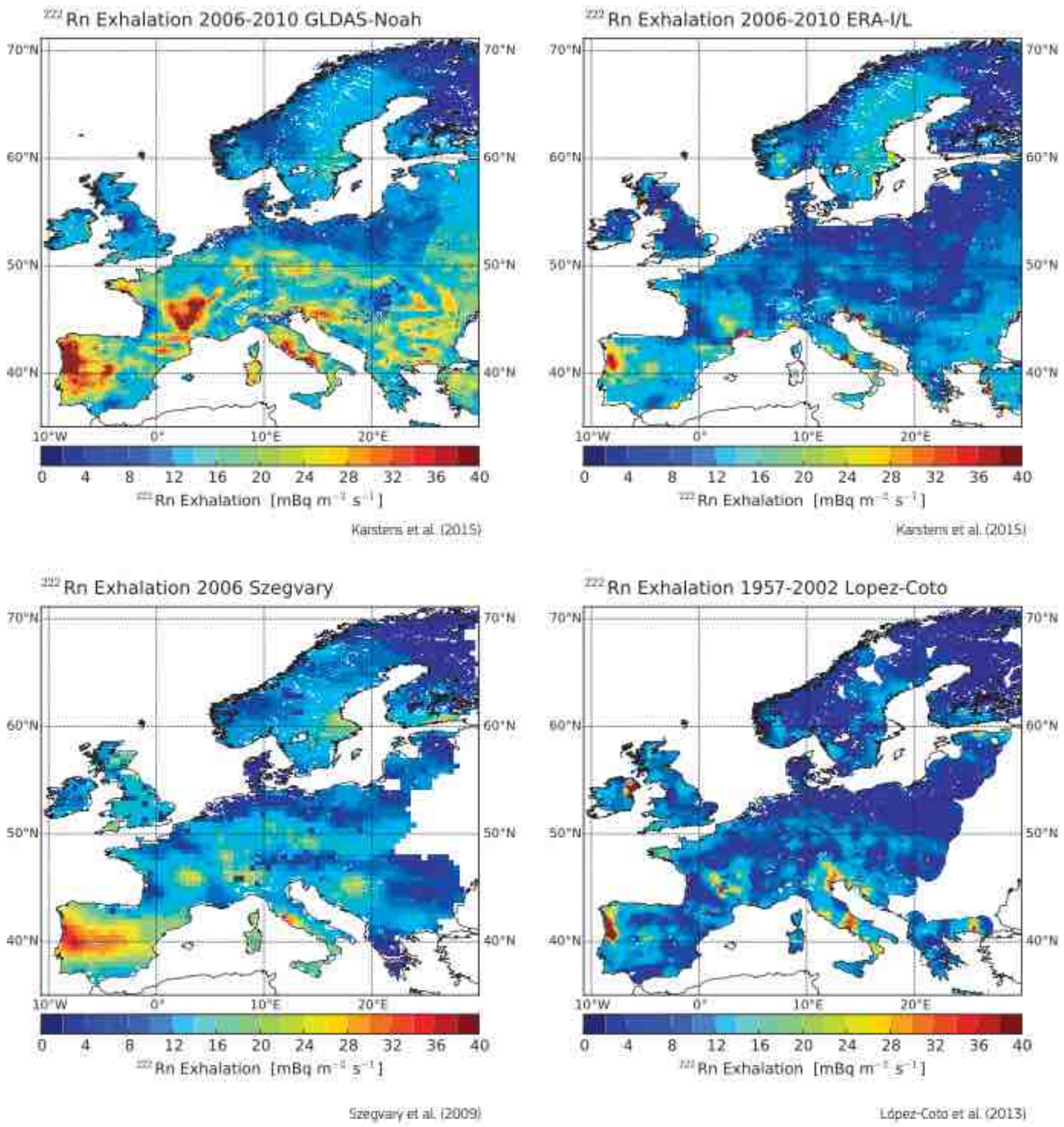

Figure 5-11
Annual mean ^{222}Rn exhalation rates for 2006-2010 from different models
Source: Karstens et al. (2015)

gases such as CO_2 and CH_4 (Livingston et al., 2005). It involves placing a chamber, known as an accumulator (Schery et al., 1989; Ferry et al., 2002), which has one open end in contact with the surface under investigation. In order to reduce superficial leakage of accumulating radon, several techniques could be used. For example, the mouth of the chamber is sealed onto the surface by inserting a short length of its cylindrical wall into the ground. The radon atoms exhaled from the surface underlying the chamber enter the headspace and gradually build up. The radon concentration is then measured at several regular intervals or, in some cases, just once at the end of the accumulation period (Jha et al., 2001). The radon concentration is measured using active monitors or instantaneous methods, such as scintillation cells or alpha spectrometry (Tuccimei & Soligo, 2008).

An accumulator can be a single-chamber or a two-part device, a collar that is inserted into the soil and a cover that is sealed onto the collar (Ferry et al., 2002). The accumulator size can vary depending upon the flux levels, portability requirements, time available for a measurement and desired resolution to map the flux across a given surface. A large base accumulator (~20–50 cm in diameter) is useful to obtain representative data over larger areas, allows more radon to enter the chamber and hence is useful for small flux levels. Smaller accumulators (around 5–10 cm in diameter) are useful for high-resolution spatial measurements, but have larger back-diffusion effects. Indeed, since the back diffusion depends on the total volume of the chamber, the height of the chamber also has to be considered. For taller accumulators, radon may not be mixed uniformly and it may be necessary to use a small fan inside the chamber. On the other hand, back-diffusion effects will be stronger in chambers with smaller heights (Ishimori et al., 2013).

In the flow-through method, a chamber working as an accumulator is placed over the surface to be investigated, even if the air in the chamber is continuously removed at a constant rate. The radon concentration in the exhaust stream is then measured by a semi-integrating technique such as a flow-through scintillation cell. Radon detection in this case allows for the presence of ^{220}Rn and its decay products by using a delay line for thoron decay prior to filtration and counting. Double-cell systems have been developed to measure simultaneously radon and thoron exhalation flux densities (Zahorowski & Whittleston, 1996). Thoron flux can also be measured using detectors that allow alpha spectrometry of the radon and thoron decay products (e.g. using electrostatic cell collection on a silicon detector).

The adsorption method for ^{222}Rn exhalation flux involves using an adsorption medium (usually activated charcoal, see Section 2.5), placed in close proximity to the soil surface. Before being used, the charcoal is heated in an oven to remove radon, moisture and other contaminants, which may have been adsorbed previously. Once prepared, the canister is sealed to prevent adsorption of ambient radon or moisture. Following exposure, the canisters are again sealed, and the activities of the radon progeny ^{214}Pb and ^{214}Bi are measured by gamma spectrometry, following a short ingrowth period for the progeny. Liquid scintillation counting may be used as a measurement technique if a higher counting efficiency is required (Ishimori et al., 2013). Moreover, track-etch detectors (see Section 2.5), placed in cups, may be used.

b. Use of models

The second approach to obtain maps of radon flux from soil is to calculate data using models based on different parameters such as gamma-ray aerial survey data, modelled soil moisture and maps of soil properties (Griffiths et al., 2010). These models need to be calibrated against a dataset of accumulation chamber measurements. Other methods, on the contrary, make use of terrestrial gamma radiation or soil radionuclides (Manohar et al., 2013) as proxies for generating radon flux maps. Among different equations applied to proxy data, one of the most popular is given by Zhuo et al. (2008). Based on an idealised model, these authors

calculated both the annual and the seasonal radon (^{222}Rn) flux densities from the soil surface at 1 099 sites in China by linking a database of soil ^{226}Ra content to a global ecosystems database containing soil temperature, soil water saturation, soil porosity and radon emanation coefficients.

According to Zhuo et al. (2008), the ^{222}Rn flux density from a semi-infinite and homogeneous soil (F, expressed as Bq m^{-2} s^{-1}) is obtained from the following equation:

$$F = A_{Ra} \cdot \rho_b \cdot \varepsilon \cdot \left(\frac{T}{273}\right)^{0.73} \cdot \sqrt{\lambda D_0 p \exp(-6Sp - 6S^{14p})} \quad (5\text{-}4)$$

where:

A_{Ra} is the soil ^{226}Ra content (Bq/kg);

ρ_b is the soil bulk density (kg/m^3);

ε is the emanation coefficient of ^{222}Rn in soil, which is a function of the soil temperature (T, in kelvin) and the water saturation fraction (S);

λ is the ^{222}Rn decay constant (s^{-1});

p is the soil porosity; and

D_0 is the ^{222}Rn diffusion coefficient in air (1.1×10^{-5} m^2/s).

For further information on the estimation of ε and S, see Zhuo et al. (2008).

Considering the key role of flux maps for the use of radon in atmospheric transport, several studies (Griffith et al., 2010; Zhuo et al., 2008; Hirao et al., 2010) resulted in high-resolution maps of the variability of ^{222}Rn exhalation from continental soils. For Europe, Figure 5-11 shows the geographical distribution of annual mean fluxes calculated by Szegvary et al. (2009); López-Coto et al. (2013) and Karstens et al. (2015), respectively.

López-Coto et al. (2013) and Karstens et al. (2015) used a similar approach. Based on theoretical equations, they parametrised ^{222}Rn production and transport in soil to calculate the ^{222}Rn flux. These studies estimate the ^{222}Rn exhalation rate based on soil properties, i.e. uranium content in the upper soil layers and modelled soil moisture, and determine its spatial and temporal variability.

On the other hand, the Szegvary et al. (2009) approach is based on proxy data, using the correlation between the ^{222}Rn flux and the terrestrial gamma-dose rate. In the study area, the total gamma-dose rate was continuously being monitored at nearly 3 600 stations, and the terrestrial component could be extracted from those measurements. This monitoring network is made available and stored on the European Radiological Data Exchange Platform (EURDEP: https://remon.jrc.europa.eu).

These maps reveal the importance of different approaches and assumptions, and the use of high-resolution datasets of soil properties, uranium content and model-derived soil moisture to calculate the ^{222}Rn flux.

Finally, analogous methodologies have been proposed for thoron (^{220}Rn) fluxes. Voltaggio et al. (2006) proposed to calculate ^{220}Rn fluxes (F) as follows:

$$F_{Th} = A_{Rn\text{-}224} \cdot \rho_b \cdot \varepsilon \cdot \sqrt{\lambda_{Th} D_0 \exp(-6Sp - 6S^{14p})} \quad (5\text{-}5)$$

where:

$A_{Rn\text{-}224}$ is the soil ^{224}Ra content (Bq/kg); and

λ_{Th} is the ^{220}Rn decay constant (s^{-1}).

For the other symbols, see Equation 5-4.

c. Laboratory measurements of soil samples

The third approach to determine radon and thoron fluxes from soil is to collect materials during field surveys and to analyse them in the laboratory. This kind of sample measurement makes use of the accumulation chamber method, but under controlled and standardised experimental conditions. Samples are generally dried in the oven because the water content could influence the recoil length of radon and thoron from mineral grains to soil pores, enhancing gas removal from the air circulating in the experimental circuit. Exhalation temperature may be kept constant during the test, in order to make measurements reproducible.

5.2.3 Application: Proposal for a classification scheme for building materials based on radon and thoron exhalation rates

The main source of indoor radon is soil gas, but other sources such as building materials and tap water contribute in an important way (Bruno, 1983). All over the world, cement bricks, red-clay bricks, gravel aggregates, Portland cements and igneous rocks are used as building materials in dwellings and workplaces (Chao et al., 1997; Tuccimei et al., 2006, 2009; Trevisi et al., 2012, 2018).

To evaluate the contribution of building materials to radon accumulation in the indoor environment, it is very important to measure radon and thoron released by geological materials used for construction. This section proposes a classification scheme for building materials, applicable to rocks, cements and mortars, based on experimental protocols to measure ^{222}Rn and ^{220}Rn exhalation rates simultaneously (see Section 5.2.2).

Special attention has to be devoted to minimise factors influencing values of exhalation rates: temperature, air mixing, humidity and grain size. The development of a specific protocol to certify building materials, evaluating their tendency to release radon gas, meets the statements of European directives concerning construction products (European Communities, 1989; European Union, 2013). This regulation stipulates requirements for building materials used in construction, among which that they should neither emit dangerous radiation nor develop toxic gases.

The protocol can be applied to cut-stone or granular material, grounded and sieved according to specific use. When analysing cut-stone material, one should consider that its exhalation rate increases considerably if the block is ground (De Martino et al., 1998; Kovler et al., 2005; Tuccimei et al., 2006). A reference grain size (if a granular material is analysed) and sample weight and volume should be introduced.

The classification of building materials proposed by Tuccimei et al. (2009) is based on an alphanumeric codex that labels the exhalation rate classes, with letters from A to E for ^{222}Rn (codex 222 in Table 5-2) and numbers from 1 to 5 for ^{220}Rn (codex 220 in Table 5-2), with which they progressively increase. The limits between classes are chosen as a function of radon exhalation rates required to reach predetermined equilibrium activity concentrations in a standard confined environment (the model room of 56 m^3, 4 × 5 × 2.8 m, reported in the EC Radiation Protection, 1999), completely covered with the investigated material.

The calculations are based on the following equation (Petropoulos et al., 2001):

$$E_0 = \lambda \cdot V \frac{(C - C_0 e^{-\lambda t})}{S(1 - e^{-\lambda t})} \quad (5\text{-}6)$$

where:

E_0 (Bq m^{-2} h^{-1}) is either E_{222} or E_{220} and λ (h^{-1}) is either λ_{222} or λ_{220}, depending on the specific calculation;

C (Bq/m^3) and C_0 (Bq/m^3) are, respectively, the equilibrium radon concentration and initial radon level in the model room; and

V (56 m^3) and S (90.4 m^2) are the volume and the inner surface of the model room.

Codex 222	Equilibrium ^{222}Rn Bq/m^3	E_{222} Bq m^{-2} h^{-1}	Codex 220	Equilibrium ^{220}Rn Bq/m^3	E_{220} Bq m^{-2} h^{-1}
A	< 100	< 0.47	1	< 100	< 2 768
B	100 - 200	0.47 - 0.94	2	100 - 200	2 768 - 5 535
C	200 - 300	0.94 - 1.40	3	200 - 300	5 535 - 8 303
D	300 - 400	1.40 - 1.87	4	300 - 400	8 303 - 11 070
E	> 400	> 1.87	5	> 400	> 11 070

Table 5-2
Proposal for a classification scheme for building materials (Tuccimei et al., 2009): Codex 222 and Codex 220 are attributed to samples based on their ^{222}Rn and ^{220}Rn exhalation rates, respectively. The combination of Codex 222 and Codex 220 (in this order) identifies the class of material (see text for explanation). Values of 0.00756 and 44.71917 h^{-1} have been used for λ_{222} and λ_{220}, respectively.
Source: Tuccimei et al., 2017

The preset values of radon equilibrium concentrations reached in the model room are 100, 200, 300 and 400 Bq/m^3 (annual average values). According to the World Health Organization (WHO, 2009), a reference level of 100 Bq/m^3 is justified from a public health perspective because an effective reduction of radon-associated health hazards for a population is hereby expected. However, if this limit cannot be implemented, the chosen reference level should not exceed 300 Bq/m^3, which represents approximately 10 mSv per year according to recent calculations made by the International Commission on Radiological Protection (ICRP), as reported by WHO (2009). Finally, the latest European Basic Safety Standards Directive (European Union, 2013) sets 300 Bq/m^3 as maximum reference level for concentration (annual average value) of indoor radon in all dwellings and workplaces.

It is worth stressing that the choice to include ^{220}Rn in this proposal for classification depends on the large thorium contents of many geological materials used for building stones or cements, resulting in significant ^{220}Rn contribution to total indoor radon activity concentration. This additional input is generally neglected because thoron released from soil is mostly negligible, even if thoron from building materials needs to be accounted for, otherwise its potential risk is underestimated. This view is clearly expressed by Steinhauser et al. (1994), who underlined at that time that the existing databases on ^{220}Rn in the environment, the experimental validation of dosimetric models and potential health effects are scarce; however, he identified circumstances where the ^{220}Rn dose becomes relevant, as in the indoor environment if building materials with high concentrations of ^{220}Rn precursor are present (Nucciatelli et al., 1998).

Finally, it is worth stressing the relevance of a building material classification scheme based on radon exhalation and the importance of a rigorous standardisation of sample preparation and laboratory measurements. If all radon determinations are carried out under the same experimental conditions, the relative strength of building materials as radon and thoron source will be respected and architects or building designers will have available a relative scale of hazard classification.

Other studies, such as Kovler (2011) and Trevisi et al. (2013), take into account radon exhalation from building materials.

5.2.4 Challenges to developing a European map

As we have seen, radon exhalation from a surface (either ground soil or a building material) can be measured, and, therefore, the following challenges must be considered when producing a radon exhalation rate map at the European scale:

1. The results should be obtained by using similar methodologies or by carrying out an inter-comparison of techniques to find out whether results can be compared. To this extent, there is an ISO standard (ISO 11665-9:2016, 2016) that could be used as starting point;
2. A map at European scale should consider two different types of materials: ground soil and building materials (i.e. a point map);
3. In the case of ground soil, typical soil parameters affecting radon exhalation rate and radon emanation have to be considered when developing mapping techniques.

Case study: Radon exhalation measurements in the laboratory

This section focuses on a methodology to measure the radon exhalation of soil-rock building-material samples in the laboratory. This approach uses an active-continuous radon monitor, a cylinder with desiccant and a vessel (modified pressure cooker) as accumulation chamber. This experimental configuration (Figure 5-12), presented by Tuccimei et al. (2009), improves that of Tuccimei et al. (2006).

The new method makes use of a continuous monitor equipped with a solid-state alpha detector, connected in line with an accumulation chamber, consisting of a 5.1 l modified stainless steel pressure cooker with a mechanical tightness system, supplied with a 9 V circulation fan (17 cm diameter) for mixing purposes (Figure 5-12). The chamber, placed in a refrigerating thermostatic bath, is connected via vinyl tubing to a gas-drying unit filled with a desiccant ($CaSO_4$, 3% $CoCl_2$ as indicator) and to a continuous radon monitor. The instrument draws air from the chamber, through the desiccant and an inlet filter (with the aim to stop the radon progeny), into the monitor.

The air is then returned to the vessel from the radon monitor outlet. The radon contained in the filtered air dacays inside the monitor chamber, producing detectable alpha-emitting progeny, particularly polonium isotopes. Alpha particles are collected on a surface barrier silicon detector thanks to an electrostatic field produced by a high voltage applied on the chamber walls. The solid-state silicon detector converts alpha radiation directly to an electrical signal, discriminating the electrical pulses generated by alpha particles from the polonium isotopes (^{218}Po, ^{216}Po, ^{214}Po, ^{212}Po) with energies of 6.0, 6.7, 7.7 and 8.8 MeV, respectively. With this approach, it is possible to use only the ^{218}Po peak for ^{222}Rn and ^{216}Po for ^{220}Rn, obtaining a rapid equilibrium between polonium and radon nuclides, because the equilibrium between ^{218}Po and ^{222}Rn is achieved in about 15 min (about five times the half-life of ^{218}Po), and between ^{216}Po and ^{220}Rn in a few seconds. The ^{222}Rn growth curve is monitored with cycle times of 2 hours per day in order to calculate the exhalation rate that is proportional to the slope of the linear part of the growth curve. The measurement allows simultaneous determination of ^{222}Rn and ^{220}Rn exhalation rates that can be referred to the surface of the material. The detection limit of the experimental apparatus is equal to 0.01 Bq/h for ^{222}Rn and to 6 Bq/h for ^{220}Rn.

^{222}Rn (E_{222}, Bq m^{-2} h^{-1}) and ^{220}Rn (E_{220}, Bq m^{-2} h^{-1}) exhalation rates are calculated using Equations 5-7 and 5-8 below:

$$E_{222} = \frac{(m + \lambda_{222} \cdot C_0) \cdot V}{S} \qquad (5\text{-}7)$$

$$E_{220} = \frac{\lambda_{220} \cdot V_0}{S} \cdot \frac{C_m}{e^{-\lambda_{220} \cdot (V_t / Q)}} \qquad (5\text{-}8)$$

where:
m (Bq m^{-3} h^{-1}) is the initial slope of the radon growth curve;
λ_{222} and λ_{220} are ^{222}Rn and ^{220}Rn decay constants (h^{-1});
C_0 is the initial radon concentration (Bq/m^3);
V is the free total volume of the analytical system (m^3);
S is the surface of the accumulation chamber (m^2);
C_m is the equilibrium ^{220}Rn concentration (Bq/m^3);
V_0 and V_t (m^{-3}) are the free volume of the accumulation chamber and the volume between the outflow of the accumulation chamber and the inflow of the radon monitor, respectively; and
Q is the flow rate in the system.

The second term of Equation 5-8 corrects for the decay of ^{220}Rn during transport in the closed system, because the thoron half-life (56 s) is comparable with the time required to complete a whole loop, causing the underestimation of thoron activity concentration (Ishimori et al., 2013).

In order to test the experimental set-up and sample preparation procedures, validation tests have been carried out using 'Tufo Rosso a Scorie Nere' (TRSN) pyroclastic flow as standard material (Tuccimei et al., 2009). This tuff, emitted from the Vico volcanic apparatus (50 km northeast of Rome, Italy), is commonly used in cut-stone and concrete masonry because of its lightness, tenacity and machinability. TRSN standard, crushed and sieved between 1 and 2 mm, has always been weighed (1 kg) and dried at 110 °C for 24 hours before beginning the experiments. Validation tests have been performed with air mixing, and the temperature has been kept constant at 20 °C, introducing the accumulator in the refrigerating thermostatic bath. Reproducible results have been obtained within the range of analytical uncertainties (about 5%).

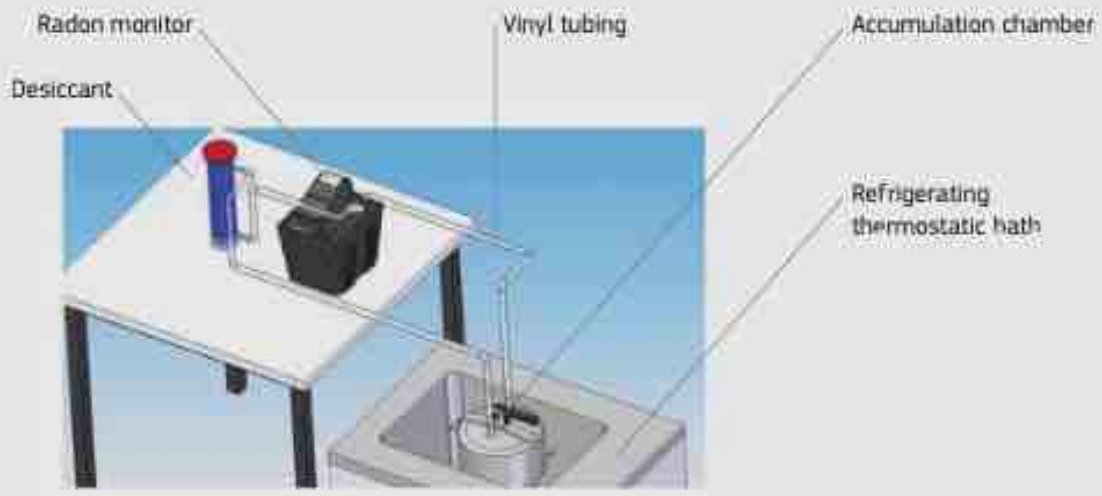

Figure 5-12
Experimental set-up used to determine radon and thoron exhalation rates from soil samples
Source: Tuccimei et al., 2009.

With the aim of investigating the influence of temperature on radon exhalation rates, Tuccimei et al. (2009) carried out another specific 19-day test on TRSN standard (Figure 5-13) without using the thermo-refrigerating bath, but allowing the sample to experience ambient temperature fluctuations. The theoretical radon accumulation curve has been modelled with Equation 5-9, using the value of m in Equation 5-7 (slope of the curve) equal to 10.44 derived from standard 24-hour tests:

$$C_t = C_0 \cdot e^{-\lambda t} + \frac{E_{222} \cdot (1 - e^{-\lambda t})}{\lambda \cdot V} \qquad (5\text{-}9)$$

where:
C_t (Bq/m^3) is the radon activity concentration at time t (h^{-1});
C_0 (Bq/m^3) is the initial radon concentration;
λ is the ^{222}Rn decay constant (h^{-1});
E_{222} is the ^{222}Rn exhalation rate (Bq/h); and
V is the free total volume of the analytical system (m^3).

As seen in Figure 5-13, the experimental ^{222}Rn growth curve is regular during the first segment of the test (up to about 250 hours, segment 1), when temperature changes are not so relevant (less than 2 °C). In the second part of the experiment (from 250 to 370 hours, segment 2), abrupt changes of radon concentration are recorded along with corresponding significant and rapid temperature fluctuations (up to 12 °C changes in a few hours). Throughout the last section of the experiment (segment 3), radon fluctuations are linked to parallel oscillations of temperature data in the frame of a general decrease of both variables.

This test clearly shows a direct correlation between large temperature changes and variations of radon concentration within the experimental set-up. A similar finding on the effect of rapid temperature increases on radon exhalation rate (as in the last 10 hours of segment 2) was reported by Kovler (2006a, b), where peaks of radon exhalation rates coincide with those of temperature measured on the surface of cement pastes, due to hydration heat development during the shrinkage phase. The author states that heating the material weakens physical adsorption of radon gas atoms on the newly formed solid surfaces, enhancing radon release. Smaller temperature changes during longer periods (as in segment 1 of Figure 5-13) do not seem to affect ^{222}Rn exhalation rates significantly.

In conclusion, validation tests suggest that the experimental procedure presented above provides exhalation rates for dried geological materials in order to remove the effect of soil moisture and to correlate meaningfully all experiments. In addition, it can be said that a 24-hour circulation of radon gas in a closed-loop circuit seems to slightly reduce the exhalation because of radon absorption by the drying agent and minor diffusion/absorption by vinyl tubings.

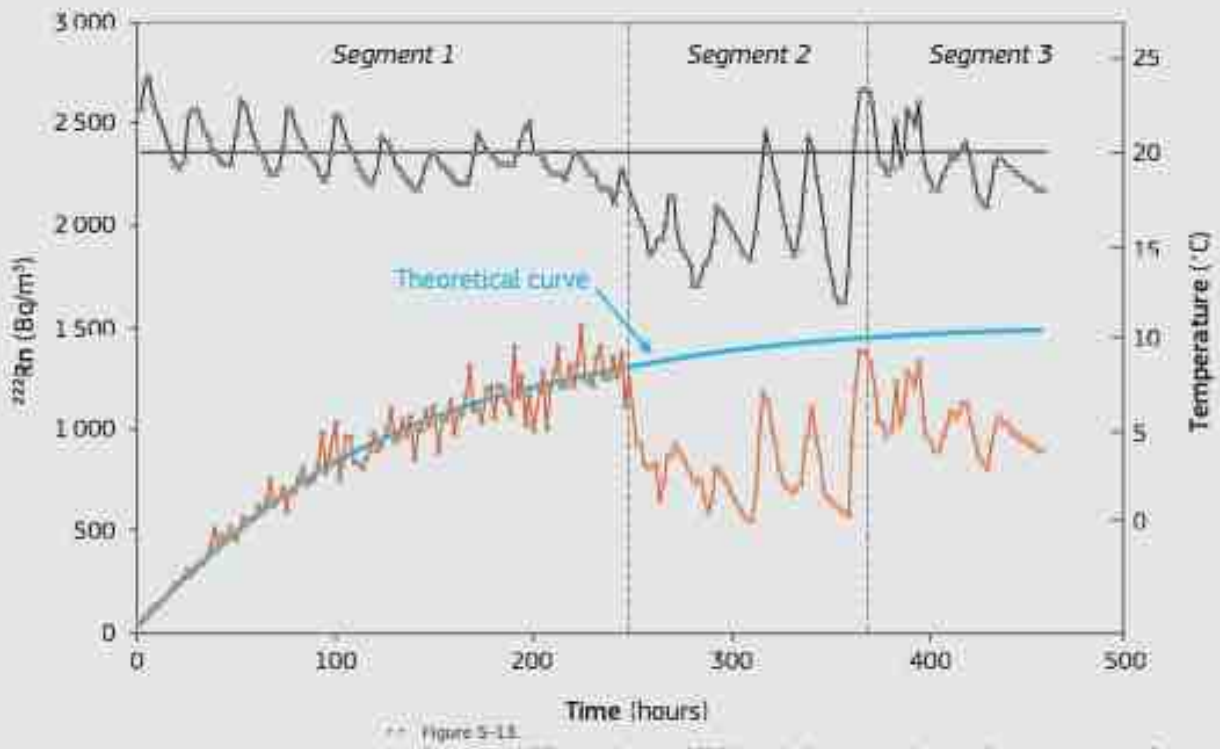

Figure 5-13
Experimental ^{222}Rn growth curve of TRSN standard (red squares) over a 19-day experiment performed at ambient conditions (variable temperature) compared with a theoretical radon curve (blue line) modelled for a constant temperature of 20 °C, with a value of m = 10.44. Temperature data are indicated with black triangles. The reference temperature of 20 °C is indicated with a full horizontal line. Errors are around 5%.
Source: Tuccimei et al., 2009.

5.3 Outdoor radon

5.3.1 Introduction

Radon (^{222}Rn) concentration in outdoor air is known to be low and to have no major impact on health (WHO, 2009). Steck and Yassin (2001) asserted that, worldwide, population-averaged radon concentration in outdoor air varies from 7 to 55 Bq/m³. According to UNSCEAR (1993), typical outdoor radon concentrations are on the order of 10 Bq/m³, a value later confirmed by subsequent publications (UNSCEAR, 2000).

In any case, outdoor radon concentrations may occasionally reach potentially hazardous levels. For example, air escaping from an open uranium mine gallery in the town of Schneeberg, Germany, contained radon with concentrations up to 10 000 Bq/m³, thus ventilation facilities had to be installed to prevent this air from entering an adjacent factory. Radon is potentially emitted by some anthropogenic sources, such as near-surface radioactive waste disposal sites (Appleton et al., 2011). Radon exhalation and releases from uranium mining and milling can potentially increase long-term radon releases into the adjacent environment relative to pre-mining baseline concentrations (Mudd, 2008). Precipitation and soil moisture can influence radon flux densities from uranium mining waste rock dumps, ore stockpiles and areas where effluents enriched in radium (^{226}Ra) have been spray-irrigated over land in wet-dry tropical regions (Lawrence et al., 2009). Outdoor measurements are needed to obtain information on natural background radon concentrations in order to identify and quantify anthropogenic contributions (i.e residues from uranium mining and milling). Moreover, the level of local concentrations of outdoor radon contributes to indoor radon concentrations, in exceptional cases being higher than that observed indoor (Vaupotič et al., 2010; Antignani, 2018); hence this has to be taken into account when establishing policies on radon in homes (Kümmel et al., 2014).

Because of the extended half-lives of uranium (^{238}U) and radium (^{226}Ra), and due to their abundance in the Earth's surface, radon is continually being formed in soil and released into the air. Owing to the relatively long half-life (about 3.8 days), monatomic radon gas can migrate through the soil and enter the atmosphere, where it reaches an altitude of several kilometres, before being lost through radioactive decay (UNSCEAR, 1982; Chen et al., 2016).

This normal emission of radon from its parent nuclide ^{226}Ra in soils is the largest single source of radon in the global atmosphere (NAS, 1999; NCRP, 1984; Planinić et al., 1994).

Radon concentration in the atmosphere is therefore directly related to the exhalation rate of radon from soil (Escobar et al., 1999). This exhalation process is influenced by several factors, including ^{226}Ra concentration, the internal structure of radium-containing mineral grain, soil type, moisture and temperature (Chen et al., 2016). In addition, the variable ambient air pressure affects the exhalation rate (Clements & Wilkening, 1974; Stranden et al., 1984; Schery, 1989; Markkanen & Arvela, 1992; Nazaroff, 1992; Ashok et al., 2011). Nazaroff (1992) explained in detail the transport mechanisms of radon from soil into the atmosphere.

The geographical location and the prevalent meteorological conditions have an impact on the concentration of radon at ground level, with significant seasonal variations. Cohen (1979) observed that, in general, radon concentrations in air typically decrease exponentially with altitude. Usually, air masses over continental regions have the highest concentrations, while air masses over the oceans or the arctic regions have the lowest ones. Mean annual values of radon concentration in outdoor air at ground level vary between 0.1 and 10 Bq/m³ (UNSCEAR, 1982). Concentration of radon in the outdoor environment is also affected by atmospheric mixing phenomena (UNSCEAR, 2006).

Once radon is in the outdoor air, its dilution/dispersion depends on atmospheric diffusion conditions related to meteorology and topography (Wilkening, 1990). A vertical gradient in activity concentration and time variations according to a daily cycle are commonly observed. Atmospheric dispersion is frequently higher during daytime, and radon concentrations are relatively weak, while it is lower during night-time temperature inversions; radon accumulates and its activity concentration increases by a factor of 10 to 100 in the atmospheric layer in contact with the ground.

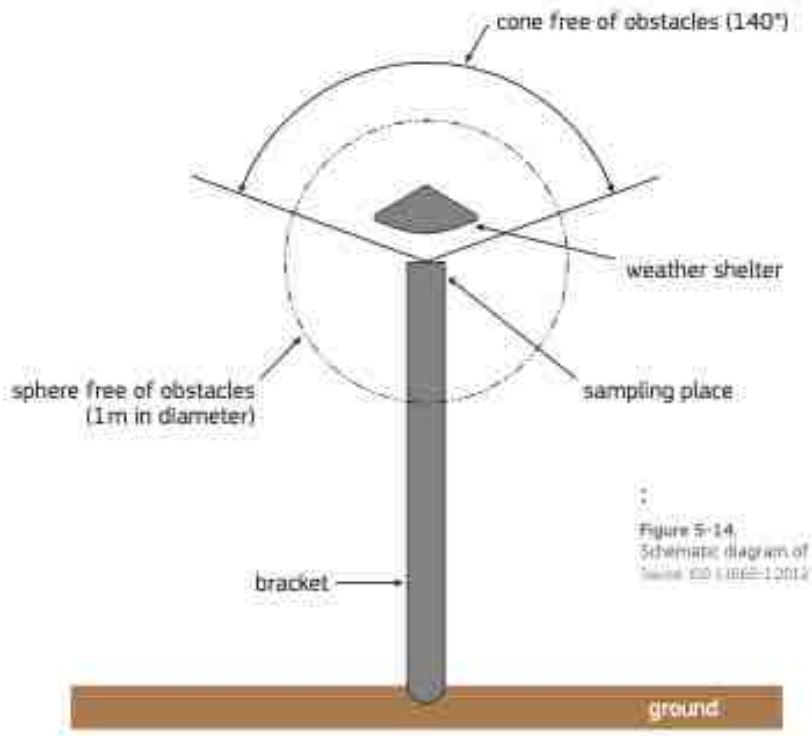

Figure 5-14
Schematic diagram of a sampling place outside a building
Source: ISO 11665-1:2012 (2012)

5.3.2 Measurement methods

Methods for measuring radon and its decay products have been described in detail in Section 2.5. Such methods can be divided into two types: active techniques which require electric power and/or the use of air pumps to collect activity from the air; and passive techniques for which the detector does not require electric power. It is also important to distinguish different sampling techniques in terms of their temporal characteristics (European Communities, 1995). The sampling time (date and hour), duration and location, and whether the sampling is active or passive, shall be specified for all measurements of radon and decay products in the environment or in a confined atmosphere.

In an open area, sampling shall be representative of the air to be measured. According to ISO 11665-1:2012 (2012), any natural and artificial obstacles (apart from weather shelters) shall be outside an inverted cone with a 140° opening at the top and the sampling point at the bottom tip, and outside a sphere with a 1 m diameter centred on the sampling location (see Figure 5-14). The sampling location shall be between 1 and 2 m above the supporting surface (e.g. ground). The installation shall not disturb the surrounding atmosphere.

Depending on their duration, radon collection and measurement methods may be classified into instantaneous, semi-integrating (also known as continuous real-time or continuous on-line) and fully-integrating (also known as time-averaging or time-integrating) modes. In the instantaneous mode, a gas sample is taken on a short timescale. In the semi-integrating mode, sampling and counting are done simultaneously, and radon concentrations are evaluated at regular intervals. Generally, the sampling is performed over periods of a few minutes to a few hours. Sample collection may be carried out either by diffusion mode or by pump-based flow-through mode. Detection can be carried out by alpha spectrometry, ionisation chamber or by gross-alpha counting techniques. An example of a semi-integrating mode is flow-through scintillation cells. Such methods are used to obtain information on rapid changes of radon concentrations in a given environment. In addition, they may be preferred over instantaneous modes owing to their superior sensitivity, reduction in the magnitude of systematic errors or their ability to measure a time-varying signal (e.g. owing to diurnal variations in the system under study).

The fully-integrating mode provides a time-integrated radon concentration for the sampling period (typically on the order of weeks or months). Sampling techniques operating in this mode must maintain an integrated record of each alpha particle impacting on the measurement medium. Once removed from the sampling site, they must maintain the exposure information until it is analysed. The passive methods are useful for obtaining long-term averages of low levels of radon concentrations. They also have the advantage of enabling large numbers of measurements over extended regions at a relatively low cost.

All three types of methods consist of primary elements such as nuclear track detectors (e.g. CR-39 and LR-115), solid-surface barrier detectors, scintillation cells (Lucas cell), electrets, activated charcoal and ionisation chambers.

It is not easy to determine the radon concentration in outdoor air and its decay products in the lower layers of the atmosphere, because concentrations there are very low, therefore it is necessary to use low background detection equipment (Burian & Otahal, 2009). A large number of radon measurements in the air above the ground surface have been made, but due to the application of different methods, these results are not comparable (Ochmann, 2005). The applicability of various systems (i.e. long-term detector systems, radon monitors) under outdoor conditions has been demonstrated in a variety of previous studies (e.g. Hopper et al., 1999; Vargas & Ortega, 2006). There are many examples of the use of both passive (e.g. nuclear track detectors such as CR-39 and LR-115) and active techniques (i.e. scintillation cells and ionisation chambers), depending on the purpose of the outdoor measurements.

Due to its good ionisation sensitivity and stability against various environmental factors, the CR-39 detector (polycarbonate material) has been used as the state-of-the-art track detector for environmental radon. One crucial point in using this detector for outdoor measurements is that the background of the material must be low. The background of CR-39 detectors varies from batch to batch, from foil to foil in the same batch, from one side to another of the same foil and within the same foil surface (Mishra et al., 2005). This could be due, apart from alpha particles from radon and its decay products, to surface defects caused by handling, microvoids or any type of imperfection left on the surface during the manufacturing processes (Mishra et al., 2005).

Examples of methods for measuring outdoor radon concentration

- In **Poland**, Ochmann (2005) investigated radon activity in the atmosphere and its behaviour. Radon activity was measured by means of long-term exposure of LR-115 (cellulose nitrate film). In order to carry out measurements of radon activity in the outdoor air, the detectors were fixed to the inner surface of a black plastic cup (of 8 cm diameter). The plastic cups provided shelter from the sunlight and precipitation. The monitoring points were situated on the outcrops of different types of rocks. Each monitoring point consisted of 4 cups fixed at 2 m, 1 m, 0.5 m and 0.05 m above the ground surface. The exposure time was 6 months, twice a year: October to March (autumn-winter period) and April to September (spring-summer period). The mean value of atmospheric radon activity was 21 Bq/m³ in the air 2 m above the ground surface. Radon activity in cup detectors close to the ground varied from 25 to 300 Bq/m³, depending on uranium and thorium content in indirect ground basement (soil and weathered rocks).
- In **Ireland**, long-term outdoor radon measurements were recorded using CR-39 track-etch detectors (Gunning et. al., 2014). The exposure period was 12 months, so as to take into account seasonal variations. In order to measure accurately the low radon concentrations expected outdoors, the measurement protocol has been specifically optimised for outdoor conditions in order to minimise the background track density of the unexposed CR-39 detectors. This protocol included pre-etching the detectors before exposure to allow radon tracks to be more easily distinguished from background.
- In **Slovenia**, a nation-wide outdoor radon survey was carried out using CR-39 detectors installed at 60 points almost uniformly distributed over the country (Vaupotič et al., 2010). At each point, a pair of detectors was fixed at a height of 1.5 m above the ground. The limitations imposed by the track-etch technique when applied outdoors were recognised. These subsisted, in contrast to indoors, by reason of detectors exposure for at least three months to substantial changes of air temperature, humidity and precipitation, both rain and snow. When manipulated through storage, exchange and mailing, the detectors were kept indoors for the shortest possible time, thus minimising the contribution from indoor air. It was also noted that on average, radon concentrations obtained with a pair of detectors at a given place differed by less than 10% in about one-third of the places, 10–30% in another third of the places, and more than 50% in the last third of the places. Although radon concentrations did not generally differ significantly between seasons at the same place, they differed substantially at a few places, most probably due to an extra exposure during improper storage, exchange or mailing of detectors.
- In **Romania**, temporal variations of radon concentration in air at 1 and 10 m height have been examined in relation to meteorological parameters such as temperature, relative humidity, air pressure, and stability (Zoran et. al. 2012). Measurements at 1 m height were carried out by means of CR-39 detectors mounted in a meteorological housing. Detectors were exposed for consecutive intervals of 10 days during one 600-day period (1 July 2010 to 1 February 2012). In Bucharest-Magurele, radon concentration in air was measured simultaneously with CR-39 also in the lower atmosphere at 10 m height between 1 August 2011 and 20 December 2011 with an active, continuous monitoring device. This compact and portable measuring system was used for continuous determination of radon and radon progeny concentrations as well as relevant climatic parameters.
- In **Germany**, the Federal Office for Radiation Protection (BfS) conducted a measuring programme over three years to determine natural radiation exposure due to outdoor radon and its short-lived decay products. The annual mean radon concentration was measured with solid-state track-etch detectors at 173 measuring points in an even grid with a grid length of approximately 50 km (Kümmel et. al, 2014). A polycarbonate film of 0.3 mm thickness in an open diffusion-chamber with a glass fibre filter and a volume of about 360 cm³ was used. The diffusion chamber was protected from mechanical and meteorological influence with a plastic cover. In order to represent breathing air, measurements were made at a standard height of 1.5 m above the ground. The system was suitable for outdoor conditions, as demonstrated by a long-term intercomparison study (3 and 6 months) with a calibrated active radon measurement system (Kummel et al., 2014).
- The measurement campaign showed radon concentrations well below the nationwide mean of 9 Bq/m³ in the northern coastal regions, intermediate values in the middle of the country and high concentrations of more than 30 Bq/m³ in the very south. The cause is linked to the influence of low radon air masses from the North and Baltic Sea that is not limited to the directly adjacent coastal regions, diminishing only gradually with increasing distance from the coast. The study also showed that in the southern regions of Germany, the influence of the local geology dominates, with typically high concentrations of ^{226}Ra in the soil and bedrock.
- Desideri et al. (2006) related the meteorological conditions and radon concentration data collected during a campaign carried out in Urbino, Central **Italy**, from 2002 to 2005. The continuous measurement of radon concentration was performed using active devices suitable for continuous monitoring of radon concentrations between 2 and 2000000 Bq/m³. The measurements mode was set to diffusion, the sampling time to 60 minutes, and the monitor was located at a height of 3 m above the ground. It was noted that the study of the time trend of radon concentration, performed by means of an active, continuous device, is a powerful tool to characterise a site, furnishing useful indication about the characteristics of the atmosphere and to uncouple pollutant concentration variations due to those in the emission fluxes from those depending on the meteorology.
- In Central **Poland**, the outdoor radon concentrations in the air layer near the ground in relation to meteorological parameters (e.g. air temperature, wind, soil heat flux, volumetric water content in soil) were studied at two sites: the city centre of Lodz and Ciosny village, a rural area about 25 km to the north of Lodz (Podstawczyńska and Kozak, 2009). Continuous measurements of radon concentration (in 60-min intervals) were performed 2 m above the ground using active, continuous devices from January to December 2008. With this instrument it was possible to study the relationship between the outdoor radon levels and the local and macroscale weather conditions.
- Another example of the use of active monitors is the continuous radon measurements in open atmosphere, including measurements of air humidity, temperature, pressure and gamma dose rate, performed in 11 different settlements of **Bulgaria** (Kunovska et. al. 2014). Measurements were made in mountains and spas, in the plain, at sea level and in uranium-mining environments in the summer period, in series of 10-min intervals over 24 hours. On the same locations, the gamma dose rate was measured (in μSv/h) 1 m above the ground using a gamma detector. Analysis of results from outdoor radon measurements in various measuring sites showed different daily variations. The relation between outdoor radon concentrations and meteorological factors as well with gamma dose rate was observed. In order to get accurate average values for several regions in Bulgaria, measurements with passive detectors were performed continuously over the year.
- Other active methods are used less frequently. Continuous measurements of outdoor radon concentration were made in two cities of the **Slovak Republic** (Müllerová et. al., 2011), using large-volume scintillation chambers. The outdoor air was sucked from a height of 1.5 m above the ground into the detection system. Subsequently, radon activity concentrations for 2-hour intervals were determined from the recorded count rates using the Ward-Borak method (Ward & Borak, 1991).
- In the **Czech Republic**, an outdoor station for measuring atmospheric radon, gamma equivalent dose rate and proper meteorological parameters such as thermal air gradient, relative air humidity, wind speed and direction and solar radiation intensity was built in the area of the National Radiation Protection Institute (Jílek et. al. 2014). It was designed to be independent of an electrical network and enables on-line wireless transfer of data. Radon gas measurements were performed continuously at a sampling height of 2.5 m above the ground using a high-volume 3 l scintillation cell connected to an evaluation unit.

5.3.3 Applications

Over the last few decades, a number of studies have documented a decrease in outdoor radon concentration with increasing height above the ground and confirmed that this is mostly due to dilution by atmospheric mixing and turbulence (Gogolak & Beck, 1980; Druilhet et. al., 1980; Bakulin et al., 1970; Pearson & Jones, 1965, 1966; Servant, 1966; Moses & Pearson, 1965). These studies found that the outdoor radon concentration can decrease to less than half in the first 10 m, but many other studies have shown decreases of only one-tenth to one-third in the first 10 m (Cohen, 1979; Gesell, 1983; NAS, 1999; UNSCEAR, 2000).

From these studies it was also observed that once radon reaches a height of approximately 1 m above the soil surface, its dispersion is mainly determined by atmospheric stability. This stability is a function of vertical temperature gradient, wind-force and direction, and turbulence. Temperature inversions (a reversal of the normal atmospheric temperature gradient) in the early morning act to produce a stable atmosphere, which keeps radon in the soil or near the ground or water surface. Solar radiation breaks up the inversion, leading to upward dispersion of radon, which reverses with radiant cooling in the late afternoon.

In a study by Chandrashekara et al. (2006), outdoor radon concentrations at 1 m above the ground were confirmed to increase during the night, peak in the very early morning, and decrease during the day.

Doi & Kobayashi (1994) studied the vertical distribution of outdoor radon and thoron in Japan. At night and in the early morning hours, atmospheric (temperature) inversion conditions were often found; these tend to trap radon closer to the ground. Outdoor radon concentrations were estimated to vary diurnally by a factor of as much as 10.

Besides atmospheric mixing phenomena, seasonal variations, in response to changes in atmospheric pressure, temperature, precipitation, or to changes in prevailing winds, also exist (UNSCEAR, 2000).

Gesell (1983), Blanchard (1989), and Harley (1990) reviewed studies of outdoor radon available from around the world and observed consistent diurnal and seasonal trends.

During temperature inversions, radon levels may reach hundreds of Bq/m³ over regions with enhanced concentrations of uranium and radium in the ground, as reported by Robé et al. (1992) and Tyson et al. (1992).

A four-year survey of outdoor radon concentrations in Milan, Italy, performed between 1997 and 2000 by Sesana et. al. (2003), showed that the mean annual outdoor radon concentrations were constant, while concentrations varied between a maximum average in winter and a minimum average in summer. Average monthly values varied from year to year according to the prevailing meteorological and climatic conditions, but on the whole, seasonal patterns were the same for all four years. This study highlighted that although daily patterns also varied according to the prevailing meteorological conditions, hourly concentrations tended to decrease during the day to a minimum in the late afternoon, and increase thereafter to a maximum concentration in the early morning. This pattern was particularly clear when there was a closed anticyclone high pressure area with a weak pressure gradient over the Po Plain.

Outdoor radon concentrations also vary with distance from other sources that can locally or regionally affect ambient radon, such as bodies of water (NAS, 1999).

Several studies have demonstrated that radon concentration in outdoor air is higher over large continents than over the sea (WHO, 2000). Furthermore, in previous studies cited in UNSCEAR (1982), it was observed that a great discontinuity in the transfer of radon to air occurs at the boundary of large land surfaces, e.g., a continent. Owing to the low radon emanation from sea water, it is to be expected that the radon concentration in surface air near the coast should be much lower when the wind blows from the sea than when it blows from the land. This effect is evident during sea breeze conditions during daytime when low radon levels occur, while off-shore wind conditions during the night usually bring higher radon levels. The radon concentration in air over the ocean at large distances from land depends on the prevailing wind direction. A low radon concentration in 'marine' air (some tens of mBq/m³) may rapidly increase by an order of magnitude or more in case of a change to 'continental' air (UNSCEAR, 1982).

The radon concentration over an island depends on the radon exhalation rate from the ground and on the meteorological conditions. If there is no wind, the radon levels are caused only by radon exhalation from the island itself. In windy weather the radon levels may increase inland, in the wind direction, and partly consist of radon from the island itself and from a distant continent (UNSCEAR, 1982).

5.3.4 Challenges to developing a European map

Traditionally, outdoor radon levels have received less attention than indoor radon values. There are many reasons for this. The fact that we spend most of our time indoors may be one. Moreover, radon diffuses into outdoor air very easily, and its outdoor concentration is very low in most cases. There are some exceptions to this fact, such as high background radiation areas, where it is common to find high levels of radon outdoors (e.g. 114 Bq/m³ in Ullensvang commune, Norway; Jensen et al., 2006). However, outdoor radon is a quantity that might be considered when carrying out national or regional studies aimed at determining radon priority areas. When using modelling approaches, the incorrect choice of the outdoor level may lead to an underestimation of the percentage of homes under the reference level which may be significant in some cases (Antignani et al., 2018). Outdoor radon is an additive component and should be removed from the measured indoor radon concentrations when assessing the radon distribution parameters (Gunby et al., 1993). According to literature at the time of this publication, information about outdoor radon levels is available (annual means) from ten European countries: Finland, Germany, Ireland, Montenegro, Norway, Poland, Russia, Slovenia, Spain and the UK. Yet other countries (e.g. Belarus) have regular monitoring programmes for measuring outdoor radon in soil, but not in air.

Table 5-4 shows results of data published from these European countries. Values are consistent with the typical outdoor radon levels in the world, as reported by UNSCEAR (UNSCEAR, 2000). In most cases, solid-state nuclear track detectors (SSNTD) have been used to measure values, but sometimes continuous monitoring is used. This is due to the fact that outdoor radon is used as a tracer in some of the reviewed papers. In addition, detectors can be installed at different heights above ground. Significant differences can be found depending on the height above ground (Kurttio & Kallio, 2014). Another remarkable outcome is the difference between results depending on the period of the year in which the measurements were carried out. Therefore, in Nordic countries (such as Finland and Norway), seasonal variations have been observed (Kurttio & Kallio, 2014; Jensen et al., 2006). Although these variations are very small, it is possible to detect them due to the good sensitivity of the radon detectors used. In the case of a study carried out in Romania (Zoran et al., 2012), the high values were mainly due to seasonal inversion layers and lack of vegetation in the winter period. This effect and the high soil permeability increase radon emanation and exhalation.

It is difficult to map these values since data have been obtained with different techniques and methods. Hence, the following challenges have been identified:

- It is important to develop standardised measurement protocols: detectors, height above ground, cover against precipitation, moist and direct sunlight etc.
- In order to protect detectors against moisture, we may need a harmonised system. Some attempts have been tested in the UK (Miles et al., 2009). The technique was further developed and has been used for monitoring outdoor radon in the UK (Ward et al., 2017).
- The problem with the background of radon detectors must be studied further. Passive detectors have been designed for indoor radon measurements, so if outdoor levels are low, the detectors are close to their detection limit. Pre-etching is recommended to reduce the background levels for those detectors intended for outdoor measurements (Gunning, 2014).

Country	Measurement method	N	Radon concentration (Bq/m³)	Uncertainty/ variability (Bq/m³)
Finland (Kurttio & Kallio, 2014)	SSNTD	58 (L)	9[1]	4[3]
Germany (Kümmel et al., 2014)	SSNTD	172 (P)	8.2[1]	1.9[2]
Ireland (Gunning et al., 2014)	SSNTD	18 (L)	5.6[1]	0.7[3]
Montenegro (Vukotić et al., 2018)	-	Theoretical calculation	7	-
Norway (Jensen et al., 2006)	SSNTD	104 (N)	19 – 114[4]	-
Poland (Podstawczyńska et al., 2010)	Continuous monitor	3 (L)	5 – 10[1]	-
Russia (Zhukovsky, 2016)	Continuous monitor	1 (L)	10.9[1]; 8.9[3] 0.03 – 43[5]	6.4[3]; 1.9[2]
Slovenia (Vaupotič et al., 2010)	SSNTD	60 (N)	11.8[1]	2.2[2]
Spain (Parages et al., 2013)	Continuous monitor	43 (L)	1.2 – 37.7[5]	6.65[3]
UK (Ward et al., 2017)	SSNTD	40 (N)	4 – 11[1]	1 – 3[3]

[1] Arithmetic mean, [2] Standard deviation, [3] Geometric mean, [4] Geometric Standard Deviation, [5] 95% confidence interval. [6] Values correspond with minimum and maximum in all locations. In the case of Russia, the minimum value is below the minimum detectable activity of the instrument. In addition, Spanish monitors are placed at a height varying from 2.5 m to 5 m above ground level depending on the station. The Russian measurements were taken at a height 5 m above ground.

Table 5-4.
Average values of radon concentration in outdoor air in several European countries. All values are given in Bq/m³. Here, N means either the number of measured points (P) or locations (L). SSNTD = solid-state nuclear track detector.

Outdoor radon detector placed 1 m above ground, Palencia province, Spain
Source: IGME (Antonio Quindós Poncela)

Case study: Continuous monitoring of outdoor radon

An example of continuous monitoring of outdoor radon levels, using both active and passive detectors, is that carried out in the Vale of Pickering in Yorkshire, England. In the UK, outdoor radon levels are generally low. Measurements made during a national survey in 1988 (Wrixon et al., 1998) established an average national value of 4 Bq/m³. The Vale of Pickering is an area selected for shale-gas extraction. Whilst most of the Vale does not have high radon potential, there are some areas with naturally elevated radon potential, called Radon Affected Areas (Miles et al., 2007); they are located close to the proposed shale-gas extraction site. In these areas at least 1% of the homes are expected to have radon levels at or above the UK Action Level of 200 Bq/m³. To determine the effect of shale-gas extraction on radon levels, baseline monitoring of radon levels was recommended (Kibble et al., 2014) prior to commencing shale-gas extraction, in order to compare baseline results with results at the same locations after extraction had begun.

Public Health England has been monitoring outdoor radon levels at various locations in the Vale of Pickering since October 2015. A good coverage of the sampling area was achieved to ensure representative monitoring results. Sampling areas were identified which included areas around the extraction site, control site and nearby areas with elevated radon potential. For outdoor radon monitoring, a sufficient number of sampling points was installed to provide good coverage of the monitored area. In this particular example the monitoring involved installing passive radon detectors at several locations: around Kirby Misperton close to the proposed shale-gas site; around Yedingham, an area with the same radon potential, to serve as a control; and around Pickering and Malton close to the extraction site but in areas of elevated radon potential.

The outdoor passive detectors should be able to perform in normal outdoor conditions which are quite different from the indoor environment. There are significant variations in outdoor temperature, sunlight and humidity, all of which can affect detector recording and reading. Wasikiewicz (2018) has shown that higher temperature and direct sunlight could affect the radon detection sensitivity. When humidity is high, water can enter the diffusion chamber of the track-etch detector and condense on the surface of the plastic, which can affect the recording of the alpha particles generated by radon and its progeny. The passive track-etch detectors were placed in sealed polyethylene bags to protect them from humidity and unwanted liquid water ingress. In addition, detectors were placed inside a plastic pot wrapped in an aluminium foil to provide protection from overheating by reflecting direct sunlight (Wasikiewicz et al., 2017). Detectors have been placed in discrete but open-air positions for several consecutive periods of 3 months or longer, to characterise both spatial and temporal variability of radon, in a number of locations in the Vale of Pickering. The detectors were deployed at the breathing height of about 1.5 m above the ground. A sufficient number of detectors per monitoring area was chosen to allow statistical analysis of the data for each area.

The average radon levels measured at all sites were low, with no observable difference between the proposed shale-gas extraction site and the controls. All the results from the first year were slightly higher to those measured in the UK national survey (Wrixon et al., 1998), but still quite close to the detection limit (5 Bq/m³) for the technique for a 3-month sampling period (Daraktchieva et al., 2017).

The results from two years of monitoring for each sampling point in the area around Kirby Misperton are given in Figure 5-15.

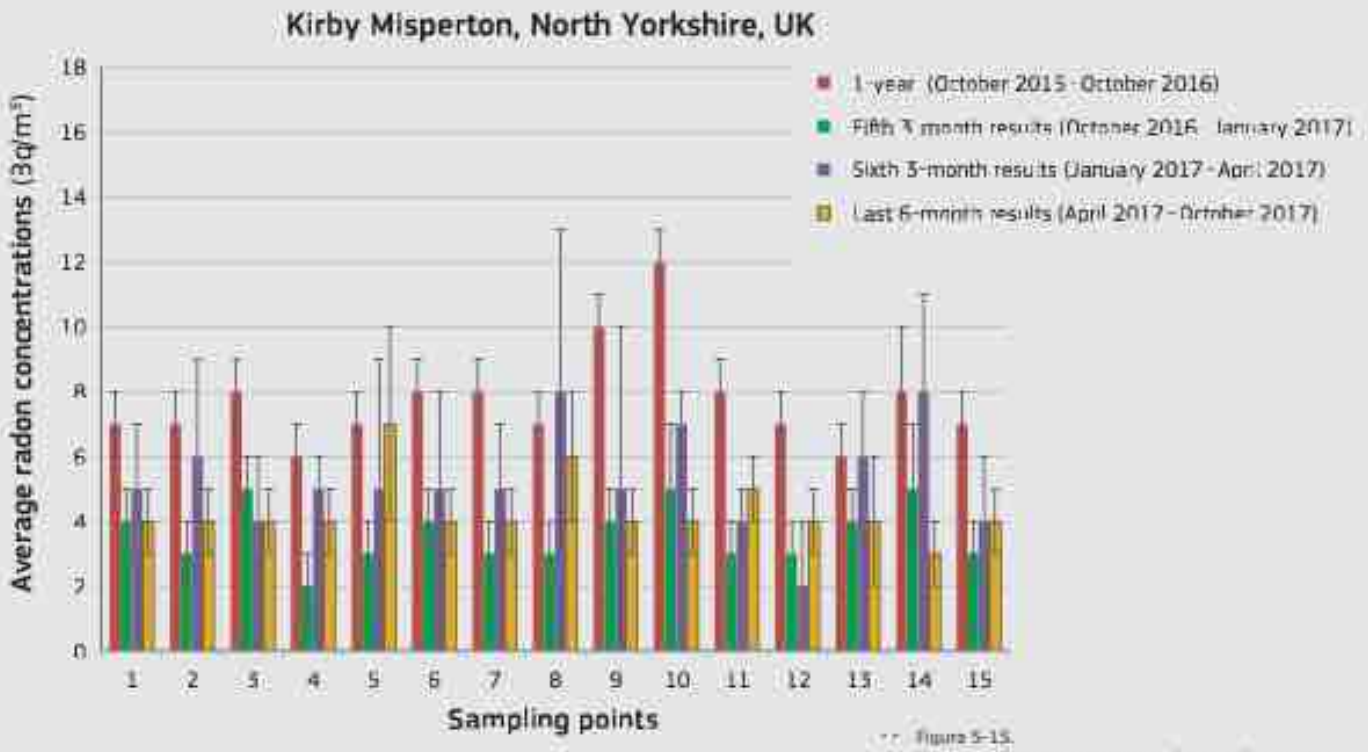

Figure 5-15.
Average radon concentrations at the sampling points around Kirby Misperton, North Yorkshire, UK
Source: Wood et al., 2017

Monitoring period	Active, continuous detector (Bq/m³)				Passive detectors (Bq/m³)	
	Range	Arithmetic Mean (AM)	Geometric Mean (GM)	Geometric Standard Deviation (GSD)	Arithmetic Mean (AM)	Standard Deviation (SD)
April 2016 - July 2016	1-46	5	5	2	4	1
July 2016 - October 2016	1-81	6	4	2.4	8	1
October 2016 - January 2017	1-50	6	4	2.5	7	1
January 2017 - April 2017	1-29	4	3	2.3	5	1
April 2017 - July 2017	1-47	5	3	2.4	-	-
July 2017 - October 2017	1-38	5	3	2.4	7	1

Table 5-3.
Range and distribution of radon measurements made with active and passive detectors in the enclosure on the extraction site
Source: Wood et al., 2017

An active, continuous radon monitor and passive detectors were placed in the enclosure at the extraction site to assess short-term variation and long-term average radon concentration at the site.

The continuous radon monitoring instrument was placed in the enclosure at the extraction site between April 2016 and October 2017, and the data were analysed. When data were processed, the background of the instrument was taken into account. The radon data, taken at 1-hour intervals, were log-normally distributed. Table 5-3 gives the distribution parameters for the above monitoring periods. The average radon concentrations measured over the six monitoring periods were from 4 to 6 Bq/m³. The average radon concentrations measured with 10 passive detectors were similar to the arithmetic means (AM) of the distributions measured with the active, continuous device for these periods, as shown in Table 5-3. This shows a good agreement between measurements with passive detectors and time-resolved active radon monitors.

A graph showing the raw data obtained by the active device, without background correction, is given in Figure 5-16.

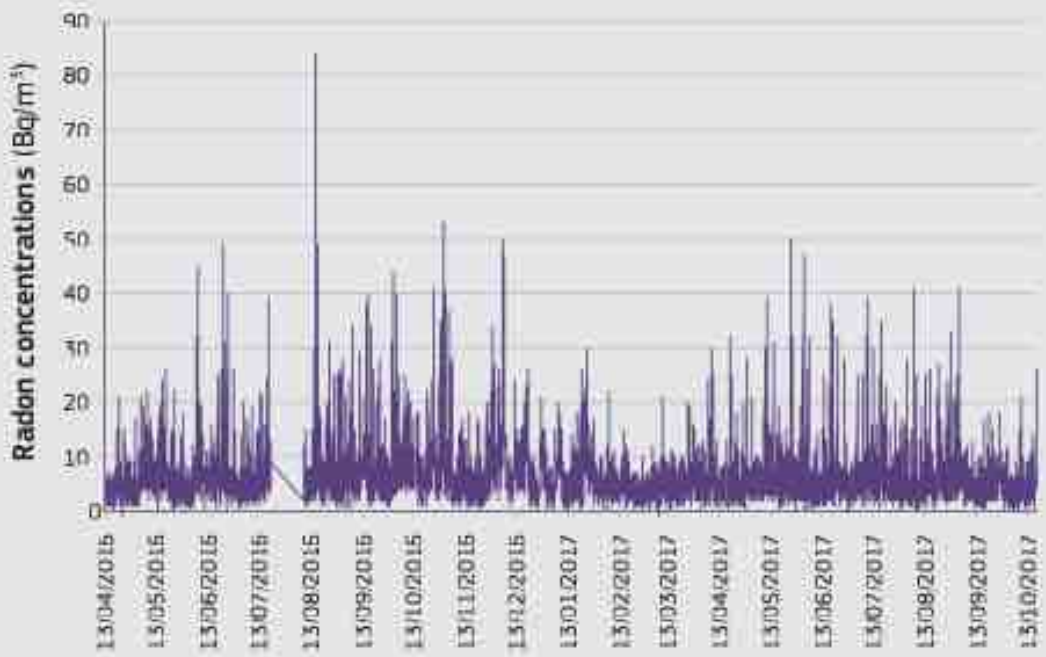

Figure 5-16.
Time series of radon concentrations recorded by the active device between April 2016 and October 2017
Source: Wood et al., 2017

5.4. Indoor radon

5.4.1 Introduction

A reminder

^{222}Rn is called radon (Rn).

^{220}Rn is called thoron (Tn).

Indoor radon is the most important source of radiation exposure to the public and the second-most common cause of lung cancer after smoking (UNSCEAR, 2008; WHO, 2009). Outdoor radon levels are generally low, but indoor radon concentration can increase significantly since radon tends to accumulate in confined spaces such as buildings. The doses from radon gas when inhaled by humans are two orders of magnitude lower than those received from its progeny. Alpha particles emitted from short-lived, solid radon progenies damage the bronchial regions of the lung. Hence the health effect from radon inhalation is the formation of carcinomas primarily in the bronchial airways (ICRP, 2017).

Long-term exposure to radon has been correlated with the probability of lung cancer (Krewski et al., 2005; Darby et al., 2005; WHO, 2009). Epidemiological studies of underground miners provided the first evidence that exposure to high radon concentrations could be associated with an increased risk of lung cancer, both for smokers and non-smokers (UNSCEAR, 2008; WHO, 2009). Furthermore, results from pooled analyses of general population data collected in Europe, North America and China revealed that exposure to indoor radon, even at low concentration, can be associated with lung cancer (Lubin et al., 2004; Darby et al., 2005, 2006; Krewski et al., 2006).

National and regional radon programmes have been initiated in many countries to reduce risk to the population. The key objectives of radon surveys for targeting residential exposure are (ICRU, 2015; WHO, 2009; IAEA, 2013):

- To obtain the distribution of the annual average radon concentration for a country or an area;
- To study seasonal variation and consider seasonal correction factors to determine the annual average radon concentration;
- To identify areas with elevated radon potential, so-called radon priority areas (RPAs).

Clear goals, appropriate design and measurement techniques have been identified as essential components of any radon survey. The main aspects that should be considered when planning radon surveys include the following (Font, 2009):

- To define the objective of the survey;
- To identify the targeted population;
- To choose an appropriate sampling design;
- To allocate resources, budget, staff, data-processing facilities;
- To choose appropriate radon detectors;
- To define the time schedule;
- To choose data-collection methods and questionnaire design.

National surveys are, in general, designed for statistical analysis based on the selected sampling methodology (see Section 2.4). Long-term radon measurements are preferable in order to average out short-term variations (Steck, 2005; Hansen et al., 2014).

Various types of spatial partitioning are used to analyse the data and present maps. Boundaries between spatial units can be administrative, geological or arbitrary (but regular) divisions, such as grid square. Nevertheless, as pointed out by Dubois et al. (2010), there are uncertainties in the indoor radon measurements inside the area boundaries mainly due to the true variability of radon concentration within the spatial unit, the number of observations in the unit and the uncertainties related to seasonal variability of indoor radon concentrations.

Indoor radon mapping

Radon is present in every soil type at low levels; however, certain geographic areas are more prone to high indoor radon concentration than others (McColl et al., 2015). The goal of indoor radon mapping is therefore to delineate radon priority areas. A detailed discussion of radon priority areas is given in Section 5.4.5. The characterisation of indoor radon distributions is to estimate the burden of disease attributable to radon exposure (i.e. lung cancer) on the general population, and to inform government policy in order to reduce the exposure to natural radioactivity (Gray et al., 2009).

The European Basic Safety Standards Directive (European Union, 2013) requires that: '*Member states shall identify areas where the radon concentration (as an annual average) in a significant number of buildings is expected to exceed the relevant national reference level*', and establishes that a national indoor radon reference level should not be higher than 300 Bq/m³ (see Section 1.2).

Protection activities should be prioritised in these areas (i.e. radon priority areas, RPAs); however, since there are no safe indoor radon levels and even low levels may have adverse health effects (Darby et al., 2005), protective measures should continue to be implemented everywhere (Bochicchio et al., 2017) according to the principle of optimisation on which the system of radiation protection is based (European Union, 2013; see Section 2.1).

The main advantage of indoor over geogenic radon maps is that radon is measured at the exposure point (i.e. dwellings, workplaces). However, map accuracy may be hampered by uncertainties in the location of the test sites, and by unsampled areas (Elio et al., 2017c). Furthermore, indoor radon has high spatial and temporal variability, and depends on multiple factors which are not easily quantified (Tollefsen et al., 2014; Gunby et al., 1993; Borgoni et al., 2014). Finally, data interpretation also requires a correct sample design (Burke & Murphy, 2011) and must take into account possible effects caused by preventive and/or remediation activities (e.g. Long et al., 2013; Finne et al., 2018).

Radon maps form the base for any radon strategy aimed to reduce exposure to this carcinogen, and have therefore profound economic and social implications (Gray et al., 2009). For example, radon maps could be helpful to intensify radon concentration measurements in areas where it is more likely to find buildings with high radon levels. Furthermore, they help to define areas where preventive measures should be installed in new buildings (McColl et al., 2015), although some basic preventive measures in all new buildings (instead of buildings in selected areas only) can be more cost-effective (Gray et al., 2009). In addition, they may also be used to build public awareness (Sainz Fernández et al., 2016).

Indoor radon concentration has high variability at small scale, and even two neighbouring houses may have indoor radon concentrations that differ by some orders of magnitude (e.g. McColl et al., 2015; US-EPA, 2001). The only way to know if a dwelling has a problem with radon is therefore to test it, and indoor radon maps should not be used for this purpose. In Ireland, for example, it was estimated that approximately 43% of the population that may live in a house with high indoor radon concentration located in areas classified as 'Non-High Radon Area' (Elio et al., 2017); thus, although radon maps are an essential tool for defining national radon action plans, they are not suitable for evaluating the risk of radon in a specific house or workplace.

Indoor radon measurements form the base for creating indoor radon maps (e.g. Fennell et al., 2002; Ferreira et al., 2016). Then geological information and other factors may be used to improve the map accuracy (e.g. Miles & Appleton, 2005; Ferreira et al., 2016; Pásztor et al., 2016; Bossew, 2014, 2015; Elio et al., 2017) since geology is the main factor controlling indoor radon (Watson et al., 2017; Appleton & Miles 2010). Indoor maps may represent the probability of having an indoor radon concentration higher than a national reference level (RL) (e.g. Fennell et al., 2002; Miles et al., 2007), or an average indoor radon concentration over large areas (e.g. Friedmann, 2005; Dubois, 2005). Recent studies, however, have also included the potentially adverse health effects of radon exposure (i.e. by estimating the number of lung cancers attributable to radon in a given area) and population density for defining radon priority areas (Elio et al., 2018).

The criteria selected to delineate RPAs therefore depend on national radiological protection strategies and the data available, and even multiple criteria may be applied in parallel to optimise a radon action plan (Elio et al., 2018). However, different strategies may lead to contradictory information, and it is common that RPAs do not match across borders. In this respect, for example, Ireland defines RPAs as areas where the probability of having an indoor radon concentration higher that the reference level of 200 Bq/m³ is 10% or higher (Fennell et al., 2002), whereas the threshold in Northern Ireland is 1% despite having the same reference level (Daraktchieva et al., 2015). Map resolution may also vary between countries, i.e. grids of 10 km × 10 km in Ireland and 1 km × 1 km in Northern Ireland. Table 5-5 presents a summary of different methods to map radon.

In France, Ielsch et al. (2010) developed a methodology to derive a map of the geogenic radon potential by determining the capacity of geological units to produce radon based on their uranium content. This initial map was then improved by taking into consideration major fault lines and underground mines, which control the preferential pathways of radon through the ground. Kropat et al. (2015) used Kernel regression to map indoor radon concentration in Switzerland. The maps were produced taking into account building styles and geology.

Estimating the number of dwellings above the reference level

Different techniques have been developed to estimate the number of dwellings exceeding action or reference levels. A log-normal model of indoor radon concentration can be used to estimate the proportion of the probability distribution above the reference or action level. The procedure explained by Miles (1998) involves subtracting the outdoor radon concentration from the measured indoor values and taking the natural logarithm, i.e. $\ln(R_i - R_o)$, where R_i and R_o are indoor and outdoor radon concentrations, respectively. The outdoor radon value to be subtracted can be estimated carrying out an analysis of quantile-quantile plot of the data, e.g. Gunby et al. (1993) and Daraktchieva et al. (2014).

Moreover, Antignani et al. (2019) studied the impact of outdoor radon concentration on estimated percentages above some reference levels.

The arithmetic mean and standard deviation of those values may then be calculated. Under the assumption of a normal distribution of $\ln(R_i - R_o)$ with mean μ and standard deviation σ, the proportion of dwellings above the reference level, N_{RL}, can be calculated using the standard cumulative distribution function Φ, as follows:

$$N_{RL} = 1 - \Phi\left(\frac{\ln(R_{RL} - R_o) - \mu}{\sigma}\right) = 1 - \int_{-\infty}^{\ln(R_{RL} - R_o)} \frac{1}{x\sqrt{2\pi\sigma^2}} e^{-\frac{(\ln x - \mu)^2}{2\sigma^2}} \quad (5.1)$$

More sophisticated techniques have been developed to reduce the influence of extreme values on the sample mean and sample standard deviation. Miles (1994) applied a sorting technique to calculate the geometric mean (GM) and geometric standard deviation (GSD). Miles and Appleton (2005) showed that Bayesian estimates of the GSD could be used to improve estimates in areas where data are scarce.

5.4.2 Materials and methods for indoor radon measurements

WHO (2009), IAEA (2013) and Bartzis et al. (2018) provide guidance on requirements for radon measurements in homes. The measurements should permit assessment of mean annual radon concentration; the measurement protocols should be standardised to ensure consistency of results; the detector type should be chosen carefully; and quality assurance and controls should be pursued in order to ensure reliability of the measurements.

It is well known that radon progeny is responsible for most of the radiation dose. Devices that measure radon progeny are excluded from this discussion because they are quite complicated to use and are not practical for estimating radon levels in dwellings. Notably, dose from radon progeny strongly depends on the aerosol size distribution, and, for the typical range of aerosol distributions that can be found in a dwelling, dose can be considered proportional to radon concentration. (e.g. Hopke et al., 1995). Only measurements of radon gas are considered in this section.

Radon measurements in dwellings are discussed in terms of the duration of the tests and the type of instrument used. The duration could range from a few days to several months, while the instrument could be passive or active. When an air sample is taken by pumping air into the measuring volume, the device is called active; whereas when air enters the measuring chamber by diffusion, the instrument is called passive. Section 2.5 describes the different devices in more detail.

Country (region)	Reference Level* (Bq/m³)	Objectives	Methods	Resolution	Reference
Austria	200 and 400	Divide the country into three classes: i.e. average annual concentration <200, 200 - 400, and >400 Bq/m³	Annual mean radon concentration in a standard situation	Administrative level (i.e. municipality)	Friedmann (2005)
			Bayesian statistics, combining indoor radon measurements (standard situation) and geology	Geological classes (scale 1:500 000)	Friedmann & Groller (2010)
Azerbaijan	200	Display the indoor radon concentration values	Arithmetic mean of indoor radon gas concentration values	10 km × 10 km and district	Hoffmann et al. (2017)
Belgium (Walloon region)	400	Percentage of dwellings above the RL taking into account geological information	Moving average between geological units	1 km × 1 km	Cinelli et al. (2011)
Hungary	200	Percentage of standard houses (i.e. one-storied, no basement houses) above the RL. Also reports the arithmetic mean and the maximum value	Lognormal model	Various: Administrative level (i.e. counties), and grids 10 km × 10 km	Minda et al. (2009)
Ireland	200	Percentage of houses above the RL based solely on indoor radon measurements RPA when P[InRn > RL] ≥ 10 %	Lognormal model	Grids 10 km × 10 km	Fennell et al. (2002)
	200	Percentage of houses above the RL based on indoor radon and geological information (i.e. bedrock geology, Quaternary geology, subsoil permeability, and soil permeability) RPA when P[InRn > RL] ≥ 10 %	Logistic regression model	Grids 1 km x 1 km	Elio et al. (2017)
	-	Estimation of radon-related lung cancer cases	Dose estimation based on average concentrations (i.e. block averages after ordinary kriging)	Administrative level (i.e. electoral division)	Elio et al. (2018)
Italy (Abruzzi region)	100, 200 and 300	Risk that a standard house exceeds the RL. Divide the country into seven categories	Bayesian spatial quantile regression, and Bayesian model for spatial cluster detection	Administrative level	Sarra et al. (2016)
Italy (Lombardy region)	200 and 400	Percentage of houses above the RLs. RPA when the RL (200 or 400 Bq/m³) is below the lower confidence limit at 95 % of the quantile 0.9 (P[InRn > RL] ≥ 10 %)	Geostatistical simulation (i.e. multi-Gaussian sequential simulation)	Administrative level (i.e. electoral division)	Borgoni et al. (2010)
Malta	100	Display the indoor radon concentration values	Average of geometric mean annual indoor radon gas concentration values for each sampling point	Grids 5 km × 5 km	Baluci et al. (2013)
North Macedonia	100 and 200	Display the probabilities of having an indoor radon concentration higher than 100 and 200 Bq/m³, and the expectation	Estimations are derived from ^{226}Ra concentration in soil	Grids 5 km × 5 km	Bossew et al. (2013)
Norway	200	Percentage of houses above the RL based on indoor radon and geological information (bedrock and Quaternary geology) RPA when P[InRn > RL] ≥ 20 %	Classify geological polygons according to local (polygon) statistics or national (class) statistics	Geological polygons	Watson et al. (2017)
Spain	300	Identify 3 radon classes	Model that uses as input data: national indoor radon databases; natural γ-radiation map (MARNA); geological maps	Geological unit	Garcia-Talavera et al. (2013)
Switzerland	100 and 300	Percentage of homes having an indoor radon concentration <100, 100 - 300, and >300 Bq/m³	Ordered logistic regression model	Grids 10 km × 10 km	Kropat et al. (2017)
United Kingdom	200	Percentage of houses above the RL taking into account geological information RPA when P[InRn > RL] ≥ 1 %	Lognormal model, corrections to account for year-to-year and random variations (i.e. Bayesian statistics)	Grids 1 km × 1 km	Miles et al. (2007); Miles et al. (2011); Daraktchieva et al. (2015)

* Reference Level (RL) reported in the cited papers, not referring to the RL in the Basic Safety Standards Directive (European Union, 2013)

Table 5-5.
Examples of different methodologies for mapping radon

Details on the most commonly used passive devices

Track-etch detectors are passive instruments that use plastic as detector material. The plastic can be a polyallyl-diglycol carbonate (PADC), cellulose nitrate (LR-115), or polycarbonate (Makrofol). The alpha particles generated by radon or radon decay products damage the surface of the plastic material and produce latent tracks. These tracks are made visible by chemical or electrochemical etching which enlarges the size of the alpha tracks, making them observable by light microscopy so that they can be counted by an automated counting device. The number of tracks per unit surface area, after subtracting background counts, is directly proportional to the radon exposure in kBq h/m³. A conversion factor obtained by controlled exposure at a calibration facility allows conversion from track density to radon concentration (Nikezic & Yu, 2004). The placement and collection protocols should be followed very carefully to obtain the best results.

There are two types of track-etch detectors: open (the plastic material is exposed to the ambient atmosphere) and closed (the material is enclosed in a container). Open track-etch detectors record alpha particles originating from radon decay products and from all radon isotopes. For these detectors the equilibrium factor F should be taken into account to estimate the number of alpha particles from radon decay only. Closed track-etch detectors allow only radon to diffuse into the closed diffusion chamber and therefore exclude the entry of ambient radon decay products. Passive track-etch detectors are not sensitive to background beta and gamma radiation.

Activated charcoal detectors are passive detectors that are used for short-term measurements of indoor radon. An airtight container with activated charcoal should be opened and placed in the measured place for 1 to 7 days. The containers could be open-faced or equipped with a diffusion barrier to extend the sampling period up to 7 days. At the end of the sampling period, the container should be sealed so that the radon decay products equilibrate with the radon collected. Detectors should be returned for analysis as soon as possible after the exposure period because of the short half-life of radon of 3.8 days. Since the response of activated charcoal detectors is affected by humidity, detectors should be calibrated to various levels of humidity. Because charcoal allows continuous adsorption and desorption of radon, the method only provides a good estimate of the average radon concentration during the exposure time if changes in radon concentration are small. The use of a diffusion barrier reduces the effects of draughts and high humidity.

Electrets are passive detectors that use an electrostatically charged disk to measure radon concentrations. The electret is situated within a small ionisation chamber. Radon diffuses through a filter into the chamber, and the charged alpha particles emitted by radon and its decay products ionise the air within the chamber volume. The negative ions are collected by the positive electret located at the bottom of the chamber. Radon concentration is proportional to the voltage drop in the electret. There are short-term and long-term electret detectors. Short-term detectors could be placed for 2 to 7 days sampling, while long-term detectors could be used for up to 12 months. The background gamma radiation during exposure could affect measurements, so results should be corrected for it (RadElec E-Perm, 2008).

A survey conducted by WHO (2007) revealed that the most popular passive radon measuring devices are track-etch detectors, activated charcoal detectors and electrets. In Europe, track-etch detectors certainly dominate.

Long-term sampling (from several months to a year) of the average radon concentration is generally performed using passive radon detectors. Although short-term sampling, lasting a few days only, could be used, it is not recommended for assessing the mean annual radon concentration. Indoor radon concentration exhibits diurnal, monthly and seasonal variations (Miles & Algar, 1998; Miles, 2001; Wrixon et al., 1998) as well as significant short-term fluctuations. To account for these variations, long-term sampling over several months is required. Radon variability is higher over shorter exposure periods (ICRU Report 88; ICRU, 2015).

In dwellings, **radon detectors** should be placed according to standard protocols for deployment and collection of detectors (IAEA, 2013; Bartzis, 2018; Daraktchieva et al., 2018). Some countries use trained personnel to place detectors, while others send detectors by post with detailed instructions on how and where to place the detectors. For example, Public Health England provides guidance to houseowners on indoor radon monitoring; see http://www.ukradon.org/information/measuringradon. The measurement protocol schedule should be appropriate for the purpose of estimating the mean annual radon concentration.

The radon concentration measured in a given place of a particular dwelling varies with time. Climate influences the amount of gas emanating from the Earth, both through air pressure and outdoor temperature. Ideally, radon should be measured in all the inhabited rooms of a dwelling in order to estimate the mean annual radon concentration that represents radon exposure of the occupants in the dwelling. This is impractical, however, so measurements are usually made in two rooms with the highest occupancy rates, typically a bedroom and a living room. Some countries measure radon in only one room situated on the ground floor. In such cases, radon concentration is probably overestimated if the dwelling has more than one floor (see Section 5.4.5). It has been shown that temperature, direct sunlight and humidity could affect detector sensitivity (Hardcastle & Miles, 1996; Moreno et al., 2013; Venoso et al., 2016; Wasikiewicz, 2018). Higher temperatures could affect radon detection sensitivity, resulting in over-readings of the integrated radon exposure. Moreover, exposing the diffusion chamber to direct sunlight would also have an adverse effect on radon measurements. In a wet environment, water can enter the diffusion chamber of the track-etch detector and condense on the surface of the PADC element, which results in an underestimation of the exposure. Therefore, detectors should be placed in areas that are far away from heat sources, direct sunlight and high humidity. For example it is recommended that detectors should be placed at least 10 cm from the wall in the normal breathing zone and away from small children and pets. The detectors should be used in normal living and ventilation conditions, and performing sampling in sealed or inhabited rooms should be avoided.

Uncertainties associated with radon exposure assessment

Indoor radon measurements with passive track-etch detectors, which are the most popular choice, are associated with uncertainties that need to be investigated and quantified. Two types of uncertainties are associated with radon exposure assessment: they are called classical and Berkson-type errors (Heid et al., 2004). The classical-type errors are statistically independent of the true variable, while the Berkson-type errors (Berkson, 1950) are statistically independent of the observed variable. The classical errors arise when values, obtained by repeated measurements, vary around the true value. The Berkson errors arise when the group average value is used instead of individual values and the true value varies randomly around the measured value. The classical-type errors can be quantified, analysed and minimised by appropriate measures, while the Berkson-type errors cannot easily be quantified but can be identified and modelled.

The typical laboratory uncertainties belong to the **classical errors** because they can be measured and quantified. These are (Miles et al., 1997; Ibrahimi et al., 2009):

- **Uncertainties in the radon calibration reference value**

In general, radon detectors are calibrated against a standard radon source or more frequently against a transferred standard. The transferred standard is a reference instrument which is calibrated against a standard radon source. The estimated uncertainty of the reference instruments can vary for different laboratories with a typical value between 6% and 10%.

- **Variations in track-etch materials**

Track-etch materials are commercially available with quality of the material varying from supplier to supplier and from manufacturing batch to manufacturing batch. Hanley et al. (2008) calculated that the typical between-sheet variability yielded 2.1% uncertainty. The processing laboratory should therefore implement rigorous quality-assurance control in order to identify the variation in the material and introduce correction measures.

- **Uncertainties due to variation in the etching process**

Variations in etching conditions can alter track sizes. Therefore, etching parameters, such as temperature, etching time and chemical composition and concentration of etchant, should be monitored and kept the same (Miles, 1992, 2004). The uncertainties associated with the etching process can be measured using a control sample of detectors.

- **Uncertainties of the automatic track counting system**

Inconsistent focusing and reading of the track-etch detectors can lead to misinterpretation of the track-etch characteristics. The focus of the counting system may drift, the track recognition may change and the scratches or the surface defects may deteriorate the signal-to-background ratio, thus increasing the measurement uncertainty. The combined uncertainty of the automatic track counting system is estimated to be 5.5% (Hanley et al., 2008).

- **Uncertainties in the linearity of response**

The detectors are exposed to a wide range of radon concentrations, varying from 20 (or even lower) to several thousands of Bq/m³. When exposure is high, more alpha particles damage the material. Therefore, the probability of a new track to lay down on top of a previous track is higher. When the tracks start to overlap, the calibration curve, which is the number of tracks as a function of radon concentrations, becomes non-linear, and a correction factor should be considered. The required degree of linearity correction depends on the size of the etched tracks.

- **Uncertainties due to chemical change of the track-etch material: ageing and fading**

Track-etch materials are subject to many changes and variations with time. Hardcastle and Miles (1996) showed that the polymer sensitivity of CR-39 to alpha radiation damage decreases over time due to ageing (i.e. the increases in cross-linking of the polymer) and fading (the partial repair of damaged trails over time). Reduction in radon sensitivity from both ageing and fading is responsible for underestimation of radon activity concentrations. As detectors are placed for a minimum of three months during a sampling, they are subject to both ageing and fading effects. The estimated uncertainties due to aging and fading given by Hanley et al. (2008) are 4.5% and 4.4%, respectively. However, the ageing and fading effect depends on the technique, including the readout system (both hardware and software) and that in some cases ageing and fading do not affect the detector sensitivity (Calamosca & Penzo, 2008).

The laboratory uncertainties can be estimated by identifying and measuring all known errors contributing to the total error δA and calculate the total uncertainty using the square root of the sum of squared errors. The quantities $a_1, a_2, a_3, \ldots a_n$ are assumed to have uncorrelated and random errors $\delta a_1, \delta a_2, \delta a_3, \ldots \delta a_n$, respectively. In this case, the uncertainties add in quadrature:

$$\delta A = \sqrt{\delta a_1^2 + \delta a_2^2 + \delta a_3^2 + \ldots + \delta a_n^2} \qquad (5.11)$$

Typical **Berkson-type errors** related to the radon exposure of the inhabitants and not to the radon measurements are:

- **Uncertainties in the results due to people's behaviour in the monitoring premises**

Radon monitors are placed in peoples' homes for several months. The measuring laboratory provides instructions for placing detectors. The exposure period is calculated from the information provided by the houseowner. The annual radon concentration is calculated according to the typical behaviour of people living in the house during the period of measurement. However, people may alter their behaviour during the monitoring period, for example by increasing or decreasing a ventilation rate of the house, compared to their usual behaviour. Such a change in ventilation rate (or non-occupation of the house during the measurement period) may undermine the results from the detectors, and therefore make them unrepresentative.

Further uncertainties can be attributed to variations of conditions during the exposure period. For example, a building may only be occupied for a part of the day or a part of the week, but detectors record constantly the radon concentration in the building.

- **Uncertainties due to spatial variation between radon activity concentrations of rooms in the dwelling.**

Variation in radon concentration in different rooms of the same house increases the overall uncertainty of the estimated radon exposure. This is the case especially when only one room has been measured. However the average radon concentration over two rooms is also affected by this source of uncertainty. Radon monitors are usually placed in the two most occupied rooms. The uncertainties arise from the fact that radon concentration in unsampled rooms may differ from that in the monitored rooms, which are used as a substitute for the concentration in the other rooms.

The radon concentration differences are higher between different floors as compared with detectors on the same floor. A coefficient of 30% has been used as the best estimate of the error in exposure estimates due to variations of radon activity concentration between rooms (Heid et al., 2004). Much lower variation (about 10% on average) was found in another study (Fisher et al., 1998), especially between rooms located on the same floor.

5.4.3 The European Indoor Radon Map

In 2005 the JRC published an overview of radon surveys conducted by that time in some 30 European countries (Dubois, 2005). It showed that no two countries had used the same approach, in terms of survey design, measurement techniques and mapping strategies. With such differences in the choice of mapped quantity and in type of visualisation, the resulting maps were heterogeneous and incompatible across borders, so that collating them on a European scale resulted in no more than a colourful patchwork.

The Euratom Treaty, mainly its Article 39 (European Union, 2016), gives the JRC the mandate to collect, present, evaluate and interpret radiological data from the EU Member States. With this in mind, in 2006 the JRC decided to create a European map of indoor radon concentration. As the above survey (Dubois, 2005) showed, indoor radon measurements were already available from most European countries; however, collecting this information from different authorities and integrating it into a common framework implied a number of conceptual and technical challenges. The decisive discussions on how to develop a European Indoor Radon Map, including determining a technical procedure, took place at the international radon workshop in Prague in 2006. As a result, both EU and non-Member States participate to the mapping effort. This map was chosen as the first step towards creating a European Atlas of Natural Radiation (Dubois et al., 2010; De Cort et al., 2011).

Methodology

The European Indoor Radon Map (EIRM) intends to show 'means over 10 km × 10 km grid cells of long-term (ideally, annual means of) indoor radon concentration in ground-floor rooms of dwellings.' The participating countries, involving national competent authorities, laboratories, universities etc., aggregate their raw data into 10 km × 10 km cells over a grid covering Europe. Finally the national competent authorities provide this input data (grid values) to the JRC. For historical reasons, this grid uses the GISCO-LAEA coordinate reference system (spherical Earth, zero-point at 9° E/48° N). Exceptions have been made for Ireland and Malta since they had already used their own 10 km × 10 km grids based on their national coordinate reference systems before participating to the European map.

The size of the grid cells has been chosen as a compromise between contradicting targets: On one hand, a small cell size implies many empty cells and poor cell statistics, since also the spatial resolution of observation is naturally limited (also, in cases of sparsely populated regions, high resolution may reveal information on individual dwellings, which conflicts with the requirement of data protection). On the other hand, small cells would have allowed revealing more local structure of the true radon field, which is lost as cell size increases.

Specifically, the national data providers fill the cells with the following statistics calculated from their original data:

- Arithmetic mean (AM);
- Standard deviation (SD);
- AM and SD of the ln-transformed data;
- Median (MED);
- Minimum (Min) and maximum (Max);
- Number of original measurements per cell (N).

This procedure was agreed upon to ensure data protection, because the original data and their exact locations are not given away, but remain at the national level, thus guaranteeing data privacy to houseowners. The methods and procedures to collect and process the raw data have been further described by Dubois et al. (2010) and Tollefsen et al. (2011).

The choice of variable to be mapped can be seen as a compromise between an indoor radon map, which would be a proxy of an exposure map, and a geogenic 'radon potential' map. Since most people in fact do not live in ground-floor rooms and are not exposed continuously (i.e. 24 hours a day, 365 days a year), the mapped variable does not reflect the radon environment to which people are actually exposed. Rather, it shows a standardised indoor concentration, namely restricted to the conditions 'ground floor' and 'annual mean'. On the other hand, the variable still includes anthropogenic factors which influence radon levels, namely building styles and living habits; hence it is not a measure of radon potential, which is defined to include only natural (geogenic), but no anthropogenic, radon controls.

Restricting the data to annual mean radon concentration in ground-floor rooms of dwellings means that data providers have to estimate this quantity, ideally from long-term measurements. Whenever measurements have been made over shorter time periods, some intermediate modelling involving seasonal corrections may be necessary to estimate annual means. As seasonal variations depend on a number of factors including climate, building styles, occupation and ventilation habits etc., no general model exists for Europe, so estimating this quantity has been entrusted to the national data providers.

As a consequence, the statistics over the chosen quantity do not represent the ones of exposure. For that purpose, detailed information about the population distribution at floor level for each country is necessary. Unfortunately, since such data are not available for all European countries, no radon exposure map could be developed for this Atlas.

Since 2010, the JRC has sent a quality-assurance questionnaire to national data providers, asking them inter alia for information about their survey designs, measurement methods, detectors used and data processing techniques applied. In most of the 20 countries that have responded to this questionnaire, the datasets represent a combination of several studies and surveys, often carried out with different purposes and therefore with different survey designs (Gruber et al., 2013). In addition to radon data collected in dwellings, some participating countries have also provided data for other building types (e.g. workplaces, schools, kindergartens) and in some cases with sampling period less than a full year.

Results and discussion

As of September 2018, 35 European countries participate to the EIRM, including all the current 28 EU Member States but one. More than 28 000 grid cells have been filled with statistical data, which are in turn based on more than 1 100 000 individual measurements in total; see Table 5.5 for descriptive statistics of the dataset which underlies the map.

As can be seen from the map (Plate 6), the **number of measurements per cell** and proportional coverage of national territory vary widely between participating countries and between regions of individual countries. The number of measurements per cell ranges from a single one up to a maximum of nearly 24 000 (for a cell in the UK). Still, there are many empty cells. The map may thus be considered to reflect the status of national surveys of indoor radon monitoring in Europe, at least up to the data prepared and released by national authorities to the JRC.

Large areas with high sampling density are found in e.g. South Finland, the Czech Republic, Austria, Switzerland, North Italy, Belgium, Luxembourg, the UK and Northern Ireland. The median number of measurements per cell equals 4, with a median absolute deviation of 4.4 (see Table 5.6). This heterogeneity of sampling density clearly influences the statistical uncertainty of the means as estimates of the expected concentration within a cell, as it does for the standard deviation and other statistics.

The wide ranges in sampling density depend on the design of the survey from which the data originate.

Some countries have mainly aimed for a homogeneous coverage of their territory, while others (e.g. Austria) have aimed for a population-weighted estimate of the radon concentration, which results in a sampling density essentially proportional to the population density. Five countries (namely Germany, the Czech Republic, Switzerland, Spain and Finland) have carried out more detailed surveys in high-radon areas. Finally, some datasets (from Greece and Poland) are mainly based on surveys in high-radon areas. As biased sampling influences the statistics, the data are not necessarily representative for the whole countries. For further discussion about representativeness and selected topics of quality assurance, see Section 2.4.7 as well as Bossew et al. (2012).

As seen from the maps, many areas of Europe are still not covered. Although a few uninhabited areas will always remain, other reasons include the following: missing data, because radon surveys are still ongoing; older surveys were conducted without recording precise geographical coordinates of the sampled dwellings; or national surveys have concentrated on high-radon areas.

The next map (Plate 7) shows the geographical distribution of **arithmetic means over the grid cells**. This map reveals a spatial trend in indoor radon concentration across Europe and essentially reflects the underlying geology. Regions of high radon concentrations are found in the granitic zones of the Bohemian Massif, the Fennoscandian Shield, the Iberian granite province, the Massif Central, Corsica, Cornwall, and the Vosges Mountains; in the crystalline rocks of the Central Alps and karst rocks of the Swiss Jura and the Dinarides; in the black shales of North Estonia; in certain volcanic structures in Central Italy; and in the lower Devonian of Ardennes, where the high radon risk may be caused by the concentration of uranium in weathering products, a result of rock history, not directly connected to its global uranium content. Apart from geology, also climatic and anthropogenic factors contribute, but their spatial structure is not evident and remains to be investigated.

The arithmetic mean of all non-empty cells in Europe (for participating countries) is 103 Bq/m³, while the median is 60 Bq/m³ (see Table 5-6). Note, however, that this spatial mean (mean over cells) is different from the mean over individual measurements (AM = 148 Bq/m³, calculated as the cell arithmetic mean weighted by the number of measurements), from the mean over country-means (AM = 97 Bq/m³) and again, in general, from the population-density-weighted mean (no value available so far).

According to the WHO Handbook on Indoor Radon (WHO, 2009), a national reference level of 100 Bq/m³ is recommended to limit the risk of individuals. Wherever this is not possible, the chosen level should not exceed 300 Bq/m³. In the recently modernised and consolidated Basic Safety Standards Directive (European Union, 2013), a reference level for workplaces and dwellings of at most 300 Bq/m³ is required (see Section 1.2).

For all the countries participating to the EIRM, 34 % of the non-empty cells have an arithmetic mean above 100 Bq/m³ and 4 % of them above 300 Bq/m³ (see Table 5-6). Similarly, exceedance probabilities have been calculated for each participating country (see Tollefsen et al., 2014, and Cinelli et al., 2018, supplementary material). In the Czech Republic, more than 90 % of the AMs of all non-empty cells exceed 100 Bq/m³. At the other end of the scale, none of the cells in the Netherlands have an AM above this level. Again, these figures can be explained by the underlying geology. However, for countries which had reported data (by September 2018) mainly from high-radon areas (e.g. Greece and Poland), such statistics should be interpreted as only regionally indicative, at least until data with national coverage become available. In any case, this variability demonstrates how differently the countries are affected by the radon problem.

Descriptive statistics for the European Indoor Radon Map		
Number of non-empty cells		28 468
Total number of measurements		1 158 888
Number of measurements per cell	MED ± MAD	4 ± 4.4
Minimum and maximum number of measurements per cell	Min/Max	1/23 993
Considering the arithmetic mean of each cell	AM ± CV %	103 Bq/m³ ± 138 %
Considering the median of each cell	MED ± MAD	60.0 ± 45.5 Bq/m³
Percentage of cells with AM > 300 Bq/m³		4.24%
Percentage of cells with AM > 100 Bq/m³		34.1%
Considering the CV (%) of each cell	MED ± MAD	(65.5 ± 34.9) %
Considering the GSD of each cell	MED ± MAD	1.87 ± 0.68

MED, median; MAD, median absolute deviation; MAD(x) = MED (|x − MED(x)|)
AM, arithmetic mean; CV, coefficient of variation, where CV = SD/AM
GSD, geometrical standard deviation (See also Section 2.4 for definition.)

Table 5-6.
Descriptive statistics for the dataset on which the EIRM is based, as of September 2018
Source: EIRM, JC-JRC, 2019

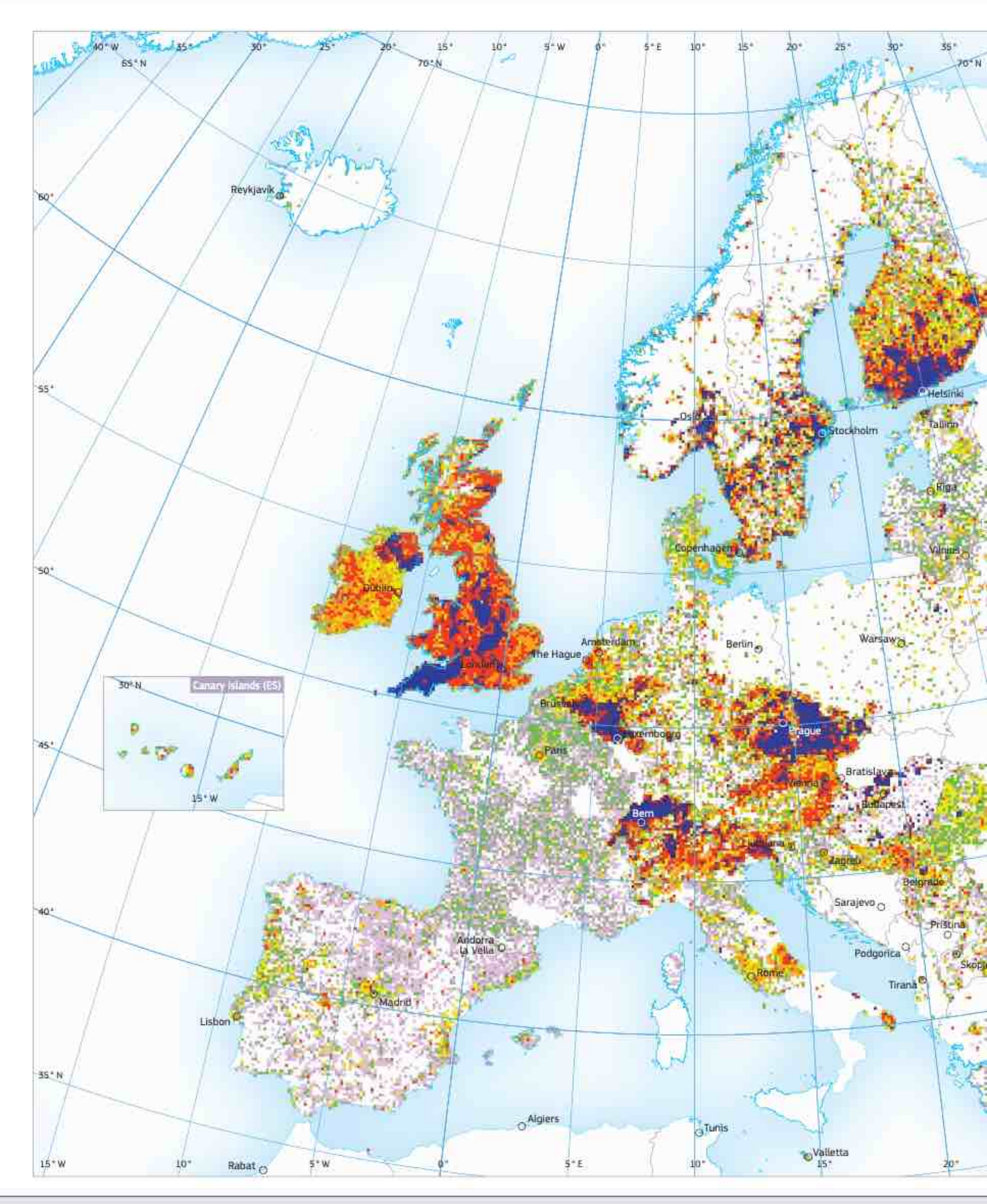
40° W
35°
30°
25°
20°
15°
10°
5° W
0°
5° E
10°
15°
20°
25°
30°
35°
65° N
70° N
70° N
60°
55°
50°
45°
40°
35° N
Reykjavik
Helsinki
Oslo
Stockholm
Tallinn
Riga
Copenhagen
Vilnius
Dublin
Amsterdam
The Hague
Berlin
Warsaw
London
Brussels
Luxembourg
Prague
Paris
Bratislava
Vienna
Budapest
Bern
Ljubljana
Zagreb
Belgrade
Sarajevo
Priština
Podgorica
Skopje
Rome
Tirana
Andorra la Vella
Madrid
Lisbon
Algiers
Tunis
Valletta
Rabat
Canary Islands (ES)
30° N
15° W

copyright © European Commission, JRC, 2019

Plate 6:
European Indoor Radon Map:
Number of measurements per grid cell

- 100 - 24000
- 50 - <100
- 20 - <50
- 10 - <20
- 5 - <10
- 3 - <5
- 2 - <3
- 1 - <2

Plate 6: European Indoor Radon Map:
Number of measurements per grid cell.
The map shows the number of measurements per 10 km × 10 km grid cell of annual indoor radon concentration in ground-floor rooms. (Data received until September 2018 included.)
Source: EANR, EC-JRC, 2019

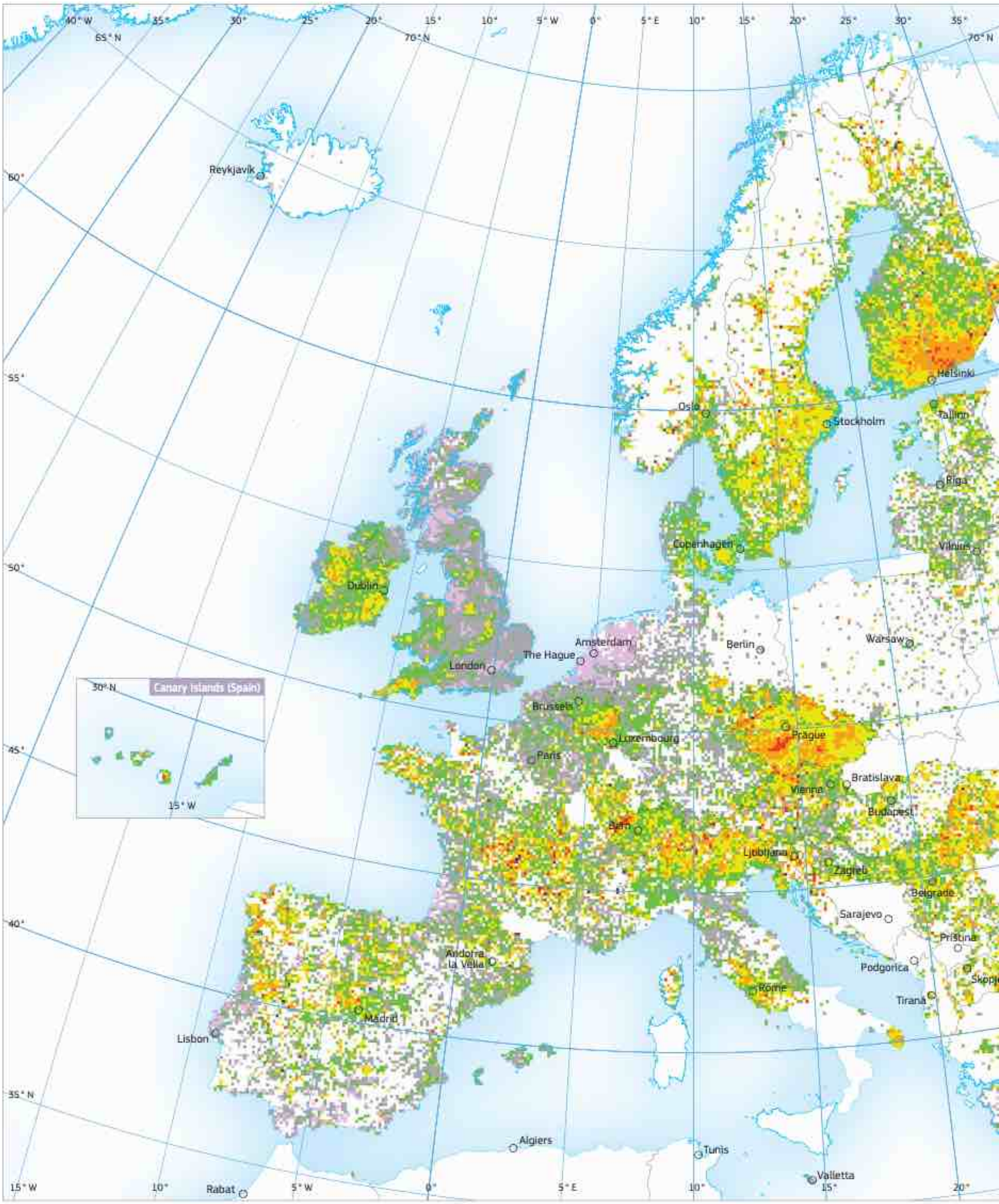
40° W
35°
30°
25°
20°
15°
10°
5° W
0°
5° E
10°
15°
20°
25°
30°
35°
65° N
70° N
70° N
60°
55°
50°
45°
40°
35° N
Reykjavik
Oslo
Stockholm
Helsinki
Tallinn
Riga
Vilnius
Copenhagen
Dublin
Amsterdam
The Hague
London
Berlin
Warsaw
Brussels
Luxembourg
Paris
Prague
Bratislava
Vienna
Budapest
Bern
Ljubljana
Zagreb
Belgrade
Sarajevo
Priština
Podgorica
Skopje
Tirana
Rome
Andorra la Vella
Madrid
Lisbon
Algiers
Tunis
Valletta
Rabat
Canary Islands (Spain)
30° N
15° W

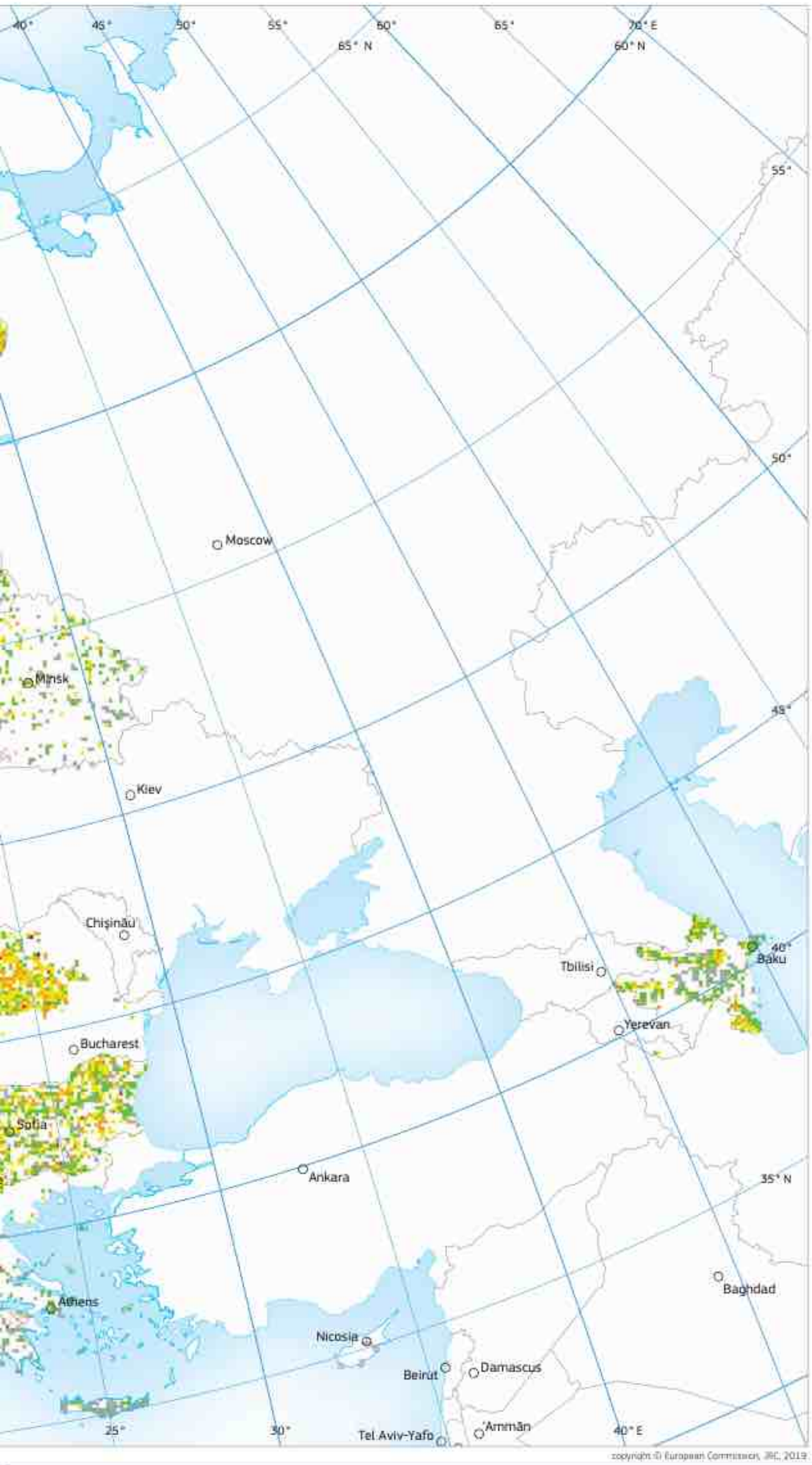

copyright © European Commission, JRC, 2019

Plate 7:
European Indoor Radon Map:
Indoor radon concentration.
Arithmetic means
per grid cell
(Bq/m³)

- 2000 - 10120
- 1000 - 2000
- 500 - 1000
- 200 - 500
- 100 - 200
- 50 - 100
- 20 - 50
- 1 - 20

Plate 7: European Indoor Radon Map: Indoor radon concentration. Arithmetic means per grid cell.
The map shows the arithmetic means (AM) over 10 km × 10 km grid cells of annual indoor radon concentration in ground-floor rooms. (Data received until September 2018 included.)
Source: EANR, EC-JRC, 2019

Limits of the EIRM due to data from ground-floor rooms

In general, the main contributor to indoor radon concentration in dwellings is gas emanating from the rock and soil underneath and in the surrounding of a building (see Section 2.2).

Indoor radon levels are likely to be higher on the lower floors of a dwelling. The highest radon concentrations are usually measured in the basements, but only few people live there. By diffusion and advection mechanisms, radon is then transferred to higher floors. Table 5-7 gives some examples of ground-floor-to-higher-floor ratios of radon concentration. The ratio of ground floor to first floor in the examples is in the range of 1.2–1.5; ground floor to second floor, 1.4–2.1 and ground floor to higher floors, 1.7–2.4. Even if the radon concentration and levels in the examples are quite different, the ratios (at least for ground floor to first floor) are comparable. In general radon concentrations stabilise with higher floors (e.g. Lorenzo-Gonzales et al., 2017), so a joint evaluation for floors above the second is acceptable. But there are also situations where radon concentrations can increase on higher floors, especially on the top floor, caused by specific building characteristics (e.g. elevators, installation ducts etc.). As examples of floor distribution of specific radon surveys are available only for some countries, it is not straightforward to use a floor model at European level.

Moreover, in order to calculate the indoor radon dose of the population, it is necessary to have detailed information about the population distribution per floor level for each country, as shown for Italy in Figure 5-17.

These data are not available for all European countries. It is not feasible to use, for example, the available data from Italy as a model for other countries, as the living situation of the population differs significantly between European countries. Table 5-8 shows the population distribution by dwelling type for a number of European countries. In Italy 50% of the population live in flats, whilst in Ireland this figure is only 7% with the rest living in semi- or detached houses. Based on this fact, the population distribution over floor numbers will differ significantly between countries.

Moreover, the data were collected only from residential dwellings; this means that in case of dose estimation the time that a person spends at work is not considered. Since it is known that radon concentrations in workplaces could differ from those in dwellings, this simplifying assumption is quite strong. There are two main reasons for this difference:

1. Workplaces generally differ in structure and usage from residential dwellings (e.g. see the case study on big buildings at the end of this chapter). This may cause a higher or lower level of indoor radon concentration.
2. Workplaces could contain additional radon sources, generally due to Natural Occurring Radioactive Material (NORM). For example, in the ceramic industry where zircon sands are used or in the phosphate fertiliser industry due to the by-product phosphogypsum. Also waterworks or underground workplaces are considered sites with potentially enhanced radon concentration.

Country (region)	Ratio GF/1st Floor	Ratio GF/2nd Floor	Ratio GF/≥3rd Floor	Reference
Italy	1.2	1.4	1.7	Bochicchio et al. (2005)
Spain (Barcelona)	1.6	2.0	1.8	Not published (personal comm. M. Garcia-Talavera)
Spain (Madrid)	1.5	2.1	2.5	Not published (personal comm. M. Garcia-Talavera)
UK	1.5			Wrixon et al. (1988)
Austria (data from 5 provinces)	1.5	2.0	2.4	Data from recent mapping survey; not published (personal comm. V. Gruber)

Table 5-7
Some examples of between-floor radon concentration ratios (GF = ground floor)

Region/country	Flat	Semi-detached house	Detached house	Other
	(% of population)			
EU-28	42.0	24.1	33.3	0.6
Euro area (EA-19)	47.7	22.7	28.9	0.7
Austria	44.5	6.9	48.0	0.6
Belgium	22.1	40.7	36.6	0.6
Bulgaria	44.0	12.4	43.2	0.4
Croatia	18.7	7.9	73.4	0.0
Cyprus	25.9	25.5	47.1	1.4
Czech Republic	52.2	10.3	37.1	0.4
Denmark	30.5	12.8	56.2	0.5
Estonia	62.6	4.7	32.1	0.5
Finland	33.7	19.3	46.5	0.5
France	31.5	23.7	44.7	0.1
Germany	57.3	15.8	25.5	1.4
Greece	56.1	10.1	33.8	0.0
Hungary	32.5	4.8	62.1	0.5
Iceland	46.7	18.8	34.1	0.3
Ireland	7.4	51.6	40.9	0.2
Italy	52.5	25.9	21.3	0.3
Latvia	65.0	3.1	31.8	0.1
Lithuania	57.4	6.3	36.1	0.2
Luxembourg	34.3	28.0	36.9	0.8
Malta	54.4	40.2	5.1	0.2
Netherlands[1]	19.9	59.9	16.6	3.6
Norway	18.6	19.8	61.2	0.3
Poland	44.1	5.2	50.6	0.1
Portugal	45.3	17.9	36.6	0.2
Romania	37.9	1.9	60.1	0.0
Serbia	23.5	10.4	66.1	0.1
Slovak Republic	51.2	1.8	46.5	0.5
Slovenia	29.6	5.0	65.1	0.3
Spain	65.9	21.0	12.7	0.5
Sweden	40.2	9.1	49.5	1.2
Switzerland[2]	60.1	12.6	24.4	3.0
United Kingdom	15.0	59.9	24.5	0.6

[1] Provisional data
[2] 2014

Table 5-8
Population distribution by dwelling type, 2015
Source: Eurostat (online data code: ilc_lvho01)

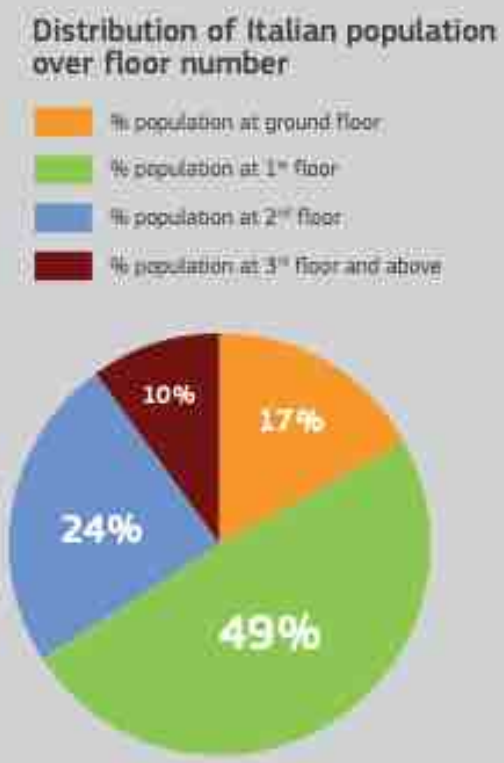

Figure 5-17
Distribution of Italian population over floor number
Source: ISTAT Italian data of 2011 Census

5.4.4 How can the dose due to radon be estimated?

The main hazard due to radon is caused by its short-lived alpha-emitting progeny (see details in Section 2.2.1). The damage which they inflict on the bronchial tissue depends on the size distribution of the radon progeny bearing clusters and aerosols that are in close contact with the tissue (UNSCEAR, 2008).

The relevant ^{222}Rn progeny are ^{218}Po (with a half-life of 3.05 min and relevant alpha energy of 6.0 MeV) and ^{214}Po (164 µs; 7.7 MeV) for the ^{238}U decay series and ^{216}Po (145 ms; 6.8 MeV) and ^{212}Po (0.3 µs; 8.8 MeV) for the ^{232}Th series (progeny of ^{220}Rn, also called thoron). Radon gas itself does not stick to lung tissue and has mostly been exhaled before it decays. This is somewhat different for ^{222}Rn and ^{220}Rn. Due to its short half-life, the latter has a higher probability of decaying while in the lung, i.e. before being exhaled, than the former. However, radon gas is soluble in tissue and contributes in this way to exposure and dose, but less than its decay products. In comparison, ^{223}Rn and ^{225}Rn have alpha energies of 5.5 and 6.3 MeV, respectively. To compare further, the parent nuclides ^{238}U, ^{226}Ra and ^{232}Th have alpha energies of 4.2, 4.8 and 4.0 MeV, the terrestrial natural nuclides ^{147}Sm and ^{144}Nd have 2.2 and 1.8 MeV, and the artificial radionuclides ^{239}Pu and ^{241}Am have 5.2 and 5.5 MeV (all data from the Lund catalogue, Chu et al., 1999). The high alpha energies of some of the ^{222}Rn and ^{220}Rn progeny, together with their capability to irradiate the lung tissue attached to small aggregates, explain their high radiological efficiency.

Radon progeny produced by radon entry indoors reacts very fast with trace gases and air vapours of the indoor air and becomes small aerosol particles with diameters of 0.5–5 nm, called clusters or 'unattached' radionuclides. Besides forming clusters, radon progenies attach to the existing aerosol particles with diameters of 10–1 000 nm, called 'attached' radionuclides (see Section 2.2.2 for more details and references, Figure 5-18). The aerosol particles, which now carry the radon progeny, diffuse in the indoor atmosphere and deposit on any available room surface. The most hazardous aggregation mode is the ultrafine one, consisting of clusters of progeny atoms. The ratio of progeny activity concentration contained in this part, to total progeny concentration, called unattached fraction, f, as well as the equilibrium factor, F, are therefore relevant parameters in radon dosimetry (see Section 2.2.1 and above).

There are different ways to quantify the health hazard:

- the organ dose to the lung generated by a given exposure to Rn or Tn progeny (dosimetric approach);
- the effective dose;
- the effective dose corresponding to exposure to a certain activity concentration of ^{222}Rn or ^{220}Rn;
- the health detriment caused by exposure (epidemiological approach).

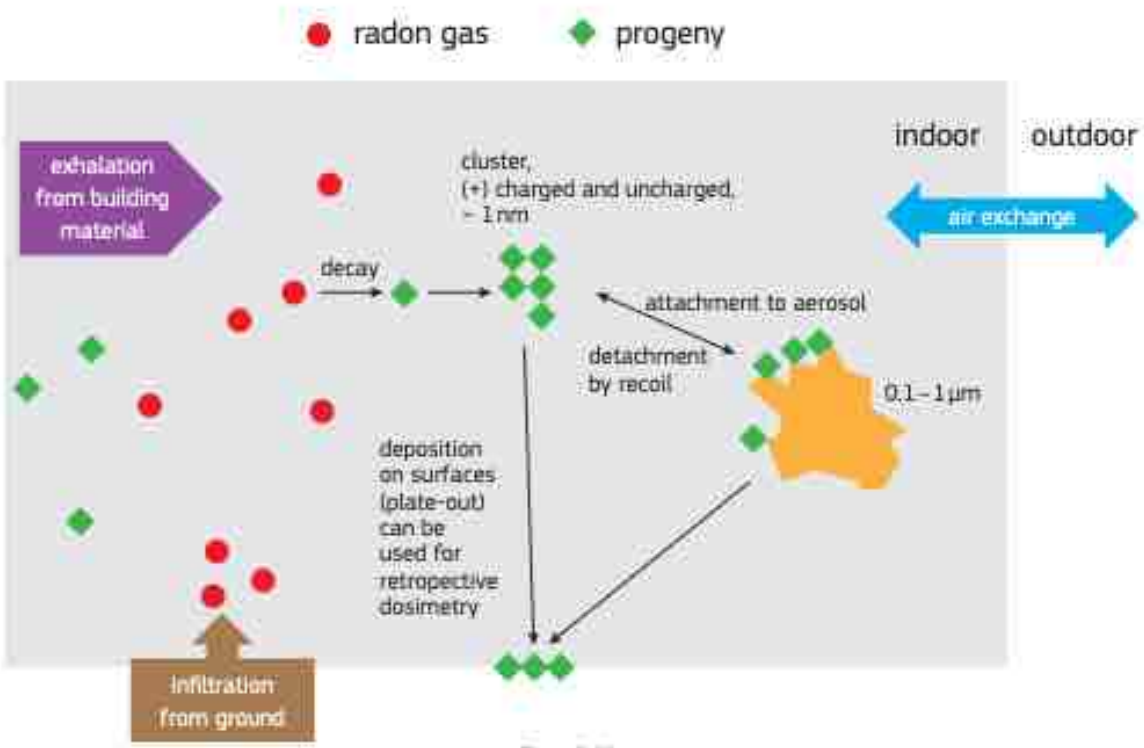

Figure 5-18
Simplification of the radon progenies behaviour in indoor air and attachment to aerosol particle (details in Figure 2.11, Section 2.2.1).
Source: Graph created by Peter Bossew.

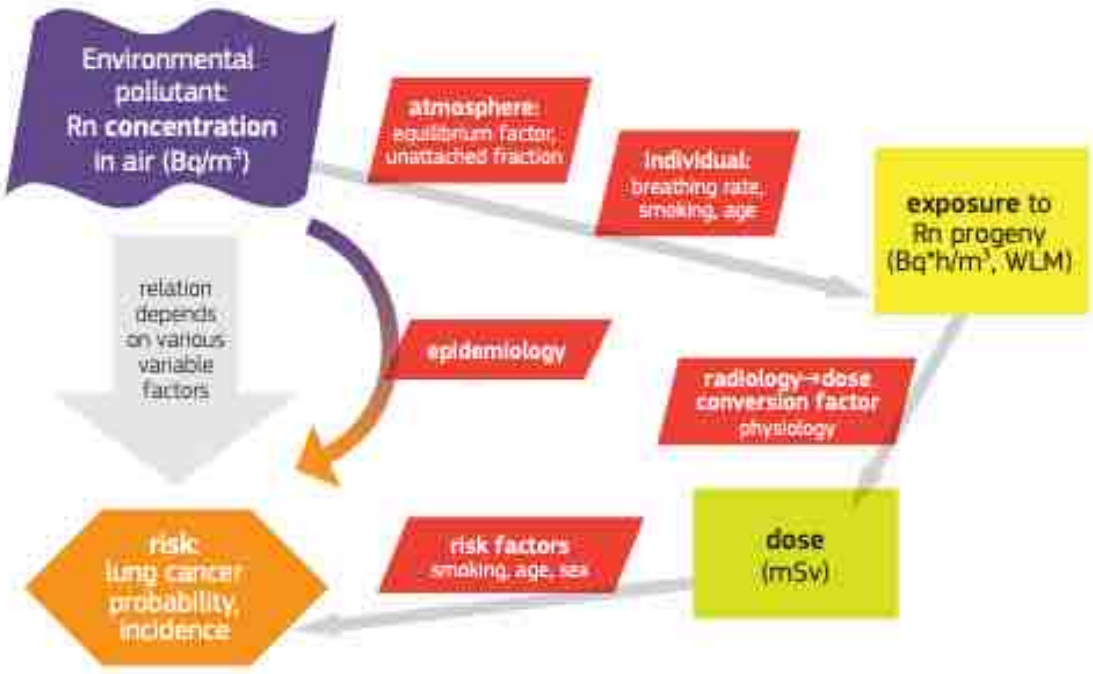

Figure 5-19
Epidemiological and dosimetric approaches to assess radon risk.
Source: Graph created by Peter Bossew.

Dose calculation

The following formula can be used to estimate the effective dose due to radon exposure:

$$D = DC \cdot EEC \cdot t \qquad (5\text{-}12)$$

where:
DC is the dose coefficient (in general Sv or Gy per $Bq_{EEC}\,h\,m^{-3}$);
$EEC = C_{Rn} \cdot F$ is the Equivalent Equilibrium Concentration (EEC) of radon daughters;
t is the exposure time;
C_{Rn} is the radon concentration in Bq/m^3;
F is the equilibrium factor.

The parameters used in Equation 5-12 could be chosen according to some hypotheses that will be described in detail below.

Dose coefficient

One of the key parameters in Equation 5-12 is the Dose Coefficient (DC). This is a tool for converting an exposure quantity into a dose quantity. Radon exposure can be expressed in working level months (WLM), as a cumulative alpha energy concentration in $mJ\,h\,m^{-3}$, or as a cumulative ^{222}Rn activity concentration in $MBq\,h\,m^{-3}$.

Historically, there have been many attempts to define the most appropriate DCs. Two different approaches have been explored: the epidemiological approach and the dosimetric approach (see Figure 5-19). In the epidemiological approach, essentially, the measured radon concentration is compared with observed lung cancer incidence or mortality. In the dosimetric approach, the causal physical chain from concentration over exposure to dose and finally to risk is modelled, based on data on atmospheric processes, properties of persons, physiology of the lung, and knowledge about biological radiation effects. Only recently could a good correspondence between the results of the two approaches be achieved (ICRP Publication 137; ICRP, 2017). Both approaches are complicated in their details and involve many sources of uncertainty.

The **epidemiological approach** is based on epidemiology studies that consist of investigating connections between lung cancer cases and radon exposures. These studies consider large numbers of case-control data, and thus they produce a factor that converts radon concentration into doses. Three main epidemiological studies have been performed respectively in Europe (Darby et al., 2005, 2006), in the US (Kremski et al., 2006) and in China (Lubin et al., 2004). In 2016, Seungsoo et al. (2016) published a review of case-control studies in the world and concluded that the risk factors attributed to lung cancer were almost the same as the classical pooling studies.

The **dosimetry approach** considers mathematical models to evaluate the dose to the lungs due to inhalation of radon gas and its daughters. An analysis of information on aerosol size distribution, unattached fraction, breathing rate, fractional deposition in the airways, mucous clearance rate, and location of the target cells in the airways should be considered. Such estimates are model-dependent and necessarily subject to all of the uncertainties associated with the input data as well as the assumptions built into the particular calculation model. The dosimetric evaluation of the absorbed dose to basal cells of the bronchial epithelium per unit exposure gives values in the range of 5–25 nGy $(Bq_{EEC}\,h\,m^{-3})^{-1}$ (UNSCEAR, 2000). The central value has been estimated by UNSCEAR to be 9 nGy $(Bq_{EEC}\,h\,m^{-3})^{-1}$ for average indoor conditions, a breathing rate of $0.6\,m^3/h$, an aerosol median diameter of 100–150 nm and an unattached fraction of 0.05.

EIRM and exposure

Again it should be emphasised that the cell mean (AM or median over cell means) is an estimate of the spatial mean of the quantity 'long-term mean radon concentration in ground-floor rooms of dwellings', but neither (a) the mean over radon in ground-floor dwellings, nor (b) the mean over all dwellings, i.e. an estimate of exposure. For (a) one would have to calculate a weighted mean with population density at ground floor by cells as weights, and for (b) the distribution of dwellings over floors would have to be included as weight, together with a model which accounts for floor level. Demographically-weighted mean radon concentrations and mean exposure are generally lower than the spatial mean of the quantity discussed here, since:

- population centres are preferentially located in valleys and flatlands, in many cases over quaternary geology which usually has lower radon potential; and
- radon concentration decreases with floor level, on the average (see Section 5.4.3, coloured box).

Several ICRP publications by ICRP over the last years have proposed different DCs. ICRP Publication 65 (ICRP, 1993) suggested using a factor of 5 mSv per WLM for workplaces and 4 mSv per WLM for homes. Published in 1993, this document was widely accepted in the community. Updated versions were published in 2007 and 2010 (ICRP Publications 103 and 115, respectively). The last one in this series is ICRP Publication 137 (ICRP, 2017). This is an interesting document since it shows a good agreement between the latest dosimetric studies and the epidemiological approach.

Working Level (WL)

Another important unit when working with radon is the Working Level (WL). This unit was originally used for uranium mines, but it can be used on environmental exposures as well. A WL is any combination of short-lived radon daughters in one litre of air that will result in the emission of 1.3×10^5 MeV of potential alpha energy (20.8 μJ/m³).

The equivalences for expressing potential alpha-energy concentration (PAEC) in relation to equilibrium equivalent concentration (EEC) are:

- PAEC of 1 J/m³ corresponds to 1.8×10^6 Bq_{eq}/m^3
- PAEC of 1 WL corresponds to 3.75×10^3 Bq_{eq}/m^3 and correspondingly the potential alpha energy exposure (PAEE):
- PAEE of 1 J h m⁻³ corresponds to 1.8×10^6 Bq_{eq} h/m³ and
- PAEE of 1 WLM corresponds to 6.37×10^5 Bq_{eq} h/m³.

In this way, one WL is roughly 3 700 Bq/m³ equilibrium equivalent concentration of radon (EEC):

$$WL = EEC\ (Bq/m^3)/3\,700 = F * C_{Rn}\ (Bq/m^3)/3\,700 \qquad (5\text{-}13)$$

Traditionally, the exposure of uranium miners and other mine workers has been expressed in units of Working Level Month (WLM). This is the exposure rate of 1 WL for a working month of 170 hours. Thus, while a miner exposed to 1 WL during a working year accumulates 12 WLM, a member of the population with continuous exposure to 1 WL accumulates about 50 WLM. In that way,

$$PAEE(WLM) = PAEC(WL) * \left(\frac{Exposure\ (h)}{170}\right) \qquad (5\text{-}14)$$

	Approach	Workers (mSv/WLM)	Members of Public (mSv/WLM)
ICRP Publication 65 (1993)	Epidemiological	5	4
ICRP Publication 137 (2017)	Dosimetric	10	10
ICRP Publication 137 (2017)	Dosimetric	20*	
Marsh & Birchall (2000) HRTM	Dosimetric		15
UNSCEAR (2006)	Average value		5.7

* For the specific situations of radon work involving substantial physical activity, and exposures in tourist caves (ICRP Publication 137, 2017)

** Table 5-8
Dose coefficients based on different models in mSv/WLM.
Source: Table created by Maria García-Talavera and José Luis Gutiérrez Villanueva

Terminology

When speaking about 'radon', sometimes one means ^{222}Rn and ^{220}Rn indiscriminately. However, more often it denotes ^{222}Rn only. ^{220}Rn is often called thoron (Tn).

To make it more confusing, if speaking about 'radon exposure' or 'exposure to radon', one means exposure to radon progeny, in most cases. Again, distinction between ^{222}Rn and ^{220}Rn (=Tn) progeny is often not made.

We recommend using exact terminology to avoid any misunderstanding. Only when addressing the hazard caused by the Rn isotopes and their progeny in a generic way may one speak about 'radon'.

Exercise on dose coefficients' influence

Figure 5-20 shows how the annual effective dose due to radon exposure depends on the values chosen for the dose coefficient. The following parameter values have been assumed to estimate the dose:

- 100 Bq/m³ Rn concentration at home;
- 0.8 as occupational factor;
- 0.4 as equilibrium factor.

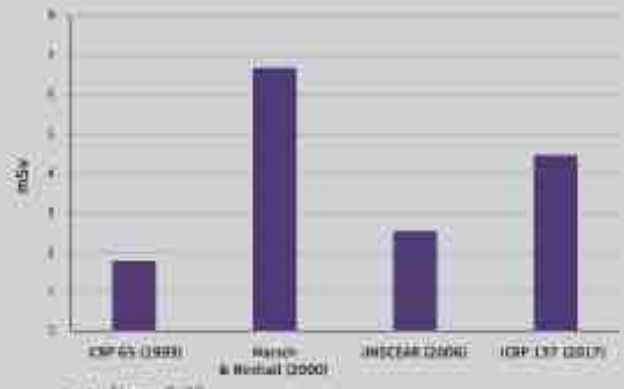

** Figure 5-20.
Comparison of the annual effective dose due to radon exposure estimated using different dose coefficients.
Source: UNSCEAR, ICRP, 2014

Exposure time

Exposure time (t) can be estimated by considering an occupancy fraction of 0.8 (UNSCEAR, 2008). The occupancy fraction is the proportion of time that a person spends indoors.

For dose calculations, the exposure time per year is generally set to 7 000 h per year (~365 d/a × 24 h/d × 0.8).

However, differences could appear between European countries due to climate and living habits. Future versions of this Atlas may include further research on this topic.

Equilibrium factor

The **equilibrium factor F** is defined as the ratio of the EEC (the radon concentration in equilibrium with its decay products that equals the potential alpha-energy concentration of the original mixture) to the radon concentration.

Based on the currently limited available F measurements, UNSCEAR (2000-2008) provides a typical value of 0.4 for indoor radon in dwellings. F increases with increasing Bq_{EEC}/m^3 aerosol particle concentration. It is thus affected by factors such as presence of tobacco smoke (Jasaitis & Grigzdy, 2013) and ventilation. For German dwellings Wicke and Postendörfer (1981) reported a range of F values from 0.3 to 0.6, for normal ventilation rates (0.1 – 1 h⁻¹). More details are provided in Section 2.2.2.

Regional variations have been observed. For Sweden a mean value of 0.44 has been obtained (Swedjemark, 1983). In Canada, long-term measurements of F gave results ranging from 0.6 to almost 1 (Harley, 2018). Measurements carried out from different studies over the years in Chinese dwellings gave an average of 0.47, whereas in India a typical value of 0.36 has been proposed (Chen & Harley, 2018). In general, warm, humid areas seem to present lower F values.

** Small, former uranium mines, Urgeiriça, Central-Eastern Portugal, close to the Spanish border.
Source: Peter Bossew

Case study: Radon measurements in large buildings

The *European Basic Safety Standards Directive* (European Union, 2013) includes regulations of *radon* in common workplaces and public buildings for the first time in radioprotection regulation. The EU Member States must transpose this Directive into national law, and even some non-Member States, although not obliged, chose to adopt regulations which closely follow it. A number of questions arose concerning the practical application of these new standards, such as how to perform representative, reproducible and legally compliant measurements of radon concentration in large buildings. As a basis for deciding further action, as laid down in the Radon Action Plans (also an obligatory part of the Basic Safety Standards Directive (European Union, 2013) transposition), measured values have to be compared with a defined reference level (RL). The BSS stipulates that EU Member States must set an RL of maximum 300 Bq/m³. The RL is valid not only for residential indoor radon, but also for workplaces and for public buildings.

In the past years, the mechanism of radon infiltration and accumulation in private dwellings has been investigated, understood and resolved in many cases. Only a few investigations have been performed in 'large' buildings such as administration edifices, schools, factories, supermarkets or business centres (Jeong et al., 2013). As one can imagine, these constructions are in general much more complex and their 'users' behave quite differently and with greater diversity (for example concerning air exchange, which is the key anthropogenic parameter that controls indoor radon concentration, together with the geogenic radon potential) than in residential buildings.

The international *Radon in Big Buildings* (Ribibui) Consortium (http://www.ribibui.org), established in February 2016 at the University of Applied Sciences and Arts (SUPSI) in Lugano, Switzerland, is investigating strategies to define a standard protocol for radon measurements in these objects. To this end, radon measurement data from 'large' buildings in various countries have been collected and analysed so far. As one can anticipate, the radon characteristics differ between types of 'large' buildings, and, consequently, a tentative classification of building types has been proposed by the consortium (see Table 5-10). Understanding the differences between building classes is a prerequisite for modelling the radon distribution and its migration pathways.

For logistic and economic reasons, only in a few cases is it possible to place radon detectors everywhere in a large building with a large number of rooms. Therefore, an important result of the project will be to propose an estimate of how many detectors are necessary within a large building, and where they have to be located, in order to be able to decide with given confidence whether further action (e.g. remediation) according to the Radon Action Plan is necessary or not. In most cases, this is a decision about compliance with the RL. Developing a method for such decision, and assessing its reliability (or the factors which determine it), is one of the objectives of this project.

To date, the majority of large buildings for radon concentration are schools, kindergartens and office buildings. In most cases, basement, ground- and first-floor rooms have been measured, but rarely rooms on higher floors because most of these measurements were performed outside the project environment. Based on experiences in dwellings, it has been assumed that also in workplace-type buildings a decrease of radon concentration with increasing floor level is the rule. Reflecting the state of knowledge around 2010, when it was developed, also the Basic Safety Standards Directive requires measurements in workplaces (when it is required at all, namely in radon priority areas) only in basement and ground floor rooms. However, the first results of the Big Buildings project have shown that in certain types of buildings one cannot rely on that rule. In fact, some measurement data show higher radon concentration on upper floors (see Figure 5-21 as an example), which might be caused by lower pressure differences between indoor/outdoor atmosphere and consequently of less natural air exchange. It is known that artificial ventilation or air conditioning systems influence the radon distribution (Kozak et al., 2014; Polednik et al., 2016). These kinds of effects have to be considered in a standard protocol. An example of the distribution of radon concentration in a building is shown in Figure 5-22, for a building without significant dependence of radon on floor level. If there is a dependence, in particular the one mostly observed in lower residential buildings, the overall frequency distribution should be assumed multimodal, reflecting distinct modes of radon entry in different compartments (floors) of the building.

Quantities for characterising the radon situation of a building could be, among others, the mean radon concentration over all rooms or the probability that any room has radon concentration levels above the RL. Finding the values of these quantities, as a basis for deciding about compliance with regulation, requires performing radon measurements, perhaps together with additional assumptions about radon distribution. A more profound understanding and analysis is required and will be performed in the near future.

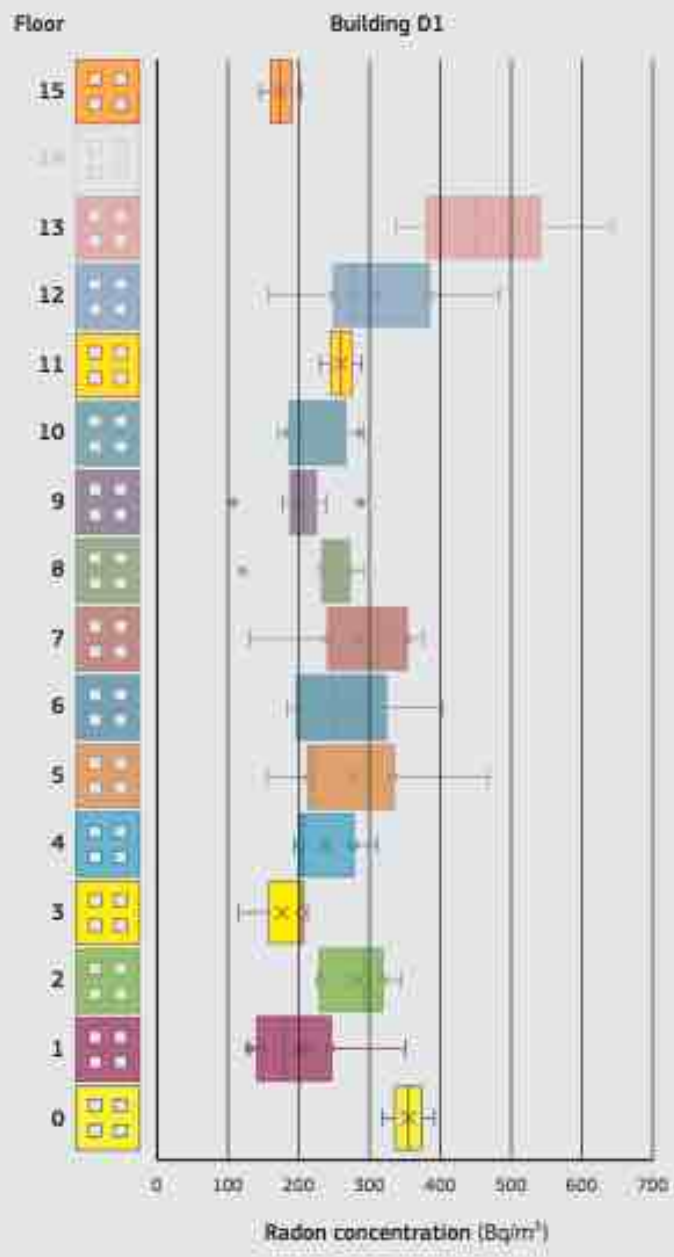

Figure 5-21.
Measured radon concentration in a building with 15 floors (floor 14 not measured). Each box ranges between the 25th and 75th percentiles, the crosses represent the mean, the black horizontal lines the median, the lines extending vertically from the boxes (whiskers) indicate variability outside the upper and lower quartiles and the points represent the outliers.
Source: Graph created by Marco Hoffmann.

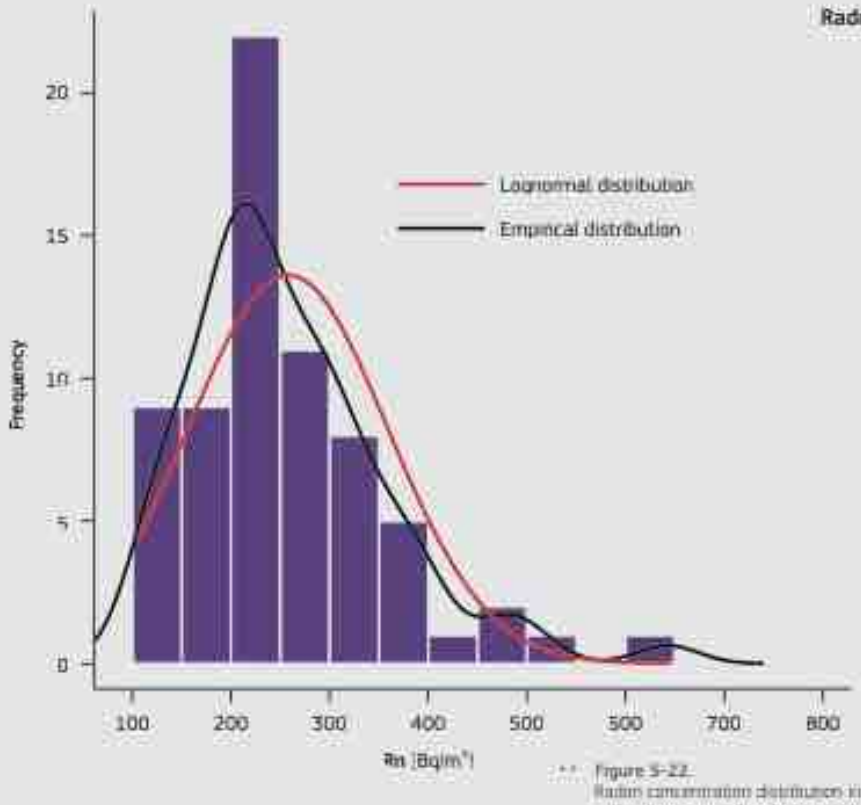

Figure 5-22.
Radon concentration distribution in a building with 15 floors, fitted with a Lognormal distribution (AM = 251, GM=228, GSD=1.55) and the empirical distribution.
Source: Graph created by Marco Hoffmann.

Type number	Building description
1	Mall or manufacturing type (large halls, large commercial centres) [$n_{floors} < 3$]
2	Flat hall type (schools, kindergartens) [$n_{floors} <= 3$]
3	Standard office type [$3 < n_{floors} < 10$]
4	Skyscraper type [$n_{floors} > 9$]
5	Sport stadium type
6	Historical buildings
7	Underground workplaces
8	Other

Table 5-10.
Building type classification by the Radon in Big Buildings project.
Source: Marco Hoffmann.

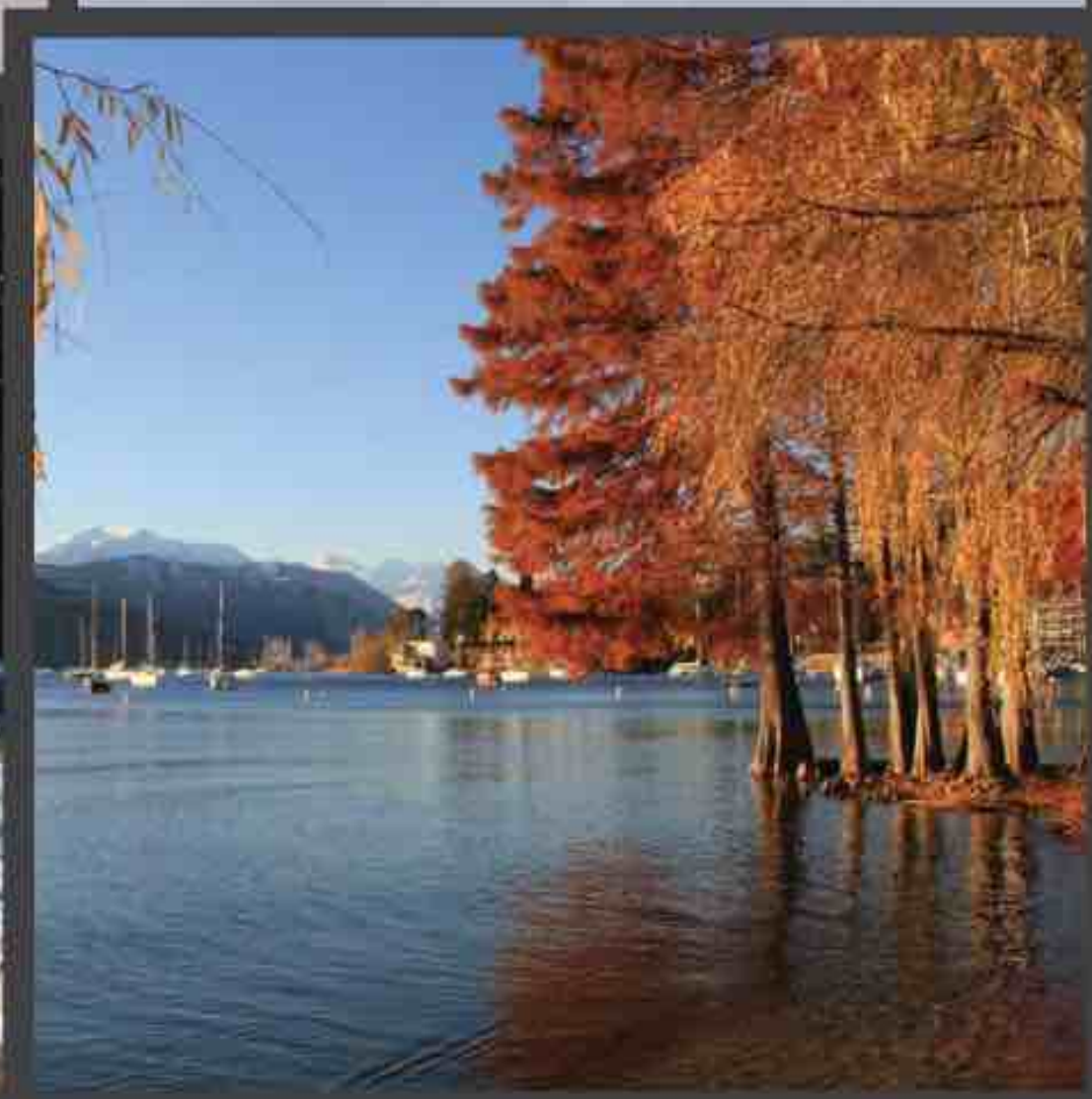

Chapter 6

Radionuclides in water and river sediments

The water we use for domestic and public consumption comes from ground and surface water. Depending on its age and chemical properties, natural water contains different natural radionuclides in varying concentration. These radionuclides, together with other mineral components, are released from rock surfaces. Water with very long contact time with rocks, e.g. ground water, may have higher radionuclide concentration, whereas surface water generally shows lower values.

Besides radionuclides in the uranium and thorium series (including radon), ^{40}K, ^{3}H, ^{14}C and other natural radionuclides may occur in water. ^{3}H and ^{14}C may also come from recent anthropogenic sources, together with ^{90}Sr, ^{131}I, transuranium products and other beta- and gamma-emitters released from industrial or medical activities.

Because radon is a highly soluble gas, its concentration in ground water is generally higher than that of the parent radium isotopes. In very old and highly mineralised ground water, radon activity may be more or less in equilibrium with that of radium. The solubility of other radionuclides in water differs as a function of their chemical properties.

In river water, radionuclides may precipitate to sediments. When fixed on high-surface matter such as clay, they are more easily immobilised or transported under turbulent conditions and thus increase radionuclide concentration in the sediment.

While uranium is chemically toxic, radium, radon and its daughter isotopes, lead and polonium, can be radioactive hazards and thus pose health challenges. Tritium and ^{14}C occur in concentrations that do not pose any health hazards, and so can be used to date ground water.

Alpha-, beta- or gamma-spectrometry is typically applied to measure radionuclide concentration in water. Water volumes and sampling procedures differ between the radionuclides, depending on their chemical properties. Gross alpha and gross beta values are determined by liquid scintillation spectrometry. To detect single radionuclides, alpha spectrometry or high-purity germanium detectors (HPGe) may be applied. These methods are often used to analyse sediments as well. The detection limits are generally below 20 Bq/l, for most radionuclides even below 0.1 Bq/l.

According to recent international studies, the concentration of natural radionuclides in water and river sediments varies at least as much as that in their host rocks. In most countries, however, this does not exceed levels in drinking water. Countries with granitic bedrocks and possibly enhanced concentrations of organic matter (due to wetlands), as in Scandinavia, are at risk of having higher concentrations of radionuclides in drinking water.

Clockwise from top-left:
Water flux during snow melt, Castellano river, Ascoli Piceno, Italy
Source: Ferdinando Cinelli
Water fall on Castellano river, Ascoli Piceno, Italy
Source: Ferdinando Cinelli
Water source, Austria
Source: Valeria Gruber
View of Lake Maggiore, Italy, which provides drinking water for bordering communities
Source: Tore Tollefsen
Waves crashing on cliffs, Vico Equense, Napoli, Italy
Source: Ferdinando Cinelli
Domestic use of water
Source: DDNet (CC BY-SA 3.0)

Radionuclides in water and river sediments

6.1 Introduction

Water is a potential source of direct exposure to radionuclides through consumption of liquids and foodstuffs (e.g. fish, shellfish, aquatic plants), but also through leisure and sports activities (e.g. fishing, swimming). Indirect human exposure arises from use of water for irrigation and watering of livestock or from use of algae or sludge as soil amendments. An additional contribution to indoor radon concentration stems from radon gas dissolved in water and released from domestic washing, showering, toilet flushing and food preparation or occupational exposure in water-supply settings.

The water we use and consume comes from two main sources: ground water and surface water. Ground water is defined as water found underground in cracks and spaces in soil, sand and rock. It is stored in and moves slowly through geologic formations of soil, sand and rocks called aquifers (from https://www.groundwater.org). Surface water comprises river, lake, or seawater.

Ground water contains naturally occurring radionuclides that originate from the thorium and uranium decay series. These can arise from natural processes in the ground or human activities, such as uranium mining and other extractive industries. For most people, the source of water for domestic consumption and other uses is ground water, often obtained from shallow, private wells, but more often obtained from public, community wells tapping the aquifer (Engelbrecht, 2012). Surface water is one of the environmental compartments to which radioactive effluents from nuclear installations are authorised to be discharged (Engelbrecht, 2012). Radionuclides in surface water can be found in the water phase or associated with suspended particles and can eventually become incorporated into sediments and living species.

Sediment is an accumulator of radionuclides that are insoluble and adsorbed on insoluble material on the aquatic system and hence an indicator of the presence of such radionuclides. Sediments in all types of water may be a source of contamination to aquatic organisms.

** Lake Fiastra during summer time, Macerata, Italy
Source: Pierangelo Crielli

Drinking water may contain radionuclides that could present a risk to human health, but this risk is normally low compared to risk from microorganisms and chemicals. Usually the radiation dose resulting from ingestion of radionuclides in drinking water is much lower than that received from other radiation sources. Naturally occurring radionuclides in drinking water usually give radiation doses higher than those provided by artificially produced radionuclides and are therefore of greater concern (WHO, 2017, 2018).

The Drinking Water Directive (Council Directive 2013/51/Euratom; European Union, 2013a) stipulates requirements for protecting public health from radioactive substances in water intended for human consumption, and specifies parametric values for radon, tritium and 'indicative dose'. For radon and tritium, the parametric values are 100 Bq/l with requirements for detection at 10 Bq/l for each. For radon, EU Member States may set national limits as judged inappropriate to be exceeded, which may be greater than 100 Bq/l but at most 1 000 Bq/l. The upper value of 1 000 Bq/l is considered through degassing to contribute around 100 Bq/m^3 to indoor air (WHO, 2011), a value comparable to the WHO Reference Level for indoor-air radon (100 Bq/m^3) recommended to minimise health hazards.

Radionuclides of anthropogenic or technological origin may be present in water from several sources (WHO, 2018), such as: radionuclides discharged from nuclear fuel cycle facilities, manufactured radionuclides (produced and used in unsealed form in medicine or industry) entered into drinking-water supplies as a result of regular or incidental discharges, and radionuclides released in the past into the environment, including drinking water sources.

^{137}Cs present in the environment stems mostly from nuclear power plant accidents. It is important to monitor its activity concentration in surface water and in sediments, especially as higher observed values of ^{137}Cs may be an indicator of some nuclear accident.

Tritium, ^{3}H, is a very important nuclide for detecting potential radioactive or nuclear contamination of surface waters, especially as its origin in water is mostly anthropogenic and not natural.

Radiocarbon, ^{14}C, is an important radioisotope for hydrogeology studies, and its origin could be natural from cosmic radiation and artificial from nuclear power plants. By monitoring the activity concentration of ^{14}C, one can evaluate if there has been a nuclear accident that directly affected surface water. After nuclear bomb testing and nuclear accidents (like Chernobyl, which mainly affected European countries), artificially produced radioisotopes such as ^{137}Cs and ^{14}C were deposited in rivers and accumulated in sediments. By measuring the activity concentrations of those two isotopes, one can construct a scale of past nuclear events and also determine some characteristics of surface water.

The most comprehensive database collections of monitoring results for isotope content in precipitations and rivers are the IAEA Global Network of Isotopes in Precipitation (GNIP) and the Global Network of Isotopes in Rivers (GNIR).

The Council Directive parametric value for indicative dose is 0.1 mSv/a, a value that EU Member States may estimate via measurements of gross alpha and gross beta activity or from specific radionuclides. Derived concentrations for radionuclides are given in the Drinking Water Directive, for which Member States can assume that the indicative doses are less than the parametric value of 0.1 mSv. WHO recommends screening water samples for gross alpha and gross beta, with guideline values of 0.5 Bq/l and 1 Bq/l, respectively (WHO, 2017).

6.2 Natural radionuclides in ground and surface water

Natural waters contain both alpha and beta emitters in widely varying concentrations which give relatively small contributions to the total dose received from natural and artificial radioactivity. In every monitoring programme, measurement of gross alpha and beta activity in a water sample is the first analysis that should be made as a screening approach. If gross alpha and/or gross beta activity concentration is higher than the recommended reference/screening levels, then some additional nuclide-specific measurement methods should be used in order to quantify the individual radioisotopes that are present in water.

Alpha activity is mostly due to dissolved uranium isotopes (^{234}U, ^{235}U and ^{238}U) and ^{226}Ra. The main source of gross beta activity in waters is ^{40}K and short-lived daughters of ^{234}U, ^{234}Th and ^{234m}Pa (Forte et al., 2007).

Natural radionuclides can be found in ground and surface water as a result of either natural processes (e.g. reaction with aquifer minerals and absorption from the soil) or technological processes involving naturally occurring radioactive materials (e.g. mining and processing of mineral sands or phosphate fertiliser production) (WHO, 2017). Anthropogenic sources of radioactivity include transuranium products, ^{14}C, ^{3}H, ^{90}Sr and ^{131}I and other gamma emitters, released in controlled/authorised quantities from nuclear installations, medical or industrial facilities, or from past bomb-testing or nuclear accidents.

The dominant radionuclides in ground and surface water that can pose a potential health hazard under natural conditions are ^{210}Po, ^{210}Pb, ^{210}Bi, ^{222}Rn, ^{226}Ra and ^{228}Ra in the ^{232}Th series. The health hazards from uranium isotopes are due more to chemo- than radiotoxicity. Other isotopes in these series are generally not present in ground water in significant quantities because of low presence, low solubility in water and/or very short half-lives. Activity of environmental ^{40}K is not considered a hazard as K is an essential element in human metabolism, and K metabolism is strongly self-regulated (more details in Section 3.3).

^{14}C also constitutes a trace proportion of natural carbon. In ground water, the contribution of carbon stems mainly from carbonate minerals with usually low ^{14}C activity. Specific activity of ^{14}C is therefore low in natural ground water, and human exposure is negligible under natural conditions.

Ground water is typically more prone than surface water to accumulate naturally-occurring radionuclides because of the influence of water-rock reactions and the large solid/solution ratios in aquifers. Furthermore, the residence time between water and the geological environment in an aquifer is usually longer. Ground water is a regionally important and strategic resource for both public and private supply. Table 6-1 shows how the proportion of water demand covered by ground water varies widely over a number of European countries.

In order to make valid judgments about management and hazards of natural radionuclides in ground water, it is necessary to understand the specific behaviour of these radionuclides in the aquifer chemical systems, which in turn requires detailed knowledge of ground water pH and redox potentials, with rock materials (Foss & Brooker, 1991). Chemical reactions, such as ion exchange, chemical complexing, and equilibration reactions with minerals, and physical processes, such as alpha recoil (Osmond & Cowart, 1976; Osmond et al., 1983, 1984), can cause considerable deviation from decay equilibrium within the uranium decay series.

Country	Percentage of water demands supplied by ground water (%)
Denmark	100
Austria	99
Italy	91
Hungary	89
Switzerland	75
Germany	73
Poland	72
Luxembourg	70
Netherlands	70
Belgium	65
Greece	64
France	57
Malta	50
Sweden	47
Finland	45
United Kingdom	30
Spain	22
Ireland	17
Norway	15
Sweden	13

** Table 6-1
Percentage of water demands supplied by ground water for a number of European countries.
Source: Stimson and Everett, 2004, table 5.1.23

6.2.1 Radon

Radon is a radioactive noble gas that exists naturally as three isotopes: ^{222}Rn, ^{220}Rn, ^{219}Rn. Radon is the heaviest of all noble gases. The most stable and environmentally relevant isotope is ^{222}Rn (hereafter called radon (Rn)), formed from alpha decay of ^{226}Ra, in the ^{238}U decay chain. ^{222}Rn is a short-lived isotope with a half-life of 3.82 days. During decay, an alpha particle is ejected, and emitted radon is propelled by kinetic energy from the decay site in the opposite direction. This alpha recoil can alter crystal lattices and enhance radon leaching from the crystal surface. By recoil, radon can be transported as a dissolved gas in pore water or be retained in the mineral structure (see Figure 6-1). See Section 2.2.2 and Chapter 5 for more details about radon.

The emanation power or emanation coefficient of radon (proportion released to ground water compared to the total radon produced) is a function of recoil and diffusion, and is affected by radium distribution in the host rock, surface geometry, grain surface moisture and rock porosity (see e.g. Nazaroff & Nero, 1988). Water-filled pores can reduce recoil into mineral grains and hence increase emanation efficiency relative to air-filled pores. Nonetheless, the emanation coefficient in saturated aquifers is typically lower than 30% (Wanty et al., 1992). More details are given in Section 2.2.2 and Chapter 5.

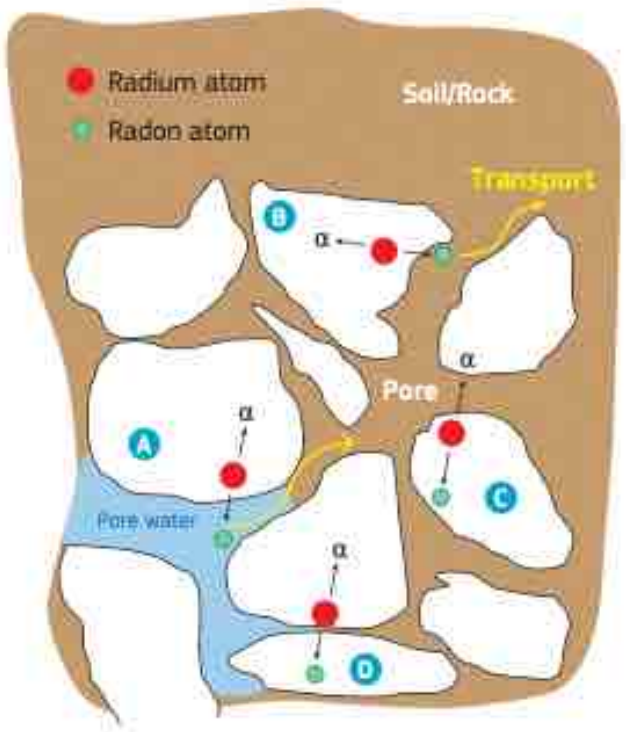

Figure 6-1.
Schematic illustration of radon recoil trajectories in and between soil/rock grains: A) Radon is released into pore water; B) Radon is released into pore air; C) Radon remains in grain; D) Radon absorbed by neighbour grain (if the thickness of the mineral grain is higher than the recoil range of 10–70 nm).
Source: modified after Nazaroff & Nero, 1988

As radon is an inert gas, its mobility in water is controlled by physical rather than chemical processes. Alpha recoil accounts for radioactive disequilibrium in ground-water systems (Wanty & Nordstrom, 1993). Radon neither precipitates in mineral phases nor participates in sorption reactions. Activities in ground water are higher than in surface water because of mineral interactions, longer contact time in host aquifers and loss by degassing from surface water.

Radon decays rapidly and does not accumulate in ground water along flow paths, because decay rates are typically faster than those of ground water flow. As a result, high radon concentrations in ground water are indicative of local uranium (radium) sources.

High radon contents in ground water are related to uranium and radium content of aquifer minerals and of the ground water, as well as ground water flow rates. For a given aquifer uranium content, higher radon concentrations in ground water are expected in rocks of lower porosity, higher density or higher emanation efficiency (Wanty et al., 1992). The extent of transport from a radium decay site is also determined by the permeability (primary or secondary) of the host rocks. High radon concentrations are typically not found in zones of high transmissivity in aquifers due to reduced rock/water ratios and dilution of emanating radon (Lawrence et al., 1991). Once radon is in ground water, its transport is controlled by advection and diffusion.

As for other gases, the solubility of radon in water is temperature-dependent, with solubility decreasing by about 3% per °C as temperature increases from 10 °C to 20 °C (Figure 6-2). Solubility is also affected by barometric pressure, though this is likely less influential than other physical controls (Lindsey & Ator, 1996; Clever, 1979; Schubert et al., 2007; Lerman, 1979).

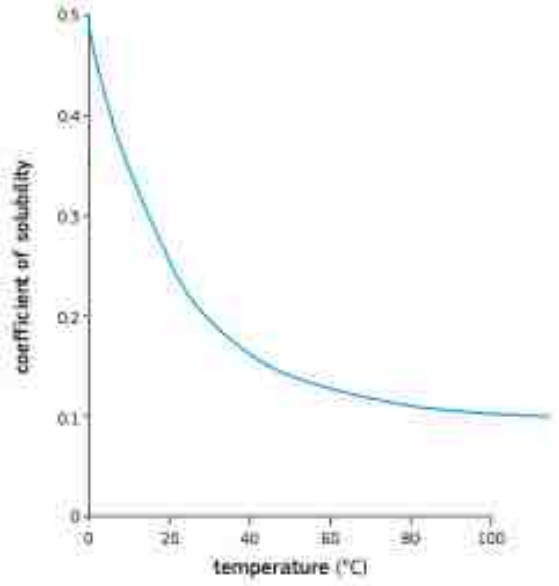

Figure 6-2.
Plot of coefficient of solubility for radon as a function of water temperature.
Source: Cothern, 1987, p. 5

Dissolved radon typically shows poor correlation with dissolved uranium and radium (Veeger & Ruderman, 1998) because of their differing states, solubilities, sorption properties and redox dependencies. Activities of radon in ground water are often much higher than can be accounted for by equilibrium decay of observed dissolved radium, suggesting the presence of additional radon from mineral surfaces (e.g. radium on adsorption sites or fracture precipitates).

High radon activities in ground water are often associated with uranium-rich rocks such as granite, granite gneiss and pegmatite (Skeppström & Olofsson, 2007; Przylibski et al., 2004; Vinson et al., 2009; Veeger & Ruderman, 1998; Knutsson & Olofsson, 2002). Some of the highest radon concentrations ever recorded, have been found in granitic terrains of Scandinavia (e.g. Banks et al., 1998; Åkerblom & Lindgren, 1997) and in Stockholm county (e.g. 63 560 Bq/l) (Skeppström & Olofsson, 2007). High values (up to 5 000 Bq/l) have also been reported from granitic areas in south-west England (Talbot et al., 2000) and parts of Scotland (up to 80 Bq/l) (Aldoorie et al., 1993). The number of measurements of radon activity in ground water, and hence the data availability, are extremely variable across Europe.

Maps of radon concentration in ground water have been prepared for some European countries, e.g. the UK (Young et al., 2015).

An evaluation of international research data (UNSCEAR, 2000) concluded that, on average, 90% of the dose attributable to radon in drinking water comes from inhalation rather than ingestion. Therefore, controlling the inhalation pathway rather than the ingestion pathway is the most effective way to control doses from radon in drinking water. The percentage of radon present in drinking water that is released into indoor air will depend on local conditions, such as the total consumption of water in the house, the volume of the house and its ventilation rate, and it is likely to be highly variable (WHO, 2017). Higher radon doses by radon inhalation may occur for workers in water supplies. In several countries, therefore, water supplies are listed as specific types of workplaces where radon in air needs to be controlled according to the Basic Safety Standards Directive, Article 54 (European Union, 2013b).

Seljalandsfoss waterfall situated on the Skógá River, Iceland at the cliffs of the former coastline.
Source: Samuel Wang on Unsplash

6.2.2 Radium

The main isotopes of radium, viz. ^{226}Ra, ^{228}Ra, and ^{224}Ra, are derived from U and Th decay. ^{226}Ra and ^{224}Ra are alpha emitters; ^{228}Ra is a beta emitter. All are relatively short-lived with half-lives of 1 600 years, 5.75 years and 3.6 days, respectively.

^{226}Ra and ^{228}Ra are the most important radium isotopes present in water. Arising respectively from the decay of ^{238}U and ^{232}Th, their concentration depends on the content of their parents in the substratum. Since thorium is about three times more abundant than uranium in the lithosphere but has a decay constant about three times that of uranium, the global inventories of ^{226}Ra and ^{228}Ra should be roughly equal; however, local specific geological structures of terrains lead to a great variability in the ratio between these two isotopes.

In general, radium concentration in fresh ground water is usually low, typically in the mBq/l range. Radium concentration in surface water is even lower than in most ground water (Eisenbud & Gesell, 1997).

Some mineral and thermal waters exhibit ^{226}Ra concentration values up to several Bq/l. ^{228}Ra, the daughter of ^{232}Th, is generally found in excess of its parent in most natural water due to the greater solubility of radium over thorium. In freshwater, radium is found in highest concentrations in limestone regions where it is more soluble in HCO-waters. ^{228}Ra is also found in excess of its parent ^{232}Th in natural waters.

Higher activities have also been found in saline ground water, including oilfield brines and other formation waters. Activities of tens to hundreds of Bq/l have been reported for ^{226}Ra and ^{228}Ra in oilfield brines from the USA (Spaite & Smithson, 1992), with activity commonly correlating positively with ground water/brine salinity.

Radium has physical properties and displays behaviour similar to that of barium, strontium and calcium, and its mobility is controlled by geochemical reactions that affect these elements (dissolution/ precipitation, sorption). Radium has only one oxidation state (+2) in natural systems. The element occurs in solution mainly as free Ra^{2+} or as $RaSO_4$ and also forms strong aqueous complexes with carbonate (Wanty & Nordstrom, 1993).

Mobility of radium in water may be enhanced by alpha recoil but limited by sorption to iron and manganese oxides, clays or co-precipitation with alkaline earth metals in $BaSO_4$, $SrSO_4$ and $CaCO_3$. Sorption of radium to metal oxides and clays is pH-dependent, being less significant under acidic conditions (e.g. Almeida et al., 2004). Loss of radium through sorption in water treatment systems has also been documented (Hill et al., 2018). Complexation of radium with chlorine, SO_4 and CO_3 ligands is possible in saline fluids. Radium activity is typically higher in anaerobic ground water due to reductive dissolution of iron oxides, in aquifers with poor sorption capacity (low iron-oxide content) and those with high concentrations of competing cations (calcium, magnesium, barium and strontium) as well as HCO_3 (Szabo et al., 2012).

As a result of co-precipitation and sorption, radium activities can be high in scale deposits (sulphates, carbonates, silicates, oxides). Many studies have been carried out on Naturally Occurring Radioactive Materials (NORM) in scales, and activities of several thousands of Bq/g have been reported in scales produced in the oil and gas industry (IAEA, 2003). Radium-bearing scales also occur in geothermal production waters.

In Europe, only a few studies have been made of radium in ground water, e.g. in Serbia (Onishchenko et al., 2010).

6.2.3 Uranium

Uranium (U) is a heavy element in the actinide series (atomic number 92) with two main natural, primordial, long-lived radionuclides, including the more abundant ^{238}U (half-life of 4.5×10^9 years, 99% of uranium total mass) and the less abundant ^{235}U (half-life of 7.0×10^8 years, 0.72% of uranium total mass), both decaying separately through long and complex radioactive decay series ending with stable lead (^{206}Pb and ^{207}Pb, respectively). Another natural uranium isotope, ^{234}U, (half-life of 2.4×10^5 years, 0.0056% of total natural uranium), is the third decay product in the ^{238}U radioactive decay series. This uranium isotope is generally considered in equilibrium (to slightly deficient) with its progenitor ^{238}U. The ^{235}U/^{238}U ratio, currently about 138, has increased over time due to faster radioactive decay of ^{235}U.

Uranium occurs in three oxidation states: U(IV), U(V) and U(VI), although U(V) is meta-stable and rarely found in nature.

In oxic conditions (with oxygen), the oxidised form, U(VI), is stable in aqueous solution, although mobility is controlled by pH and concentrations of inorganic and organic carbon. In oxic water at pH<5, uranyl, $U(VI)O_2^{2+}$, is the dominant dissolved form. At neutral pH, the mobility of U(VI) may be diminished by adsorption to iron oxides (e.g. Villalobos et al., 2001; Payne et al., 1994), phosphate minerals, organic matter and clays (Ivanovich, 1994). The affinity of U(VI) is especially strong for poorly-structured iron oxides (Kohler et al., 2004). Sorption of U(VI) is generally less strong at high pH≥8.

Dissolved U(VI) concentrations can be high in acidic mine waters. At higher pH, the uranyl ion forms stable complexes with carbonate ions, notably $UO_2(CO_3)_2^{2-}$ and at higher pH, $UO_2(CO_3)_3^{4-}$. Complexes with phosphate can occur at near-neutral pH (Drever, 1997) and with sulphide and fluoride under acidic conditions (Langmuir, 1978; Drever, 1997). Chlorine and SO_4 may be important ligands in saline waters (Porcelli & Swarzenski, 2003). Uranium(VI) also forms complexes with dissolved organic carbon at pH values between 3.5 and 7 (Higgo et al., 1993; Arey et al., 1999; Cothern & Lappenbusch, 1983), although U(VI) may be removed by sorption to humic acid (Wanty & Nordstrom, 1993).

In most continental waters (glaciers, rivers and lakes, i.e.

surface water excluding seawater), the uranium concentration ranges from less than 0.1 to 10 µg/l (approximately from <2.5 to 250 mBq/l). In Germany, regionally highly variable ^{238}U concentrations (from 0.5 to 310 mBq/l) were reported (Diehl, 2003). In Austria ^{238}U concentrations were found in the same ranges, up to 1 Bq/l for some ground waters from granite areas (Gruber et al., 2009).

In some regions of the world, where naturally radioactive minerals are particularly abundant, uranium concentration can reach much higher values, up to several mg/l. In areas with uraniferous granitic intrusions, e.g. in Finland, ^{238}U activity concentrations higher than 100 Bq/l have been detected (Saloneri & Huikuri, 2002).

Although ^{234}U and ^{238}U should be in secular equilibrium in rock, the energetic recoil associated with disintegration of ^{238}U, different chemical properties of intermediates (^{234}Th and ^{234}Pa) in the decay chain and differences in oxidation states between the two uranium isotopes often lead to a relative enrichment of ^{234}U in water. Uranium is much less mobile under reducing conditions. The reduced U(IV) form may be stabilised as uraninite (UO_2), although sorption of U(IV) to organic matter and clays has also recently been demonstrated (Bone et al., 2017).

Modern laboratory analysis by inductively coupled plasma mass spectrometry (ICP-MS) has facilitated collection of data for U in European water.

Uranium has no known metabolic function in the human body. Furthermore, due to its chemical properties, it is, like other heavy metals, nephrotoxic. The radiotoxic effect of uranium is considered to be low.

6.2.4 Thorium

Thorium (Th) is an actinide series element with an atomic number of 90 and atomic mass of 232. Thorium is radioactive with one main natural isotope, the primordial long-lived radionuclide ^{232}Th, which has the longest half-life (1.41×10^{10} years) of all known radioactive isotopes and comprises 99.98 % of thorium total mass. Thorium decays through a long radioactive decay series ending with the stable lead isotope ^{208}Pb.

The fate and mobility of thorium in environmental media are governed by its chemical and biological behaviour. The quadrivalent thorium compounds are very stable towards reducing agents. Thorium discharged as ThO_2 into surface waters from mining, milling and processing will be present as suspended particles or sediments in water because of its low solubility. Other soluble thorium ions in water will hydrolyse, forming a Th(OH)4 precipitate or hydroxy complexes. The hydroxy complexes will be adsorbed by particulate matter in water, with the result that most of the thorium will be present in suspended matter or sediment, and the concentration of soluble thorium in water will be very low. In most cases, sediment resuspension and mixing may control the transportation of particle-sorbed thorium in water; but in some cases, the concentration of dissolved thorium in waters may increase due to formation of soluble complexes with carbonate, humid materials or other ligands in the water. (Extract from Guogang et al., 2008.)

Low activity concentrations of ^{230}Th, ^{234}Th and ^{232}Th, up to 1 mBq/l, 0.4 mBq/l and 0.4 mBq/l, respectively, are found in shallow ground waters (IAEA, 2003), and they are typically not detectable at all. As such, Th activities and concentrations are rarely measured or reported in ground water studies. Low activities and concentrations are a function of paucity of Th-bearing minerals, slow dissolution, and preferential sorption (Langmuir & Herman, 1980).

6.2.5 Lead and polonium

^{210}Pb is a radioactive isotope of lead (Pb; Z=82) and is a member of the ^{238}U decay series, separated from ^{222}Rn by six short-lived alpha- and beta-emitters. ^{210}Pb is a beta-emitter with a half-life of 22.3 years. The ^{210}Pb isotope decays to ^{210}Po (polonium, Po) via the intermediate ^{210}Bi (bismuth, Bi) and has a half-life of 5 days by beta-decay. ^{210}Po (Z=84) has a half-life of 138 days and is an alpha-emitter.

^{210}Pb and ^{210}Po are therefore ubiquitously distributed in the rocks and soils making up Earth's crust, and in the atmosphere and natural waters as a result of decay of ^{222}Rn and subsequent deposition. The natural distribution of ^{210}Po in the environment is integrally dependant on that of its progenitor, ^{210}Pb. With a half-life of 22.3 years, ingrowth of ^{210}Pb is slow and its environmental transport largely controls the distribution of ^{210}Po. If ^{222}Rn decays in situ then the chemistry of ^{210}Pb will largely control the fate of ^{210}Po subsequently produced. In river/estuarine systems, for example, the concentrations of ^{210}Po and ^{210}Pb in water and sediments depend on the geology of the watershed and weathering conditions, while the geochemistry of the parent ^{238}U and its speciation also play a significant role. In surface and coastal waters, the deposition of ^{222}Rn decay products from the atmosphere is assumed to provide the main flux of ^{210}Po, particularly deposition of ^{210}Pb, while for deeper oceans it is more associated with in situ decay of ^{226}Ra. In marine and estuarine sediments ^{210}Po associates with settling and deposited materials, and its residence time in coastal waters may vary from a few months to 2 years. Applications of ^{226}Ra, ^{210}Pb and ^{210}Po allow estimation of rates at which reactive elements are removed from water by adsorption onto particles [see Section 6.5.5]. The possibility of health effects for humans and other organisms associated with ^{210}Po arises because of its α-particle emission—although, again, ^{210}Pb is also associated with relatively high radiation exposure (UNSCEAR, 2000). Indeed, ^{210}Po is considered to be one of the most toxic naturally occurring radionuclides, and one of the most important environmental radionuclides due to its wide distribution and potential for human radiation exposure through ingestion and inhalation. It has been widely reported that ^{210}Po is concentrated in many marine organisms, particularly in the digestive glands of molluscs and crustaceans, and is the largest contributor to the radiation dose received by marine organisms.
(Extract from Matthews et al., 2007)

6.2.6 Tritium

Natural tritium is produced in the atmosphere from the interaction of cosmic radiation with atmospheric nitrogen (Madruga, 2008). Anthropogenic production has disturbed the natural levels of tritium by nuclear weapons tests, and tritium is being released into the atmosphere through weapons manufacturing, the operation of nuclear power plants and reprocessing of nuclear fuels (Pujol & Sanchez-Cabeza, 1999; Nikolov et al., 2013). The average natural (cosmogenic) concentration of tritium in environmental waters has been estimated to range from 0.12 to 0.9 Bq/l (Mook, 2001; Palomo et al., 2007; Baeza et al., 2001). Tritium most commonly enters the environment in gaseous form (T_2) or as a replacement for one of the hydrogen atoms in water (HTO, called 'tritiated water' instead of ordinary, non-radioactive H_2O) (Budnitz, 1971; Nikolov et al., 2013). HTO's properties are very similar to those of water because of their relatively small difference in atomic weight. HTO is taken up by organisms and environmental media far more readily than molecular tritium. When tritiated water enters the body, it acts just like normal water, spreading throughout the body and delivering a uniform radiation dose to all soft tissues, with a biological half-life of about 10 days (Diehl, 2003; McKone et al., 1997).

Beginning in 1953, atmospheric testing of fusion weapons dramatically increased the inventory of tritium on the Earth's surface, with the highest increase resulting from nuclear tests in 1962 (Eriksson, 1965; Carter & Moghissi, 1977). These atmospheric bursts more than doubled the tritium inventory on the Earth's surface, with most of the tritium finally ending up in the world oceans (Miskel, 1973; Michel, 2005).

Tritium activity concentration is commonly reported in tritium units (TU). The TU is the ratio of tritium atoms to stable hydrogen-1 atoms or $^{3}H/^{1}H$, prior to weapons testing, and represents the number of tritium atoms per 10^{18} hydrogen atoms. Hence, one TU is equivalent to 0.118 Bq/kg of water.

Prior to nuclear testing, tritium concentrations in rain were of the order of a few tritium units, with the highest ones found in mid-continental areas. During 1963 tritium concentrations in precipitation peaked in the northern hemisphere, rising to a few thousand tritium units in most mid-continental locations (IAEA, 1981, 1992). Smaller increases were seen in the tritium concentrations of oceanic and continental surface waters in the mid-1960s (Stewart, 1966; Dockins et al., 1967). After deposition on the continents, tritium entered into vadose zones, surface water and ground water (Michel, 2005).

Tritium is important as a global transient tracer for studying dynamics in the hydrological cycle, recharge, renewal rate, flow velocity, and in conjunction with radiocarbon to determine ground water age (Libby, 1953; Pujol & Sanchez-Cabeza, 1999), see Section 6.3.

6.3 Measurement methods

6.3.1 Introduction

Typical radiometric procedures for measuring radioisotopes in water and sediments are alpha, beta and gamma spectrometry, liquid scintillation counting (LSC) or gas-flow proportional counting. Table 6-2 (EPA, 2000) presents the most commonly used procedures for some radionuclides. In Section 2.5 the methods are discussed in general. In this chapter the sample preparation process and determination for the radionuclides in water and sediments are discussed in detail.

Sample type	Radionuclides or radiation measured	Procedure
Water	Gross alpha	Liquid scintillation spectrometer Gas-flow proportional counter Solid-state scintillation detector
	Gross beta	Liquid scintillation spectrometer Gas-flow proportional counter
	^{137}Cs, ^{60}Co, ^{226}Ra (^{214}Bi), ^{232}Th (^{228}Ac), ^{234,235,238}U, ^{40}K	HPGe spectrometer, NaI(Tl)
	^{234,235,238}U; ^{238,239,240}Pu; ^{227,228,230,232}Th; other alpha emitters	Alpha spectrometry with multichannel analyser –solvent extraction; surface barrier detector; pulse height analyser
	^{3}H	Liquid scintillation spectrometer
	^{222}Rn	Gamma-ray spectrometry, emanometry, liquid scintillation counting
Sediment	^{137}Cs, ^{60}Co, ^{226}Ra (^{214}Bi), ^{232}Th (^{228}Ac), ^{234,235,238}U, ^{40}K	HPGe spectrometer, NaI(Tl)
	^{234,235,238}U; ^{238,239,240}Pu; ^{227,228,230,232}Th; other alpha emitters	Alpha spectrometry with multichannel analyser –pyrosulfate fusion and solvent extraction; surface barrier detector; pulse height analyser; 1-g sample; 16-h

Table 6-2
Typical radiometric procedures for radioisotope measurements in surface water and sediments (EPA, 2000)
Source: Modified from EPA, 2000

As a minimum, any method used to determine radionuclides in water must be capable of measuring activity with detection limits as specified in the Drinking Water Directive (European Union, 2013a); see Table 6-3.

Parameters and radionuclides	Detection limit (Bq/l)
Tritium	10
Radon	10
Gross alpha activity	0.04
Gross beta activity	0.4
^{238}U	0.02
^{234}U	0.02
^{226}Ra	0.04
^{228}Ra	0.02
^{210}Pb	0.02
^{210}Po	0.01
^{14}C	20

Table 6-3
Detection limit for methods used for radionuclides in water determination
Source: European Union, 2013a

6.3.2 Sampling of water and sample pre-treatment

In general, sampling and preparation of water samples for analysis is not an easy task due to various problems that may occur, which are not common to other sample matrices.

The problems are principally caused by two situations: the samples are two-phase systems (i.e., the water contains some

Water sampling in a pump house of a waterworks, Austria
Source: Tamara Gruber

insoluble material) and the sometimes unpredictable behaviour of many substances at very low concentrations (Engelbrecht, 2012). Another issue could be various compositions of available natural waters as well as different pre-treatment procedures needed for different analyses. In the case of ground water samples, the sample composition may vary according to the geology surrounding the natural spring.

Since some radionuclides may stick to the wall of sampling vials, the sample is usually acidified in order to reduce this risk. The longer the storage time before analysis, the more important it is to acidify water samples (Engelbrecht, 2012). In most cases acidification is a good option, but, when measuring ^{222}Rn in water by some direct method with available alpha detectors, acidised samples may cause problems during measurements. Also for measuring ^{14}C concentration in ground water in the case of some hydrological study, acidification of water sample allows ^{14}C to escape from the volume. Most environmental waters are close to neutral, and acidification of 0.1-0.5 N is adequate. At this acidity, radioactive substances in particles in the sample can be leached (perhaps slowly) and appear in the solution, resulting in a considerable increase in the original soluble radioactivity (Engelbrecht, 2012). Another way to prevent sorption of radionuclides on vial's walls between sampling and analysis is to freeze samples. This method is only practical for small samples, and there could be some problems with treating insoluble portions.

If the sample has been stored before analysis, particularly at its natural acidity, it is advisable to transfer the sample to a second container with a solution, usually an acid, in which the sought-for activity is soluble (Engelbrecht, 2012). The 'wash' solution can be added to the original solution or analysed separately. Special attention has to be given to verifying the washing procedure; it has to be verified experimentally. If suspended and dissolved fractions need to be separated for the analysis, then the safest pre-treatment procedure is to filter water through membrane filter paper during sample collection on the field and acidify the sample immediately after collection. The acid can already be introduced into the receiving flask during filtration. This is the only way to ensure that water is not in contact with container walls until after acidification.

During sampling in the field, it is sometimes impractical to follow a pre-defined method, in which case the water sample can only be collected *in situ*, and as soon it arrives in the laboratory, it has to be acidified immediately prior to filtration. Any inactive carriers or radioactive tracers used in the analysis should be added as soon as possible to the sample, preferably before any other pre-treatment method (acidification, filtration or evaporation).

When measuring water samples with gamma spectrometry, it is essential to pay special attention to possible change in counting geometry which will affect the efficiency of the measurement. Changes in counting geometry may occur when finely divided species become fixed on the container walls during counting. It is important to filter the sample, evaporate and acidify it if the suspended material is soluble in diluted acid.

MnO_2 coprecipitation can be used for pre-concentration of radionuclides from large water volumes. In this method, the water sample is collected in a large container and with some intermediate steps (adding HCl, $KMnO_4$ and NaOH; see Lehto et al., 2011), a MnO_2 suspension is built and the radionuclides will coprecipitate with MnO_2. The precipitate formed is collected after settling down to the bottom of the container. The MnO_2 precipitate is finally dissolved in a small volume (<5 l) and transferred to a plastic bottle, which is prepared for gamma-spectrometry analysis (Lehto et al., 2011).

For measuring ^{222}Rn concentration in water, there are some methods which require special sampling techniques; this will be explained in Section 6.3.5. For simultaneous measurements of different radioisotopes in water samples, it is essential to collect water samples in glass bottles and to take the first sample for ^{222}Rn in water measurement or to collect a separate sample for this analysis. After that, the rest of sample should be acidified, and by bubbling air through the water all remaining ^{222}Rn could be completely expelled. There are some conventional radiochemical analysis procedures which are used for sample preparation for different measurement methods of separate radionuclides of interest.

For surface water some of the sampling methods are automatic and continuous, generally designed to give an early warning in case of an accidental release. In all cases, additional information on the river flow rate is very important. Samples can be taken continuously (or daily) and are then bulked into a monthly or quarterly analysis; or alternatively, spot samples are taken periodically and analysed individually. The time and frequency of sampling are very important for rivers with large seasonal hydrological variations (Engelbrecht, 2012). In collecting surface water from rivers, care should be taken to avoid stagnant areas. Lake water samples should not be taken near the shoreline.

International Standards dealing with water sampling are the ISO 5667 group, under the general title: Water quality – Sampling. They provide guidance for different water samplers (ISO 5667-1:2006 and ISO 5667-3:2018); lakes (ISO 5667-4:2016), rivers and streams (ISO 5667-6:2014), marine water (ISO 5667-9:1992), and ground water (ISO 5667-11:2009).

6.3.3 Determination of gross alpha/beta activities

Gross alpha/beta activity measurements are widely applied as a screening technique as the first analysis of any kind of water sample. These analyses are obligatory for drinking water according to many different national and international standards and recommendations. The main advantages of the gross alpha/beta methods are the relatively low costs, rapidity and simplicity (Jobbagy et al., 2014). Although gross alpha/beta measurement is one of the simplest methods, it is also one of the most disputed radioanalytical methods because the determination of gross alpha and beta activities faces some specific problems that may affect measuring results. There are many sources of interference in gross alpha/beta measurements that may corrupt the reliability of the measurement results (Arndt & West, 2004; Rusconi et al., 2006; Semkow et al., 2004; Montaña et al., 2012). During gross alpha/beta activity measurement, a mixed radionuclide composition must simultaneously be measured (Jobbagy et al., 2014). Drinking-water samples may contain different, naturally occurring alpha (^{238}U, ^{234}U, ^{232}Th, ^{226}Ra and ^{210}Po) and beta (^{40}K, ^{228}Ra and ^{210}Pb) emitters, and artificial radionuclides (^{241}Am, ^{90}Sr) in various concentrations (UNSCEAR, 2000). Moreover, most of these are members of a complex decay chain; therefore, the ingrowths of the daughter products influence the measurement result.

The most common approach for analysing drinking water for gross alpha and gross beta activities (excluding radon) is to evaporate a known volume of the sample to dryness and measure the activity of the residue (Engelbrecht, 2012). When water samples have a high content of total dissolved solids, there is a concern that reliability and sensitivity of the method for alpha determination may be reduced as alpha radiation is easily absorbed within a thin layer of solid material. The determination of gross beta activity using the evaporation method includes the contribution from ^{40}K (Engelbrecht, 2012). An additional analysis of total potassium is therefore required if the gross beta screening value is exceeded. The co-precipitation technique excludes the contribution due to ^{40}K; therefore, determination of total potassium is not necessary. This method is not applicable for assessing water samples containing certain fission products, such as ^{137}Cs. However, under normal circumstances, concentrations of fission products in ground water used for drinking water (natural springs and wells) are extremely low, below the detection limits.

According to the Drinking Water Directive (Council Directive 2013/51/Euratom; European Union, 2013a), the analysis method used for gross alpha and gross beta measurements in water must, as a minimum, be capable of measuring activity concentrations with a detection limit of 0.04 Bq/l and 0.4 Bq/l respectively. The screening level recommended for gross alpha activity is 0.1 Bq/l and for gross beta activity is 1.0 Bq/l. The most common standard methods for gross alpha/beta measurements are proportional counter or solid-state scintillation counters (ISO 9696, 2007; ISO 9697, 2008; ISO 10704, 2009). The counting efficiency of these methods is strongly affected by the total dissolved solids and the surface density of the sample (Jobbagy et al., 2014).

In addition to the above techniques, ultra-low-level alpha/beta discrimination liquid scintillation counters (LSCs), because of their high detection efficiency (up to 100%) and low background rate, are useful tools for determining alpha- and beta-emitting radionuclides (Schönhofer, 1995). The basic steps of the chemical pre-treatment during sample preparation for LSC are relatively simple. The main steps are thermal pre-concentration, pH adjustment and sample mixing with scintillation cocktail (ISO 11704, 2009). There are a lot of advantages in using LSC for gross alpha/beta measurements:

- samples do not suffer from self-absorption;
- LSC methods show the best results for measuring low-energy beta emitters such as ^{3}H and ^{14}C (Schönhofer, 1995);
- and LSC is a very accurate method for measuring radon in water (Salonen, 2010; Todorović et al., 2014; Gruber et al., 2009; Nikolov, 2018).

Furthermore, semi-qualitative information can be obtained in the form of alpha-beta spectra. The main disadvantage is quenching (chemical, colour and physical), which reduces the counting efficiency especially in the case of ground water measurements as that water can very often be coloured and/or contain some other chemical elements and impurities. To overcome this problem, there are some possibilities in adjusting appropriate Pulse Shape Analysis (PSA) parameters (Stojković et al., 2017). Another issue could be the separation of beta energies from all alpha energies, which can be difficult because it depends on many factors in LSC counting (Rusconi et al., 2006; Schönhofer, 2012). So, the optimal setting of the different parameters (type of vial, cocktail, alpha/beta pulse discrimination, counting efficiency) is essential for gross alpha/beta measurements by LSC (Jobbagy et al., 2014; Stojković et al., 2017).

It has been shown that gross methods are not as simple as usually stated (Montaña et al., 2012; Semkow et al., 2004), and that they are far from accurate (Jobbagy et al., 2014). Advances in gamma spectrometry, alpha spectrometry, and LSC and spectrometry for alpha and beta emitters have obviated many of the reasons for measuring total activity, but low-cost gross measurements, preferably applying alpha/beta-separated LSC measurements (Pujol & Sanchez-Cabeza, 1999; Zapata-García, et al., 2009; Palomo et al., 2011), may still serve as a screening procedure (Engelbrecht, 2012). Some recommendations say that gross alpha/beta measurement should be avoided and only used for monitoring after the radionuclide composition is known from radionuclide-specific analysis of representative samples (Jobbagy et al., 2014).

6.3.4 Measurement methods for uranium and its daughter radioisotopes

Because of their greater mobility, uranium and ^{230}Ra are usually depleted relative to ^{230}Th on the surfaces of soil or rock particles, e.g., minerals and particulate organics (Engelbrecht, 2012). ^{238}U, ^{234}U, and ^{226}Ra are, therefore, present in greater abundance in ground water than ^{230}Th. ^{222}Rn enters the water by alpha recoil and/or leaching, and migrates. ^{210}Po and ^{210}Pb also migrate to a lesser extent and are in disequilibrium with other isotopes in the ^{238}U series (Upchurch et al., 1991).

Determination of uranium by measuring radioactivity is a highly sensitive technique; it requires, however, knowledge of the other radionuclides present in the sample. Either the uranium must be separated from interfering radionuclides, or it must be possible to make appropriate corrections for their interference. Uranium in equilibrium with its decay products may be conveniently determined by measuring the gamma activity of its daughters. There are different techniques used to determine uranium in ground water samples, such as **alpha spectrometry, Neutron Induced Fission Technique, and Inductively Coupled Plasma Mass Spectrometry (ICP-MS)** (see Section 2.5).

The main advantage of the ICP-MS technique is its ability to measure multiple isotopes of the same element. ICP-MS instrumentation can also precisely measure isotope ratios. Rapid techniques with ICP-MS have been developed e.g. by Qiao & Xu (2018).

There are numerous alpha-counting methods available for uranium that has been separated from other alpha-emitting nuclides. But there are also some complications in those analyses. The most important source of error results from the variation in abundance of the uranium isotopes. The abundance ratios vary more in natural ground waters than in primary uranium minerals, as is to be expected from geochemical considerations of the uranium series (Barker et al., 1965). Alpha spectrometry, using solid-state detectors, is a method frequently used to determine individual uranium isotopes, even when other alpha emitters are present. Neutron-activation methods are suitable for analysing uranium in very low concentrations.

Isotopic analysis for most of the above radionuclides could be performed with LSC using ultra-low-level spectrometers. To measure $U_{natural}$ and ^{226}Ra, it is very important to acidify samples with HNO_3 down to a pH of about 2 and filter to remove the suspended solid particles (Pereira et al., 2015). ^{226}Ra can be measured by an indirect method using ^{222}Rn as a tracer after isotopic equilibrium is reached following the procedure described by Forte et al. (2007). It is very important to remove all radon present in the sample before measuring ^{226}Ra. The uranium isotopes have to be previously extracted with a mixture of a scintillation cocktail and bis-(2-ethylhexyl) phosphate in accordance with Salonen (1993) and Salonen & Hukkanen (1999). The Pulse Shape Analysis (PSA) and the best counting time have to be previously evaluated for each sample. The detection limits that can be achieved for the activity of uranium isotopes are 1.5 mBq/l (0.15 µBq/l, for $U_{natural}$), 0.01 Bq/l for ^{226}Ra. Liquid-liquid extraction, ion-exchange chromatography, and barium sulphate or barium carbonate precipitation are the usual separation techniques used for ^{226}Ra. Analysis of ^{226}Ra may involve inferring the radium activity from measuring the ingrown daughter, ^{222}Rn (Engelbrecht, 2012), or by applying pulse shape analysis to determine ^{226}Ra alpha particles.

To determine low-level activity concentrations of ^{210}Po in water samples, large-volume samples (> 1 l) have to be provided (Engelbrecht, 2012). The samples have to be pre-concentrated, since direct evaporation of large volumes is very time-consuming and susceptible to loss of polonium. Therefore, co-precipitation with iron hydroxide, followed by a solvent extraction step with an extractant, has commonly been used. Additional chemical purification using strontium resin (Vajda et al., 1997) or various solvent extractions prior to the final auto-deposition of polonium may be applied. Methods to determine ^{226}Ra, ^{228}Ra, ^{210}Pb and ^{210}Po are discussed by e.g. Landstetter & Katzlberger (2005).

6.3.5 Radon

Most of the methods used for ^{226}Ra in water measurements rely on an indirect method using ^{222}Rn as a tracer after isotopic equilibrium is reached about 30 days after sampling. So the methods described for ^{222}Rn in water measurements may also be used for ^{226}Ra in water measurements.

^{222}Rn in water is mainly of concern in ground water as it mostly originates from the surrounding bedrock. There are international standards dedicated to radon in water measurements such as ISO 13164-3 (ISO 13164-3, 2013) and ISO 13164-4 (ISO 13164-4, 2015). Beside the technical parts, they describe the principles of the methods, some of the sampling issues and approaches, transportation and storage conditions. Those aspects are the most important and challenging ones for measuring ^{222}Rn in water in order to get a representative sample and reliable measurement results (Gruber et al., 2009, Jobbagy et al., 2017).

The most commonly used measuring methods for ^{222}Rn in water measurements are **gamma-ray spectrometry, emanometry and Liquid Scintillation Counting (LSC)** (Jobbagy et al., 2017) (see Section 2.5 for a general description of the methods). Those methods cover a wide range of techniques from simple, cheap but straightforward ones to more sophisticated and expensive detection techniques. The Drinking Water Directive from 2013 (European Union, 2013a) allows EU Member States to use various screening strategies to indicate the presence of radioactivity in water intended for human consumption, but these methods have to be reliable (Jobbagy et al., 2017). There are some requirements for minimal detection limits and sampling techniques from drinking water supplies. According to the directive, techniques for measuring radon concentration in water have to be capable of measuring activity concentrations with a detection limit of 10 Bq/l for radon, which is 10% of its parametric value of 100 Bq/l (European Union, 2013a; Jobbagy et al., 2017). All the aforementioned detection techniques comply with this detection limit requirement.

Measurement methods for radon in water can be grouped according to some key aspects, such as the application of phase transfer, analysis location, detection systems (Jobbagy et al., 2017). A technique that does not require any phase transfer is a direct measurement of the sample by gamma spectrometry. Some other techniques involve phase transfer; during this process ^{222}Rn is transferred from the aqueous phase to another phase. In the case of emanometry techniques, it is transferred from liquid to gas phase. In the case of liquid scintillation counting, the target matrix is an organic phase of a liquid scintillation cocktail which traps ^{222}Rn and prevents it from emanating from water to outer air. Contrary to those *in situ*, laboratory measurements require careful transport of the samples and storage under well-defined conditions (Jobbagy et al., 2017). Samples should be measured as soon as possible after sampling due to the short half-life of ^{222}Rn (3.8 days), and decay corrections must be applied not only for time elapsed between sampling and measurement but also in the case of methods which require longer measurement times.

The sampling of water presents the main source of error in measuring radon in water for both *in situ* and in laboratory measurement methods, so it is not easy to get a reliable and representative sample for the analysis. There are different approaches with the same aim: if possible it is necessary to assure that water will not be in contact with air during sampling and sample preparation. One way to overcome this is to take the samples directly into measuring vials. For the LSC method the best option is to put the liquid scintillation cocktail in the measuring vial and then to add an appropriate volume of water directly *in situ*; after mixing water with appropriate scintillation cocktail the risk of losing some ^{222}Rn activity concentrations is minimal.

In **gamma spectrometry**, ^{222}Rn activity concentration is measured via activity concentrations of its daughter products ^{214}Bi and ^{214}Pb. As those radioisotopes have a short half-life, secular radioactive equilibrium is established within 3 hours. The main problem for measuring radon in water by gamma spectrometry is the presence of ^{226}Ra in water. When ^{226}Ra is present in the water sample, due to constant production of new radon in the sample it is necessary to wait for secular equilibrium between ^{226}Ra and ^{222}Rn, which is established after more than one month. Subsequently, the measurement should be repeated in order to precisely determine the activity concentration of ^{222}Rn in water. Solid-state scintillation detectors based on NaI are used only for screening, while qualitative and quantitative analysis by gamma spectrometry requires detectors with better resolution, so high-purity Germanium (HPGe) detectors are mostly used. A lot of factors can affect the efficiency of detection, and therefore the accuracy of the performed measurement of radon in water, such as sample density, homogeneity which is directly correlated to the water temperature, suspended materials and air bubbles. It is necessary to purge the immediate surroundings of the detector and sample during measurement as recommended by ISO 13164 standard (ISO 13164-3, 2013) in order to diminish the influence of radon in the air which could be present in the laboratory (from outdoors and/or building materials).

Emanometry is based on sample degassing followed by alpha-particle detection by various detection systems (Jobbagy et al., 2017). When a water sample is degassed, ^{222}Rn is transferred to a measurement cell either by an inert gas flow or air circulation or vacuum. Several detection techniques can be applied to determine radon activity concentration in the gas phase, including scintillation cells such as Lucas cell, semiconductor silicon detector and ionisation chamber. Most emanometry techniques are sensitive to water temperature, but even more important is detector contamination. As ^{222}Rn also has longer-living daughter products (like ^{210}Po), it is essential to check detector contamination prior to measurement in order to ensure that there is no build-up. Another issue is that some waters can contain ^{220}Rn (thoron) which can affect the measurement results, but there are instruments which can differentiate those two radioisotopes. One degassing approach is to place a water sample in a degassing cell and introduce radon-free air or inert gas in a closed system (Jobbagy et al., 2017). This allows radon to be purged from the sample and directed to the counting cell or detector by the appropriate pump. A second degassing approach will be to inject a small volume of sample directly into a partially vacuumed scintillation cell with a syringe. This approach ensures that radon is released from the water, after which by introducing radon-free or inert gas the pressure is adjusted to normal ambient pressure. There are few instruments specially designed for radon measurements, with some additional kits for radon in water measurements, that are a good choice especially for *in situ* and rapid low-cost measurements. However, if better accuracy is needed, then they do not perform as well as the laboratory measurement methods.

Liquid scintillation counting (LSC) for radon measurement is based on the extraction of ^{222}Rn from the water to the immiscible scintillation cocktail (Jobbagy et al., 2017). Mixing an appropriate volume of water sample (around 10 ml) with water immiscible scintillation cocktail which is already in the measuring vial gives a two-phase sample, with clearly separated phases. All ^{222}Rn from the water sample is transferred to the scintillation cocktail and trapped in it. It is important to take the samples well below the surface and to introduce them slowly into the LSC vial below the cocktail by using a gas-tight syringe. After preparation (mixing and shaking) of the sample, the LSC vial is stored in a dark place and at a stable temperature for around 3 hours, after which time the sample is ready for measurement. For LSC measurements the most important issue is to adjust alpha/beta discrimination and to avoid effects of photoluminescence and chemiluminescence. There are different scintillation cocktails that can be used for measuring ^{222}Rn in water. The degree of extraction of ^{222}Rn progenies and therefore the calibration errors depend on the scintillation cocktail, and it is suggested that the cocktails should be studied case-by-case (Jobbagy et al., 2017). The great advantage of this method is the volume of the sample needed for analysis, for one measuring sample only 10 ml, and stability of the obtained sample; once radon is trapped in the scintillation cocktail, it cannot escape easily.

For all the above methods for measuring ^{222}Rn in water, the measurement uncertainties are typically below 20% (coverage factor, k=1). The main difference between these methods is the initial sampled volume; it varies from 10 ml up to a few litres, duration of the measurement and the possibility to perform *in situ* measurements. Emanometry methods are usually portable, and there are some small LSC detectors which can also be used in the field, but they do not have appropriate shielding, and therefore those LSC detectors are not suitable for measuring low-activity concentrations of ^{222}Rn in water. It is almost impossible to use *in situ* gamma spectrometry to measure ^{222}Rn in water due to a very high background in the case of HPGe detectors and very poor resolution in the case of NaI detectors.

The biggest problem that all methods suffer from measuring ^{222}Rn in water is to calibrate the instruments. To improve the situation of the available calibration options, there were some international efforts to make reliable primary radon standards and to further develop secondary standards (De Felice, 2007; Jobbagy et al., 2017). Due to the short half-life of ^{222}Rn, the method most commonly used to calibrate instruments is the

^{226}Ra calibration approach, but there are also some practical examples of radon-in-water standard sources (Forte et al., 2007). For calibrating gamma detectors there are two options, experimentally by means of a ^{226}Ra standard source or by using Monte Carlo simulations, which need a lot of precise parameters as input. On the other hand, emanometry methods allow calibration of alpha counting efficiency of a scintillation cell by using radon in air calibration chambers with accurately established ^{222}Rn activity concentrations (Jobbagy et al., 2017). In the case of LSC, the ^{226}Ra standard is usually used (Todorović et al., 2014).

All the above methods have low detection limits and fulfil the requested 10% from guidance levels for specific radioisotopes.

6.3.6 Measurement methods for tritium

Natural levels of tritium, especially in ground water, are very low, so the water samples have to be purified by distillation, followed by an isotopic enrichment procedure using electrolysis through a direct current (Florkowski, 1992). In order to increase the tritium concentration to an easily measurable level, electrolytic enrichment must be applied (Nikolov et al., 2013). The best method for measuring low activity concentrations of ^{3}H in water samples is LSC. After electrolysis and distillation, one aliquot of water is withdrawn to a scintillation vial with a scintillation cocktail. Tritium (and its daughter ^{3}He) can also be measured using mass spectrometry, but other dissolved gases (H_2O, CO_2, O_2, N_2, etc.) must be removed first (Clark & Fritz, 1997). Due to the specific characteristics of tritium (gas, relatively easily oxidised to HTO), combined with the omnipotent presence of water vapour, the assay of low levels of tritium requires consideration of various types of contamination, the magnitude of which depends strongly on specific procedures of sample handling, on the ambient tritium concentrations during sampling, storage and analysis, and on the type of containers used to store the samples before the analysis (Engelbrecht, 2012). With the electrolytic enrichment technique, detection limits on the order of 0.1 – 0.01 TU (11.8 – 1.18 mBq/kg) is achievable (see Section 6.2.5 for the definition of TU). In ground water the expected activity concentrations of ^{3}H are in the range of 1-3 TU, which means that electrolytic enrichment is necessary for the analysis of ground water samples as the results are mainly used in hydrological studies.

6.3.7 Radionuclides in river sediments

Sediment is an indicator and accumulator of radionuclides that are insoluble and adsorbed on insoluble material of the aquatic system. Sediment in all types of water may be a source of contamination to aquatic organisms. For example, contaminated sedimentary materials used as fertilisers may increase the radioactivity levels of soil (IAEA, 1989).

Sampling procedure

Conventional collection of sediment is done by a dredge dropped from a boat. The dredge mechanism is activated by contact with the benthos. For river sediments, it is of interest to describe the stream flow conditions that lead to benthal deposition and the movement of the sediment, as well as the characteristics of the sediment such as particle-size distribution, soil type, ion-exchange capacity, and organic content. Drying at low temperatures (50 °C) to avoid the loss of radionuclides from the soil and hand mixing of soils or sediments prior to sub-sampling should be acceptable for gamma spectrometry where a relatively large sub-sample is used (e.g. 150 - 500 g). However, drying, grinding, and sieving prior to sub-sampling should be carried out where a small sub-sample (e.g. 5-10 g) is to be taken for radiochemical analysis (Engelbrecht, 2012). Commercially available grinders, mills, pulverisers, mixers and blenders are suitable. Hardened metals are best for the grinding surfaces, and it is not likely that radioactive contamination will be introduced into a sample with this equipment, except by cross-contamination from a highly radioactive sample. To prevent this, thorough cleaning of equipment between samples is advisable. At this stage, a portion may be taken for gamma-ray spectrometry.

If vegetation and organic debris are not discarded, the roots, mat and vegetation should be cut into very fine particles so as to be distributed evenly; if they are to be discarded, these materials should be collected and weighed. Stones should be collected, weighed, and discarded. It can be assumed that the large rocks contain an insignificant fraction of the activity and are in effect voids in the sample. The mass of the discarded material should be taken into account, but not in calculating the specific activity of the sediment. It provides, however, additional information to indicate the overall makeup of the growing area.

The sediment should be crushed, ground or pulverised to a particle size predetermined by the analytical requirements. The need for preparing the material will also depend on the nature of the soil; for example, beach sand may not need grinding. In general, the soil should pass a mesh size of 2 mm. Activity in soil sediment samples is reported on a dry weight basis in Bq/kg and on an area basis in Bq/m^2 (Engelbrecht, 2012).

Methods for sample preparation

Analysis of beta emitters

Laboratory sample preparation is an important step in the analysis of sediment samples for beta-emitting radionuclides. The laboratory will typically have a sample preparation procedure that involves drying the sample and grinding the soil so that all of the particles are less than a specified size to provide a homogeneous sample. A small portion of the homogenised sample is usually all that is required for the individual analysis (Engelbrecht, 2012).

Analysis of gamma emitters

There is no special sample preparation required for counting sediment samples using a germanium detector or a sodium iodide detector beyond placing the sample in a known geometry for which the detector has been calibrated. The samples can be measured as they arrive at the laboratory, or the sample can be dried, ground to a uniform particle size, and mixed to provide a more homogeneous sample.

Gross beta analysis

Once the sediment sample has been prepared, a small portion is dissolved, fused or leached to provide a clear solution containing the radionuclide of interest. The only way to ensure that the sample is solubilised is to completely dissolve the sample. However, this can be an expensive and time-consuming step in the analysis. In some cases, leaching with strong acids can consistently provide greater than 80% recovery of the radionuclide of interest and may be acceptable for certain applications. Gross beta measurements may be performed on the material that has not been dissolved. After dissolution, the sample is purified using a variety of chemical reactions to remove bulk chemical and radionuclide impurities. The objective is to provide a chemically and radiologically pure sample for measurement. Examples of purification techniques include precipitation, liquid-liquid extraction, ion-exchange chromatography, distillation, and electrodeposition.

6.4 Activity concentration of natural radionuclides in water

Table 6-4 shows the results of some studies performed in European countries to determine the radionuclide content in ground and surface water.

Table 6-4
Concentration of natural radionuclides in water in some European countries (means and ranges), methods used for the analysis, objectives of the study and spatial resolution

Country	Media	Radioisotope	Reference level (Bq/l)	Activity concentration (Bq/l)	Methods	Objectives	Spatial resolution	Reference
Finland	Ground water: drilled and dug wells	^{226}Ra	0.5	Drilled wells: median: 0.06 mean: 0.30 maximum: 9.5	Gamma spectrometry 5" × 4" NaI(Tl)	Determination in 308 drilled and 58 dug wells in Helsinki region	Study area of about 400 km^2; geologically highly variable, dominated by granites, amphibolites and migmatites	Asikainen et al. (1979)
				Dug wells: median: 0.004 mean: 0.015 maximum: 0.37				
		^{222}Rn	100	Drilled wells: median: 925 mean: 2.04×10^3 maximum: 23.6×10^3	Gamma spectrometry 5" × 4" NaI(Tl)			
				Dug wells: median: 31.5 mean: 96.2 maximum: 1.37×10^3				
	Drinking water from drilled, dug wells and springs; ground water in bedrock and soil	^{222}Rn	100	Drilled wells: mean: 2.4×10^3 Dug wells: mean: 220 Ground water in bedrock: mean: 1.02×10^3 Ground water in soil: mean: 92	Liquid scintillation counter	Systematic study of natural radioactivity in drinking water in Finland		Salonen (1988)

Country	Media	Radioisotope	Reference level (Bq/l)	Activity concentration (Bq/l)	Methods	Objectives	Spatial resolution	Reference
Finland (cont'd)	Drinking water from drilled, dug wells and springs; ground water in bedrock and soil (cont'd)	Gross alpha	0.1	Ground water in bedrock: mean: 2.4 Ground water in soil: mean: 0.17	Conventional radiochemical procedure	Systematic study of natural radioactivity in drinking water in Finland		Salonen (1988)
		Gross beta	1	Ground water in bedrock: mean: 2.3 Ground water in soil: mean: 0.33				
		U	For ^{238}U: 3.0 For ^{234}U: 2.8	Drilled wells: ^{238}U mean: 3.9 Dug wells: ^{238}U mean: 1.8 Ground water in bedrock: mean: 4.2 Ground water in soil: mean: 0.61	Alpha spectrometry			
		^{226}Ra	0.5	Drilled wells: mean: 0.55 Dug wells: mean: 0.23 Ground water in bedrock: mean: 0.44 Ground water in soil: mean: 0.04	Separation with a barium sulphate method, zinc-sulphide scintillation counter			
		^{210}Pb	0.2	Drilled wells: mean: 0.43 Dug wells: mean: 0.076 Ground water in bedrock: mean: 0.43 Ground water in soil: mean: 0.08	Alpha spectrometry			
		^{210}Po	0.1	Drilled wells: mean: 0.22 Dug wells: mean: 0.035 Ground water in bedrock: mean: 0.22 Ground water in soil: mean: 0.04	Alpha spectrometry			
	Drinking water	^{222}Rn	100	mean: 460	Liquid scintillation counter spectrometer	Random sampling: 500 wells (all drilled wells and a random sample of dug wells)		Vesterbacka et al. (2005)
		^{226}Ra	0.5	mean: 0.05	Alpha spectrometry			
		^{234}U	3.0	mean: 0.35				
		^{238}U	2.8	mean: 0.26				
		^{210}Pb	0.2	mean: 0.04				
		^{210}Po	0.1	mean: 0.05				
Greece and Cyprus	Drinking water	^{222}Rn	100	Greece: range: 0.8–24 mean: 5.4	Alpha spectrometry	Cyprus and Greece (Attica, Crete), 42 water samples collected from various sites		Nikolopoulos et al. (2008)
				Cyprus: range: 0.3–219 mean: 5.9				
Hungary	Drinking water	^{222}Rn	100	mean: 5.56 maximum: 24.3	Lucas cell	125 tap water, 29 wells, 27 springs frequently visited and regularly used in Hungary		Somlai et al. (2007)
	Spring water	^{222}Rn	100	range: 153–219	Liquid scintillation spectrometry	Csaoka Spring in Sopron Mountains, West Hungary	Mainly gneiss and mica schists, formed from granitic and clastic sedimentary rocks	Freiler et al. (2016)
Poland	Ground water	^{222}Rn	100	median: 2.03 mean: 541.4 maximum: 3.04×10^5	Ultra-low-level liquid scintillation spectrometer	Analysis of ground water from southern Poland, focused on shallow-circulation ground water from first aquifer; >500 measurements from 2008–2013	Mainly Sudeten Mountains, north-east part of Bohemian Massif (the largest crystalline massif in Central Europe)	Przylibski et al. (2014)
		^{226}Ra	0.5	median: 0.05 mean: 0.19 maximum: 1.77				
Spain	Ground water, wells and springs	^{222}Rn	100	< 30	Alpha spectrometry	La Garrotxa volcanic region, Catalonia, Spain, with 53 points selected to measure radon concentration (42 private and public wells and 11 springs)	La Garrotxa region mainly consists of quaternary volcanic and non-volcanic formations over a tertiary substratum	Moreno et al. (2014)
	Spring water	^{222}Rn	100	range: 1.4–104.9	Ultra-low-level liquid scintillation counting	Spring water in the south of Catalonia (15 samples)	Natural spring water located in two contrasting lithologies: igneous rocks (granites) and soils of marine origin (e.g. limestones, marls and clays and carbonate formations)	Fonollosa et al. (2016)
		^{226}Ra	0.5	range: $2–91 \times 10^{-3}$	Zinc-sulphide scintillator counter			
		^{238}U; ^{234}U	For ^{238}U: 3.0 For ^{234}U: 2.8	For ^{238}U: $< 0.2–21.6 \times 10^{-3}$ For ^{234}U: $4–55 \times 10^{-3}$	Alpha spectrometry			

6.5 Applications

6.5.1 Introduction

Most of the world's population is directly affected by the availability of water resources and the means to supply them. All natural or anthropogenic processes that modify the water flux and quality have a direct influence on human lives. Radioactive tracers can be extremely useful for studying such processes, and thus help to investigate the common problems and find adequate solutions. Problems such as water pollution, erosion, river sedimentation, and the loss of storage capacity of water reservoirs, thereby reducing fish stocks, can cause great damage and negatively affect the well-being of local populations (IAEA, 2015). There are several radionuclides commonly used as environmental tracers (e.g. Tritium (HTO), ^{82}Br, ^{198}Au, ^{210}Pb/^{210}Po, U/Th/Ra isotopes and the geological dating). Also anthropogenic radionuclides still available in the environment from nuclear weapons tests and nuclear accidents can be used as tools for environmental studies (e.g. ^{137}Cs). This topic is not within the scope of this Atlas, but more details can be found in e.g. IAEA (2015). Also natural radionuclides are used for environmental studies and applications such as ground water dating, mixing of fresh and saline water or sedimentation rates. These applications are studied in more detail below.

6.5.2 Ground water dating

Natural radionuclides have a wide range of applications for assessing ground water age, provenance, processes and fluxes. Radionuclides can be used to trace the time since exposure at surface and hence date the ground water recharge.

One of the radioisotopes most widely used for age dating is ^{14}C which is produced by cosmic-ray bombardment in the upper atmosphere and decays by beta-emission with an established half-life of 5730 years. Although complications arise with the contribution of other sources of carbon (biogenic and rock carbonate) and require appropriate corrections, this method has been effective for determining ground water age up to around 35 000 years. Applications of measuring ^{4}He, which is produced in the deep subsurface by radioactive decay of uranium and thorium, can supplement age data acquired from ^{14}C.

Tritium has also been widely used for age dating. Tritium is also produced naturally by cosmic-ray bombardment in the upper atmosphere and decays to ^{3}He through beta emission with a half-life of 12.4 years. Activities of ^{3}H rose sharply in the atmosphere as a result of atomic bomb testing in the 1950s, providing a greatly enhanced tracer for hydrogeological applications. Since then, however, its value has gradually diminished as the ^{3}H activities of atmospheric precipitation has decayed from a 1963 peak to near-background values, and age estimates do not give solutions. Hydrogeologists tend to quote ^{3}H in tritium units (where 1 TU is equivalent to 0.118 Bq/l). Today, precipitation in the northern hemisphere has a ^{3}H activity of around 5–30 TU and in the southern hemisphere slightly lower value of 2–10 TU, compared to previous values in the thousands, making ^{3}H a much less distinctive isotopic tracer in modern investigations.

Short ground water residence times also have been investigated using the combined ^{3}H-^{3}He technique, which extends the capability of ^{3}H as a tracer. The amounts of ^{3}He and of ^{3}H remaining, together establish the total original ^{3}H, which in turn determines the date of ground water recharge. The ^{3}H-^{3}He method has been useful for determining age up to around 40 years (Plummer et al., 2001).

By contrast, the long-lived ^{36}Cl and ^{81}Kr radionuclides have been successfully used to investigate very old ground water on long flow paths in aquifers, and beyond the scope of ^{14}C dating (Edmunds et al., 2003; Shand & Edmunds, 2009). ^{36}Cl decays with a half-life of 301 000 years and is potentially suitable for dating ground water of around 1 million years or more. ^{81}Kr decays with a half-life of 229 000 years with a similar age-range capability (Sturchio et al., 2004). As the radionuclide ^{129}I occurs both naturally as a result of cosmic-ray bombardment and from nuclear weapons testing and has a half-life of 15.7 million years, it has potential applications for dating very old ground water and for tracing modern ground water.

6.5.3 Ground water flux

Measurements of radon and radium activities in surface water have been widely used to estimate ground water discharge fluxes (Avery et al., 2018; Gleeson et al., 2018; Cook et al., 2003), both onshore and offshore (Burnett et al., 2006). These measurements can be especially effective when used in combination with other tracers (e.g. CFCs, SF_6, δ18O, δ2H, water temperature, CH_4).

Observing increased radon activity in ground water has also been suggested as a precursor, and therefore warning system, for major seismic activity (Hauksson, 1981; Wakita, 1996), although evidence for causal links between the two remains inconclusive.

6.5.4 Ground water provenance and processes

Many of the radionuclides described above can also be used to study ground water provenance, weathering processes, flow paths, redox controls and sources of contaminants (Ivanovich, 1994). Among others, radon, radium and uranium, ^{234}U/^{238}U and ^{87}Sr/^{86}Sr ratios have been used to distinguish between ground water and baseflow from distinctive rock types (e.g. granite, mineralised rocks) (e.g. Riotte & Chabaux, 1999). Some of the radionuclides are pH- and redox-sensitive, giving insight into weathering and redox processes. Uranium is redox-sensitive, and uranium and radium behave differently in different redox conditions. ^{234}U/^{238}U activity ratios have been used to delineate redox boundaries (Andrews & Kay, 1982). Measurements of ^{234}U/^{238}U activity ratios have also been used to identify uranium-bearing fertilisers (Bigalke et al., 2018; Barisic et al., 1992). Moreover, radionuclides also have obvious applications for investigating processes, flow paths, reaction kinetics and environmental impacts in the context of nuclear facilities and repositories.

6.5.5 Sedimentation rates

The radioactive isotopes ^{137}Cs (half-life of 30.2 years) and ^{14}C (half-life of 5730 years) are used as suitable tools to study lake sediments. Global changes in the atmosphere have been reflected in the whole environment, and they are particularly noticeable in lake sediments that preserve records of anthropogenic alterations. Therefore, the record of ^{137}Cs and ^{14}C radioisotopes in recent carbonate sediments can be used to determine sedimentation rate, the response of the lake environment/sediment to anthropogenic contamination of the atmosphere, as well as to follow environmental processes of carbon geochemistry (Horvatinčić et al., 2014).

^{210}Pb occurs naturally as one of the radioisotopes in the ^{238}U decay series. In sediments ^{210}Pb has two sources: The first one is ^{222}Rn, produced in local rocks and sediments, escapes to the atmosphere and decays there via short-lived isotopes to ^{210}Pb. ^{210}Pb is removed from the atmosphere by adsorption to aerosols and in precipitation or dry deposition and is incorporated into the upper sediment layer (unsupported or excess ^{210}Pb). The other source is ^{210}Pb produced in the sediments *in situ* (supported). The ^{210}Pb method is based on the radioactive decay of unsupported ^{210}Pb, which has been calculated as the difference between total ^{210}Pb and supported ^{210}Pb. With a half-life of 22.3 years, ^{210}Pb is an ideal indicator of modern sedimentation rates. Several models based on ^{210}Pb (unsupported) measurements in sediment columns have been extensively used (Horvatinčić et al., 2014). As ^{137}Cs is derived from a different source than ^{210}Pb, it provides a valuable cross-check of the ^{210}Pb results.

The activity concentration ratio of ^{228}Ra/^{226}Ra has been used as an indicator of the geochemical source of sediment particles along the Danube River (Maringer et al., 2009, 2015).

6.6 Challenges to improving radioactivity measurements in water and developing a European map

Comparable and fit-for-purpose results are an essential requirement for decisions based on radioactivity measurements, and international standards of tested and validated radionuclides test methods are an important tool for producing such measurements. It is essential that all testing laboratories use agreed and appropriate methods and procedures for sampling, handling, transporting, storing and preparing of test samples, the test method, and for calculating measurement uncertainty. In this framework, the normative approach based on international standards aims to ensure the accuracy or validity of the test results through calibrations and measurements traceable to The International System of Units (SI, abbreviated from the French *Le Système international d'unités*). The test laboratory should establish traceability of its own measurement methods and measuring instruments to the SI by means of an unbroken chain of calibrations or comparisons, linking them to relevant primary standards of the SI units of measurement. This approach guarantees that radioactivity test results on the same type of samples are comparable over time and between different test laboratories worldwide.

Quality assurance is required by the IAEA Basic Safety Standards (IAEA, 2014), and, hence, should be an integral part of environmental monitoring programs (Engelbrecht, 2012). As a minimum, an adequate quality assurance program satisfies the general requirements established by the regulatory body. In order to minimise incidents, such as mixing up samples or biased analyses, quality control and quality assurance concepts have been developed to assist the laboratory personnel in the following objectives: to achieve a higher degree of transparency of procedures; to minimise potential sources of error; to standardise the handling of samples, instruments, and data; and, in the end, to decrease the rate of nonconforming results.

Uncertainty in environmental monitoring results arises primarily from design errors, the non-representativeness of samples and/or measurements, and measurement uncertainty. These uncertainties, as well as human errors, cannot be fully eliminated but can be reduced as far as possible.

Non-representativeness occurs when the sampling or field measurement is unable to capture the complete extent of variability that exists for the radionuclide distribution in a survey unit. Since it is impossible to always measure the residual radioactivity at every point in space and time, the results will be incomplete to some degree. It is also impossible to know with complete certainty the residual radioactivity at locations that were not measured, so the incomplete survey results give rise to uncertainty. The greater the natural or inherent variation in residual radioactivity, the greater the uncertainty associated with a decision based on the survey results. Representativeness in sampling and/or in field measurements can be optimised by means of an appropriate sampling and measurement scheme as described above.

In the case of water and sediment measurements, sampling is the biggest challenge and determines the quality/reliability of the measurement result. It is not easy to collect a representative and reliable sample. Due to different characteristics of water, different mixing of water, the measured activity concentration of radioisotopes in a sample does not always give a clear picture of the present radioisotopes in water. Also, sampling frequency should be clearly defined. Sampling frequency of drinking water is defined in The Drinking Water Directive (European Union, 2013a), and IAEA has established the Global Network of Isotopes in Precipitation (GNIP) and Global Network of Isotopes in Rivers (GNIR) for river water.

In some cases, gross alpha/beta should be the first screening method performed. On the other hand, according to the conclusions from a European interlaboratory comparison exercise (Jobbagy et al., 2014), gross alpha/beta methods are not fit to be used as an independent method to assess activity concentration. Gross measurement should be used for monitoring only after the radionuclide composition is known from radionuclide-specific analysis of representative samples. It can be used as a complementary or substitute method for radionuclide-specific measurement only with some important restrictions: (1) no temporary change is expected in the radiochemical composition (no significant growth of progenies during the measurement); (2) no complex decay chains are present; (3) a true, standardised method is used; and (4) the measurement parameters are fixed. Radionuclide-specific analysis should be repeated on a regular basis in accordance with the Drinking Water Directive from 1998 concerning check and audit monitoring (European Communities, 1998). Any suspected change in parameters requires more frequent nuclide-specific analysis.

However, due to different requirements for sample pre-treatment for different radioisotope techniques, simultaneous measurements methods should be improved. It is important to have all radioisotopes measured in the same sample whenever it is possible.

Mapping natural radionuclides in water at European level is not an easy task and it has not been sufficiently explored in the present version of the Atlas. Hence, the following challenges have been identified:

- Collect data on sampling and measurements of natural radionuclides in water;
- Work on harmonisation procedures since data of natural radionuclides in water have been obtained with different techniques and methods;
- Explore different mapping methodologies.

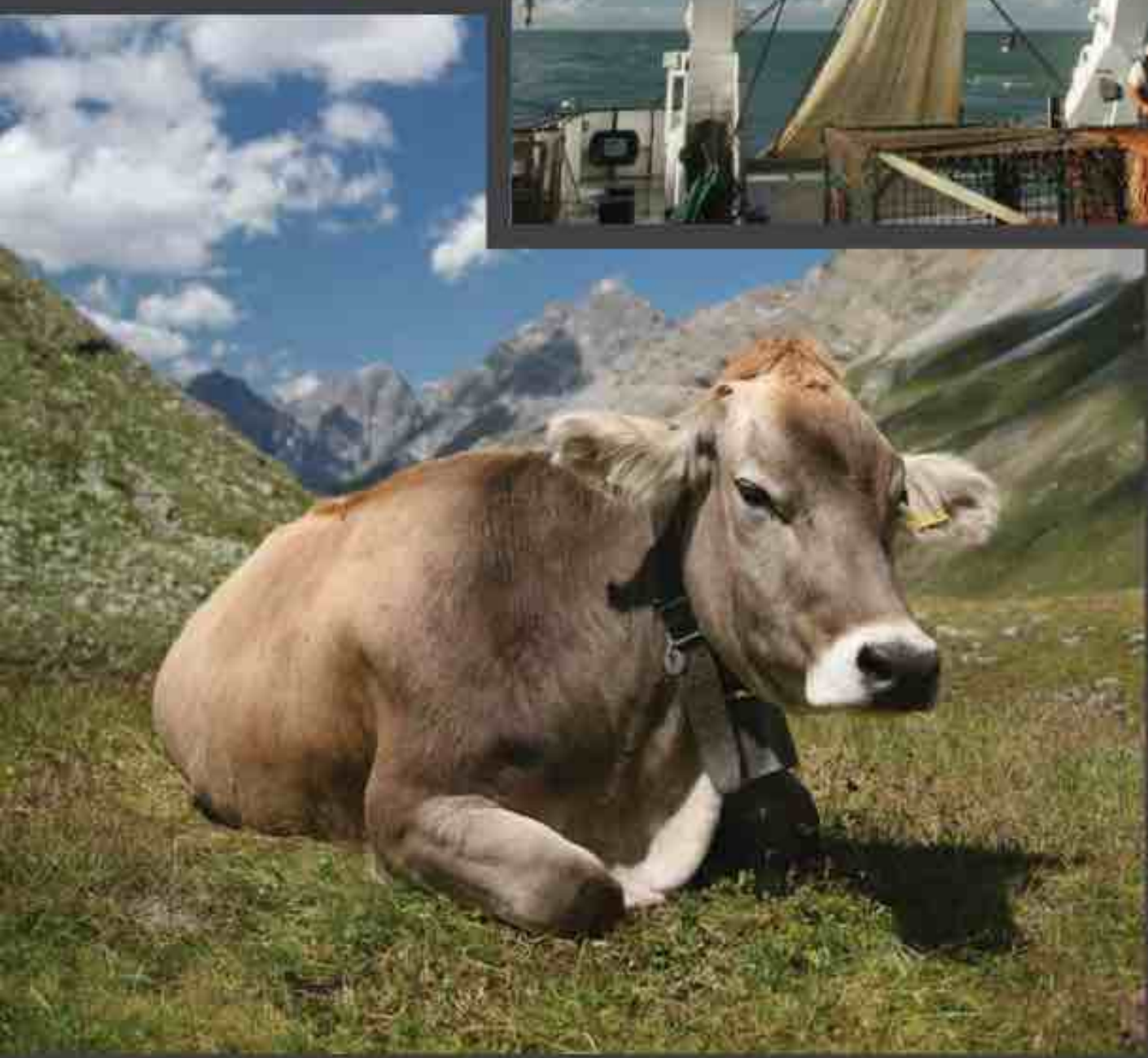

Chapter 7

Radionuclides in food

As described in Section 2.2, natural radioactivity is found in all rock and soil types. From there, radionuclides are taken up by plants and animals and thus enter the food chain. That is why all types of food contain natural radionuclides and consumption of food contributes to the total radiation dose of an individual.

This chapter describes the pathways of natural radionuclides from soil to food, the relevant radionuclides, as well as methods for measuring radioactivity in foodstuffs. Furthermore, typical activity concentrations in various foodstuffs are quoted for various European countries, and finally the main factors controlling dose due to ingestion of food are illustrated.

In general, the levels of natural radionuclides in food and drinking water are very low and thus safe for human consumption. On average, the dose due to food consumption accounts for about 10% of the average radiation dose from all natural sources for an individual.

However, concentrations of natural radionuclides vary widely between but also within food categories such as vegetables, fruit, meat and fish. Therefore, it is important to control radioactivity levels in food and inform consumers about the risk. National food monitoring programs in some countries include natural radionuclides, but generally such programmes focus on artificial (man-made) radionuclides e.g. from nuclear power plants or nuclear weapons tests.

Clockwise from top-left:

Oats, barley and derived products.
Source: Public Domain By Peggy Greb United States Department of Agriculture, Agricultural Research Service https://commons.wikimedia.org/w/index.php?curid=2963310

Cabbage cultivation in Dojran region, Macedonia.
Source: Ksenija Pulin (CC BY 2.0)

Orange grove.
Source: Hans Braxmeier (CC0)

Braunvieh cow below Fuorcla Sesvenna in the Engadin, Switzerland.
Source: Daniel Schwen (CC BY-SA 3.0)

Commercial free-range hens.
Source: Adam Wolf (CC BY-SA 2.0)

Commercial fishing off Zeebrugge, Belgium.
Source: © Hans Hillewaert, CC BY-SA 4.0, https://commons.wikimedia.org/w/index.php?curid=11787420

Radionuclides in food

Introduction

All types of food contain some natural radionuclides that are transferred from the soil to the crops on land and from water to fish in rivers, lakes and the sea (Figure 7-1). The levels of natural radionuclides in food and drinking water are generally very low and safe for human consumption. However, concentrations of radionuclides of natural origin vary between different types of food because of different environmental conditions, agricultural practices and other factors that affect radionuclide transfer from the environment to crops and animal products (UNSCEAR, 2000b). Concentrations of natural radionuclides differ between food categories and inside each category, such as vegetables, cereals, fruits, meat and fish. In addition, doses due to food consumption vary, depending on the food types that are consumed in the various countries (IAEA, 2016). Therefore, it is important to know radioactivity levels in food and inform consumers about potential risks. Radiation doses from the consumption of foodstuffs typically range from a few tens to a few hundreds of μSv per year (IAEA, 2016; FAO/WHO, 2001). On average, the global population receives a total radiation dose of about 0.3 mSv each year due to radionuclides of natural origin in the diet. Typically, this represents 10% of the average annual radiation dose of 3 mSv from all sources received by an individual (IAEA, 2016).

Total Diet Studies

One way to monitor food doses is through Total Diet Studies. This method is recommended by the European Food Safety Authority (EFSA), Food and Agriculture Organization of the United Nations (FAO) and the World Health Organization (WHO), in order to determine the mean concentration levels of substances in the average human diet (EFSA, 2011). A Total Diet Study consists of selecting and collecting types of food representing the overall diet of a population, which are prepared as they are consumed and pooled into representative food groups before the radionuclides contents in the food are analysed. Combined with food consumption data, the results allow scientists to calculate the amount of each radionuclide that is being consumed by a specific population as part of their typical diet (EFSA, 2011).

Because of authorised or accidental releases from the nuclear power industry, military facilities as well as nuclear weapons tests, anthropogenic radionuclides such as ^{137}Cs or ^{90}Sr are also present in the environment and often the main target of food monitoring programs. According to Articles 35 and 36 of the Euratom Treaty, all EU Member States are required to monitor mostly artificial radioactivity in the environment, hence many national legislations include maximum levels of radionuclides, mostly artificial, in food (Máté et al., 2015). Unfortunately, only some countries monitor both artificial and naturally occurring radioisotopes by radionuclide. Mostly, ^{226}Ra, and in some cases also uranium and ^{210}Po, are examined (Máté et al., 2015).

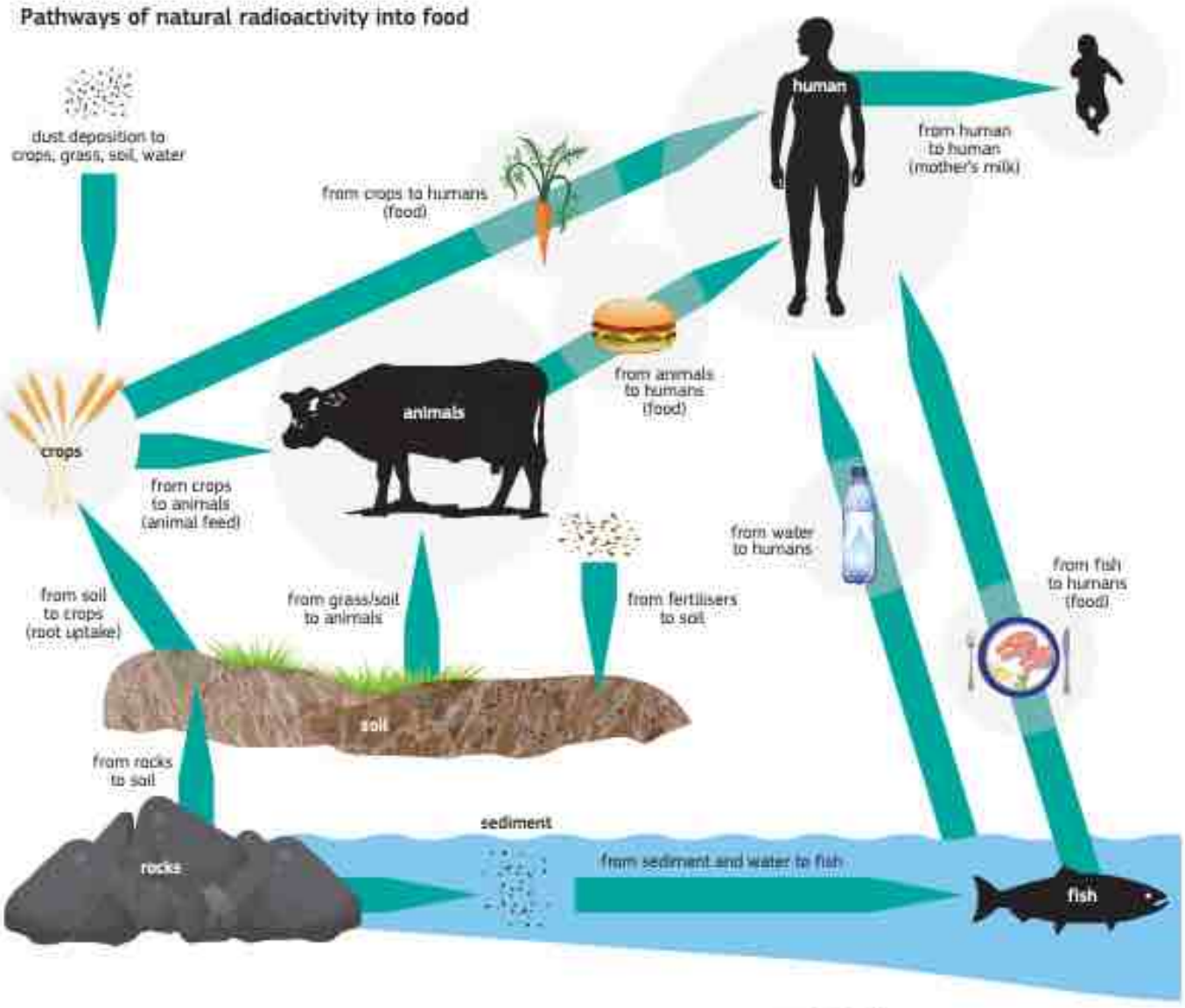

Figure 7-1.
Pathways of natural radioactivity into the food chain.
Source: Figure created by Michaela Arnetz

Food group	Natural radionuclide	Artificial radionuclide
Beverages	^{210}Pb, ^{210}Po, ^{226}Ra, ^{238}U	^{90}Sr, ^{131}I, ^{137}Cs
Cereals	^{40}K, ^{210}Pb, ^{210}Po, ^{226}Ra, ^{228}Ra, ^{234}U, ^{238}U	^{90}Sr, ^{131}I, ^{137}Cs
Fish and shellfish	^{210}Pb, ^{210}Po, ^{226}Ra, ^{234}U, ^{238}U, ^{40}K	^{99}Tc, ^{137}Cs, Pu, Am
Fruit	^{14}C, ^{210}Pb, ^{210}Po, ^{226}Ra, ^{228}Ra, ^{234}U, ^{238}U, ^{40}K	^{35}S
Game/venison meat	^{210}Po	^{137}Cs
Honey	^{14}C	^{137}Cs
Meat and offal	^{40}K, ^{210}Pb, ^{210}Po, ^{226}Ra, ^{234}U, ^{238}U	^{90}Sr, ^{137}Cs, Pu, Am
Milk and dairy products	^{14}C, ^{40}K, ^{210}Pb, ^{210}Po, ^{226}Ra, ^{234}U, ^{238}U	^{90}Sr, ^{131}I, ^{137}Cs
Vegetables	^{40}K, ^{210}Pb, ^{210}Po, ^{226}Ra, ^{228}Ra, ^{234}U, ^{238}U	^{90}Sr, ^{131}I, ^{137}Cs

Table 7-1.
Food groups and radionuclides of major interest in radiological monitoring programmes.
Source: Petroni, 2006; Benaud et al. 2013a; Benaud et al. 2013b; D'Amato et al. 2013; Smith-Briggs & Bradley, 1989; Petrova-Tin et al., 1993a.

7.1 Materials and methods

7.1.1 Natural radioactivity in food

Detailed knowledge of radionuclide activity concentrations in food products is needed to determine the effective dose for the population, since food intake is the most significant route for the intake of radionuclides for the public (ICRP, 2008). Natural radioactivity of terrestrial origin, which contributes to the dose to an average person from ingestion, is represented by potassium-40 (^{40}K), uranium-thorium series (more details in Section 2.2) (Meli et al., 2016; Mehra et al., 2010; Navas et al., 2002; Wallova et al., 2012). Here, ^{40}K and ^{210}Po, a radionuclide of the ^{238}U series, are the nuclides that give the largest contribution (Meli et al., 2016).

Plants and animals routinely absorb radioactivity because of similar chemical properties of radionuclides and essential nutrients. The concentration of radionuclides absorbed by plants and animals depends on the radioactivity of the source media, e.g. the soil or water, the nutrients present and the dynamics of radionuclides in the soil-plant-animal system influenced by both the characteristics of the soil and the species-specific capacity of the crop to bioconcentrate the element from the soil and transfer it from the roots to the different vegetative organs, thereby becoming available for further redistribution within food chains (Figure 7-1) (Linsalata, 1994).

Carbon-14

Carbon-14 (^{14}C) is a radioactive isotope present in infinitesimal quantities in the atmosphere. Indeed, ^{14}C is about 10-12 times less abundant than stable carbon. Cosmic radiation produces neutrons that interact with nitrogen in the upper atmosphere to produce ^{14}C at a fairly constant rate ($^{14}_{7}N + ^{1}_{0}n \rightarrow ^{14}_{6}C + ^{1}_{1}p$). This ^{14}C is distributed worldwide throughout the environment, and, because carbon is a key component of all living material, ^{14}C is present in plants and animals and hence throughout the food chain.

Food high in fatty acids normally contains a large amount of carbon, and therefore also ^{14}C. Examples of such food are milk and milk products, oils, almonds, walnuts, avocados and fish such as mackerel, trout and salmon (O'Connor et al., 2014).

Potassium-40

Potassium-40 (^{40}K) has a half-life of 1.25×10^{9} years and is ubiquitous on the Earth.

^{40}K represents a very small fraction of naturally occurring potassium, which is an element found in large amounts throughout nature. Potassium is the seventh most abundant element in the crust of the Earth and the sixth most abundant element in solution in the oceans. Potassium is a key element involved in regulating body functions such as digestion, heart rate and the water content of cells. For that reason, the potassium content of the body is held constant by metabolic processes, although some variability between men and women as well as with age has been observed. Natural potassium is made of 0.012% by weight of ^{40}K which is naturally radioactive, and no control can reasonably be exercised over the dose from ^{40}K in the diet (O'Connor et al., 2014). The annual effective dose due to the presence of ^{40}K in the body is typically about 0.165 mSv for adults and 0.185 mSv for children (UNSCEAR, 2000b).

Radium

Radium-228 (^{228}Ra) is a radioactive decay product in the thorium-232 (^{232}Th) decay series, and most of the dose attributed to ^{232}Th is in fact produced by ^{228}Ra (O'Connor et al., 2014). ^{232}Th is found in the Earth's crust and is, on average, three times more abundant than uranium and as abundant as lead. The ^{232}Th decay chain ends with stable lead-208 (^{208}Pb).

The highest thorium concentrations are usually found in igneous rocks such as granites, while the lowest concentrations are found in carbonate rocks such as limestones.

Radium-226 (^{226}Ra) is a radioactive decay product in the uranium-238 (^{238}U) decay series and is the precursor to radon-222 (^{222}Rn).

People may ingest radium that is naturally contained in food and/or water, and may also inhale it from dust particles suspended in the air. Most of the radium taken in by ingestion (about 80%) will promptly leave the body in faeces. The remaining parts (20%) enter the bloodstream and are carried to all parts of the body. The metabolic behaviour of radium in the body is similar to that of calcium. For this reason, an appreciable fraction is preferentially deposited in bone and teeth.

Radium can also be produced in the body from its parent radionuclide (uranium) that has been inhaled or swallowed, but this is normally not a significant source (O'Connor et al., 2014).

Uranium, polonium and lead

Natural uranium is composed of three main isotopes, all of which are radioactive. The two isotopes most abundant are uranium-238 (^{238}U) and uranium-235 (^{235}U), both of which have existed since the Earth's creation. The third isotope is uranium-234 (^{234}U), which is produced by alpha disintegration of ^{238}U and represents only a minute fraction of all uranium isotopes. ^{238}U is also found in the Earth's crust in concentrations that vary from a few to several thousand ppm. ^{238}U decays through a series of steps to produce lead-206 (^{206}Pb). Radioactive decay of ^{238}U produces radon gas (^{222}Rn) which, in turn, produces polonium-210 (^{210}Po) and lead-210 (^{210}Pb) which, through inhalation, significantly contribute to the overall dose.

^{210}Pb and ^{210}Po are relatively long-lived radionuclides with half-lives of 22 years and 140 days respectively, and both occur widely in nature albeit in very small quantities (trace). The main exposure pathway of ^{210}Pb and ^{210}Po is ingestion. Indeed, most of the ingestion dose from the ^{238}U series is due to the presence of ^{210}Po in foodstuffs. ^{210}Pb also contributes significantly to the total radiation dose received by the population because of its long residence time in the human body, particularly in the skeleton (O'Connor et al., 2014).

The average annual individual dose from radionuclides in the uranium and thorium series in the total diet (food and drinking water together) for the general population is 0.12 mSv (UNSCEAR, 2008).

The losses in food preparation and the associated variation in intakes of natural radionuclides can additionally be used to estimate the ingestion of radionuclides to ensure that doses are not systematically overestimated. Drying food increases the concentration in the product, typically by a factor of 5 compared to fresh food (UNSCEAR, 2000a). Boiling foodstuff such as meat considerably reduces the radionuclide content. Radionuclide contents in vegetables and fruits are also significantly affected by washing, peeling and cooking. However, there are no specific recommendations for these calculations (UNSCEAR, 2000a).

7.1.2 Measurement of natural radionuclides in food

Radioactivity analysis of food samples is a very important issue, especially with regard to dose assessments based on these measurements. The first important step is a comprehensive sample plan and subsequent sample collection. In substantial studies, like Total Diet Studies, it can take several months to evaluate food samples because detailed food surveys are needed in the population (Leclercq et al., 2009).

Sample preparation is a process in which samples are taken through several steps to carry out the qualitative and quantitative analysis of natural and/or artificial radionuclides that may be present.

It is important to use guidelines on sampling methods, treatments, sample preparations and preservations, and standardisations of the analysis for the comparability of the results obtained.

For foodstuff this means thorough shredding and homogenisation of food samples. Depending on the type of measurement and type of food, there follow sometimes several drying and combustion steps and crushing again the food ashes.

The radioactivity analyses often used for food include liquid scintillation spectrometers, α/β-spectrometry as well as gamma-ray spectrometers (see Table 7-2) (Poeschl, 2006). Many naturally occurring radionuclides, e.g. members of the uranium, thorium and actinium decay series, are mainly alpha-emitters. Since alpha-particle spectrometry is a very sensitive technique with a very low counting background, it is necessary that source samples be present in a thin layer to reduce self-absorption of the alpha-particles. To generate an extremely thin sample layer, a source sample chemical preparation is essential. After precipitation reactions or chromatographic methods, these thin layers containing radionuclides such as ^{210}Po or $^{234+238}$U can be generated for example by deposition on silver or steel discs (see Table 7-2) and alpha radiation measured. The main advantages of using alpha/beta spectrometry are the low detection limits and elimination of other possible interferences by chemical separation at the cost of sample destruction. The main disadvantage is the great effort on source sample preparation and chemical separation. A non-destructive method to capture radionuclide content in foodstuff is gamma-ray spectrometry. Low-level gamma spectrometry allows qualitative and quantitative determination of radionuclides in the sample generally by using semiconductor detectors on the basis of pure germanium. The analysis of photo peak areas (after correction of the peak area for background, energy and efficiency calibrations) and the processing of data in terms of radionuclide content require homogenised samples in given geometries. The detection limit of the method is strictly correlated to the efficiency of the detector, radionuclide of interest, the measuring time, the composition and density of the sample and the acquisition geometry.

Country	Radionuclide	Analysis	Reference
Austria	^{40}K	Low-level gamma spectrometry	Landstetter et al., 2013
Germany	^{210}Pb	Co-precipitation to Fe-hydroxides, extraction chromatography, liquid scintillation counter (LSC) measurement of beta radiation	modified to BMU, 2018
	^{226}Ra	Co-precipitation with barium sulfate, measurement of alpha radiation	
	^{228}Ra	Co-precipitation with barium sulfate and transfer to carbonate, extraction chromatography (Re-spec), measurement of beta radiation	
	^{234}U	Extraction chromatography, electrochemical precipitation, measurement of alpha radiation	
	^{238}U	Extraction chromatography, measurement of alpha radiation	
France	^{210}Pb	Gamma-ray spectrometry	Renaud et al., 2015c
	^{210}Po	Acid digestion, deposition onto a stainless steel disc, measurement of alpha radiation	
	^{226}Ra	Gamma-ray spectrometry	Renaud et al., 2015b
	^{228}Ra		
Italy	^{40}K	Gamma-ray spectrometry	Desideri et al., 2014
	^{210}Po	Extraction chromatography, precipitation, electrodeposition on silver discs, measurement of alpha radiation	Meli et al., 2014
	^{226}Ra	Direct gamma-ray spectrometry	Desideri et al., 2014
	^{228}Ra		
	^{232}Th		
	^{238}U		
Poland	^{210}Pb	Precipitation of lead chromate, deposition on Ni discs, detection limit measurement of beta radiation	Pietrzak-Flis et al., 1997a
	^{210}Po	Electrodeposition on silver discs, measurement of alpha radiation	
	^{226}Ra	Emanation method, co-precipitation with barium sulphate, measurement of alpha radiation	
	^{228}Th, ^{230}Th, ^{232}Th	Extraction chromatography, measurement of alpha radiation	Pietrzak-Flis et al., 2001
	^{234}U	Extraction chromatography, measurement of alpha radiation	
	^{238}U	Extraction chromatography, measurement of alpha radiation	
Romania	^{40}K	Low-level gamma spectrometry	Ferdes and Cojocaru, 1996
Spain	^{40}K	Low-level gamma spectrometry	Hernandez et al., 2004
	^{210}Pb		
	^{210}Po	Radiochemical purification, alpha spectrometry	Nadal et al., 2010
	^{226}Ra	Low-level gamma spectrometry	Hernandez et al., 2004
	^{228}Ra		
	^{238}U		
	U_{nat}	Coupled plasma mass spectrometry, acid microwave digestion	Bellés et al., 2013
United Kingdom	^{210}Pb	Manganese dioxide precipitate, measurement of beta radiation	Smith-Briggs et al., 1986
	^{210}Po	Acid digestion, spontaneous deposition onto a silver disc, measurement of alpha radiation	Smith-Briggs & Bradley, 1984
	^{226}Ra	Alpha scintillation cell measurement	
	^{230}Th, ^{232}Th	Ion exchange, extraction chromatography, measurement of alpha radiation	Ham et al., 2001
	^{234}U		
	^{238}U		

Table 7-2
Analysis methods for natural radionuclides in food samples taken in some European countries.

7.1.3 Activity concentration of natural radionuclides in food

Activity concentration of natural radionuclides in food is usually expressed in terms of mass or volume; the units are Bq/g or Bq/l (see Section 2.1 for the definition of becquerel (Bq)).

Table 7-5 presents mean/median concentration values of natural radionuclides in various types of food in some European countries; it includes selected data from UNSCEAR (UNSCEAR, 2000a), with updates from other sources. Sometimes, the samples analysed originate from areas with higher concentrations of natural radionuclides (BfS, 2003) in soil or have only been sampled locally (Hernandez et al., 2004; Pietrzak-Flis et al., 1997b); hence, they cannot be used to make a representative dose assessment estimation for the whole country. In general, specific activities vary a lot depending on country, natural radionuclide, sampling campaign and measurement method.

Table 7-5
Concentration of natural radionuclide in various types of food in some European countries (means and ranges). Values marked with * are additional figures taken from UNSCEAR 2000 Annex B, Table 15 (UNSCEAR, 2000a).

Radionuclide concentration in milk and milk products (Bq/kg)								
Country	^{40}K	^{238}U	^{226}Ra	^{210}Pb	^{210}Po	^{228}Ra	^{228}Th	References
Finland	-	-	-	-	-	-	-	-
France	-	-	0.017 (0.007-0.059)	-	-	42	-	Renaud et al., 2015c
Germany	50 (35-65)	-	0.025 (0.001-0.13)/0.002-0.130*	0.04 (0.004-0.26)/0.005-0.280*	0.024 (0.003-0.07)/0.002-0.080*	-	-	BfS, 2003
Ireland	40-60	-		15	15		-	O'Connor et al., 2014
Italy	82 (1.7-109)	-	1.85 /0.003-0.019*	-	0.0315	2.4	0.7	Desideri et al., 2014; Meli et al., 2014
Poland	-	0.0030/0.0026*	0.00957 (1997) 0.0126 (2001)/0.01*	0.0178/0.018*	0.0159/0.016*	-	-	Pietrzak-Flis et al., 2001; Pietrzak-Flis et al., 1997a
Portugal	-	-		0.5050	0.5900	-	0.0001	Carvalho, 1995
Spain	-	-	-	-	-	-	-	-
United Kingdom	-	0.0001-0.0049	<0.0004-200*	0.042/0.035-0.088*	0.0085/0.020-0.22*	-	-	Smith-Briggs & Bradley, 1984

Radionuclide concentration in cereals and cereal products (Bq/kg)								
Country	^{40}K	^{238}U	^{226}Ra	^{210}Pb	^{210}Po	^{228}Ra	^{228}Th	References
Finland	-	-	-	0.3367 (0.08-0.56)	-	-	-	Turtiainen et al., 2011
France	-	-	0.18 (0.056-1.5)	-	-	0.18 (0.047-5.55)	-	Renaud et al., 2015b
Germany	150 (87-246)/ 0.020-0.400*	0.1 (0.02-0.4)	0.2 (0.04-1.54)/0.020-2.9*	0.9 (0.04-10.2)/0.040-4.0	0.35 (0.2-7.94)/0.037-1.9*	-	-	BfS, 2003
Ireland		-		0.05	0.06	-	-	O'Connor et al., 2014
Italy	152 (90-237.9)	-	4.2667 (2.2-7.2)	-	0.0487 (0.020-0.114)	5.67 (2.2-9.0)	3.3 (1.7-5.0)	Desideri et al., 2014
Poland	-	0.0031/ 0.0047-0.011*	0.0962 (1997) 0.0551(2001)/ 0.080-0.110*	0.1335 /0.11-0.16	0.1141/0.090-0.140*	-	16	Pietrzak-Flis et al., 2001
Portugal	-	-	-	0.1987 (0.066-0.27)	0.2867 (0.14-0.49)	-	-	Carvalho, 1995
Spain	-	-	-	-	-	-	-	Hernández et al., 2004
United Kingdom	-	0.0062-0.035*	0.0007-5.2*	0.523/0.056-0.120	0.041/0.027-0.260	-	0.18-2.3	Smith-Briggs & Bradley, 1984

Radionuclide concentration in green/leafy vegetables (Bq/kg)								
Country	^{40}K	^{238}U	^{226}Ra	^{210}Pb	^{210}Po	^{228}Ra	^{228}Th	References
Finland	-	-	-	-	-	-	-	-
France	-	-	0.09 (0.018-1.22)	0.34 (0.08-4.2)	-	0.09 (0.020-1.97)	-	Renaud et al., 2015b; Renaud et al., 2015c
Germany	130 (59-196)	0.3 (0.02-0.75) 0.006-2.2	0.2 (0.01-0.68)/0.006-1.15*	0.3 (0.004-1.28)/0.004-4.1*	0.2 (0.004-1.13)/0.004-7.4*	-	-	BfS, 2003
Ireland	20-150	-	-	0.08	0.10	-	-	O'Connor et al., 2014
Italy	163 (62.4-447.9)	-	2.6 (0.7-4.7)/0.027-0.044*	-	0.129 (0.007-0.651)	2.9 (0.9-7.5)	2.9 (0.4-31.7)	Desideri et al., 2014; Meli et al., 2014
Poland	-	0.0076 (0.0011-0.0136)	0.0531 (0.0147-0.137)/ 0.037-0.043*	0.046 (0.043-0.0507)/ 0.043-0.051*	0.0521 (0.0399-0.0669)/0.040-0.067*	-	0.0145 (0.0037-0.0114)	Pietrzak-Flis et al., 1997a; Pietrzak-Flis et al., 2001
Portugal	-	-	-	0.3300	0.0540	-	-	Carvalho, 1995
Spain	-	-	-	-	-	-	-	-
United Kingdom	-	0.0098-0.40	0.0022-0.170	0.031 / 0.016-3.3	0.0096 / 0.037-3.3	-	-	Smith-Briggs & Bradley, 1984

Radionuclide concentration in fruit vegetables and other vegetables (Bq/kg)								
Country	^{40}K	^{238}U	^{226}Ra	^{210}Pb	^{210}Po	^{228}Ra	^{232}Th	References
Finland	-	-	-	-	-	-	-	-
France	-	-	-	-	-	-	-	-
Germany	-	0.4 (0.1-1.26)	0.1 (0.01-0.68)	-	0.1 (0.004-1.19)	-	-	BfS, 2003
Ireland	60-80	-		-	-	-	-	O'Connor et al., 2014
Italy	135 (60-437.7)	-	1.5 (0.6-3.3)	-	0.015 (0.005-0.039)	2.4 (0.9-6.2)	1.3	Desideri et al., 2014
Poland	-	0.0040 (0.0005-0.0102)	0.0177 (0.0087-0.0109)	0.0347 (0.0244-0.0413)	0.0524 (0.0279-0.0821)	-	0.0046 (0.0019-0.0104)	Pietrzak-Flis et al., 1997a, Pietrzak-Flis et al., 2001
Portugal	-	-	-	0.1600	0.0565	-	-	Carvalho, 1995
Spain	116 (53-260)	-	-	-	-	0.34	-	Hernández et al., 2004
United Kingdom		-	-	0.0680	0.0350	-	-	Smith-Briggs & Bradley, 1984

Radionuclide concentration in fruit (Bq/kg)								
Country	^{40}K	^{238}U	^{226}Ra	^{210}Pb	^{210}Po	^{228}Ra	^{232}Th	References
Finland	-	-	-	-	-	-	-	-
France	-	-	-	-	-	0.18	-	Renaud et al., 2015b
Germany	95 (23-190)	0.5 (0.02-0.89)	1.2 (0.005-5.38)	4.3 (0.02-14.8)	-	-	-	BfS, 2003
Ireland	60-100	-	-	-	-	-	-	O'Connor et al., 2014
Italy	92 (60.2-150.0)	-	1.3 (0.7-2.19)	-	0.034 (0.006-0.069)	1.8 (0.9-6.8)	1.1 (0.6-3.4)	Desideri et al., 2014
Poland	-	0.0029 (0.0013-0.0053)	0.0239 (0.0016-0.0053)	0.0523 (0.0296-0.0934)	0.1057 (0.0492-0.213)	-	0.0063 (0.0015-0.0053)	Pietrzak-Flis et al., 2001; Pietrzak-Flis et al., 1997a
Portugal	-	-	-	0.0350	0.0450	-	-	Carvalho, 1995
Spain	8 (41-185)	-	-	-	-	0.23 (0.14-0.3)	-	Hernández et al., 2004
United Kingdom	-	-	-	0.0470	0.0130	-	-	Smith-Briggs & Bradley, 1984

Radionuclide concentration in root vegetables (Bq/kg)								
Country	^{40}K	^{238}U	^{226}Ra	^{210}Pb	^{210}Po	^{228}Ra	^{232}Th	References
Finland	-	-	-	-	-	-	-	-
France	-	-	-	0.1200	-	0.12	-	Renaud et al., 2015b; Renaud et al., 2015c
Germany	125 (72-194)	0.65 (0.02-3.09)	0.2 (0.02-1.3)	0.35 (0.02-4.9)	0.35 (0.02-5.2)	-	-	BfS, 2003
Ireland	140-180	-	-	0.03	0.04	-	-	O'Connor et al., 2014
Italy	-	-	-	-	-	-	-	Desideri et al., 2014
Poland	-	0.0029 (0.0013-0.0047)	0.0402 (0.0192-0.0594)	0.0407 (0.032-0.0458)	0.0367 (0.0281-0.0491)	-	0.0098 (0.0089-0.0140)	Pietrzak-Flis et al., 2001; Pietrzak-Flis et al., 1997a
Portugal	-	-	-	0.1800	0.1800	-	-	Carvalho, 1995
Spain	105	-	-		-	-	-	Hernández et al., 2004
United Kingdom	-	-	-	0.0160	0.0069	-	-	Smith-Briggs & Bradley, 1984

Radionuclide concentration in meat (Bq/kg)								
Country	^{40}K	^{238}U	^{226}Ra	^{210}Pb	^{210}Po	^{228}Ra	^{232}Th	References
Finland	-	-	-	-	-	-	-	-
France	-	-	-	-	-	-	-	-
Germany	90 (60-120)	0.01 (0.001-0.02)/0.001-0.020*	0.1 (0.03-0.18)/0.030-0.22*	0.5 (0.1-1)/0.10-1.0*	2 (0.2-4)/0.037-4.0*	-	-	BfS, 2003
Ireland	80-200	-		0.08	0.06	-	-	O'Connor et al., 2014
Italy	-	-	-		-	-	-	-
Poland	-	0.0032 (0.0023-0.0041)/ 0.0016-0.0056*	0.0149 (1997)/0.071 (2001)/0.011-0.019*	0.1017/0.098-0.105*	0.1005/0.099-0.102*	-	0.0059	Pietrzak-Flis et al., 2001; Pietrzak-Flis et al., 1997a
Portugal	-	-	-	0.3475 (0.12-0.55)	0.4925 (0.15-0.86)	-	-	Carvalho, 1995
Spain	66 (54-130)	-	3	2.4	-	0.55 (0.19-1.15)	-	Hernández et al., 2004
United Kingdom	-	0.0049*	0.0026-0.074*	0.292 (0.043-0.651)/ 0.040-3.7*	0.0085 (0.0026-0.014)/ 0.062-67*	-	0.022-0.093*	Smith-Briggs & Bradley, 1984

Radionuclide concentration in eggs (Bq/kg)								
Country	^{40}K	^{238}U	^{226}Ra	^{210}Pb	^{210}Po	^{228}Ra	^{232}Th	References
Finland	-	-	-	-	-	-	-	-
France	-	-	0.15 (0.136-0.190)	-	-	0.087 (0.07-0.11)	-	Renaud et al., 2015b
Germany	-	-	-	-	-	-	-	-
Ireland	-	-	-	-	-	-	-	-
Italy	87 (59.1-103.8)	-	2.5 (1.3-3.2)	-	0.07 (0.020-0.230)	2.8 (2.4-3.5)	1.4 (1.2-1.7)	Desideri et al., 2014
Poland	-	0.0014	0.0996	-	-	-	0.0201	Pietrzak-Flis et al., 2001
Portugal	-	-	-	0.1400	0.25	-	-	Carvalho, 1995
Spain	90	-	-	-	-	0.30		Hernández et al., 2004
United Kingdom	-	-	-	0.0880	0.0520	-	-	Smith-Briggs & Bradley, 1984

Radionuclide concentration in fish (Bq/kg)								
Country	^{40}K	^{238}U	^{226}Ra	^{210}Pb	^{210}Po	^{228}Ra	^{232}Th	References
Finland	-	-	-	-	-	-	-	-
France	-	-	0.13 (0.015-0.48)/0.037*	-	-	0.1265	-	Renaud et al., 2015b
Germany	100 (80-120)	4.1 (0.5-7.4)	1.5 (0.05-7.8)/0.1- 7.4*	0.8 (0.02-4.42) / 0.02-4.4*	1.1 (0.05-5.2)/ 0.05-5.2*	-	-	BfS, 2003
Ireland	100-170	-	-	0.20	2	-	-	O'Connor et al., 2014
Italy	54.9-235.9	-	0.08 (0.052-0.12)	<0.7	0.3-44.6	-	-	Desideri et al., 2011; Desideri et al., 2014
Poland	-	0.0101	0.028-0.043*	0.0869/0.081-0.093*	3.449/3.1-3.8*	-	0.0058	Pietrzak-Flis et al., 2001
Portugal	618	-	-	0.53 (0.12-1.9)	3.9 / 0.08-120*	-	-	Carvalho, 1995; Malta et al., 2013
Spain	-	-	-	-	-	-	-	-
United Kingdom	-	0.004 / 0.0025*	0.04/ 0.0085-2.1*	0.182/ 0.042/ 0.18-4.8*	0.0085 /0.82*/ 0.060-53.0*	-	0.005/ 0.056-0.7*	Smith-Briggs & Bradley, 1984; Environment Agency et al., 2017

7.2 Applications

7.2.1 Dose calculation

Radioactivity alone, measured in becquerel (Bq), does not provide enough information to evaluate possible risks associated with the intake of radionuclides, for it depends on:

- the amount of energy deposited in tissues that can cause biological effects in the affected tissues, whose magnitude varies according to the energy released (intensity and type);
- the organ involved;
- the age of the person.

The radiation energy imparted per gram of tissue, the type of radiation (alpha, beta, gamma), the distribution of the particular radionuclide in the body and its rate of excretion, and the different vulnerability to radiation of different tissues and organs must all be taken into account. Following procedures developed by the International Commission for Radiological Protection (ICRP) and taking into consideration all these factors, the effective dose can be calculated. It is an approximate measure of the actual ('effective') risk of genetic and somatic radiation damage to a human over a lifetime. Unless the full term is required for clarification, we will refer to it as 'dose'. The unit of dose is called the sievert (Sv), and 1 Sv is defined as 1 J/kg (Diehl, 2003). More details about dose estimation can be found in Section 2.1.

Three sources of information are required to assess the doses received from consumption of foodstuffs:

1. the radioactivity concentration in the food consumed;
2. the amount of food consumed (consumption rate);
3. and the dose received per unit intake of the radionuclides present in the food.

The dose received from food consumption depends on the characteristics of the radionuclides ingested, e.g. its biological behaviour, its half-life, and the type of radiation.

The dose varies depending on the different radionuclides that are found in varying amounts in different types of food.

This is due to several factors, one of which is the chemical properties of the radionuclide in question (O'Connor et al., 2014).

Identifying the type and amount of food consumed by the general population or by a specific group of individuals (consumption habits) is normally performed by carrying out a habit survey which often involves interviewing individuals and asking them to identify the types of food and quantities thereof that they consume (O'Connor et al., 2014). However, it would be helpful to use a more appropriate database on habit data or to generate a new common European database, where all EU countries get access and can enter local habits. Table 7-4 shows the consumption rates of foodstuff for different age groups, according to various authorities in European countries.

Cows in mountain pasture, North Piedmont, Italy
Source: Tore Tydéhen

Additional information on the ingestion process

In the case of ingestion, the soluble compounds may cross the barrier formed by the gastrointestinal mucosa; they arrive in the blood plasma and from there in various organs and bodily tissues. The fraction that reaches the plasma and the fraction that passes from the plasma to the organs and tissues, varies from compound to compound. Excretion of the radionuclides is predominantly with urine. The insoluble compounds simply transit through the gastrointestinal system, during which they can give doses to the mucous membranes (beta particles, alpha and gamma rays) as well as to the abdomen (gamma rays). Expulsion with human faeces occurs 1 – 3 days after ingestion (Polvani, 1993).

Food group (l/a or kg/a)	Adult			Reference / Country
Milk	250			IAEA, 2001 / Europe
Grain, root crops, vegetables, fruits	410			
Beef	100			

Food group (l/a or kg/a)	Infant (1 y.o.)	Child (10 y.o.)	Adult	Reference / Country
Milk	320	240	240	ICRP, 2006 / Europe
Green vegetable	30	35	80	
Beef	20	30	45	

Food group (l/a or kg/a)	Infant (1 y.o.)	Child (10 y.o.)	Adult	Reference / Country
Milk products	120	110	105	UNSCEAR, 2000b / Europe
Grain products	45	90	140	
Leafy vegetables	20	40	60	
Roots and fruits	60	110	170	
Meat products	15	35	50	
Fish products	5	10	15	

Food group (l/a or kg/a)	≤ 1 y.o.	1 y.o.	2–6 y.o.	7–11 y.o.	12–16 y.o.	≤ 17 y.o.	Reference / Country
Mother's milk, milk products with drinking water	200	-	-	-	-	-	Ziegler, 2017 / Germany
Milk, milk products	45	160	160	170	170	130	
Cereals, cereal products	12	30	80	95	110	110	
Leaf vegetables	3	6	7	9	11	13	
Local fruits, fruit products, juices	25	45	65	65	60	35	
Vegetables, vegetable products, juices	5	17	30	35	35	40	
Potatoes, root vegetables, juices	30	40	45	55	55	55	
Meat, sausage, eggs	5	13	50	65	80	90	
Fish	0.5	3	3	4.5	5	7.5	

Food group (l/a or kg/a)	Infant (< 1 y.o.)	Child (7–12 y.o.)	Adult (>17 y.o.)	Reference / Country
Milk	256	91	80	ISPRA, 2010 / Italy
Milk products	4	11	15	
Cereals	18	88	110	
Leafy vegetables	9	37	55	
Vegetables	9	91	124	
Fruit	18	73	95	
Meat	14	43	60	
Eggs	5	9	11	
Fish	7	9	11	

Food group (l/a or kg/a)	6–12 months	10–11 y.o.	14–15 y.o.	16–64 y.o.	Reference / Country
Milk	120	110	110	95	Byrom et al., 1995 / United Kingdom
Butter, cheese, other milk products	15	15	15	20	
Cereals	15	45	50	50	
Green and other domestic vegetables	5	10	15	30	
Imported fruit	9.5	10	10	25	
Domestic fruit	7.5	15	10	15	
Potatoes and root vegetables	15	50	65	60	

Table 7-4
Consumption rates for ingestion of foodstuff for different age groups, according to some international organisations and a few European national authorities (y.o. denotes years old).

Often there can be considerable variability in the dose received by different age groups for the same intake, and this is another factor that must be taken into account for dose assessments.

In case radionuclides are taken up by the human body (internal contamination), one must realise that the irradiation will continue until the introduced radionuclide is removed from the body. The dose received in a certain organ or tissue during this period is called the committed effective dose.

The committed effective dose is obtained by multiplying the activity intake by the effective dose coefficient for ingestion, and it is computed within a specified period (50 years for adults and up to 70 years for children) according to recent metabolic data and models.

These effective dose coefficients are conversion factors which provide numerical links between dose and measurable quantities; they are published by the International Commission on Radiological Protection (ICRP, 2008) and are derived from a combination of theoretical calculations and experimental observations which are regularly updated.

7.2.2 Example of dose assessment of public exposure for food ingestion

The assessment of public exposure is based on three input parameters: the radionuclides, their activity concentration in foodstuffs, and information on habit data with regard to food consumption. The annual effective dose by ingestion E (Sv) received by an individual in any given year is calculated from the following equation:

$$E = \sum_j \sum_i A_i \times B_j \times e_{i,ing} \qquad (7.1)$$

where:

A_i is the mean activity concentration of radionuclide i in the ingested foodstuff (in Bq/kg);

B_j is the annual amount of food item j for average consumption (in kg); and

$e_{i,ing}$ is the effective dose coefficient for ingestion of radionuclide i for a member of the public (in Sv/Bq).

Dose coefficients for 3-month-old infants, 1-, 5-, 10-, and 15-year-old children and adults are cited in ICRP Publication 119 (ICRP, 2012).

This calculation has to be carried out and summed for every radionuclide i and for every food item j.

The computation could be simplified if the measurement refers to a complete meal and the radionuclide concentration is referred to total content of annual consumption.

Hence the total annual dose received by an adult by consuming this mixed diet sample has been estimated to be 262 µSv from natural radioactivity in food for the Irish population. The computation excluded artificial ^{14}C contribution but included the dose contributions from ^{40}K, ^{87}Rb, ^{228}Ra, ^{226}Ra (O'Connor et al., 2014).

A simple example from Ireland

The Radiological Protection Institute of Ireland (now part of the Environmental Protection Agency) gave a simple example of dose assessment from ingestion of natural radionuclides (see 'Radiation Doses Received by the Irish Population' by O'Connor et al., 2014). This estimation was based on a sample of mixed diet and average concentrations, as quoted in Table 7-5 below. The Irish Universities Nutrition Alliance Survey indicates that an adult consumes an average of 440 kg of food per year (O'Connor et al., 2014).

Nuclide	A_i (Bq/kg)[1]	B (kg/a)	C_i (Sv/Bq)[2]	E_i (µSv)
^{14}C	31	440	5.8×10^{-10}	8[3]
^{210}Po	0.089	440	1.2×10^{-6}	47
^{210}Pb	0.086	440	6.9×10^{-7}	26

[1] Average concentrations of natural radionuclides expressed in Bq/kg of fresh weight.
[2] Dose conversion factors ICRP Publication 119: Compilation of Dose Coefficients based on ICRP Publication 60 for the public (adults) (ICRP, 2012).
[3] This value includes the average annual dose from ingestion of artificial ^{14}C equal to 2µSv.

Table 7-5
Irish data used to estimate dose by ^{14}C, ^{210}Po and ^{210}Pb from foodstuff for the public (adults).

7.3 Discussion and conclusions

The uptake of natural radionuclides depends on their content in foodstuff, which is influenced by differing background levels, climate as well as agricultural conditions, and metabolic behaviour.

Potassium (and with it ^{40}K) is an essential mineral under close homeostatic control in the body. Carbon (and with it ^{14}C) is contained in all types of food. The elements of the uranium and thorium series are present in most types of food of plant or animal origin, although at very low concentrations. Populations living in areas where the soils are rich in uranium/thorium minerals or individuals regularly consuming reindeer meat, brazil nuts, or shellfish can reach annual exposure levels of 1 000 µSv (Diehl, 2003). For example, the uptake of ^{40}K with food leads to an average specific activity of 60 Bq/kg body weight. Radionuclides from the uranium and thorium decay chain, specifically ^{210}Pb and ^{210}Po, contribute to the radiation exposure with an average age-balanced supply of 30 Bq/a and 58 Bq/a, respectively (UNSCEAR, 2000a). The high concentration of ^{210}Po in shellfish can greatly affect the radiation dose in individuals that consume large quantities of shellfish. The total annual effective dose for adults due to inhalation and ingestion of terrestrial radionuclides is estimated to be 0.29 mSv, of which 0.17 mSv is due to ^{40}K and 0.12 mSv to the long-lived radionuclides in the uranium and thorium series. In some cases, there may be large uncertainties in these values.

All in all, the average radiation dose from natural sources is composed of external exposure, for example cosmic rays as well as terrestrial gamma rays, and internal exposure, namely inhalation (mainly radon) and ingestion. The worldwide average annual effective dose from these natural sources is altogether about 2.4 mSv, to which ingestion contributes only 0.3 mSv (UNSCEAR, 2000c).

Nevertheless, it is important to control food continuously for levels of radioactivity and inform consumers about potential risks.

The consumption of food and water by individuals varies widely around the world, depending on climate, food availability and cultural, dietary preferences.

Locally produced or gathered food is now usually greatly supplemented by food imported from other regions or countries.

Moreover, it is difficult to obtain accurate estimates for food consumption: there are considerable individual variations, and many types of food are of a seasonal nature.

Average rates in countries may be indicated by food balance analysis, taking into account local production, imports, and exports. These rates will be overestimated, however, if losses from wastage or preparation are not taken into account (UNSCEAR, 2000).

The activity concentration of natural radionuclides in diet has not yet been systematically studied in all European countries. To provide a more complete overview of radiological implications for EU countries caused by the ingestion of food, it would be useful to make a systematic effort to sample and compile such data in a common database.

Mother sheep with lambs in Knockranea, Ireland
Source: Heather Mount on Unsplash

Greenhouse-grown leafy vegetables
Source: Bernd Kaiser on Unsplash

Free-range pig farming in Herdern, Switzerland
Source: Pascal Bitzenmann on Unsplash

Tomato crops in Hüttendorf, Erlangen, Germany
Source: Markus Spiske on Unsplash

Cereal crop harvesting in Biatorbágy, Hungary
Source: Bence Balla-Schottner on Unsplash

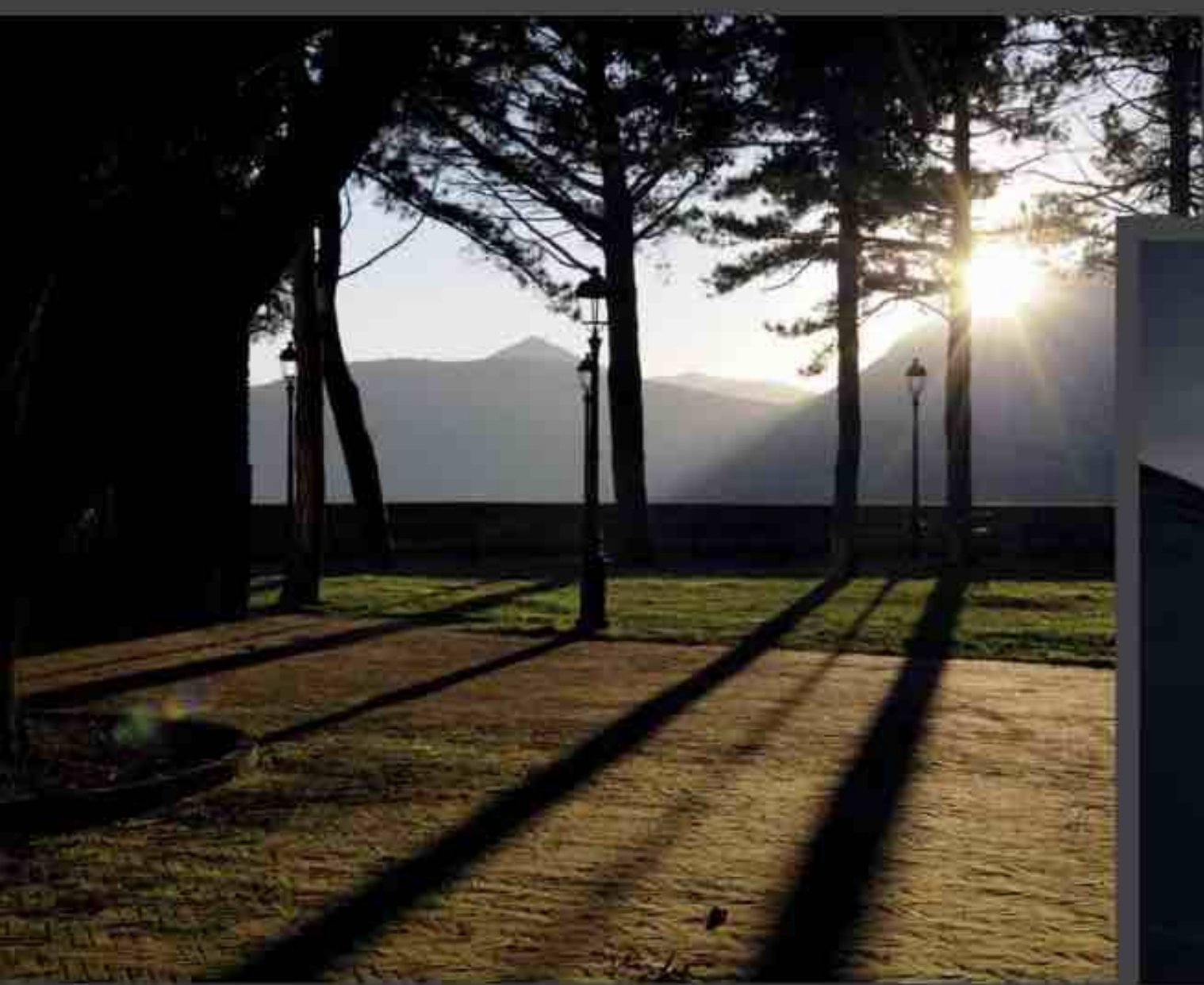

Chapter 8

Cosmic radiation and cosmogenic radionuclides

This chapter addresses the effects of cosmic radiation. Cosmic rays are atomic nuclei accelerated to high energy levels, thus creating electrons, gamma rays, neutrons and mesons when interacting with atmospheric nuclei.

Cosmic-radiation flux depends highly on altitude above sea level.

The intensity of cosmic radiation also depends on solar activity and variations in the geomagnetic field; together with other factors, this triggers a 50 % variation in production rates of cosmogenic radionuclides on the Earth. Cosmogenic radionuclides are created when cosmic rays interact with gases and particulate matters in the Earth's atmosphere.

The first section describes the rationale of the Annual Cosmic-Ray Dose Map, which has been developed by the Joint Research Centre of the European Commission. This map has a resolution of 1 km × 1 km and shows that the cosmic-ray dose mean value in Europe is about 390 microsievert (μSv). It also shows a strong correlation between dose and altitude, with the highest dose levels occurring in the Alps, the Pyrenees and in eastern Turkey, all mountain regions.

The dose map section illustrates annual effective dose per capita per country; it shows that Turkey has the highest value (399 μSv/a) and Iceland the lowest (298 μSv/a), with an average of 334 μSv/a for the countries studied.

The next section addresses cosmogenic radionuclides. Concentration of cosmogenic radionuclides depends on the interaction between cosmic radionuclide production, decay, transport and deposit at the Earth's surface. Examples of different cosmogenic radionuclides are listed, along with illustrative applications showing how measurements of cosmogenic radionuclides can be used. For example, specific radionuclides may be used to date soil sediments and ground water in aquifers. Radionuclides are also useful for studying global climate change and air quality, thus making measurements important regionally and globally.

Monitoring beryllium-7 (^{7}Be) activity concentration is of special interest. This radioisotope is created in the stratosphere and in the upper troposphere, attaches to aerosols and is transported horizontally and vertically by wind and gravity. Then it is removed from the atmosphere through the mechanism that also governs aerosols. Therefore, monitoring ^{7}Be can greatly help in research on mass exchange between the stratosphere and troposphere as well as on local meteorological conditions.

Clockwise from top-left:

NGC 4414, a typical spiral galaxy in the constellation Coma Berenices, is about 55 000 light-years in diameter and approximately 60 million light-years from Earth.
Source: The Hubble Heritage Team (AURA/STScI/NASA)/NASA Headquarters - Greatest Images of NASA (NASA-HQ-GRIN)

Camerino hills. Sun on the hills, Camerino, Italy.
Source: Ferdinando Cinelli

Monte Vettore sunrise. Sunrise, Monte Vettore, Sibillini Mountains National Park, Italy.
Source: Ferdinando Cinelli

Camerino panorama. Panoramic viewpoint from Rocca dei Borgia, Camerino, Italy.
Source: Ferdinando Cinelli

Sun during the Venus transit of June 2012.
Source: Marc De Cort

Cosmic radiation and cosmogenic radionuclides

The Earth is constantly bombarded by high-energy cosmic-ray particles which, upon entering the Earth's atmosphere, interact with its gaseous and particulate constituents to produce a variety of cosmogenic radioisotopes. This chapter presents and describes the European Annual Cosmic-Ray Dose Map. It displays the annual effective dose that a person may receive from cosmic rays at ground level. Moreover, the cosmogenic radionuclides will be described, focusing on their application as tracers in environmental studies.

The cosmic radiation is composed of penetrating ionising radiation (both particulate and electromagnetic). By observing them, it has been established that cosmic rays are ordinary atomic nuclei accelerated to very high energy levels (e.g. Drury, 2012) which move through space at almost light speed.

Depending on their origin, the cosmic rays vary greatly in their composition. Almost 90% of cosmic rays are galactic in origin, and are composed of high-energy particles (0.1–10 GeV) in the form of protons (87%), helium nuclei (alpha particles, about 12%) and heavy nuclei (about 1%) (Masarik & Beer, 1999). On the contrary, solar cosmic rays, with lower energies (< 100 MeV), have a much higher proton content (98%) and lower alpha particle contribution (2%), but do not have any heavier nuclei or energetic electrons. For the physical background and details, we refer to Wissmann et al. (2005) and to Gaisser et al. (2016).

The intensity of cosmic rays presents a wide variety of timescales as well as spatial modulation in the Earth's atmosphere. Many field studies have been designed to assess the understanding of spatial and temporal variations in cosmic rays in the heliosphere, and their relation to effects of the Sun (e.g. Heber et al., 2013). The worldwide neutron monitor network (http://w3.nmdb.eu/), which is considered as a reliable network of ground-based detectors of cosmic rays, records many cosmic-ray variations.

Variations in elevation and atmospheric conditions influence the amount of cosmic radiation received. The intensity of the cosmic-ray flux increases greatly as a function of altitude. At 6–9 km above the Earth's surface, it is 30 times greater than at ground level (e.g. Monem, 2012). In addition, cosmic radiation is partly screened and modulated by the Earth's magnetic field and the atmosphere (Turekian & Graustein, 2003). The heliospheric environment considerably modulates the intensity of the cosmic radiation reaching the Earth. On short timescales, Forbush decreases (also known as Forbush effects) (Forbush, 1954) are sudden decreases in the intensity of cosmic radiation and in the amplitude of a few percent for several days. They occur after an increase in solar activity, such as coronal mass ejections. On a longer timescale and with stronger influence, the intensity of cosmic rays is influenced by the degree of solar activity and to variations in the geomagnetic field. Many studies have investigated and demonstrated the rigidity dependence of the galactic cosmic-ray and solar activity (e.g. Dorman et al., 2001), reporting that high sunspot activities are highly correlated with low cosmic-ray intensity, and vice versa. In particular, the number of sunspots, which can be considered an indicator of disturbances in the Sun's magnetic field, varies from year to year and exhibits a nearly 11-year cycle. In this line, some works (e.g. Sloan & Wolfendale, 2013; Stozhkov et al., 2017) cite solar activity, either directly or through its effect on cosmic rays, as an underestimated contributor to global warming.

All these factors may trigger variations of 50% in production rates of cosmogenic radionuclides on the Earth, which are radioactive isotopes produced and distributed within the Earth's system. Cosmogenic activation strongly depends on the nucleon flux, neutron-to-proton ratio and energies available. For instance, at sea level, radionuclide production is mainly dominated by neutrons at low energies because of charged particles being absorbed in the atmosphere; whereas if materials are flown at high altitude, cosmic flux is much greater, energies at play are larger and activation by protons cannot be neglected (Lal & Peters, 1967).

Production of this kind of radionuclides can be described in three main stages: the production of (i) primary cosmic rays, (ii) secondary cosmic rays (see Figure 8-1) and (iii) nuclides via nucleonic reactions (spallation, neutron capture, or muon capture) in the atmosphere or at Earth's surface (Gosse & Phillips, 2001). The radionuclides with the highest activity concentrations in the environment are: ^{7}Be, ^{36}Cl, ^{39}Cl and ^{38}S (see Table 8-1).

Radionuclide	Half-life	Major radiations	Target nuclides	Typical concentrations (Bq/kg)		
				Air (troposphere)	Rainwater	Ocean water
^{10}Be	$1.6*10^{6}$ a	β	N, O			$2*10^{-4}$
^{26}Al	$7.2*10^{5}$ a	β⁻	Ar			$2*10^{-19}$
^{36}Cl	$3*10^{5}$ a	β	Ar			$1*10^{-3}$
^{81}Kr	$2.3*10^{5}$ a	K X ray	Kr			
^{14}C	$5.7*10^{3}$ a	β	N, O			$5*10^{-3}$
^{32}Si	$1.7*10^{2}$ a	β	Ar			$4*10^{-7}$
^{39}Ar	$2.7*10^{2}$ a	β	Ar			$6*10^{-4}$
^{3}H	$1.2*10^{2}$ a	β	N, O	$1.2*10^{-3}$		$7*10^{-4}$
^{22}Na	2.60 a	β⁻	Ar	$1*10^{-4}$	$2.8*10^{-4}$	
^{35}S	87.4 d	β	Ar	$1.3*10^{-4}$	$7.7\text{-}107*10^{-3}$	
^{7}Be	53.3 d	γ	N, O	$1*10^{-2}$	$6.6*10^{-1}$	
^{37}Ar	35.0 d	K X ray	Ar	$3.5*10^{-4}$		
^{33}P	25.3 d	β	Ar	$1.3*10^{-3}$		
^{32}P	14.3 d	β	Ar	$2.3*10^{-4}$		
^{28}Mg	20.9 h	β	Ar			
^{24}Na	15.0 h	β	Ar		$3.0\text{-}5.9*10^{-3}$	
^{38}S	2.83 h	β	Ar		$6.6\text{-}21.8*10^{-2}$	
^{31}Si	2.62 h	β	Ar			
^{18}F	110 min	β⁻	Ar			
^{39}Cl	56.2 min	β	Ar		$1.7\text{-}8.3*10^{-1}$	
^{38}Cl	37.2 min	β	Ar		$1.5\text{-}25*10^{-1}$	
^{38m}Cl	32.0 min	β⁻	Ar			

Table 8-1
Cosmogenic radionuclides, induced in the Earth's atmosphere by cosmic rays, listed in order of decreasing half-life
Source: Eisenbud, 1997

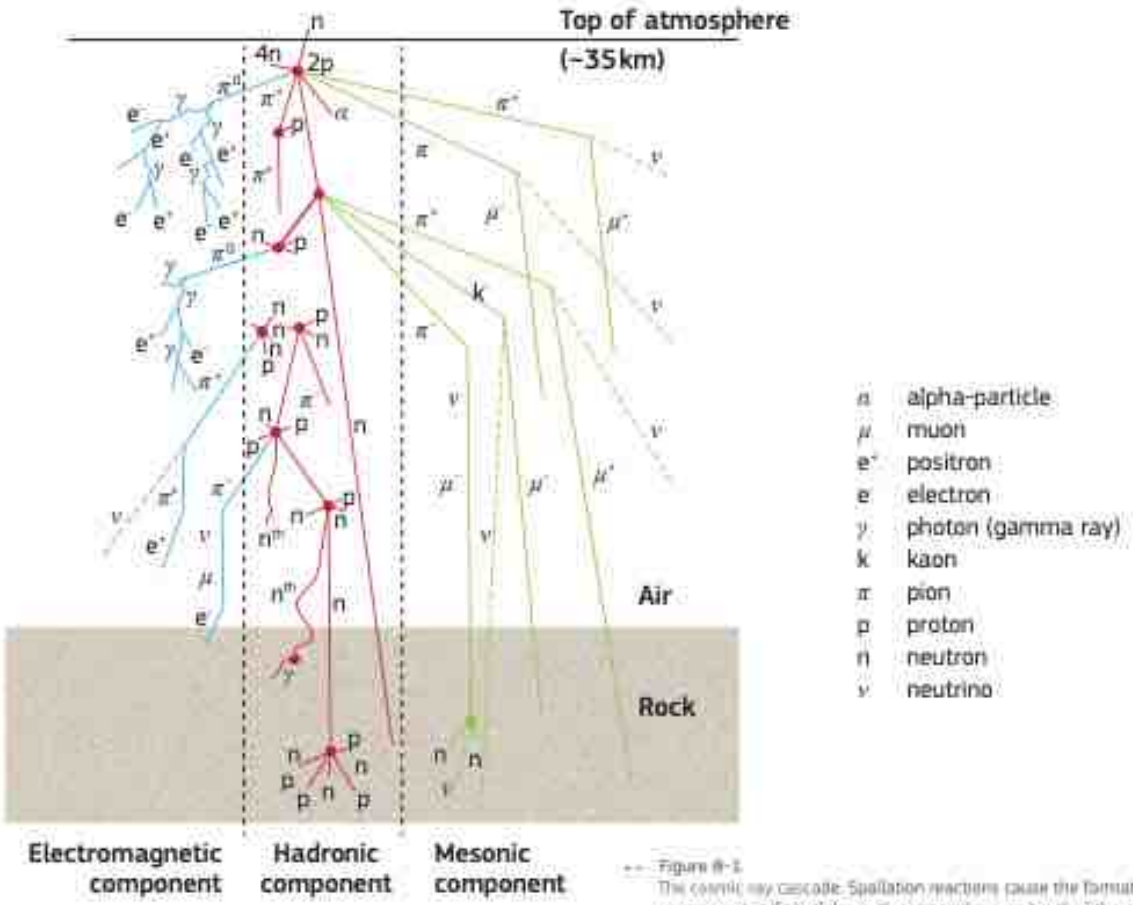

Figure 8-1
The cosmic ray cascade. Spallation reactions cause the formation of new cosmogenic radionuclides in the atmosphere and in the lithosphere
Source: www.AtlasofGaines.org after Gosse & Phillips, 2001

Primary cosmic rays (mainly protons) are stable, charged particles that have been accelerated to enormous energy levels by astrophysical sources located somewhere in our universe. Secondary cosmic radiation is generated when primary rays penetrate into the Earth's magnetic field and interact with atmospheric gas nuclei. This radiation is composed of high-energy nucleons (e.g. protons and neutrons) and mesons (e.g. muons). In its displacement to the Earth's surface, secondary ray particles collide with atoms in the atmosphere. The interaction with nuclei causes a 'spallation' reaction, i.e. a nuclear reaction where a highly energetic nucleon collides with a target nucleus. Spallation reactions cause the release of multiple particles (protons, neutrons and clusters). These accelerated particles cause a wave of secondary interactions and, again, spallation reactions as they strike more atmospheric nuclei. The result of this cascade of reactions is the creation of cosmogenic nuclides and high-energy radiation (neutrons), although, through successive interactions, energy is lost until the particles have insufficient energy to cause a spallation reaction upon collision with another particle.

By far, spallation is the most common mode of production of cosmogenic radionuclides in the atmosphere; but other reactions such as fragmentation, induced fission or capture can be very important for some nuclei (Lal & Peters, 1967). Indeed, processes such as neutron and slow muon capture commonly produce cosmogenic radionuclides (also called terrestrial cosmogenic radionuclides) at the Earth's surface (e.g. Darvill et al., 2013). In this sense, most terrestrial cosmogenic radionuclides are hence formed within the top few centimetres of a rock, as the cosmic-ray intensity flux becomes attenuated with depth.

Notably, natural background radiation is the largest contributor to the average radiation dose received by individuals. Among the natural sources, cosmic rays represent about 13% of the total effective dose received by the population at ground level, with only a very small contribution (0.4%) due to cosmogenic radionuclides (UNSCEAR, 2008). However, as altitude increases, there is less air to act as a shield, and hence exposure to cosmic radiation also increases.

8.1 Cosmic-ray dose map

Part of this Section has been adapted from a paper written by Cinelli et al. (2017): 'European annual cosmic-ray dose: estimation of population exposure'.

8.1.1 Introduction

As described above, interactions between primary particles and atmospheric nuclei produce electrons, gamma rays, neutrons, and mesons (Grieder, 2001). At ground level the dominant component of the cosmic-ray field is muons with energies mostly between 1 and 20 GeV (UNSCEAR, 2008: Volume 1, Annex B, p. 231). Only 0.05% of primary protons penetrate to sea level (Eisenbud & Gesell, 1997: Chapter 6).

Cosmic radiation (photons, direct ionising and neutron components) represents about 13% of the total effective dose received by the population (UNSCEAR, 2008).

For radiation protection of aircrew and frequent flyers it is important to assess exposure to cosmic radiation on board aircraft (ICRP, 2016; European Communities, 1996a; European Union, 2004). According to the latest Basic Safety Standards (BSS) Directive (European Union, 2013), exposure of aircrew to cosmic radiation should be managed as a planned exposure situation (European Communities, 1996b; European Union, 2009; European Union, 2013: art. 35.3). It is worth noting that the BSS Directive explicitly excludes exposure of members of the public or workers other than air- or space crew to cosmic radiation in flight or in space from the scope of the Directive (see Section 1.2 for further details on legal aspects). However, assessing cosmic-ray exposure at ground level is indispensable to understanding population exposure to ionising radiation (Chen et al., 2009; Sato, 2016b; Poje et al., 2012). Several studies have been conducted to estimate and map outdoor gamma dose rate and their components (i.e. terrestrial, cosmic, radon etc.), using different geostatistical techniques (Yeşilkanat et al., 2016; Bossew et al., 2017; Szabó et al., 2017).

The Joint Research Centre of the European Commission has developed the European Annual Cosmic-Ray Dose Map (at 1 km × 1 km resolution) (Cinelli et al., 2017). It displays the annual effective dose, on average over its temporal variability, that a person will receive from cosmic rays at ground level, if she/he spends all the reference time at that elevation. Our simple and easy approach to estimate the cosmic-ray dose, based only on elevation data, has been compared with more sophisticated models, such as EXPACS (Sato, 2016a) and CARI-6 (O'Brien et al., 1996; O'Brien et al., 2005), which consider both latitude and longitude dependences of the cosmic-ray doses, the water density in the ground (EXPACS) and the date (solar cycle variation).

Thanks to the availability of maps showing the geographical distribution of the European population (Batista e Silva et al., 2013a, 2013b; Lavalle & Jacobs-Crisioni, 2016), it is possible to extend the analysis by including population data. In Cinelli et al. (2017), the annual cosmic-ray collective dose, i.e. the total dose incurred by a population, has been evaluated using population data available at the European level. The collective dose is the sum of all individual doses to members of the population. Therefore the population-weighted average annual effective dose due to cosmic rays has been estimated for each European country considered in this study, as well as for all of them together. The coverage of the European Annual Cosmic-Ray Dose Map is conditioned by the availability of the population data (Batista e Silva et al., 2013a, 2013b; Lavalle & Jacobs-Crisioni, 2016).

8.1.2 Materials and methods

Dose calculation

Several software programmes are available for calculating cosmic-ray dose rates at aviation altitudes. A detailed overview is given in the EURADOS 2012-2013 report (Bottollier-Depois et al., 2012), and a comparison of programmes assessing radiation exposure of aircrew can be found in the Radiation Protection 173 issue of the European Commission (European Union, 2012). In general, given geographical information (latitude, longitude and altitude) and time (date), these codes are used to calculate the cosmic-ray dose rate. These programmes are mainly used to assess radiation doses for aircrew members.

Here, cosmic-ray dose rate at ground level has been estimated for most European countries, using the same methods as those for UNSCEAR (UNSCEAR, 2008: Volume 1, Annex B, Chapter 2). The photons and direct ionising component of cosmic radiation are considered separately from the neutron ones. The dose rate value may be considered as averages over the 11-year solar cycle, with a range of variation of about 10% (UNSCEAR, 2000: Annex B, Chapter 1; Bouville & Lowder, 1988). The only spatial variable considered is the altitude effect, and not the latitude. The altitude data used in this study are described below.

Photons and direct ionising component of cosmic radiation

To estimate the dose rates from photons and direct ionising component of cosmic radiation at ground level (at different altitudes), the following formula (Bouville and Lowder, 1988) was used:

$$\dot{E}_1(z) = \dot{E}_1(0)\,[0.21e^{-1.649z} + 0.79e^{0.4528z}] \qquad (8\text{-}1)$$

where z is altitude in km and $\dot{E}_1(0)$ the annual effective dose rate at sea level, which is 240 μSv/a. The latter quantity has been estimated by assuming a dose rate of 32 nGy/h at sea level (UNSCEAR, 2000: Annex A), a value deemed appropriate for the latitudes considered here (between 30° N and 70° N). This value agrees with that of 32.7 nGy/h cited by Wissmann et al. (Wissmann et al., 2005), measured at a latitude of 52° 17' N and a longitude of 10° 28' E. Only altitude has been considered, because at ground level, doses from photons and the direct ionising component of cosmic radiation depend strongly on altitude, and weakly on latitude. The dose rate is about 10% lower at the geomagnetic equator than at high latitudes (UNSCEAR, 2008: Annex B). At sea level, variation in dose rate has been estimated to be around 10% over the 11-year solar cycle (Wissmann, 2006).

A mean shielding factor of 0.8, and an indoor occupancy factor of 0.8 have been assumed (UNSCEAR, 2000: Annex A).

Neutron component of cosmic radiation

To estimate the neutron component of cosmic radiation is more complicated. Both altitude and latitude variation should be taken into account because both quantities strongly affect exposure rates. The approach described in UNSCEAR (2000: Annex A, Chapter 2) has been used. In this work a fixed latitude of 50° has been assumed as an average value for Europe, our area of interest.

A neutron fluence rate of 0.013 $cm^{-2}s^{-1}$ at sea level has been assumed (UNSCEAR, 2000: Annex A, p. 28), and its attenuation with altitude is described using Equation 8-2, where p is the atmospheric depth in g/cm^2. The following relation between height, h, in km, above sea level and atmospheric depth, p, is used:

$$h = 44.34 - 11.86\,p^{0.19} \qquad (8\text{-}2)$$

A neutron fluence energy distribution weighting factor of 200 pSv cm^2 (that is 720 nSv/h per neutron $cm^{-2}s^{-1}$) has been applied (UNSCEAR 2000: Annex A, p. 28).

As for photons and direct ionising component, a shielding factor of 0.8 and an occupancy factor of 0.8 were assumed for the neutron component (UNSCEAR, 2000: Annex A).

Geographical information: altitude

In order to obtain altitude data for this work, a global digital elevation model (DEM), called the GTOPO30 dataset (https://www.usgs.gov/media/images/gtopo30-elevation-source-data) was used. This raster dataset has been derived from several raster and vector sources of topographic information and is georeferenced with a horizontal grid spacing of 30 arc seconds (approximately 1 km).

With the aim of overlaying the altitude data grid and the population data grid, described in the next section, and hence for proceeding with the calculation, it was necessary to transform the original DEM to Lambert azimuthal equal-area (LAEA) projection (http://spatialreference.org/ref/epsg/etrs89-etrs-laea/). Then, to align the DEM grid with the population grid, the re-projected DEM was resampled using the resample' tool in ArcGIS® (Esri, 2011).

Population data

The European Population Map 2006 (Batista e Silva et al., 2013a, 2013b; Lavalle & Jacobs-Crisioni, 2016), created by the Joint Research Centre of the European Commission and by the Centro de Estudos de Geografia e Ordenamento do Território of Portugal, was used as reference in this study. This database was chosen because it is the most recently updated and complete European population grid map.

The data are organised in a digital raster grid that lists the number of residents (night-time population) in 100 m × 100 m cells. It has been produced by downscaling census population data, at the finest resolution available, to the 100 m grid-cell level given pycnophylactic constraints (redistribution or 'disaggregation' of data given on input support such as administrative polygons into grid cells, preserving total 'volume', i.e. population numbers in this case). This downscaling is done by using data on land use (a refined version of the Corine Land Cover from 2006) and soil-sealing. In addition, the final outcome of this cartographic exercise was validated against reference data.

This level of resolution (100 m × 100 m cells) was then reduced to 1 km × 1 km to compare it with the information included in the European Annual Cosmic-Ray Dose Map (1 km × 1 km cells). This upscaling process was performed using the 'aggregate' tool in ArcGIS® (Esri, 2011) so that each output cell contains the sum of the input cells (100 m × 100 m) enclosed by that cell.

Aurora Borealis, 25 February 2017, Tromsø, Norway.
Source: Dancing Lights, Tromsø, www.tromsodancinglights.com

Reykjavik
Oslo
Helsinki
Stockholm
Tallinn
Riga
Copenhagen
Vilnius
Dublin
Amsterdam
The Hague
Berlin
Warsaw
London
Brussels
Luxembourg
Prague
Paris
Vienna
Bratislava
Budapest
Bern
Ljubljana
Zagreb
Belgrade
Sarajevo
Pristina
Podgorica
Andorra la Vella
Rome
Tirana
Madrid
Lisbon
Algiers
Tunis
Valletta
Rabat
Canary Islands (Spain)
30° N
15° W
40° W
35°
30°
25°
20°
15°
10°
5° W
0°
5° E
10°
15°
20°
25°
30°
35°
65° N
70° N
60°
55°
50°
45°
40°
35° N

copyright © European Commission, JRC, 2019

Plate 8: The European Annual Cosmic-Ray Dose Map

(μSv)

- < 350
- 350 - 400
- 400 - 500
- 500 - 700
- 700 - 1 100
- >1 100

Plate 8: The European Annual Cosmic-Ray Dose Map shows the annual effective dose, on average over its temporal variability, that a person should receive from cosmic rays at ground level, if she/he spends all the reference time at that elevation, considering a shielding factor of 0.8 and an indoor occupancy fraction of 0.8. The annual effective dose resulting from cosmic radiation (photons, direct ionising and neutron components) has been calculated following a simple methodology based only on elevation data. A global digital elevation model (DEM), called the GTOPO30 dataset (https://www.usgs.gov/media/images/gtopo30-elevation-source-data), was used as reference for elevation data, so that the grid used for rendering the map is the same as for the DEM, with a horizontal grid spacing of 30 arc seconds (approximately 1 kilometre).

Source: Cinelli et al. (2017)

8.1.3 Discussion and conclusions

Cosmic-Ray Dose Rate Map

The effective dose due to cosmic radiation (photons, direct ionising and neutron components) at ground level has been calculated following the methodology and using the elevation data described above. In turn, the annual cosmic-ray dose at ground level has been calculated by summing the components. The map displays the European annual cosmic-ray dose at 1 km × 1 km resolution. Each value on the map shows the annual effective dose that a person may receive from cosmic rays at ground level if she/he stays there all the reference time with an occupancy factor of 0.8 at that altitude considering a shielding factor of 0.8 (UNSCEAR, 2008). Descriptive statistics of the Annual Cosmic-Ray Dose at 1 km × 1 km resolution are listed in Table 8-2.

The spatial distribution of the cosmic-ray dose rate over Europe clearly reflects elevation above sea level. The map shows that for half the territory considered, the annual cosmic-ray dose is below 360 µSv and for less than 1 % above 1 000 µSv. The highest values are found in the highest-lying areas of Europe, such as the Alps, the Pyrenees and in eastern Turkey (with mountains above 3 000 m.a.s.l.), reaching a maximum value of 3 955 µSv in the latter. Intermediate values, ranging from 400 to 900 µSv, also reflect the natural elevation, for instance in Spain with a medium elevation of 600 m or in the European Plain, which stretches 2 000 km from the French Atlantic coast to the Ural Mountains. On the contrary, the minimum value of 301 µSv at sea level coincides mainly with coastal locations. Exceptions are cliffs and mountains diving into the sea, as for example in Norway.

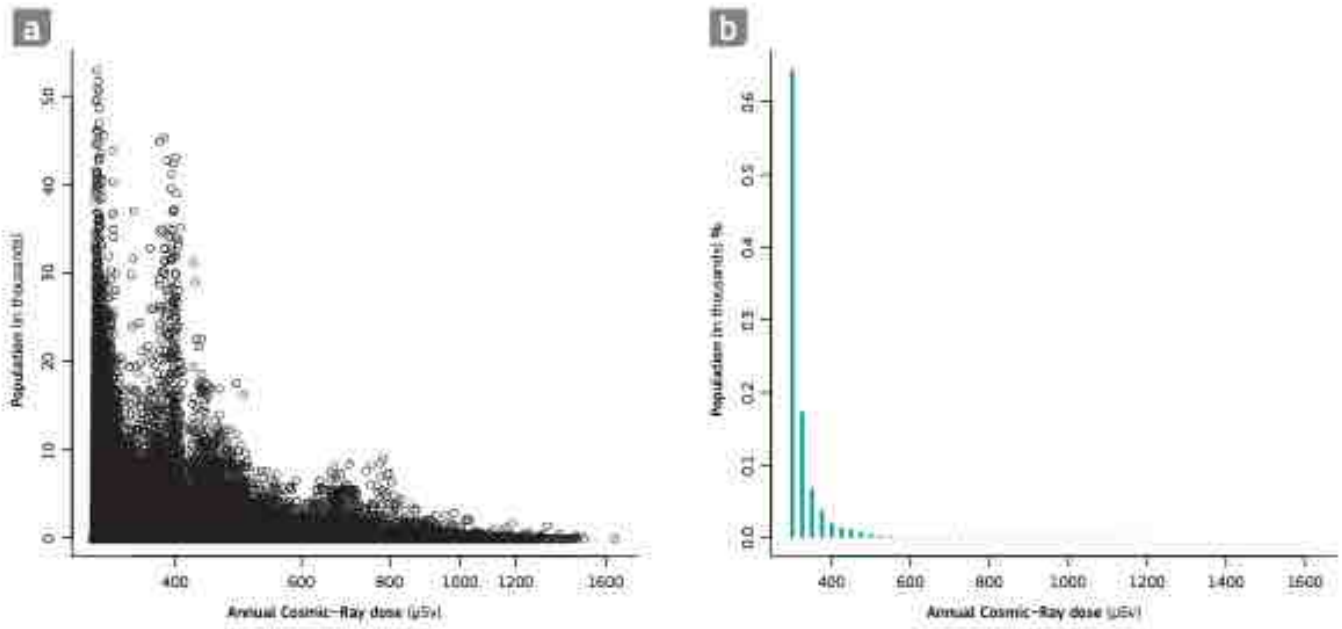

Figure 8-2
a) Population density (inhabitants per 1 km × 1 km cell) versus annual cosmic-ray dose (µSv)
b) Histogram showing fraction of population in annual cosmic-ray dose classes of 25 µSv starting from 300 µSv
Source: Cinelli et al. (2017)

Descriptive statistics for the Annual Cosmic-Ray Dose Map at 1 km × 1 km resolution	
Statistic	Dose (µSv)
Mean	388.7
Median	355.8
Minimum	301.4
Maximum	3 955
1st Quartile	317.3
2nd Quartile	403.1

Table 8-2
Descriptive statistics for the Annual Cosmic-Ray Dose Map at 1 km × 1 km resolution
Source: Cinelli et al. 2017

Cinelli et al. (2017) compared this simple and easy approach to estimate the cosmic-ray dose, based only on elevation data, with more sophisticated models, such as EXPACS (Sato, 2016a) and CARI-6 (O'Brien et al., 1996; O'Brien et al., 2005), that consider the latitude and longitude dependence of the cosmic-ray doses, the water density in the ground (EXPACS) and the date (solar cycle variation). The results of comparative analysis are satisfactory: the difference (below 15 %) between this simple and the more sophisticated EXPACS and CARI-6 models are of the same magnitude as variation due to other parameters (such as solar modulation, building shielding effects, ground condition, indoor occupancy etc.). Thus, we consider that this simple method is adequate for the purpose of developing this European map.

Population exposure

The collective dose for Europe has been estimated by taking as reference the population data for 2006 described in Section 5.1.2. The collective, annual cosmic-ray dose has been calculated for each cell (1 km × 1 km) by multiplying the annual cosmic-ray dose value with the number of residents in that cell.

First, we explored how many persons are exposed to a certain annual cosmic-ray dose that, of course, depends on the elevation at which they live. To this end, we analysed the relation between annual cosmic-ray dose and population at cell level (1 km × 1 km), has been analysed in Figure 8-2a, the majority of cells show values below 400 µSv, which are those with the highest population values. Indeed the few cells above 1 000 µSv coincide with the least populated areas.

This distribution of the results means that only a few percent of the population receive the highest cosmic-ray dose rate (i.e. at the highest altitudes); no person should receive an annual cosmic-ray dose at ground level above 1650 µSv (about 3 270 m.a.s.l.). At ground level, only 0.02 % of the population (138 000 inhabitants) may receive an annual dose due to cosmic-ray levels higher than 1 000 µSv (Figure 8-2b). The majority of the population, about 65 %, will receive values below 325 µSv (about 200 m.a.s.l.); and 92 %, below 400 µSv (about 700 m.a.s.l.).

The population-weighted average (per capita) annual effective dose due to cosmic-ray per country considered is displayed in Figure 8-3. The values range between 399 µSv (Turkey) to 298 µSv (Iceland) per capita. The average value for all the countries considered is 334 µSv per capita. Only Turkey presents a value above the global mean of 390 µSv cited by UNSCEAR (2008).

Cinelli et al. (2017) compared the estimated population-weighted average annual effective dose due to cosmic ray for each European country considered here, with those reported by Sato (Sato, 2016b), based on different population data and methodology. The comparison is satisfying, considering that in the two studies different models and different population data are used. However the differences are comparable with the variation due to solar cycle, measurements uncertainty and so on.

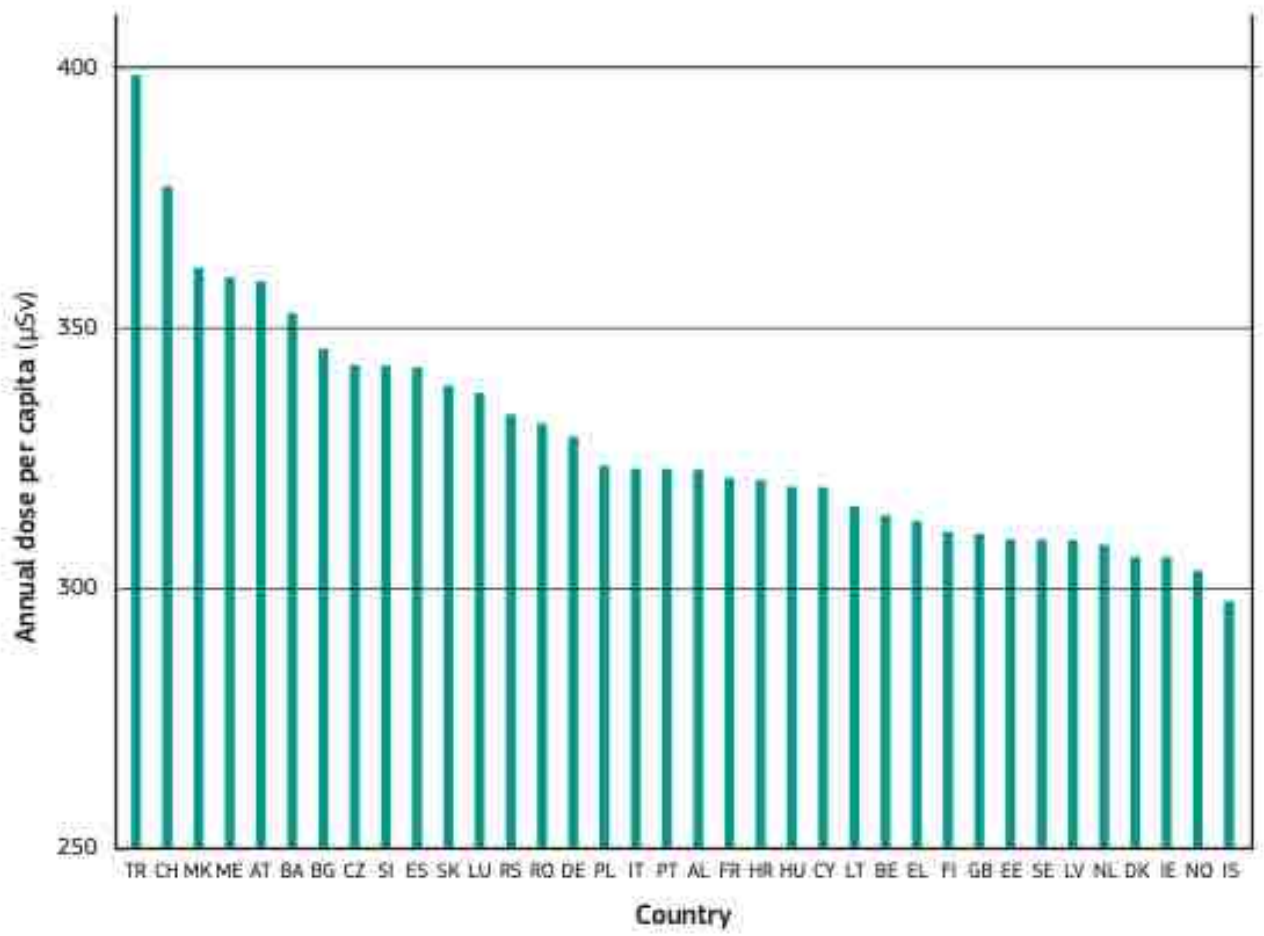

Figure 8-3
Population-weighted average (per person) annual effective dose (annual dose per capita) due to cosmic-ray for each country considered (the ISO country code is quoted for each country, see Appendix 2 for explanations)
Source: Cinelli et al. (2017)

8.2 Cosmogenic radionuclides

8.2.1 Introduction

Since cosmic radionuclides were first discovered, there has been a wide interest in studying their production induced by galactic cosmic rays (e.g. Libby, 1946; Beer et al., 2012). In accordance with the variation in the intensity of cosmic rays, the cosmogenic radionuclide production:

- increases with altitude because the decreasing mass of the overlying atmosphere corresponds to a reduced attenuation of cosmic rays;
- increases with latitude because cosmic rays strike the Earth subparallel to geomagnetic field lines at high latitudes and are thus deflected less than at lower latitudes (Lal & Peters, 1967); and
- varies in relation to the intensity and orientation of the geomagnetic field that modulate the primary cosmic-ray flux (e.g. Pigati & Lifton, 2004).

Therefore, the production rate of cosmic radionuclides primarily depends on the cosmic-ray particle flux at the top of the Earth's atmosphere, whereas the concentration of cosmogenic radionuclides is the result of an interplay between four processes, namely production, decay, transport, and deposition at the Earth's surface. Below, examples of different kinds of production of cosmogenic radionuclides are briefly given:

- **Beryllium-10** (^{10}Be) ($t_{1/2}$ = 1.6 × 10^6 a) is produced in the lower stratosphere and upper troposphere by cosmic ray–induced spallation reactions involving O_2 and N_2. Peak production rates occur at approximately 16–20 km at mid-latitudes. ^{10}Be is also generated when spallation products reach crust (mostly constituted by O, Mg, Si, Fe).
- **Beryllium-7** (^{7}Be) ($T_{1/2}$ = 53.3 d) is a cosmogenic radionuclide produced primarily in the stratosphere and upper troposphere as a natural product of cosmic ray spallation of nitrogen and oxygen nuclei. Once produced, ^{7}Be rapidly forms BeO or $Be(OH)_2$ through ionic reactions, then attaches to sub-micrometre atmospheric aerosol particles and diffuses throughout the atmosphere.
- **Chlorine-36** (^{36}Cl) ($T_{1/2}$ = 3.01 × 10^5 a) and **aluminium-26** (^{26}Al) ($T_{1/2}$ = 7.16 × 10^5 a) are produced by cosmic-ray interaction with ^{35}Cl, ^{39}K, ^{40}Ca and ^{40}Ar (Phillips et al., 1997). They are also generated when spallation products reach the Earth's crust (oxygen, magnesium, silicon and iron).
- **Tritium** or **hydrogen-3** (^{3}H) ($T_{1/2}$ = 12.32 a) is produced by reactions of cosmic rays on ^{14}N or ^{16}O. In addition, this nuclide has anthropogenic origins, since it is formed due to the explosion of nuclear devices in the atmosphere and by the operation of nuclear reactors and particle accelerators.
- **Carbon-14** (^{14}C) ($T_{1/2}$ = 5 730 a) is produced in the atmosphere by a low-energy cosmic-ray neutron reaction with nitrogen. Its production rate is the highest of all cosmogenic radionuclides, because nitrogen is the most abundant element in the atmosphere and has a very large thermal neutron absorption cross-section.
- **Phosphorus-32** (^{32}P) ($T_{1/2}$ =14.28 d) and **phosphorus-33** (^{33}P) ($t_{1/2}$ = 25.3 d) are mainly produced by the spallation reactions induced by neutron on atmospheric argon. In the ocean, an additional source derives from spallation reactions with chlorine and sulphur and, to a lesser extent, with potassium and calcium.
- **Silicon-32** (^{32}Si) ($T_{1/2}$ = 160 a) is when neutrons from cosmic radiation bombard ^{40}Ar atoms in the atmosphere. Its daughter product is the strong beta-emitter ^{32}P. The cosmogenic ^{32}Si activity increased about 4 times during the second half of the 1960s, as a result of bomb-produced ^{32}Si.
- **Krypton-81** (^{81}Kr) ($T_{1/2}$ = 2.2 × 10^5 a) and **krypton-85** (^{85}Kr) ($T_{1/2}$ = 10.6 a) are produced in the upper atmosphere by cosmic-ray spallation involving protons and by reactions from the stable ^{80}Kr and ^{84}Kr isotopes, respectively. So far, there is neither significant subsurface production nor an appreciable anthropogenic source for ^{81}Kr, while ^{85}Kr is also produced by nuclear fission.
- **Sodium-22** (^{22}Na) ($T_{1/2}$ = 2.6 a) is produced by cosmic rays which induce spallation of atmospheric Ar. ^{22}Na is a suitable isotope for detecting solar cycle intensity variations in meteorites, because it is averaging sufficiently well over the orbit, but not over the 11-year cycle. ^{22}Na is also produced by nuclear weapons tests.

8.2.2 Environmental applications

Froehlich (2010) justified using environmental radionuclides as ideal tracers of environmental processes indicating the following properties:

- A tracer must behave in the system exactly (physical and dynamic characteristics) as the traced matter in the particular process to be studied.
- A tracer must have at least one property that distinguishes it from the tracer material (e.g. radioactive decay). This definition implies that an ideal tracer should have neither sources nor sinks in the system other than those to be studied.
- A tracer should move with the same velocity in the system (air, water, soil and sediment) as the material to be traced.
- A tracer should not be confused with trace elements, which have no corresponding major or minor components; thus, the behaviour of trace elements depends on their own concentration and properties.

Specifically, a wide range of cosmogenic radionuclides can be used as tracers since their source functions, together with the large range of different physical and chemical properties and half-lives, are fairly well known (Table 8-1); in particular, due to their different properties, the ultimate choice of the appropriate tracer depends on the physical, chemical, geological and biological process at hand.

Variation in half-lives (extending from seconds to millions of years) as well as their incorporation in the different Earth system reservoirs including the atmosphere, the hydrosphere, the biosphere, the cryosphere and the lithosphere allow the use of cosmogenic radionuclides as chronological markers and general tracers. Excellent summaries of the principles of cosmogenic radionuclide dating include Cerling & Craig (1994), Kurz & Brook (1994), Gosse & Phillips (2001) and Dunai (2010).

There is an extensive bibliography on the use of cosmogenic radionuclides in dating sediments (e.g. Granger & Muzikar, 2001; Balco et al., 2005; Von Blanckenburg, 2005), continental ice sheets (e.g. Lal & Jull, 1992; Balco et al., 2007), ground water (e.g. Fröhlich, 1990; IAEA, 2013; Kazemi et al., 2005), timing of geologic processes and rates of change in the Earth's surface (e.g. Fabel & Harbor, 1999; Gosse & Phillips, 2001) and atmospheric processes (e.g. Young et al., 2009; Lal & Baskaran, 2012). More information is available in Darwill (2013), who presents a complete summary of the range of applications for which cosmogenic radionuclide dating have been used (e.g. volcanic landforms, floods, desert pavements).

For example, the long half-life of ^{81}Kr allows radiometric dating in the 50 000–1 500 000-year age range (Loosli & Oeschger, 1969). ^{81}Kr has already been used to determine the residence time of ground water in old aquifers (e.g. Sturchio et al., 2004), while its trapping in bubbles in glacial ice allows it to be used to date polar ice (e.g. Bruizert et al., 2014). The use of this cosmogenic radionuclide allows accurate dating of up to 1.5 million-year-old ice. Other examples of dating the terrestrial glacial record is the use of ^{26}Al and ^{10}Be ratios in quartz to determine the age of deeply buried palaeosols and underlying till layers (Balco et al., 2005), or to analyse millennial-scale glacial advances by *in-situ* cosmogenic, ^{10}Be, ^{26}Al, and ^{3}He exposure ages, supported by limiting ^{40}Ar/^{39}Ar and ^{14}C ages (Kaplan et al., 2004).

Rilhimaki & Libarking (2007) discuss the theory behind cosmogenic-nuclide palaealtimetry, sampling strategies, and practical limitations of the technique. Palaealtimetry is a method for estimating quantitatively past elevation of the land surface. The terrestrial cosmogenic nuclides are produced in rock when secondary cosmic rays interact with rock at the Earth's surface. In particular, Rilhimaki & Libarking (2007) present the terrestrial cosmogenic nuclides that are of interest to palaealtimetry (stable nuclides: ^{21}Ne, ^{36}Ar, ^{38}Ar, ^{126}Xe; radionuclides ^{3}H, ^{10}Be, ^{14}C, ^{26}Al, ^{36}Cl, ^{41}Ca, ^{53}Mn, ^{81}Kr, ^{129}I). Summaries of other geological applications of cosmogenic isotopes are included in Gosse & Phillips (2001) and Bierman (1994). ^{10}Be and ^{26}Al cosmic radionuclides have been measured to investigate the erosion rates in selected rock samples from the Antarctic mountains (Nishiizumi et al., 1991), and to measure middle Pleistocene erosion rates in buried alluvial sediments (e.g. Balco & Stone, 2005).

Distributions of both cosmogenic and anthropogenic ^{14}C have also been used to study the interaction of the atmosphere with the surface water layer and the oceanic deep waters (e.g. Bard et al., 1994; Matsumoto & Yokoyama, 2013). ^{14}C is also widely used in dating soil organic matter (SOM) (e.g. Pessenda et al., 2001; Blyth et al., 2017), although it is considered a controversial subject, mainly due to the complexity of the soil formation. The main problem with ^{14}C dating of SOM is the different components with different ages of the SOM due to the invasion of roots, infiltration of organic compositions dissolved in water, influence of microorganisms, and of the soil fauna, resulting in the rejuvenation of the estimated ages (Nowaczyk & Pazdur, 1990). Lal et al. (1970) demonstrated that ^{32}Si could be used in ground-water studies, where a comparison of ^{32}Si and ^{14}C ages would be extremely valuable for delineating ground-water characteristics.

Measurements of cosmic radionuclides at mountain peak stations out of the tropospheric boundary layer, i.e. the station lies freely exposed in the advection layer, can be used to draw conclusions about the atmospheric circulation and exchange processes between atmospheric layers. These kinds of location are exposed to air mass transport from far away and, hence, can also serve as good early warning monitoring stations for radioactivity. A good example using these strategic measurement sites to study chemical-physical characteristics and climatology of the free troposphere, as well as to carry out studies regarding stratosphere-to-troposphere exchange (STE), is the Italian climate observatory 'O. Vittori', which forms part of the Global Atmosphere Watch network of the World Meteorological Organization (WMO-GAW, 2004) global station 'Monte Cimone' (Cristofanelli et al., 2018).

High-volume air sampler located at 2 550 m in Sierra Nevada, Spain, in the framework of the FRESA Project (CGL2015-70741-R).
Source: FRESA Project

Concentrations of ^{3}H and ^{14}C, at different latitude belts, have provided deeper insight into the time scales of interhemispheric exchange in the troposphere, rates of meridional transport within the two hemispheres, mixing time scales of air masses within Hadley and Polar cells (Lal, 2002). ^{7}Be and ^{10}Be (Lal & Peters, 1967) are considered as tracers of stratospheric-upper tropospheric influence and subsidence processes, as well as of air mass transport and can be used to test global circulation models (e.g. Liu et al., 2001). In turn, once their potential to correctly reproduce the radionuclides pattern is established, these can be used to analyse the impact of transport, convection and deposition on their seasonal and interannual variability (e.g. Brattich et al., 2017). Due to differences in tropospheric lifetimes, concentrations and isotopic ratios of different nuclides (e.g. ^{10}Be/^{7}Be, ^{10}Be/^{36}Cl, ^{7}Be/^{22}Na) may be used as tracers of mid-latitude wet deposition and storm type, air mass history, and season (Knies, 1994). These studies also show the need for integrating the tracer-based information, i.e. their temporal and spatial variability, with meteorological information in order to fully understand the atmospheric dynamics. In this sense, and as an example, Heikkila et al. (2008) studied production and climate-related changes of ^{10}Be and ^{7}Be transport and deposition to polar regions during two climatically different periods.

8.2.3 Databases

The previous section covered a wide spectrum of *in-situ* applications of cosmogenic isotopes, together with specific and generic examples of exposure dating and erosion. Since then, it has been recognised that cosmogenic radionuclides are useful in a global monitoring network for atmospheric composition to support global climate-change and air-quality research, and therefore they are measured at many of the regional, global, and contributing partner stations in the WMO-GAW network.

Because cosmogenic radionuclides are important as tracers and contribute to natural background radiation, measurements of these nuclides are incorporated into databases. In general, environmental radioactivity databases contribute to scientific knowledge of the processes affecting radionuclides distribution and the sources introducing radioactivity into the environment. They provide critical inputs to the evaluation of environmental radionuclide levels at regional and global scales, deliver information on temporal trends of radionuclide levels and identify gaps in available information. This information is used as a basis to estimate radiation doses to local, regional and global human populations and biota. The purpose of this kind of repository is to provide a better understanding of the past, which is key to predicting the future.

An example of worldwide monitoring and repository in large databases of cosmogenic radionuclides (e.g. ^{22}Na, ^{24}Na, ^{7}Be) is the International Monitoring System (IMS), set up by the Comprehensive Nuclear-Test-Ban Treaty Organization (CTBTO; www.ctbto.org/). CTBTO is an international organisation which aims to achieve the object and purpose of the Comprehensive Nuclear-Test-Ban Treaty (CTBT), to ensure the implementation of its provisions, including those for international verification of compliance with the Treaty; and to provide a forum for consultation and cooperation among its Member States. The IMS consists of 321 monitoring stations and 16 laboratories built worldwide to monitor the planet for any sign of a nuclear explosion conducted on Earth – underground, underwater or in the atmosphere. The radionuclide network comprises 80 measuring stations, of which more than 60 are certified. At a global level, radionuclide stations aim to monitor radioactive aerosols and radioactive noble gases.

Another example of a cosmogenic radionuclides repository (such as ^{7}Be) is the Radioactivity Environmental Monitoring Database (REMdb) (https://rem.jrc.ec.europa.eu/RemWeb/), which is maintained by the Joint Research Centre of the European Commission, located in Ispra, Italy. Further details on this database are given in the box on the right.

Additional information on the Radioactivity Environmental Monitoring Database

The Radioactivity Environmental Monitoring Database (REMdb) database contains a unique collection of environmental radioactivity measurements, as reported from a wide number of sources, media and countries from 1984 onwards. The REMdb collects information received under the terms of Article 36 of the Euratom Treaty (European Union, 2016) from EU Member States, according to which they shall periodically communicate information on environmental radioactivity levels to the European Commission. In this way, the database has two main objectives:

- to keep a historical record of the Chernobyl accident, for further scientific study; and
- to store environmental radioactivity data provided by the EU Member States, thus allowing the Joint Research Centre to prepare annual monitoring reports. Through these reports, citizens of the EU Member States are informed on radioactivity levels in their environment, as stated in Articles 35 and 36 of the Euratom Treaty.

Commission Recommendation 2000/473/Euratom (European Union, 2000) addresses the application of Article 36 of the Euratom Treaty concerning the monitoring of the levels of radioactivity in the environment for the purpose of assessing the exposure of the population as a whole. Table 8-3 shows the combinations of sampling media and measurements categories for which the EU Member States are required to forward monitoring results to the European Commission.

Sampling medium	Measurement category	
	Dense network	Sparse network
Airborne particulates	^{137}Cs, gross beta	^{137}Cs, ^{7}Be
Surface water	^{137}Cs, residual beta	^{137}Cs
Drinking water	Tritium, ^{90}Sr, ^{137}Cs	Tritium, ^{90}Sr, ^{137}Cs
Milk	^{137}Cs, ^{90}Sr	^{137}Cs, ^{90}Sr, ^{40}K
Mixed diet	^{137}Cs, ^{90}Sr	^{137}Cs, ^{90}Sr, ^{14}C

Table 8-3
Sampling media and measurement categories for the monitoring results that EU Member States should forward to the Commission (European Union, 2000, Annex 1). The terms 'dense' and 'sparse' are explained below.
Source: DAMS EC JRC, 2019

More information about samples, treatment and measurements of each sampling media can be found in the annual monitoring reports produced by the REM group to inform the Member States about the radioactivity levels in the environment in the European Community (https://rem.jrc.ec.europa.eu/RemWeb/Reports.aspx):

- Airborne particulates are measured due to their great radiological significance because they may be deposited and hence remain in the local environment.
- Surface water is one of the compartments into which authorised discharges of radioactive effluents from nuclear installations are made. Radionuclides in surface water can be found in the water phase or associated with suspended particles and can eventually become incorporated into sediments and living species.
- Drinking water is monitored because of its vital importance to human beings, even though a severe radioactive contamination of this medium is rather improbable.
- Consumption of milk and dairy products has been shown to be one of the most important pathways for uptake of radionuclides from environment to man.
- The aim of measuring radioactivity in mixed diet is to get 'integral' information on the uptake of radionuclides by human beings from the food chain.

In Table 8-3, the 'dense network' refers to sampling locations which are distributed all over EU Member States' territories, and which allow the European Commission to compute regional averages (except for surface water, for which data from single sample locations are reported). On the contrary, sampling locations within the 'sparse network' are more representative mainly because of high-sensitivity measurements. Therefore, the main distinction between the dense and sparse networks lies in a higher measurement sensitivity in the sparse network, which gives a more transparent representation of actual levels and trends of radioactivity levels.

As of 2019, the REMdb contains nearly 5 million records of data on radioactivity levels in airborne particulates, surface and drinking water, milk and mixed diet. Continuous or semi-continuous monitoring of air and water is undertaken by each EU Member State. Monitoring of food products, such as milk and mixed diet, is considered to be an acceptable surrogate for the Article 35 requirement of the Euratom Treaty to monitor soil.

From the REMdb, measurement data made before 2012 are publicly available, while access to data from 2012 onwards may be granted upon explicit request. This fact makes the REMdb a useful and unique pillar on which to perform environmental radioactivity studies at the European level; thus, it can be considered as a liaison platform between national and international scientific groups conducting collaborative research.

8.2.4 An overview of research activities on beryllium-7

This section provides an overview of research activities undertaken by the scientific community based on beryllium-7 (^{7}Be) activity concentration data. These results represent attempts to understand the distribution of ^{7}Be better, as well as its use as a tracer of different atmospheric processes. Here, we focus on ^{7}Be because:

- its high activity concentration in the air (troposphere), the highest one for any cosmogenic radionuclide (see Table 8.1);
- its wide use in understanding the roles of transport and/or scavenging in controlling the behaviour of radioactively active trace gases and aerosols (e.g. Koch et al., 1996);
- and its contribution, however small, to annual effective doses 0.03 µSv (UNSCEAR, 2000).

Briefly, ^{7}Be is a cosmogenic radionuclide generated by cosmic-ray spallation reactions with nitrogen and oxygen (Lal et al., 1958). Once produced, mainly in the stratosphere (67%) and secondarily in the upper troposphere, ^{7}Be rapidly attaches to ubiquitous submicron aerosol particles in the ambient air (e.g. Ioannidou et al., 2005). Aerosols are transported by wind and redistributed vertically through gravitational sedimentation and are ultimately removed mainly by wet and secondarily by dry deposition in the lower troposphere. Therefore, in addition to its radioactive decay, ^{7}Be is removed from the atmosphere by the same removal mechanisms as for fine aerosols.

Several factors affect ^{7}Be distribution in surface air (Feely et al., 1989), such as air-mass exchange between the stratosphere and troposphere, vertical transport in the troposphere, horizontal transport from subtropics and mid-latitudes to the tropics and polar regions, as well as regional-local meteorological conditions and their seasonal variations (e.g. rainfall, temperature and winds). All these parameters make it difficult to describe ^{7}Be activity in surface air.

Because of its global distribution in surface air, its unique source and sink characteristics, ^{7}Be is considered as a suitable tracer for atmospheric dynamics. For example, Terzi & Kalinowski (2017) analysed ^{7}Be activity concentrations from the International Monitoring System (IMS) to visualise the location of the Hadley-Ferrel convergence zone (HFCZ), the Polar-Ferrel convergence zone (PFCZ) and the intertropical convergence Zone (ITCZ) through ^{7}Be maps covering the whole world and demonstrating the seasonal shift of these zones at longitudinal bands over the course of one year. Usoskin et al. (2009) analysed short-term production and synoptic influences on atmospheric ^{7}Be concentration by using a series of daily measurements of ^{7}Be concentration in near-surface air at eleven sites all around the world.

Many studies have described airborne ^{7}Be activity concentrations and temporal evolution in Europe (in italics are indicated works carried out at high-altitude stations):

- Croatia: Franic et al. (2008);
- Czech Republic: Rulík et al. (2009); Pöschl et al. (2010);
- Finland: Leppanen et al. (2010, 2012); Leppanen & Paatero (2013); Ajtić et al. (2016); Sarvan et al. (2017);
- France: *Bourcier et al. (2011)*;
- Greece: Papastefanou & Ioannidou (1991); Gerasopoulos et al. (2003); Ioannidou et al. (2005); Papandreou et al. (2011); Ioannidou (2012); Ioannidou et al. (2014);
- Greenland: Dibb (2007);
- Italy: *Tositti et al. (2014); Brattich et al. (2017a,b)*; Cannizzaro et al. (2004); Cristofanelli et al. (2018);
- Monaco: Pham et al. (2011); Pham et al. (2013);
- Portugal: Carvalho et al. (2013);
- Russia: Buraeva et al. (2007);
- Serbia: Todorovic et al (1999, 2005, 2010); Krmar et al. (2007); Ajtić et al. (2013); Samolov et al. (2014); Rajačić et al. (2016);
- Slovak Republic: Ďurana et al. (1996); Sýkora et al. (2017);
- Spain: Rodenas et al. (1997); Azahra et al. (2003, 2004); Lozano et al. (2011, 2012); Dueñas et al. (2009, 2011); Piñero Garcia et al. (2012); Rodas Ceballos et al. (2015); Grossi et al. (2016); Bas et al. (2016, 2017); Gordo et al. (2015); Hernandez-Ceballos et al. (2017);
- Sweden: Aldahan et al. (2001); Kulan (2006);
- Switzerland: *Zanis et al. (1999); Gerasopoulos et al. (2005); Steinmann et al. (2013)*;
- United Kingdom (England only): Daish et al. (2005); Likuku (2006).

In addition to the previous studies, several others deal with long-term distribution of the cosmogenic isotope ^{7}Be in surface air all over Europe. Kulan et al. (2006) analysed ^{7}Be collected on air filters over three decades, 1972–2003, at five sampling stations located in Sweden, the Czech Republic and France.

At European level, Hernandez-Ceballos et al. (2015) characterised the spatial and temporal distribution of the ^{7}Be activity concentration in surface air for 34 sampling sites available in the REMdb using data from 1984 to 2011.

Moreover, Hernandez-Ceballos et al. (2016), applied a cluster analysis to identify spatial patterns in ^{7}Be concentrations in Europe: results showed the presence of three distinguishable cluster groups (south, central and north of Europe, respectively)

clearly differentiated in terms of both intensity and time trends of concentration levels, and with a latitudinal distribution of the sampling stations.

These regions were also identified in an analysis of seasonal and spatial patterns of extremely high ^{7}Be surface concentrations (values exceeding the 95th percentile in each site) recorded over the 2001–2010 period across Europe (Ajtić et al., 2017). This study reported that most of the extremes occur during the March–August period, while at least 10% of the total number of extremes takes place during autumn and winter (Figure 8-4). The extreme ^{7}Be events are thought to be caused by particular meteorological conditions, different from the average European patterns (Ajtić et al., 2017; Hernández-Ceballos et al., 2017). In the northernmost parts of Europe, the Scandinavia teleconnection index seems to be a good indicator of these occurrences (Ajtić et al., 2016, 2018).

Furthermore, some of the extremely high ^{7}Be surface concentrations in Scandinavia during winter were linked to a perturbed Stratosphere-Troposphere Exchange (STE) that accompanies sudden stratospheric warmings of the Artic polar vortex (Ajtić et al., 2018). Hernandez-Ceballos et al. (2016) investigated the connection between ^{7}Be activity concentrations and heat-wave events in Spain. On average, the ^{7}Be activity concentrations during these events show an increase of around 20% in central and southern areas of Spain and a decrease of 13% in northern parts. This increase was associated with the arrival of distant westerly air masses.

The behaviour of ^{7}Be activity concentrations at high altitude sites, under the direct influence of air masses from the free troposphere, has often been investigated to understand stratosphere-to-troposphere exchange dynamics (Gerasopoulos et al., 2001, 2005; Zanis et al., 2003; Bourcier et al., 2011; Jasiulionis & Wershofen, 2005; Simon et al., 2009; Tositti et al., 2014; Brattich et al., 2017; Cristofanelli et al., 2018). In particular, Gerasopoulos et al. (2001) characterised the climatological features of ^{7}Be in combination with a set of meteorological and atmospheric parameters such as the tropopause height, relative and specific humidity, and with 3D back-trajectories at four European high-altitude sites. Because of the latitudinal variation of ^{7}Be production, ^{7}Be activity concentrations in northern Europe have also been extensively analysed. For example, Leppanen & Paatero (2013) analysed the surface air ^{7}Be concentrations in Finland according to solar cycle. Sarvan et al. (2017) investigated a ^{7}Be dataset for Helsinki, Finland, that spanned 25 years and found that over short time intervals, the activity concentrations were strongly autocorrelated, while over longer intervals, there were periods of anticorrelation in the data records, which led them to conclude that changes in the dynamics of this radionuclide are slow and evident only over time scales of several years. Ajtić et al. (2016) also analysed the Helsinki ^{7}Be records, but from a perspective of extremely high values occurring during the colder half of the year. In these works, the impact of higher tropopause height (TPH) on ^{7}Be, and therefore, on the spatial distribution of ^{7}Be in Europe, was also suggested. Further, a number of studies have shown a strong link between temperature and ^{7}Be surface concentrations (Ajtić et al., 2018; Ioannidou et al., 2005) that, in turn, suggests that this radionuclide could be one of the climate change indicators. A study of Jiwen et al. (2013) showed a decreasing trend of ^{7}Be activity concentration over 1970–1997, which could be a result of changes in vertical transport, caused by changes in temperature, but also changes in precipitation patterns.

The impact of the 11-year solar modulation on the ^{7}Be concentrations in air is well known. As ^{7}Be is produced in the atmosphere through interaction of cosmic rays with atmospheric molecules, its production rate varies with solar modulation of galactic cosmic rays invading the heliosphere (Masarik & Beer, 1999), which is controlled by the solar magnetic field and, in turn, by solar activity (Figure 8-5). Therefore, the ^{7}Be concentration is inversely related to the number of sunspots.

At surface layers, ^{7}Be activity concentrations may vary due to various atmospheric processes. Generally, the increase in ^{7}Be in ground level air from March to May is ascribed to the more efficient and higher frequency of STE, whereas the further increase in ^{7}Be during summer is due to the stronger convective mixing and TPH. The influence of the tropopause height on ^{7}Be was investigated in detail by Ioannidou et al. (2014), where the time-lag between the elevation of tropopause and the concentration of ^{7}Be in near-surface air is defined. Following the same methodology, Hernández-Ceballos et al. (2016) addressed the impact of tropopause height on ^{7}Be distribution and evaluated the time-lag between tropopause height and ^{7}Be at European level. These results show a larger tropopause height influence on ^{7}Be during summer and a large spatial variability of TPH on ^{7}Be levels with a clear gap between southern and northern Europe in the area of the polar front jet.

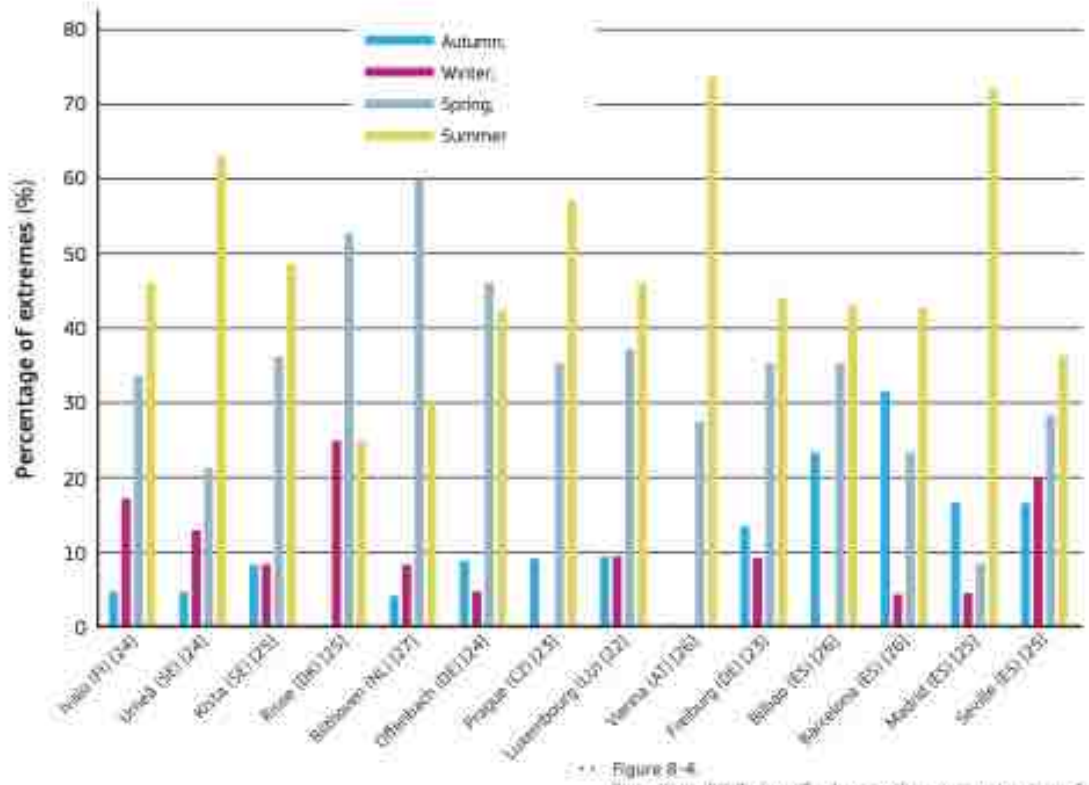

Figure 8-4
Percentage distribution of extreme values over seasons, as observed between 2001 and 2010 at a number of locations in Europe, in order of decreasing latitude (in brackets, the number of extremes). Here, extreme values are defined as those above the 95th percentile
Source: adapted from Ajtić et al. (2017)

^{7}Be has been used as an indicator of parcels of stratospheric air that have entered the troposphere, especially in connection with other tracers to investigate ozone (O_3) behaviour and to investigate vertical transports from the stratosphere to the troposphere. In fact, in atmospheric studies, ^{7}Be has been used to investigate STE and STT (Stratosphere-to-Troposphere Transport) events, starting from the pioneering work of Reiter et al. (1983) at Zugspitze in Germany. STT events, sometimes associated with mid-latitude tropopause folds, are characterised by anomalously high potential vorticity (PV), high ozone, and low water vapour mixing ratio. Previous studies carried out at high-mountain sites especially within the VOTALP (Vertical Ozone Transport in the Alps) and STACCATO (Influence of STE in A Changing Climate on Atmospheric Transport in the Alps) (e.g., Zanis et al., 1999; Cristofanelli et al., 2006, 2009) indicate that air mass transport from the stratosphere to surface levels occurs either in a direct way, with vigorous vertical transport (tropospheric age < 2 days), or in an indirect way, with a multi-step of synoptic and regional transport processes when the STT area is located thousands of kilometres away (longer tropospheric age). Several studies present case of concurrent STE events down to the surface in which high concentrations of the cosmogenic radionuclide ^{7}Be are measured. While Gerasopoulos et al. (2006) presented a complex case in northern Greece, Hernandez-Ceballos et al. (2017) identified vigorous stratospheric-to-troposheric events in Spain; Galani et al. (2003) investigated STE events over the southeastern Mediterranean region, during 2000–2002. An overview of ^{7}Be data collected simultaneously at four high altitude stations in Europe (Monte Cimone, Italy; Sonnblick, Austria; Jungfraujoch, Switzerland; and Zugspitze, Germany) (Gerasopoulos et al., 2001) have provided a tool for analysing STE characteristics on a larger-than-usual spatial scale.

Using ^{7}Be together with other tracers such as the ^{210}Pb nuclide, which like ^{7}Be, travels attached to fine aerosols and therefore follows the same rate of fine stable aerosol (Brattich et al., 2016), proved useful (especially used as activity ratio) for understanding regional circulation processes, as well as processes controlling PM10 variability at the Monte Cimone site (Tositti et al., 2014; Brattich et al., 2017b; Cristofanelli et al., 2018).

In addition to its use as radiotracer in atmospheric studies or to regional circulation understanding, ^{7}Be has been used as a tracer in studies of soil erosion (e.g. Wallbrink & Murray, 1996; Dercon et al., 2012) or soil redistribution (Schuller et al., 2006), even though the Food and Agriculture Organization (FAO) of the United Nations and IAEA with a dedicated joint research programme indicated ^{137}Cs as tracer to measure soil erosion (FAO, 2017). Papastefanou et al. (1999) measured ^{7}Be concentration in soils and grass in the Thessaloniki area of Northern Greece in order to study their fate in natural ecosystems. Iurian et al. (2013) analysed the spatial distribution of ^{7}Be in soils of Lower Austria after heavy rains to estimate the erosion rates, based on the assumption that the deposition of ^{7}Be fallout associated with the erosive event is spatially uniform.

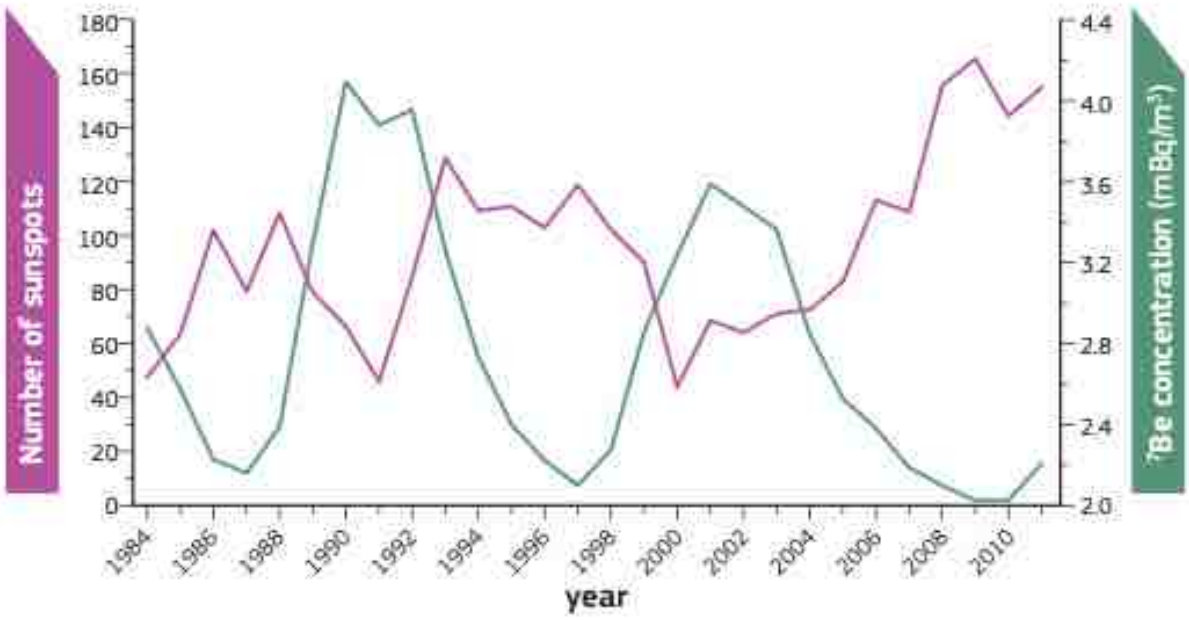

Figure 8-5
Yearly variation in the ^{7}Be activity concentrations and sunspots number from 1984 to 2011
Source: Hernández-Ceballos et al. (2015)

8.2.5 Conclusions

All living organisms are continuously exposed to a background radiation from the air (cosmic-ray and cosmogenic radionuclides), soil, rock, water, and building materials. The amount of background radiation differs as a function of elevation, the amount of nuclei in the soil, and the geographical conditions of different regions.

The source functions, together with a wide range of different physical and chemical properties and half-lives of the cosmogenic radionuclides, are fairly well known. Hence it is possible to select the most appropriate tracer, depending on the specific study to be carried out, and, specifically, in order to understand better the physical, chemical, geological and biological processes at hand. For example, cosmogenic radionuclides can be used to determine directly the timing of events and rates of change in the Earth's surface. This is achieved by measuring their production due to cosmic-ray-induced reactions in rocks and sediments. Numerical simulations of atmospheric production rates of radionuclides, as a function of altitude, latitude, solar and geomagnetic fields, have recently progressed; this has helped to understand this production process better.

Due to the importance of cosmogenic radionuclides as tracers and their contribution to natural background radiation, they are measured and the results are compiled and managed in databases. The purpose is threefold: to provide critical input for evaluating environmental radionuclide levels at regional and global scale; to deliver information on temporal trends of radionuclide levels, and to identify gaps in available information. This will foster a better understanding of the past, which is key to predicting the future.

Since it appears to be an excellent tracer for atmospheric circulation, ^{7}Be is measured routinely at surface monitoring stations all around the world. Temporal variations in surface ^{7}Be radioactivity have been reported from many of these sites. Considering its relatively short half-life of 53.3 days, it is a useful tracer for studying air mass motions on short timescales in the atmosphere, as well as processes controlling its activity concentration in surface air, such as wet and dry removal.

A cloud chamber in Deutsches Museum, Munich, Germany
Source: Tue Marks (CC BY-SA 3.0)

Beta radiation detected in an isopropanol cloud chamber (after insertion of an artificial source strontium-90)
Source: Nuenki (CC BY-SA 4.0 https://creativecommons.org/licenses/by-sa/4.0)

Case study: An overview of beryllium-7 concentrations in Europe in 2006

The following case study analyses beryllium-7 (^{7}Be) concentration in a number of EU Member States using data from 2006 as submitted to the REM Database. This year has been chosen as reference because it has the highest number of ^{7}Be measurements of all those covered by the annual monitoring reports on environmental radioactivity prepared by the Joint Research Centre of the European Commission. Only the stations that reported at least one result per month have been considered (Figure 8-6).

The frequency distribution shown in Figure 8-7 indicate the existence of a large variability in ^{7}Be activity concentrations over these countries. All sampling stations display a positive asymmetrical distribution (positively skewed) of the values, as the upper quartile (P75) is farther from the median than the lower one (P25). This fact confirms the greater variability observed for higher values (P50 upward) than for lower values (P50 downward). This result is also confirmed by observing that the mean is always larger than the median, implying the dominance of low ^{7}Be values as well as the large impact of occasionally high values.

The seasonal variability of surface-air ^{7}Be concentration is displayed for each station in Figure 8-8. We point out the similarity of observed trends in all stations of increasing activity in spring and summer and decreasing in winter and autumn. Therefore, this indicates the existence of a strong seasonal pattern for ^{7}Be.

Different reasons for the seasonal variations in the surface-air ^{7}Be concentrations (Figure 8-8) include:

1. seasonal variations in the amount of precipitation;
2. increased stratosphere-to-troposphere exchange during the late winter and early spring; and
3. increased vertical transport of ^{7}Be from the upper troposphere to the middle and lower troposphere, due to decreased stability of the troposphere during summer months.

copyright © European Commission, JRC, 2010

Figure 8-6.
Map of the sampling stations for ^{7}Be concentration in airborne particulates, as reported by EU Member States to the REM Database (reference year 2006).
Source: DAME EC-JRC, 2010

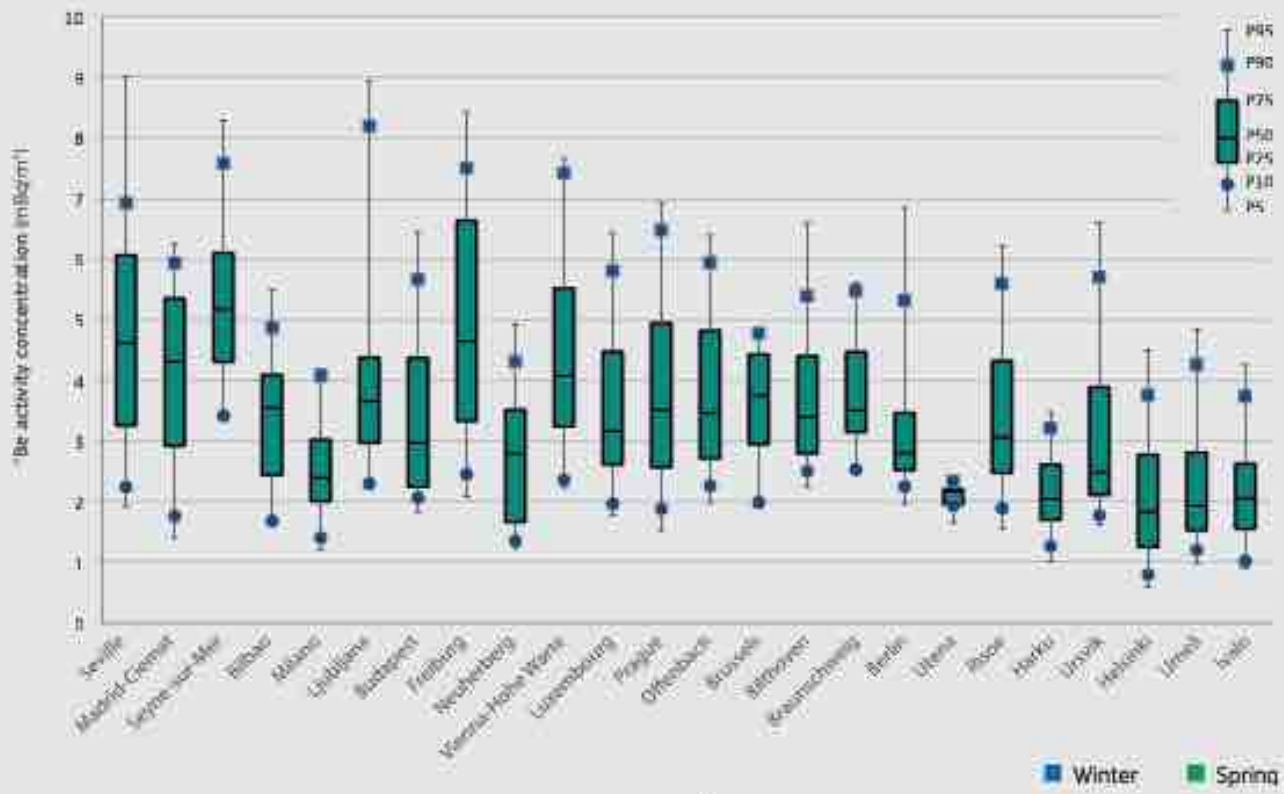

Figure 8-7.
Box plots of ^{7}Be frequency distribution at different sampling stations in a number of EU Member States for 2006. The stations are ordered by latitude from low (left side) to high (right side). P stands for Percentile. The rectangle represents 50 % of the data interquartile range from 25th to 75th percentile; the continuous horizontal line inside the rectangle identifies the median (50th percentile); the small circle and square identify the 10th and 90th percentiles respectively; and the whiskers extend each end of the box to the 5th and 95th percentiles, respectively.
Source: DAME EC-JRC, 2010

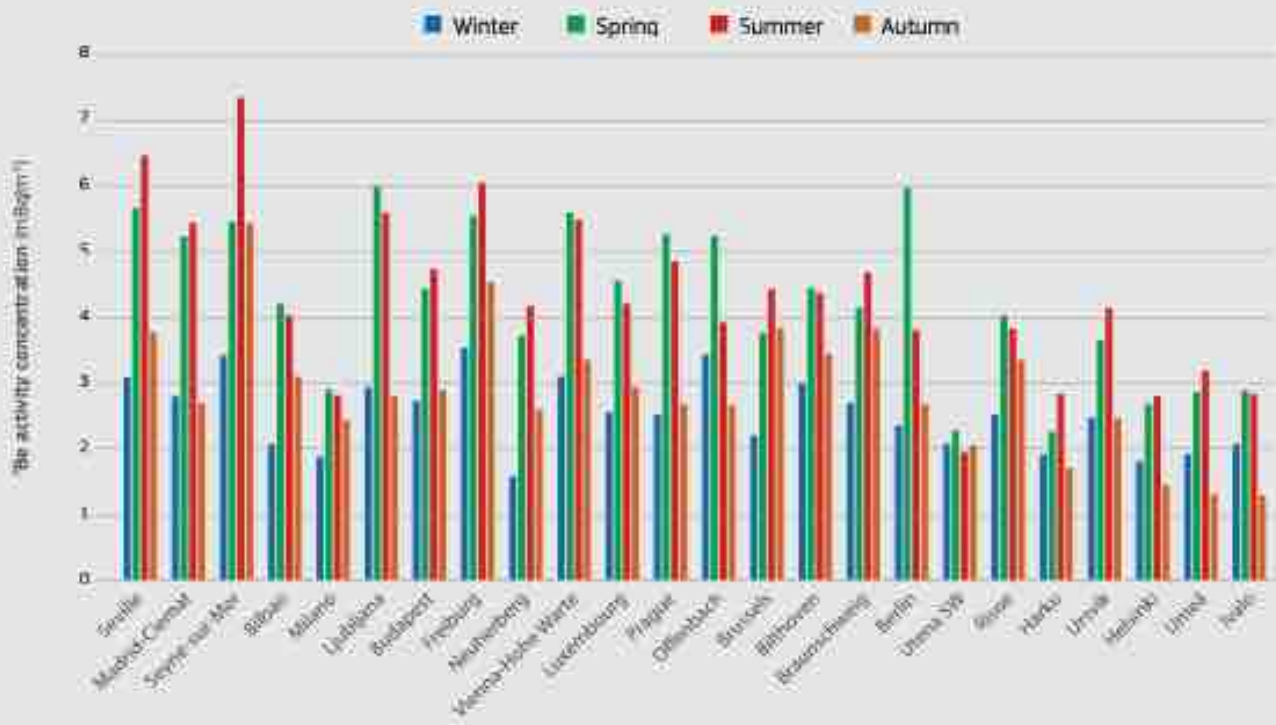

Figure 8-8.
Seasonal average of ^{7}Be concentrations at the different sites. The stations are ordered by latitude from low (left side) to high (right side).
Source: DAME EC-JRC, 2010

Long-exposure photograph capturing the apparent motion of stars and planets (Angus, Scotland, UK).
Source: © Peter Dolan Photography (www.peterdolan.com. Special permission granted for this image to be used specifically for the European Atlas of Natural Radiation)

Chapter 9

Annual effective dose from natural environmental radiation

This chapter presents a method for estimating the annual effective dose to the European population due to exposure to natural environmental radiation. Essentially, it extends methods from previous chapters for estimating internal and external dose from terrestrial and cosmic radiation. However, it should be noted that doses from ingestion and inhalation (apart from indoor radon and progeny) of terrestrial radionuclides are taken from literature. For the first time, the availability of European population maps makes it possible to give an overall European estimate of the annual dose. In this approach, collective doses were estimated in each 10 km × 10 km cell for most European countries by multiplying the annual effective dose by the number of persons living in each cell. These estimates took into account indoor occupancy rates, shielding, and elevation above sea-level which are important factors for estimating doses from radon, external radiation and cosmic radiation, respectively.

We present details for most European countries on the various contributions from natural radiation to dose. Notably, doses from radon and progeny are the major contributors in all these countries, and on the European level they represent about 60 % of the total dose of 3.2 mSv/a, as compared to about 50 % of the total dose of 2.4 mSv/a on a global basis. Between the European countries considered here, total estimated doses range from 1.48 mSv/a in the Netherlands to 5.83 mSv/a in the Czech Republic. This fourfold increase in total dose essentially reflects the tenfold increase in radon doses from 0.43 mSv/a in the Netherlands to 4.47 mSv/a in the Czech Republic. Moreover, within countries exposure and dose may vary significantly, reflecting the varied regional geology which affects both external radiation and radon exposures. In regions where the underlying geology is composed of granites, exposures due to external radiation and radon can be comparatively high. Due to a lack of representative data, certain components of exposure, such as those due to natural radionuclides in building materials, are not included here. Finally, in keeping with the core rationale of this Atlas, this chapter deals only with doses from natural sources; that is, no comparison is made here with doses from anthropogenic sources such as nuclear accidents or medical doses. As indoor radon exposures are due to the design, construction and usage of buildings, it can be argued that although radon itself is natural, the doses from indoor radon are also anthropogenic.

Annual effective dose from natural environmental radiation

9.1 Introduction

The overall goal of this Atlas is to estimate the annual effective dose that the European population may receive from natural radiation.

In general, estimating dose to the public is not based on direct measurements, but on environmental data and models for environmental exposure scenarios. Different approaches exist to estimate the dose, but they mainly depend on data availability (UNSCEAR, 2000: Annex A). Indeed, in this work, effective doses have been estimated by combining all the information from the various natural sources of exposure discussed in previous chapters.

Table 9-1 summarises the main sources of natural exposure for the general public and their contribution to internal and external doses. External exposure arises from radiation sources located outside the human body; it is mainly due to gamma radiation (see Section 2.1). As opposed to external exposure, internal exposure occurs when the sources of ionising radiation are located inside the human body. This is due to the intake of radionuclides through ingestion (food and drinking water) or inhalation of radionuclides.

Unfortunately, except for inhalation of indoor radon and its progeny, data on ingestion and inhalation exposures have not been collected for this study (Table 9-1). For the missing exposure sources, however, data from literature have been used.

Thanks to the availability of European population maps (Batista e Silva et al., 2013a, 2013b; Lavalle & Jacobs-Crisioni, 2016), it has been possible to estimate a population-weighted average of the annual effective dose due to natural sources for the European countries considered as well as for all of them together, giving, therefore, an overall European estimate.

Exposure sources	Doses		
	Internal		External
	Ingestion	Inhalation	
Terrestrial radionuclides	^{40}K, uranium and thorium series	^{40}K, uranium and thorium series	Terrestrial radiation (^{40}K, uranium and thorium series)
	Radon, thoron and their progenies	Radon and its progeny	Radon, thoron and their progenies
		Thoron and its progeny	
Cosmic radiation	Cosmogenic radionuclides	Cosmogenic radionuclides	Directly ionising, photon and neutron component

Table 9-1.
Main sources of natural exposure for the general public and their contributions to internal and external doses. The data available at the European level and presented in this Atlas are highlighted in darker green.
Source: UNSCEAR, EC-JRC, 2013

9.2 Materials and methods

9.2.1 Dose calculation

In order to estimate the annual dose received from natural radiation sources for the European countries considered, as well as for all of them together, the following procedure has been followed, giving, therefore, a European estimate:

a. resampling all input data to 10 km × 10 km resolution to compare all the information included in the European maps developed in this Atlas;
b. estimating the collective doses (cosmic, radon and terrestrial) in each 10 km × 10 km grid cell, by multiplying the annual effective dose with the number of people living in that cell;
c. estimating the population-weighted average annual effective doses (cosmic, radon and terrestrial) for the European countries considered, as well as for all of Europe; and
d. by considering literature data for missing exposure sources, estimating the population-weighted average total annual effective doses, for each European country considered, as well as for all of Europe.

9.2.2 Input data

a. Cosmic sources

Cosmic radiation

The Joint Research Centre of the European Commission has developed the European Annual Cosmic-Ray Dose Map (at 1 km × 1 km resolution); it is described in detail in Chapter 8. The effective dose due to cosmic radiation (photons, direct ionising and neutron components) at ground level has been calculated following methods used by UNSCEAR and based only on elevation data (UNSCEAR, 2008: Annex B).

The map displays the annual effective dose (external dose) that a person could receive from cosmic radiation (photons, direct ionising and neutron components) at ground level, if she/he spends all the reference time at that elevation, considering a shielding factor of 0.8 and an indoor occupancy rate of 0.8 (UNSCEAR, 2000, Annex B).

The 1 km × 1 km grid-cell resolution was reduced to 10 km × 10 km. This upscaling process was performed using the 'aggregate' tool in ArcGIS® (Esri, 2011), so that the output cell contains the sum of the input cells (1 km × 1 km) enclosed by that cell.

Cosmogenic radionuclides

As discussed in Chapter 8, cosmogenic radionuclides are relevant mainly as tracers. Only a few cosmogenic radionuclides, viz. ^{14}C, ^{3}H, ^{22}Na and ^{7}Be, contribute to radiation doses through ingestion (food and water) and inhalation. However, their contribution to the public exposure from natural radiation sources is less than 0.1% (UNSCEAR, 2008: Annex B).

Unfortunately, for this Atlas, no data on concentrations of cosmogenic radionuclides in air, food and water have been collected at the European level. Therefore, the annual effective dose due to cosmogenic radionuclides could not be estimated for European countries, and it has been considered as a fixed value, viz. that as reported by UNSCEAR (2008: Annex B), estimated at 0.01 mSv/a globally.

b. Terrestrial sources

Terrestrial radiation

The European Annual Indoor Radon Dose Map (at 10 km × 10 km resolution) displays the annual effective dose (external dose) that a person could expect to receive from terrestrial radiation, if she/he were to spend all the reference time in a location in which the soil has fixed uranium, thorium and potassium concentration, considering an indoor occupancy rate of 0.8 and a shielding factor of buildings of 1.4.

The dose has been estimated using geochemical concentration of uranium, thorium and potassium in soils, according to the UNSCEAR formula (UNSCEAR, 2008: Annex B), under some assumptions. More details on the methodology are provided in Chapter 4.

Radon (^{222}Rn)

The European Annual Indoor Radon Dose Map displays the annual effective dose (internal dose) that a person may receive from radon inhalation when spending 0.8 of the time indoor at ground floor of a dwelling. The dose coefficient used in this work is the one proposed by UNSCEAR in 2000 (UNSCEAR, 2000: Annex A) and an equilibrium factor of 0.4. More details on the methodology are provided in Section 5.4. Assuming, for lack of more detailed data, that all persons spend 0.8 of their time indoor at ground floor in dwellings, the dose might be overestimated. For some countries or areas (such as large cities), where many people live in flats on higher floors, the dose might be overestimated; whereas for countries where most people live in detached or semi-detached houses, overestimation will be limited. However, this is the best that could be achieved at the time this Atlas was written.

Thoron (^{220}Rn)

Unfortunately, no data on thoron concentration in indoor air could be collected for this Atlas, because varying amounts of such data. Therefore, the annual effective dose due to inhalation of thoron and its progeny could not be estimated for European countries, and it has been considered as a fixed value, viz. that reported by UNSCEAR (UNSCEAR, 2008: Annex B), estimated at global level as 0.1 mSv/a.

Terrestrial Radionuclides (other than radon)

Radionuclides of the uranium and thorium series and ^{40}K enter human beings through inhalation and ingestion.

Natural radionuclides are present in dust particles and can be inhaled. Inhalation of natural radionuclides, other than radon and its decays products, gives rise to a minor contribution, less than 0.01%, to the dose due to natural radiation sources (UNSCEAR, 2008: Annex B).

Ingestion of ^{40}K and of ^{238}U and ^{232}Th series radionuclides comes from foods and drinking water. The effective dose received by ingestion depends on the consumption rates of food and water and on the radionuclides concentrations, and varies widely.

Unfortunately, no data on concentrations of radionuclides in air, food and water have been collected at European level for this Atlas. Therefore, the annual effective dose (internal dose) due to ingestion and inhalation of terrestrial radionuclides (other than radon) could not be calculated for European countries, and it has been estimated as a fixed value, the same as reported in UNSCEAR (UNSCEAR, 2008: Annex B), assessed at global level as 0.29 mSv/a.

c. Population

The European Population Map 2006, created by the Joint Research Centre of the European Commission and by the Centro de Estudos de Geografia e Ordenamento do Território of Portugal (Batista e Silva et al., 2013a, 2013b; Lavalle & Jacobs-Crisioni, 2016), was used as reference for estimating dose. This database was chosen because it is the most recently updated European population grid map; for many European countries, data are still distributed at coarser geographical units such as municipalities.

The data are organised in a digital raster grid that reports the number of residents (night-time population) in 100 m × 100 m grid cells. It has been produced by downscaling census population data, at the finest available resolution, to the 100 m × 100 m grid-cell level given pycnophylactic interpolation constraints (redistribution or 'disaggregation' of data given on input support like administrative polygons into grid cells, preserving total 'volume', i.e. population number in this case). This downscaling was performed using data on land use (a refined version of the Corine Land Cover data from 2006) and soil-sealing. In addition, the final outcome of this cartographic exercise was validated against reference data.

Here, this resolution level (100 m × 100 m cells) was reduced to 10 km × 10 km to compare it with the information included in the European maps (10 km × 10 km cells). This upscaling process was performed using the 'aggregate' tool in ArcGIS® (Esri, 2011), so that the output cell contains the sum of the input cells (100 m × 100 m) enclosed by that cell.

9.3 Results

Table 9-2 and the pie charts in Figure 9-1 invite several observations for each source of natural radiation:

- **Radon (^{222}Rn) and its progeny** represent the most important contribution to the dose from natural sources of radiation due to inhalation. In the budget estimated for Europe, they amount to about 60 % of the total dose, while at global level to about 50 %. This contribution would change if newer dose conversion factors were applied (see Section 5.4.4 for further details about dose conversions factors). Thoron (^{220}Rn) progeny generally contribute less, although in certain situations (e.g. with clay as building material), they may even be dominant. The contribution of radon and its progeny differs significantly between countries, from about 30 % in the Netherlands and Cyprus to more than 75 % in the Czech Republic and Finland. This reflects differences in the geogenic radon contribution due to different geology. Moreover, different construction styles play a role, as they are influenced by climate: air exchange (which is inversely related to indoor radon) can, on average, be expected to be lower in Northern than in Southern Europe. (Please note that these percentages would change if different dose conversion factors were applied for radon and its progeny.)
- The second important contribution is due to **terrestrial external radiation**, on average. The value estimated at the European level is 0.50 mSv/a, similar to the one at global level, 0.48 mSv/a. In Europe, terrestrial external radiation represents 15 % of the total dose due to natural radiation. At country level, terrestrial external radiation presents different values due to varying geology, from 0.85 mSv/a in Portugal, via 0.6 mSv/a in Bulgaria, Croatia, Sweden and the Czech Republic, to the lowest values, around 0.3 mSv/a, found in Poland, the Netherlands, Denmark and Cyprus.
- The dose due **to cosmic radiation** depends essentially on altitude above sea level, so that low-lying countries, e.g. the Netherlands, Denmark and Baltic countries, are less affected than Turkey, Switzerland or Austria. The value estimated at European level is 0.34 mSv/a, similar to the global one of 0.38 mSv/a. For European countries, it ranges from 0.31 mSv/a in Denmark, Estonia, Finland, Ireland, Latvia, the Netherlands and Sweden, to 0.41 mSv/a in Switzerland and 0.42 mSv/a in Turkey.
- For the **other sources of natural radiation** (terrestrial radionuclides, ingestion-inhalation other that radon, thoron and its progeny, cosmic radionuclides), data from literature have been used, and in total they contribute about 0.39 mSv/a, which represents about 12 % at the European level.

Population-weighted average annual effective doses (mSv)							
Dose	External		Internal (ingestion/inhalation)		Internal (inhalation)		Total*
Exposure sources	Cosmic radiation	Terrestrial radiation	Cosmic radionuclides	Terrestrial radionuclides (no radon)	Radon and progeny*	Thoron and progeny	
World (UNSCEAR 2008)	0.38	0.48	0.01	0.29	1.15	0.1	2.41
Europe	0.34	0.5	0.01	0.29	1.96	0.1	3.20
Country							
Albania	0.34	0.49	0.01	0.29	2.82	0.1	4.05
Austria	0.39	0.54	0.01	0.29	2.53	0.1	3.86
Azerbaijan	na	na	0.01	0.29	na	0.1	
Belgium	0.32	0.46	0.01	0.29	1.54	0.1	2.72
Belarus	na	na	0.01	0.29	na	0.1	
Bosnia and Herzegovina	0.37	0.6	0.01	0.29	na	0.1	
Bulgaria	0.36	0.63	0.01	0.29	2.85	0.1	4.24
Croatia	0.33	0.61	0.01	0.29	2.39	0.1	3.73
Czech Republic	0.35	0.61	0.01	0.29	4.47	0.1	5.83
Cyprus	0.33	0.37	0.01	0.29	0.49	0.1	1.59
Denmark	0.31	0.34	0.01	0.29	2.22	0.1	3.27
Estonia	0.31	0.53	0.01	0.29	2.67	0.1	3.91
Finland	0.31	0.51	0.01	0.29	4.94	0.1	6.16
France	0.33	0.49	0.01	0.29	1.82	0.1	3.04
Germany	0.33	0.47	0.01	0.29	1.44	0.1	2.64
Greece	0.34	0.46	0.01	0.29	1.82	0.1	3.02
Hungary	0.32	0.45	0.01	0.29	2.37	0.1	3.54
Ireland	0.31	0.42	0.01	0.29	2.49	0.1	3.62
Iceland	0.32	na	0.01	0.29	0.34	0.1	
Italy	0.34	0.64	0.01	0.29	2.64	0.1	4.02
Latvia	0.31	0.44	0.01	0.29	1.62	0.1	2.77
Lithuania	0.32	0.42	0.01	0.29	1.39	0.1	2.53
Luxembourg	0.34	0.5	0.01	0.29	2.26	0.1	3.50
Malta	na	na	0.01	0.29	na	0.1	
Montenegro	0.39	0.56	0.01	0.29	na	0.1	
Netherlands	0.31	0.34	0.01	0.29	0.43	0.1	1.48
North Macedonia	0.39	0.63	0.01	0.29	2.98	0.1	4.40
Norway	0.33	0.46	0.01	0.29	2.13	0.1	3.32
Poland	0.33	0.31	0.01	0.29	1.73	0.1	2.77
Portugal	0.33	0.85	0.01	0.29	1.66	0.1	3.24
Romania	0.34	na	0.01	0.29	3.76	0.1	
Serbia	0.34	0.58	0.01	0.29	2.74	0.1	4.06
Spain	0.36	0.53	0.01	0.29	1.79	0.1	3.08
Slovak Republic	0.35	0.54	0.01	0.29	na	0.1	
Slovenia	0.36	0.6	0.01	0.29	3.43	0.1	4.79
Sweden	0.31	0.67	0.01	0.29	3.01	0.1	4.39
Switzerland	0.41	0.55	0.01	0.29	2.69	0.1	4.05
Turkey	0.42	na	0.01	0.29	na	0.1	
United Kingdom	0.32	0.41	0.01	0.29	0.84	0.1	1.97

* Assuming that all persons spend 0.8 of their time indoor as ground floor in dwellings, the dose due to radon inhalation might be overestimated and hence also the total dose for each country considered and for Europe.

** Table 9-2
Population-weighted average annual effective dose (in mSv) for each natural radiation source and their sum for each European country considered and for Europe as a whole. For global comparison, data are reported (UNSCEAR, 2008). na: not available.
Source: EANR JRC, 2019

Annual effective dose from natural environmental radiation

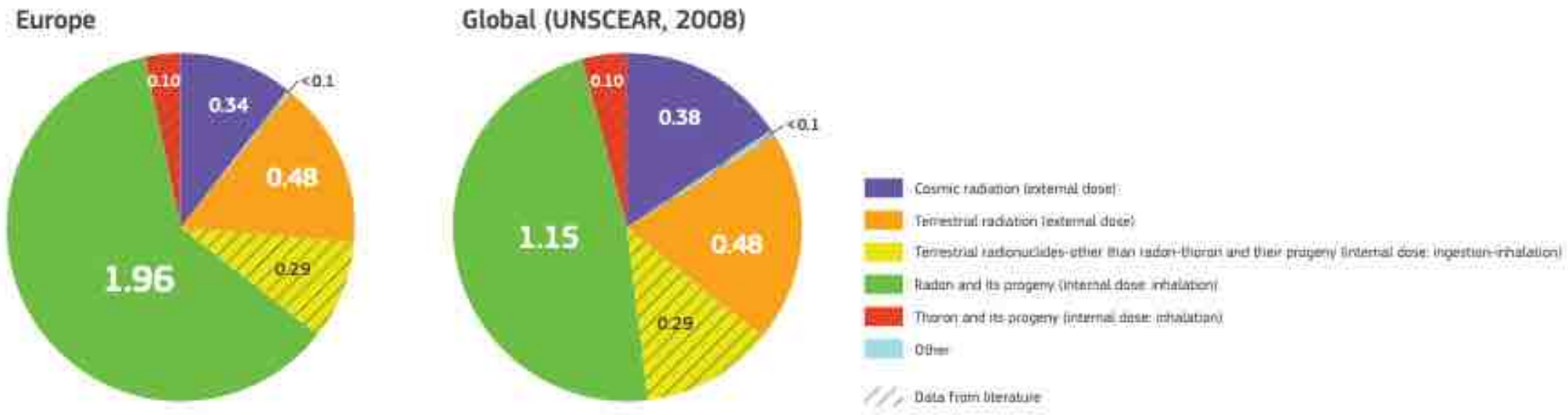

Figure 9-1:
Pie charts showing the population-weighted average annual effective dose (in mSv/a) for each natural radiation source considering European and global populations, respectively.
Source: UNSCEAR, 2008

Except for radon dose, European and global values are not very different, according to UNSCEAR. The difference observed for radon could be because only ground-floor indoor radon data have been considered at the European level and that, globally, many regions have lighter construction styles than in Europe due to a milder climate, which mitigates the radon hazard.

While Table 9-2 reports country averages, exposure and dose can vary significantly within countries as well. In particular, this applies to countries with varied geology. Comparatively high exposure due to external terrestrial radiation and radon occurs in regions whose geological base is made of certain granites (mainly Variscan and Alpine), such as the Iberian Peninsula, the Massif Central in France and the Bohemian Massif in Austria, the Czech Republic, or the granites of Southern Finland. In the same countries, other regions, mainly sedimentary plains and limestone, have lower exposure. However, also in such regions high-exposure areas can occur, as for example the Swiss Jura (karst limestone) or certain post-glacial formations show. Concerning exposure from cosmic radiation, the evident reason for heterogeneity within a country is the variety between mountains and low-lying plains.

Certain components of exposure could not be discussed here due to lack of data. It can be expected that gamma radiation from building materials would contribute visibly in some areas. Since building materials often come from local sources, typically bricks and limestone from local clay quarries, a geographical trend can be expected for these components as well. The matter is probably more complicated with natural radionuclides in food. These days, only a relatively small fraction of consumed foodstuff is produced locally; this seems to apply increasingly even for rural regions. Therefore, one can expect that the geographical distribution of exposure originating from foodstuff is relatively even, but this is only a hypothesis as long as sufficient data to test it are not available.

Table 9-2 and the pie charts in Figure 9-1 only show doses from natural sources. Qualitatively, comparison with anthropogenic sources would give the following picture:

- Fallout and air contamination from nuclear accidents can contribute locally and over short time periods. The only relevant contribution comes from global fallout of atmospheric nuclear bomb tests made in the 1950s to 1960s, which gave rise to problematic doses in Scandinavia (due to particular food chains) and from the Chernobyl accident on 26 April 1986. In parts of Europe, this led to short-time (days) exposure by inhalation of contaminated air, to mid-term (months) exposure by ingestion of contaminated foodstuff (vegetables, milk), some of which remain effective until today (e.g. certain mushrooms, wild boar), and long-term exposure by gamma radiation of fallout in the ground. However, the geographical exposure pattern is very patchy and heterogeneous (De Cort et al., 1998). Today, the most important contribution is from ground gamma radiation (^{137}Cs). This can amount to few percent of terrestrial radiation in areas of Europe that have been more severely hit (parts of Scandinavia, Austria and Bavaria and spots in Northern Italy, Greece etc.). The situation is different in the heavily affected zones of Ukraine, Belarus and Russia, where relatively high doses are encountered more than 30 years after the accident. Other events led to minor doses over Europe, such as the Fukushima accident on 11 March 2011. Averaged over the years, their contribution is negligible and could not even be visualised in the pie chart.
- On the other hand, medical exposure due to radiotherapy and diagnosis can be considerable and even exceed the natural doses (UNSCEAR, 2008: Annex B). Certain treatments can lead to very high doses, which are considered justified only by weighing risks against benefits. Evidently, this contribution to dose only concerns a fraction of the population, while most are not affected at all.

References

Foreword

(p93)

[1] Encyclopaedia Britannica (2019). Europe continent. Written by: Berentsen, W.H.; East, W.G.; Worden, B.E. & Poulsen, T.M. https://www.britannica.com/place/Europe

[2] European Communities (1998). Atlas of Cesium Deposition on Europe after the Chernobyl Accident. Office for Official Publications of the European Communities. ISBN 92-828-3140-X. https://rem.jrc.ec.europa.eu/RemWeb/PastActivities.aspx?id=Atlas

[3] European Union (2013). Council Directive 2013/59/Euratom of 5 December 2013 laying down basic safety standards for protection against the dangers arising from exposure to ionising radiation, and repealing Directives 89/618/Euratom, 90/641/Euratom, 96/29/Euratom, 97/43/Euratom and 2003/122/Euratom. Official Journal of the European Union, OJ L13, 17.01.2014, pp. 1 – 73. https://eur-lex.europa.eu/legal-content/EN/TXT/?uri=OJ:L:2014:013:TOC

[4] European Union (2016). Consolidated version of the Treaty establishing the European Atomic Energy Community. Official Journal of the European Union, C 203, 07.06.2016, pp. 1 – 112. https://eur-lex.europa.eu/legal-content/EN/TXT/?uri=OJ:C:2016:203:TOC

Chapter 1 – Rationale

(pp10-15)

[1] European Communities (1989). Council Directive 89/618/Euratom of 27 November 1989 on informing the general public about health protection measures to be applied and steps to be taken in the event of a radiological emergency. Official Journal of the European Communities, L-357, 07.12.1989, p. 31. https://eur-lex.europa.eu/legal-content/EN/TXT/PDF/?uri=CELEX:31989L0618&from=EN

[2] European Communities (1990a). Commission Recommendation 90/143/Euratom of 21 February 1990 on the protection of the public against indoor exposure to radon. Official Journal of the European Communities L-80, 27.03.1990, p. 26. https://eur-lex.europa.eu/legal-content/EN/TXT/PDF/?uri=CELEX:31990H0143&from=EN

[3] European Communities (1990b). Council Directive 90/641/Euratom of 4 December 1990 on the operational protection of outside workers exposed to the risk of ionizing radiation during their activities in controlled areas. Official Journal of the European Communities, L-349, 13.12.1990, p. 21. http://eur-lex.europa.eu/LexUriServ/LexUriServ.do?uri=CELEX:31990L0641:EN:HTML

[4] European Communities (1996). Council Directive 96/29/Euratom of 13 May 1996 laying down basic safety standards for the protection of the health of workers and the general public against the dangers arising from ionising radiation. Official Journal of the European Communities, L-159, 30.06.1996, p. 1. https://eur-lex.europa.eu/legal-content/EN/TXT/PDF/?uri=CELEX:31996L0029&qid=1524139391074&from=EN

[5] European Communities (1997). Council Directive 97/43/Euratom of 30 June 1997 on health protection of individuals against the danger of ionising radiation in relation to medical exposure. Official Journal of the European Communities, L-180, 09.07.1997, p. 22. https://eur-lex.europa.eu/legal-content/EN/TXT/PDF/?uri=CELEX:31997L0043&qid=1524139510307&from=EN

[6] European Communities (1998). Atlas of Cesium Deposition on Europe after the Chernobyl Accident. Office for Official Publications of the European Communities. ISBN 92-828-3140-X. https://rem.jrc.ec.europa.eu/RemWeb/PastActivities.aspx?id=Atlas

[7] European Communities (1998). Council Directive 98/83/EC of 3 November 1998 on the quality of water intended for human consumption (concerns the quality of water intended for human consumption). Official Journal of the European Communities, L 330, 05.12.1998, p. 32 – 54. https://eur-lex.europa.eu/legal-content/EN/TXT/PDF/?uri=CELEX:31998L0083&qid=1524159207724&from=EN

[8] European Union (2003). Council Directive 2003/122/Euratom of 22 December 2003 on the control of high-activity sealed radioactive sources and orphan sources. Official Journal of the European Union, L 346, 31.12.2003, p. 57 – 64. https://eur-lex.europa.eu/legal-content/EN/TXT/PDF/?uri=CELEX:32003L0122&qid=1524159128792&from=EN

[9] European Union (2011). Regulation (EU) No 305/2011 of the European Parliament and of the Council of 9 March 2011 laying down harmonised conditions for the marketing of construction products and repealing Council Directive 89/106/EEC Text with EEA relevance. Official Journal of the European Union OJ L 88, 4.4.2011, p. 5 – 43. https://eur-lex.europa.eu/legal-content/EN/TXT/PDF/?uri=CELEX:32011R0305&qid=1524138761759&from=EN

[10] European Union (2013a). Council Directive 2013/51/Euratom of 22 October 2013 laying down requirements for the protection of the health of the general public with regard to radioactive substances in water intended for human consumption. Official Journal of the European Union OJ L 296, 7.11.2013, p. 12 – 21. https://eur-lex.europa.eu/legal-content/ENTXT/PDF/?uri=CELEX:32013L0051&from=EN

[11] European Union (2013b). Council Directive 2013/59/Euratom of 5 December 2013 laying down basic safety standards for protection against the dangers arising from exposure to ionising radiation, and repealing Directives 89/618/Euratom, 90/641/Euratom, 96/29/Euratom, 97/43/Euratom and 2003/122/Euratom. Official Journal of the European Union OJ L13, 17.1.2014, p. 1 – 73. https://eur-lex.europa.eu/legal-content/EN/TXT/?uri=OJ:L:2014:013:TOC

[12] European Union (2016). Consolidated version of the Treaty establishing the European Atomic Energy Community. Official Journal of the European Union, C 203, 07.06.2016, p. 1 – 112. https://eur-lex.europa.eu/legal-content/EN/TXT/?uri=OJ:C:2016:203:TOC

[13] ICRP (2007). The 2007 Recommendations of the International Commission on Radiological Protection. ICRP Publication 103. Ann. ICRP 37 (2-4). http://www.icrp.org/publication.asp?id=ICRP%20Publication%20103

Chapter 2 – General background information

(pp. 16-57)

[1] Aliyu, A.S. & Ramli, A.T. (2015). The world's high background natural radiation areas (HBNRAs) revisited: A broad overview on the dosimetric, epidemiological and radiobiological issues. Radiation Measurements, 73: 51–59. https://doi.org/10.1016/j.radmeas.2015.01.007

[2] Allain, C. & Clotre, M. (1981). Characterizing the lacunarity of random and deterministic fractal sets. Physical Review A 44 (8): 8552 – 8558.

[3] Andersen, C.E., Ulbak, K., Damkjær, A., Rønnegaard, P. & Gravesen, P. (2001). Mapping indoor radon-222 in Denmark: Design and test of the statistical model used in the second nationwide survey. Science of the Total Environment, 272(1–3): 231–241.

[4] Artioli, A., Lucci, C., Guidetti, E. & Pizzi, J. (eds.) (2003). Map Projections for Europe. European Commission, Report EUR 20120 EN. http://magicref.org/Library/Documents/MapProjectionsForEurope-EUR-20120.pdf

[5] Annunziatellis, A., Cioni, G., Lombardi, S. & Nolasco, F. (2005). Short- and long-term gas hazard: The release of toxic gases in the Albani Hills volcanic area (central Italy). Journal of Geochemical Exploration, 77(1–3): 93–108. doi:10.1016/j.gexplo.2002.09.074

[6] Arnaldi, L. (1998). Exploratory spatial data analysis in a geocomputational environment. In P. Longley et al. (ed.): Geocomputation, A Primer. John Wiley and Sons, New York, USA.

[7] Asch, K. (2005). IGME 5000 : 1 : 5 Million International Geological Map of Europe and Adjacent Areas – Trial version for the internet. BGR, Hannover, Germany. https://www.bgr.bund.de/EN/Themen/Sammlungen-Grundlagen/GG_geol_Info/Karten/International/Europa/IGME5000/IGME_Project/IGME_Downloads.html?nr=154623.0

[8] Bailey, T.C. & A. Gatrell, A. (1995). Interactive Spatial Data Analysis. Longman Scientific & Technical, Harlow, United Kingdom.

[9] Ball, T.K. & Miles, J.C.H. (1993). Geological and geochemical factors affecting the radon concentration in homes in Cornwall and Devon, United Kingdom. Environmental Geochemistry and Health, 15(1): 27–36. doi: 10.1007/BF02148290

[10] Barros-Dios, J.M., Barnett, M.A., Ruano-Ravina, A. & Figueiras, A. (2002). Exposure to residential radon and lung cancer in Spain: a population-based case-control study. American Journal of Epidemiology 156(6): 548–555. PMID: 12226082

[11] Beaubien, S.E., Ciotoli, G. & Lombardi, S. (2002). Carbon dioxide and radon gas hazard in the Alban Hills area (central Italy). Journal of Volcanology and Geothermal Research, 123 (1–2): 63–80. https://doi.org/10.1016/S0377-0273(02)00328-5

[12] Beaubien, S.E., Jones, D.G., Gal, F., Barkwith, A.K.A.P., Brabant, G., Baubron, J.-C., Ciotoli, G., Graziani, S., Lister, T.R., Lombardi, S., Michel, K., Quattrocchi, F. & Strutt, M.H. (2013). Monitoring of near-surface gas geochemistry at the Weyburn, Canada, CO2 site, 2001–2011. International Journal of Greenhouse Gas Control, 16(S1): S236–S262. doi:10.1016/j.ijggc.2013.01.015

[13] Bender, F. & Nesbor, H.-D. (2017). Geologische Karte von Hessen 1:25 000 (GK25), Blatt 5217: Gladenbach. Second edition. Hessisches Landesamt für Umwelt und Geologie, Wiesbaden, Germany.

[14] Behrmann, J., Ziegler, P.A., Schmid, S.M., Heck, B. & Granet, M. (Eds.) (2005). EUCOR-URGENT – Upper Rhine Graben: evolution and neotectonics. International Journal of Earth Sciences, 94(4): 585–506. https://doi.org/10.1007/s00531-005-0513-0

[15] Ben Gal, I. (2005). Outlier detection. In: Maimon O. and Rokach L. (Editors.) Data Mining and Knowledge Discovery Handbook: A Complete Guide for Practitioners and Researchers. Kluwer Academic Publishers. http://www.eng.tau.ac.il/~bengal/outlier.pdf

[16] Bennett, B.G. (1995). Exposures from worldwide release of radionuclides. Proceeding of an international symposium on environment impact of radioactive release. IAEA, Vienna, May 8–12 1995. pp. 3–32.

[17] Berger, J.-P., Reichenbacher, B., Becker, D., Grimm, M., Grimm, K., Picot, L., Storni, A., Pirkenseer, C. & Schaefer, A. (2005). Eocene-Pliocene time scale and stratigraphy of the Upper Rhine Graben (URG) and the Swiss Molasse Basin (SMB). International Journal of Earth Sciences, 94(4): 711–731. https://doi.org/10.1007/s00531-005-0479-y

[18] Bivand, R.S., Pebesma, E.& Gómez-Rubio, V. (2013). Applied Spatial Data Analysis with R. Springer, ISBN 978-0-387-78170-6

[19] Blanckenburg, F.V. & Davies, J.H. (1995). Slab breakoff: A model for syncollisional magmatism and tectonics in the Alps. Tectonics, 14(1): 120–131. https://doi.org/10.1029/94TC02051

[20] Blanchy, J. & Wood, D. (2003). Mineral-melt partitioning of uranium, thorium and their daughters. Reviews in Mineralogy and Geochemistry, 52(1): 99–123. https://doi.org/10.2113/0520099

[21] Bobrov, O.V., Eurskiy, D.S., Malyuk, B.I. et al. (2006). Ukraine: Carpathians and Ukrainian Shield. Geological excursion guidebook. Ukrainian State Geological Research Institute Publishing, Kiev, Ukraine. https://www.researchgate.net/publication/272486747_Ukraine_Carpathians_and_Ukrainian_Shield

[22] Bone, S.E., Dynes, J.J., Cliff, J. & Bargar, J.R. (2017). Uranium (IV) adsorption by natural organic matter in anoxic sediments. Proceedings of the National Academy of Sciences of the United States of America, 114 (4): 711–716. http://doi.org/10.1073/pnas.1611918114

[23] Bossew, P. (2014). Spatial sampling design for radon surveys. https://my.cleanline.com/Portlet/europe/Spatial_sampling_design

[24] Bossew, P. (2012). Radon: Explaining the log-normal mystery. Journal of Environmental Radioactivity, 101(10): 826–834. https://doi.org/10.1016/j.jenvrad.2010.05.005

[25] Boundon, B. & Sims, K.W. (2003). U-series and isotopic magmatism in U-series geochemistry and applications. In: Bourdon, B., Henderson, G.M., Lundstrom, C.C. & Turner, S.P. (eds): Uranium-Series Geochemistry. Mineralogical Society of America: 39–123.

[26] Brady, B.T. & Rice, R.S. (1977). Helium determinations as an exploration technique at the Ambrosia Lake uranium district, McKinley County, New Mexico. United States Geological Survey, Open File Report, 77-669. https://doi.org/10.3133/ofr77669.

[27] Breitner, D., Arvela, H., Hellmuth, K.-H. & Reinsel, T. (2010). Effect of moisture content on emanation at different grain size fractions – A pilot study on granitic esker sand sample. Journal of Environmental Radioactivity, 101(11): 1002–1006. https://doi.org/10.1016/j.jenvrad.2010.07.008

[28] Carlini, C., Rinzenu, P., Giovani, C. & Gannaioglio, M. (2014). Definition of radon prone areas in Friuli Venezia Giulia region, Italy, using geostatistical tools. Journal of Environmental Radioactivity, 138: 208 – 219. http://doi.org/10.1016/j.jenvrad.2014.09.003

[29] Capaccioni, B., Cinelli, G., Mostacci, D. & Tassi, L. (2012). Long-term risk in a recently active volcanic system: Evaluation of doses and indoor radiological risk in the quaternary Vulsini Volcanic District (Central Italy). Journal of Volcanology and Geothermal Research 247–248: 26–36. https://doi.org/10.1016/j.jvolgeores.2012.07.014

[30] Chabaux, F., Riotte, J. & Dequincey, O. (2003). U-Th-Ra Fractionation During Weathering and River Transport. Reviews in Mineralogy and Geochemistry, 52(1): 533–576. doi: 10.2113/0520533

[31] Chen, J. (2018). A review of radon equilibrium factors for the assessment of radon dose to the lung. CARST 2018. An Elemental Approach: Radon in EARTH AIR WATER. https://www.carst.ca/resources/Conference%202018/Presentations2018/Chen-CARST-Feq%20v2.pdf

[32] Chen, W., Honghui, H., Bai, T. & Jiang, S. (2017). Geochemistry of monazite within carbonatite-related REE deposits. Resources, 6(4): 51. https://doi.org/10.3390/resources6040051

[33] Cheng, Q. (1999). Multifractality and spatial statistics. Computers & Geosciences, 25 (8): 949 – 961. DOI: 10.1016/S0098-3004(99)00060-6

[34] Chilès, J.-P. & Delfiner, P. (2012). Geostatistics: Modeling Spatial Uncertainty, 2nd Edition. ISBN: 978-0-470-18315-1

[35] Chung, A.P., Sousa, T., Pereira, A. & Morais, P.V. (2014). Microorganisms – Tools for bioremediation of uranium contaminated environments. Procedia Earth and Planetary Science, 8: 53–58. https://doi.org/10.1016/j.proeps.2014.09.012

[36] Cinelli, G. & Tondini, F. (2015). Log-normality of indoor radon data in the Walloon region of Belgium. Journal of Environmental Radioactivity, 143: 100–109. doi: 10.1016/j.jenvrad.2015.02.014

[37] Ciotoli, G., Bigi, S., Tartarotti, C., Sacco, P., Lombardi, S., Arcone, A. & Mazzoli, S. (2014). Soil gas distribution in the main coseismic surface rupture zone of the 1983, Ms = 6.9, Ipsina earthquake (southern Italy). Journal of Geophysical Research Solid Earth, 119(5): 2440–2461. doi:10.1002/2013JB010508

[38] Ciotoli, G., Etiope, G., Guerra, M. & Lombardi, S. (1999). The detection of concealed faults in the Ofanto Basin using the correlation between soil-gas fracture surveys. Tectonophysics, 301(3–4): 321–332. https://doi.org/10.1016/S0040-1951(98)00220-0

[39] Ciotoli, G., Guerra, M., Lombardi, S. & Vittori, E. (1998). Soil-gas survey for tracing seismogenic faults: A case study in the Fucino basin, Central Italy. Journal of Geophysical Research Solid Earth, 103(B10): 23781–23794. doi:10.1029/98JB01553

[40] Ciotoli, G., Lombardi, S. & Annunziatellis, A. (2007). Geostatistical analysis of soil gas data in a high seismic intermontane basin: Fucino Plain, central Italy. Journal of Geophysical Research Solid Earth, 112 (B05407). doi:10.1029/2005JB004044

[41] Ciotoli, G., Sciarra, A., Ruggiero, L., Annunziatellis, A. & Biagi, S. (2016). Soil gas geochemical behaviour across buried and exposed faults during the 24 August 2016 central Italy earthquake. Annals of Geophysics, 59, Fast Track 5, 2016. doi: 10.4401/ag-7242

[42] Ciotoli, G., Voltaggio, M., Tuccimei, P., Soligo, M., Pasculli, A., Beaubien, S.E. & Bigi, S. (2017). Geographically weighted regression and geostatistical techniques to construct the geogenic radon potential map of the Lazio region: A methodological proposal for the European Atlas of Natural Radiation. Journal of Environmental Radioactivity, 168 (Part 2): 355–375. https://doi.org/10.1016/j.jenvrad.2016.05.010

[43] Clark, I. & Harper, W.V. (2001). Practical Geostatistics 2000. Geostokes (Ecosse) Limited, United Kingdom.

[44] Clark, P.J. & Evans, F.C. (1954). Distance to nearest neighbor as a measure of spatial relationships in populations. Ecology, 35 (4): 445 – 453.

[45] Cochran, W.G. (1977). Sampling Techniques, Third Edition. John Wiley & Sons, New York, USA. ISBN 0-471-16240-X

[46] Cocks, L.R.M., McKerrow, W.S. & Staal, C.R. van (1997). The margins of Avalonia. Geological Magazine, 134(3): 627–636.

[47] Cole, J.M., Rasbury, E.T., Montañez, I.P., Padoria, V.A., Landstrom, A. & Hanson, G.N. (2004). Petrographic and trace element analysis of uranium-rich tufa calcite, middle Miocene Barstow Formation, California, USA. Sedimentology, 51(3): 455–453. https://doi.org/10.1111/j.1365-3091.2004.00631.x

[48] Cressie, N. (1990). The origins of kriging. Mathematical Geology, 22: 239–252. http://dx.doi.org/10.1007/BF00889887.

[49] Cressie, N. (1993). Statistics for spatial data. John Wiley & sons. ISBN 0-471-00255-0

[50] Cumberland, S.A., Douglas, G., Grice, K. & Moreau, J.W. (2016). Uranium mobility in organic matter rich sediments: A review of geological and geochemical processes. Earth-Science Reviews, 159: 160–185. doi: 10.1016/j.earscirev.2016.05.010

[51] Cuney, M. (2014). Felsic magmatism and uranium deposits. Bulletin de la Société géologique de France, 185(2): 75–92.

[52] Dadlez, R. (2006). The Polish Basin – interbetween crystalline, consolidated and sedimentary crust. Geological Quarterly, 50(1): 43–58. DOI: https://doi.org/10.7306/gq.v50i1.7397

[53] Danielchenko, Z., Miles, J.C.H. & McColl, N. (2014). Radon, the lognormal distribution and deviation from it. Journal of Radiological Protection, 34(1): 183–190. doi: 10.1088/0952-4746/34/1/183

[54] Darby, S., Hill, D., Auvinen, A., Barros-Dios, J.M., Baysson, H., Bochicchio, F., Deo, H., Falk, R., Forastiere, F., Hakama, M., Heid, I., Kreienbrock, L., Kreuzer, M., Lagarde, F., Makeläinen, I., Muirhead, C., Oberaigner, W., Pershagen, G., Ruano-Ravina, A., Ruosteenoja, E., Rosario, A.S., Tirmarche, M., Tomásek, L., Whitley, E., Wichmann, H.E. & Doll, R. (2005). Radon in homes and risk of lung cancer: collaborative analysis of individual data from 13 European case-control studies. British Medical Journal, 330: 223–226. doi: 10.1136/bmj.38308.477650.63.

[55] Dawood, Y.H. & Abd El-Naby, H.H. (2007). Mineral chemistry of monazite from the black sand deposits, northern Sinai, Egypt: a provenance perspective. Mineralogical Magazine, 71(4): 389–408. https://doi.org/10.1180/minmag.2007.071.4.389

[56] De Marbou, S., Sabbarese, C. & Menetti, G. (1998). Radon emanation and exhalation rates from soils measured with an electrostatic collector. Appl. Radiat. Isot., 49: 407–413.

[57] De Vivo, B., Ippolito, F., Capaldi, G. & Simpson, P.R. (1984). Uranium geochemistry, mineralogy, geology, exploration and resources. London: Institution of Mining and Metallurgy. ISBN-13: 978-94-009-6062-6. DOI: 10.1007/978-94-009-6060-2

[58] Del Claro, F., Paschuk, S.A., Corrêa, J.N., Denyak, V., Kappke, J., Perna, A.F.N., Martins, M.N., Santos, T.O., Rocha, Z. & Schelin, H.R. (2017). Radioisotopes present in building materials of workplaces. Radiation Physics and Chemistry, 140: 141 – 145. https://doi.org/10.1016/j.radphyschem.2017.02.037

[59] Delmelle, E. (2008). Spatial Sampling. In Fotheringham, A.S. & Rogerson, P.A. (eds.) Sage Handbook of Spatial Analysis. Sage Publication, The Cromwell press Ltd, United Kingdom.

[60] Deutsch, C.V. & Journel, A.G. (1992). GSLIB Geostatistical Software Library and User's Guide. Oxford University Press, Oxford, United Kingdom; 340 pp.

[61] Dixon, C. & Leach, B. (1977). Sampling methods for geographical research. CAO MOG 17.

[62] DOE (1982). DOE Fundamentals Handbook instrumentation and control. Volume 2 of 2. DOE-DBK-10132-92. United States Department of Energy, Washington, US. (1992).

[63] Domingos, F. & Pereira, A. (2018). Implications of alteration processes on radon emanation, radon production rate and W-Sn exploration in the Panasqueira ore district. Science of the Total Environment, 622–623: 825–840. doi: 10.1016/j.scitotenv.2017.

[64] Ielsin, M., Bijelijac, S.J., Badourov, M. & Barbaric, L. (2016). Mechanisms of radon loss from zircon: Microstructural control on emanation and diffusion. Geochimica et Cosmochimica Acta, 184: 212–226. https://doi.org/10.1016/j.gca.2016.04.024

[65] Eisenbud, M. & Gesell, T. (1997). Chapter 6 - Natural Radioactivity. In Environmental Radioactivity (Fourth Edition). Academic Press, San Diego, 1997, Pages 134-200. ISBN 9780122351549. https://doi.org/10.1016/B978-0122351549-5/50010-4

[66] Eisman, L., Lee, T. & Wanke, S. (1995). Eisenian and Saalian deposits in their type area in central Germany. In: Ehlers, J., Kozarski, S. & Gibbard, P.L. (Eds.) Glacial deposits in North-East Europe. Balkema, Rotterdam, the Netherlands, pp. 433 – 454.

[67] EPA (2000). Multi-Agency Radiation Survey and Site Investigation Manual (MARSSIM) Revision 1. - Sampling and Preparation for Laboratory Measurements (Chapter 7). Environmental Protection Agency (EPA), August 2000.

[68] European Union (2013). Council Directive 2013/59/Euratom of 5 December 2013 laying down basic safety standards for protection against the dangers arising from exposure to ionising radiation, and repealing Directives 89/618/Euratom, 90/641/Euratom, 96/29/Euratom, 97/43/Euratom and 2003/122/Euratom. Official Journal of the European Union OJ L13, 17.1.2014, pp. 1–73. https://eur-lex.europa.eu/legal-content/EN/TXT/?uri=OJ:L:2014:013:TOC

[69] Faust, H. (2009). Historische Geologie. In German. 8th Grifft, Stuttgart, Germany. ISBN: 9783825221492

[70] Fjellskaar, W., Lindholm, C., Dehls, J.F. & Fjeldskaar, I. (2000). Postglacial uplift, neotectonics and seismicity in Fennoscandia. Quaternary Science Reviews, 19(14-15): 1413–1422. https://doi.org/10.1016/S0277-3791(00)00079-6

[71] Fotheringham, A.S., Brunsdon, C. & Charlton, M. (2002). Geographically Weighted Regression: The Analysis of Spatially Varying Relationships. John Wiley & Sons, Chichester, UK. 284 pp. ISBN: 978-0-471-49615-8

[72] Frechen, M., Oches, E.A. & Kohfeld, K.E. (2003). Loess in Europe – mass accumulation rates during the Last Glacial Period. Quaternary Science Reviews, 22(18-19): 1835 – 1857. https://doi.org/10.1016/S0277-3791(03)00149-5

[73] Frechen, M., Vanneste, K., Verbeeck, K., Paulssen, E. & Camelbeeck, T. (2001). The deposition history of the coversands along the Bree Fault Escarpment, NE Belgium. Netherlands Journal of Geosciences, 80(3-4): 171–185. https://doi.org/10.1017/S0016774600023829

[74] Friedmann, H. (2001). Final results of the Austrian radon project. Health Physics, 80(4): 335–346. doi: 10.1097/01.HP.0000157228.19115.17

[75] Frisch, W. & Meschede, M. (2009). Plattentektonik. Kontinentverschiebung und Gebirgsbildung. In German. Primus Verlag, Darmstadt, Germany. 136 pp. ISBN 978-3896786562

[76] Fritzhem, H., Fladerska, D. & Schuster, R. (2008). Alpine tectonics of the Alps and Western Carpathians. In: McCann, T. (Ed.): The Geology of Central Europe, Vol. 2: Mesozoic and Cenozoic. Geological Society, London, United Kingdom, pp. 1141–1232. DOI: 10.1144/CEV2P6.

[77] Gauss, C.F. (1828). Disquisitiones generales circa superficies curvas. https://archive.org/details/disquisitionesgO0gauugoogle/page/n6/, p.24 f.

[78] Gish, T., Occolson, D., Cheslock, M. & Shaybakeh, E. (1991). Fluxes rate of radon from soil: Effect of sorption isotherm, moisture content, and temperature. Health Physics, 61 (3): 355–365. DOI: 10.1097/00004032-199109000-00005

[79] George, A.C. (1984). Passive integrated measurement of indoor radon using activated carbon. Health Phys., 46: 867–872.

[80] Goldschmidt, V.M. (1937). The principles of distribution of chemical elements in minerals and rocks. The seventh Hugo Muller Lecture, delivered before the Chemical Society. Journal of the Chemical Society, D: 655–673.

[81] Good, I.J. (1983). The philosophy of exploratory data analysis. Philosophy of Science, 50(2): 283–295. University of Chicago Press, Chicago, USA. https://www.jstor.org/stable/188015

[82] Goovaerts, P. (1997). Geostatistics for Natural Resources Evaluation (Applied Geostatistics). Oxford University Press, Oxford, United Kingdom. 496 pp. ISBN-13: 978-0195115383

[83] Grassberger, P. & Procaccia, I. (1983). Measuring the strangeness of strange attractors. Physica D 9, 189–208.

[84] Grasman, D. & Rose, A. (1995). Factors controlling the emanation of radon and thoron in soils of the eastern U.S.A. Chemical Geology, 129: 1–14.

[85] Gwinner, M.P. (1978). Geologie der Alpen in German. Schweizerbart, Stuttgart, Germany. 480 pp. ISBN 978-3-510-65315-7

[86] Hammer, Ø., Harper, D.A.T. & Ryan, P.D. (2001). PAST. Paleontological statistics software package for education and data analysis. Paleontologia Electronica 4(1): 9pp. http://palaeo-electronica.org/2001_1/past/issue1_01.htm. Current version: Past 3.20. https://folk.uio.no/ohammer/past/ (acc. 12 July 2018)

[87] Hänninen, K., Toth, E., Lasnen, A. & Mjönda, M. (2006). Some remarks on the indoor radon distribution in a country. Applied Radiation and Isotopes, 64(8): 859–863. doi: 10.1016/j.apradiso.2006.02.088

[88] Handy, M.R., Schmid, S.M., Bousquet, R., Kissling, E. & Bernoulli, D. (2010). Reconciling plate-tectonic reconstructions of Alpine Tethys with the geological-geophysical record of spreading and subduction in the Alps. Earth Science Reviews, 102(3-4): 121–158. https://doi.org/10.1016/j.earscirev.2010.06.002

[89] Hansen, M.H., Madow, W.G. & Tepping, B.J. (1983). An Evaluation of Model-Dependent and Probability-Sampling Inferences in Sample Surveys. Journal of the American Statistical Association, 78 (384): 776–793. https://doi.org/10.1080/01621459.1983.10477018

[90] Hassan, N.M., Hosoda, M., Ishikawa, T., Sorimachi, A., Sahoo, S.K., Tokonami, S. & Fukushi, M. (2009). Radon migration process and its influence factors: review. Japan Journal of Health Physics, 44(2): 218–231. doi: 10.5453/jhps.44.218

[91] Hazen, R.M., Ewing, R.C. & Sverjensky, D.A. (2009). Evolution of uranium and thorium minerals. American Mineralogist, 94(10): 1293–1311. https://doi.org/10.2138/am.2009.3298

[92] Heerd, T., Heuvelink, G.B.M. & Rossiter, D.G. (2007). About regression-kriging: From equations to case studies. Computers & Geosciences, 33(10): 1301–1315. https://doi.org/10.1016/j.cageo.2007.05.001

[93] Henk, A. (1993). Subsidenz und Tektonik des Saar-Nahe-Beckens (SW-Deutschland). In German. Berlin, Geologische Rundschau, 82(1): 3–19.

[94] Hinck, J.E., Linder, G., Finger, S., Little, E., Tillitt, D. & Rohne, W. (2010). Biological pathways of exposure and ecotoxicity values for uranium and associated radionuclides. In: Alpine, A.E. (ed.): Hydrological, geological, and biological site characterization of breccia pipe uranium deposits in Northern Arizona. Reston, Virginia, US Geological Survey, pp. 287–354. doi: 10.3133/sir20105250.

[95] Hinkle, M.E. (1994). Environmental conditions affecting concentrations of He, CO_2, O2 and N2 in soil gases. Applied Geochemistry, 9(1): 53–63. https://doi.org/10.1016/0883-2927(94)90052-3

[96] Hofmann, A.W. (1988). Chemical differentiation of the Earth: the relationship between mantle, continental crust, and oceanic crust. Earth and Planetary Science Letters, 90: 297–314. doi: 10.1016/0012-821X(88)90132-X

[97] Hosoda, M., Kavasi, N., Sorimachi, A., Hassan, N.M., Sahoo, S.K., Ishikawa, T., Tokonami, S. & Uchida, S. (2008). Influence of soil particle size on radon emanation and exhalation. Proc. of the 7th International conference on nuclear and radiochemistry.

[98] HPA (Health Protection Agency) (2009). Radon and Public Health. Report prepared by the Subgroup on Radon Epidemiology of the Independent Advisory Group on Ionising Radiation. Documents of the Health Protection Agency. Health Protection Agency, United Kingdom.

[99] IAEA (1990). The environmental behaviour of radium. Technical Report Series no. 310. International Atomic Energy Agency, Vienna.

[100] IAEA (2007). IAEA safety glossary: terminology used in nuclear safety and radiation protection, 2007 edition. Vienna: International Atomic Energy Agency, 2007. ST/PUB/1290

[101] IAEA (2014). The environmental behaviour of radium: revised edition. Technical Report Series no. 30, International Atomic Energy Agency, Vienna.

[102] ICRP (1993). Protection Against Radon-222 at Home and at Work. ICRP Publication 65. Ann. ICRP 23 (2).

[103] ICRP (2017). Occupational Intakes of Radionuclides: Part 3. ICRP Publication 137. Ann. ICRP 46(3/4).

[104] ICRP (2007). The 2007 Recommendations of the International Commission on Radiological Protection. Elsevier.

[105] ICRP-65 (1994). Protection Against Radon-222 at Home and at Work. Pergamon, Oxford, UK.

[106] INSPIRE (2007). Directive 2007/2/EC of the European Parliament and of the Council of 14 March 2007 establishing an Infrastructure for Spatial Information in the European Community (INSPIRE). https://eur-lex.europa.eu/legal-content/EN/TXT/?uri=CELEX:32007L0002

[107] INSPIRE (2014). Data Specification on Coordinate Reference Systems – Technical Guidelines. https://inspire.ec.europa.eu/id/document/tg/crs

[108] International Atomic Energy Agency (2013). National and Regional Surveys of Radon Concentration in Dwellings. Review of Methodology and Measurement Techniques. IAEA Analytical Quality in Nuclear Application Series, No. 33, Report IAEA/AQ/33. https://www-pub.iaea.org/MTCD/Publications/PDF/IAEA-AQ-33_web.pdf

[109] Ioannides, K., Papachristodoulou, C., Stamoulis, K., Karamanis, D., Pavlidis, S.

Chaizpetrov, A. & Karakaia, E. (2013). Soil gas radon: a tool for exploring active fault zones. Applied Radiation and Isotopes, 59(2–3): 205–213. https://doi.org/10.1016/S0969-8043(03)00164-7.

[110] Isaaks, E.J. & Srivastava, R.M. (1989). An Introduction to Applied Geostatistics. Oxford University Press, New York, USA. 561 pp. ISBN 92-0-100707-8.

[111] Ishimori, Y., Lange, K., Martin, P., Mayya, Y.S. & Phaneuf, M. (2013). Measurement and Calculation of Radon Releases from NORM Residues. Technical Reports Series No. 474. International Atomic Energy Agency, Vienna.

[112] Iskandar, D., Yamazawa, H. & Iida, T. (2004). Quantification of the dependency of radon emanation power on soil temperature. Appl. Radiat. Isot., 60: 971–973. DOI: 10.1016/j.apradiso.2004.02.003.

[113] Ivanov, S.N., Perfilieva, V. & Protchenko, V.N. (1977). Les traits principaux de la structure géologique de l'Oural. In: La chaîne varisque d'Europe moyenne et occidentale. In French. Colloquer Internationaux du CNRS, 243: 571–581.

[114] Iyer, M.R. (2013). Origin of thorium deposits in Kerala beach sands. Radiation Protection and Environment, 36(3): 98–101. doi: 10.4103/0972-0464.169381.

[115] Jacobi, W. (1972). Activity and potential energy of Radon-222 and Radon-220 (thoron) in different air atmospheres. Health Phys. 22: 441–450.

[116] Johnston, K., Ver Hoef, J.M., Krivoruchko, K. & Lucas, N. (2001). Using ArcGIS Geostatistical Analyst. ESRI, Redlands, California, USA.

[117] Journel, A.G. & Huijbregts, C.J. (1978). Mining Geostatistics. Academic Press, New York, USA. 600 pp.

[118] Journel, A.G. & Rossi, M.E. (1989). When do we need a trend model in kriging? Mathematical Geology, 21(7): 715–739. https://doi.org/10.1007/BF00893318.

[119] Kanevski, M., Pozdnoukhov, A. & Timonin, V. (2009). Machine Learning for Spatial Environmental Data. Theory, Applications and Software. EPFL Press, 377 pp. DOI: 10.1201/9781439808085.

[120] Kanevski, M., Timonin, V. & Pozdnoukhov, A. (2009). Machine Learning for Spatial Environmental Data. Theory, Applications, and Software. EPFL Press. ISBN-13: 978-0849382376.

[121] Kepplar, H. & Wyllie, P.J. (1999). Role of fluids in transport and fractionation of uranium and thorium in magmatic processes. Nature, 348: 531–533.

[122] Khoury, H.N., Salameh, E.M. & Clark, I.D. (2014). Mineralogy and origin of surficial uranium deposits hosted in travertine and calcrete from central Jordan. Applied Geochemistry, 43: 49–65. https://doi.org/10.1016/j.apgeochem.2014.02.003.

[123] Knoll, G.F. (2000). Radiation Detection and Measurement, 3rd Edition. Wiley, New York, US.

[124] Kunzl, V. (editor) (2000). Principy a praxe radiační ochrany. 1. vyd. Praha: Státní úřad pro jadernou bezpečnost. 613 pp. ISBN 8023817036 (in Czech).

[125] Knutson, E.O., George, A.C., Knuth R.H., & Koh B.R. (1984). Measurements of Radon daughters' particle size. Radiation Protection Dosimetry, 7: 121–125.

[126] Kockel, F. (2002). Rifting processes in NW-Germany and the German North Sea sector. Netherlands Journal of Geosciences, 81(52): 148–158. https://doi.org/10.1017/S0016774600022381.

[127] Kossmat, F. (1927). Gliederung des varistischen Gebirgsbaues. In German. Leipzig, Abh. Sächs. Geol. L.-Amt., Leipzig, Germany.

[128] Kovalenko, G.D. (2013). Radioecology of Ukraine. Kharkiv, Ukraine. http://www.nsc.gov.ua/terchpu/ru/radioecology/index.html.

[129] Kozler, K. (2017). The national survey of natural radioactivity in concrete produced in Israel. Journal of Environmental Radioactivity, 168: 46–53. https://doi.org/10.1016/j.jenvrad.2016.03.002.

[130] Krivoruchko, K. & Gribov, A. (2014). Pragmatic Bayesian kriging for non-stationary and moderately non-Gaussian data. Mathematics of Planet Earth. In Pardo-Igúzquiza, E., Guardiola-Albert, C., Heredia, J., Moreno-Merino, L., Durán, J. & Vargas-Guzmán, J. (eds.) Mathematics of Planet Earth. Lecture Notes in Earth System Sciences. Springer, Berlin, Heidelberg, Germany, pp. 61–64. https://doi.org/10.1007/978-3-642-32408-6_15.

[131] L'Annunziata, M.F. (2016). Radioactivity. Introduction and History. From the Quantum to Quarks. Amsterdam: Elsevier. ISBN 978-0444527158.

[132] Lahiani, T.P. (2004). Geologie der Schweiz. In German. Otto Verlag, Thun, Switzerland. 211 pp. ISBN 978-3722567624.

[133] Lamas, M.C. (2005). Factors affecting the availability of uranium in soils. Landbauforschung Völkenrode Sonderheft, 278. Braunschweig: Federal Agricultural Research Centre (FAL).

[134] Langmuir, D. (1978). Uranium solution-equilibria at low temperatures with applications to sedimentary Ore deposits. Geochimica et Cosmochimica Acta, 42(6): 547–569. https://doi.org/10.1016/0016-7037(78)90001-7.

[135] Levine, J. CrimeStat: A Spatial Statistics Program for the Analysis of Crime Incident Locations. Ned Levine & Associates, Houston, TX, and the National Institute of Justice, Washington, DC. Version 3.3. https://www.icpsr.umich.edu/CrimeStat/; version 4.02. https://nij.gov/topics/technology/maps/pages/crimestat.aspx (acc. 12 July 2016).

[136] Li, J. & Heap, A.D. (2011). A review of comparative studies of spatial interpolation methods in environmental sciences: Performance and impact factors. Ecological Informatics, 6(5–6): 228–241. https://doi.org/10.1016/j.ecoinf.2010.12.003.

[137] List, T., Schmincke, H.U., Frechen, M. & Schlüchter, C. (2008). Quaternary. In: McCann, T. (Ed.) The Geology of Central Europe. Vol. 2: Mesozoic and Cenozoic. Geological Society, London, 1287 – 1340.

[138] Liu, C. (2001). A comparison of five distance-based methods for spatial pattern analysis. Journal of Vegetation Science, 12(5): 411–416. doi: 10.2307/3236855.

[139] Lombardi, A. & Vellutoni, N. (2010). Rn, He and CO_2: soil gas geochemistry for the study of active and inactive faults. Applied Geochemistry, 25(8): 1206–1220. https://doi.org/10.1016/j.apgeochem.2010.05.006.

[140] Mandelbrot, B. (1967). How Long is the Coast of Britain? Statistical Self-Similarity and Fractional Dimension. Science 156 (3775): 636 – 638. doi: 10.1126/science.156.3775.636.

[141] Markkanen, M. & Arvela, H. (1992). Radon emanation from soils. Radiat. Prot. Dosim., 45: 269–272. https://doi.org/10.1093/rpd/45.1-4.269.

[142] Masoccho, M., Righi, S., Bargossi, G.M. & Gasparotto, G. (2011). Natural radionuclides content and radiological hazard of commercial ornamental stones: an integrated calorimetric and mineralogical-petrographic study. Radiation Measurements, 46(5): 538–545. https://doi.org/10.1016/j.radmeas.2011.03.017.

[143] Matheron, G. (1963). Principles of geostatistics. Economic Geology, 58(8): 1246–1266. https://doi.org/10.2113/gsecongeo.58.8.1246.

[144] Maxwell, O., Wagner, H., Ibrahim, N., Lee S.K., Embong, Z. & Upasoki, P.S. (2015). Natural radioactivity and geological influence on subsurface layers at Kubwa and Gosa area of Abuja, Northcentral Nigeria. Journal of Radioanalytical and Nuclear Chemistry, 303(1): 821–830. https://doi.org/10.1007/s10967-014-3442-1.

[145] McCann, T. (1998). The Rotliegend of the NE German Basin: Background and prospectivity. Petroleum Geoscience, 4(1): 17–27. doi: 10.1144/petgeo.4.1.17.

[146] McCann, T., Pascal, C., Timmerman, M.J., Krzywiec, P., Lopez-Gomez, J., Wetzel, A., Krawczyk, C.M., Rieke, H. & Lamarche, J. (2006). Post-Variscan (end Carboniferous-Early Permian) basin evolution in Western and Central Europe. In: Gee, D. G. & Stephenson, R.A. (eds.) European Lithosphere Dynamics. Geological Society, London, Memoirs, 32: 355–388. https://doi.org/10.1144/GSL.MEM.2006.032.01.22.

[147] McGregor, D.S. (2007). Chapter 8: Detection and Measurement of Radiation. In: Shultis, J.K. & Faw, R.E. (Eds.) Fundamentals of Nuclear Science and Engineering, 2nd Edition. CRC Press, Boca Raton, US.

[148] Miles, J. (2004). Methods of radon measurement and devices. In: Proceedings of the 4th European conference on protection against radon at home and at work. Czech Republic. https://ris.utwente.nl/ws/portalfiles/portal/6066210/360108024.pdf?locale=en.

[149] Milne, G.A., Davis, J.L., Mitrovica, J.X., Scherneck, H.-G., Johansson, J.M., Vermeer, M. & Koivula, H. (2001). Space-geodetic constraints on glacial isostatic adjustment in Fennoscandia. Science, 291(5512): 2381–2385. DOI: 10.1126/science.1057022.

[150] Mojzl, B.A., Nazaroff, W.W. & Sextro, R.G. (1988). Soil as a source of indoor radon: Saturation, migration and entry. In: Nazaroff, W.W. & Nero, A.V. (Eds.) Radon and its Decay Products in Indoor Air. John Wiley and Sons, New York, pp. 57–112.

[151] Moran, P.A.P. (1950). Notes on continuous stochastic phenomena. Biometrika, 37(1–2): 17–23. doi: 10.2307/2332142.

[152] Morawska, L. & Jefferies, C. (1994). Distribution of radium in mineral sand grains and its potential effect on radon emanation. Radiation Protection Dosimetry, 56 (1–4): 199–200.

[153] Morawska, L. & Phillips, C. (1992). Dependence of the radon emanation coefficient on radium distribution and internal structure of the material. Geochimica et Cosmochimica, 57: 1783–1797.

[154] Morawska, L. & Phillips, C.R. (1993). Dependence of the radon emanation coefficient on radium distribution and internal structure of the material. Geochimica et Cosmochimica Acta, 57: 1783–1797.

[155] Morales, V., Bach, J., Zarraca, M., Font, L., Roque, C. & Linares, R. (2018). Characterization of radon levels in soil and groundwater in the North Maladeta Fault area (Central Pyrenees) and their effects on indoor radon concentration in a thermal spa. Journal of Environmental Radioactivity, 189: 1–13. https://doi.org/10.1016/j.jenvrad.2018.03.001.

[156] Moore, R.J. & Fisk, W.J. (1988). Modeling the effects of exhaust ventilation on ^{222}Rn entry rates and indoor ^{222}Rn concentrations. Health Physics 54, 491–501.

[157] Müller, W.G. (2007). Collecting Spatial Data – Optimum Design of Experiments for Random Fields. Springer. ISBN 978-3-540-31174-4.

[158] Murphy, J. B., Keppie, J. D., Nance, R. D. & Dostal, J. (2010). Comparative evolution of the Iapetus and Rheic Oceans: A North America perspective. Gondwana Research, 17(2–3): 482–499. https://doi.org/10.1016/j.gr.2009.08.009.

[159] Nance, R.D., Gutiérrez-Alonso, G., Keppie, J.D., Linnemann, U., Murphy, J.B., Quesada, C., Strachan, R.A. & Woodcock, N.H. (2010). Evolution of the Rheic Ocean. Gondwana Research, 17(2–3): 194–222. https://doi.org/10.1016/j.gr.2009.08.001.

[160] Nazaroff, W.W. (1992). Radon transport from soil to air. Reviews of Geophysics, 30 (2): 137–160.

[161] Nazaroff, W.W. & Nero, A.V. (1988). Soil as a source of indoor radon: generation, migration and entry. In: Radon and its decay products in indoor air. (Nazaroff, W.W. & Nero, V. eds). Wiley, New York, US.

[162] Meßner, H.-D. (2019). Paläozoisches Grundgebirge – Geotektonisch-paläogeographische Entwicklung Mitteleuropas. In: HLNUG (Hrsg.). Geologie von Hessen. Schweizerbart, Stuttgart, Germany.

[163] Nikolaev, A.M., Ziegler, P.A., Stephenson, R.A., Cloetingh, S.A.P.L., Furne, A.V., Fokin, P.A., Erofeev, A.V., Baistrov, S.N., Korniliev, M.V., Aleksejev, A.S., Gorbachev, V.I., Shipilov, E.V., Lankreijer, A., Bembinova, E.Yu. & Shalimov, I.V. (1996). Late Precambrian to Triassic history of the East European Craton: dynamics of sedimentary basin evolution. Tectonophysics, 268(1–4): 23–63. DOI: 10.1016/S0040-1951(96)00228-4.

[164] Nuccetelli, C., Risica, S., Ginevri, S., Leonardi, F. & Trevisi, R. (2017). Natural radioactivity in building materials in the Europe Union: a database of activity concentrations, radon emanation and radon exhalation rates. ISTISAN 17/36, ISSN 2384-8936.

[165] Olaussen, S., Larsen, B.T. & Steel, R. (1994). The Upper Carboniferous–Permian Oslo Rift: basin fill in relation to tectonic development. In: Embry, A.F., Beauchamp, B. & Glass, D.J. (eds). Pangea: Global Environments and Resources. Canadian Society of Petroleum Geology, Memoirs, 17: 175–197.

[166] Osmond, J.K. & Ivanovich, M. (1992). Uranium series mobilization and surface hydrology. In: Uranium-series Disequilibrium: Applications to Earth, Marine, and Environmental Sciences (M. Ivanovich and R.S. Harmon, eds.). Clarendon Press, Oxford, UK, pp. 259–289.

[167] Park, G. (2014). The making of Europe – A geological history. Dunedin Academic Press, Edinburgh, United Kingdom, 176 pp. ISBN 978-1780460437.

[168] Park, G. (2015). Die Geologie Europas. Translated from English by Heiner Fiek. WBG Academic, Darmstadt, Germany. 200 pp.

[169] Pastor-Galán, D., Gutiérrez-Alonso, G., Murphy, J. B., Fernández-Suárez, J., Hofmann, M. & Linnemann, U. (2013). Provenance analysis of the Paleozoic sequences of the northern Gondwana margin in NW Iberia: Passive margin to Variscan collision and orocline development. Gondwana Research, 23 (3): 1089–1105. https://doi.org/10.1016/j.gr.2012.06.015.

[170] Penck, A. (1879). Die Geschiebeformation Norddeutschlands. Zeitschrift der Deutschen Geologischen Gesellschaft, 31: 117–228.

[171] Pfiffner, O.A. (1992). Alpine orogeny. In: Blundell, D., Freeman, R. & Mueller, S. (editors). A Continent Revealed: The European Geotraverse. Cambridge University Press, Cambridge, UK, pp. 180–190. ISBN 0-521-42848-8 paperback.

[172] Pielou, E.C. (1959). The use of point to plant distances in the study of the pattern of populations. Journal of Ecology 47(1): 607–613. DOI: 10.2307/2257299.

[173] Plotnick, R.E. (1993). Lacunarity indices as measures of landscape texture. Landscape Ecology, 8(3): 201–211.

[174] Plotnick, R.E., Gardner, R.H., Hargrove, W.W., Prestegaard, K. & Perlmutter, M. (1996). Lacunarity analysis: A general technique for the analysis of spatial patterns. Physical Review E 53(5): 5461–5468. DOI: 10.1103/physreve.53.5461.

[175] Porstendörfer, J. & Reineking, A. (1992). Indoor behaviour and characteristics of radon progeny. Radiation Protection Dosimetry, 45: 303–311. https://doi.org/10.1093/rpd/45.1-4.303.

[176] Porstendörfer, J. (1994). Behaviour of radon daughter products in indoor air. Radiation Protection Dosimetry, 7: 107–113.

[177] Porstendörfer, J. (1991). Properties and behaviour of radon and thoron and their decay products in the air. Tutorial sessions, in Proceedings of Natural Radiation Environment V (ELR 14411). Salzburg, Austria, September 22–28, 1991, pp. 69–150.

[178] Porstendörfer, J. (1994). Properties and behaviour of radon and thoron and their decay products in the air. Journal of Aerosol Science, 25(2): 219–263.

[179] Porstendörfer, J., Pagelkopf, P. & Scrandel, M. (2006). Fraction of the positive ^{218}Po and ^{214}Pb clusters in indoor air. Radiation Protection Dosimetry, 113(3): 342–351. doi: 10.1093/rpd/nel465.

[180] Radlac'k-Pyrm (2008). Sistema per la misura del gas Radon, Manuale d'uso, m.am s.r.l.

[181] Radiation Protection 112 (1999). Radiological Protection Principles concerning the Natural Radioactivity of Building Materials. European Commission, Directorate-General Environment, Nuclear Safety and Civil Protection.

[182] Rafique, M., Rahman, S.U., Mahmud, T., Rahman, S., Matullah & Rahman S.U. (2011). Radon exhalation rate from soil, sand, bricks, and sedimentary samples collected from Azad Kashmir, Pakistan. Russian Geology and Geophysics, 52(4): 450–457. https://doi.org/10.1016/j.rgg.2011.03.007.

[183] Rantisch, G. (2004). Geochemical exploration in a mountainous area by statistical modeling of polypopulational data distributions. Journal of Geochemical Exploration, 82(1): 79–95. doi: 10.1016/j.gexplo.2004.01.003.

[184] Rao, D.D. (2012). Radioactivity in human body and its detection. Radiat Prot Environ35:57-8. DOI: 10.4103/0972-0464.112337.

[185] Rapp, G., Tucci, M. & Bruno, R. (1987). Reconstruction of rainfall fields by combining ground raingauges data with radar maps using external drift method. In: Basli, E.T. & Schofield, N.A. (eds.). Geostatistics Wollongong '88. Kluwer Academic Publishers, Dordrecht, the Netherlands, pp. 945–956.

[186] Rasser, M.W., Harzhauser, M., Anistratenko, O.Y., Anistratenko, V.V., Bassi, D., Belak, M., Berger, J.-P., Borhetski, G., Dick, S., Cosovic, V., Dolakova, N., Drobne, K., Filipescu, S., Gurs, K., Hladkova, S., Hrvatovic, H., Jelen, B., Kaunicki, J.R., Kovac, M., Kralj, P., Marjanac, T., Marton, E., Mietto, P., Moro, A., Nagymarosy, A., Nebocsok, J.H., Nehyba, S., Ogorelec, B., Oszczypko, N., Pavelic, D., Pavlovec, R., Pavsic, J., Petrova, P., Piwocki, M., Poljak, M., Pugliese, N., Radzevicic, R., Rifelj, H., Roetzel, R., Skaberne, D., Stica, C., Standke, G., Turac, G., Vass, D., Wagreich, M. & Wessely, G. (2008). Paleogene and Neogene. In: McCann, T. (Ed.). The Geology of Central Europe, Vol. 2: Mesozoic and Cenozoic. Geological Society, London, United Kingdom, pp. 1031 – 1139. DOI: https://doi.org/10.1144/CSJGS.2.

[187] Raumer, J.F., Bussy, F., Schaltegger, U., Schulz, B. & Stampfli, G.M. (2013). Pre-Mesozoic Alpine basements — their place in the European Paleozoic framework. Geological Society of America Bulletin, 125(1–2): 89–108. https://doi.org/10.1130/B30654.1.

[188] Raumer, J.F. & Stampfli, G.M. (2008). The birth of the Rheic Ocean – Early Paleozoic subsidence patterns and subsequent tectonic plate scenarios. Tectonophysics, 461(1–4): 9–20. https://doi.org/10.1016/j.tecto.2008.04.012.

[189] Rees, D.M., Bradley, E.J. & Green, B.M.R. (2011). Radon in homes in England and Wales: 2010 data review. HPA-CRCE-015. Health Protection Agency, Chilton, UK.

[190] Reichertz, K., Frotzheim, N., Jaroszewski, M., Baldura, J., Frentzel, H.J., Hansen, M., Hubscher, C., Müller, R., Pagnacs, P., Reise-Sor, J., Stockebrandt, W., Voigt, T., von Eynatten, H. & Zachmann, W. (2008). Alpine tectonics north of the Alps. In: McCann, T. (Ed.). The Geology of Central Europe. Volume 2: Mesozoic and Cenozoic. Geological Society, London, United Kingdom, 1233 – 1286. DOI: https://doi.org/10.1144/CSJGS.2.7.

[191] Reimann, E. & Filzmoser P. (2000). Normal and lognormal data distribution in geochemistry: death of a myth. Consequences for the statistical treatment of geochemical and environmental data. Environmental Geology, 39(9): 1001–1014. doi: 10.1007/s002549900081.

[192] Reimer, G.M. (1990). Reconnaissance techniques for determining soil gas radon concentrations: an example from Prince George's County, Maryland. Geophysical Research Letters, 17: 809–812.

[193] Reineking, A. & Porstendörfer, J. (1990). Unattached fraction of short-lived Rn-decay products in indoor and outdoor environments: An improved single-screen method and results. Health Phys., 58: 715–727.

[194] Reiss, M.A., Lemmens, B., Hämmerer, A. & Ahammer H. (2018). Tug-of-war lacunarity—A novel approach for estimating lacunarity. Chaos, 28 (113107). https://doi.org/10.1063/1.4966539.

[195] Renyi, A. (1959). On the dimension and entropy of probability distributions. Acta Mathematica Academiae Scientiarum Hungarica, 10(1–2): 193–215. doi: org/10.1007/BF02063299.

[196] Rey, P. & Fjeldskaar, W. (1992). On the magnitude of the Late Tertiary and Quaternary erosion and its significance for the uplift of Scandinavia and the Barents Sea. Norwegian Petroleum Society Special Publications, 1: 163–185. https://doi.org/10.1016/B978-0-444-88607-1.50016-4.

[197] Roberts, A.A., Friedman, I., Donovan, T.J. & Denton, E.H. (1975). Helium survey: a possible technique for locating geothermal reservoirs. Geophysical Research Letters, 2: 209–210.

[198] Röhl, H.-J., Schmid-Röhl, A., Oschmann, W., Frimmel, A. & Schwark, L. (2001). The Posidonia Shale (Lower Toarcian) of SW-Germany: an oxygen-depleted ecosystem controlled by sea level and paleoclimate. Palaeogeography, Palaeoclimatology, Palaeoecology, 165: 27–52. DOI: 10.1016/S0031-0182(00)00152-8.

[199] Rudnick, R.L. & Fountain, D.M. (1995). Nature and composition of the continental crust: a lower crustal perspective. Reviews of Geophysics, 33(3): 267–309. doi: 10.1029/95RG01302.

[200] Rudnick, R.L. & Gao, S. (2003). Composition of the continental crust. In: Rudnick, R.L., Holland, H. D. & Turekian, K. K. (eds.). Treatise on Geochemistry. Volume 3. Elsevier, Amsterdam, the Netherlands, pp. 1–64.

[201] Rutherford, E., Chadwick, J. & Ellis, C. D. (1951). Radiations from radioactive substances. Cambridge University Press, Cambridge, UK. ISBN 978-0511707179. https://doi.org/10.1017/CBO9780511707179.

[202] Ruzicka, V. (1993). Vein uranium deposits. Ore Geology Reviews, 8(3–4): 247–276. https://doi.org/10.1016/0169-1368(93)90019-U.

[203] Sakoda, A., Hanamoto, K., Ishimori, Y., Katagiri, T., Kawabe, A. & Yamaoka, K. (2010). First model of the effect of grain size on radon emanation. Applied Radiation and Isotopes, 68(6): 1169–1172. https://doi.org/10.1016/j.apradiso.2009.11.070.

[204] Sakoda, A., Ishimori, Y. & Yamaoka, K. (2011). A comprehensive review of radon emanation measurements for inorganic rock, soil, mill tailing and fly ash. Appl. Radiat. Isot., 69(10): 1422–1435. doi: 10.1016/j.apradiso.2011.06.009.

[205] Sakoda, A., Nishiyama, Y., Hanamoto, K., Ishimori, Y., Yamamoto, Y., Katagiri, T., Kawabe, A. & Yamaoka, K. (2010). Differences of natural radioactivity and radon emanation fraction among constituent minerals of rock or soil. Applied Radiation and Isotopes, 68: 1180–1184. DOI: 10.1016/j.apradiso.2009.12.036.

[206] Schäfer, A. & Karsch, R.C. (1998). Formation and sediment fill of the Saar-Nahe Basin (Permo-Carboniferous, Germany). Zeitschrift der Deutschen Geologischen Gesellschaft, 149(2): 233–269. Schweizerbart Science Publishers, Stuttgart, Germany.

[207] Schmidt, S. & Gechter, J.K. (2010). Radium and radium daughter nuclides in carbonates: a brief overview of strategies for determining chronologies. Journal of Environmental Radioactivity, 101(7): 538–537. https://doi.org/10.1016/j.jenvrad.2009.10.006.

[208] Schmid, S.M., Fugenschuh, B., Kissling, E. & Schuster, R. (2004). Tectonic map and overall architecture of the Alpine orogeny. Eclogae Geologicae Helvetiae, 97(1): 93–117. https://doi.org/10.1007/s00015-004-1113-x.

[209] Schumann, R. & Gundersen, L. (1996). Geological and climatic controls on the radon emanation coefficient. Environment International, 22 (Suppl. 1): S439–S448.

[210] Schueregger, F. & Kissling, E. (2015). Slab roll-back progeny in the Alps and evolution of the Swiss Molasse basin. Nature Communications, 6: 8826. DOI: 10.1038/ncomms9605.

[211] Schuster, R. & Stowe, R. (2010). Die Geologie der Alpen im Zentralraum. Mitteilungen des naturwissenschaftlichen Vereines für Steiermark, 140: 5 – 21.

[212] Scotese, C.R. (2003). The Paleomap Project. Available from: http://www.scotese.com.

[213] Segovia, N., Seidel, J.L. & Monnin, M. (1987). Variations of radon in soils induced by external factors. Journal of Radioanalytical and Nuclear Chemistry, 119(1): 199–209. https://doi.org/10.1007/BF02162265.

[214] Semkow, T. (1990). Recoil emanation theory applied to radon release from mineral grains. Geochimica et Cosmochimica, 54: 425–440.

[215] Sinclair, A.J. (1991). A fundamental approach to threshold estimation in exploration geochemistry: Probability plots revisited. Journal of Geochemical Exploration, 41: 1–22. doi 10.1016/0375-6742(91)90071-3.

[216] Snyder, J.P. (1987). Map projections. A working manual. US Geological Survey Professional paper 1395. https://pubs.usgs.gov/pp/1395/report.pdf.

[217] Sousa, T., Chung, A.P., Pereira, A., Piedade, A.P. & Morais, P.V. (2013). Aerobic uranium immobilization by Rhodanobacter A2-61 through formation of intracellular uranium-phosphate complexes. Metallomics, 5(4): 390–397. doi: 10.1039/c3mt00192d.

[218] Stanley, S.M. (2001). Historische Geologie. Second Edition. In German. Spektrum Akademischer Verlag, Heidelberg, Germany. 710 pp.

[219] Stoulos, S., Manolopoulou, M. & Papastefanou, C. (2003). Assessment of natural radiation exposure and radon exhalation from building materials in Greece. Journal of Environmental Radioactivity, 69(3): 225–240. https://doi.org/10.1016/S0265-931X(03)00081-X.

[220] Strand, E., Rosstad, A.K. & Lind B. (1984). The influence of moisture and temperature on radon emanation. Radiat. Prot. Dosim., 7: 55–58.

[221] Strong, K.P. & Levins, D.M. (1982). Effect of moisture content on radon emanation from uranium ore and tailing. Health Phys., 42: 27–32.

[222] Stowe, K.S. & Homberger, R. (2011). Die Geologie der Alpen aus der Luft. Weishaupt Publisher, Graz, Austria. 236 pp. ISBN 978-3-7059-0314-2.

[223] Suksi, J. (2001). Natural uranium as a tracer in radionuclide geosphere transport studies. Academic dissertation, University of Helsinki, Finland. 56 pp.

[224] Swank, R. (1954). Characteristics of scintillators. Annual Review of Nuclear Science 4: 111–140. https://doi.org/10.1146/annurev.ns.04.120154.000551.

[225] Swedjemark, G.A. (1983). The equilibrium factor F. Health Phys., 45: 453–462.

[226] Talavada, T., Cortizo, A.M., García, C. & García-Rodeja, E. (2006). Uranium and thorium in weathering and pedogenetic transects developed on granitic rocks from NW Spain. Science of the Total Environment, 356: 192–206.

[227] Tait, J.A., Bachtadse, V., Franke, W. & Soffel, H.C. (1997). Geodynamic evolution of the European Variscan fold belt: paleomagnetic and geological constraints. Geologische Rundschau, Berlin, Germany.

[228] Tanner, A. (1964). Radon migration in the ground: A review. In: The Natural Radiation Environment, pp. 161–190. University of Chicago Press, Chicago, US.

[229] Tanner, A.B. (1978). Radon migration in the ground. In: The Natural Radiation Environment, Houston, US.

[230] Tanner, A.B. (1980). Radon migration in the ground: A supplementary review. In: The Natural Radiation Environment, Vol. 3, pp. 5–56. National Technical Information Service, Springfield, USA.

[231] The Great Soviet Encyclopaedia. Third Edition (1970–1979). Eastern European Platform. https://encyclopedia2.thefreedictionary.com/Eastern+European+Platform.

[232] Theiler, J. (1990). Estimating fractal dimensions. Journal of the Optical Society of America A, 7(6): 1055–1073. https://doi.org/10.1364/JOSAA.7.001055.

[233] Tobler, W. (1970). A computer movie simulating urban growth in the Detroit region. Economic Geography, 46 (supp): 234–240. doi: 10.2307/143141.

[234] Torsvik, T.H. & Rehnström, E.F. (2003). The Tornquist Sea and Baltica–Avalonia docking. Tectonophysics, 362: 67–82. doi:10.1016/S0040-1951(02)00631-5.

[235] Torsvik, T.H., Eide, E.A., Meert, J.G., Smethurst, M.A. & Walderhaug, H.J. (1998). The Oslo Rift: new paleomagnetic and $^{40}Ar/^{39}Ar$ age constraints. Geophysical Journal International, 135: 1045–1058.

[236] Tositti, L., Cinelli, G., Bratkič, E., Galgani, A., Mostacci, D., Mazzoli, C., Massiani, M. & Sassi, R. (2017). Assessment of lithogenic radioactivity in the Euganean Hills magmatic district (NE Italy). Journal of Environmental Radioactivity, 166(Pt 2): 259–269. doi: 10.1016/j.jenvrad.2016.07.011.

[237] Trench, A. & Torsvik, T.H. (1992). The closure of the Iapetus Ocean and Tornquist Sea: new paleomagnetic constraints. London, J. Geol. Soc., 149(6): 867–870. doi: 10.1144/gsjgs.149.6.0867.

[238] Trevisi, R., Leonardi, F., Risica, S. & Nuccetelli, C. (2018). Updated database on natural radioactivity in building materials in Europe. Journal of Environmental Radioactivity, 187: 90–105. https://doi.org/10.1016/j.jenvrad.2018.01.024.

[239] Tu, K.W. & Knutson, E.O. (1988). Indoor radon progeny particle size distribution measurements made with two different methods. Radiation Protection Dosimetry, 24: 251–255.

[240] Tuccimei, P., Mollo, S., Soligo, M., Scarlato, P. & Castelluccio, M. (2015). Real-time set-up to measure radon emission during rock deformation: implications for geochemical surveillance. Geoscientific Instrumentation, Methods and Data Systems, 4: 111–119. https://doi.org/10.5194/gi-4-111-2015.

[241] Tukey, J.W. (1977). Exploratory Data Analysis. Addison-Wesley, Boston, USA.

[242] U.S. Geological Survey (USGS) (1992). The Geology of Radon. https://pubs.usgs.gov/gip/7000028/report.pdf.

[243] UNSCEAR (1993). United Nations Scientific Committee on the Effects of Atomic Radiation. United Nations, New York, US.

[244] UNSCEAR (2000). United Nations Scientific Committee on the Effects of Atomic Radiation. Source and Effects of Ionizing Radiation. United Nations, New York, US.

[245] UNSCEAR (2008). United Nations Scientific Committee on the Effects of Atomic Radiation. Source and Effects of Ionizing Radiation. New York. Annex E. Sources-to-Effects Assessment for Radon in Homes and Workplaces. United Nations, New York, US.

[246] UNSCEAR (2008). United Nations Scientific Committee on the Effects of Atomic Radiation. Source and Effects of Ionizing Radiation. New York. Annex B. United Nations, New York, US.

[247] Valente, E., Ascione, A., Dosso, G., Cuzzolino, M., Porfido, S. & Sciarra, A. (2018). Do moderate magnitude earthquakes generate seismically induced ground effects? The case study of the Mw = 5.16, 29th December 2013 Matese earthquake (Southern Apennines, Italy). International Journal of Earth Science, 107(2): 517–537. https://doi.org/10.1007/s00531-017-1506-5.

[248] Velikanov, V.Ya. & Bakarovich, M.M. (2005). Tectonic zoning of Ukraine. In: Gozak, P.F. (ed.). Lithosphere of Ukraine. Atlas. Kiev, Geographic Publishing, Ukraine, p. 59.

[249] Walter, R. (2007). Geologie von Mitteleuropa (The Geology of Central Europe). Seventh Edition. In German. Schweizerbart Science Publishers, Stuttgart, Germany. 511 pp. ISBN 978-3-510-65225-9.

[250] Webster, R. & Oliver, M.A. (2001). Geostatistics for environmental science. John Wiley and Sons, Toronto, Canada. 271 pp.

[251] Wedepohl, K.H. (Editor) (1978). Handbook of Geochemistry. Volume II/5. Elements La(57) to U(92). Springer-Verlag, Berlin, Heidelberg & New York.

[252] Winke, A. & Porstendörfer, J. (1981). Application of surface barrier detectors for the measurement of environmental radon and radon daughters in air. Presented at the International meeting on radon-radon daughter measurements, 27–28 August 1981, Montgomery, Alabama, US. Proceedings, pp. 34–46. https://inis.iaea.org/Search/21059304.pdf.

[253] Wilson, M. & Downes, H. (2006). Tertiary-Quaternary intra-plate magmatism in Europe and its relationship to mantle dynamics. In: Stephenson, R. & Gee, D. (Eds.). European Lithosphere Dynamics. Geological Society, London, Memoirs, 32: 147–166. DOI: 10.1144/GSL.MEM.2006.032.01.09.

[254] World Health Organization (WHO) (2009). WHO Handbook on Indoor Radon – a public

References

Health perspective. ISBN 978 92 4 154767 3. http://www.who.int/ionizing_radiation/environ/elnino1.html (accessed on 30 October 2018).

[255] Zanzonico, P., Quan, L. & Strauss, H.W. (2016). Radiobiology in Cardiovascular Imaging. JACC: Cardiovascular Imaging, 9(12), 1446–1461. https://doi.org/10.1016/j.jcmg.2016.09.013.

[256] Zhang, E., Markham, F.T., Hinde, J. & Grieve, I.H. (2005). Statistical characterisation of a large geochemical database and effect of sample size. Applied Geochemistry, 20, 1887–1904. doi:10.1016/j.apgeochem.2005.06.006.

Chapter 3 – Terrestrial radionuclides

(pp. 58-87)

[1] Adams, J.A.S. & Weaver, C.E. (1958). Thorium-to-uranium ratios as indicators of sedimentary processes – Example of Concept of Geochemical Facies. Bulletin of the American Association of Petroleum Geologists, 42, 387-430.

[2] Alloway, B.J. (2013). Chapter 26 Uranium. In: Alloway, B.J. (Ed.). Heavy Metals in Soils, 656-577. Springer, Netherlands.

[3] Ayora, C., Garcia-Veigas, J. & Pueyo, J. (1994). The chemical and hydrological evolution of an ancient potash-forming evaporite basin as constrained by mineral sequence, fluid inclusion composition, and numerical simulation. Geochimica et Cosmochimica Acta, 58 (16), 3379-3394 (30). https://doi.org/10.1016/0016-7037(94)90093-0.

[4] Baker, G. R. & Jackson, I. (2001). OneGeology-Europe. Final Report (CP-2001-GEO-684 31700). (www.onegeology-europe.org).

[5] Barthel, F. H. & Tuisku, H. (2014). Thorium Occurrences, Geological Deposits and Resources. In: International Atomic Energy Agency. IAEA International Symposium on Uranium Raw Material for Nuclear Energy (URAM 2014), 23-27 June 2014, Vienna, Austria.

[6] Batista, M. J., Torres, L., Leite, J., Prazeres, C., Saraiva, J. & Carvalho, J. (2013). Carta Radiométrica de Portugal (1:500000). Laboratório Nacional de Energia e Geologia, Lisboa, Portugal.

[7] Beaubien, S. E., Ciotoli, G. & Lombardi S. (2003). Carbon dioxide and radon gas hazard in the Alban Hills area (central Italy). Journal of Volcanology and Geothermal Research, 123 (1-2), 63-80. DOI: 10.1016/S0377-0273(03)00028-3.

[8] Benisa, R., Lopez-Ruiz, J., Cebria, J. M., Hertogen, J., Dobosi, G., Ingram, G. A., Harmon, R. S. & Scharbert, H. G. (1993). The Petrogenesis of Pliocene Alkaline Volcanic Rocks from the Pannonian Basin, Eastern Central Europe. Journal of Petrology, 34 (2), 317-343. DOI: 10.1093/petrology/34.2.317.

[9] Berka, R., Katzlberger, C., Philippitsch, R., Schubert, G., Kiernan, M., Lenhardtner, C., Metschka, K., Pühl, H., Seath, J., Drasler, A. & Herman, T. (2014). Radionuklide in Grundwässern, Gesteinen und Bauhölzen mittels Osterreichs 1:500000. Geologische Bundesanstalt, Wien.

[10] Birke, M., Reimann, C. & Fabian, K. (2014). Analytical Methods Used in the GEMAS Project. Chapter 5 in: Reimann, C., Birke, M., Demetriades, A., Filzmoser, P., O'Connor, P. (Eds.). Chemistry of Europe's Agricultural Soils. Part A. Geologisches Jahrbuch (Reihe B), Schweizerbarth, pp. 41–46.

[11] Bonja R., Cinelli, G., Tollefsen, T. & De Cort M. (2015). Bedrock U-Th-K signatures in the ongoing European Atlas of Natural Radiation. Proceedings of the International Workshop on the European Atlas of Natural Radiation, Verbania, Italy.

[12] Chen, S. B., Zhu, Y.G. & Hu, Q.H. (2005). Soil to plant transfer of ^{238}U, ^{226}Ra and ^{232}Th on a uranium mining-impacted soil from southeastern China. Journal of Environmental Radioactivity 82: 223-236. DOI: 10.1016/j.jenvrad.2005.01.009.

[13] Cicchella, D., Albanese, S., Birke, M., De Vivo, B., De Vos, W., Dinelli, E., Lima, A., O'Connor, P.J., Salpeteur, I. & Tarvainen, T. (2014). Natural radioactive elements U, Th and K in European soil. Chapter 8 in Reimann, C., Birke, M., Demetriades, A., Filzmoser, P., O'Connor, P. (Eds.). Chemistry of Europe's Agricultural Soils. Part B. Geologisches Jahrbuch (Reihe B), Schweizerbarth, pp. 145-159.

[14] Cinelli, G., Tositti, L., Capaccioni, B., Brattich, E. & Mostacci, D. (2015). Soil gas radon assessment and development of a radon risk map in Bolsena, Central Italy. Environmental Geochemistry and Health, 37, 305-319. DOI: 10.1007/s10653-014-9649-9.

[15] Cumberland, S. A., Douglas, G., Grice, K. & Moreau, J. W. (2016). Uranium mobility in organic matter-rich sediments: A review of geological and geochemical processes. Earth-Science Reviews, 159, 160-185. (DOI: 10.1016/j.earscirev.2016.05.010).

[16] Damiata, A.G., Bjelkhagen, H., Bakhiev, M., Gustavsson, N., Kovalchuk, P.V., Plant, J.A., Steenfelt, A., Taylorful, M., Xueqing, X., Garrett, R.G. & Hall, G.E.M. (1995). A global geochemical database for environmental and resource management: Final report of IGCP Project 259, Earth Sciences, 19. UNESCO Publishing, Paris, 122 pp.

[17] Demetriades, A., Reimann, C., Filzmoser, P. (2014). Evaluation of GEMAS Project Quality Control Results. Chapter 6 in: Reimann, C., Birke, M., Demetriades, A., Filzmoser, P., O'Connor, P. (Eds.). Chemistry of Europe's Agricultural Soils. Part A. Geologisches Jahrbuch (Reihe B), Schweizerbarth, pp. 145–158.

[18] De Vivo, B., Ippolito, F., Capaldi, G. & Simpson, P. R. (1984). Uranium geochemistry, mineralogy, geology, exploration and resources. London, Institution of Mining and Metallurgy.

[19] De Vos, W. & Tarvainen, T. (ed.) et al. (2006). Geochemical Atlas of Europe. Part 2 – Interpretation of Geochemical Maps, Additional Tables, Figures, Maps, and Related Publications. Geological Survey of Finland, Otamedia Oy, Espoo, 692 pp.

[20] ECHA (European Chemicals Agency) (2008). Guidance on information requirements and chemical safety assessment. Appendix R.7.15-2: Environmental risk assessment for metals and metal compounds. 78 pp.

[21] Embey-Isztin, A., Downes, H., James, D. E., Upton, B. G. J., Dobosi, G., Ingram, G. A., Harmon, R. S. & Scharbert, H. G. (1993). The Petrogenesis of Pliocene Alkaline Volcanic Rocks from the Pannonian Basin, Eastern Central Europe. Journal of Petrology, 34 (2), 317-343. (DOI: 10.1093/petrology/34.2.317).

[22] European Union (2006). Regulation (EC) No 1907/2006 of the European Parliament and of the Council of 18 December 2006 concerning the Registration, Evaluation, Authorisation and Restriction of Chemicals (REACH), establishing a European Chemicals Agency, amending Directive 1999/45/EC and repealing Council Regulation (EEC) No 793/93 and Commission Regulation (EC) No 1488/94 as well as Council Directive 76/769/EEC and Commission Directives 91/155/EEC, 93/67/EEC, 93/105/EC and 2000/21/EC (Text with EEA relevance). https://eur-lex.europa.eu/legal-content/EN/TXT/PDF/?uri=CELEX:02006R1907-20140410&from=EN.

[23] FitzPatrick, E. A. (1986). An introduction to soil science. 2nd ed. Longman Scientific & Technical, London, United Kingdom.

[24] Garrett, R. G., Reimann, C., Smith, D. B. & Xie, X. (2008). From geochemical prospecting to international geochemical mapping: a historical review. Geochemistry: Exploration, Environment, Analysis, 8, 205-217. DOI: 10.1144/1467-7874.08-174.

[25] Geological Survey of Japan (2005). Atlas of Eh-pH diagrams. Intercomparison of thermodynamic databases. National Institute of Advanced Industrial Science and Technology, Report number: 419.

[26] Green, B. M. R., Hughes, J. S. & Lomas, P. R. (1992). Radiation Atlas: Natural Sources of Ionising Radiation in Europe. National Radiological Protection Board, Oxon, UK.

[27] Greenhut, V. A. & Dowiatt, C. J. (2012). Secondary Data Analysis: An Important Tool for Addressing Developmental Questions. Journal of Cognition and Development, 13 (1), 2-18. (DOI: 10.1080/15248372.2012.648613).

[28] Harr, J.R. (1962). Study and interpretation of the Chemical Characteristics of Natural Water. US Geological Survey Water Supply Paper 2254. United States Government Printing Office, Washington, US.

[29] Jelach, G., Cuney, M., Bourcel, F., Rossi, F., Leon, A. & Duching, M. E. (2017). Estimation and mapping of uranium content of geological units in France. Journal of Environmental Radioactivity, 166, 210-219. (DOI: 10.1016/j.jenvrad.2016.09.022).

[30] Kabata-Pendias, A. (2011). Trace elements in soils and plants. Taylor and Francis Group, London.

[31] Lahtinen, R. (2012). Main geological features of Fennoscandia. Mineral deposits and metallogeny of Fennoscandia. Geological Survey of Finland, Special Paper 53, 19–28.

[32] Lecomte, A., Cathelineau, M., Michels, R., Peiffert, C. & Bouchot, V. (2017). Uranium mineralisation in the Alum Shale Formation (Sweden): Evolution of a U-rich marine black shale from sedimentation to metamorphism. Ore Geology Reviews, 88, 71-98. https://doi.org/10.1016/j.oregeorev.2017.04.021.

[33] Lovering, J.F. & Morgan, J. W. (1963). Comparative uranium and thorium analyses of basic and ultra-basic rocks. Nature, 199 (4892), 479-480. DOI: 10.1038/199479b0.

[34] Mackenzie, D. & Lizeganka, P. (2014). Preparation of GEMAS Project Samples and Standards. Chapter 4 in: Reimann, C., Birke, M., Demetriades, A., Filzmoser, P., O'Connor, P. (Eds.). Chemistry of Europe's Agricultural Soils. Part A. Geologisches Jahrbuch (Reihe B), Schweizerbarth, pp. 145-159.

[35] Martin, W. C., Hagan, L., Reader, J. & Sugal, J. (1974). Ground levels and ionization potentials for Lanthanides and Actinide atoms and ions. Journal of Physical and Chemical Reference Data, 3 (3), 771-779. DOI: 10.1063/1.3253147.

[36] Morton, L.S., Evans, C.V., Hallmark, C. & Esles, D.O. (2001). Pedogenic fractionation and bioavailability of uranium and thorium in naturally radioactive spodosols. Soil Sci. Soc. Am. J., 65, 1197-1203.

[37] Negrel, P., Sadeghi, M., Ladenberger, A., Reimann, C., Birke, M. (2015). Geochemical fingerprinting and source discrimination of agricultural soils at continental scale. Chem. Geol., 396, 1-15. https://doi.org/10.1016/j.chemgeo.2014.12.004.

[38] Negrel, P., De Vivo, B., Reimann, C., Ladenberger, A., Cicchella, D., Albanese, S., Birke, M., De Vos, W., Dinelli, E., Lima, A., O'Connor, P., Salpeteur, I. & Tarvainen, T. (2016). U-Th signatures of agricultural soil at the European continental scale (GEMAS): Distribution, weathering patterns and processes controlling their concentrations. Science of the Total Environment, 622-623, 1277-1293.

[39] Neves, L. J. P. F., Stephens, W. E., Pereira, A. J. S. C., Godinho, M. M. & Fallick, A. E. (1990). The São Pedro do Sul granite (Central Portugal): an HHP Through rock of the Hercynian Massif. Anais da Academia Brasileira Ciências, 71, 51-65.

[40] Nogarotto, A. (2018). Mapping the bedrock K, U and Th concentration in Italy – Towards the European Atlas of Natural Radiation. Unpublished thesis. University of Bologna, Italy.

[41] Paul, D., White, W. M. & Turcotte, D. L. (2003). Constraints on the ^{232}Th/^{238}U ratio of the continental crust. Geochemistry, Geophysics, Geosystems, 4 (12), 1-17. DOI: 10.1029/2002GC000457.

[42] Peccerillo, A. (2005). Plio-Quaternary volcanism in Italy: petrology, geochemistry, geodynamics. Berlin-New York, Springer.

[43] Pereira, A., Lamas, R., Miranda, M., Domingos, F., Neves, L., Ferreira, N. & Costa, L. (2017). Estimation of the radon production rate in granite rocks and evaluation of the implications for geogenic radon potential maps: A case study in Central Portugal. Journal of Environmental Radioactivity, 166, 270-277. (DOI: 10.1016/j.jenvrad.2016.08.022).

[44] Plant, J.A., Reeder, S., Salminen, R., Smith, D.B., Tarvainen, T., De Vivo, B., Petersen, M.G. (2001). The distribution of uranium over Europe: geological and environmental significance. Geol. Earth Sci. 112, 221-238. https://doi.org/10.1179/037174503225005152.

[45] Reimann, C., Birke, M., Demetriades, A., Filzmoser, P., O'Connor, P. (Eds.) (2014a). Chemistry of Europe's agricultural soils – Part A. Methodology and interpretations of the GEMAS Dataset. Geologisches Jahrbuch (Reihe B). Schweizerbarth, Stuttgart, Germany, 528 pp.

[46] Reimann, C., Birke, M., Demetriades, A., Filzmoser, P., O'Connor, P. (Eds.) (2014b). Chemistry of Europe's agricultural soils – Part B. General Background Information and Further Analysis of the GEMAS Dataset. Geologisches Jahrbuch (Reihe B). Schweizerbarth, Stuttgart, Germany, 352 pp.

[47] Reimann, C. (2014). Sample Material, Site Selection and Sampling. Chapter 3 in: Reimann, C., Birke, M., Demetriades, A., Filzmoser, P., O'Connor, P. (Eds.). Chemistry of Europe's Agricultural Soils. Part A. Geologisches Jahrbuch (Reihe B), Schweizerbarth, pp. 31–36.

[48] Reimann, C., Filzmoser, P., Garrett, R.G., Dutter R. (2008). Statistical data analysis explained: Applied Environmental Statistics with R. Chichester: Wiley, 343 pp.

[49] Rudnick, R. L. & Fountain, D. M. (1995). Nature and composition of the continental crust: a lower crustal perspective. Reviews of Geophysics, 33 (3), 267-309. DOI: 10.1029/94RG01802.

[50] Rudnick, R.L., Gao, S. (2003). Composition of the continental crust. In: Holland, H.D., Turekian, K.K., Rudnick, R.L. (Eds.). Treatise on Geochemistry. The Crust, vol. 3. Elsevier-Pergamon, Oxford, United Kingdom, pp. 1–64.

[51] Salminen, R., Tarvainen, T., Demetriades, A., Duris, M., Fordyce, F.M., Gregorauskiene, V., Kahelin, H., Kivisilla, J., Klaver, G., Klein, H., Larson, J.O., Lis, J., Locutura, J., Marmina, A., Martinova, N., McArthur, C., O'Connor, P., Odor, L., Ottesen, G., Paukola, T., Plant, J.A., Reimann, C., Schermann, O., Sewerin, U., Steenfelt, A., Van der Sluys, J., De Vivo, B. & Williams, L. (1998). FOREGS Geochemical mapping field manual. Geological Survey of Finland, Guide Number 47, Espoo, Finland, 42 pp. http://www.gtk.fi/foregs/geochem/fieldman.pdf.

[52] Salminen, R. (Chief-editor), Batista, M.J., Bidovec, M., Demetriades, A., De Vivo, B., De Vos, W., Duris, M., Gilucis, A., Gregorauskiene, V., Halamic, J., Heitzmann, P., Lima, A., Jordan, G., Klaver, G., Klein, P., Lis, J., Locutura, J., Marmina, N., Mazreku, A., O'Connor, P.J., Olsson, S., Ottesen, R.T., Petersell, V., Plant, J.A., Reeder, S., Salpeteur, I., Sandstrom, H., Siewers, U., Steenfelt, A. & Tarvainen, T. (2005). FOREGS Geochemical atlas of Europe. Part 1: Background information, methodology and maps. Geological Survey of Finland, Otamedia Oy, Espoo, Finland, 525 pp.

[53] Salminen, R., Batista, M.J., Demetriades, A., Lis, J. & Tarvainen, T. (2005a). Sampling. In: R. Salminen (Chief-editor), M.J. Batista, M. Bidovec, A. Demetriades, B. De Vivo, W. De Vos, M. Duris, A. Gilucis, V. Gregorauskiene, J. Halamic, P. Heitzmann, A. Lima, G. Jordan, G. Klaver, P. Klein, J. Lis, J. Locutura, K. Marsina, A. Mazreku, P.J. O'Connor, S.A. Olsson, R.T. Ottesen, V. Petersell, J.A. Plant, S. Reeder, I. Salpeteur, H. Sandstrom, U. Siewers, A. Steenfelt, & T. Tarvainen, FOREGS Geochemical Atlas of Europe. Part 1. Background information, Methodology and Maps. Geological Survey of Finland, Otamedia Oy, Espoo, Finland, p. 67-79.

[54] Sandstrom, H., Reeder, S., Bartha, A. et al., (2005). Sample Preparation and Analysis. In: R. Salminen (Chief-editor), M.J. Batista, M. Bidovec, A. Demetriades, B. De Vivo, W. De Vos, M. Duris, A. Gilucis, V. Gregorauskiene, J. Halamic, P. Heitzmann, A. Lima, G. Jordan, G. Klaver, P. Klein, J. Lis, J. Locutura, K. Marsina, A. Mazreku, P.J. O'Connor, S.A. Olsson, R.T. Ottesen, V. Petersell, J.A. Plant, S. Reeder, I. Salpeteur, H. Sandstrom, U. Siewers, A. Steenfelt, & T. Tarvainen, FOREGS Geochemical Atlas of Europe. Part 1. Background information, Methodology and Maps. Geological Survey of Finland, Otamedia Oy, Espoo, Finland, p. 80-93.

[55] Sheppard, S. C. & Evenden, W. G. (1988). Critical Compilation and Review of Plant/Soil Concentration Ratios for Uranium, Thorium and Lead. Journal of Environmental Radioactivity, 8(3), 255-285. https://doi.org/10.1016/0265-931X(88)90051-3.

[56] Sinclair, A. J. (1976). Applications of probability graphs in mineral exploration. Special Volume 4. Association of Exploration Geochemists, Toronto, Canada, 95 pp.

[57] Steenfelt, A. & Tarvainen, T. (2005). FOREGS Geochemical Atlas of Europe. Part 1. Background information, Methodology and Maps. Geological Survey of Finland, Otamedia Oy, Espoo, Finland, p. 67-79.

[58] Sukel, J. (2011). Natural uranium as a tracer in radionuclide geosphere transport studies. Academic dissertation, University of Helsinki, Finland, 56pp.

[59] Tye, A.M., Mikodowski, A.E. & Smedley, P.L. (2017). Distribution of Natural Radioactivity in the Environment, British Geological Survey Open Report, OR/17/011, 77pp.

[60] Tukey, J. W. (1977). Exploratory data analysis. Addison-Wesley, Reading, Massachusetts, USA, 506pp.

[61] UNSCEAR (2000). Annex B. Sources and Effects of Ionizing Radiation. United Nations Scientific Committee on the Effects of Atomic Radiation 2000 Report, Volume I. Sources. Annex B (Exposures from natural radiation sources). United Nations, New York, US.

[62] UNSCEAR 2008, Annex B. Sources and Effects of Ionizing Radiation. United Nations Scientific Committee on the Effects of Atomic Radiation 2008 Report, Volume I, Annex B (Exposures of the public and workers from various sources of radiation). United Nations, 2010.

[63] UNSCEAR (United Nations Scientific Committee on the effects of Atomic Radiation) (2010). Sources and effects of ionizing radiation. Report to General Assembly, Annex B. United Nations, New York.

[64] Verouglasiene, V. & Schneiders (2014). REACH and GEMAS. Chapter 2 in: Reimann, C., Birke, M., Demetriades, A., Filzmoser, P., O'Connor, P. (Eds.). Chemistry of Europe's Agricultural Soils. Part A. Geologisches Jahrbuch (Reihe B), Schweizerbarth, pp. 27-29.

[65] Vlasyuk, S. V. & Czapowski C. (2007). Generation of primary saline: the fluid inclusion data from the Upper Permian (Zechstein) evaporites, SW Poland. In: Schreiber, B. C., Lugli, S. & Babel, M. (eds.). Evaporites Through Space and Time. Geological Society of London, pp. 275-284. (DOI: 10.1144/SP285.16).

[66] Webb, J. S., Fortescue, J., Nichol, I. & Thorne, J. S. (1964). Regional geochemical Reconnaissance in the Namwala Concession area, Zambia. Geochemical Prospecting Research Centre, Technical Communication, 47.

[67] Wedepohl, K.H. (Ed.) (1978). Handbook of Geochemistry. Volume II/2. Elements (14) to V(23). Springer-Verlag, Berlin, Heidelberg & New York.

[68] Wedepohl, K.H. (Ed.) (1978a). Handbook of Geochemistry. Volume II/3. Elements La(57) to U(92). Springer-Verlag, Berlin, Heidelberg & New York.

[69] White, R. E. (2006). Principles and practice of soil science: the soil as a natural resource. 4th ed. Blackwell Science Ltd, Oxford.

Chapter 4 – Terrestrial radiation

(pp. 88-107)

[1] Adams, J.S. & Gasparini, P. (1970). Gamma-ray spectrometry of rocks. Elsevier Publishing Company, Amsterdam, the Netherlands.

[2] Albini M., Balderacchi M., Bettarelli C., Chiarelli E., Fiorentino G., Raptis K.G.C., Realini E., Regazzoni M., Rossi L., Sampietro D., Strati V., Marrisuoh F. (2017). Accuracy of Flight Altitude Measured with Low-Cost GNSS, Radar and Barometer Sensors: Implications for Airborne Radiometric Surveys. Sensors 17 (1888), 1 – 21, doi:10.3390/s17081888.

[3] Beck, H.L., DeCampo, J., Gogolak, C. (1972). In situ Ge(Li) and NaI(Tl) gamma-ray spectrometry. Health and Safety Laboratory, U.S. Atomic Energy Commission, report HASL-258.

[4] Bilinga, S.D., Minty, B.R., Newsam, G.N. (2003). Deconvolution and spatial resolution of airborne gamma-ray survey. Geophysics 68 (4), 1257 – 1266. https://gfzpublic.gfz-potsdam.de/pubman/item/item_1126642_5/component/file_1126643/GP2003.pdf.

[5] Blaha, M., Doll, H. & Stehlik, U. (2014). Long-term inter-comparison experiment for dose rate and spectrometric probes. Radiation Protection Dosimetry 160 (4), 306 – 310. doi:10.1093/rpd/nsu039.

[6] Bossew, P., Cinelli, G., Tollefsen, T., De Cort M. (2016). Gamma radiation from Radon peaks – association with factors related to geogenic radiation sources and meteorology. Presentation, Rad 2016 14th Intl. Conf. on Radiation and Application in Various Fields of Research, Niš, Serbia, 23-27.5.2016. https://onedrive.live.com/?authkey=%21KFEOPVaBMNgkpk&id=36E85E2D8D5B3CBF!986&cid=36E85E2D8D5B3CBF.

[7] Bossew, P. & Kirchner, G. (2004). Modelling the vertical distribution of radionuclides in soil. Part 1: the convection-dispersion equation revisited. Journal of Environmental Radioactivity, 73(2), 127 – 150. https://doi.org/10.1016/j.jenvrad.2003.08.008.

[8] Bossew, P., Kirchner, G., De Cort, M., de Vries G., Hofer A., de Felice L. (2012). Radioactivity from Fukushima Dai-ichi in air over Europe, part 1: Spatial-temporal analysis. Journal of Environmental Radioactivity, 114, 22 – 34. doi: 10.1016/j.jenvrad.2011.11.018.

[9] Bossew, P., Cinelli, G., Hernández-Ceballos, M., Cinelli, G., Hernández-Ceballos, M., Cinelli, G., Hernández-Ceballos, M., Cernohlawek, N., Gruber, V., Baumgartner, A., Hofmann, P., Hofer, M., Stöhlker, U., Hellmann, I., Weiler, F., Tollefsen, T., Tognoli, P.V., De Cort M. (2017). Estimating the terrestrial gamma dose rate by decomposition of the ambient dose equivalent rate. 2. Environmental Radioactivity 166, 296 – 308. http://dx.doi.org/10.1016/j.jenvrad.2016.02.013.

[10] Camp, A & Vargas, A. (2014). Ambient dose estimation H*(10) from LaBr3(Ce) spectra. Rad. Prot. Dosimetry 160 (4) 264 – 268. https://doi.org/10.1093/rpd/nct342.

[11] Chiozzi, P., Pasquale, V., Verdoya, M., Meloto S. (2001). Natural gamma-radiation in the Aeolian volcanic arc. Applied Radiation and Isotopes 55 (5), 737 – 744.

[12] Chiozzi, P., Pasquale, V., Verdoya, M., Meloto, S. (2003). Gamma-ray activity in the volcanic islands of the Southern Tyrrhenian Sea. Journal of Environmental Radioactivity 67 (3), 235 – 246. DOI: 10.1016/S0265-931X(03)00026-2.

[13] Cinelli, G., Faletti, P., Chiaberto, E., Cucchi, A. & Magnani, M. (2019). European Terrestrial Gamma Dose Rate. In: Proceedings from XXXVI Congresso Nazionale AIRP – il radiometrame, 17. – 19 October 2018, Bergamo, Italy, pp. 48- 63. (ISBN 9788888484860). http://www.airp.eos.it/wp-content/uploads/convegni/2019_bergamo/ATTI.pdf.

[14] Dainel, J., Lubyanetki, I. & Stercz, M. (1997). Geochemical Atlas of the Slovak Republic, Part II: Natural Radioactivity.

[15] Degerlier, M. & Doger, G. (2008). Assessment of gamma dose rates in air in Adana / Turkey. Radiation Protection Dosimetry 132 (3), 350 – 356; doi:10.1093/rpd/ncn295.

[16] Dennewarder, C.P., Hoogeboom, K. & Van Turnes, S.T. (2001). The national radioactivity monitoring network of the Netherlands. Nukleonika 46(4), 131–135.

[17] Devoron, J.P., Siegers, W., Gillard, J., Piernal, J.M. & Cuir, J.P. (1988). Survey of the natural radiation of Belgian territory as determined by different methods. Radiation Protection Dosimetry 24 (1 – 4), 347 – 351.

[18] Dickson, B.L. & Scott, K.L. (1997). Interpretation of aerial gamma ray surveys adding the geochemical factors. AGSO Journal of Australian Geology and Geophysics, 17(2), 187-203.

[19] Dombrowski, H., Neumaier, S., Thompson, I.M.G. & Wissmann, F. (2009). EURADOS intercomparison 2006 to harmonise European early warning dosimetry systems. Radiation Protection Dosimetry 135 (1), 1 – 20. https://doi.org/10.1093/rpd/ncp090.

[20] Dombrowski, H. (2014). Area dose rate values derived from NaI or LaBr3 spectra. Rad. Prot. Dosimetry 160 (4) 269 – 276. https://doi.org/10.1093/rpd/nct349.

[21] Dragovic, S., Jankovic, Lj., Dojcinovic, M. (2008). Assessment of gamma dose rates from terrestrial exposure in Serbia and Montenegro. Radiation Protection Dosimetry 131 (3), 297 – 302; doi:10.1093/rpd/nct099.

[22] Drakes E. (2016). Processing of Airborne Gamma-Ray Spectrometry using Interpolation. ASEG-PESA-AIG 2016 conference, Adelaide, Australia. www.publish.csiro.au/ex/pdf/ASEG2016ab147.

[23] EURAMET (2017). Metrology for radiological early warning networks in Europe. https://www.euramet.org/research-innovation/search-research-projects/details/euramet/Displ_project_show%5Bproject%5D=126%5EeurametDispl_project%5Bback%5D=40%5EHash=41b1bd1e2ffb609351d0129f5e124ca. Extended summary available.

[24] EURAMET (2018). Metrology for mobile detection of ionising radiation following a nuclear or radiological incident. https://www.euramet.org/research-innovation/search-research-projects/details/euramet/Displ_project_show%5Bproject%5D=147%5EeurametDispl_project%5Bback%5D=34%5EHash=a7a5c0a4a839f28e9a3975e41085438c. Short project description available.

[25] European Communities et al. (1998). Atlas of Caesium Deposition on Europe after the Chernobyl accident. Report EUR 16733. Office for Official Publications of the European Communities, Luxembourg. https://rem.jrc.ec.europa.eu/RemWeb/Browse.aspx?path=Atlas.

[26] Garcia-Talavera, M., Matarranz, J.L., Martinez, M., Salas, R. & Ramos, R. (2007). Natural ionizing radiation exposure of the Spanish population. Radiation Protection Dosimetry 124 (4), 355 – 359. doi:10.1093/rpd/nm211.

[27] Garcia-Talavera, M., Garcia-Perez, A., Rey, C. & Ramos, L. (2013). Mapping radon-prone areas using γ-radiation dose rate and geological information. J. Radiol. Prot. 33, 605 – 620. DOI: 10.1088/0952-4746/33/3/605.

[28] Grasty, R. (1987). The design, construction and application of airborne gamma ray calibration pads – Thailand. Geological Survey of Canada Paper 87-10.

[29] Grasty, R.L., Holman, P.B., Blanchard, Y.B. (1991). Transportable calibration pads for ground and airborne gamma ray spectrometers. Geol. Survey of Canada Paper 90-23.

[30] Guastaldi, E., Baldoncini, M., Bezzon, G., Broggini, C., Buso, G., Caciolli, A., Carmignani, L., Callegari, I., Colonna, T., Dule, N., Fiorentini, G., Xhaxha, M.K., Mantovani, F., Massa, G., Menegazzo, R., Mou, L., Rosa Alvarez, C., Strati, V., Shaha, G., Zanin, A. (2013). A multivariate spatial interpolation of airborne γ-ray data using the geological constraints. Remote Sensing of the Environment 137, 1 – 11. https://doi.org/10.1016/j.rse.2013.05.023.

[31] International Atomic Energy Agency (1976). Radiometric reporting Methods and Calibration in uranium Exploration. Technical Reports Series No. 174, IAEA, Vienna.

[32] International Atomic energy Agency (1978). Gamma-Ray Surveys in uranium exploration. Technical Reports Series No. 186, IAEA, Vienna.

[33] International Atomic Energy Agency (1987). Preparation and Certification of IAEA Gamma Ray Spectrometry Reference Materials RGU-1, RGTh-1 and RGK-1. Technical Report-IAEA/RL/148, IAEA, Vienna.

[34] International Atomic Energy Agency (1989). Construction and Use of Calibration Facilities for Radiometric Field Equipment. Technical Reports Series No. 309, IAEA, Vienna.

[35] International Atomic Energy Agency (1991). Airborne Gamma Ray Spectrometer Surveying. Technical Reports Series No. 323, IAEA, Vienna.

[36] IAEA (1997). Uranium exploration data and techniques applied to the preparation of radioelement maps. IAEA-TECDOC-980. https://www-pub.iaea.org/MTCD/publications/PDF/P074_scr.pdf.

[37] International Atomic Energy Agency (2003). Guidelines for radioelement mapping using gamma ray spectrometry data. IAEA-TECDOC-1363, IAEA, Vienna.

[38] International Atomic Energy Agency (2010). Radioelement Mapping. IAEA Nuclear Energy Series No. NF-T-1.3, IAEA, Vienna.

[39] International Atomic Energy Agency (2013). Advances in Airborne and Ground Geophysical Methods for Uranium Exploration. Nuclear Energy Series No. NF-T-1.5, IAEA, Vienna.

[40] ICRP (2007). The 2007 Recommendations of the International Commission on Radiological Protection. Ann. ICRP 37 (2-4). http://www.icrp.org/publication.asp?id=ICRP+Publication+103.

[41] ICRU (2011). Report 85: Fundamental Quantities and Units for Ionizing Radiation (Revised). Journal of the International Commission on Radiation Units and Measurements, 11(1). https://doi.org/10.1093/jicru/ndr012.

[42] International Commission on Radiation Units and Measurement (1994). Gamma-Ray Spectrometry in the Environment. ICRU Report 53, Bethesda.

[43] Kapdan, E., Varilioglu, A. Karahan, A. (2012). Outdoor radioactivity and health risks in Balikesir, north-western Turkey. Radiation Protection Dosimetry 148 (3), 301 – 309. doi:10.1093/rpd/nrc098.

[44] Kogan, F.M., Nazarov, I.M., Fridman S.D. (1969). Fundamentals of gamma ray spectrometry of natural environments. Gosatomizdat, Moscow.

[45] Lahtinen, R. (2012). Main geological features of Fennoscandia. Mineral deposits and metallogeny of Fennoscandia. Geological Survey of Finland, Special Paper 53, 19–28.

[46] Lindberg, I. (1984). The calibration of portable and airborne gamma ray spectrometers – theory, problems and facilities. Report Risø-M-2450, Roskilde.

[47] Malina, A., Okumura, M. Machida, M., Takemiya, H., Saito, K. (2015). Fields of view for environmental radioactivity. arXiv:1509.00125v1.

[48] Marousk, M. & Matolin, M. (1999). Radiometric map of the Czech Republic 1:500 000. Czech Geological Survey, Prague, 1 – 19.

[49] Matern, S. & Tardy, M. (1984). Introduction to Applied Geophysics. D. Reidel Publishing Company, Dordrecht, the Netherlands.

[50] Martin, P.G., Payton, O.D., Fardoulis, J.S., Richards, D.A. & Scott, T.B. (2015). The use of unmanned aerial systems for the mapping of legacy uranium mines. J. Environmental Radioactivity 143, 135 – 140. https://doi.org/10.1016/j.jenvrad.2015.02.004.

[51] Mascom O. et al. (2011). Tracking of Airborne Radionuclides from the Damaged Fukushima Dai-ichi Nuclear Reactors by European Networks. Environmental Science and Technology 45 (18), 7670 – 7677. DOI: 10.1021/es2017158.

[52] Matern, M. (2017). Verification of the radiometric map of the Czech Republic. Journal of Environmental Radioactivity, 166 (2017), 288-295.

[53] Miller A.M. & Stelzel P. (1993). In situ gamma-ray spectrometry. A tutorial for environmental radiation scientists. Environmental Measurement Laboratory, U.S. Department of Energy, report EML-557. https://inis.iaea.org/search/search.aspx?orig_q=RN:25033475.

[54] Minty, B., Franklin, R., Milligan P., Richardson, L.M. & Wilford, J. (2009). The radiometric map of Australia. Paper presented at the 20th Int. Geophysical Conference and Exhibition, Australian Soc. of Exploration Geophysicists, Adelaide.

[56] Neumaier, S. & Dombrowski, H. (2014). EURADOS intercomparisons and the harmonisation of environmental radiation monitoring. Radiation Protection Dosimetry 160 (4): 297 – 305. doi:10.1093/rpd/nct002

[57] Osmen, S.F., Bozkurtoum, I., Yavuz, M., Tunç, M.H. (2014). Determination of gamma radioactivity levels and associated dose rates of soil samples of the Akesu / Manyas using high-resolution gamma-ray spectrometry. Radiation Protection Dosimetry 158 (4): 461 – 465. doi:10.1093/rpd/nct267

[58] Otcenas, P., Karahan, G., Kam, E., Baruz, I., Tosun H. (2012). Assessment of natural radioactive concentrations and gamma dose rate levels in Kayseri, Turkey. Radiation Protection Dosimetry 148 (2): 227 – 236. doi:10.1093/rpd/nc023

[59] Rahbvandic, B., Avdic, S., Gadic, I., Osmanovic, A. (2016). Measurement of natural environmental radioactivity and estimation of population exposure in Bihac, Bosnia and Herzegovina. J. Radioanalytical and Nuclear Chemistry 311 (3): xx. DOI 10.1007/s10967-016-5155-0

[60] Quindós Poncela, L.S., Fernández, P.L., Gómez Arozamena, J., Fernández, J.A., Suárez Mahou, E., Martín Matarranz, J.L. & Cascón, M.C. (2004). Natural gamma radiation map (MARNA) and indoor radon levels in Spain. Environment International 29 (8): 1091 – 1096. doi:10.1016/S0160-4120(03)00102-8

[61] Rybach, L., Bachler, D., Bucher, B., Schwarz, G. (2003). Radiation doses of Swiss population from external sources. J. Environmental Radioactivity 62 (3): 277 – 288. PMID: 12164632

[62] Sáez-Vergara, J.C., Thompson, I.M.G., Gunnarsson, K., Dombrowski, H., Funck, E. & Neumaier, S. (2007). The second EURADOS intercomparison of national network systems used to provide early warning of a nuclear accident. Radiation Protection Dosimetry 123 (2): 190 – 208. https://doi.org/10.1093/rpd/nc1112

[63] Sahin, L., Cevik, M. (2008). Natural radioactivity measurements in soil samples of Central Anatolia (Turkey). Radiation Protection Dosimetry 131 (4): 526 – 530. doi:10.1093/rpd/ncn243

[64] Sainz Fernández, C., Fernández Villar, A., Fuente Merino, I., Gutiérrez Villanueva, J.L., Martín Matarranz, J.L., García-Talavera, M., Casaño Ordás, S., Quindós Poncela, L.S. (2014). The Spanish indoor radon mapping strategy. Radiation Protection Dosimetry 162 (1-2): 58 – 62. doi:10.1093/rpd/nct218

[65] Strebl, F., Gerzabek, M., Kirchner, G., Ellison S. & Bossew, P. (2008). Vertical migration of radionuclides in undisturbed grassland soils. In IAEA Tecdoc 1616: Quantification of Radionuclide Transfer in Terrestrial and Freshwater Environments for Radiological Assessments. ISBN 978-92-0-104509-6. International Atomic Energy Agency, Vienna, Austria. www-pub.iaea.org/mtcd/publications/PubDetails.aspx?pubId=8103

[66] Strzelecki, R., Walkowicz, S., Szewczyk, J. & Lewandowski, P. (1994). Radioecological maps of Poland. Part V. Warsaw, Poland.

[67] Szegvary, T., Conen, F., Stichler W., Dubois, G., Bossow, P., de Vries, B. (2007). Mapping terrestrial γ-dose rate in Europe based on routine monitoring data. Rad. Meas. 42, 1561 – 1572. https://doi.org/10.1016/j.radmeas.2007.09.002

[68] Szegvary, T., Conen, F., Ciais, P. (2009). European ^{222}Rn inventory for applied atmospheric studies. Atmospheric Environment 43 (8): 1536 – 1539.

[69] Taschl, M. & Gnesly, R.L. (2002). Natural background radioactivity of the Earth's surface – essential information for environmental impact studies. The Uranium Production Cycle and the Environment. IAEA-CSP-10/P, IAEA, Vienna.

[70] Tschiff, E., Baumann, W., Neppel, R., Vychytil, P. (1975). Strahlenkarte Österreichs. Bundesministerium für Gesundheit und Umweltschutz. (In German)

[71] Turhan, S., Arikan, I.H., Oguz, F., Ordemir, T., Yücel, B., Varoğlu, A. & Köse A. (2012). Gamma dose rate survey of natural background gamma dose rate in Çanakkale region, Turkey. Radiation Protection Dosimetry 148 (1): 45 – 50. doi:10.1093/rpd/nq293

[72] UNSCEAR (2000). United Nations Scientific Committee on the Effects of Atomic Radiation. Source and Effects of Ionizing Radiation. United Nations, New York, US.

[73] UNSCEAR (2008). United Nations Scientific Committee on the Effects of Atomic Radiation. Source and Effects of Ionizing Radiation. New York. Annex B. United Nations, New York, US.

[74] Vargas, A. (2018). WG 3 – Environmental Dosimetry. http://eurados.org/media/Files/Eurados/documents/Working_Groups/2018/progressreport/WG03_2018.pdf?srv=kshash=A3E7D01D97358F70B9B08785A2457B0687AF512

[75] Wedepohl, K.H. (Editor) (1978). Handbook of Geochemistry. Volume II/5 Elements La(57) to U(92). Springer-Verlag, Berlin, Heidelberg & New York.

[76] Wissmann, F. & Sáez-Vergara, J.C. (2008). Dosimetry of environmental radiation – a report on the achievements of EURADOS WG3. Radiation Protection Dosimetry 118 (2): 167 – 179. https://doi.org/10.1093/rpd/ncl015

[77] Yi, E.-H., J.-S. Jun, H.-S. Chai, J.-J.-Oh & J.-Y. Yun (1997). Measurement of ambient dose equivalent using a NaI(Tl) scintillation detector. Rad. Prot. Dosimetry 74 (4): 271 – 278. https://doi.org/10.1093/oxfordjournals.rpd.a032207

[78] Will, W., Bunzel, H. H., Mielcarek, J., Malinowski, D. & Sarnau, D. (1997). Ortsdosisleistung für terrestrischen Dosiseintrag in den östlichen Bundesländern Deutschlands. (In German) German Federal Office for Radiation Protection, report BfS-SY-13/97

[79] Will, W., Mielcarek, J., Schkade, U.-K. (2003). Ortsdosisleistung der terrestrischen Gammastrahlung in ausgewählten Regionen Deutschlands. (In German) German Federal Office for Radiation Protection, report BfS-SW-01/03

[80] Zahringer, M. & Serpau, J. (1998). The assessment of the representativeness of data from dose rate monitoring stations. Radiation Protection Dosimetry 64 (4): 275 – 282. https://doi.org/10.1093/oxfordjournals.rpd.a011584

[81] Zähringer, M. & Serpau, J. (1997). Calibration factors for dose rate probes in environmental monitoring networks obtained from Monte Carlo simulations. German Federal Office for Radiation Protection, report BfS-AR-2/97

Chapter 5 – Radon

(pp. 108-137)

[1] Åkerblom, G., Pettersson, B. & Rosen, B. (1988). Radon i bostader. Markradon. Rapport från BFR. In Swedish. ISBN 91-540-4937-7.

[2] Abramaitytė, R., Pilkytė, I. & Markūnas, L. (2005). Radon risk investigation in Panevėžys city development area. Health Sciences, 13: 32–35.

[3] Åkerblom, G. & Wilson, C. (1980). Radon gas – A radiation hazard from radioactive bedrock and building materials. Bulletin of the International Association of Engineering Geology, 23(1): 55–61. https://doi.org/10.1007/BF02594726.

[4] Åkerblom, G. & Wilson, C. (1981). Radon – geological aspects of an environmental problem. In International Meeting on Radon – Radon Progeny Measurements, 27–28 August 1981, Montgomery, Alabama, US. Geological Survey of Sweden. Reports and communications no. 30. Uppsala 1982. 47 pp. ISBN 91-7158-271-1.

[5] Åkerblom, G. (1986). Investigation and mapping of radon risk areas. In: International Symposium on Geological Mapping in the Service of Environmental Planning. Commission for the Geological Map of the World, Trondheim, Norway, 5–9 May, 1986. In Wolff, F.C. (ed.): Geology for Environmental planning. Geological of Survey of Norway, Special Papers 2: 15 pp.

[6] Åkerblom, G., Pettersson, B. & Rosén, B. (1988). A handbook of investigation of the radon situation in areas before building. The Swedish Council for Building Research and the Swedish National Board for Physical Planning and Building. Report 88:8 1988. Revised edition 1990. 160 pp. ISBN 91-540-4937-7.

[7] Alharbi, W.R. & Abbady, A.G.E. (2013). Measurement of radon concentrations in soil and the extent of their impact on the environment from Al-Qassim, Saudi Arabia. Natural Science, 5(1): 93–98. doi:10.4236/ns.2013.51015.

[8] Alonso, H., Rubiano, J.G., Arnedo, M.A., Gil, J.M., Rodríguez, R., Florido, R. & Martel, P. (2010). Determination of the radon potential for volcanic materials of the Gran Canaria island. In: Barnet I., Neznal M. and Pacherova P., eds. Proc. 10th international workshop on the geological aspects of radon risk mapping. Czech Geological Survey, Radon v.o.i., Prague 2010. ISBN 978-80-7075-754-3, pp. 7 – 14. http://www.radon.eu/workshop2010/

[9] Andersson, P., Cavenagi, D. & Åkerblom, G. (1983). Radon i bostader – Mätbara invankar på radonhalt och gammastrålning dominus. In Swedish. Statens råd för byggnadsforskning. Rapport 89: 1983.

[10] Annunziatellis, A., Beaubien, S.E., Bigi, S., Ciotoli, G., Coltella, M. & Lombardi, S. (2008). Gas migration along fault systems and through the vadose zone in the Latera caldera (central Italy): implications for CO_2 geological storage. International Journal of Greenhouse Gas Control, 2(3): 353–372. https://doi.org/10.1016/j.ijggc.2008.02.003

[11] Antignani, S., Venoso, G., Carpentieri, C. & Bochicchio, F. (2018). Analytical method for evaluating (and correcting) the impact of outdoor radon concentration on the estimates of percentage of dwellings exceeding reference levels. Journal of Environmental Radioactivity. Available online 19 April 2018. doi: 10.1016/j.jenvrad.2017.12.021.

[12] Appleton, J.D. & Ball, T.K. (1995). Radon and background radioactivity from natural sources: characteristics, extent and the relevance to planning and development in Great Britain. British Geological Survey Technical Report WP/95/2.

[13] Appleton, J.D., Miles, J.C.H. & Tellam, D.K. (2003). Dealing with radon emissions in respect of new development: Evaluation of mapping and site investigation methods for targeting areas where new development may require radon protective measures. British Geological Research Report RR/00/12. ISBN 0 85272 377 6.

[14] Appleton, J.D. & Miles, J.C.H. (2010). A statistical evaluation of the geogenic controls on indoor radon concentrations and radon risk. Journal of Environmental Radioactivity, 101 (10): 799–803. https://doi.org/10.1016/j.jenvrad.2009.06.002.

[15] Appleton, J.D., Cave, M.R., Miles, J.C.H. & Sumerling, T.J. (2011). Soil radium, soil gas radon and indoor radon: empirical relationships to assist in post-closure impact assessment related to near-surface radioactive waste disposal. Journal of Environmental Radioactivity, 102(3): 221–234. doi: 10.1016/j.jenvrad.2010.09.007.

[16] Arvela, H., Holmgren, O. & Hänninen, P. (2016). Effect of soil moisture on seasonal variation in indoor radon concentration: modeling and measurements in 326 Finnish houses. Radiation Protection Dosimetry, 168(2): 277–290. doi: 10.1093/rpd/nc182.

[17] Ashok, G.V., Nagaiah, N., Shiva Prasad, N.G. & Anilkka, M.R. (2011). Study of radon exhalation rate from soil, Bangalore, South India. Radiation Protection and Environment, 34(4): 233–238. doi: 10.4103/0972-0464.106093.

[18] Baklushin, V.N., Simko, E.E. & Starikov, B. (1970). Investigation of turbulent exchange and wash-out by measurement of natural radioactivity in surface air. Journal of Geophysical Research, 75(18): 3669–3674. https://doi.org/10.1029/JC075i018p03669.

[19] Balzan, C., Vincenti, K., Tabuck, B., Conchan, S., Farrugia, S. & Grech, D. (2013). National mapping survey of indoor radon levels in the Maltese Islands (2010-2011). Malta Medical Journal, 25 (4): 33–39.

[20] Barnet, I., Miklosova, J. & Procházka, J. (1998). Radon database and radon risk map 1:500 000 of the Czech Republic. In: Barnet, I. & Neznal, M. (eds.): Radon investigations in the Czech Republic VI and the Fourth International Workshop on the Geological Aspects of Radon Risk Mapping, pp. 1–5, Prague, Czech Republic.

[21] Barnet, I., Miklosova, J., Tomas, R. & Kunnova, J. (2000). Radon risk mapping of the Czech Republic on a scale 1:50 000. In: Barnet, I., Neznal, M. (eds.): Radon investigations in the Czech Republic VIII and the Fifth International Workshop on the Geological Aspects of Radon Risk Mapping. Czech Geological Survey and Radon Corp. Prague, Czech Republic. https://ths.aha.org/collection/HCU/Collection/Stories/_Pub-lic/32003/32003561.pdf (accessed 7 November 2018).

[22] Barnet, I., Pacherová, P., Neznal, M. & Neznal, M. (2008). Radon in geological environment – Czech experience. Czech Geological Survey Special Papers 19, 70 pp. Czech Geological Survey, Prague, Czech Republic.

[23] Barnet, I. & Pacherová, P. (2011). Impact of the deeper geological basement on soil gas and indoor radon concentrations in areas of Quaternary fluvial sediments (Bohemian Massif, Czech Republic). Environmental Earth Sciences, 63(3): 551–557. https://doi.org/10.1007/s12665-010-0722-0.

[24] Barnet, I. & Pacherová, P. (2013). Increased soil gas radon and indoor radon concentrations in Neoproterozoic siliciclastones of the Teplá-Barrandian unit (Czech Republic). Environmental Earth Sciences, 69(5): 1601–1607. https://doi.org/10.1007/s12665-012-1996-1.

[25] Barnet I., Pacherová P. & Rahael M. (2019). Detection of faults using the soil-file measurements of radon concentration and gamma dose rate (Bohemian Massif, Czech Republic). Environmental Earth Sciences 77, 330. https://doi.org/10.1007/s12665-018-7513-4.

[26] Barregin, R.M., Arellano, V.M., Portugal, E. & Segovia, N. (2008). Effects of changes in reservoir thermodynamic conditions on 222 Rn composition of discharged fluids: study for two wells at Los Azufres geothermal field (Mexico). Geofluids, 8 (4): 252–262. https://doi.org/10.1111/j.1468-8123.2008.00229.x.

[27] Bartos, J., Alvela, H., Bochicchio, F., Bradley, J., Colligan, B., Fenton, D., Fujikawa, I., Gray, A., Grasche, B., Grusson, M., Holmgren, O., Huda, J., Jiranek, M., Kahrmann, K., Kephalopoulos, S., Kreuzer, M., Laughlin, J.M., Ringer, W., Rovensky, K., Schlesinger, D., Venoso, G. & Zeeb, H. 2012. Radon Prevention and Remediation: The RADPAR Recommendations. https://doi.org/10.1314/JRS.2.2.12952.08964.

[28] Baroni e Silva, F. & Lavalle, C. (2013). A high-resolution grid map for Europe. Journal of Maps, 9 (1): 16 – 26. https://doi.org/10.1080/17445647.2013.764830.

[29] Baubron, J.C., Rigo, A. & Toutain, J.P. (2002). Soil gas profiles as a tool to characterize active tectonic areas: The Jaut Pass example (Pyrenees, France). Earth and Planetary Science Letters, 196(1-2): 69–81. https://doi.org/10.1016/S0012-821X(01)00591-8.

[30] Beckman, I.N. & Balek, V. (2002). Theory of emanation thermal analysis: III. Radon diffusion as the probe of microstructure changes in solids. Journal of Thermal Analysis and Calorimetry, 67(1): 49–61. https://doi.org/10.1023/A:1013735702559.

[31] Berg, S.S. & Skar, T. (2005). Controls on damage zone asymmetry of a normal fault zone: Outcrop analyses of a segment of the Moab fault, SE Utah. Journal of Structural Geology, 27(10): 1803–1822. https://doi.org/10.1016/j.jsg.2005.04.012.

[32] Berkson, J.D. (1950). Are there two regressions? Journal of the American Statistical Association, 45 (250): 164–180.

[33] Bigi, S., Beaubien, S.E., Ciotoli, G., D'Ambrogio, C., Doglioni, C., Tavarnelli, V., Lombardi, S.

[34] Blanchard, R.L. (1980). Ambient Outdoor Radon Concentrations in the United States. Contract No. 68- 03-4375 for USEPA, Office of Radiation Programs. Cuneo and Associates, McLean, Virginia, USA.

[35] Blachowicz, P., Campos-Venuti, G., Piermarini, S., Risica, S., Tommasino, L., Torri, G., Magnoni, M., Agnesod, G., Sgorbati, G., Bonomi, M., Minach, L., Trotti, F., Malisan, M.R., Maggioni, S., Gandolfi, L., Guarnerio, C., Bongioni, A., Lombardi, M., Cherubini, G., D'Ostilio, S., Cristofaro, C., Pugliese, M., Martucci, V., Crispino, A., Dubourieux, P., Sansone Santamaria, R. & Cappai, M. (2005). Annual average and seasonal variations of residential radon concentration for all the Italian Regions. Radiation Measurements 40 (2005): 686–694. https://doi.org/10.1016/j.radmeas.2004.12.023.

[36] Bochicchio, F., Venoso, G., Antignani, S. & Carpentieri, C. (2017). Radon Reference Levels and Priority Areas: Considering Optimisation and Avertable Lung Cancers. Radiation Protection Dosimetry, 177 (1-2): 87–90. doi: 10.1093/rpd/ncx130.

[37] Borgoni, R., Quatto, P., Somà, G. & de Bartolo, G. (2010). A geostatistical approach to define guidelines for radon prone area identification. Statistical Methods and Applications, 19 (2): 253–276. https://doi.org/10.1007/s10260-009-0128-x.

[38] Borgoni, R., De Francesco, D., De Bartolo, D. & Tzavidis, N. (2014). Hierarchical modeling of indoor radon concentration: how much do geology and building factors matter? Journal of Environmental Radioactivity, 138: 227–237. doi:org/10.1016/j.jenvrad.2014.08.022.

[39] Bossew, P., Dubois, G. & Tollefsen, T. (2006a). Investigations on indoor Radon in Austria, part 2: Geological classes as categorical external drift for spatial modelling of the Radon potential. Journal of Environmental Radioactivity, 59(1): 81–97. doi: 10.1016/j.jenvrad.2007.06.013.

[40] Bossew, P., Dubois, G. & Tollefsen T. (2006b). Geological classes as categorical external drift for spatial modelling of the Radon potential. Journal of Environmental Radioactivity, 89 (1): 81 – 97. doi: 10.1016/j.jenvrad.2007.06.013.

[41] Bossew, P., Gruber, V., Tollefsen, T. & De Cort, M. (2012). The European map of indoor radon concentrations: status and questions of quality assurance. Kerntechnik, 77 (3): 176 – 183. https://doi.org/10.3139/124.110264.

[42] Bossew, P. Stojanovska, Z., Zunic, Z.S. & Ristova, M. (2013). Prediction of indoor radon risk from radium concentration in soil: Republic of Macedonia case study. Romanian Reports of Physics, 58 (SUPPL.): 1–15. ISSN 1221-146X.

[43] Bossew, P. (2014). Determination of radon prone areas by optimized binary classification. Journal of Environmental Radioactivity, 139: 121–132. doi: 10.1016/j.jenvrad.2013.12.015.

[44] Bossew, P. (2015). Estimation of radon prone areas through binary classification, part 2: radon prone geologies. Journal of Environmental Radioactivity, 141: 44–50. doi: 10.1016/j.jenvrad.2014.11.020.

[45] Bossew, P., Gruber, G., Tollefsen, T. & De Cort, M. (2017). The geogenic radon hazard index – another attempt. Proc. NEANR 2017, 2nd International Workshop on the European Atlas of Natural Radiation, Verbania, Italy, 6 – 9 Nov 2017. http://www.nrpi.fr/nrpi/wp-content/uploads/2018/07/Bossew_NEANR2017_Rn.pdf

[46] Breitner, D., Arvela, H., Helmuth, K.-H. & Renault, T. (2010). Effect of moisture content on emanation at different grain size fractions – a pilot study on granite, esker sand sample. Journal of Environmental Radioactivity, 101(11): 1002–1006. doi: 10.1016/j.jenvrad.2010.07.008.

[47] Brunt, R.C. (1985). Sources of Indoor Radon in Houses: A Review. Journal of the Air Pollution Control Association, 35(2): 105–109. https://doi.org/10.1080/00022470.1985.10465550.

[48] Burian, I. & Ditalal, P. (2009). Radon and its decay products in outdoor air. Applied Radiation and Isotopes, 67(5): 881–883. doi:10.1016/j.apradiso.2009.01.008.

[49] Burke, O. & Murphy, P. (2011). The use of volunteer radon measurements for radon mapping purposes: an examination of sampling bias issues. Journal of Radiological Protection, 31(3): 319–328. doi: 10.1088/0952-4746/31/3/001.

[50] Burnett, W.C. & Dulaiova, H. (2003). Estimating the dynamics of groundwater input into the coastal zone via continuous radon-222 measurements. Journal of Environmental Radioactivity, 69 (1-2): 21–35. https://doi.org/10.1016/S0265-931X(03)00084-6.

[51] Burnett, W.C., Aggarwal, P.K., Aureli, A., Bokuniewicz, H., Cable, J.E., Charette, M.A., Kontar, E., Krupa, S., Kulkarni, K.M., Loveless, A., Moore, W.S., Oberdorfer, J.A., Oliveira, J., Ozyurt, I.N., Povinec, P., Privitera, A.M.G., Rajar, R., Ramessur, R.T., Scholten, J., Stieglitz, T., Taniguchi, M. & Turner, J.V. (2006). Quantifying submarine groundwater discharge in the coastal zone via multiple methods. The Science of the Total Environment, 367(2-3): 498–543. doi: 10.1016/j.scitotenv.2006.05.009.

[52] Caine, J.S., Evans, J.P. & Forster, C.B. (1996). Fault zone architecture and permeability structure. Geology, 24(11): 1025–1028. https://doi.org/10.1130/0091-7613(1996)024<1025:FZAAPS>2.3.CO;2.

[53] Calderoni, M. & Pinza, S. (2008). Are ageing and fading really a problem for the quality of the passive radon measurements? Radiation Measurements, 43: 5422–5426. https://doi.org/10.1016/j.RADMEAS.2008.03.018.

[54] Carmina, G., Ganzaglia, M., Magnani, S., Valli, G. & Vecchi, R. (1997). Natural radioactivity and radon exhalation in stony materials. Journal of Environmental Radioactivity, 34(2): 145–159. https://doi.org/10.1016/0265-931X(96)00025-2.

[55] Ciotoli, G., Lombardi, S. & Annunziatellis, A. (2007). Geostatistical analysis of soil gas data in a high seismic intermontane basin: Fucino Plain, central Italy. J. Geophys. Res. 112, B05407. http://dx.doi.org/10.1029/2005JB004044.

[56] Ciotoli, G., Ascione, A., Bigi, S., Lombardi S. & Mazzoli S. (2014). Soil gas distribution in the main coseismic surface rupture zone of the 1980, Mw=6.9, Irpinia earthquake (southern Italy). Journal of Geophysical Research, 119(3), 2440–2461. doi: 10.1002/2013JB010508.

[57] Ciotoli, G., Sciarra, A., Ruggieri, L., Annunziatellis, A. & Bigi, S. (2016). Soil gas geochemical behaviour across tunnel and exposed faults during the 24 August central Italy earthquake. Annals of Geophysics, 59, Fast Track 5, 2016. doi: 10.4401/ag-7242.

[58] Ciotoli, G., Voltaggio, M., Tuccimei, P., Soligo, M., Pascucci, A., Beaubien, S.E. & Bigi, S. (2017a). Geographically weighted regression and geostatistical techniques to construct the geogenic radon potential map of the Lazio region: A methodological proposal for the European Atlas of Natural Radiation. Journal of Environmental Radioactivity, 166 (Part 2): 355–375. https://doi.org/10.1016/j.jenvrad.2016.05.010.

[59] Ciotoli, G., Ruggieri, L., Bossew, P. & Pereira A.J.S.C. (2017b). Geogenic radon as geophysical / geothermal tracer of active faults: an overview. Proceedings of the 4th International Conference on Environmental Radioactivity / Radionuclides as Tracers of Environmental Processes. ENVRA 2017, 29 May – 3 June 2017, Vilnius, Lithuania, pp. 56 – 43. ISBN 978-609-95511-4-2.

[60] Ciotoli, G., Ruggieri, L., Cannata, G.P., Modesti, L., Bigi, S. & Romano, V. (2018). Geogenic radon as geophysical tracer of active faults: the Fucino Plain (central Italy). 87° Convegno Nazionale del GNGTS, Session 2.2 'Processi tettonici attivi: dati e modelli', Bologna, 19-22 November 2018. http://www3.ogs.trieste.it/gngts/files/2018/512/Russian/Contributi.pdf

[61] Clavensjö, B. & Åkerblom, G. (1994). The Radon Book – Measures against radon. The Swedish Council for Building Research, Stockholm, Liungbäls Offset AB. ISBN 91-540-5407-8.

[62] Clements, W.E. & Wilkening, M.H. (1974). Atmospheric pressure effects on ^{222}Rn transport across the Earth-air interface. Journal of Geophysical Research, 79(33): 5025–5029. https://doi.org/10.1029/JC079i033p05025.

[63] Clever, H.L. (Ed.) (1979). Solubility Data Series, Volume 2: Krypton, Xenon and Radon — Gas Solubilities. 0-08-022352-4, Pergamon Press, Oxford, United Kingdom.

[64] Cloos, M., Matthews, M., Burkitt, L., Abraham, P. & Scott D. (2014). Use of radon to characterise surface water recharge to groundwater. Journal of Hydrology (New Zealand), 53 (2): 115–127. https://www.jstor.org/stable/43945059.

[65] Cohen, B.L. (1979). Radon: Characteristics, natural occurrence, technological enhancement, and health effects. Progress in Nuclear Energy, 4(1): 1–24. https://doi.org/10.1016/0149-1970(79)90007-6.

[66] Collettini, C., Castellini, C., Chiaraluce, G., De Paola, N., Holdsworth, R.E. & Smith, S.A.F. (2008). Fault weakening due to CO_2 degassing in the Northern Apennines: short- and long-term processes. In: Wibberley, C.A.J., Kurz, W., Imber, J., Holdsworth, R.E., Collettini, C. (Eds.). The Internal Structure of Fault Zones: Implications for Mechanical and Fluid-Flow Properties. Geological Society, London, pp. 175–194.

[67] Cornelis, J., Sohir, A. & Turki, K. (2011). Messungen der Radonkonzentration in der Bodenluft – Wie zuverlässig sind die Messwerte? Strahlenschutzpraxis 3/2011, 56 – 60.

[68] Cosma, C., Cucos, A., Dicu, A., Papp, B., Begy, R. & Sainz, C. (2013). Soil and building material as main sources of indoor radon in Baia-Sim radon prone area (Romania). Journal of Environmental Radioactivity, 116: 174–179. doi: 10.1016/j.jenvrad.2012.09.006.

[69] Crawley, D., Ciotoli G., Cinelli, G., Ellis, J., Bossew, P., McKinley, J., Lomnl, R. & Mitzer A. (2018). Tectonically enhanced geogenic radon (TEGR). EGU general assembly, Vienna 9 – 13 April 2018. http://meeting.copernicus.org/EGU2018-9348_presentation.pdf

[70] Cucos, D.A., Papp, B., Dicu, T., Moldovan, M., Burghele, D.B., Moraru, I.T., Tender, A. & Cosma, C. (2017). Residential, soil and water radon surveys in north-western part of Romania. Journal of Environmental Radioactivity, 166(Pt 2): 412–416. doi: 10.1016/j.jenvrad.2016.10.003.

[71] Cinelli, G., Tondeur, F., Dehandschutter, B., Bossew, P., Tollefsen, T. & De Cort, M. (2017). Mapping uranium concentration in soil: Belgian experience towards a European map. Journal of Environmental Radioactivity, 166(Pt 2): 220–234. doi: 10.1016/j.jenvrad.2016.04.026.

[72] Cinelli, G., Tollefsen, T., Bossew, P., Gruber, V., Bogdanovics, K., De Felice, L. & De Cort, M. (2018). Digital version of the European Atlas of Natural Radiation. Journal of Environmental Radiation. doi: 10.1016/j.jenvrad.2018.02.008.

[73] Cotal, G., Guerra, M., Lombardi, S. & Vitari, E. (1998). Soil gas survey for tracing seismogenic faults: a case study in the Fucino basin, Central Italy. Journal of Geophysical Research, Solid Earth 103 (B10): 23781–23794. https://doi.org/10.1029/98JB01553.

[74] Cotal, G., Etiope, G. & Guerra, M. (1999). The detection of concealed faults in the Ofanto Basin using the correlation between soil gas fracture surveys. Tectonophysics, 301(3-4): 321–332. https://doi.org/10.1016/S0040-1951(98)00220-0.

[75] Cotal, G., Lombardi, S. & Annunziatellis, A. (2007). Geostatistical analysis of soil gas data in a high seismic intermontane basin: Fucino Plain, central Italy. J. Geophys. Res. 112, B05407. http://dx.doi.org/10.1029/2005JB004044.

[76] Cotal, G., Ascione, A., Bigi, S., Lombardi S. & Mazzoli S. (2014). Soil gas distribution in the main coseismic surface rupture zone of the 1980, Mw=6.9, Irpinia earthquake (southern Italy). Journal of Geophysical Research, 119(3), 2440–2461. doi: 10.1002/2013JB010508.

[77] Cotal, G., Sciarra, A., Ruggieri, L., Annunziatellis, A. & Bigi, S. (2016). Soil gas geochemical behaviour across tunnel and exposed faults during the 24 August central Italy earthquake. Annals of Geophysics, 59, Fast Track 5, 2016. doi: 10.4401/ag-7242.

[78] Cotal, G., Voltaggio, M., Tuccimei, P., Soligo, M., Pascucci, A., Beaubien, S.E. & Bigi, S. (2017a). Geographically weighted regression and geostatistical techniques to construct the geogenic radon potential map of the Lazio region: A methodological proposal for the European Atlas of Natural Radiation. Journal of Environmental Radioactivity, 166 (Part 2): 355–375. https://doi.org/10.1016/j.jenvrad.2016.05.010.

[79] Cotal, G., Lombardi, S. & Annunziatellis, A. (2007). Geostatistical analysis of soil gas data in a high seismic intermontane basin: Fucino Plain, central Italy. J. Geophys. Res. 112, B05407. http://dx.doi.org/10.1029/2005JB004044.

[80] Cotal, G., Ruggieri, L., Cannata, G.P., Modesti, L., Bigi, S. & Romano, V. (2018). Geogenic radon as geophysical tracer of active faults: the Fucino Plain (central Italy). 87° Convegno Nazionale del GNGTS, Session 2.2 'Processi tettonici attivi: dati e modelli', Bologna, 19-22 November 2018. http://www3.ogs.trieste.it/gngts/files/2018/512/Russian/Contributi.pdf

[81] Clavensjö, B. & Åkerblom, G. (1994). The Radon Book – Measures against radon. The Swedish Council for Building Research, Stockholm, Liungbäls Offset AB. ISBN 91-540-5407-8.

[82] Clements, W.E. & Wilkening, M.H. (1974). Atmospheric pressure effects on ^{222}Rn transport across the Earth-air interface. Journal of Geophysical Research, 79(33): 5025–5029. https://doi.org/10.1029/JC079i033p05025.

[83] Clever, H.L. (Ed.) (1979). Solubility Data Series, Volume 2: Krypton, Xenon and Radon — Gas Solubilities. 0-08-022352-4, Pergamon Press, Oxford, United Kingdom.

[84] Cloos, M., Matthews, M., Burkitt, L., Abraham, P. & Scott D. (2014). Use of radon to characterise surface water recharge to groundwater. Journal of Hydrology (New Zealand), 53 (2): 115–127. https://www.jstor.org/stable/43945059.

[85] Cohen, B.L. (1979). Radon: Characteristics, natural occurrence, technological enhancement, and health effects. Progress in Nuclear Energy, 4(1): 1–24. https://doi.org/10.1016/0149-1970(79)90007-6.

[86] Collettini, C., Castellini, C., Chiaraluce, G., De Paola, N., Holdsworth, R.E. & Smith, S.A.F. (2008). Fault weakening due to CO_2 degassing in the Northern Apennines: short- and long-term processes. In: Wibberley, C.A.J., Kurz, W., Imber, J., Holdsworth, R.E., Collettini, C. (Eds.). The Internal Structure of Fault Zones: Implications for Mechanical and Fluid-Flow Properties. Geological Society, London, pp. 175–194.

[87] Cornelis, J., Sohir, A. & Turki, K. (2011). Messungen der Radonkonzentration in der Bodenluft – Wie zuverlässig sind die Messwerte? Strahlenschutzpraxis 3/2011, 56 – 60.

[88] Cosma, C., Cucos, A., Dicu, A., Papp, B., Begy, R. & Sainz, C. (2013). Soil and building material as main sources of indoor radon in Baia-Sim radon prone area (Romania). Journal of Environmental Radioactivity, 116: 174–179. doi: 10.1016/j.jenvrad.2012.09.006.

[89] Crawley, D., Ciotoli G., Cinelli, G., Ellis, J., Bossew, P., McKinley, J., Lomnl, R. & Mitzer A. (2018). Tectonically enhanced geogenic radon (TEGR). EGU general assembly, Vienna 9 – 13 April 2018. http://meeting.copernicus.org/EGU2018-9348_presentation.pdf

[90] Cucos, D.A., Papp, B., Dicu, T., Moldovan, M., Burghele, D.B., Moraru, I.T., Tender, A. & Cosma, C. (2017). Residential, soil and water radon surveys in north-western part of Romania. Journal of Environmental Radioactivity, 166(Pt 2): 412–416. doi: 10.1016/j.jenvrad.2016.10.003.

[91] Daraktchieva, Z., Appleton, J.D., Rees, M.D., Allam, K.A.M., Myers, A.H., Hodgson, S.A., McCall, W.P., Wasson, G.R. & Peake, L.J. (2015). Radon in Northern Ireland: Indicative Atlas. Report PHE-CRCE-017. ISBN 978-0-85951-765-2. 22 pp.

[92] Daraktchieva, Z., Howarth, C.B. & Algar, R. (2011). Results of the 2011 HPA inter-comparison of Passive Radon Detectors, HPA-CRCE-033. ISBN 978-0-85951-715-7. 27 pp.

[93] Daraktchieva, Z., Miles, J.C.H. & McCall, N. (2014). Radon, the lognormal distribution and deviation from it. Journal of Radiological Protection, 34(1): 183–190. DOI: 10.1088/0952-4746/34/1/183.

[94] Daraktchieva, Z., Wankewicz, J.M.,

References

Howarth, C.B. & Bradley, E.J. (2017). Baseline monitoring around a potential shale gas development site in Yorkshire, England. Radiation Protection Dosimetry, 177(1–2): 140–143. doi: 10.1093/rpd/ncx134.

[96] Danakjiseva, Z., Howarth, C.B., Sowerby, T.D., Bradley, E.J. & Hull, N. (2016). Validation Scheme for Organisations Making Measurements of Radon in UK Buildings: 2018 Revision. Manuscript submitted for publication.

[96] Darby, S., Hill, D., Auvinen, A., Barros-Dios, J.M., Baysson, H., Bochicchio, F., Deo, H., Falk, R., Forastiere, F., Hakama, M., Heid, I., Kreienbrock, L., Kreuzer, M., Lagarde, F., Makeläinen, I., Muirhead, C., Oberaigner, W., Pershagen, G., Ruosteenoja, E., Schaffrath Rosario, A., Tirmarche, M., Tomásek, L., Whitley, E., Wichman, H.E. & Doll, R. (2005). Radon in homes and risk of lung cancer: collaborative analysis of individual data from 13 European case-control studies. BMJ 330: doi: 10.1136/bmj.38308.477650.63.

[97] Darby, S., Hill, D., Deo, H., Auvinen, A., Barros-Dios, J.M., Baysson, H., Falk, R., Farchi, S., Figueiras, A., Hakama, M., Heid, I., Hunter, N., Kreienbrock, L., Kreuzer, M., Lagarde, F., Makeläinen, I., Muirhead, C., Oberaigner, W., Pershagen, G., Ruosteenoja, E., Rosario, A., Tirmarche, M., Tomásek, L., Whitley, E., Wichman, H.E. & Doll, R. (2006). Residential radon and lung cancer – detailed results of a collaborative analysis of individual data on 7148 persons with lung cancer and 14 208 persons without lung cancer from 13 epidemiologic studies in Europe. Scandinavian Journal of Work Environmental Health, 32, Suppl. 1: 1–83.

[98] De Cort, M. (ed.) (2010). Advances in radon mapping. Journal of Environmental Radioactivity, 101(10): 785. doi: 10.1016/j.jenvrad.2010.04.012.

[99] De Cort, M., Gruber, V., Tollefsen, T., Bossew, P. & Janssens, A. (2011). Towards a European Atlas of Natural Radiation: Goal, status and future perspectives. Radioprotection, 46: 5737 – 5745. doi: 10.1051/radiopro/2011187 in.

[100] De Meyer, V., Cinelli, G., Cotoli, G., Tondeur, F., Dehandschutter, B., Lecour, C. & Gerardy, I. (2017). First steps in the multivariate analysis of Belgian radon data. In: Tollefsen, T., Cinelli, G. & De Cort, M. (eds.) 2nd International Workshop on the European Atlas of Natural Radiation: Book of Abstracts, pp. 56–57. EUR 28820 EN. Publications Office of the European Union, Luxembourg. ISBN 978-92-79-74131-9. doi: 10.2788/72011. JRC108701.

[101] De Martino, S., Sabbarese, C. & Monetti, G. (1998). Radon emanation and exhalation rates from soils measured with an electrostatic collector. Applied Radiation & Isotopes, 49(4): 407–413. https://doi.org/10.1016/S0969-8043(98)00300-4.

[102] De Simone, G., Cocchetti, C., Pompili, F., Galli, G., Tuccimei, P., Cuccaro, P. & Gaeng, H. (2017). Soil radon survey to assess NAPL contamination from an ancient spill: Do kerosene vapors affect radon partition? Journal of Environmental Radioactivity, 171, 138–147. doi: 10.1016/j.jenvrad.2017.02.014.

[103] Deb, A., Guo, M., & Barman, C. (2016). Anomalous soil radon fluctuations – signal of earthquakes in Nepal and eastern India regions. Journal of Earth System Science, 125(8): 1657–1665. https://doi.org/10.1007/s12040-016-0757-z.

[104] Dematteis, D., Rizzello, C., Feduzi, L., Mei, M.A. (2008). Monitoring the atmospheric stability by using radon concentration measurements: A study in a Central Italy site. Journal of Radioanalytical and Nuclear Chemistry, 277(3): 523–530. https://doi.org/10.1007/s10967-006-0458-1.

[105] Di Piazza, A., Conti, F.La, Viola, F., Eccel, E., Noto, L.V. & (2015). Comparative analysis of spatial interpolation methods in the Mediterranean area: Application to temperature in Sicily. Water (Switzerland) 7, 1866–1888. doi:10.3390/w7051866.

[106] Doi, M. & Kobayashi, S. (1994). Vertical distribution of outdoor radon and thoron in Japan using a new discriminative dosimeter. Health Physics, 67(4): 385–392. PMID: 8083051.

[107] Druffel, A.O., Guedalia, D. & Fontan, J. (1980). Use of natural radioactive tracers for the determination of vertical exchanges in the planetary boundary layer. In: Gesell, T.F. & Lowder, W.M. (eds.) Natural Radiation Environment III. Report No CONF-780422, Vol. 1: 226–241. Technical Information Centre, Department of Energy, Oak Ridge, Tennessee, USA.

[108] Dubois, G. (ed.) (2005). An overview of radon surveys in Europe. Office for Official Publication of the European Communities, Luxembourg. 172 pp. EUR 21932 EN. ISBN 92-79-01366-2. Available from: https://remtnjrc.ec.europa.eu/About/Publications.htm.

[109] Dubois, G., Bossew, P., Tollefsen, T. & De Cort, M. (2010). First steps towards a European atlas of natural radiation: status of the European indoor radon map. J. Environ. Radioact., 101 (10): 786–798. doi: 10.1016/j.jenvrad.2010.03.007.

[110] Dubeikova, H., Petersen, R., Burnett, W. & Lane-Smith, D. (2005). A multi-detector continuous monitor for assessment of 222Rn in the coastal ocean. Journal of Radioanalytical and Nuclear Chemistry, 263(2): 361–363. https://doi.org/10.1007/s10967-005-0595-y.

[111] Ellis, J., Crowley, Q., Scanlon, R., Hodgson, J. & Long, S. (2017a). Detection of radon priority areas by in-situ radon soil gas measurements: a case study in the Cooley Peninsula (County Louth, Ireland). Presented at the 2nd International Workshop on the European Atlas of Natural Radiation, 6–9 November 2017. Verbania, Italy. https://onedrive.live.com/?authkey=%21AJeJmr1BUYlQ2q4&cid=353A200A8F4E58C7&id=353A200A8F4E58C7%21261&parId=353A200A8F4E58C7%21247&o=OneUp (accessed 7 November 2018).

[112] Ellis, J., Crowley, Q., Scanlon, R., Hodgson, J., Lee, G.-S. & Cooper, M. (2017b). Mapping naturally occurring radioactive materials (U, Th and K) in Ireland: implications for radon mapping. Presented at the 2nd International Workshop on the European Atlas of Natural Radiation, 6–9 November 2017. Verbania, Italy. https://onedrive.live.com/?authkey=%21AJeJmr1BUYlQ2q4&cid=353A200A8F4E58C7&id=353A200A8F4E58C7%21261&parId=353A200A8F4E58C7%21247&o=OneUp (accessed 7 November 2018).

[113] Ellis, J., Crowley, Q., Scanlon, R., Hodgson, J. & Zgajga, L. (2017c). Logistic regression models for detecting radon prone areas in Ireland. Science of the Total Environment, 599–600: 1317–1329. https://doi.org/10.1016/j.scitotenv.2017.05.071.

[114] Ellis, J., Crowley, Q., Scanlon, R., Hodgson, J. & Zgajga, L. (2018). Estimation of residential radon exposure and definition of Radon Priority Areas based on expected lung cancer incidence. Environment International, 114: 69–78. https://doi.org/10.1016/j.envint.2018.02.015.

[115] Escobar, V.G., Tome, F.V. & Lozano, J.C. (1998). Procedures for the determination of 222Rn exhalation and effective 226Ra activity in soil samples. Applied Radiation Isotopes, 50(6): 1039–1047. PMID: 10355105.

[116] European Communities (1990). European radiation action. Indoor air quality and its impact on man: Radon in indoor air. Report EUR 16123 EN. Office for Official Publication of the European Communities, Luxembourg. 60 pp. ISBN 92-827-0115-0. http://www.buildingecology.com/publications/EIA_Report15.pdf (accessed 21 November 2018).

[117] European Commission and the European Soil Bureau Network, 2004. ESDB v2.0 (2004). The European Soil Database Distribution Version 2.0, CD-ROM, EUR 19945 EN.

[118] European Communities (1988). Council Directive of 21 December 1988 on the approximation of laws, regulations and administrative provisions of the Member States relating to construction products. Official Journal L 040, 11/02/1989: 12–26. https://eur-lex.europa.eu/legal-content/EN/TXT/PDF/?uri=CELEX:31989L0106&from=EN.

[119] European Communities (1990). Commission Recommendation 90/143/Euratom of 21 February 1990 on the protection of the public against indoor exposure to radon. Official Journal L 080, 27/03/1990: 26–28. https://eur-lex.europa.eu/legal-content/EN/TXT/PDF/?uri=CELEX:31990H0143&from=EN.

[120] European Communities (1999). Radiological protection principles concerning the natural radioactivity of building material. Radiation Protection 112. https://publications.europa.eu/en/publication-detail/-/publication/88bf3243-5259-43c5-b621-fbff862dedc0/language-en.

[121] European Union (2013). Council Directive 2013/59/Euratom of 5 December 2013 laying down basic safety standards for protection against the dangers arising from exposure to ionising radiation, and repealing Directives 89/618/Euratom, 90/641/Euratom, 96/29/Euratom, 97/43/Euratom and 2003/122/Euratom. Official Journal of the European Union OJ L13: 17.1.2014, pp. 1–73. https://eur-lex.europa.eu/legal-content/EN/TXT/?uri=OJ:L:2014:013:TOC.

[122] European Union (2016). Consolidated version of the Treaty establishing the European Atomic Energy Community. Official Journal of the European Union, C 203, 07/06/2016, p. 1 – 112. https://eur-lex.europa.eu/legal-content/EN/TXT/?uri=OJ:C:2016:203:TOC.

[123] Faulkner, D.R., Jackson, C.A.L., Lunn, R.J., Schlische, R.W., Shipton, Z.K., Wibberley, C.A.J. & Withjack, M.O. (2010). A review of recent developments concerning the structure, mechanics and fluid flow properties of fault zones. Journal of Structural Geology, 32(11): 1557–1575. https://doi.org/10.1016/j.jsg.2010.06.009.

[124] Favara, R., Grassa, F., Inguaggiato, S. & Valenza, M. (2001). Hydrogeochemistry and stable isotopes of thermal springs: earthquake-related chemical changes along Belice Fault (Western Sicily). Applied Geochemistry, 16(1): 1–17. https://doi.org/10.1016/S0883-2927(00)00015-9.

[125] Fennell, S.G., Madin, I.M., Madden, J.S., McGarry, A.T., Duffy, J.T., O'Colmán, M., Colgan, P.A. & Folland, D. (2002). Radon in Dwellings: The Irish National Radon Survey. Report RPII-02/1. Radiological Protection Institute of Ireland. 47 pp. http://www.epa.ie/pubs/reports/radiation/radon/nwell-english/irishnationalradonsurvey.html (accessed June 2018).

[126] Ferreira, A., Dashchenko, Z., Blaumis, D., Kirkwood, C., Lister, T.R., Cave, M., Wragg, J. & Lee, K. (2016). Indoor radon measurements in south west England explained by topsoil and stream sediment geochemistry, airborne gamma-ray spectrometry and geology. Journal of Environmental Radioactivity, 161: 152–171. doi: 10.1016/j.jenvrad.2016.05.007.

[127] Ferry, C., Richon, P., Beneito, A. & Robé, M.C. (2002). Evaluation of the effect of a cover layer on radon exhalation from uranium mill tailings: transient radon flux analysis. Journal of Environmental Radioactivity, 63(1): 49–64. PMID: 12230135.

[128] Finne, I.E., Klaustad, T., Larsson, M., Olsen, B., Prendergast, J. & Rudjord, A.L. (2018). Significant reduction in indoor radon in newly built houses. Journal of Environmental Radioactivity, 196: 259–263. https://doi.org/10.1016/j.jenvrad.2018.01.013.

[129] Fisher, E.C., Field, R.W., Smith, B.J., Lynch, C.F., Steck, D.J. & Neuberger, J.S. (1998). Spatial variation of residential radon concentrations. Health Physics, 75: 500–513. https://doi.org/10.1097/00004032-199811000-00007.

[130] Flleacher, R., Hart, H.R. & Magro-Campero, A. (1980). Radon emanation over an ore body: Search for long distance transport of radon. Nuclear Instruments and Methods, 173: 169–181. https://doi.org/10.1016/0029-554X(80)90584-4.

[131] Fojtíková, I., Žemlová, I. & Tomásek, J. (2017). Radon in workplaces – Czech approach to EU BSS implementation. Radiation Protection Dosimetry, 177, (1 – 2), 104 – 111. https://doi.org/10.1093/rpd/ncx180.

[132] Font, L.I., Baeza, C., Morera, V. & Bach, J. (2008). Soil radon levels across the Amer fault. Radiation Measurements, 43(1): 1519–1523. https://doi.org/10.1016/j.radmeas.2008.04.072.

[133] Font, L.I. (2009). On radon surveys: design and interpretation. Radiation measurements, 44(9 – 10): 964–968. http://dx.doi.org/10.1016/j.radmeas.2009.10.044.

[134] Fossen, H., Schultz, R.A., Rundhovde, E., Rotevatn, A. & Buckley, S.J. (2010). Fault linkage and graben stepovers in the Zuidwestelijk Delfland and the North Sea Viking Graben, with implications for hydrocarbon migration and accumulation. AAPG Bulletin, 94 (5): 597–613. doi: 10.1306/10130809088.

[135] Friedmann, H. (2006). Final results of the Austrian Radon Project. Health Physics, 89 (4): 339–348. doi: 10.1097/01.HP.0000197228.18113.27.

[136] Friedmann, H. & Sroller, J. (2010). An approach to improve the Austrian Radon Potential Map by Bayesian statistics. Journal of Environmental Radioactivity, 101 (10): 804–808. doi: 10.1016/j.jenvrad.2009.11.009.

[137] Friedmann, H., Baumgartner, A., Bernhardt, M., Gruber, J., Gruber, V., Kahrer, F., Kienzler, H., Maringer, F.J., Ringer, W., Seidel, C. & Wurm, G. (2017a). Indoor radon, geogenic radon surrogates and geology – investigations on their correlation. Journal of Environmental Radioactivity, 166 (Part 2): 382–389. https://doi.org/10.1016/j.jenvrad.2016.04.028.

[138] Fu, C.C., Yang, T.F., Du, J., Walia, V. & Chen, Y.G. (2008). Variations of helium and radon concentrations in soil gases from an active fault zone in Southern Taiwan. Radiat. Meas. 43 (11): 5348–5352. https://doi.org/10.1016/j.radmeas.2008.03.035.

[139] Fu, C.C., Yang, T.F., Tsai, M.C., Lee, L.C., Liu, T.K., Walia, V., Chen, C.H., Cheng, W.Y., Kumar, A. & Lai, T.M. (2017). Exploring the relationship between soil degassing and seismic activity by continuous radon monitoring in the Longitudinal Valley of eastern Taiwan. Chem. Geol., 469: 163–175. https://doi.org/10.1016/j.chemgeo.2016.12.042.

[140] Fukui, M. (1987). Soil water effects on concentration profiles and variations of 222Rn in a vadose zone. Health Physics, 53 (2): 181–186.

[141] Garavaglia, M., Dal Moro, G. & Zadro, M. (2001). Radon and tilt measurement in a seismic area: temporalow effects. Phys. Chem. Earth (A), 26: 233–237.

[142] García-Talavera, M., García-Pérez, A., Rey, C. & Ramos, L. (2013). Mapping radon-prone areas using γ-radiation dose rate and geological information. Journal of Radiological Protection, 33 (3): 605–620. doi: 10.1088/0952-4746/33/3/605.

[143] Gesell, T. (1983). Background atmospheric 222Rn concentrations outdoors and indoors: A review. Health Physics, 45(2): 289–302. PMID: 6885450.

[144] Ghosh, D., Deb, A. & Sengupta, R. (2009). Anomalous radon emission as precursor of earthquake. Journal of Applied Geophysics, 69(2): 67–81. https://doi.org/10.1016/j.jappgeo.2009.06.001.

[145] Giammanco, S., Sims, K.W.W. & Neri, M. (2007). Measurements of 222Rn and 220Rn and CO_2 emissions in soil and fumarole gases on Mt. Etna volcano (Italy): implications for gas transport and shallow ground fracture. Geochem. Geophys. Geosyst., 8, Q10001. doi: 10.1029/2007GC001644.

[146] Gogolak, C.V. & Beck, H.L. (1980). Diurnal variations of radon daughter concentrations in the lower atmosphere. In: Gesell, T.F. & Lowder, W.M. (eds.) Natural Radiation Environment III. Report No. CONF-780422, Vol. 1: 259–280. Technical Information Service, Department of Energy, Oak Ridge, Tennessee, USA.

[147] Gun, J., Dvorkin, D., Cheslack, M. & Shaviv, A. (1991). Fluence rate of radon from soil. Effect of sorption barriers, moisture content, and temperature. Health Physics, 61 (3): 355–365.

[148] Gray, A., Read, S., McGale, P. & Darby, S. (2009). Lung cancer deaths from indoor radon and the cost effectiveness and potential of policies to reduce them. BMJ (Clinical research ed.), 338: a3110. https://doi.org/10.1136/bmj.a3110.

[149] Greeman, D. & Rose, A. (1995). Factors controlling the emanation of radon and thoron in soils of the eastern U.S.A. Chemical Geology, 129: 1–14.

[150] Gregorič, A., Zmazek, B. & Vaupotič, J. (2009). Radon concentration in thermal water as an indicator of seismic activity. Collegium Antropologicum, 32(S2): 95–98. PMID: 19138014.

[151] Griffiths, A.D., Zahorowski, W., Element, A. & Werczynski, S. (2010). A map of radon flux at the Australian land surface. Atmospheric Chemistry and Physics, 10: 8969–8982.

[152] Grossi, C., Vargas, A., Camacho, A., López-Coto, I., Bolívar, P., Yu Xia & Correa, F. (2011). Inter-comparison of different direct and indirect methods to determine radon flux from soil. Radiation Measurements, 46 (1): 112–118. https://doi.org/10.1016/j.radmeas.2010.07.021.

[153] Gruber, V., Bossew, P., De Cort, M. & Tollefsen, T. (2013a). The European map of the geogenic radon potential. Journal of Radiological Protection, 33(2): 51–80. doi: 10.1088/0952-4746/33/1/51.

[154] Gruber, V., Tollefsen, T. & De Cort, M. (2013b). The European Indoor Radon Map – questionnaire results and evaluation for quality assurance. JRC Scientific and Policy Reports. JRC87017.

[155] Guida, D., Guida, M., Cuomo, A., Scaglione, D. & Sarno, V. (2010). Radon-prone area assessment by means of multi-scale hierarchical approach. Case study of the Campania region, Southern Italy. In: Barnet, I., Neznal, M. & Pacherova, P. (Eds.): Proc. 10th international workshop on the geological aspects of radon risk mapping. Czech geological survey, Radon v.o.s., Prague 2010. ISBN 978-80-7075-754-3, pp. 122 – 139. http://www.radon-workshop.2010/.

[156] Gunby, J.A., Darby, S.C., Miles, J.C., Green, B.M. & Cox, D.R. (1993). Factors affecting indoor radon concentrations in the United Kingdom. Health Physics, 64 (1): 2–12. PMID: 8416211.

[157] Gundersen, L.C.S., Randall Schumann, R., Otton, J.K., Dubiel, R.F., Owen, D.E., Dickinson, K.A. 1992. Geology of radon in the United States. In: Gates, A.E. & Gundersen, L.C.S. (Eds.): Geologic Controls on Radon. Geological Society of America. ISBN 0813722719. https://doi.org/10.1130/SPE271-p1.

[158] Gundersen, L.C.S. & Schumann, R.R. (1996). Mapping the radon potential of the United States: examples from the Appalachians. Environ. Int., 22 (Suppl. 1): 829–837.

[159] Gunning, G.A., Pollard, D. & Finch, E.E. (2014). An outdoor radon survey and remapping the uncertainties in low level measurements using CR-39 detectors. Journal of Radiological Protection, 34(2): 457–467. doi: 10.1088/0952-4746/34/2/457.

[160] Hanley, O., Gutiérrez-Villanueva, J.L., Curran, D. & Pollard, D. (2008). Assessment of the uncertainties in the Radological Protection Institute of Ireland (RPII) radon measurements service. Journal of Environmental Radioactivity 99 (10): 1578–1582. https://doi.org/10.1016/j.jenvrad.2007.12.018.

[161] Hansen, M.F., Moss, G.R., Fews, A.P. & Henshaw, D.L. (2014). Improving the uncertainty on short-term radon measurements using PADC detector. Radiat. Prot. Dosim., 160 (1–3): 181–185. doi: 10.1093/rpd/nct078.

[162] Hardcastle, G.D. & Miles, J.C.H. (1996). Ageing and fading of alpha particle tracks in CR-39 exposed to air. Radiation Protection Dosimetry, 67 (4): 295–298. https://doi.org/10.1093/oxfordjournals.rpd.a031832.

[163] Harley, J.H. (1966). Radon is not to Cross, F.T. (ed.): Indoor radon and lung cancer: reality or myth? 29th Hanford symposium on health and the environment. Battelle Press, Columbus, Ohio, USA.

[164] Hashemi, S., Negarestani, A., Nasrnejad, M. & Nasab, S.M.M. (2013). An analytical algorithm for designing radon monitoring network to predict the location and magnitude of earthquakes. J. Radioanal. Nucl. Chem., 295(3): 2249–2262. https://doi.org/10.1007/s10967-012-2510-0.

[165] Hassan, N.M., Hosoda, M., Ishikawa, T., Sorimachi, A., Sahoo, S.K., Tokonami, S. & Fukushi, M. (2009). Radon Migration Process and its Influence Factors: Review. Japan Journal of Health Physics, 44 (3): 219–231.

[166] Hatuda, Z. (1955). Radon content and its change in soil air near the ground surface. Mem. Coll. Sci., Univ. Kyoto.

[167] Heinicke, J., Italiano, F., Koch, U., Martinelli, G. & Tassi, L. (2010). Anomalous fluid emission of a deep borehole in a seismically active area of Northern Apennines (Italy). Applied Geochemistry, 25 (4): 555–571. doi: 10.1016/j.apgeochem.2010.01.012.

[168] Hessbom, A. (1985). Radon in soil gas: A study of methods and instruments for determining radon concentrations in the ground. Uppsala, Sweden, Sveriges Geologiska Undersökning, ser. C, no. 803, pp. 1–68.

[169] Hirao, S., Yamazawa, H. & Moriizumi, J. (2010). Estimation of the global 222Rn flux density from the Earth's surface. Japan Journal of Health Physics, 45(2): 161–171.

[170] Hoffmann, M. Akçay, Ş.Y., Feyzullayev, A.A., Baghirli, R.I., Veliyeva, F.F., Fazylov, L., Valcangiacomo, C., Tollefsen, T. & Cinelli, G. (2017). First Map of Residential Indoor Radon Measurements in Azerbaijan. Radiation Protection Dosimetry, 175 (2): 186–195. doi: 10.1093/rpd/ncw284.

[171] Holub, R.F. & Brady, B.T. (1981). The effect of stress on radon emanation from rock. Journal of Geophysical Research Atmospheres, 86(B5): 1776–1784. doi: 10.1029/JB086iB05p01776.

[172] Hopke, P.K., Jensen, B., Li, C.S., Montassier, N., Wasiolek, P., Cavallo, A.J., Gaimbo, K., Socolow, R.H. & James, A.C. (1995). Assessment of the exposure to and dose from radon decay products in normally occupied homes. Environ. Sci. Technol., 29: 1359–1364. https://doi.org/10.1021/es00005a031.

[173] Hopper, R.D., Steinhaussler, F. & Renne-Bertsch, M. (1990). IAEA/EPA international climatic test program for integrating radon detectors. Health Physics, 77(3): 303–308. PMID: 2045650.

[174] Hosoda, M., Omori, M., Sugino, M., Furukawa, M. & Fukushi, M. (2007a). Effect of soil moisture content on radon and thoron exhalation. Journal of Nuclear Science and Technology, 44: 664–672.

[175] Hosoda, M., Tamamoto, Y., Hanada, K., Nori, T., Fukushi, M. & Shimo, M. (2007b). Experimental interpretation of physical and chemical characteristics of soil materials up on the radon and thoron exhalation rate. Japan Journal of Health Physics, 42: 88–97.

[176] Hosoda, M., Kavasi, N., Sorimachi, A., Hassan, N.M., Sahoo, S.K., Ishikawa, T., Tokonami, S. & Uchida, S. (2008). Influence of soil particle size on radon emanation and exhalation. Proc. of the 7th international conference on nuclear and radiochemistry.

[177] IAEA (2013). National and Regional Surveys of Radon Concentration in Dwellings: Review of Methodology and Measurement Techniques. IAEA Anal. Qual. Nucl. Appl., IAEA/AQ/33. International Atomic Energy Agency, Vienna, Austria.

[178] Ibrahim, Z.F., Howarth, C.B. & Miles, J.C.H. (2008). Sources of error in etched-track radon measurements and a review of passive detectors using results from a series of radon intercomparisons. Radiation Measurements, 44 (9–10): 750–754. https://doi.org/10.1016/j.radmeas.2009.10.009.

[179] ICRP (2017). Occupational Intakes of Radionuclides: Part 3. ICRP Publication 137. Ann. ICRP 46(3/4). https://doi.org/10.1177/0146645317734903.

[180] ICRU (International Commission on Radiation Units and Measurements) (2015). Report 88. Measurement and Reporting of Radon Exposures. Journal of the ICRU, 12 (2): 1–191. doi: 10.1093/jicru/ndv019.

[181] Ielsch, G. & Hemdey, D. (2001). Mise au point d'une méthodologie cartographique d'élaboration d'un outil (carte) prédictif en vue d'identifier les zones potentiellement exposées à de fortes concentrations de radon (2 Volumes). Programme Environnement et Santé 1997. Rapport IPSN-INRCM Ref. IPSN/DPRE/SERGD RT 01-05.

[182] Ielsch, G., Ferry, C., Tymen, G. & Robé, M.C. (2002). Study of a predictive methodology for quantification and mapping of the radon 222 exhalation rate. Journal of Environmental Radioactivity, 63(1): 15–33. https://doi.org/10.1016/S0265-931X(01)00133-3.

[183] Ielsch, G. (2005). Méthodologie de cartographie prédictive du potentiel d'exhalation du radon à la surface des sols: bilan des projets de recherche et validation complémentaire. Rapport IRSN/DEI-SARG 05-02.

[184] Ielsch, G., Cushing, M.E., Combes, Ph. & Cuney, M. (2015). Mapping of the geogenic radon potential in France to improve radon risk management: methodology and first application to region Bourgogne. Journal of Environmental Radioactivity, 103(10): 813–820. doi: 10.1016/j.jenvrad.2013.04.008.

[185] Ielsch G., Cuney, M., Buscail, F., Rossi, F., Leon, A. & Cushing, M.E. (2017). Estimation and mapping of uranium content of geological units in France. Journal of Environmental Radioactivity, 166 (Part 2): 210–219. https://doi.org/10.1016/j.jenvrad.2016.05.022.

[186] Igarashi, G., Saeki, S., Takahara, N. & Tunakawa, K., Tanaka, S., Sasaki, Y., Takahashi, M. & Sano, Y. (1995). Ground-water radon anomaly before the Kobe earthquake in Japan. Science, 269(5220): 60–61. doi: 10.1126/science.269.5220.60.

[187] International Commission on Radiological Protection (ICRP) (1993). Protection against radon-222 at home and at work. ICRP Publication 65. Ann. ICRP 23 (2).

[188] International Commission on Radiological Protection (ICRP) (2007). The 2007 Recommendations of the International Commission on Radiological Protection. ICRP Publication 103. Ann. ICRP 37(2–4), 2007. Elsevier. ISBN 978-0702041042.

[189] International Commission on Radiological Protection (ICRP) (2010). Lung Cancer Risk from Radon and Progeny and Statement on Radon. ICRP Publication 115. Ann. ICRP 40(1). Elsevier, 2010. ISBN 978-0702049774.

[190] International Commission on Radiological Protection (ICRP) (2017). Occupational Intakes of Radionuclides: Part 3. ICRP Publication 137. Ann. ICRP 46(3-4).

[191] Ioannides, K., Papachristodoulou, C., Stamoulis, K., Karamanis, D., Pavlides, S., Chalkiopoulos, A. & Karakala, E. (2003). Soil gas radon: a tool for exploring active fault zones. Applied Radiation and Isotopes, 59(2–3): 205–213. https://doi.org/10.1016/S0969-8043(03)00164-7.

[192] Ishimori, Y., Lange, K., Martin, P., Mayya, Y.S., & Phillips, M. (2013). IAEA Measurement and Calculation of Radon Releases from NORM Residues. International atomic energy agency. Technical Reports Series Number: 474.

[193] Iskandar, D., Yamazawa, H. & Iida, T. (2004). Quantification of the dependency of radon emanation power on soil temperature. Appl. Radiat. Isot., 60: 971–973.

[194] ISO 11665-1:2012 (2012). Measurement of radioactivity in the environment – Air: radon-222 — Part 1: Origins of radon and its short-lived decay products and associated measurement methods. pp. 30.

[195] ISO 11665-7:2012 (2012). Measurement of radioactivity in the environment – Air: radon-222 — Part 7: Accumulation method for estimating surface exhalation rate.

[196] ISO 11665-9:2016 (2016). Measurement of radioactivity in the environment – Air: radon-222 — Part 9: Test methods for exhalation rate of building materials. pp. 38.

[197] ISO 11665-11:2016 (2016). Measurement of radioactivity in the environment – Air: radon-222 — Part 11: Test method for soil gas with sampling at depth. pp. 25.

[198] Jaacks, J.A. (1984). Meteorological influence upon mercury, radon and helium soil gas emissions. Ph.D. thesis, Colorado School of Mines, Golden, Colorado, US. 170 pp.

[199] Jaksics, D. & Gergely, A. (2013). The investigation of tobacco smoke influence on the changes of indoor radon and its short-lived decay products volumetric activities. Journal of environmental engineering and landscape management, volume 21(1): 55–66. doi:10.3846/16486897.2012.745415.

[200] Jensen, C.L., Sundal, A.V. & Åneslad, K. (2006). Radon concentrations in outdoor air. Presentation of results from radon measurements in outdoor air in six selected Norwegian areas. Norwegian Radiation Protection Authority. Report number: 2006:20 (in Norwegian).

[201] Jha, S., Khan, A.H. & Mishra, U.C. (2001). A study of the technologically modified sources of 222Rn and its environmental impact in an Indian U mineralised belt. Journal of Environmental Radioactivity, 53(2): 183–197. https://doi.org/10.1016/S0265-931x(00)00124-7.

[202] Jiránek, M., Barošová, M. & Thomas, J. (2014). Diurnal and seasonal variability of outdoor radon concentration in the area of the Nrp Prague. Radiation Protection Dosimetry, 160(1–3): 57–61. doi: 10.1093/rpd/nsu091.

[203] Jiránek, M. (2000). Diffusive and convective transport of radon through cracks in the building substructure. In: Barnet, I. & Neznal, M. (eds.): Radon investigations in the Czech Republic VIII and the Fifth International Workshop on the Geological Aspects of Radon Risk Mapping, pp. 65–70. Czech Geological Survey and Radon Corp., Prague. Czech Republic. https://inis.iaea.org/collection/NCLCollectionStore/_Public/32/002/32002563.pdf (accessed 7 November 2018).

[204] Jeong, S. & Chon, H.T. (2013). Indoor radon measurements of the multi-storey buildings in Seoul, Korea. Geosystem Engineering, 2013 Vol. 16, No. 4, 289–295. DOI: 10.1080/12269328.2013.861642.

[205] Jobbágy, V., Altzitzoglou, T., Malo, P., Tanner, V. & Hult, M. (2017). A brief overview on radon measurements in drinking water. Journal of Environmental Radioactivity, 173: 18 – 24. https://doi.org/10.1016/j.jenvrad.2016.08.019.

[206] Johansen, T.E.S., Fossen, H. & Kluge, R. (2005). The impact of syn-faulting porosity reduction on damage zone architecture in porous sandstone: an outcrop example from the Moab Fault, Utah. Journal of Structural Geology, 27(8): 1469–1485. https://doi.org/10.1016/j.jsg.2005.01.014.

[207] Johansson, S., Fiandaca, G. & Dahlin, T. (2015). Influence of non-aqueous phase liquid configuration on induced polarization parameters: conceptual models applied to a time-domain field case study. Journal of Applied Geophysics, 123: 295–309. https://doi.org/10.1016/j.jappgeo.2015.08.010.

[208] Johnn, H.U. & Surbeck, H. (2001). Soil gas measurements below foundation depth improve indoor radon prediction. The Science of the Total Environment, 272(1–3): 337–341. https://doi.org/10.1016/S0048-9697(01)00712-4.

[209] Karstens, U., Schwingshackl, C., Schmithüsen, D. & Levin, I. (2015). A process based 222radon flux map for Europe and its comparison to long-term observations. Atmospheric Chemistry and Physics, 15: 12845–12865. https://doi.org/10.5194/acp-15-12845-2015.

[210] Kemski, J., Klingel, R. & Siehl, A. (1996). Classification and mapping of radon-affected areas in Germany. Environment International, 22 (5): 789–798. https://doi.org/10.1016/S0160-4120(96)00185-7.

[211] Kemski, J., Lehmann, R., Siehl, A., Siegmann, R. & Valdivia-Manchego, M. (2000). Radon Mapping in Germany – State of Investigations and Future Work. In: Barnet, I. & Neznal, M. (eds.): Radon investigations in the Czech Republic VIII and the Fifth International Workshop on the Geological Aspects of Radon Risk Mapping, pp. 86–91. Czech Geological Survey and Radon Corp., Prague. Czech Republic. https://inis.iaea.org/collection/NCLCollectionStore/_Public/32/002/32002563.pdf.

[212] Kemski, J., Siehl, A., Siegmann, R. & Valdivia-Manchego, M. (2001). Mapping the geogenic radon potential in Germany. Science of the Total Environment, 272(1–3): 217–230. https://doi.org/10.1016/S0048-9697(01)00696-9.

[213] Kemski, J., Klingel, R., Siehl, A. & Siegmann, R. (2005). Radon transfer from ground to houses and prediction of indoor radon in Germany based on geological information. Radioactivity in the Environment, 7: 821–832. https://doi.org/10.1016/

51669-4060(04)07103-7

[214] Kemski, J., Klingel, R., Siehl, A., Hennig, M. & Mahlke, M. (2012). Erarbeitung fachlicher Grundlagen zum Beurteilung der Vergleichbarkeit unterschiedlicher Messmethoden zur Bestimmung der Radonkonzentrationen – BfS. Forschungsvorhaben 3609510003. 2 volumes. Available in https://doro.bfs.de/ipa/katalog/um.nsf/de.0221-20120325784 and https://doro.bfs.de/ipa/suchanfrage/um.nsf/de.0221-20120325785 (in German only)

[215] Kibble, A., Cabanes, T., Darakchieva, Z., Gooding, T., Smithard, J., Krawczyk, G., McColl, N.P., Singh, M., Mitchen, J., Lamb, P., Vandvalais, S. & Kamaryan, R. (2014). Review of the Potential Public Health Impacts of Exposures to Chemical and Radioactive Pollutants as a Result of the Shale Gas Extraction Process. Report PHE-CRCE-005. Public Health England, Chilton, UK.

[216] Kikaj, D., Jeran, Z., Bahtijari, M. & Dragna, P. (2016). Radon in soil gas in Kosovo. Journal of Environmental Radioactivity, 164: 245 – 252. https://doi.org/10.1016/j.jenvrad.2016.07.017

[217] King, C.Y. (1986). Gas geochemistry applied to earthquake prediction: An overview. Journal of Geophysical Research – Solid Earth, 91 (B12): 12269–1228. https://doi.org/10.1029/JB091iB12p12269

[218] King, C.Y., King, B.S., Evans, W.C. & Zhang, W. (1996). Spatial radon anomalies on active faults in California. Applied Geochemistry, 11(4): 497–510. doi: 10.1016/0883-2927(96)00003-0

[220] Koarashi, J., Amano, H., Andoh, M. & Iida, T. (2008). Estimation of Rn222 flux from ground surface based on the variation analysis of Rn222 concentration in a closed chamber. Radiation Protection Dosimetry, 87 (2): 123–131.

[221] Kobe, K., Inishinaga, T. & Asaue, H. (2006). Radon concentrations in soil gas, considering radioactive equilibrium conditions with application to estimating fault zone geometry. Environ. Geol., 56(6): 1533–1540. https://doi.org/10.1007/s00254-008-1252-x.

[222] Kojima, H. & Fujiwara, H. (2005). Simulation of radon exhalation at Kanto Loam with very low permeability. J. Atomic. Elect., 25(1): 1–9

[223] Kovach, E.M. (1945). Meteorological influences upon the radon content of soil gas. Eos Transactions, American Geophysical Union, 26(2): 241–248. https://doi.org/10.1029/TR026i002p00241

[224] Kovács, T., Szeiler, G., Fábián, F., Kandó, R., Gregorič, A. & Vaupotič, J. (2013). Systematic survey of natural radioactivity of soil in Slovenia. Journal of Environmental Radioactivity, 122: 70–78. https://doi.org/10.1016/j.jenvrad.2013.02.007.

[225] Kovler, K., Perevalov, A., Steiner, V. & Metzger, L.A. (2005). Radon exhalation of cementitious materials made with coal fly ash: Part 1 – scientific background and testing of the cement and fly ash emanation. Journal of Environmental Radioactivity, 82(3): 321–324. doi: 10.1016/j.jenvrad.2005.02.004.

[226] Kovler, K. (2009a). Measurements of radon exhalation rate for monitoring cement hydration. Materials and Structures, 40(4): 419–430. https://doi.org/10.1617/s11527-006-9149-1.

[227] Kovler, K. (2009b). Radon exhalation of hardening concrete: monitoring cement hydration and prediction of radon concentration in construction site. Journal of Environmental Radioactivity, 80(3): 354–366. doi: 10.1016/j.jenvrad.2005.10.005.

[228] Kovler, K. (2011). Legislative aspects of radiation hazards from both gamma emitters and radon exhalation of concrete containing coal fly ash. Construction and Building Materials, 25(8): 3404–3409. https://doi.org/10.1016/j.conbuildmat.2011.03.031.

[229] Kozak, K., Grządziel, D., Polednik, B., Mazur, J., Dudzińska, M.R., & Mroczek, M. (2014). Air conditioning impact on the dynamics of radon and its daughters concentration. Radiation Protection Dosimetry, Vol. 162, No. 4, pp. 663–673. DOI: 10.1093/rpd/nct347.

[230] Kozłowska, B., Mazur, J., Kozak, K., Walencik-Łata, A. & Bać, B. (2016). Investigation of the influence of chamber construction parameters on radon exhalation rate. Nukleonika, 61(3): 269 – 273. doi: https://doi.org/10.1515/nuka-2016-0045.

[231] Kraner, H.W., Schroeder, G.L., & Evans, R.D. (1964). Measurements of the effects of atmospheric variables on radon 222 flux and soil gas concentrations. In: Adams, J.A.S. and Lowder, W.M. (eds.) The natural radiation environment. Chicago, Ill., University of Chicago Press, pp. 191–215.

[232] Krewski, D., Lubin, J.H., Zielinski, J.M., Alavanja, M., Catalan, V.S., Field, R.W., Klotz, J.B., Letourneau, E.G., Lynch, C.F., Lyon, J.L., Sandler, D.P., Schoenberg, J.B., Steck, D.J., Stolwijk, J.A., Weinberg, C. & Wilcox, H.B. (2005). Residential radon and risk of lung cancer: a combined analysis of 7 North American case-control studies. Epidemiology, 16: 137–145.

[233] Krewski, D., Lubin, J.H., Zielinski, J.M., Alavanja, M., Catalan, V.S., Field, R.W., Klotz, J.B., Letourneau, E.G., Lynch, C.F., Lyon, J.L., Sandler, D.P., Schoenberg, J.B., Steck, D.J., Stolwijk, J.A., Weinberg, C. & Wilcox, H.B. (2006). A combined analysis of North American case-control studies of residential radon and lung cancer. J. Toxicol. Environ. Health A, 69 (7): 533–597.

[234] Kropat, G., Bochud, F., Jaboyedoff, M., Laedermann, J.-P., Murith, C., Palacios Gruson, M. & Baechler, S. (2013). Predictive analysis and mapping of indoor radon concentrations in a complex environment using kernel estimation: An application to Switzerland. Science of the Total Environment, 505: 137–148. doi: 10.1016/j.scitotenv.2014.09.064

[235] Kropat, G., Bochud, F., Murith, Ch., Palacios Gruson, M. & Baechler, S. (2017). Modeling of geogenic radon in Switzerland based on ordered logistic regression. Journal of Environmental Radioactivity, 166 (Part 2): 289–295. doi: 10.1016/j.jenvrad.2016.04.013.

[237] McColl, N., Auvinen, A., Kesminiene, A., Espina, C., Erdmann, F., de Vries, E., Grosche, B., Harrison, J. & Schüz, J. (2015). European Code against Cancer, 4th Edition: ionising and non-ionising radiation and cancer. Cancer Epidemiology, 39 (Suppl. 1): S93–S100. doi: 10.1016/j.canep.2015.03.016.

[236] Kummel, M., Dubbe, E., Müller & Gehrcke, K. (2014). Outdoor ^{222}Rn-concentrations in Germany – part 1 – natural background. Journal of Environmental Radioactivity, 132: 123–130. doi: 10.1016/j.jenvrad.2014.01.012.

[237] Kunovska, B., Ivanova, K., Stojanovska, Z. & Badzakov, V. (2014). Measurements of outdoor radon concentration over 24 hour periods in different settlements in Bulgaria. In: Proceedings of the Second International Conference on Radiation and Dosimetry in Various Fields of Research, Niš, Serbia, 27–30 May 2014, pp. 5–8. ISSN 978-86-6125-101-6.

[238] Kuo, T., Su, C., Chang, C., Lin, C., Chang, W., Liang, H., Lewis, C. & Chang, C. (2010). Application of recurrent radon precursors for forecasting large earthquakes (Mw > 6.0) near Antung, Taiwan. Radiation Measurements, 45(8): 1049–1054. https://doi.org/10.1016/j.radmeas.2010.08.009.

[239] Kurtiss, P. & Kalio, A. (2014). Radon oleskeleissa. Ympäristön säteilyvaikutusten tiiviystaajeinna STUK, Finland. ISBN 978-952-309-230-3 (in Finnish). Available from http://urn.fi/URN:978-952-309-230-3 (accessed 20 November 2018).

[240] Lawrence, C.E., Akber, R.A., Bollhöfer, A. & Martin, P. (2009). Radon 222 exhalation from open ground on and around a uranium mine in the wet-dry tropics. Journal of Environmental Radioactivity, 100(1): 1–8. doi: 10.1016/j.jenvrad.2008.09.003.

[241] Lee, S.C., Kim, C.K., Lee, C.K. & Kang, H.D. (2001). Natural radionuclides contents and radon exhalation rates in building materials used in South Korea. Radiation Protection Dosimetry, 94(3): 269–274. PMID: 11487810.

[242] Li, J. & Heap, A.D. (2008). A Review of Spatial Interpolation Methods for Environmental Scientists. Geosci. Aust. Rec. 2008/23. SpCat# RR. 137. doi:http://www.ga.gov.au/image_cache/GA12526.pdf

[243] Lindmark, A. & Rosen, B. (1985). Radon in soil gas – exhalation tests and in situ measurements. The Science of the Total Environment, 45: 397–404. PMID: 4081740.

[244] Livingston, G.P., Hutchinson, G.L. & Spartalian, K. (2005). Diffusion theory improves chamber-based measurements of trace gas emissions. Geophysical Research Letters, 32(24): 817. https://doi.org/10.1029/2005GL024744.

[245] Long, S., Fenton, D., Damon, M. & Morgan, A. (2013). The effectiveness of radon preventive and remedial measures in Irish homes. Journal of Radiological Protection, 33 (1): 141–149. doi: 10.1088/0952-4746/33/1/141.

[246] López-Coto, I., Mas, J.L. & Bolívar, J.P. (2013). A 40-year retrospective European radon flux inventory including climatological variability. Atmospheric Environment, 73: 22–33. doi:10.1016/j.atmosenv.2013.02.043.

[247] Lorenzo-Gonzalez, M., Ruano-Ravina, A., Pino, J., Pineiro, M. & Barros-Dios, J.M. (2017). Residential radon in Galicia: a cross-sectional study in a radon-prone area. J. Radiol. Prot. 2017 Sep; 37(3): 728–741.

[248] Lubin, J.H., Wang, Z.Y., Boice Jr, J.D., Xu, Z.Y., Blot, W.J., De Wang, L. & Kleinerman, R.A. (2004). Risk of lung cancer and residential radon in China: pooled results of two studies. International Journal of Cancer, 109: 132–137.

[249] Lyle, S. (2007). The geology of radon in Kansas. Kansas Geological Survey, Public Information Circular (PIC) 25.

[250] Malczewski, D. & Żaba, J. (2007). ^{222}Rn and ^{220}Rn concentrations in soil gas of Karkonosze–Izera Block (Sudetes, Poland). Journal of Environmental Radioactivity, 92(3): 144–164. https://doi.org/10.1016/j.jenvrad.2006.11.001.

[251] Manohar, S.N., Meijer, H.A.J. & Herber, M.A. (2013). Radon flux maps for the Netherlands and Europe using terrestrial gamma radiation derived from soil radionuclides. Atmospheric Environment, 81: 399 – 413. https://doi.org/10.1016/j.atmosenv.2013.09.009.

[252] Mazzoni, F.J., Alvarado, M.D., Kalander, K., Alroth, P., Krakik, C., Lettner, H., Luxbacher, S., Nadschläger, E., Ringer, W., Rulik, H., Schernthaler, F., Sperker, S., Stadlmann, H., Steger, F., Steinhäusler, F., Tschurlovits, M. & Winkler, R. (2011). Results and conclusions of the Austrian radon mitigation project "SARAH". The Science of the Total Environment, 2721–3): 159–167. PMID: 21379904.

[253] Mustikainen, M. & Arvela, H. (1992). Radon emanation from soils. Radiation Protection Dosimetry, 45(1–4): 269–272. https://doi.org/10.1093/oxfordjournals.rpd.a081541.

[254] Marsh, J.W. & Birchall, A. (2008). Sensitivity analysis of the weighted equivalent dose per unit exposure from radon progeny. Radiation Protection Dosimetry, 87, 167–178.

[255] Matolín, M. & Prokop, P. (1991). Statistical significance of radon determination in soil air. In: Barnet I. (ed.) Radon investigations in CS. Vol. 2. Czech Geological Survey, Prague, pp. 20–24.

[256] Matolín, M. (2017). Verification of the radiometric map of the Czech Republic. Journal of Environmental Radioactivity, 166 (Part 2): 289–295. doi: 10.1016/j.jenvrad.2016.04.013.

[257] McColl, N., Auvinen, A., Kesminiene, A., Espina, C., Erdmann, F., de Vries, E., Grosnert, R., Harrison, J. & Schüz, J. (2015). European Code against Cancer, 4th Edition: ionising and non-ionising radiation and cancer. Cancer Epidemiology, 39 (Suppl. 1): S93–S100. doi: 10.1016/j.canep.2015.03.016.

[258] Mennigi, K. & Mamuni, T. (1973). Radon and thoron exhalation from the ground. Journal of Geophysical Research, 78(11): 1804–1808. https://doi.org/10.1029/JB078i011p01804.

[259] Megumi, K. & Mamuni, T. (1974). Emanation and exhalation of radon and thoron gases from soil particles. Journal of Geophysical Research, 79: 5357–5360.

[260] Miles, J.C.H. (1992). Quality assurance for passive radon measurements. Applied Radiation and Isotopes, 43 (1/2): 87–93.

[261] Miles, J.C.H. (1994). Mapping the proportion of the housing stock exceeding a radon reference level. Radiation Protection Dosimetry, 56: 207–210.

[262] Miles, J.C.H. & Algar, R.A. (1998). Variations in radon 222 concentrations. J. Radiol. Prot., 8 (2): 103–106.

[263] Miles, J.C.H. (1998). Mapping radon-prone areas by lognormal modelling of house radon data. Health Physics, 74 (3): 370–379.

[264] Miles, J.C.H. (2001). Temporal variation of radon levels in houses and implications for radon measurement strategies. Radiation Protection Dosimetry, 95 (4): 369–376.

[265] Miles, J.C.H., Kendall, G.M., Ibrahimi, Z.-F. & Howorth, C.B. (2004). Practical procedures for a radon etched-track dosimetry service. Journal of Radiological Protection, 24: 165–171.

[266] Miles, J.C.H. & Appleton, J.D. (2005). Mapping variation in radon potential both between and within geological units. Journal of Radiological Protection, 25 (3): 257–276. doi: 10.1088/0952-4746/25/3/003.

[267] Miles, J.C.H., Appleton, J.D., Rees, D.M., Green, B.M.R., Adams, K.A.N. & Myers, A.H. (2007a). Indicative Atlas of Radon in England and Wales, Report HPA-RPD-033. Health Protection Agency, Chilton, UK. ISBN 978-0-85951-608-2.

[268] Miles, J., Appleton, J. & Rees, D. (2007b). Indicative atlas of radon in England and Wales. Report HPA-RPD-033. Health Protection Agency and British Geological Survey.

[269] Miles, J., Ibrahimi, Z.-F. & Birch, K. (2009). Moisture-resistant passive radon detectors. Journal of Radiological Protection, 29(2): 269–271. doi: 10.1088/0952-4746/29/2/N01.

[270] Miles, J.C.H. (2011). Calibration and Standardisation of Etched Track Detectors. In: Durrani, S.A., Bi, R. & Miles, J.C.H. (Eds.). Radon Measurements by Etched Track Detectors, 143–154. https://doi.org/10.1142/9789812830197_0007.

[271] Mollo, S., Orlando, L., Ruggiero, L., Tartaglia, M.C. & Sacco, F. (2014). Mantle-derived CO_2 migration along active faults within an intracontinental basin margin (Fiumicino, Rome, Italy). Tectonophys, 637:137–149. DOI: 10.1016/j.tecto.2014.10.001.

[272] Minda, M., Tóth, G., Horváth, I., Barnet, I., Hámor, K. & Tóth, E. (2009). Indoor radon mapping and its relation to geology in Hungary. Environmental Geology, 57 (3): 601–608. https://doi.org/10.1007/s00254-008-1329-6.

[273] Molina, R., Omede, C., Tommasino, L., Tonnarini, R. & Trevisi, R. (2005). A better understanding of the background of CR-39 detectors. Radiation Measurements, 40(2–6): 525–528. https://doi.org/10.1016/j.radmeas.2004.11.010.

[274] Mitev, K., Georgiev, S., Dimitrova, I. & Pressyanov, D. (2018). Radon-222 in soil gas measurements by compact dfocs: Comparison to diffusion chamber measurements. Radiation Protection Dosimetry 181, 38 – 41.

[275] Mjönes, L., Bladh, A. & Swedjemark, G.A. (1984). Radonhalter i svenska bostäder. Resultat av en landsomfattande undersökning. In Swedish. SSI ø84-23. Statens strålskyddsinstitut.

[276] Moed, B.A., Nazaroff, W.W. & Sextro, R.G. (1988). Soil as a source of indoor radon: Generation, migration and entry. In: Nazaroff, W.W. & Nero Jr., A.V. (eds.) Radon and its Decay Products in Indoor Air. John Wiley and Sons, New York, pp. 57–112.

[277] Mogro-Campero, A., Fleischer, R.L. & Likes, R.S. (1980). Changes in subsurface radon concentration associated with earthquakes. Journal of Geophysical Research, 85 (B6): 3055–3057. https://doi.org/10.1029/JB085iB06p03053.

[278] Mojzeš, A., Matúš, P., Porubčanová, B. & Bartolová, A. (2017). Radon measurements in an area of tectonic zone: A case study in Central Slovakia. Journal of Environmental Radioactivity, 166 (Part 2): 278–288. doi: 10.1016/j.jenvrad.2016.08.012.

[279] Molina, S., Tuccimei, P., Heap, M.J., Vinciguerra, S., Sciotti, M., Castelluccio, M. & Dingwell, D.B. (2011). Increase in radon emission due to rock failure: An experimental study. Geophysical Research Letters, 38, L14304. doi: 10.1029/2011GL047962.

[280] Molin, S., Tuccimei, P., Galli, G., Izzo, G. & Scarlato, P. (2017). The impact of thermally induced devolatilization phenomena on radon signal: Implications for the geochemical survey in volcanic areas. Geophysical Journal International, 211(1): 558–571. https://doi.org/10.1093/gji/ggx314.

[281] Morawska, L. & Phillips, C.R. (1993). Dependence of the radon emanation coefficient on radium distribution and internal structure of the material. Geochimica et Cosmochimica Acta, 57: 1783–1797. https://doi.org/10.1016/0016-7037(93)90113-8.

[282] Morawska, L. & Jeffries, C. (1994). Distribution of radium in mineral sand grains and its potential effect on radon emanation. Radiation Protection Dosimetry, 56 (1–4): 199–202.

[283] Moreno, V., Baixeras, C. & Font, L. (2013). Experimental study on the effect of high humidity environments on the response of long-term exposed nuclear track detectors. Radiation Measurements, 50: 207–211. https://doi.org/10.1016/j.radmeas.2012.11.014.

[284] Moore, H. & Poreda, J.E. (1985). Radiological Physics Division Annual Report July 1984 June 1985. Report ANL-2060. Argonne National Laboratory, Chicago, Illinois, USA.

[285] Mudd, G.M. (2008). Radon releases from Australian uranium mining and milling projects: assessing the UNSCEAR approach. Journal of Environmental Radioactivity, 99(2): 288–315. doi: 10.1016/j.jenvrad.2007.08.001.

[286] Mullerová, M., Holý, K. & Bulko, M. (2011). Results of outdoor radon monitoring in Bratislava and Novaky. Radiation Protection Dosimetry, 145(2–3): 123–128. doi: 10.1093/rpd/nrr068.

[287] NAWRC (National Academies/National Research Council) (1999). Health Effects of Exposure to Radon: BEIR VI. Washington: National Academy Press. Washington DC.

[288] National Academy of Sciences (1999). Risk assessment of radon in drinking water. National Academy of Sciences, Washington (DC), USA. PMID: 25101450.

[289] Nazaroff, W.W. & Nero, A.V. (1988). Radon and its decay products in indoor air. John Wiley and Sons, New York, USA.

[290] Nazaroff, W.W. (1992). Radon transport from soil to air. Reviews of Geophysics, 30(2): 137–160. https://doi.org/10.1029/91RG00055.

[291] NCRP (National Council on Radiation Protection and Measurements) (1984). Evaluation of occupational and environmental exposures to radon and radon daughters in the United States. National Council on Radiation Protection and Measurements NCRP Report No. 78. National Council on Radiation Protection and Measurements. ISBN 0-913392-68-5.

[292] Neri, M., Ferrera, E., Giammanco, S., Currenti, G., Cinerchi, G., Patanè, G. & Zanon, V. (2016). Soil radon measurements as a potential tracer of tectonic and volcanic activity. Scientific Reports, Volume 6, Article number: 24581. https://www.nature.com/articles/srep24581 (accessed 29 March 2018).

[293] Neznal, M., Sokal, A. & Thomas, J. (1996). Radon contamination of natural gas in a storage cavern. Environment International, 22 Suppl.1, S425 – S427. https://doi.org/10.1016/S0160-4120(96)00141-8.

[294] Neznal M., Neznal M. (2005). Permeability as an important parameter for radon risk classification of foundation soils. Annals of Geophysics 48 (1), 125 – 180. DOI: 10.4401/ag-3192.

[295] Neznal, M. (2015). Soil gas radon concentration measurements, radon risk classification – 25 years experience. Presented at International Workshop on the European Atlas on Natural Radiation, 10–13 October 2015, Verbania, Italy. https://mycloudme.com/#radonsurpet/WEAN8%20Verbania%202015 (accessed 1 April 2018).

[296] Neznal, M., Neznal, M. & Smanta, J. (1994). Variability of radon with depth in various soil profiles. In: Barnet, I. & Neznal, M. (eds.) Radon investigations in the Czech Republic. Vol. 5. Czech Geological Survey, Prague, pp. 55–61.

[297] Neznal, M., Neznal, M. & Smanta, J. (1995). Temporal Variability of Soil Gas Radon Concentration – Some Remarks. In: Dubois, C. ed. Gas Geochemistry. Northwood: Science Reviews, 529–534.

[298] Neznal, M., Neznal, M. & Smanta, J. (1996). Assessment of radon potential of soils – A five-year experience. Environment International, 22 (5): 5819–5828. https://doi.org/10.1016/S0160-4120(96)00189-4.

[299] Neznal, M., Neznal, M., Matolín, M., Barnet, I. & Miklovič, J. (2004). The new method for assessing the radon risk of building sites. Czech Geological Survey Special Papers 16. Czech Geological Survey, Prague, 47 pp. http://www.neznam.cz/pdf/metodika.pdf

[300] Nikezic, D. & Yu, K.N. (2004). Formation and growth of tracks in nuclear track materials. Materials Science and Engineering R: Reports 46(3–5): 51–123. https://doi.org/10.1016/j.mser.2004.07.003.

[301] Nuccetelli, C. & Risica, S. (1998). The Italian issue: Monitoring activities, measuring techniques and dose conversion factors. Radiation Protection Dosimetry, 78 (1): 55–64. https://doi.org/10.1093/rpd/rpd/rpd/a012334.

[302] Ochman, A.R. (2005). Distribution of radon activity in the atmosphere above Wzgórza Niemczańsko-Strzelińskie (South-West Poland) and its dependence on uranium and thorium content in the underlying rock and indirect (round basement). Annals of Geophysics, 48(1). doi: https://doi.org/10.4401/ag-3186.

[303] Oh, Y. & Kim, G. (2015). A radon-thoron isotope pair as a reliable earthquake precursor. Scientific Reports, 5: 13084. doi:10.1038/srep13084.

[304] Organzi A., Ballabio C., Panagos P., Jones A., Fernández-Ugalde O. (2018). LUCAS Soil, the largest expandable soil dataset for Europe: a review. European Journal of Soil Science, 69, 140–153. doi: 10.1111/ejss.12499.

[305] Paragas Pérez del Hierro, C., García Talavera J.P. & de la Vega Rivas, R. (2013). Red de estaciones automáticas de vigilancia radiológica ambiental (REA) del CSN. Operación y resultados años 2010 y 2011. Colección informes técnicos 39.2013. Consejo de seguridad nuclear. (in Spanish.)

[306] Pásztor, L., Szabó, K., Szatmári, Laborczi, A. & Horváth, A. (2016). Mapping geogenic radon potential by regression kriging. Science of the Total Environment, 544: 883–891. https://doi.org/10.1016/j.scitotenv.2015.11.175.

[307] Pearson, J.E. & Jones, G.E. (1966). Emanation of radon 222 from soils and its use as an atmospheric tracer. Journal of Geophysical Research, 70(20): 5279–5290. https://doi.org/10.1029/JZ070i020p05279.

[308] Pearson, J.E. & Jones, G.E. (1966). Soil concentrations of emanating radon 222 and the emanation of radon 222 from soils and plants. Tellus, 18:655.

[309] Pereira, A.J.S.C., Godinho, M.M. & Neves, L.J.P.F. (2010). On the influence of faulting on small-scale soil gas radon variability: a case study in the Iberian Uranium Province. Journal of Environmental Radioactivity, 101(10): 875–882. doi: 10.1016/j.jenvrad.2010.05.014.

[310] Petermann, E. & Bossew, P. (2018). Estimation of spatial continuous soil gas air permeability using physical and statistical models as a support for geogenic radon risk mapping. Workshop, GARM, Geological Aspects of Radon Risk Mapping, Prague, Czech Republic, 18 – 20 September 2018.

[311] Petersell, V., Akerblom, G., Ek, B.M., Eisk, M., Mittus, V. & Tahi, K. (2005). Radon Risk Map of Estonia: Explanatory text to the Radon Risk Map Set of Estonia at scale of 1:500 000. Report 2005:16. Swedish Radiation Protection Authority (SSI), Tallinn.

[312] Petersell, V., Junada, K., Raukas, A., Shogenkenko, M. & Tahi-Kok, K. (2013). Quaternary deposits and weathered bedrock material as a source of dangerous radon emissions in Estonia. Geologos, 21(2): 139–147. doi: 10.1515/logos-2015-0006.

[313] Petersell, V., Karimov, M., Tahi-Kok, K., Stotskuenko, M., Nõgi, S., Szavik, K. & Mihek, H. (2017a). Keskkonnaministeerium, Eesti Geoloogiateenistus. Eesti pinnase radioonilisi ja looduslikkuse atlas (The Atlas of Radon Risk and Natural Radiation in Estonian Soil). Geological Survey of Estonia, Tallinn, Estonia, 89 pp. ISBN 978-9985-815-89-2. https://www.envir.ee/sites/default/files/eesti_rn_atlas_2017_ke-janistatud.pdf

[314] Petersell, V., Tahi-Kok, K., Karimov, M., Mihek, H., Nõgi, S., Raha, M. & Szavik, K. (2017b). Radon in the soil air of Estonia. Journal of Environmental Radioactivity, 166 (Part 2): 235–241. https://doi.org/10.1016/j.jenvrad.2016.08.004.

[315] Petrakis, E., Nikolopoulos, D., Panagiotaras, D., Cantzos, D., Yannakopoulos, P., Nomicos, C. & Stonham, J. (2015). Radon-222: A Potential Short-Term Earthquake Precursor. J. Earth Sci. Clim. Change 6: 282. doi: 10.4172/2157-7617.1000282.

[316] Petropoulou, M.P., Anagnostakis, M.J. & Simopoulos, S.E. (1999). Building materials radon exhalation rates: ERRICA intercomparison exercise results. Science of the Total Environment, 272(1–3): 109–118. doi: 10.1016/S0048-9697(01)00674-X.

[317] Piersanti, A., Cannelli V. & Galli, G. (2015). Long-term continuous radon monitoring in a seismically active area. Ann. Geophysics 58 (84), S0437, doi:10.4401/ag-6755.

[318] Pinault, J.L. & Baubron, J.C. (1996). Signal processing of soil gas radon, atmospheric pressure, moisture, and soil temperature data. A new approach for radon concentration modeling. Journal of Geophysical Research, 101(B2), 3157–3171. https://doi.org/10.1029/95JB03121.

[319] Planinić, J., Suveljak, R. & Faj, Z. (1994). Radon distribution in dwellings. Journal of Radiological Protection, 14(3): 235–239.

[320] Planinic, J., Radolić, V., & Lazaro, Z. (2001). Temporal variations of radon in soil related to earthquakes. Applied Radiation and Isotopes, 55(2): 267–272. https://doi.org/10.1016/S0969-8043(00)00387-0.

[321] Planinic, J., Radolić, V., Faj, Z., Stanić, D. & Vukovic, B. (2002). Radon risk mapping in Croatia. Proceedings of the Sixth International Workshop on the Geological Aspects of Radon Risk Mapping, Prague 2002, pp. 71–77.

[322] Podstawczyńska, A. & Kozak, K. (2009). Outdoor radon (^{222}Rn) concentration in urban and rural area (central Poland) in relation to meteorological parameters. Presented at the Seventh International Conference on Urban Climate, 29 June – 3 July 2009, Yokohama, Japan.

[323] Podstawczyńska, A., Kozak, K., Pawlak, W. & Mazur, J. (2010). Seasonal and diurnal variation of outdoor radon (^{222}Rn) concentrations in urban and rural area with reference to meteorological conditions. Nukleonika 55(4): 545–547.

[324] Pawlska, P., Kozak, K., Mazur, J., Dudzińska, M. & Grządziel, D. (2016). Radon and its decay products in an air-conditioned auditorium in correlation with indoor air parameters. Indoor and Built Environment 26(5): 621–630. DOI: 10.1177/1420326X15626295.

[325] Porstendörfer, J. (1994). Properties and Behavior of Radon and Thoron and their decay products in the air. Journal of Aerosol Science, 25(3): 219–263. https://doi.org/10.1016/0021-8502(94)90077-9.

[326] Pressyanov, D., Buyuk, I., Poffijn, A., Meesen, G. & Van Deynse, R. (2003). The compact desk air radon detector: a laboratory study of the method. Health Physics 84, 642 – 651.

[327] Pressyanov, D., Mitev, K., Georgiev, S. & Dimitrova, I. (2010). Radon mapping by retrospective measurements – an approach based on CDs/DVDs. Journal of Environmental Radioactivity 101 (11), 821 – 825. doi:10.1016/j.jenvrad.2010.02.009.

[328] Pressyanov, D., Georgiev, E., Georgiev, S., Dimitrova, I. & Mitev, K. (2014). Traceability of CDs/DVDs used as retrospective ^{222}Rn detectors to reference SSR laboratory. Radiation Measurements 59: 165 – 171. https://doi.org/10.1016/j.radmeas.2013.06.002.

[329] Pressyanov, D., Mitev, K., Georgiev, S. & Dimitrova, I. (2015). Optimization of etching conditions of CDs/DVDs used as detectors for ^{220}Rn. Radiation Measurements 83, 36 – 40.

[330] Pressyanov, D., Dimitrova, I. & Dimitrov, D. (2018). High sensitivity passive radon detector for measuring radon in low-background nuclear/particle physics laboratories. 2018 IEEE Nuclear Science Symposium and Medical Imaging Conference, Conference Records (in press). ISSN 978-1-5386-0495-5.

[331] Quindos, L., Soto, J., Fernandez, P. & Rodenas, C. (1992). Estimate of external gamma exposure outdoors in Spain. Radiation Protection Dosimetry, 45(1–4): 527–529. https://doi.org/10.1093/oxfordjournals.rpd.a081596.

[332] Quindos, L.S., Fernandez-Navarro, P.L., Bolivar-Molina, M.L., Gomez-Arozamena, J., Sainz, C. & Arteche, J. (2002). Medida de la exhalación de radón en el suelo. Nuclenor, 32: 10–15 (in Spanish).

[333] Radtec E-Perm (2006). Sistema per la misura del gas Radon. Manuale d'uso. m-ism s.r.l.

[334] Radolić, V., Miklavčić, I., Stanić, D., Poje, M., Kopan, I., Mužinić, M., Perinac, B. & Vukovic, B. (2014). Identification and mapping of radon-prone areas in Croatia-preliminary results for Lika-Senj and the southern part of Karlovac counties. Radiation Protection Dosimetry, 162(1–2): 29–35. doi: 10.1093/rpd/nsr212.

[335] Radolić, V., Sorić, M.P., Miklavčić, I. & Vukovic, B. (2017). The influence of geological formations on geogenic radon potential and/or indoor radon in Croatia. Presented at the 2nd International Workshop on the European Atlas of Natural Radiation, 6–9 November 2017, Verbania, Italy. https://onedrive.live.com/?authkey=%21AJbVnfWVK2q4kcid=353A2006BF4E5BC7&id=353A2006BF4E5BC7%21247&parId=353A2006BF4E5BC7%21247&o=OneUp (accessed 7 November 2018).

[336] Ramola, R.C., Singh, M., Sandhu, A.S., Singh, S. & Virk, H.S. (1990). The use of radon as an earthquake precursor. Nuclear Geophysics, 4(2): 275–287.

[337] Ramola, R.C., Prasad, Y., Prasad, G., Kumar, S. & Choubey, V.M. (2008). Soil gas radon as seismotectonic indicator in Garhwal Himalaya. Applied Radiation and Isotopes, 66(10): 1523–1530. https://doi.org/10.1016/j.apradiso.2008.04.006.

[338] Ramola, R.C. (2010). Relation between spring water radon anomalies and seismic activity in Garhwal Himalaya. Acta Geophysica, 58(5): 814–827. https://doi.org/10.2478/s11600-009-0047-0.

[339] Reddy, D.V. & Nagabhushanam, P. (2011). Groundwater electrical conductivity and soil radon-gas monitoring for earthquake precursory studies in Koyna, India. Applied Geochemistry, 26 (5): 731–737. https://doi.org/10.1016/j.apgeochem.2011.01.031.

[340] Rice, T., Sinicola, A., Bante-Calvarese, S., Deicher, E., Alparone, S., Gambino, S. & Milazzo, V. (2015). Hydrothermal fluid flow disruptions evidenced by subsurface changes in heat transfer mobility: the La Fossa cone of Vulcano (Italy) case study. Geology, 43: 959–962. doi: 10.1130/G37013.1.

[341] Rice, J. (1980). The mechanics of earthquake rupture. In: Dziewonski, A.M. & Boschi, E. (eds.) Physics of the Earth's Interior. Amsterdam: the Netherlands, pp. 555–649.

[342] Riggio, A. & Santulin, M. (2015). Earthquake forecasting: a review of radon as seismic precursor. Bollettino di Geofisica Teorica ed Applicata, 56 (2): 95–114. doi: 10.4430/bgta0148.

[343] Robé, M.C., Rantou, A. & Le Brusc, J. (1992). Radon measurement in the environment in France. Radiation Protection Dosimetry, 45(1–4): 453–457. https://doi.org/10.1093/oxfordjournals.rpd.a081580.

[344] Rose, A.R., Ciukosz, E.J. & Washington, J.W. (1990). Effects of regional and seasonal variations in soil moisture and temperature on soil gas transport. In: Proceedings of the International Symposium on Radon and Radon Reduction Technology, Volume

References

III Proceeds. EPA/600/9-90/005c. Atlanta, GA, USA, 19-23 February 1990. C-VI-5.

[345] Rotevatn, A. & Fossen, H. (2011). Simulating the effect of subseismic fault tails and process zones in a siliciclastic reservoir analogue: Implications for aquifer support and trap definition. Marine and Petroleum Geology 28, 1648–1662. doi:org/10.1016/j.marpetgeo.2011.07.005

[346] Saad, A.F., Abdallaha, R.M. & Hussein, N.A. (2018). Physical and geometrical parameters controlling measurements of radon emanation and exhalation from soil. Applied Radiation and Isotopes, 137, 273–279. https://doi.org/10.1016/j.apradiso.2018.03.022

[347] Sanz Fernández, C., Quindós Poncela, L.S., Fernández Villar, A., Fuente Merino, I., Gutiérrez-Villanueva, J.L., Celaya González, S., Quindós López, L., Quindós López, J., Fernández, E., Remondo Tejerina, J., Martín Matarranz, J.L. & García Talavera, M. (2016). Spanish experience on the design of radon surveys based on the use of geogenic information. Journal of Environmental Radioactivity, 166 (Pt 2), 390–397. doi: 10.1016/j.jenvrad.2016.07.007

[348] Sakoda, A., Hamamoto, K., Ishimori, Y., Kataoka, T., Kawase, A. & Yamaoka, K. (2010). First model of the effect of grain size on radon emanation. Applied Radiation and Isotopes, 68(6): 1159–1172. doi: 10.1016/j.apradiso.2009.11.070

[349] Sakoda, A., Ishimori, Y. & Yamaoka, K. (2011). A comprehensive review of radon emanation measurements for mineral, rock, soil, mill tailing and fly ash. Applied Radiation and Isotopes, 69(10): 1422–1435. doi: 10.1016/j.apradiso.2011.05.000

[350] Sarra, A., Fontanella, L., Valentini, P. & Palarmi, S. (2016). Quantile regression and Bayesian cluster detection to identify radon prone areas. Journal of Environmental Radioactivity, 164: 354–364. https://doi.org/10.1016/j.jenvrad.2016.06.014

[351] Scarlato, P., Tuccimei, P., Mollo, S., Soligo, M. & Castellucci, M. (2013). Contrasting radon background levels in volcanic settings: clues from ^{222}Rn activity concentrations measured during long-term deformation experiments. Bulletin of Volcanology, 75: 751. https://doi.org/10.1007/s00445-013-0751-0

[352] Schery, S. & Gaeddert, D. (1982). Measurements of the effect of cyclic atmospheric pressure variation on the flux of Rn-222 from the soil. Geophysical Research Letters, 9(8): 835–838.

[353] Schery, S.D., Whittlestone, S., Hart, K.P. & Hill, S.E. (1989). The flux of radon and thoron from Australian soils. Journal of Geophysical Research: Atmospheres, 94(D6): 8567–8576. doi: 10.1029/JD094iD06p08567

[354] Shirai-Schwarz M., Volkan U. (1997). Mapping radon-prone areas - a geophysical approach. Environmental Geology 31 (3- 4), 167 – 173. DOI: 10.1007/s002540050176

[355] Schulz, C.H., Sykes, L.R. & Aggarwal, Y.P. (1973). Earthquake prediction: a physical basis. Science, 181 (4102): 803–810. doi: 10.1126/science.181.4102.803

[356] Schubert, M. (2015). Using radon as environmental tracer for the assessment of subsurface Non-Aqueous Phase Liquid (NAPL) contamination – A review. The European Physical Journal Special Topics, 224(4): 717–730. https://doi.org/10.1140/epjst/e2015-02402-3

[357] Schumann, R.R., Owen, D.E. & Ashley, R.P. (1989). Weather factors affecting soil gas radon concentrations at a single site in the semi-arid western U.S. In: Proceedings of the 1989 PA Symposium on Radon Production Technology v.2, Publ. EPA/600/9-89/008, Environ. Protect. Agency, Wellington, D.C., USA, 3.1–3.13.

[358] Schumann, R.R., Owen, D.E. & Ashley, R.P. (1992). Effects of weather and soil characteristics on temporal variations in soil–gas radon concentrations. In: Gates, A.E. & Gundersen, L.C.S. (Eds.): Geology Controls on Radon, Geological Society of America. ISBN9780813722719. DOI: https://doi.org/10.1130/SPE271-p65

[359] Schumann, R.R. (ed.) (1993a). Geologic radon potential of EPA region (1-10). U.S. Geological Survey Open-File Report 93-292, parts A-J, various authors.

[360] Schumann, R.R. (1993b). Geologic radon potential of the glaciated Upper Midwest. In: Proceedings. The 1992 International Symposium on Radon and Radon Reduction Technology, vol. 2, Symposium Oral Papers, Technical Sessions VII-XII. Research Triangle Park, N.C., U.S. Environmental Protection Agency Rept. EPA-600/R-93/078b, p. 8-33–8-49.

[361] Schumann, R. & Gundersen, L. (1996). Geological and climatic controls on the radon emanation coefficient. Environment International, 22 (5): 543–546. https://doi.org/10.1016/S0160-4120(96)00144-4

[362] Sciarra, A., Cinelli, G., Ruggieri, L., Annunziatella, A., Bigi, S. & Giuliani, S. (2017). Soil gas profiles across buried fault and exposed cataclasic ruptures during the Amatrice and Norcia earthquakes, Central Italy. Geophysical Research Abstracts, Vol. 19, EGU2017-13552.

[363] Seminsky, K.Zh. (2003). Inner Structure of Continental Fault Zones: Tectonophysical Aspect (in Russian) (ed. SO RAN, Filial "Geo", Novosibirsk.

[364] Seminsky, K.Zh. & Bobrov, A.A. (2009). Comparative assessment of radon activity for different Fault Types and scale ranks in the Baikal Rift and South of the Siberian platform. Doklady Earth Sciences, 427(6): 915–919. doi: 10.1134/S1028334X09060603.

[365] Seminsky, K.Zh., Bobrov, A.A. & Demberel, S. (2014). Variations in radon activity in the crustal fault zones: Spatial characteristics. Izvestiya Physics of the Solid Earth, 50(6): 795–813. doi: 10.1134/S1069351314060081.

[366] Semkow, T. (1990). Recoil emanation theory applied to radon release from mineral grains. Geochimica et Cosmochimica Acta, 54(2): 425–440. https://doi.org/10.1016/0016-7037(90)90303-E.

[367] Sempere, L., Hopkins, D.S. & Tasker, B.R. (2006). Laboratory, field, and modeling studies of Radon-222 as a natural tracer for monitoring NAPL contamination. Transport in Porous Media, 38(1–2): 223–240. https://doi.org/10.1023/A:1006671519145

[368] Servant, J. (1966). Temporal and spatial variations of the concentration of the short-lived decay products of radon in the lower atmosphere. Tellus, 18(2–3): 661–671. https://doi.org/10.3402/tellusa.v18i2-3.9201

[369] Sesana, L., Caprioli, E. & Marcazzan, G.M. (2003). Long period study of outdoor radon concentration in Milan and correlation between its temporal variation and dispersion properties of atmosphere. Journal of Environmental Radioactivity, 65(2): 147–60. PMID: 12527232.

[370] Sheen, S., Lee, K.S., Chung, W.Y., Nam, S., Kang, D.R.K. (2016). An updated review of case–control studies of lung cancer and indoor radon-is indoor radon the risk factor for lung cancer?. Annals of Occupational and Environmental Medicine, 28:9. DOI: 10.1186/s40557-016-0094-3

[371] Shipton, Z.K. & Cowie, P.A. (2003). A conceptual model for the origin of fault damage zone structures in high-porosity sandstone. Journal of Structural Geology, 25(3): 333–344. https://doi.org/10.1016/S0191-8141(02)00037-8.

[372] Shipton, Z.K., Evans, J.P. & Thompson, L.B. (2005). The geometry and thickness of deformation band fault core and its influence on sealing characteristics of deformation band fault zones. In: Sorkhabi, R. & Tsuji, Y. (eds.) Faults, fluid flow, and petroleum traps. American Association of Petroleum Geologists Memoir 85: 181–195. ISBN 0891813667.

[373] Shroe-Schwartz, M. & Volkan, U. (1997). Mapping radon-prone areas - a geophysical approach. Environmental Geology 31 (3- 4), 167 – 173. DOI: 10.1007/s002540050176

[374] Shweikani, R., Giaddui, T.G. & Durham, E.A. (1995). The effect of soil parameters on the radon concentration values in the environment. Radiation Measurement, 25(1–4): 581–584. https://doi.org/10.1016/1350-4487(95)00188-K

[375] Sibson, R.H. (2000). Fluid involvement in normal faulting. Journal of Geodynamics, 29(3–5): 469–499. https://doi.org/10.1016/S0264-3707(99)00042-3

[376] Siehl, A., Stegemann, R., Lehmann, R. & Valdivia Manchego, M. (2000). Mapping of the geogenic radon potential in Germany - the state of matters. In: Barnet, I. & Neznal, M. (eds.): Radon investigations in the Czech Republic VIII and the Fifth International Workshop on the Geological Aspects of Radon Risk Mapping. Czech Geological Survey Radon Corp., Prague, Czech Republic.

[377] Singh, M., Kumar, M., Jain, V.K. & Chaturdh, R.P. (1999). Radon in ground water related to seismic events. Radiation Measurements, 30(4): 465–469. https://doi.org/10.1016/S1350-4487(99)00049-9

[378] Skeppström, K. & Olofsson, B. (2007). Uranium and radon in groundwater: An overview of the problem. European Water 17/18: 51–62. E.W. Publications.

[379] Smethurst, M.A., Watson, R.J., Baranwal, V.C., Rudjord, A.L. & Finne, I. (2017). The predictive power of airborne gamma ray survey data on the locations of domestic radon hazards in Norway: A strong case for utilizing airborne data in large-scale radon potential mapping. Journal of Environmental Radioactivity, 166 (Part 2): 321–340. doi: 10.1016/j.jenvrad.2016.04.006.

[380] Stack, D.J. (1992). Spatial and Temporal Indoor Radon Variations. Health Physics, 62 (4): 353–359.

[381] Stack, D.J. & Yasun, S.S. (2001). Variation of atmospheric radon and radon progeny in central North America. In: Proceedings of the 5th International Conference on Rare Gas Geochemistry, Debrecen, Hungary, 30 August–3 September 1999, pp. 107–116.

[382] Steinhausler, F., Hofman, W. & Lettner, H. (1994). Thoron exposure of man: a negligible issue? Radiation Protection Dosimetry, 56(1): 1–44. DOI: 10.1093/oxfordjournals.rpd.a082436

[383] Stoop, P., Glasius, P., Hiemstra, T., de Vries, L. & Lambrechts, J. (1998). Results of the second Dutch national survey on radon in dwellings. RIVM Report no. 610056008. National Institute for Public Health and the Environment, Bilthoven, the Netherlands. 45 pp.

[384] Strandén, E., Kolstad, A.K. & Lind, B. (1984). Radon exhalation: moisture and temperature dependence. Health Physics, 47(3): 480–484. PMID: 6510953.

[385] Strandén, E., Kolstad, A.K. & Lind, B. (1984). The influence of moisture and temperature on radon exhalation. Radiation Protection Dosimetry, 7(1–4): 55–58. https://doi.org/10.1093/oxfordjournals.rpd.a082962.

[386] Strong, K.P. & Levins, D.M. (1982). Effect of moisture content on radon emanation from uranium ore and tailing. Health Phys ics, 42(1): 27–32. PMID: 7056644.

[387] Sugisaki, R., Ariga, H., Adachi, M. & Ui, H. (1980). Geochemical features of gases and rocks along active faults. Geochemical Journal, 14(3): 101–112. https://doi.org/10.2343/geochemj.14.101

[388] Sundal, A.V., Henriksen, H., Soldal, O. & Strand, T. (2004). The influence of geological factors on indoor radon concentrations in Norway. Science of the Total Environment, 338(1–3): 41–53. doi: 10.1016/j.scitotenv.2004.02.011

[389] Surbeck, H. (1995). Radon Monitoring in Soils and Water. Nuclear Tracks and Radiation Measurements, 22(1–4): 463–466. https://doi.org/10.1016/1359-0189(95)80110-P.

[390] Swakoń, J., Paszkowski, M., Janik, M., Hajduk, T., Loskiewicz, J. & Olko, P. (2000). Radon measurements in soil-tests in Krakow agglomeration. In: Barnet, I. & Neznal, M. (eds.): Radon investigations in the Czech Republic VIII and the Fifth International Workshop on the Geological Aspects of Radon Risk Mapping. Czech Geological Survey, RADON v.o.s., Prague, Czech Republic: 215–221.

[391] Swakoń, J., Kozak, K., Paszkowski, M., Gradziński, R., Loskiewicz, J., Mazur, J., Janik, M., Bogacz, J., Horwacik, T. & Olko, P. (2004). Radon concentration in soil gas around local conjunctive tectonic zones in the Krakow area. Journal of Environmental Radioactivity, 78(2): 137–149. doi: 10.1016/j.jenvrad.2004.04.004.

[392] Swedemark, G.A. (1985). The equilibrium factor F. Health Phys 49: 453–462(10): 10.1097/00004032-198509000-00021.

[393] Szabó, K.Z., Jordan, G., Horváth, Á. & Szabó, C. (2014). Mapping the geogenic radon potential: methodology and spatial analysis for central Hungary. Journal of Environmental Radioactivity, 214 (129): 107–120. doi: 10.1016/j.jenvrad.2013.12.008.

[394] Szabó, K.Z., Jordan, G., Petrik, A., Horváth, Á. & Szabó, C. (2017). Spatial analysis of ambient gamma dose equivalent rate data by means of digital image processing techniques. Journal of Environmental Radioactivity, 168 (Part 2): 308–320. doi: 10.1016/j.jenvrad.2016.07.013.

[395] Szegvary, T., Conen, F. & Ciais, P. (2009). European ^{222}Rn inventory for applied atmospheric studies. Atmos. Environ. 43: 1536–1539. doi:10.1016/j.atmosenv.2008.11.035.

[396] Tale Kok, K., Petersen, V. & Štukavskis, M. (2012). High concentrations of Rn in soil air reveal a fracture zone in the bedrock of the Tapa area. In: Barnet, I., Neznal, M. & Pacherova, P. (eds.) Proceedings of the 11th International Workshop on the Geological Aspects of Radon Risk Mapping. Czech Geological Survey, RADON v.o.s., Prague, Czech Republic: 216–221.

[397] Talpale, T.T. & Wrayford, R. (1985). Seasonal variations in soil gas radon concentration. Science of the Total Environment, 45: 121 – 126.

[398] Tanner, A. (1964). Radon migration in the ground: A review. In: The Natural Radiation Environment, pp. 161–190. University of Chicago Press, Chicago, USA.

[399] Tanner, A.B. (1980). Radon migration in the ground: A supplementary review. In: The Natural Radiation Environment, Vol. 3, pp. 5–56. National Technical Information Service, Springfield, Virginia, USA.

[400] Tanner A.B. (1988). A tentative protocol for measurement of radon availability from the ground. Radiation Protection Dosimetry 24 (1 – 4): 87 – 83. https://doi.org/10.1093/oxfordjournals.rpd.a080246

[401] Tollefsen, T., Cinelli, G., Bossew, P., Gruber, V. & De Cort, M. (2014). From the European indoor radon map towards an atlas of natural radiation. Radiation Protection Dosimetry, 162 (1–2): 129–134. doi: 10.1093/rpdncu244.

[402] Tollefsen, T., De Cort, M., Cinelli, G., Gruber, V. & Bossew, P. (2010-03). Indoor radon concentration. European Commission, Joint Research Centre (JRC) [Dataset] PID: http://data.europa.eu/89h/jrc-ener-03_indoor-radon-measurements.

[403] Tollefsen, T., De Cort, M., Cinelli, G., Gruber, V. & Bossew, P. (2010-03). Indoor Radon – Number of Measurements. European Commission, Joint Research Centre (JRC) [Dataset] PID: http://data.europa.eu/89h/jrc-ener-03_indoor-radon-measurements.

[404] Tollefsen, T., Gruber, V., Bossew, P. & De Cort, M. (2011). Status of the European indoor radon map. Radiation Protection Dosimetry 145 (2–3): 110–116. doi: 10.1093/rpd/ncr072.

[405] Torkar, G., Zmazek, B., Vaupotič, J. & Kobal, I. (2010). Application of artificial neural networks in simulating radon levels in soil gas. Chemical Geology, 270 (1–4): 1–8. https://doi.org/10.1016/j.chemgeo.2008.09.017.

[406] Toutain, J.P. & Baubron, J.C. (1999). Gas geochemistry and seismotectonics: a review. Tectonophysics, 304(1–2): 1–27. https://doi.org/10.1016/S0040-1951(98)00295-9.

[407] Trevisi, R., Risica, S., D'Alessandro, M., Paradisi, D. & Nuccetelli, C. (2012). Natural radioactivity in building materials in the European Union: a database and an estimate of radiological significance. Journal of Environmental Radioactivity, 105: 11–20. https://doi.org/10.1016/j.jenvrad.2011.10.001.

[408] Trevisi, R., Nuccetelli, C. & Risica, S. (2013). Screening tools to limit the use of building materials with enhanced/elevated levels of natural radioactivity: Analysis and application of index criteria. Construction and Building Materials, 49: 448–454. https://doi.org/10.1016/j.conbuildmat.2013.08.059.

[409] Trevisi, R., Leonardi, F., Risica, S. & Nuccetelli, C. (2018). Updated database on natural radioactivity in building materials in Europe. Journal of Environmental Radioactivity, 187: 90–105. https://doi.org/10.1016/j.jenvrad.2018.01.024.

[410] Tuccimei, P., Salvati, R., Capelli, G., Delitala, M.C. & Pomavera, P. (2005). Groundwater fluxes into a submerged sinkhole area, Central Italy, using radon and water chemistry. Applied Geochemistry, 20(10): 1831–1847. https://doi.org/10.1016/j.apgeochem.2005.04.005.

[411] Tuccimei, P., Moroni, M. & Norcia, D. (2006). Simultaneous determination of ^{222}Rn and ^{220}Rn exhalation rates from building materials used in Central Italy with accumulators chambers and a continuous solid state alpha detector: influence of particle size, humidity and precursors concentration. Applied Radiation and Isotopes, 64(2): 254–263. doi: 10.1016/j.apradiso.2005.07.016.

[412] Tuccimei, P. & Soligo M. (2008). Correcting for CO_2 interference in soil radon flux measurements. Radiation Measurements, 43(1): 102–105. https://doi.org/10.1016/j.radmeas.2007.05.056.

[413] Tuccimei, P., Castellucci, M., Soligo, M. & Moroni, M. (2009). Radon exhalation rates of building materials: experimental, analytical protocol and classification criteria. In: Comeau D.N. & Haro, J.L. (eds.): Building materials: Properties, Performance and Applications. Nova Science Publishers, Hauppauge, New York, USA, pp. 259–273.

[414] Tung S., Leung I.K.C., Lee J.I., Wiegand J., Wattenberg W. (2013). Assessment of soil radon potential in Hong Kong, China, using a 10-point evaluation system. Environmental Earth Sciences 68 (3): 679 – 689. https://doi.org/10.1007/s12665-012-1782-0.

[415] Turek, K., Bednář, J., Neznal, M. (1997). Parallel track-etch detector arrangement for radon measurement in soil. Radiation measurement 28 (1 – 6): 751 – 754. https://doi.org/10.1016/S1350-4487(97)00138-9.

[416] Turek, K., Geles, M. & Dimov, I. (2004). Comparative measurements of soil gas radon concentration using thermoluminescent and track detectors. Radiation Measurement 38 (4 – 6): 843 – 846. doi:10.1016/j.radmeas.2004.02.011.

[417] Tyson, J.L. et al. (1993). Elevated radon levels in ambient air. In: Saarela, K., Kalliokoski & P., Sippanen, O. (eds.): Indoor Air '93. Proceedings of the 8th International Conference on Indoor Air Quality and Climate, Helsinki, Finland, 4–8 July 1993, Vol. 4: 443–448. Indoor Air '93, Helsinki, Finland.

[418] U.S. Geological Survey Bulletin (1971). Field Studies of Radon in Rocks, Soils, and Water.

[419] U.S. Geological Survey (USGS) (1992). The Geology of Radon. ISBN 0-16-037974-1. https://doi.org/10.3133/b1971.

[420] Ulomov, V.I., & Mavashev, B.Z. (1971). Forerunners of the Tashkent earthquake. Izv. Akad. Nauk Uzbekskoy SSR, pp. 188–200.

[421] UNSCEAR (2000). Sources and Effects of Ionizing Radiation. Vol. II: Effects, Annex B. United Nations, New York.

[422] UNSCEAR (United Nations Scientific Committee on the Effects of Atomic Radiation) (1993). Sources and Effects of Ionizing Radiation. Report to the General Assembly, with scientific annexes. United Nations, New York, USA.

[423] UNSCEAR (United Nations Scientific Committee on the Effects of Atomic Radiation) (1982): Ionizing Radiation: Sources and Biological Effects. Report to the General Assembly, with scientific annexes. United Nations, New York, USA.

[424] UNSCEAR (2000). Sources and effects of ionizing radiation: sources. United Nations Publications.

[425] UNSCEAR (2008) Effects of ionizing radiation, Vol. 1, 2008. Report to the General Assembly, with Scientific Annexes (New York: United Nations Publication 2008).

[426] US-EPA (2001). Building Radon Out: A Step-by-Step Guide On How To Build Radon-Resistant Homes. https://www.epa.gov/radon/building-radon-out-step-step-guide-how-build-radon-resistant-homes (accessed June 2018).

[427] Van Giap, P. (2003). Use of radon-222 as tracer to estimate groundwater infiltration velocity in a river bank area. Nuclear Science and Technology, 2(2): 12–17. ISSN 1810-5408.

[428] Vargas, A. & Ortega, X. (2006). Influence of environmental changes on integrating radon detectors: results of an intercomparison exercise. Radiation Protection Dosimetry, 123(4): 529–536. doi: 10.1093/rpd/nci116.

[429] Vaupotič, J., Gregorič, A., Kobal, I., Žvab, P., Kozak, K., Mazur, J., Kozłowska, E. & Grządziel, D. (2010a). Radon concentration in soil gas and radon exhalation rate at the Ravne Fault, in NW Slovenia. Natural Hazards & Earth System Sciences, 10: 895–899. http://www.nat-hazards-earth-syst.net/10/895/2010/.

[430] Vaupotič, J., Kobal, I. & Krušman, M.J. (2010b). Background outdoor radon levels in Slovenia. Radiometrika, 35(4): 579–582.

[431] Venoso, G., Ampolini, M., Antignani, S., Carpentieri, C. & Bochicchio, F. (2016). In-field evaluation of the impact of ageing and fading effects on annual radon concentration measurements for two different techniques. Journal of Radiological Protection, 36(4): 922–933. DOI: 10.1088/0952-4746/36/4/922.

[432] Verbaggio, A., Masi, U., Scardoni, M. & Zampetti, G. (2006). A methodology for assessing the maximum expected radon flux from soils in Northern Latium (Central Italy). Environmental Geochemistry and Health, 28(6): 541–551. doi: 10.1007/s10653-006-9051-3.

[433] Verbaggio, M. (2012). Radon progeny in hydrometeors at the earth's surface. Radiation Protection Dosimetry, 150(3): 334–341. doi: 10.1093/rpd/nci402.

[434] Vukotic, P., Antovic, N., Djurovic, A., Sekulic, K., Svrkota, N., Antovic, T., Svrkota, R., Mrdak, R., Bakica, N., Djurovic, T., Dubljevic, A. & Bogicevic, M. (2018). Radon survey in Montenegro – A base to set national radon reference and 'urgent action' level. Journal of Environmental Radioactivity. Available online 28 February 2018. https://doi.org/10.1016/j.jenvrad.2018.01.009.

[435] Wakita, H., Nakamura, Y., Notsu, K., Noguchi, M. & Asada, T. (1980). Radon anomaly: A possible precursor of the 1978 Izu-Oshima-Kinkai earthquake. Science, 207 (4433): 882–883. doi: 10.1126/science.207.4433.882.

[436] Walia, V., Yang, T.F., Hong, W.L., Lin, S.J., Fu, C.C., Wan, K.L. & Chen, C.H. (2009). Geochemical variation of soil-gas composition for fault trace and earthquake precursory studies along the Hsinchang fault in NW Taiwan. Applied Radiation and Isotopes, 67(10): 1855–1863. https://doi.org/10.1016/j.apradiso.2009.07.004.

[437] Ward, D.C. & Borak, T.B. (1991). Determination of time varying ^{222}Rn concentrations using flow through scintillation flasks. Health Physics, 61(6): 799–807. PMID: 1955324.

[438] Ward, R.S., Smedley, P.S., Allen, G., Baptie, B.J., Daraktchieva, Z., Horleston, A., Jones, D.G., Jordan, C.J., Lewis, A., Lowry, D., Purvis, R.M. & Rivett, M.O. (2017). Environmental Baseline Monitoring Project: Phase II, final report, 163 pp. Report OR/17/048. British Geological Survey. http://nora.nerc.ac.uk/id/eprint/517889.

[439] Washington, J.W. & Rose, A.W. (1990). Regional and temporal relations of radon in soil gas to soil temperature and moisture. Geophysical Research Letters, 17(6): 829–832. https://doi.org/10.1029/GL017i006p00829.

[440] Wasiukiewicz, J.M. (2018a). Impact of environmental factors on PADC radon detector sensitivity during long term storage. Radiation Physics and Chemistry, 142: 141–145. https://doi.org/10.1016/j.radphyschem.2017.01.002.

[441] Wasiukiewicz, J.M., Daraktchieva, Z. & Howarth, C.B. (2018b). Passive etched track detectors application in outdoor radon monitoring. Radiation Measurement. Manuscript submitted for publication.

[442] Watson, R.J., Smethurst, M.A., Baranwal, V.C., Finne, I. & Rudjord, A.L. (2017). The use of mapped geology as a predictor of radon potential in Norway. Journal of Environmental Radioactivity, 166 (Part 2): 341–354. https://doi.org/10.1016/j.jenvrad.2016.05.031.

[443] Wiegand, J. (2001). A guideline for the evaluation of the soil radon potential based on geogenic and anthropogenic parameters. Environmental Geology 40, 949 – 963. DOI: 10.1007/s002540100287.

[444] Wiegand, J. (2005). A semi quantitative method to evaluate the soil radon potential. The 10 point system. Hydrogeologie und Umwelt 35 (1): 1 – 10.

[445] WHO (World Health Organization) (2000). Air Quality Guidelines for Europe, Second Edition. WHO Regional Publications, Euro-pean series, No. 91, 273 pp. Copenhagen, Denmark. ISBN 92 890 1358 3.

[446] WHO (World Health Organization) (2007). World Health Organization International Radon Project: Survey on Radon Guidelines, Programmes and Activities. WHO Press, Geneva. http://www.who.int/ionizing_radiation/env/radon/WP_Survey_on_Radon.pdf.

[447] WHO (World Health Organization) (2009). WHO Handbook on Indoor Radon: A Public Health Perspective. World Health Organization, Geneva. ISBN 978 92 4 154767 3. http://www.who.int/ionizing_radiation/env/radon/en/index1.html.

[448] Wicke, A. & Pandendorfer, J. (1981). Radon daughter equilibrium in dwellings. In: 2nd Special Symposium on Natural Radiation Environment. Proceedings of conference held 19–23 January 1981, Bombay, India. Bhabha Atomic Research Centre: 132–135.

[449] Wiegand, J. (2001). A guideline for the evaluation of the soil radon potential based on geogenic and anthropogenic parameters. Environmental Geology, 40(8): 949–963. https://doi.org/10.1007/s002540100287.

[450] Wilkening, M.H., Clements, W.E. & Stanley, D. (1974). Radon 222 flux in widely separated regions. In: Adams, J.A.S., Lowder, W.M. & Gesell, T.F. (eds.): The Natural Radiation Environment, Vol. 2, pp. 717–730. University of Chicago Press, Chicago, US.

[451] Wilkening, M. (1980). Radon in the Environment. Studies in Environmental Science, in: Environmental Science 4. Elsevier, Amsterdam, the Netherlands. ISBN: 9780444418232.

[452] World Health Organization (WHO) (2009). Handbook on indoor radon: a public health perspective. World Health Organization, Geneva, Switzerland. ISBN 978 92 4 154767 3.

[453] Wrixon, A.D., Green, B.M.R., Lomas, P.R., Miles, J.C.H., Cliff, K.D., Francis, E.A., Driscoll, C.M.H., James, A.C. & O'Riordan, M.C. (1988). Natural Radiation Exposure in UK Dwellings. Report NRPB-R190. National Radiation Protection Board, Chilton, UK.

[454] Wysocka, M., Skowronek, J. & Skubacz, K. (1995). Changes of radon concentration in soil gas over some main faults in Upper Silesia Coal Basin. In: Proceedings of the 5th International Conference on Rare Gas Geochemistry, 30 August – 3 September, Debrecen, Hungary.

[455] Yang, T.F., Walia, V., Chyi, L.L., Fu, C.C., Chen, C.H., Liu, T.K., Song, S.R., Lee, C.Y. & Lee, M. (2005). Variations of soil radon and thoron concentrations in a fault zone and prospective earthquakes in the Taiwan. Radiation Measurements, 40 (2–6), 496–502. https://doi.org/10.1016/j.radmeas.2005.05.017.

[456] Zahorowski, W. & Whittlestone, S. (1996). A fast portable emanometer for field measurement of radon and thoron flux. Radiation and Protection Dosimetry, 67(2): 109–120. doi: 10.1093/oxfordjournals.rpd.a031802.

[457] Zang, L., Guo, Q. & Ida, T. (2004). Atmospheric radon levels in Beijing, China. Radiation Protection Dosimetry, 112(3): 449–453. doi: 10.1093/rpd/nch407.

[458] Zhang, W., Zhang, D., Wu, L., Li, J. & Cheng, J. (2016). Radon release from underground strata to the surface and uniaxial compressive test of rock samples. Acta Geodyn. Geomater., 13(4): 407–416. doi: 10.13168/AGG.2016.0023.

[459] Zhu, H.C., Charlet, J.M. & Poffijn, A. (2001). Radon risk mapping in southern Belgium: an application of geostatistical and GIS techniques. The Science of the Total Environment, 272(1–3): 203–210. https://doi.org/10.1016/S0048-9697(01)00693-3.

[460] Zhukovsky, M. (2016). The effect of meteorological conditions on diurnal dynamic of atmospheric radon in urban environment. Presented at the 13th International Workshop on the Geological Aspects of Radon Risk Mapping, 15–16 September 2016, Prague, Czech Republic.

[461] Zhuo, W., Guo, Q., Chen, B., & Cheng, G. (2008). Estimating the amount and distribution of radon flux density from the soil surface in China. Journal of Environmental Radioactivity, 99(7): 1143–1148. https://doi.org/10.1016/j.jenvrad.2008.01.011.

[462] Zmazek, B., Todorovski, L., Džeroski, S., Vaupotič, J. & Kobal, I. (2003). Application of decision trees to the analysis of soil radon data for earthquake prediction. Applied Radiation and Isotopes, 58(6): 697–706. https://doi.org/10.1016/S0969-8043(03)00094-0.

[463] Zmazek, B., Živčić, M., Todorovski, L., Džeroski, S., Vaupotič, J., & Kobal, I. (2005). Radon in soil gas: How to identify anomalies caused by earthquakes. Applied Geochemistry, 20(6): 1106–1119. https://doi.org/10.1016/j.apgeochem.2005.01.014.

[464] Zmazek, B., Todorovski, L., Živčić, M., Džeroski, S., Vaupotič, J., & Kobal, I. (2006). Radon in a thermal spring: identification of anomalies related to seismic activity. Applied Radiation and Isotopes, 64(6): 725–734. doi: 10.1016/j.apradiso.2005.12.016.

[465] Zoran, M., Savastru, R. & Savastru, D. (2012). Ground based radon (^{222}Rn) observations in Bucharest, Romania and their application to geophysics. Journal of Radioanalytical and Nuclear Chemistry, 295(3): 877–888. doi: 10.1007/s10967-012-1761-7.

[466] Żmudź, Z.S., Rizzuto, K., Cerioli, G., Ramola, R.C., Kochowska, E., Ujić, P., Čeliković, I., Mazur, J., Janik, M., Dorenjo, A., Strnisťjev, A., Bochicchio, F., Yarmoshenko, I.V., Krysiuk, D. & Ilić, P. (2007). A campaign of discrete radon concentration measurements in soil of Niška Banja town, Serbia. Radiation Measurements, 42(10): 1695–1702. doi: 10.1016/j.radmeas.2007.06.010.

Chapter 6 – Radionuclides in water and river sediments

(pp. 138 – 147)

[1] Andrews, J. N. & Kay, R. L. F. (1982). ^{222}Rn activity ratios of dissolved uranium in groundwaters from a Jurassic limestone aquifer in England. Earth and Planetary Science Letters, 57: 139–151.

[2] Ajay, J. S., Seaman, J. C. & Bertsch, P. M. (1998). Immobilization of uranium in contaminated sediments by hydroxyapatite addition. Environmental Science & Technology, 33(2): 337–342. doi:10.1021/es980425+.

[3] Amitt, M.F. & West, I.E. (2004). A Study of the factors affecting the gross alpha measurement, and a radiochemical analysis of some groundwater samples from the state of Wisconsin exhibiting an elevated gross alpha activity. Wisconsin groundwater management practice monitoring project. DNR-176. Available at: http://www.uh.wisc.edu/wp-content/uploads/2013/10/dnr-final.pdf.

[4] Asikainen, M. & Kahola H. (1979). Anomalously high concentrations of uranium, radium and radon in water from drilled wells in the Helsinki region. Geochim. Cosmochim. Acta 43 1681–1686.

[5] Avery, E., Bibby, R., Visser, A., Esser, B. & Moran, J. (2016). Quantification of Groundwater Discharge in a Subalpine Stream Using Radon-222. Water, 10(2):100.

https://doi.org/10.3390/w10020100.

[6] Baeza, A., Bragueria, A. M., Camero, M. C., Garcia, E., Gil, J. M., Mas, C., Sequeira, M. M. & Teixeira M. M (2001). Spatial and temporal evolution of the levels of tritium in the Tagus river in its passage through Cáceres (Spain) and Alentejo (Portugal). Water Research 35:705–714.

[7] Barker, F.B., Johnson, J.D., Edwards, K.W. & Robinson, B.P. (1965). Determination of Uranium in Natural Waters. U.S. Government Printing Office.

[8] Banks, D., Frengstad, B., Midtgård, A.K., Krog, J.R. & Strand, T. (1998). The chemistry of Norwegian groundwaters. I. The distribution of radon, major and minor elements in 1604 crystalline bedrock groundwaters. Science of the Total Environment, 222(1–2): 71–91. https://doi.org/10.1016/S0048-9697(98)00291-5.

[9] Barisic, D., Lulic, S. & Miletic, P. (1992). Radium and uranium in phosphate fertilizers and their impact on the radioactivity of waters. Water Research, 26: 607–611.

[10] Bigalke, M., Schwab, L., Rehmann, A., Tonda, P. & Floch, M. (2018). Uranium in agricultural soils and drinking water wells on the Swiss Plateau. Environmental Pollution, 233, 943–953. doi: 10.1016/j.envpol.2017.09.061.

[11] Bone, S.E., Dynes, J.J., Cliff, J. & Bargar, J.R. (2017). Uranium(VI) adsorption by natural organic matter in anoxic sediments. Proceedings of the National Academy of Sciences, 114(4): 711–716. doi: 10.1073/pnas.1611918114.

[12] Budnitz, R. J. (1971). Tritium Instrumentation for Environmental and Occupational Monitoring, Health Physics 26:163–169.

[13] Burnett, W.C., Aggarwal, P.K., Aureli, A., Bokuniewicz, H., Cable, J.E., Charette, M.A., Kontar, E., Krupa, S., Kulkarni, K.M., Loveless, A., Moore, W.S., Oberdorfer, J.A., Oliveira, J., Ozyurt, N., Povinec, P., Privitera, A.M.G., Rajar, R., Ramessur, R.T., Scholten, J., Stieglitz, T., Taniguchi, M. & Turner, J.V. (2006). Quantifying submarine groundwater discharge in the coastal zone via multiple methods. Science of the Total Environment, 367: 498–543. doi: 10.1016/j.scitotenv.2006.05.009.

[14] Carter, M. W. & Moghissi, A. A. (1977). Three decades of nuclear testing. Health Phys. 33:55–71.

[15] Clark, I. & Fritz, P. (1997). Environmental Isotopes in Hydrogeology. Lewis Publishers, Boca Raton.

[16] Clever H.L. (Ed.) (1979). Solubility Data Series. Volume 2. Krypton, Xenon and Radon — Gas Solubilities. 0-08-022352-4, Pergamon Press, Oxford.

[17] Cook, P. G., Favreau, G., Dighton, J. C. & Tickell, S. (2003). Determining natural groundwater influx to a tropical river using radon, chlorofluorocarbons and ionic environmental tracers. Journal of Hydrology, 277(1–2): 74–88. https://doi.org/10.1016/S0022-1694(03)00087-8.

[18] Cothern, C.R. & Lappenbusch, W.L. (1983). Occurrence of uranium in drinking water in the U.S. Health Physics, 45, 89–99.

[19] Cothern, C.R. (1987). Environmental Radon. Plenum Press, New York, pp. 363. ISBN 0-306-42707-9.

[20] De Felice, P. (2007). Primary standards of radon. Metrologia 44: 82–86. DOI: 10.1088/0026-1394/44/1/11.

[21] Dietl, J. (2003). Radioactivität in Lebensmitteln (WILEY-VCH GmbH & Co).

[22] Dockins, K. D., Bainbridge, A. E., Hausermann, J. C. & Sueiss, H. E. (1967). Tritium in the mixed layer of the North Pacific Ocean. Radioactive Dating and Methods of Low-Level Counting, IAEA, Vienna, 129–142.

[23] Drever, J. I. (1997). The Geochemistry of Natural Waters, Prentice Hall, New Jersey, US.

[24] Edmunds, W.M., Guendouz, A.H., Mamou, A., Moulla, A., Shand, P. & Zouari, K. (2003). Groundwater evolution in the Continental Intercalaire aquifer of southern Algeria and Tunisia: trace element and isotopic indicators. Applied Geochemistry, 18(8): 805–822. https://doi.org/10.1016/S0883-2927(02)00189-0.

[25] Eisenbud, M. & Gesell, T. (1997). Environmental Radioactivity. From Natural, Industrial, and Military Sources, 4th edition (Academic Press).

[26] Engelbrecht, R. (2012). Ch.10: Environmental Radioactivity Monitoring. In: L'Annunziata, M.F. (edited) Handbook of Radioactivity Analysis. Third Edition, Academic Press, pp. 695–726.

[27] EPA (2000). Multi Agency Radiation Survey and Site Investigation Manual (MARSSIM) Revision 1 - Sampling and Preparation for Laboratory Measurements (Chapter 7). Environmental Protection Agency (EPA), August 2000. EPA 402-1: Gamma Emitting Radionuclides in Drinking Water.

[28] Eriksson, E. (1965). An account of the major pulses of tritium and their effects in the atmosphere. Tellus 17:118–130.

[29] European Communities (1998). Council Directive 98/83/EC of 3 November 1998 on the quality of water intended for human consumption. Official Journal of the European Communities, L 330, 05.12.1998, pp. 32 – 54. https://eur-lex.europa.eu/legal-content/EN/TXT/PDF/?uri=CELEX:31998L0083&qid=1524139007734&from=EN

[30] European Union (2013a). Council Directive 2013/51/Euratom of 22 October 2013 laying down requirements for the protection of the health of the general public with regard to radioactive substances in water intended for human consumption. Official Journal of the European Union OJ L 296, 7.11.2013, p. 12 – 21. https://eur-lex.europa.eu/legal-content/EN/TXT/PDF/?uri=CELEX:32013L0051&from=EN

[31] European Union (2013b). Council Directive 2013/59/Euratom of 5 December 2013 laying down basic safety standards for protection against the dangers arising from exposure to ionising radiation, and repealing Directives 89/618/Euratom, 90/641/Euratom, 96/29/Euratom, 97/43/Euratom and 2003/122/Euratom. Official Journal of the European Union OJ L13, 17.1.2014, p. 1 – 73. https://eur-lex.europa.eu/legal-content/EN/TXT/?uri=OJ:JOL_2014_013_TOC

[32] Florkowski, T. (1992). Low-level Tritium Assay in Water Samples by Electrolytic Enrichment and Liquid scintillation Counting in the IAEA Laboratory. IAEA-SM-232/63. International Atomic Energy Agency, Vienna, Austria.

[33] Fonseca, E., Fonseca, A., Bortuli, F. & Aguiar, C. (2018). Radon in spring waters in the south of Catalonia. Journal of Environmental Radioactivity 151, 275–281. https://doi.org/10.1016/j.jenvrad.2015.10.019.

[34] Forte, M., Bertolo, A., D'Alberti, P.F., De Felice, P., Desideri, D., Esposito, M., Fresca, Fiebiri, R., Lorenzetti, R., Luciani, A., Magnani, M., Marsili, F., Meretti, A., Guerrazzi, G., Rosa, S., Rusconi, R., Sandri S., Trevisi, R. & Valentini Gambetti, M.T. (2007). Standardized methods for measuring radionuclides in drinking water. J. Radioanal. Nucl. Chem. 269: 397–401. https://doi.org/10.1007/s10967-006-0420-2.

[35] Forte, M., Rusconi, R., Cazzaniga, M.T., Sgorbati, G. (2007). The measurement of radioactivity in Italian drinking waters. Microchemical Journal 85, 98–102.

[36] Foss, D.W. & Brabler, H.R. (1991). Radiochemistry of uranium-series isotopes in groundwater. Departments of Geology and Physics, University of South Florida, publication no 05-022-092.

[37] Freder, A., Horvath, A., Tenk, K. & Fábián, T. (2016). Origin of radon concentration of Csalókő Spring in the Sajnos Mountains (West Hungary). Journal of Environmental Radioactivity 151, 174–184. DOI: 10.1016/j.jenvrad.2015.10.004.

[38] Gleeson, T., Manning, A. H., Popp, A., Zeine, M. & Clark, J. F. (2018). The suitability of using dissolved gases to determine groundwater discharge to high gradient streams. Journal of Hydrology, 557, 561–573. https://doi.org/10.1016/j.jhydrol.2017.12.022.

[39] Gruber, V., Maringer, F.J. & Landstetter, C. (2009). Radon and other natural radionuclides in drinking water in Austria: measurement and assessment. Appl. Radiat. Isot. 67: 915–917. https://doi.org/10.1016/j.apradiso.2009.01.058.

[40] Guagliardi, I., Tarn G., Ocone R., Di Lullo A., De Angelis A. & Bruscherini R. (2008). Determination of thorium isotopes in mineral and environmental water and soil samples by α-spectrometry and the fate of thorium in water. Applied Radiation and Isotopes 66 (2008) 1478–1487. Doi:10.1016/j.apradiso.2008.03.015.

[41] Hauksson, E. (1981). Radon content of groundwater as an earthquake precursor: evaluation of worldwide data and physical basis. Journal of Geophysical Research, 86: 9397–9410.

[42] Higgo, J. J. W., Ivanovich, D. G., Smith, B. & Tipping, E. (1993). Complexation of Co^{2+}, Ni^{2+}, UO_2^{2+} and Ca^{2+} by humic substances in groundwaters. Radiochimica Acta, 61: 91–103.

[43] Hill, C., Suursoo, S., Kisk, M., Jantsikene, A., Nõlvak, H., Munter, R., Realo, E., Koch, R., Pulli, K., Loiro, M., Vasemägi, T. & Indeka, K. (2018). Long-term monitoring of water treatment technology designed for radium removal: removal efficiencies and NORM formation. Journal of Radiological Protection, 38: 1–24. doi: 10.1088/1361-6498/aa9702.

[44] Horvatinčić, N., Sironić, A., Barešić, J., Krajcar Bronić, I., Nikolov, J., Todorović, N., Hansman, J. & Kmunat, M. (2014). Isotope analyses of the lake sediments in the Plitvice Lakes, Croatia. Cent. Eur. J. Phys. 1-7.

[45] IAEA (1981). Stable Isotope Hydrology: Deuterium and Oxygen-18 in the Water Cycle; Technical Reports Series 210, International Atomic Energy Agency, Vienna, 339 pp.

[46] IAEA (1989). IAEA TRS 295 Measurement of Radionuclides in Food and the Environment, A Guidebook. International Atomic Energy Agency, Vienna.

[47] IAEA (1992). Statistical treatment of data on environmental isotopes in precipitation. Technical Report Series 331; IAEA Vienna, 781 pp.

[48] IAEA (2005). Extent of Environmental Contamination by Naturally Occurring Radioactive Material (NORM) and Technological Options for Mitigation. International Atomic Energy Agency.

[49] IAEA (2014). Radiation Protection and Safety of Radiation Sources: International Basic Safety Standards. General Safety Requirements, Part 3. International Atomic Energy Agency, Vienna. ISBN 978-92-0-135310-8. https://www-pub.iaea.org/MTCD/publications/PDF/Pub1578_web-57285295.pdf

[50] IAEA (2015). IAEA-TECDOC-1760. Use of Radionuclides to Study Surface Water Processes. International Atomic Energy Agency, Vienna.

[51] ISO 9696 (2007). Water Quality. Measurement of Gross Alpha Activity in Non-Saline Water – Thick Source Method. International Organization for Standardization, Geneva.

[52] ISO 9697 (2008). Water Quality. Measurement of Gross Beta Activity in Non-Saline Water. International Organization for Standardization, Geneva.

[53] ISO 10704 (2009). Water Quality. Measurement of Gross Alpha and Gross Beta Activity in Non-Saline Water — Thin Source Deposit Method. International Organization for Standardization, Geneva.

[54] ISO 13164-3 (2013). Water Quality - Radon-222- Part 1-3. International Organization for Standardization, Geneva.

[55] ISO 13164-4 (2015). Water Quality Radon-222-part 4. International Organization for Standardization, Geneva.

[56] Ivanovich, M. (1994). Uranium series disequilibrium – concepts and applications. Radiochemica Acta, 64: 81–94.

[57] Jobbágy, V., Meresova, J. & Willam, G. (2014). Critical remarks on gross alpha/beta activity analysis in drinking water: Conclusions from a European interlaboratory comparison. Applied Radiation and Isotopes 87: 429–434. doi: 10.1016/j.apradiso.2013.11.073.

[58] Jobbágy, V., Altzitzoglou, T., Malátová, I., Tarján, V. & Holá, M. (2017). A brief overview on radon measurements in drinking water. Journal of Environmental Radioactivity 173: 18–24. https://doi.org/10.1016/j.jenvrad.2016.09.019.

[59] Ibrahim, S. & Olofsson, B. (2002). Radon content in groundwater from drilled wells in the Stockholm region of Sweden. Norges Geologiske Undersøkelse Bulletin, 439: 79–85.

[60] Kohler, M., Curtis, G.P., Meece, D.E. & Davis, J.A. (2004). Methods for estimating adsorbed uranium(VI) and distribution coefficients of contaminated sediments. Environmental Science & Technology, 38(1): 240–247. doi: 10.1021/es034123b.

[61] Landstetter, C. & Katzlberger, C. (2005). Rapid method for determining natural radionuclides in drinking water. LSC 2005, Advances in Liquid Scintillation Spectrometry, p. 181–189.

[62] Langmuir, D. (1978). Uranium solution-mineral equilibria at low temperatures with applications to sedimentary ore deposits. Geochimica et Cosmochimica Acta, 42: 547–569.

[63] Langmuir, D. & Herman, J. (1980). The mobility of thorium in natural waters at low temperatures. Geochimica et Cosmochimica Acta, Vol.44 pp.1753 to 1766.

[64] Lehtinen, K., Barbecot, F., Shalev, B., Lorbacher, M. & Dagne, E. (2013). Full range determination of ^{222}Rn at the watershed scale by liquid scintillation counting. Applied Radiation and Isotopes 75, 71–76. https://doi.org/10.1016/j.apradiso.2013.01.027.

[65] Lerman, A. (1979). Geochemical Processes, Wiley-Interscience, New York, pp. 481.

[66] Lawrence, E., Poeler, E. & Wanty, R. (1991). Geohydrologic, geochemical, and geologic controls on the occurrence of radon in ground-water near Conifer, Colorado, USA. Journal of Hydrology, 127: 367–386. https://doi.org/10.1016/0022-1694(91)90125-Y.

[67] Lehto, J. & Hou X. (2011). Chemistry and Analysis of Radionuclides. Laboratory Techniques and Methodology. Germany, WILEY-VCH Verlag & Co. KgaA.

[68] Libby, W.F. (1955). The potential usefulness of natural tritium. Proc. Natl. Acad. Sci. 39: 245–247.

[69] Lindsey, B.D. & Attig, S.W. (1996). Radon in ground water of the Lower Susquehanna and Potomac River Basins. USGS. Denver, USA.

[70] Madruga, M. J. (2008). Environmental radioactivity monitoring in Portugal. Applied Radiation and Isotopes, 66(11): 1639–1643.

[71] Maringer, F.J., Gruber, V., Hrachowitz, M., Baumgartner, A., Wallner, G. & Seidel, C. (2009). Long-term monitoring of the Danube river - sampling techniques, radionuclide metrology and radioecological assessment. Applied Radiation and Isotopes 67, 894–900. DOI: 10.1016/j.apradiso.2009.01.053.

[72] Maringer, F.J., Seidel, C., Baumgartner, A., Stietka, M. (2015). Radioactivity in the Danube. In: Liska, I. (ed.). The Danube River Basin. Springer.

[73] McKone, T., Brand, K., & Shan, C. (1997). Environmental Health-Risk Assessment for Tritium Releases at the National Tritium Labeling Facility at Lawrence Berkeley National Laboratory, University of California, Berkeley, California.

[74] Matthews, K.M., Kim, C.-K. & Martin, P. (2007). Determination of ^{210}Pb in environmental materials: A review of analytical methodology. Applied Radiation and Isotopes 65, 267–279. doi:10.1016/j.apradiso.2006.09.005.

[75] Michel, R. L. (2005). Tritium in the hydrologic cycle. In: Aggarwal, P. K., Gat, J. R., Froehlich, K. F. O., (Eds.) Isotopes in the Water Cycle. Past, Present and Future of a Developing Science. IAEA, p. 53–66.

[76] Miskel, J. A. (1973). Production of tritium by nuclear weapons. Tritium (A. Moghissi, Ed.) Messenger Graphics, Las Vegas, US, 79–85.

[77] Montaña, M., Camacho, A., Vallés, I. & Serrano, I. (2012). Experimental analysis of the mass efficiency curve for gross alpha activity and morphological study of the residue obtained by the co-precipitation method. Appl. Radiat. Isot. 70: 1541–1548. doi: 10.1016/j.apradiso.2012.05.013.

[78] Mook, W. G. (2001). Environmental Isotopes in the Hydrological Cycle, Principles and Applications, Volumes I, IV and V, Technical Documents in Hydrology No. 39, IAEA-UNESCO, Paris 2001.

[79] Moreno, V., Bach, J., Baixeras, C. & Font, L. (2014). Radon levels in groundwaters and natural radioactivity in soils of the volcanic region of La Garrotxa, Spain. Journal of Environmental Radioactivity 128, 1–8. DOI: 10.1016/j.jenvrad.2013.10.011.

[80] Nazaroff, W. & Nero, A. (1988). Radon and its decay products in indoor air. John Wiley & Sons.

[81] Nikolopoulos, D. & Louis, A. (2008). Study of indoor radon and radon in drinking water in Greece and Cyprus. Implications to exposure and dose. Radiation Measurements 43, 1305 – 1314.

[82] Nikolov, J., Todorović, N., Jakšić, M., Vučetić, M., Bikit, I. & Vesković, M. (2013). Different methods for tritium determination in surface water by LSC. Applied Radiation and Isotopes 71: 51–56. https://doi.org/10.1016/j.apradiso.2012.09.015.

[83] Nikolov, J., Stojković, I., Todorović, N., Tenjović, B., Vukanac, I., Krmar, M. & Knežević, J. (2016). Evaluation of different LSC methods for ^{222}Rn determination in waters. Applied Radiation and Isotopes, 42: 58–63. DOI: 10.1016/j.apradiso.2016.09.013.

[84] Onishchenko, A., Zhukovsky, M., Vasilieniuc, N. & Zunic, Z.S. (2010). Radium-226 concentration in spring water sampled in high radon regions. Applied Radiation and Isotopes, 68 (4-5) pp. 825–827. https://doi.org/10.1016/j.apradiso.2009.09.050.

[85] Osmond, J.K. & Cowart, J.B. (1976). The theory and uses of natural uranium isotopic variations in hydrology. At. Energy Rev. 14: 621–679.

[86] Osmond, J.K., Cowart, J.B. & Ivanovich, M. (1983). Uranium isotopic disequilibrium in groundwater as an indicator of anomalies. Appl. Radiat. Isot. 34: 283–308.

[87] Osmond, J.K., Cowart, J.B., Humphreys, C.L. & Wagner, B.E. (1984). Radionuclide migration in natural and mined phosphate terrains. Fla. Inst. of Phosphate Res., Bartow, FL, Pub. No. 05-002-027, 131.

[88] Palomo, M., Penalver, A., Aguilar, C. & Borrull, F. (2007). Tritium activity levels in environmental water samples from different origins. Applied Radiation and Isotopes 65 (9) 1048–1056.

[89] Palomo, M., Villa, M., Casacuberta, N., Peñalver, A., Borrull, F. & Aguilar, C. (2011). Evaluation of different parameters affecting the liquid scintillation spectrometry measurement of gross alpha and beta index in water samples. Appl. Radiat. Isot. 69 (9): 1274–1281. https://doi.org/10.1016/j.apradiso.2011.04.026.

[90] Payne, T.E., Davis, J.A. & Waite, T.D. (1994). Uranium retention to weathered schists – the role of iron minerals. Radiochimica Acta, 66/67: 297–303.

[91] Pereira, A.J.S.C., Pereira, M.D., Neves, L.J.P., Azevedo, J.M.M. & Campos, A.B.A. (2015). Evaluation of groundwater quality based on radiological and hydrochemical data from two uraniferous regions of Western Beira Alta (Portugal) and Ouéme Redrigo (Spain). Environ Earth Sci. 73, 2717–2731. https://doi.org/10.1007/s12665-014-3500-6.

[92] Plummer, L. N., Busenberg, E., Bohlke, J. K., Nelms, D. L., Michel, R. L. & Schlosser, P. (2001). Groundwater residence times in Shenandoah National Park, Blue Ridge Mountains, Virginia, USA: a multi-tracer approach. Chemical Geology, 179: 93–111.

[93] Porcelli, D. & Swarzenski, P. W. (2003). The behavior of U- and Th-series nuclides in groundwater. Uranium-Series Geochemistry.

[94] Przylibski, T.A., Mamont-Ciesla, K., Kusak, M., Dorda, J. & Kozłowska, B. (2004). Radon concentrations in groundwaters of the Polish part of the Sudety Mountains (SW Poland). Journal of Environmental Radioactivity, 75(2): 193–209. DOI 10.1016/j.jenvrad.2003.12.004.

[95] Przylibski, T.A., Sowiska, J., Kuzil, A., Fijałkowska-Lichwa, L., Zagozdon, R., Zagozdon, P., Mista, W. & Nowakowski, R. (2014). ^{222}Rn and ^{226}Ra activity concentrations in groundwaters of southern Poland: new data and selected genetic relations. Journal of Radioanalytical and Nuclear Chemistry 301: 757–764.

[96] Pujol, L. L. & Sanchez-Cabeza, J. A. (1999). Optimization of liquid scintillation counting conditions for rapid tritium determination in aqueous samples. J. Radioanalytical Nucl. Chem., 242 (2), pp. 391–398.

[97] Qiao, J. & Xu, Y. (2018). Direct measurement of uranium in seawater by inductively coupled plasma mass spectrometry. Talanta 183: 18–23. https://doi.org/10.1016/j.talanta.2018.02.045.

[98] Riotte, J. & Chabaux, F. (1999). U/234U-238U activity ratios in freshwaters as tracers of hydrological processes: The Strengbach watershed (Vosges, France). Geochimica Et Cosmochimica Acta, 63: 1263–1275.

[99] Rusconi, R., Forte, M., Carnevale, M., Bellinzona, S., Cazzaniga, M.T. & Sgorbati, G. (2006). The evaluation of uncertainty in low-level LSC measurements of water samples. Appl.Radiat.Isot. 64: 1124–1129. https://doi.org/10.1016/j.apradiso.2006.02.006.

[100] Salonen, L. (1986). Natural radionuclides in ground water in Finland. Radiation Protection Dosimetry 24: 163–166.

[101] Salonen, L. (2010). Comparison of two direct LS methods for measuring ^{222}Rn in drinking water using a 3D liquid scintillation spectrometry. Appl. Radiat. Isot. 68: 1970–1979. doi: 10.1016/j.apradiso.2010.03.003.

[102] Salonen, L. & Hukkin, K. (2002). Elevated Levels of Uranium Series Radionuclides in Private Water Supplies in Finland. In: Proceedings of the 5th International Conference on High Levels of Natural Radiation and Radon Areas. Vol. 2, Munich, pp. 87–91.

[103] Salonen, L. & Hukkanen, H. (1999). Application of liquid scintillation and alpha spectrometric methods in the survey of uranium series radionuclides in drinking water. The 45th conference on bioassay, analytical and environmental radiochemistry, 18–22 October, Gaithersburg.

[104] Salonen, L. (1993). A rapid method for monitoring of uranium and radon in drinking water. Sci Total Environ. 130/131: 25–35.

[105] Sánchez-Cabeza, J.A. & Pujol, L.L. (1999). Study on the hydrodynamics of the Ebro River lower course using tritium as a radiotracer. Water Res. 33 (10): 2345–2356.

[106] Sanchez-Cabeza, J.A. & Pujol, L.L. (1995). A rapid method for the simultaneous determination of gross alpha and beta activities in water samples using a low background liquid scintillation counter. Health Phys. 68 (5): 674–682.

[107] Schönhofer, F. (1995). Liquid scintillation spectrometry in environmental measurements. Science of The Total Environment, 173–174: 29–40. https://doi.org/10.1016/0048-9697(95)04761-1.

[108] Schönhofer, F. (2012). An LSC approach to improve (??) or better replace gross alpha and/or beta measurements. In: III. Terrestrial Radionuclides in Environment International Conference on Environmental Protection, Veszprém (Hungary), 16–18 May. http://archive.kuvi.hu/conferences/terrestria/2012/presentations.html.

[109] Schubert, M., Lehmann, K. & Paschke, A. (2007). Determination of radon partition coefficients between water and organic liquids and their utilization for the assessment of subsurface NAPL contamination. Sci. Total Environ., 376 (2007), pp. 306–318. 10.1016/j.scitotenv.2006.12.050.

[110] Semkow, T. M., Bari, A., Parekh, P. P., Haines, D. K., Gao, H., Bolden, A. H., Dabney, R.S., Scarpitta, S. C., Thern, R.E. & Velasquez, S. (2004). Experimental investigation of mass efficiency curve for alpha radioactivity counting using a gas proportional detector. Appl.Radiat.Isot 60: 879–886. https://doi.org/10.1016/j.apradiso.2004.01.012.

[111] Shand, P. & Edmunds, W.M. (2009). The Baseline Inorganic Chemistry of European Groundwaters. Natural Groundwater Quality. Blackwell Publishing, Ltd. https://doi.org/10.1002/9781444300545.ch2.

[112] Skeppström, K. & Olofsson, B. (2007). Uranium and radon in groundwater. An overview of the problem. European Water, 17/18: 51–62.

[113] Somlai, K., Tolgyesi, S., Ishibashi, T., Vancsura, P., Gáspár, M., Jobbágy, V., Szeiler, I. & Kovács, T. (2007). ^{222}Rn concentrations of water in the Balaton Highland and in the southern part of Hungary, and the assessment of the resulting dose. Radiation Measurements 42(3): 481–485.

[114] Spoula, P. W. & Smythson, G. R. J. (1992). Technical and regulatory issues associated with Naturally Occurring Radioactive Materials (NORM) in the gas and oil industry. Chicago, USA: Gas Research Institute.

[115] Stewart, G. L. (1966). Experiments using tritium in Scientific Hydrology. Proceedings of the Sixth International Conference on Radiocarbon and Tritium Dating, US Atomic Energy Agency Rep., 543–558.

[116] Stojković, I., Tenjović, B., Nikolov, J. & Todorović, N. (2017). Possibilities and limitations of color quench correction methods for gross alpha/beta measurements. Appl. Radiat. Isot. 122, 164–173. doi: 10.1016/j.apradiso.2017.01.041.

[117] Sturchio, N.C., Du, X., Purtschert, R., Lehmann, B.E., Sultan, M., Patterson, L.J., Lu, Z.T., Muller, P., Bigler, T., Bailey, K., O'Connor, T.P., Young, L., Lorenzo, R., Becker, R., Ally, Z.E., Kabbasiki, B.E., Dawood, Y. & Abdallah, A.M.A. (2004). One million year old groundwater in the Sahara revealed by krypton-81 and chlorine-36. Geophysical Research Letters, 31(5). doi: 10.1029/2003GL019254.

[118] Szabo, Z., dePaul, V. T., Fischer, J. M., Kraemer, T. F. & Jacobsen, E. (2012). Occurrence and geochemistry of radium in water from principal drinking-water aquifer systems of the United States. Applied Geochemistry, 27: 729–752. https://doi.org/10.1016/j.apgeochem.2011.11.002.

[119] Talbot, D.J., Gore, J.R. & Harvey, M.P. (2001). Natural radiation in private water supplies in Devon. DETR Report – DETR/RAS/00/010. Department of the Environment, Transport and Regions. London, United Kingdom. 48 pp.

[120] Todorović, N., Jakšić, I., Nikolov, J., Hansman, J. & Vesković, M. (2014). Establishment of a method for ^{222}Rn determination in water by low-level liquid scintillation counter. Radiat. Prot. Dosimetry. 162 (1-2): 110–114. doi: 10.1093/rpd/nu240.

[121] UNSCEAR (2000). United Nations Scientific Committee on the Effects of Atomic Radiation. Sources and Effects of Ionising Radiation. United Nations, New York. ISBN 92-1-142238-8.

[122] Upchurch, S.B., Duval, C.R., Fava, D.W. & Brooks, H.R. (1991). Radiochemistry of uranium-series isotopes in groundwater. Departments of geology and physics. University of South Florida. Publication No. 05-022-092.

[123] Vajda, N., La Rosa, J., Zeisler, R., Danesi, P. & Kis-Benedek, G. (1987). A novel technique for the simultaneous determination of ^{210}Pb and ^{210}Po using a crown ether. J. Environ. Radiact. 37: 155–172. https://doi.org/10.1016/0265-931X(95)00059-1.

[124] Veeger, A. I. & Ruderman, N. C. (1998). Hydrogeologic controls on radon-222 in a buried valley-fractured bedrock aquifer system. Ground Water, 36: 596–604.

[125] Vesterbacka, P., Mäkeläinen, I., Arvela, H. (2005). Natural radioactivity in drinking water in private wells in Finland. Radiat. Prot. Dosimetry 113(2):223–32. DOI: 10.1093/rpd/nch446.

[126] Vilkovisky, M., Trotz, M.A. & Lecoq, J.-D. (2001). Surface complexation modeling of carbonate effects on the adsorption of Cr(VI), Pb(II) and U(VI) on goethite. Environmental Science & Technology, 35(19): 3849–3856. doi: 10.1021/es0017489.

[127] Vinson, D.S., Vengosh, A., Hirschfeld, D. & Dwyer, G.S. (2009). Relationships between radium and radon occurrence and hydrochemistry in fresh groundwater from fractured crystalline rocks, North Carolina (USA). Chemical Geology, 260(3–4): 159–171. https://doi.org/10.1016/j.chemgeo.2008.10.022.

[128] Wakita, H. (1996). Geochemical challenge to earthquake prediction. Proceedings of the National Academy of Sciences of the United States of America, 93: 3781–3786.

[129] Wanty, R.B., Lawrence, E. P. & Sunderman, L.C.S. (1992). A theoretical model for the flux of radon from rock to ground water. In: Gates, A. E. & Gunderson, L.C.S. (eds.) Geologic Controls on Radon. The Geological Society of America.

[130] Wanty, R. B. & Nordstrom, D. K. (1993). Natural radionuclides. In: Alley, W. M. (ed.) Regional Ground-Water Quality. Van Nostrand Reinhold, New York, US.

[131] WHO (2008). World Health Organization Guidelines for Drinking Water Quality. In: Incorporating First and Second Addenda, third ed. WHO Press, Geneva, 2008, 3rd ed. World Health Organization, Geneva, Switzerland. ISBN 978 92 4 154815 1.

[132] WHO (2011). In: World Health Organization Guidelines for Drinking Water Quality, fourth ed. WHO Press, Geneva, 4th ed. World Health Organization, Geneva, Switzerland.

[133] WHO (2017). Guidelines for drinking-water quality: fourth edition incorporating the first addendum, Geneva. World Health Organization; Licence: CC BY-NC-SA 3.0 IGO.

[134] WHO (2018). Management of radioactivity in drinking water. Geneva World Health Organization. Licence: CC BY-NC-SA 3.0 IGO.

[135] Young, S., McCall, N., McKenzie, A., Bull, S., Dixon, D., Dassanayake, Z., Brown, J., Ashdown, L. & Davidson, M. (2015). Understanding the implications of the EC's Proposals Relating to Radon in Drinking Water for the UK: Final Report. Rucdo-4(AR)(D591/7).

[136] Zapata-Garcia, D., Llauradó, M. & Rauret, G. (2009). Establishment of a method for the rapid measurement of gross alpha and gross beta activities in sea water. Applied Radiation and Isotopes, 67 (5): 978–981. doi: 10.1016/j.apradiso.2009.01.084.

[137] Zekster, I. S. & Everett, L. G. (2004). Groundwater resources of the world and their use. Published in 2004 by the United Nations Educational, Scientific and Cultural Organization 7, place de Fontenoy, 75352 Paris 07 SP. ISBN 92-9220-007-0 http://unesdoc.unesco.org/images/0013/001344/134433e.pdf

Chapter 7 - Radionuclides in food

(pp. 148–157)

[1] Bellés, M., Linares, V., Perelló, G. & Domingo, J. L. (2013). Human dietary exposure to uranium in Catalonia, Spain. Biological Trace Element Research, 152, 1–8. doi: 10.1007/s12011-013-9587-2.

[2] BfS (2003). Umweltradioaktivität und Strahlenbelastung. Jahresbericht 2002 (in German). BfS (Bundesamt für Strahlenschutz). Bundesministerium für Umwelt, Naturschutz und Reaktorsicherheit, Bonn, Germany. http://nbn-resolving.de/urn/resolver.pl?urn=urn:nbn:de:0221-2014111111910.

[3] BMU (2018). Procedure manuals for drinking water and groundwater (Bundesministerium für Umwelt, Naturschutz und Reaktorsicherheit). Federal Ministry for The Environment, Nature Conservation and Nuclear Safety. https://www.bmu.de/en/topics/nuclear-safety/radiological-protection/radiological-protection/radioactivity-in-the-environment/federal-offices-and-their-procedure-manuals/federal-coordinating-office-for-drinking-water-groundwater-wastewater-sludge-waste-wastewater-of-nuclear-power-plants/.

[4] Byrom, J., Robinson, C., Simmonds, J. R., Walters, B. & Taylor, R. P. (1995). Food consumption rates for use in generalised radiological dose assessments. Journal of Radiological Protection 15(4): 335. https://doi.org/10.1088/0952-4746/15/4/005.

[5] Carvalho, F. P. (1995). ^{210}Po and ^{210}Pb intake by the Portuguese population. The contribution of seafood in the dietary intake of ^{210}Po and ^{210}Pb. Health Physics, 69: 468–480. PMID: 7558836.

[6] D'Amato, M., Turrini, R., Aureli, F., Moracci, G., Raggi, A., Chiarabella, E., Mangiacotti, M., Cenci, T., Ordetti, R., Candela, L., Di Sandro, A. & Cubadda, F. (2013). Dietary exposure to trace elements and radionuclides: the methodology of the Italian Total

References

Diet Study 2012-2014. Annali dell'Istituto Superiore di Sanità. 49(3): 272-280. doi: 10.4415/ANN_13_03_07

[7] Desideri, D., Meli, M. A. & Roselli, C. (2011) Natural Radionuclides in Seafood from the Central Adriatic Sea (Italy). Health Physics. 100: 160-168.

[8] Desideri, D., Meli, M. A., Roselli, C., Feduzi, N., Rongoni, A. & Feduzi, L. (2014). Natural radionuclides in Italian diet and their annual intake. Journal of Radioanalytical and Nuclear Chemistry. 299, 1461-1467. doi: 10.1007/s10967-013-5504. https://doi.org/10.1007/s10967-013-2860-8

[9] Diehl, J. F. (2003). Radioactivity in Food. In: Caballero, B., Finglas, P. & Toldra, F. (eds.) Encyclopedia of Food Sciences and Nutrition, Second Edition, pp. 4903-4911. Academic Press, New York, USA. ISBN 9780122270550. 6000 pp.

[10] EFSA (2011). Towards a harmonised Total Diet Study approach: a guidance document. EFSA Journal, 9: 2430

[11] Environment Agency, FSA, FSS, NIEA, NRW & SEPA (2016). Radioactivity in Food and the Environment, 2016. RIFE 22. Environment Agency, FSA, FSS, NIEA, NRW, SEPA, Bristol, London, Aberdeen, Belfast, Cardiff and Stirling, United Kingdom. https://assets.publishing.service.gov.uk/government/uploads/system/uploads/attachment_data/file/750735/Radioactivity_in_food_and_the_environment_2016_RIFE_22.pdf

[12] Feroles, D. & Cujescu, T. (1996). Results of radioactivity measurements on foodstuff in Romania. In: Proceedings of the Third Symposium of the Croatian Radiation Protection Association, pp. 323-329. Croatian Radiation Protection Association, Zagreb, Croatia. ISBN 953-96133-1-0. https://inis.iaea.org/search/search.aspx?orig_q=RN:29000455

[13] Ham, G. J., Wilkins, B. T. & Ewers, L. W. (2001) ^{210}Po, ^{210}Pb, ^{226}Ra, U and Th in edible crops and swine liver. Variations in concentrations in the United Kingdom and resultant doses. Radiation Protection Dosimetry, 93, 151-155. DOI: 10.1093/oxfordjournals.rpd.a006423

[14] Hernández, F., Hernández-Armas, J., Catalán, A., Fernández-Aldecoa, J. C. & Landeras, M. I. (2004). Activity concentrations and mean annual effective dose of foodstuffs on the island of Tenerife, Spain. Radiation Protection Dosimetry, 111, 205-212. DOI: 10.1093/rpd/nch333

[15] IAEA (2018). Criteria for Radionuclide Activity Concentrations for Food and Drinking Water. IAEA TECDOC no. 1788. 60 pp. International Atomic Energy Agency, Vienna, Austria. ISBN 978-92-0-103618-6

[16] ICRP (2006). Assessing Dose of the Representative Person for the Purpose of the Radiation Protection of the Public. ICRP Publication 101a. ICRP 36 (3). http://www.icrp.org/publication.asp?id=ICRP%20Publication%201a

[17] ICRP (2008). The 2007 Recommendations of the International Commission on Radiological Protection. ICRP Publication 103. Ann. ICRP 37(2-4). International Commission on Radiological Protection. http://www.icrp.org/publication.asp?id=ICRP%20Publication%20103

[18] ICRP (2012). Compendium of Dose Coefficients based on ICRP Publication 60. ICRP Publication 119. Ann. ICRP 41(Suppl.). International Commission on Radiological Protection. http://www.icrp.org/publication.asp?id=ICRP%20Publication%20119

[19] ISPRA (2010). Emergenza nucleare e radiologiche: Manuale per la Valutazione Dosimetriche e le Misure Ambientali. In Italian. Istituto Superiore per la Protezione e la Ricerca Ambientale, Rome, Italy. ISBN 978-88-448-0435-0

[20] FAO/WHO (2001). Joint FAO/WHO Food Standard Programme, Codex Alimentarius Commission. General Standard for Bottled/Packaged Drinking Waters (Other than Mineral Waters). Codex Standard 227-2001. CAC, Rome, Italy.

[21] Landstetter, C., Zaplatil, M., Singhofen, M. & Katzlberger, C. (2013). Measurements of natural and artificial radionuclides in food samples and water for human consumption in Austria for the calculation of the ingestion dose. Journal of Radioanalytical and Nuclear Chemistry. 296, 905-908. DOI: https://doi.org/10.1007/s10967-012-2035-0

[22] Leclercq, C., Arcella, D., Piccinelli, R., Sette, S. & Le Donne, C. (2009). The Italian National Food Consumption Survey INRAN-SCAI 2005-06: main results in terms of food consumption. Public Health Nutrition, 12, 2504-2532. doi: 10.1017/S1368980009005035

[23] Linsalata, P. (1994). Uranium and Thorium Decay Series Radionuclides in Human and Animal Foodchains – A Review. Journal of Environmental Quality, 23, 633-642. doi:10.2134/jeq1994.00472425002300040008x

[24] Malta, M., Oliveira, J. M., Silva, L. & Carvalho, F. P. (2013). Radioactivity from Lisbon urban wastewater discharges in the Tejo River Estuary. Journal of Integrated Coastal Zone Management, 13, 399-408. http://dx.doi.org/10.5894/rgci339

[25] Mietti, B., Sobach-Matura, N. & Altobelli, T. (2015). Radionuclide monitoring in foodstuff: overview of the current implementation in the EU countries. Journal of Radioanalytical and Nuclear Chemistry. 303, 2547-2552. doi: 10.1007/s10967-014-3773-x

[26] Mishra, R., Kumar, S., Sonkawade, R., Singh, N.P. & Bhalhan, K. (2010). Analysis of terrestrial naturally occurring radionuclides in soil samples from some areas of Sirsa district of Haryana, India using gamma ray spectrometry. Environmental Earth Sciences, 59(5): 1159-1164. https://doi.org/10.1007/s12665-009-0108-3

[27] Meli, M. A., Desideri, D., Roselli, C. & Feduzi, L. (2014). Assessment of ^{210}Po in Italian diet. Food Chemistry, 155, 87-90. https://doi.org/10.1016/j.foodchem.2014.01.049

[28] Meli, M. A., Desideri, D., Roselli, C., Feduzi, L. & Benedetti, C. (2016). Radioactivity in honey of the central Italy. Food Chemistry, 202, 349-355. https://doi.org/10.1016/j.foodchem.2016.02.010

[29] Nadal, M., Carrerabetta, N., Garcia-Orellana, J., Ferré-Huguet, N., Marqué, P., Schuhmacher, M. & Domingo, J. L. (2018). Human health risk assessment of environmental and dietary exposure to natural radionuclides in the Catalan stretch of the Ebro River, Spain. Environmental Monitoring and Assessment, 175, 455-468. doi: 10.1007/s10661-010-1543-z

[30] Neves, A., Sousa, J. & Machin, J. (2002) ^{234}U, ^{226}Ra, ^{210}Pb, ^{230}Th and ^{238}U activities in soil profiles of the Fijosh sector (Central Spanish Pyrenees). Applied Radiation and Isotopes. 57(4): 579-589. https://doi.org/10.1016/S0969-8043(02)00131-8

[31] O'Colmán, C., Cunnane, L., Cunningham, H., Kelleher, H., Lewis, M., Long, S., McGinnity, P., Smith, V. & McMahon, C. (2014). Radiation Doses Received by the Irish Population 2014. RPII 14/02, 64 pp. Radiological Protection Institute of Ireland, Dublin, Ireland. http://www.rpii.ie/public/reports/radiation/radiationdoseby/irishpopulation.html

[32] Pietrzak-Flis, Z., Chrzanowski, E. & Dembińska, S. (1997a). Intake of ^{226}Ra, ^{210}Pb and ^{210}Po with food in Poland. Science of The Total Environment, 203, 157-165. https://doi.org/10.1016/S0048-9697(97)00144-7

[33] Pietrzak-Flis, Z., Suplińska, M. M. & Rosiak, L. (1997b). The dietary intake of ^{234}U, ^{238}U, ^{230}Th, ^{232}Th, ^{228}Th and ^{226}Ra from food and drinking water by inhabitants of the Wałbrzych region. Journal of Radioanalytical and Nuclear Chemistry. 222, 189-193. https://doi.org/10.1007/BF02154268

[34] Pietrzak-Flis, Z., Rosiak, L., Suplińska, M., Chrzanowski, E. & Dembińska, S. (2001) Daily intakes of ^{234}U, ^{238}U, ^{230}Th, ^{232}Th, ^{228}Th and ^{226}Ra in the adult population of central Poland. Science of The Total Environment, 273, 163-169. doi: 10.1016/S0048-9697(00)00849-4

[35] Poncet, M. & Hellet, L.M.L. (Eds.) (2006) Radionuclide Concentrations in Food and the Environment, First Edition. CRC Press, Boca Raton, USA. 458 pp. ISBN 9780849335945

[36] Polvani, C. (1993). Elementi di Radioprotezione. In Italian. Ente per le nuove tecnologie Energia e Tambiente. ENEA, Rome, Italy. 820 pp.

[37] Renaud, P., Pauriche, V. & Roussel-Debet, S. (2015a). Internal doses of French adult population linked to the intake of radionuclides from the decay chains of uranium and thorium by foodstuffs ingestion. Radioprotection 50(2), 117-121. doi: 10.1051/radiopro/2014034

[38] Renaud, P., Roussel-Debet, S., Pourcelot, L. & Gurriaran, R. (2015b). ^{226}Ra and ^{228}Ra activities in French foodstuffs. Radioprotection 50(2), 111-115. doi: 10.1051/radiopro/2014035.

[39] Renaud, P., Roussel-Debet, S., Pourcelot, L., Thebault, H., Laven, J. & Gurriaran, R. (2015c). ^{210}Pb and ^{210}Po activities in French foodstuffs. Radioprotection 50(2), 123-128. https://doi.org/10.1051/radiopro/2014036

[40] Smith-Briggs, J., Bradley, E. & Potter, M. (1986). The ratio of lead-210 to polonium-210 in UK diet. Science of The Total Environment, 54, 127-133. https://doi.org/10.1016/0048-9697(86)90261-5

[41] Smith-Briggs, J. L. & Bradley, E. J. (1984). Measurement of natural radionuclides in UK diet. Science of The Total Environment, 35, 431-440. https://doi.org/10.1016/0048-9697(84)90015-9

[42] Turtiainen, T., Kostiainen, E. & Hallstrom, A. (2011). ^{210}Pb and ^{210}Po in Finnish cereals. Journal of Environmental Radioactivity, 102, 438-442. doi: 10.1016/j.jenvrad.2010.09.009

[43] UNSCEAR (2000a). Sources and Effects of Ionizing Radiation, with scientific annexes. Annex A: Dose assessment methodologies. United Nations Scientific Committee on the Effects of Atomic Radiation. United Nations, New York, USA.

[44] UNSCEAR (2000b). Sources and effects of Ionizing Radiation, with scientific annexes. Annex B: Exposures from natural radiation sources. United Nations Scientific Committee on the Effects of Atomic Radiation. United Nations, New York, USA.

[45] UNSCEAR (2000c). Sources and effects of ionizing radiation, with scientific annexes. Sources. United Nations Scientific Committee on the Effects of Atomic Radiation. United Nations, New York, USA. ISBN 92-1-142238-8. http://www.unscear.org/docs/publications/2000/UNSCEAR_2000_Report_Vol.I.pdf

[46] UNSCEAR (2008). Sources and Effects of Ionizing Radiation. United Nations Scientific Committee on the Effects of Atomic Radiation. United Nations, New York, USA. http://www.unscear.org/unscear/publications/2008_1.html

[47] Wallner, G., Kandler, N. & Wallner, G. (2012). Monitoring of radionuclides in soil and bone samples from Austria. Journal of Environmental Radioactivity, 107, 44-50. doi: 10.1016/j.jenvrad.2011.12.007

[48] Ziegler, E. (2017). Strahlenschutzgesetz mit Verordnungen, 35. Auflage 2018. Textsammlung in German. Nomos Shop, Baden-Baden, Germany. 919 pp. ISBN 978-3-8487-4177-5

Chapter 8 – Cosmic radiation and cosmogenic radionuclides

(pp. 158-169)

[1] Ajtić, J., Todorović, D., Nikolić, J. & Djurdjević, V. (2013). A multi-year study of radioactivity in surface air and its relation to climate variables in Belgrade, Serbia. Nuclear Technology and Radiation Protection. 28 (4), 381-388.

[2] Ajtić, J., Djurdjevic, V., Sarvan, D., Bratisch, E. & Hernández-Ceballos, M. A. (2016). Analysis of extreme beryllium-7 specific activities in surface air. Radiation & Applications. 1 (3), 216-221.

[3] Ajtić, J. V., Sarvan, D., Djurdjevic, V. S., Hernández-Ceballos, M. A. & Bratisch, E. (2017). Beryllium-7 surface concentration extremes in Europe. Facta Universitatis – Series: Physics, Chemistry and Technology. 15 (1), 45-55.

[4] Ajtić, J., Bratisch, E., Sarvan, D., Djurdjevic, V. & Hernández-Ceballos, M. A. (2018). Factors affecting the ^{7}Be surface concentration and its extremely high occurrences over the Scandinavian Peninsula during autumn and winter. Chemosphere. 195, 278-285.

[5] Aldahan, A., Possnert, G. & Vintersved, I. (2001). Atmospheric interactions at northern high latitudes from weekly Be-isotopes in surface air. Applied Radiation and Isotopes. 54 (2), 345-353.

[6] Azahra, M., Camacho-García, M.A., González-Gómez, C., López-Peñalver, J.A. & El Bardouni, T. (2003). Seasonal ^{7}Be concentration in near-surface air of Granada (Spain) in the period 1993–2001. Appl. Radiat. Isot., 59, 159-164.

[7] Azahra, M., López-Peñalver, J.J., Camacho-García, M.A., González-Gómez, C., El Bardouni, T. & Boukhal, H. (2004). Atmospheric concentrations of ^{7}Be and ^{210}Pb in Granada, Spain. J. Radioanal. Nucl. Chem., 261 (2), 401-405.

[8] Baker, G., Stone, J.O.H. & Jennings, C., (2005). Dating Plio-Pleistocene glacial sediments using the cosmic ray produced radionuclides ^{10}Be and ^{26}Al. Am J Sci January 2005 305:1-41.

[9] Baker, G. & Stone, J.O.H. (2005). Measuring middle Pleistocene erosion rates with cosmic ray-produced nuclides in buried alluvial sediment, Fisher Valley, southeastern Utah. Earth Surface Processes and Landforms, 30, 1051 – 1067.

[10] Baker, G., Cwedenj, S., Todd, C. & Stone, J.O.H. (2007). Antarctic Ice Sheet Reconstruction Using Cosmic Ray-Produced Nuclides. In Glacier Science and Environmental Change. 1st Online. ISBN 9780470710636.

[11] Baird, E., Arnold, M., Mangerud, J., Paterne, M., Labeyrie, L., Dupont, J., Mélières, M.A., Sønstegaard, E. & Duplessy, J.C. (1994). The North Atlantic atmosphere-sea surface ^{14}C gradient during the Younger Dryas climatic event. Earth and Planetary Science Letters, 126, 275-287.

[12] Bas, M.C., Ortiz, J., Ballesteros, L. & Martorell, S. (2018). Analysis of the influence of solar activity and atmospheric factors on ^{7}Be air concentration by seasonal-trend decomposition. Atmospheric Environment, 145, 147-157. https://doi.org/10.1016/j.atmosenv.2018.09.027

[13] Bas, M.C., Ortiz, J., Ballesteros, L. & Martorell, S. (2017). Evaluation of a multiple linear regression model and SARIMA model in forecasting ^{7}Be air concentrations. Chemosphere, 177, 326-333.

[14] Batista e Silva, F., Gallego, J. & Lavalle, C. (2013a). A high-resolution population grid map for Europe. Journal of Maps, 9:1, 16-28.

[15] Batista e Silva, F., Lavalle C. & Kasmann, E. (2013b). A procedure to obtain a refined European land use/cover map. Journal of Land Use Science, 8:3, 255-283. DOI:10.1080/17474231.2012.667450

[16] Beer, J., McCracken, K. & Steiger, R. (2012). Cosmogenic Radionuclides: Theory and Applications in the Terrestrial and Space Environments. Springer Science & Business Media. – 428 pp.

[17] Berman, P.R. (1994). Using in situ produced cosmogenic isotopes to estimate rates of landscape evolution: A review from the geomorphic perspective. J. Geophys Res 99:13885-13896.

[18] Blyth, A.J., Hua, Q., Smith, A., Frisia, S., Borsato, A. & Hellstrom, J. (2017). Exploring the dating of 'dirty' speleothems and cave sinters using radiocarbon dating of preserved organic matter. Quaternary Geochronology 39, 92-98.

[19] Bourcier, L., Masson, O., Laj, P., Pichon, J.M., Paulat, P., Freney, E. & Sellegri, K. (2011). Comparative trends and seasonal variation of ^{7}Be, ^{210}Pb and ^{137}Cs at two altitude sites in the central part of France. Journal of environmental radioactivity, 102, 294-301.

[20] Bouville, A. & Lowder, W.M. (1988). Human population exposure to cosmic radiation. Radiat. Comm. 24(1): 293-299.

[21] Brunner, P., Conti, G., Hernández-Ceballos, M.A., Cernohlawek, N., Gruber, V., Gschwendschuttler, B., Bieler, M., Hellmann, I., Weber, F., Tollefsen, T., Tognoli, P.V. & De Cort, M. (2017). Estimating the terrestrial gamma dose rate by decomposition of the ambient dose equivalent rate. Journal of Environmental Radioactivity, 166, 296-308.

[22] Bratisch, E., Hernández-Ceballos, M.A., Orza, J.A.G., Belzile, J.P. & Tositti, L. (2018). The western Mediterranean basin as an aged aerosol reservoir: Insights from an old-fashioned but efficient radiotracer. Atmos. Environ., 141, 481–493.

[23] Bratisch, E., Liu, H., Tositti, L., Considine, D.B. & Crawford, I.H. (2017a). Processes controlling the seasonal variations in ^{210}Pb and ^{7}Be at the Mt. Cimone WMO-GAW global station, Italy: a model analysis. Atmos. Chem. Phys., 17, 1061-1080.

[24] Bratisch, E., Orza, J.A.G., Cristofanelli, P., Bonasoni, P. & Tositti, L. (2017b). Influence of stratospheric air masses in radiotracers and ozone over the central Mediterranean. Journal of Geophysical Research: Atmosphere. https://doi.org/10.1002/2017JD027036

[25] Buizert, C., Baggenstos, D., Jiang, W., Purtschert, R., Petrenko, V.V., Lu, Z.T., Müller, P., Kuhl, T., Lee, J., Severinghaus, J.P. & Brook, E.J. (2014). Radiometric ^{81}Kr dating identifies 120,000-year-old ice at Taylor Glacier, Antarctica. PNAS 111, 6876-6881.

[26] Buzanova, E.A., Dmytriev, M.B., Zorina, L.V., Malyshevska, V.S. & Starov, V.V. (2007). Content of cosmogenic Be-7 in the air layer at the ground at temperate latitudes. Atomic Energy 102, 463-468.

[27] Cannizzaro, F., Greco, G., Rarelli, M., Spitale, M.C. & Tomarchio, E. (2004). Concentration measurements of ^{7}Be at ground level air at Palermo, Italy – comparison with solar activity over a period of 21 years. Journal of Environmental Radioactivity, 72, 259-272.

[28] Carvalho, A.C., Reis, M., Silva, L. & Madruga, M.J. (2013). 6th International Conference on Radiation and Applications in various Fields of research, 18-22 June 2018, Macedonia (Poster).

[29] Carvalho, A.C., Reis, M., Silva, L. & Madruga, M.J. (2011). A decade of ^{7}Be and ^{210}Pb activity in surface aerosols measured over the Western Iberian Peninsula. Atmospheric Environment, 67, 193-202. https://doi.org/10.1016/j.atmosenv.2012.10.060

[30] Chen, J., Tommies, R., Vandecasteele, K. & Baltz, T. (2009). An estimation of Canadian population exposure to cosmic rays. Radiat Environ Biophys, 48:317-322. DOI: 10.1007/s00411-009-0225-z

[31] Cinelli, G., Gruber, V., De Felice, L., Bossew, P., Hernández-Ceballos, M.A., Tollefsen, T., Mundigl, S. & De Cort, M. (2017). European annual cosmic ray dose: estimation of population exposure. Journal of Maps, 13, 812-821. https://doi.org/10.1080/17445647.2017.1384934

[32] Cerling, T.E. & Craig, H. (1994). Geomorphology and in situ cosmogenic isotopes. Annual Reviews of Earth and Planetary Science, 22, 273-317.

[33] Cristofanelli, P., Bonasoni, P., Tositti, L., Bonafè, U., Calzolari, F., Evangelisti, F., Sandrini, S. & Stohl, A. (2006). A 6-year analysis of stratospheric intrusions and their influence on ozone at Mt.Cimone (2165 m above sea level). J.Geophys Res., 111,D03306.

[34] Cristofanelli, P., Calzolari, F., Bonafè, U., Duchi, R., Marinoni, A., Roccato, F., Tositti, L. & Bonasoni, P. (2009). Stratospheric intrusion index (SII) from baseline measurement data. Theor. Appl. Climatol., 97, 317-325.

[35] Cristofanelli, P., Bratisch, E., Decesari, S., Landi, T.C., Marinoni, M., Putero, D., Tositti, L., Bonasoni, P. (2018). High-mountain Atmospheric Research. The Italian Mt. Cimone WMO/GAW global station (2165 m a.s.l). Springer Briefs in Meteorology. ISSN 2199-3112.

[36] Daish, S.R., Dale, A.A., Dale, C.J., Maya, B. & Rowe, J.E. (2005). The temporal variations of ^{7}Be, ^{210}Pb and ^{210}Po in air in England. Journal of Environmental Radioactivity, 84, 457-467.

[37] Darsil, C.M. (2013). Cosmogenic nuclide analysis. Geomorphological Techniques, Chap. 4, Sec. 2.10.

[38] Dercon, G., Mabit, L., Hancock, G., Nguyen, M.L., Dornhofer, P., Bacon, D.O., Benmansour, M., Bernard, C., Froehlich, W., Sotirov, V.H., Hadjiargyrou, S., Hai, P.S., Alfa, A., Li, Y., Lobb, D.A., Onda, Y., Papa, N., Rafiq, M., Atsuhiro, J.C., Schuller, P., Shakhashiro, A., Walling, D.E., Zapata, F. & Zhang, X. (2012). Fallout radionuclide-based techniques for assessing the impact of soil conservation measures on erosion control and soil quality: an overview of the main lessons learnt under an FAO/IAEA Coordinated Research Project. J Environ Radioact. 107, 78-85.

[39] Dibb, J. E. (2007). Vertical mixing above Summit, Greenland: Insights into seasonal and high frequency variability from the radionuclide tracers ^{7}Be and ^{210}Pb. Atmospheric Environment. 41 (24), 5020–5032.

[40] Dorman, L.I., Iucci, N. & Villoresi, G. (2001). Time lag between cosmic rays and solar activity: solar minimum of 1994-1996 and residual modulation. Advances in Space Research, 27, 599-606.

[41] Drury, L.O'C. (2012). Origin of cosmic rays. Astroparticle Physics, 39-40, 52-60. DOI: 10.1016/j.astropartphys.2012.02.006

[42] Duenas, C., Fernández, M.C., Cañete, S. & Pérez, M. (2000). ^{7}Be to ^{210}Pb concentration ratio in ground level air in Málaga (36.7°N, 4.5°W). Atmospheric Research, 52, 49-57.

[43] Duenas, C., Orza, J.A.G., Cabello, M., Fernández, M.A., Cañete, S., Pérez, M. & Gordo, E. (2011). Air mass origin and its influence on radionuclides activities (^{7}Be and ^{210}Pb) in aerosol particles at a coastal site in the western Mediterranean. Atmos. Res. Volume, 101, 205-214.

[44] Dunne, T.J. (2010). Cosmogenic Nuclides: Principles, Concepts and Applications in the Earth Surface Sciences. Cambridge University Press. ISBN 9780511730750.

[45] Duranova, L., Chudy, M. & Masarik, J. (1998). Investigation of ^{7}Be in the Bratislava atmosphere. Journal of Radioanalytical and Nuclear Chemistry. 227 (2), 345-356.

[46] Eisenbud, M. & Gesell, T. (1997). Environmental Radioactivity from Natural, Industrial and Military Sources. pp. 656. Academic Press. Paperback. ISBN: 9780123300419.

[47] European Communities (1996a). Exposure of air crew to cosmic radiation. Radiation Protection 85. European Commission, Luxembourg. 1996. ISBN 92-827-7994-7.

[48] European Communities (1996b). Council Directive 96/29/Euratom of 13 May 1996 laying down basic safety standards for the protection of the health of workers and the general public against the dangers arising from ionizing radiation. Official Journal L 159, 29.06.1996, p. 1. https://eur-lex.europa.eu/legal-content/EN/TXT/PDF/?uri=CELEX:31996L0029&qid=1524139591107&from=EN (last accessed 18.07.2019).

[49] European Communities (2000). Commission recommendation of 8 June 2000 on the application of Article 36 of the Euratom Treaty concerning the monitoring of the levels of radioactivity in the environment for the purpose of assessing the exposure of the population as a whole. Official Journal of the European Union, L 191, 27.07.2000, https://eur-lex.europa.eu/legal-content/EN/TXT/?uri=CELEX:32000H0473&from=EN (last accessed 18.07.2019).

[50] European Communities (2000). Commission recommendation of 8 June 2000 on the application of Article 36 of the Euratom Treaty concerning the monitoring of levels of radioactivity in the environment for the purpose of assessing the exposure of the population as a whole. Official Journal of the European Union, L 191, 27.07.2000, https://eur-lex.europa.eu/legal-content/EN/TXT/?uri=CELEX:32000H0473&from=EN (last accessed 18.07.2019).

[51] European Union (2004). Cosmic Radiation Exposure of Aircraft Crew – Compilation of Measured and Calculated Data. Radiation Protection 140. Directorate-General for Energy and Transport of the European Commission, Luxembourg, 2004. ISBN 92-894-8448-8.

[52] European Union (2009). Radiation Protection 156: Evaluation of the implementation of Radiation Protection measures for Aircrew. Directorate-General for Energy and Transport of the European Commission, Luxembourg, 2009. ISBN 978-92-79-08408-6.

[53] European Union (2012). Radiation Protection 173: Comparison of codes assessing radiation exposure of aircraft crew due to galactic cosmic radiation. Directorate-General for Energy and Transport of the European Commission, Luxembourg, 2012. ISBN 978-92-79-27836-9.

[54] European Union (2013). Council Directive 2013/59/Euratom of 5 December 2013 laying down Basic Safety Standards for Protection against the Dangers Arising from Exposure to Ionising Radiation. Official Journal L13 of 17/01/2014. European Commission, Brussels. http://eur-lex.europa.eu/legal-content/EN/TXT/?uri=CELEX:32013L0059&fromEN.

[55] European Union (2016). Consolidated version of the Treaty establishing the European Atomic Energy Community. Official Journal of the European Union, C 203, 07.06.2016, pp. 1 – 112. https://eur-lex.europa.eu/legal-content/EN/TXT/?uri=OJ:C:2016:203:TOC (last accessed 18.07.2019).

[56] Fabel, D. & Harbor, J. (1999). The use of in situ produced cosmogenic radionuclides in glaciology and glacial geomorphology. Annals of Glaciology 28, 103-110.

[57] Feely, H.W., Larsen, R.J. & Sanderson, C.G. (1989). Factors that cause seasonal variations in Beryllium-7 concentrations in surface air. Journal of Environmental Radioactivity, 9 (3), 223-249.

[58] Forbush, S.E. (1954). World-wide Cosmic-Ray Variations, 1937-1952. J. Geophys. Res., 59, 525.

[59] Franic, Z., Marovic, G. & Sencar, J. (2008). Long-term investigations of radioactive matter in the air of Zagreb, Croatia. Atmospheric Research. 89 (4), 391-395.

[60] Froehlich, K. (2010). Environmental radionuclides. Tracers and timers of terrestrial processes. Radioactivity in the environment, 18.

[61] Fröhlich, P. (1990). On dating of old groundwater: hydrogeologic isotopes in Environmental and Health Studies, 26, 557-560.

[62] Gaisser, T.K., Engel, R. & Resconi, E., (2016). Cosmic rays and particle physics. Cambridge University Press. ISBN 9781139192194. https://doi.org/10.1017/CBO9781139192194

[63] Galani, E., Balis, D., Zanis, P., Zerefos, C., Papayannis, A., Wernli, H. & Gerasopoulos, E. (2003). Observations of stratosphere-to-troposphere transport events over the eastern Mediterranean using a ground-based lidar system. Journal of Geophysical Research. 108, D12, 8527.

[64] Gerasopoulos, E., Zanis, P., Stohl, A., Zerefos, C.S., Papastefanou, C., Ringer, W., Tobler, L., Hubener, S., Guggenmoser, H.W., Kanter, H.J., Tositti, L. & Sandini, S. (2001). A climatology of ^{7}Be at four high-altitude stations at the Alps and the Northern Apennines. Atmos. Environ., 35, 6347-6360.

[65] Gerasopoulos, E., Zerefos, C. S., Papastefanou, C., Zanis, P. & O'Brien, K. (2003). Low-frequency variability of beryllium-7 surface concentrations over the Eastern Mediterranean. Atmospheric Environment 37, 1745–1756.

[66] Gerasopoulos, E., Zanis, P., Zerefos, C.S., Papastefanou, C., Ringer, W., Gaeggeler, H., Tobler, L. & Kanter, H.J. (2005). Factors and processes controlling the concentration of the cosmogenic radionuclide ^{7}Be at high-altitude Alpine stations: Radioactivity in the Environment 7,863-870.

[67] Gerasopoulos, E., Zanis, P., Papastefanou, C., Zerefos, C.S., Ioannidou, A. & Wernli, H. (2006). A complex case study of down to the surface intrusions of persistent stratospheric air over the Eastern Mediterranean. Atmospheric Environment 40, 4113-4125.

[68] Gosse, J.C., & Phillips, F.M. (2001) Terrestrial in situ cosmogenic nuclides: theory and application. Quaternary Science Reviews 20, 1475-1560.

[69] Granger, D.E. & Muzikar, P.F. (2001). Dating sediment burial with in situ-produced cosmogenic nuclides: theory, techniques, and limitations. Earth and Planetary Science Letters 188, 269-281.

[70] Grieder, P. (2001). Cosmic Rays At Earth. Elsevier Science 2001, pages 1112. ISBN 97-804-4450-7105.

[71] Grossi, C., Ballester, J., Simons, C., Gallmann, S., Camacho, A., Curcoll, R., Morguí, J.A., Rödó, X. & Duch, M.A. (2016). Influence of long-range atmospheric transport pathways and climate teleconnection patterns on the variability of surface ^{210}Pb and ^{7}Be concentrations in southwestern Europe. Journal of Environmental Radioactivity, 165, 103-114.

[72] Haber, R., Rizzo, J. & Von Steiger, R. (2013). Cosmic Rays in the Heliosphere – Temporal and Spatial Variations. Springer-Verlag New York. Hardcover. ISBN: 978-1-4614-9199-6.

[73] Heikkila, U., Beer, J. & Feichter, J. (2008). Modeling cosmogenic radionuclides ^{10}Be and ^{7}Be during the Maunder Minimum using the ECHAM5-HAM General Circulation Model. Atmos. Chem. Phys., 8, 2797–2809.

[74] Hernández-Ceballos, M.A., Marín-Ferrer, M., Cinelli, G., Tollefsen, T., De Felice, L., Navolio, E., Tognoli, P.V., Vanzi, S. & De Cort, M. (2015). A climatology of ^{7}Be in surface air in European Union. Journal of Environmental Radioactivity, 141, 62-70. https://doi.org/10.1016/j.jenvrad.2014.12.003

[75] Hernández-Ceballos, M.A., Bratisch, E., Cinelli, G., Ajtić, J. & Djurdjevic, V. (2016). Seasonality of ^{7}Be concentrations in Europe and influence of tropopause height. Tellus B. 68 (5), May, https://doi.org/10.3402/tellusb.v68.25534, 2016.

[76] Hernández-Ceballos, M.A., Bratisch, E., Lozano, R.L. & Cinelli, G. (2017). ^{7}Be behaviour and meteorological conditions associated with ^{7}Be peak events in Spain. Journal of Environmental Radioactivity, 166, 17-26. https://doi.org/10.1016/j.jenvrad.2016.03.019

[77] International Atomic Energy Agency (IAEA) (2013). Isotope methods for dating old groundwater. IAEA Library Cataloguing in Publication Data. ISBN 978-92-0-137210-8.

[78] International Atomic Energy Agency (IAEA) (2016). Safety glossary. Terminology used in nuclear safety and radiation protection – Revision.

[79] Ioannidou, A., Manolopoulou, M. & Papastefanou, C. (2005). Temporal changes of ^{7}Be and ^{210}Pb concentrations in surface air at temperate latitudes (40 °N). Applied Radiation and Isotopes. 63, 277–284.

[80] Ioannidou, A. (2012). ^{7}Be aerosols and their deposition on the sea: a possible method to estimate trace metals deposition on the sea. Journal of Radioactivity, 108, 29-32.

[81] Ioannidou, A., Vandoulakis, A. & Melas, D., (2014). Time lag between the tropopause height and ^{7}Be activity concentrations on surface air. Journal of Environmental Radioactivity, 129, 80–85.

[82] Ishan, R., Tokuda, R., Aslu-Gulemi, A. & Cosma, C. (2013). Spatial distribution of ^{7}Be in soils of Lower Austria after heavy rains. Journal of Radioanalytical and Nuclear Chemistry 298(3): 1857-1863. DOI:10.1007/s10967-013-2683-8 https://doi.org/10.1007/s10967-013-2683-8

[83] Jacobsen, B. & Weinhofer, H. (2005). A study of the vertical diffusion of the cosmogenic radionuclides ^{7}Be and ^{22}Na in the atmosphere. J Environ Radioact, 79:137-59.

[84] Jiwen, L., Shuiyuanova, V. N. & Webb, D. P. (2013). Long term variations in the surface air ^{7}Be concentration and climatic changes. Journal of Environmental Radioactivity. 116, 42-47.

[85] FAO/IAEA (2017). Use of ^{137}Cs for soil erosion assessment. Fulajtar, E., Mabit, L., Renschler, C.S., Lee Zhi Yi, A., Food and Agriculture Organization of the United Nations, Rome, Italy. 640.

[86] Kaplan, R.M., Ackert, R.P., Singer, B.S., Douglass, D.C. & Kurz, M.D. (2004). Cosmogenic nuclide chronology of millennial-scale glacial advances during O-isotope stage 2 in Patagonia. GSA Bulletin 116, 308-321.

[87] Kizomi, G.A., Lahr, J.H. & Pennochet, P. (2003). Groundwater age. Wiley Online Library. ISBN 9780471718193.

[88] Kneis, D.L. (1994). Cosmogenic Radionu-

cides in Precipitation. Thesis (PhD.) — Purdue University. Dissertation Abstracts International, Volume: 56-02, Section: B, page: 0865.

[89] Koch, D.M., Jacob, D.J. & Graustein, W.C. (1996). Vertical transport of tropospheric aerosols as indicated by ^{7}Be and ^{210}Pb in a chemical tracer model. J. Geophys. Res., 101, 18651-18666.

[90] Kovacs, M., Radnóczi, G., Balázs, S. & Molnár, M. (2007). Possible use of terrestrial mosses in detection of atmospheric deposition of ^{7}Be over large areas. Journal of Environmental Radioactivity 95, 53-61. https://doi.org/10.1016/j.jenvrad.2007.01.011.

[91] Kulan, A. (2006). Seasonal ^{7}Be and ^{137}Cs activities in surface air before and after the Chernobyl event. Journal of Environmental Radioactivity 90 (2), 140-150.

[92] Kurz, M.D. & Brook, E.J. (1994). Surface exposure dating with cosmogenic nuclides, in Beck, C., ed., Dating in exposed and surface contexts. Albuquerque, University of New Mexico Press, p. 139-159.

[93] Lal, D., Malhotra, P.K. & Peters, B. (1958). On the production of radioisotopes in the atmosphere by cosmic radiation and their application to meteorology. Journal of Atmospheric and Terrestrial Physics, 12, 306-328.

[94] Lal, D. & Peters, B. (1967). Cosmic-ray produced radioactivity on the earth. S. Flugge (Ed.), Handbuch der Physik XLVI/2, Springer Verlag, Berlin, 551-612.

[95] Lal, D., Nijampurkar, V.N. & Rama, S. (1970). Silicon-32 hydrology. Isotope Hydrology, 847-868.

[96] Lal, D. (1999). New Nuclear Methods for Studies of Soil Dynamics Utilizing Cosmic Ray Produced Radionuclides. 1044-1052 in: D.E. Stott, R.H. Mohtar and G.C. Steinhardt (eds). 2001. Sustaining the Global Farm. Selected papers from the 10th International Soil Conservation Organization Meeting held May 24-29, 1999 at Purdue University and the USDA-ARS National Soil Erosion Research Laboratory.

[97] Lal, D. & Jull, A.J.T. (1992). Cosmogenic nuclides in ice sheets. Radiocarbon, 34, 227-233.

[98] Lal, D. & Baskaran, M. (2012). Applications of Cosmogenic Isotopes as Atmospheric Tracers. Baskaran (ed.), Handbook of Environmental Isotope Geochemistry: Advances in Isotope Geochemistry, 575- 589.

[99] Lavalle, C. & Jacobs-Crisioni, C. (2016). INPUT - European Population Map 2006. European Commission, Joint Research Centre (JRC) [Dataset] PID: http://data.europa.eu/89h/jrc-luisa-europopmap06.

[100] Leppänen, A.-P., Pacini, A.A., Usoskin, I.G., Aldahan, A., Echer, E., Evangelista, H., Klemola, E., Kovaltsov, G.A., Mursula, K. & Possnert, G. (2010). Cosmogenic ^{7}Be in air: a complex mixture of production and transport. J. Atmos. Sol. Ter. Phys., 72, 1036-1043.

[101] Leppänen, A.-P., Usoskin, I.G., Kovaltsov, G.A. & Paatero, J. (2012). Cosmogenic ^{7}Be and ^{22}Na in Finland: production, observed periodicities and the connection to climatic phenomena. J. Atmos. Sol. Ter. Phys., 74, 164-180.

[102] Leppänen, A.-P. & Paatero, J. (2013). ^{7}Be in Finland during the 1999-2001 solar maximum and 2007-2009 solar minimum. J. Atmos. Sol. Ter. Phys., 97, 1-10.

[103] Libby, W.F. (1946). Atmospheric helium three and radiocarbon from cosmic radiation. Phys. Rev. 69,671-672.

[104] Lieuka, A.S. (2006). Factors influencing ambient concentrations of ^{210}Pb and ^{7}Be over the city of Edinburgh (55.9 N, 03.2 W). J. Environ. Radioact., 87, 289-304.

[105] Liu, H., Jacob, D.J., Bey, I. & Yantosca, R.M. (2001). Constraints from ^{210}Pb and ^{7}Be on wet deposition and transport in a global three-dimensional chemical tracer model driven by assimilated meteorological fields. Journal of Geophysical Research: Atmospheres 106 (D11), 12109-12128.

[106] Lopez, H.H. & Oeschger, H. (1969). ^{39}Ar and ^{85}Kr in the atmosphere. Earth Planet. Sci. Lett. 7(1),67-71.

[107] Lozano, R.L., San Miguel, E.G., Bolívar, J.P. & Bolívar, M. (2011). Depositional fluxes and concentrations of ^{7}Be and ^{210}Pb in bulk precipitation and aerosols at the interface of Atlantic and Mediterranean coast in Spain. J. Geophys. Res., 116, D10213.

[108] Lozano, R.L., Hernández-Ceballos, M.A., San Miguel, E.G., Adame, J.A. & Bolívar, J.P. (2012). Meteorological factors influencing the ^{7}Be and ^{210}Pb concentrations in surface air from the southwestern Iberian Peninsula. Atmospheric Environment, 63, 168-178.

[109] Masarik, J. & Beer, J. (1999). Simulation of particle fluxes and cosmogenic nuclide production in the Earth's atmosphere. Climate and Atmospheric Physics, 104, 12099-12111.

[110] Matsumoto, K. & Yokoyama, Y. (2013). Atmospheric Δ^{14}C reduction in simulations of Atlantic overturning circulation shutdown. Global Biogeochemical Cycles, 27, 296-304. DOI: 10.1002/gbc.20035.

[111] Mansour, A.A.A. (2012). Cosmogenic Radionuclides in the Atmosphere: Origin and Applications. XI Radiation Physics & Protection Conference, 25-28 November 2012, Nasr City - Cairo, Egypt.

[112] National Research Council. (1998). Committee on Evaluation of EPA Guidelines for Exposure to Naturally Occurring Radioactive Materials. Washington (DC): National Academies Press (US).

[113] Nishiizumi, K., Kohl, C.P., Arnold, J.R., Klein, J., Fink, D. & Middleton, R. (1991). Cosmic ray produced ^{10}Be and ^{26}Al in Antarctic rocks: exposure and erosion history. Earth and Planetary Science Letters, 104, 440-454.

[114] Nowaczyk, B. & Pazdur, M.F. (1990). Problems concerning the ^{14}C dating of fossil dune soils. Quaestiones Geographicae 11/12, 135-51.

[115] O'Brien, K., Friedberg, W., Sauer, H.H. & Smart, D.F. (1996). Atmospheric cosmic rays and solar energetic particles at aircraft altitudes. Environ Int 22(Suppl 1):539-544.

[116] O'Brien, K., Felsberger, E. & Kindl, P. (2006). Application of the heliocentric potential to aircraft dosimetry. Radiat Prot Dosim 118:336-342.

[117] Papastefanou, S.M.A., Sarva, M.I., Xanthopoulos, K.I., Karangelos, D.J., Anagnostakis, M.J. & Simopoulos, S.E. (2011). Monitoring of ^{7}Be atmospheric activity concentration using short term measurements. Nuclear Technology & Radiation Protection, 26 (2), 101-108.

[118] Papastefanou, C. & Ioannidou, A. (1991). Deposition fluxes and other physical characteristics of atmospheric beryllium-7 in the temperate zones (40 N) with a dry (precipitation-free) climate. Atmos. Environ., 25A, 2335-2343.

[119] Papastefanou, C., Manolopoulou, M., Stoulos, M.S., Ioannidou, A. & Simopoulos, E. (1998). Soil-to-plant transfer of ^{137}Cs, ^{40}K and ^{7}Be. Journal of Environmental Radioactivity 45, 59-65.

[120] Pessenda, L.C.R., Gouveia, S.E.M. & Aravena, R. (2001). Radiocarbon dating of total soil organic matter and humin fraction and its comparison with ^{14}C ages of fossil charcoal. Radiocarbon, 43, 595-601.

[121] Pham, M.K., Betti, M., Nies, H. & Povinec, P.P. (2011). Temporal changes of ^{7}Be, ^{137}Cs and ^{210}Pb activity concentrations in surface air at Monaco and their correlation with meteorological parameters. J. Environ. Radioact., 102, 1045-1054.

[122] Pham, M.K., Povinec, P.P., Nies, H. & Betti, M. (2013). Dry and wet deposition of ^{7}Be, ^{210}Pb and ^{137}Cs in Monaco air during 1998-2010: Seasonal variations of deposition fluxes. Journal of Environmental Radioactivity 128, 45-57.

[123] Phillips, F.M., Zreda, M.G., Gosse, J.C., Klein, J., Evenson, E.B., Hall, R.D., Chadwick, O.A. & Sharma, P. (1997). Cosmogenic ^{36}Cl and ^{10}Be ages of Quaternary glacial and fluvial deposits of the Wind River Range, Wyoming. Geol. Soc. Am. Bull., 109, 1453-1463.

[124] Pigati, J.S. & Lifton, N.A. (2004). Geomagnetic effects on time-integrated cosmogenic nuclide production with emphasis on in situ ^{14}C and ^{10}Be. Earth Planet. Sci. Lett., 226, pp. 193-205.

[125] Piñero García, F., Ferro García, M.A. & Araina, M. (2022). ^{7}Be behaviour in the atmosphere of the city of Granada January 2005 to December 2009. Atmos. Environ., 47, 84-93.

[126] Poje, M., Vukovic, B., Radolić, V., Miklavčić, I., Faj, D., Varga Pajtler, M. & Planinić, J. (2012). Mapping of cosmic radiation dose in Croatia. Journal of Environmental Radioactivity 103, 30-33.

[127] Ptochi, M., Brunčik, T. & Hanák, J. (2010). Seasonal and inter-annual variation of Beryllium-7 deposition in birch tree leaves and grass in the northeast upland area of the Czech Republic. Journal of Environmental Radioactivity 101, 744-750.

[128] Rajsić, M.M., Todorović, D.J., Kmezić, N.V., Janković, M.M. & Djordjević, V.S. (2016). The Fourier analysis applied to the relationship between ^{7}Be activity in the Serbian atmosphere and meteorological parameters. Environmental Pollution 216, 915-923.

[129] Ramachandran, T.V. (2011). Background radiation people and the environment. Iran J Radiat Res. 9:65-76.

[130] Reiter, R., Munzert, K., Kanter, H.-J. & Pötzl, K. (1983). Cosmogenic radionuclides and ozone at a mountain station at 3.0 km a.s.l. Arch. Met. Geophr. Biocl. B, 32, 131-160.

[131] Rehmski, C.A. & Lisiecki, J.C. (2007). Terrestrial Cosmogenic Nuclides as Paleoseismic Proxies. Reviews in Mineralogy & Geochemistry 66, 269-278. DOI: https://doi.org/10.1007/BF02279371.

[132] Ribeiro, C., Gómez, J., Quindós, L.S., Fernández, P.L. & Soto, J. (1997). ^{7}Be concentrations in air, rain water and soil in Cantabria (Spain). Applied Radiation and Isotopes, 48, 545-548.

[133] Rodas Ceballos, M., Borrás, A., Gamiz, E., Estela, J.M. & Ferrer, L. (2016). Monitoring of ^{7}Be and gross beta in particulate matter of surface air from Mallorca Island, Spain. Chemosphere, 152, 481-489.

[134] Rulík, P., Malá, H., Bečková, V., Holý, Z., Schlesingerová, E., Svítík, I. & Šimkal, J. (2009). Low level air radioactivity measurements in Prague, Czech Republic. Applied Radiation and Isotopes, 67 (5), 969-973.

[135] Samolov, A., Dragović, S., Daković, M. & Bačić, G. (2014). Analysis of ^{7}Be behaviour in the air by using a multilayer perceptron neural network. Journal of Environmental Radioactivity, 137, 198-203.

[136] Sarvan, D., Stratimirović, D., Blagić, S., Djordjević, V., Milošević, V. & Ajtić, J. (2017). Dynamics of beryllium-7 specific activity in relation to meteorological variables, tropopause height, teleconnection indices and sunspot number. Physica A: Statistical Mechanics and its Applications, 469, 813-823.

[137] Sato, T. (2016a). Analytical Model for Estimating the Zenith Angle Dependence of Terrestrial Cosmic Ray Fluxes. PLoS ONE 11(8): e0160390. https://doi.org/10.1371/journal.pone.0160390.

[138] Sato, T. (2016b). Evaluation of World Population-Weighted Effective Dose due to Cosmic Ray Exposure. Scientific Reports 6, Article number: 33932. doi:10.1038/srep33932.

[139] Schuler, P., Inoue, A., Walling, D.E., Mancilla, N.H., Castillo, A. & Trumper, R.S. (2006). Use of Beryllium-7 to Document Soil Redistribution Following Forest Harvest Operations. Journal of Environmental Quality Abstract - Landscape and Watershed Processes, 35, 1756-1763.

[140] Shahbazi-Gahrouei, D., Gholami, M. & Setayandeh, S. (2013). A review on natural background radiation. Adv Biomed Res. 2013; 2: 65.

[141] Simon, J., Meresin, J., Sykora, I., Jeskovsky, M. & Holy, K. (2009). Modeling of temporal variations of vertical concentration profile of ^{7}Be in the atmosphere. Atmospheric Environment, 43, 2000-2004. https://doi.org/10.1016/j.atmosenv.2009.01.015.

[142] Sloan, T. & Wolfendale, A.W. (2013). Cosmic rays, solar activity and the climate. Environmental Research Letters, 8, 045022 (7 pages).

[143] Steinmann, P., Zeller, M., Baumit, P., Ferreli, D. & Estier, S. (2013). Cosmogenic ^{7}Be and ^{22}Na in ground level air in Switzerland (1994-2011). J. Environ. Radioact., 124, 68-73. https://doi.org/10.1016/j.jenvrad.2013.03.013.

[144] Stozhkov, Y.I., Bazilevskaya, G.A., Makhmutov, V.S., Svirzhevsky, N.S., Svirzhevskaya, A.K., Logachev, V.I. & Obridko, V.N. (2017). Cosmic Rays, Solar Activity, and Changes in the Earth's Climate. Bulletin of the Russian Academy of Sciences: Physics, 2017, 81, 252-254.

[145] Sturchio, N.C., Du, X., Purtschert, R., Lehmann, B.E., Sultan, M., Patterson, L.J., Lu, Z.T., Müller, P., Bigler, T., Bailey, K., O'Connor, T.P., Young, L., Lorenzo, R., Becker, R., El Alfy, Z., El Kaliouby, B., Dawood, Y. & Abdallah, A.M.A. (2004). One million year old groundwater in the Sahara revealed by krypton-81 and chlorine-36. Geophys Res Lett 31:L05503.

[146] Szabó, K.Z., Jordan, G., Petrik, A., Horváth, Á. & Szabó, C. (2017). Spatial analysis of ambient gamma dose equivalent rate data by means of digital image processing techniques. Journal of Environmental Radioactivity 166 (2017) 309-320.

[147] Talerko, I., Holý, K., Jeřábková, M., Müllerová, M., Bulko, M. & Povinec, P.P. (2017). Long-term variations of radionuclides in the Bratislava air. Journal of Environmental Radioactivity, 166 (1): 27-35.

[148] Terzi, L. & Kalnajavadi, M. (2017). World-wide seasonal variation of ^{7}Be related to large-scale atmospheric circulation dynamics. J. Environ Radioact. 178-179:1-15.

[149] Todorovic, D., Popovic, D. & Djuric, G. (1999). Concentration measurements of ^{7}Be and ^{137}Cs in ground level air in the Belgrade city area. Environment International 1, 55-66.

[150] Todorovic, D., Popovic, D., Djuric, G. & Radenkovic, M. (2005). ^{7}Be to ^{210}Pb concentration ratio in ground level air in Belgrade area. Journal of Environmental Radioactivity 79 (3), 297-302.

[151] Todorovic, D., Popovic, D., Nikolic, J., Djuric, G. (2010). Radioactivity monitoring in ground level air in Belgrade urban area. Radiation Protection Dosimetry, 142(2-4), 308-313.

[152] Treitli, L., Brattich, E., Cinelli, G. & Baldoncini, D. (2014). 12 years of ^{7}Be and ^{210}Pb in Mt. Cimone and their correlation with meteorological parameters. Atmospheric Environment, 87,108-122.

[153] Turekian, K.K. & Graustein, W.C. (2003). Natural Radionuclides in the Atmosphere. Treatise on Geochemistry, Volume 4. Editor: Ralph F. Keeling. Executive Editors: Heinrich D. Holland and Karl K. Turekian. pp. 347. ISBN 0-08-043751-6. Elsevier, p.261-279.

[154] UNSCEAR (1988). United Nations Scientific Committee on the Effects of Atomic Radiation. Sources, effects and risks of ionizing radiation. Report to the General Assembly, with annexes.

[155] UNSCEAR (2000). United Nations Scientific Committee on the Effects of Atomic Radiation. Sources and effects of ionizing radiation (Report to General Assembly). New York, NY: United Nations.

[156] UNSCEAR (2008). United Nations Scientific Committee on the Effects of Atomic Radiation. Sources and effects of ionizing radiation (Report to General Assembly, Annex B). New York, NY: United Nations.

[157] Usoskin, I.G., Field, C.V., Schmidt, G.A., Lieuppanen, A.P., Aldahan, A., Kovaltsov, G.A., Possnert, G. & Unger, R.K. (2009). Short-term production and synoptic influences on atmospheric ^{7}Be concentrations. Journal of Geophysical Research, 114, D06108.

[158] Von Blanckenburg, F. (2005). The control mechanisms of erosion and weathering at basin scale from cosmogenic nuclides in river sediment. Earth and Planetary Science Letters 237, 462-479.

[159] Walbrek, P.J. & Murray, A.S. (1996). Distribution and Variability of ^{7}Be in Soils Under Different Surface Cover Conditions and Its Potential for Describing Soil Redistribution Processes. Water Resources Research, 32,

Chapter 9 - Annual effective dose from natural environmental radiation

(pp. 170-175)

[1] Batista e Silva, F., Gallego, J. & Lavalle, C. (2013a). A high-resolution population grid map for Europe. Journal of Maps, 9:1, 16-28. https://doi.org/10.1080/17445647.2013.764830.

[2] Batista e Silva, F., Lavalle, C. & Koomen, E. (2013b). A procedure to obtain a refined European land use/cover map. Journal of Land Use Science, 8:3, 255-283. DOI:10.1080/17474230.2012.667450.

[3] Esri (2011). ArcGIS Desktop: Release 10. Redlands, CA: Environmental Systems Research Institute. www.esri.com.

[4] Lavalle, C. & Jacobs-Crisioni, C. (2016). INPUT - European Population Map 2006. European Commission, Joint Research Centre (JRC) [Dataset] PID: http://data.europa.eu/89h/jrc-luisa-europopmap06.

[5] UNSCEAR (2000). United Nations Scientific Committee on the Effects of Atomic Radiation. Source and Effects of Ionizing Radiation. Annex A. United Nations, New York, US. ISBN 92-1-142238-8.

[6] UNSCEAR (2008). United Nations Scientific Committee on the Effects of Atomic Radiation. Source and Effects of Ionizing Radiation. Annex B. United Nations, New York, US. ISBN 978-92-1-142274-0.

Appendix 1 – The International System of Units (SI)

Source material:

SI brochure: The International System of Units (SI) (8th ed.), 2006; updated in 2014. Paris Bureau International des Poids et Mesures. Retrieved from: https://www.bipm.org/en/publications/si-brochure/.

Cohen E. R. and Giacomo P., 1987 (2010 reprint). Symbols, units, nomenclature and fundamental constants in physics. http://iupap.org/wp-content/uploads/2014/05/A4.pdf

Quantity	Symbol	Base Unit	Symbol	Definition of Unit
length	l, h, r, x	metre	m	The metre is the length of the path travelled by light in vacuum during a time interval of 1/299 792 458 of a second.
mass	m	kilogram	kg	The kilogram is the unit of mass; it is equal to the mass of the international prototype of the kilogram.
time, duration	t	second	s	The second is the duration of 9 192 631 770 periods of the radiation corresponding to the transition between the two hyperfi ne levels of the ground state of the caesium atom.
electric current	I, i	ampere	A	The ampere is that constant current which, if maintained in two straight parallel conductors of infinite length, of negligible circular cross-section, and placed 1 metre apart in vacuum, would produce between these conductors a force equal to 2×10^{-7} newton per metre of length.
thermodynamic temperature	T	kelvin	K	The kelvin, unit of thermodynamic temperature, is the fraction 1/273.16 of the thermodynamic temperature of the triple point of water.
amount of substance	n	mole	mol	The mole is the amount of substance of a system which contains as many elementary entities as there are atoms in 0.012 kilogram of carbon-12. When the mole is used, the elementary entities must be specified and may be atoms, molecules, ions, electrons, other particles, or specified groups of such particles.
luminous intensity	Iv	candela	cd	The candela is the luminous intensity, in a given direction, of a source that emits monochromatic radiation of frequency 540×10^{12} hertz and that has a radiant intensity in that direction of 1/683 watt per steradian.

Table A1-1
The seven base units of the SI provide the reference used to define all the measurement units of the International System

Some important and widely used units do not properly fall within the SI. For this reason, special names and symbols of those units have been accepted. These are simply a compact form for the expression of combinations of base units that are used frequently. There are 22 special names for units approved for use in the SI at present, and these are listed in Table AI-2.

Derived quantity	Name of derived unit	Symbol for unit	Expression in terms of other units
plane	angle	radian	m/m = 1
solid angle	steradian	sr	$m^2/m^2 = 1$
frequency	hertz	Hz	s^{-1}
force	newton	N	$m\ kg\ s^{-2}$
pressure, stress	pascal	Pa	$N/m^2 = m^{-1}\ kg\ s^{-2}$
energy, work, amount of heat	joule	J	$N\ m = m^2\ kg\ s^{-2}$
power, radiant flux	watt	W	$J/s = m^2\ kg\ s^{-3}$
electric charge	coulomb	C	s A
electric potential difference	volt	V	$W/A = m^2\ kg\ s^{-3} A^{-1}$
capacitance	farad	F	$C/V = m{-}2\ kg^{-1}\ s^4\ A^2$
electric resistance	ohm	Ω	$V/A = m^2\ kg\ s^{-3}\ A^{-2}$
electric conductance	siemens	S	$A/V = m^{-2}\ kg^{-1}\ s^3\ A^2$
magnetic flux	weber	Wb	$V\ s = m^2\ kg\ s^{-2}\ A^{-1}$
magnetic flux density	tesla	T	$Wb/m^2 = kg\ s^{-2}\ A^{-1}$
inductance	henry	H	$Wb/A = m^2\ kg\ s^{-2}\ A^{-2}$
Celsius temperature	degree Celsius	°C	K
luminous flux	lumen	lm	cd sr = cd
illuminance	lux	lx	$lm/m^2 = m^{-2}\ cd$
activity referred to a radionuclide	becquerel	Bq	s^{-1}
absorbed dose	gray	Gy	$J/kg = m^2\ s^{-2}$
dose equivalent	sievert	Sv	$J/kg = m^2\ s^{-2}$
catalytic activity	katal	Kat	s^{-1} mol

Table A1-2
Coherent derived units in the SI with special names and symbols

The prefixes should be used to indicate decimal multiples or submultiples of a unit (base or derived). The SI prefixes are listed in Table AI-3.

Factor	Name	Symbol
10^{24}	yotta	Y
10^{21}	zetta	Z
10^{18}	exa	E
10^{15}	peta	P
10^{12}	tera	T
10^{9}	giga	G
10^{6}	mega	M
10^{3}	kilo	K
10^{2}	hector	H
10^{1}	deca	da
10^{-1}	deci	d
10^{-2}	centi	c
10^{-3}	milli	m
10^{-6}	micro	μ
10^{-9}	nano	n
10^{-12}	pico	p
10^{-15}	femto	f
10^{-18}	atto	a
10^{-21}	zepto	z
10^{-24}	yocto	y

Table A1-3
SI prefixes

The SI is the only system of units that is universally recognised, so that it has a distinct advantage in establishing an international dialogue. Other units, i.e. non-SI units, are generally defined in terms of SI units. The use of the SI also simplifies the teaching of science. For all these reasons the use of SI units is recommended in all fields of science and technology.

Nonetheless, some non-SI units are still widely used. A few, such as the minute, hour and day as units of time, will always be used because they are so deeply embedded in our culture. Others are used for historical reasons, to meet the needs of special interest groups, or because there is no convenient SI alternative. It will always remain the prerogative of a scientist to use the units that are considered to be best suited to the purpose. However when non-SI units are used, the conversion factor to the SI should always be quoted. For a more complete list, see the SI Brochure, or the BIPM website.

Appendix 2 – Country ISO codes

ISO code	Country name
AL	Albania
AT	Austria
AZ	Azerbaijan
BA	Bosnia & Herzegovina
BE	Belgium
BG	Bulgaria
BY	Belarus
CH	Switzerland
CY	Cyprus
CZ	Czech Republic
DE	Germany
DK	Denmark
EE	Estonia
ES	Spain
FI	Finland
FR	France
GB	United Kingdom
GR	Greece
HR	Croatia
HU	Hungary
IE	Ireland
IS	Iceland
IT	Italy
LT	Lithuania
LU	Luxembourg
LV	Latvia
ME	Montenegro
MK	North Macedonia
MT	Malta
NL	Netherlands
NO	Norway
PL	Poland
PT	Portugal
RO	Romania
RS	Serbia
SE	Sweden
SI	Slovenia
SK	Slovak Republic
TR	Turkey
UA	Ukraine

Appendix 3 – List of national competent authorities

List of the national competent authorities that provided input indoor radon data for the maps displayed in Plate 6 and Plate 7:

Country	National competent authorities
Albania	Institute of Applied Nuclear Physics
Austria	University of Vienna
Azerbaijan	Azerbaijan National Academy of Science
Belarus	Joint Institute for Power and Nuclear Research 'Sosny' of the National Academy of Sciences of Belarus
Belgium	Agence fédérale de contrôle nucléaire
Bulgaria	National Centre of Radiobiology and Radiation Protection
Croatia	University of Osijek
Czech Republic	Czech Geological Survey
Cyprus	Ministry of Labour, Welfare and Social Insurance
Denmark	Danish Health Authority
Estonia	Environmental Board
Finland	Radiation and Nuclear Safety Authority
France	Institut de radioprotection et de sûreté nucléaire
Germany	Bundesamt für Strahlenschutz
Greece	Greek Atomic Energy Commission
Hungary	National 'FJC' Research Institute for Radiobiology and Radiohygiene; University of Pannonia, and Rad Lauder Labor
Iceland	Icelandic Radiation Safety Authority
Ireland	Environmental Protection Agency
Italy	Istituto Superiore per la Protezione e la Ricerca Ambientale
Latvia	Radiation Safety Centre of State Environmental Service of Latvia
Lithuania	Radiation Protection Centre
Luxembourg	Ministry of Health
Malta	Ministry for Energy and Health
Netherlands	National institute for Public Health and the Environment
North Macedonia	Institute of Public Health
Norway	Norwegian Radiation and Nuclear Safety Authority
Poland	Wroclaw University of Science and Technology
Portugal	Instituto Tecnológico e Nuclear
Romania	Babeş-Bolyai University
Serbia	Serbian Radiation Protection and Nuclear Safety Agency
Slovenia	Jožef Stefan Institute
Spain	Consejo de Seguridad Nuclear
Sweden	National Board of Housing, Building and Planning
Switzerland	Bundesamt für Gesundheit
United Kingdom	British Geological Survey and Public Health England

Appendix 4 – Periodic Table of the Elements

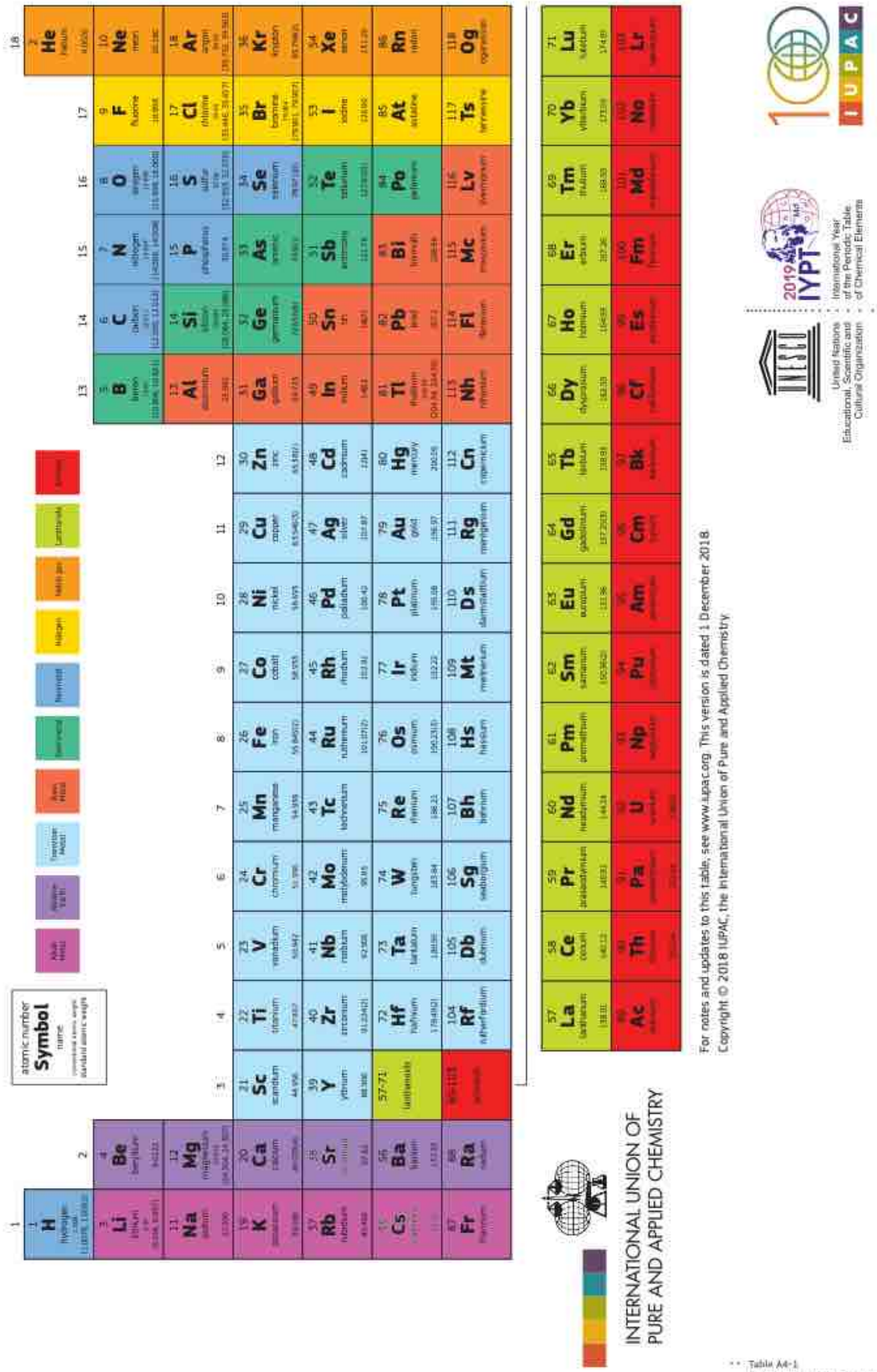

Table A4-1
Periodic Table of the Elements
Source: Copyright © 2018 IUPAC, the International Union of Pure and Applied Chemistry. Modified by EANR JC-JRC 2019

This QR code points to the full online version of the Atlas, where the most updated content may be freely accessed :

Do you know what natural ionising radiation is?

Where can you find natural sources of radiation?

What are the levels of natural sources of radiation in Europe?

Do you know the pathways of ionising radiation?

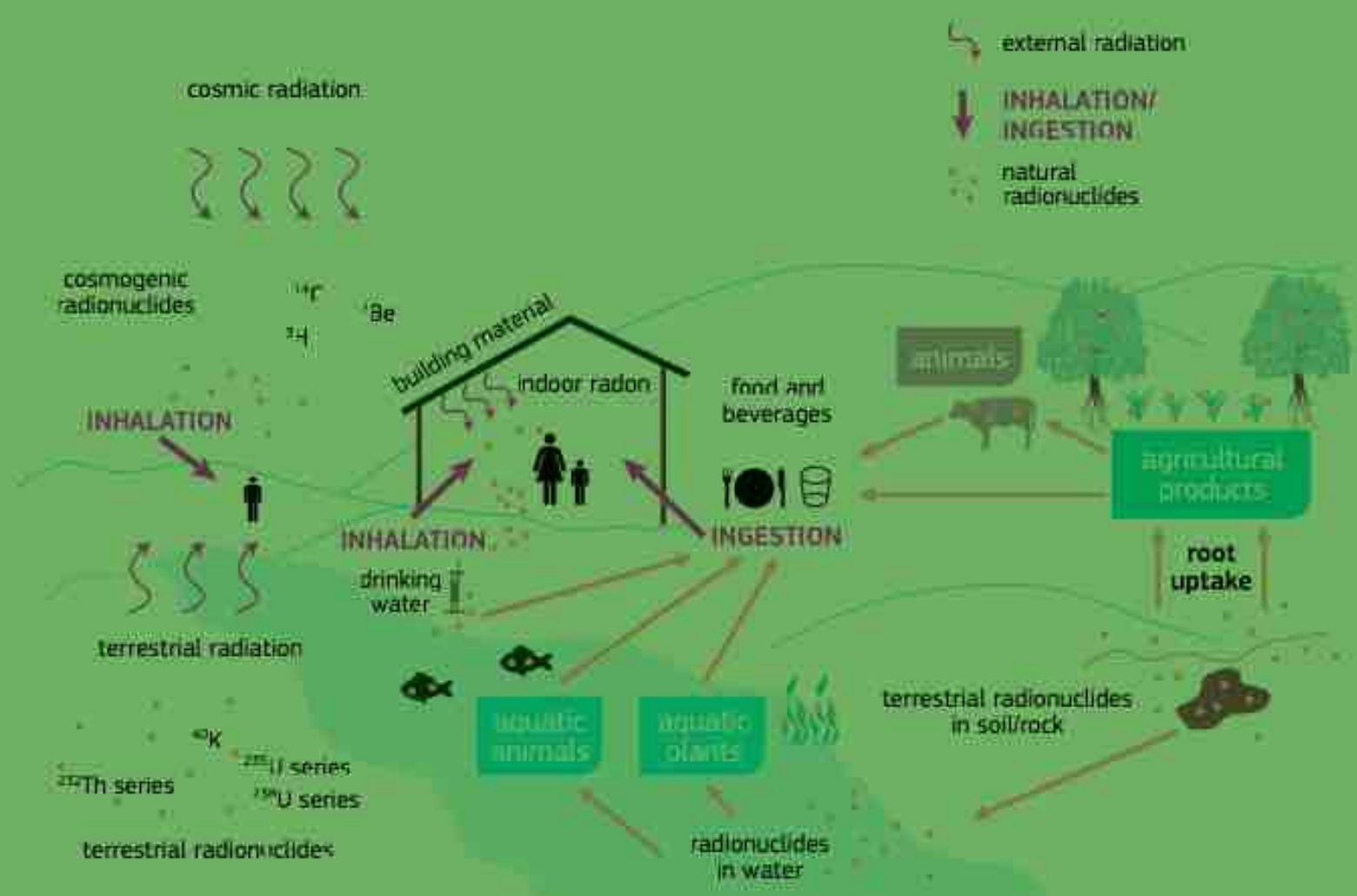

Simplified pathways of natural radionuclides through the environment and different exposure pathways for humans

Source: EAR, DG RTD, 2020

Natural radionuclides, both terrestrial and cosmogenic, migrate in the environment through different pathways: air, water, rock, soil and the food chain. Radionuclides may then enter the human body through ingestion (food and drinking water) and inhalation giving, so-called, internal exposure. External exposure is due to cosmic radiation and radiation from terrestrial radionuclides present in soil, rocks and building materials.

The first ever European Atlas of Natural Radiation uses informative texts, stunning photographs and striking maps to answer and explain these and other questions.

Publications Office of the European Union

EUR 19425 EN · **Price** (excluding VAT) in Luxembourg **€25**